Title
Slow Photoelectron Velocity-Map Imaging and Infrared Photodissociation Spectroscopy of Cryo-Cooled Molecular and Cluster Anions

Author
Weichman, Marissa Liana

Publication Date
2017

Peer reviewed|Thesis/dissertation

Slow Photoelectron Velocity-Map Imaging and Infrared Photodissociation Spectroscopy of Cryo-Cooled Molecular and Cluster Anions

by

Marissa Liana Weichman

A dissertation submitted in partial satisfaction of the

requirements for the degree of

Doctor of Philosophy

in

Chemistry

in the

Graduate Division

of the

University of California, Berkeley

Committee in charge:

Professor Daniel M. Neumark, Chair
Professor Richard J. Saykally
Professor Holger Müller

Spring 2017

Slow Photoelectron Velocity-Map Imaging and Infrared Photodissociation Spectroscopy of Cryo-Cooled Molecular and Cluster Anions

Abstract

Slow Photoelectron Velocity-Map Imaging and Infrared Photodissociation Spectroscopy of Cryo-Cooled Molecular and Cluster Anions

by

Marissa Liana Weichman

Doctor of Philosophy in Chemistry

University of California, Berkeley

Professor Daniel M. Neumark, Chair

Two high-resolution techniques, slow photoelectron velocity-map imaging (SEVI) spectroscopy and infrared photodissociation (IRPD) spectroscopy, are used to probe cryogenically cooled anionic molecules and clusters. The systems studied here fall into four categories: astrochemical species, aromatic radicals, transition metal oxide clusters, and the reactive potential energy surfaces of bimolecular reactions.

Anion photoelectron spectroscopy (PES) is a versatile technique for studying transient neutral species via photodetachment of a stable anion. SEVI is a variant of anion PES which combines tunable laser energy and a velocity-map imaging detection scheme. Slow photoelectrons are preferentially detected, yielding sub milli-electronvolt (meV) spectra over a narrow electron kinetic energy range. SEVI yields detailed information on the geometry, vibrational frequencies, and electronic structure of the neutral molecule. Cryogenic cooling of anions in a radio frequency ion trap prior to photodetachment eliminates spectral congestion and allows for analysis of complex systems.

IRPD spectroscopy is a method complementary to cryo-SEVI for structural characterization of complex gas-phase ions. Anions (A^-) are mass selected, collected in a cryogenic ring-electrode ion trap, and messenger-tagged with D_2. The trapped ions are irradiated with intense, tunable IR light, then extracted into a time-of-flight mass spectrometer. The IR absorption spectrum of A^- is constructed by measuring the depletion of the A^-D_2 species as the wavelength is scanned. IRPD spectra yield vibrational frequencies with meV precision. Geometries and vibrational modes are assigned through comparison with simulation.

Carbon clusters are structurally complex and of great interest in interstellar, plasma, and combustion chemistry. The cryo-SEVI spectrum of the C_5 carbon cluster shows vibrational fine structure and subtle vibronic coupling effects not previously resolved. The cyanomethyl radical, CH_2CN, is important astrochemically as an open-shell carbon-containing species, and its corresponding anion may be a carrier of a diffuse interstellar band. Temperature-dependent SEVI spectra show new rotational and vibrational structure of CH_2CN, CH_2CN^-, and their deuterated isotopologs.

The *ortho*-hydroxyphenoxy (*o*-HOC_6H_4O) radical is a model for the photochemistry of larger biomolecules. Characterizing excited state surfaces and the dynamics of non-radiative relaxation pathways in these species can elucidate the chemistry subsequent to photoexcitation of biological systems. The SEVI spectra of the first three electronic states of *o*-HOC_6H_4O clarify the energetics and vibrational frequencies of these states. The deprotonated polycyclic aromatic hydrocarbon radicals α- and β-naphthyl ($C_{10}H_7$) and 9-, 1-, and 2-anthracenyl ($C_{14}H_9$) are intermediates in the combustion of organic matter and soot formation, and may be present in the interstellar medium. A gas-phase synthesis technique using trimethylsilyl-substituted precursors allows for the acquisition of isomer-specific SEVI spectra for these species. Detailed vibrational structure of the ground and first excited states of each isomer is reported and assigned.

Transition metal oxides catalyze many reactions fundamental to chemistry. Small gas-phase clusters can serve as models for catalytically active point defect sites on surfaces, which often demonstrate distinct bonding and stoichiometry from the bulk. The cryo-SEVI spectra of the ferromagnetic iron suboxide clusters Fe_4O and Fe_5O, model systems for oxygen-deficient metal oxide catalytic sites, illuminate the vibrational and electronic structure of these species. Bulk titanium dioxide is of great interest as a water-splitting photocatalyst to generate sustainable hydrogen fuel. We report IRPD spectra of the anionic clusters $(TiO_2)_n^-$ (n=3–8) and the reactive complexes of $(TiO_2)_n^-$ (n=2–4) with D_2O. With comparison to calculations, these spectra confirm the most stable cluster geometries and provide detailed information on their vibrational structure. These results aid in understanding the size-dependent evolution of the properties and reactivity of $(TiO_2)_n^-$ clusters, and their potential utility as model systems for water-splitting catalysts.

Anion PES is one of the few ways to gain spectroscopic access to the transition states of neutral bimolecular reactive surfaces. In a transition state spectroscopy experiment, photodetachment of a bound anion similar in geometry to the desired neutral transition state can yield a spectrum showing structure very sensitive to the shape of the neutral potential energy surface. In particular, it is possible to observe discrete quantum resonances that are bound or quasibound along the reaction coordinate. Such resonances are an exceptional point of comparison between theory and experiment. Cryo-SEVI is used to study the benchmark $F + H_2$ reaction through photodetachment of the FH_2^- anion. We report previously unresolved peaks that are attributed to long-predicted reactive scattering resonances. We also discuss a cryo-SEVI study of the seven-atom $F + CH_3OH$ hydrogen abstraction reaction based on photodetachment of CH_3OHF^-. This measurement reveals structure associated with a manifold of vibrational Feshbach resonances and bound states supported by the post-transition-state potential well. For both the $F + H_2$ and $F + CH_3OH$ studies, high-level quantum dynamical calculations yield excellent agreement with experimental results, allow assignment of structure, and demonstrate the utility of cryo-SEVI transition state spectroscopy experiments as benchmarks for the study of increasingly complex bimolecular reactions.

For Grandpa and for Nanny

The good life is one inspired by
love and guided by knowledge.

Bertrand Russell,
What I Believe

Contents

Acknowledgments

My Ph.D. years have been a time of enormous personal growth, learning, and adventure. I owe many thanks to the wonderful people who were a part of them.

Thanks first and foremost to the inimitable Herr Prof. Dr. Daniel Milton Neumark, for his pragmatism and sterling advice, for fostering my self-confidence and development, for both having my back and pushing me out of the nest, and for once making 100 physical chemists sing me Happy Birthday at the Dynamics of Molecular Collisions conference.

All my thanks to Michelle Haskins for keeping the gears running smoothly 200% of the time and for her limitless patience and incredible ability to fix any problem, big or small.

Thanks to the SEVI elders and progeny. Thanks to Jongjin Kim, for teaching me essentially everything I know, for instilling in me equal doses of common sense, bravery, and obsession, and for staging what I hope will remain the most memorable kidnapping of my life. Thanks to Tara Yacovitch and Christian Hock for early advice and encouragement. Thanks to Jessalyn DeVine and Mark Babin, the next champions of SEVI, for picking up the torch and running with it. Godspeed!

Thanks to the Neumark group, past, present, and future. Thanks to Holly Williams and Mark Shapero, my Neumark soul-siblings, for their camaraderie and senses of humor. Thanks to Annelise Beck and Camila Bacellar for board games, coffee, and story-swapping, and to Maggie Yandell-Zhao for gossip and life guidance. Thanks to Aaron Harrison for being provocative and a great Australian tour guide. Thanks to Weili Li, Mikhail Ryazanov, Bethan Nichols, Madeline Elkins, Sarah King-Zimmer, and Neil Cole-Filipiak for their patience and experimental expertise. Best of luck to soon-to-be senior students Alice Kunin, Erin Sullivan, Isaac Ramphal, and Blake Erickson.

Thanks to Knut Asmis, Xiaowei Song, Mattias Fagiani, Sreekanta Debnath, John Kelly, and all the free electron laser folks for being wonderful collaborators, hosts, and friends during my visits to the Fritz Haber Institute. My research trips to Berlin were a joy and a highlight of my Ph.D., even accounting for clogged ablation sources and sleepless beamtime nights.

Thanks to the many theory collaborators we've worked with during my Ph.D., from whom I've learned a great deal: Millard Alexander, David Manolopoulous, Hua Guo, John Stanton, Joachim Sauer, Uwe Manthe, Bess Vlaisavljevich, and Hrant Hratchian.

Thanks to Eric Granlund in the machine shop for being such a tremendous resource, especially in times of dire experimental crisis.

Thanks to Mitchio Okumura and the Okumurons, particularly Kana Takematsu, Leah Dodson, Thinh Bui, and Matt Sprague, for giving me my first footholds in spectroscopy and for remaining an incredibly supportive network to this day.

Thanks to David Osborn for great advice and ideas, and for the wonderful opportunity to be involved with the Pacific Conference on Spectroscopy and Dynamics from early in my graduate career.

Thanks to Scott Kable and his very friendly research group for inviting me Down Under and teaching me all about cricket, drop bears, and roaming trajectories.

Thanks to friends old and new, near and far. Thanks to my bestie Patrick Xia for adventure, counsel, and patient help with even the most basic electronics. Thanks to Daniel Levine, my go-to consultant of all things chemistry, for responding quickly to text messages like "I'm about to try to press red phosporous into an ablation target - is this a bad idea?" Thanks to Tobias Sjölander for his Scandinavian wit and for patiently making us *para*-hydrogen (and *ortho*-deuterium) repeatedly until the stars aligned. Thanks to Allan Oliveira of the Lineberger group for being my lab troubleshooting pen-pal.

Thanks to all the rest of Berkeley gang for puzzle hunts, board games, movie nights, dinner parties, brunch potlucks, finger painting, and endless conversations about science, culture, politics, and everything in between, especially Danie Monahan, Daniel Freeman, Paul Romer, Elaina Present, Katie Klymko, David Herlihy, and David Litt.

Thanks to Mom, Dad, and Benji, and to Grandpa, Grandma, and Nanny. I couldn't have done this without you, and I ain't done yet.

Part I

Background and Methods

No observational problem will not be solved by more data.

Vera Rubin

Chapter 1

Introduction

1.1 Anion Photoelectron Spectroscopy

Anion photoelectron spectroscopy (PES) is a versatile tool to study neutral species of interest. Nearly any neutral can be probed with anion PES, provided that the corresponding anion can be synthesized, and that the electron affinity of the neutral falls within an energy range accessible by laser. This technique provides spectroscopic access to a wide array of exotic and reactive neutrals: radicals, clusters, and even metastable or unbound species. Anions are also quite convenient species to work with, as they are charged and can therefore be easily manipulated with electromagnetic fields, which allows for experimental capabilities like mass selection and ion trapping for buffer gas cooling applications.

Experimentally, a packet of molecular anions, A^-, is intersected with a laser beam. If the laser photon energy ($h\nu$) exceeds the binding energy of the electron to the anion, a photoelectron may be detached:

$$A^- \xrightarrow{h\nu} A + e^- \tag{1.1}$$

The kinetic energy distribution of the nascent electrons is measured, and can show discrete features corresponding to detachment to specific neutral electronic and vibrational quantum states. The energy given to the system by the photon must be conserved between overcoming the binding energy of the electron to a given neutral state (eBE) and the kinetic energy of the outgoing photoelectron after detachment (eKE):

$$\text{eBE} = h\nu - \text{eKE} \tag{1.2}$$

The energetics of this process are shown schematically in Fig. 1.1. Generally, photoelectron spectra are plotted in eBE, because it is independent of the choice of photon energy.

An anion photoelectron spectroscopy experiment often directly yields the electron affinity (EA) and relative energetics of electronic and vibrational levels of the neutral. Relative intensities of features in the spectra provide more indirect information about the difference in equilibrium geometries between the anionic and neutral states.

1.1.1 A Brief History

Anion PES derives historically from the PES of neutrals;[1] many techniques used in anion PES were originally developed for neutral experiments. Early applications of anion PES were carried out with continuous ion sources, intracavity continuous-wave (cw) argon ion lasers, and detection of eKE distributions using hemispherical energy analyzers. The first such anion PES experiment was reported in 1967 by Jan Hall and coworkers, and measured the electron affinity of the helium atom.[2] Over the following decades, even as new anion PES technologies were developed, cw anion PES remained a workhorse technique, and was applied

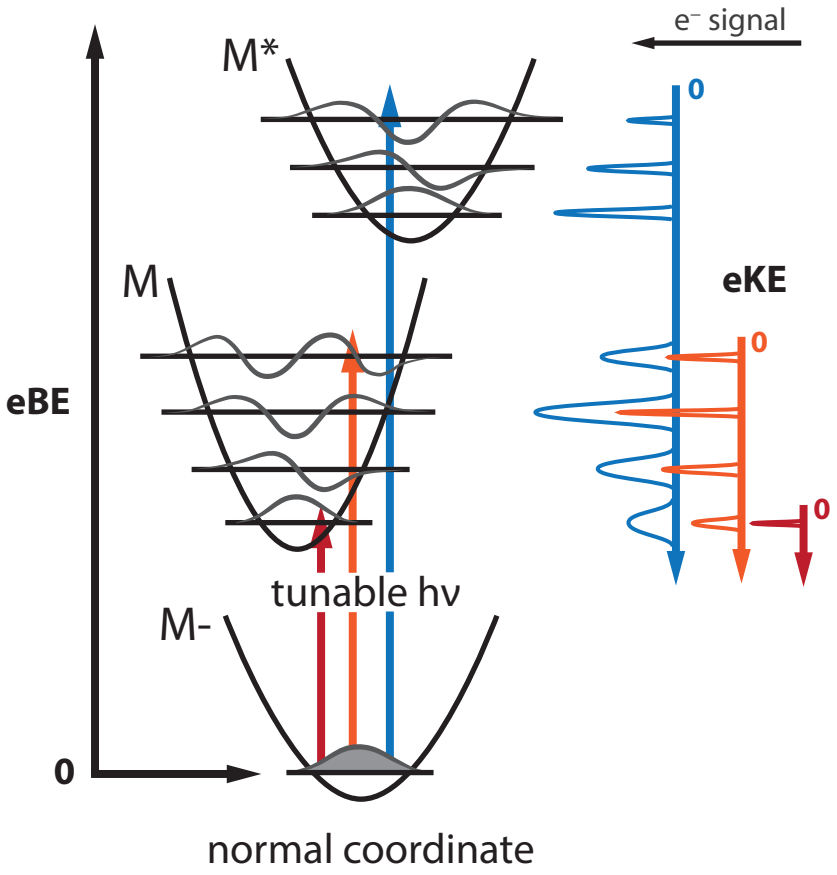

Figure 1.1: Energetic principles of anion photoelectron spectroscopy.

to an extensive array of atomic species,[3,4] small molecules,[5,6] clusters,[7], metal complexes,[8] and transition states of unimolecular reactions.[9,10]

The first pulsed anion PES report came in 1986.[11] The transition to pulsed experiments was motivated by the desire to use more flexible and shorter wavelength pulsed laser sources for photodetachment, and to study anion clusters that were generated more readily in pulsed free jet expansion sources. The eKE distributions for early pulsed anion PES experiments were measured via the time-of-flight (TOF) of the detached electrons, either with a field-free TOF or with a magnetic bottle scheme.[12]

With the development of ion imaging[13] and velocity-map imaging (VMI)[14] techniques, VMI became an attractive alternative to measure eKE distributions,[15,16] due to high photoelectron collection efficiency and the ability to measure photoelectron angular distributions alongside eKEs. Additionally, VMI detection is sensitive to low-eKE electrons which could not be detected with TOF methods.

Despite its flexibility and applicability to an incredibly diverse range of systems,[17] the utility of anion PES has historically been limited by the energy resolution of the eKE detection

methods. Energy resolution is around $50\,\mathrm{cm}^{-1}$ for the hemispherical analyzer,[6] 40–$80\,\mathrm{cm}^{-1}$ at best for conventional TOF eKE measurements,[18] and around $150\,\mathrm{cm}^{-1}$ for magnetic bottle TOF analyzers.[19] The energy resolution of a VMI spectrometer is dependent on the eKE of the detached photoelectrons, with a relatively constant $\Delta\mathrm{eKE/eKE} \sim 3\%$ for the original Eppink-Parker design.[14] With the Eppink-Parker VMI lens, energy resolution is therefore limited to $\sim$$250\,\mathrm{cm}^{-1}$ for electron kinetic energies of 1 eV, though more recent VMI designs have substantially improved upon this as discussed in Chap. 2.

These techniques allow resolution of electronic bands, and partially resolved vibrational structure. Only in favorable systems with amenable FC structure are vibrations clearly resolved, with extractable fundamental frequencies. Resolution poses a particular problem for species with FC active low frequency vibrations, and in cases where warm ion temperatures lead to hot bands and spectral congestion.

Zero electron kinetic energy (ZEKE) spectroscopy, another technique first motivated by neutral PES experiments,[20] was one approach to improve the energy resolution of anion PES. The laser wavelength is scanned, and only electrons detached at threshold, with essentially zero electron kinetic energy, are detected. Anion ZEKE, as developed in the Neumark group, had an impressive instrumental resolution down to 1–$2\,\mathrm{cm}^{-1}$ for atomic anions. Molecular systems demonstrated more typical peak widths of 8–$10\,\mathrm{cm}^{-1}$ due to rotational broadening.[21,22]

However, anion ZEKE proved to be experimentally challenging, and only suitable for a small fraction of systems. In ZEKE spectroscopy of neutrals, electrons are excited to high-lying Rydberg states, and are pulsed-field-ionized shortly before detection.[23] With the absence of Rydberg states in anions, the physics of anion ZEKE is quite different, and collection of ZEKE electrons without distortion by stray fields was incredibly difficult.

Depending on symmetry, photodetachment transitions can also suffer from poor threshold cross section. As governed by the Wigner threshold law (Section 1.1.5), photodetachment transitions that produce photoelectrons with outgoing angular momentum $l > 0$ have vanishing threshold cross section, and cannot be measured with ZEKE.[24] Even some photodetachment transitions expected to demonstrate partial $l = 0$ detachment were not found to yield ZEKE signal.

ZEKE spectroscopy was successfully applied to a number of anions in the Neumark group, including carbon,[25,26] silicon,[24,27,28] and germanium clusters,[29,30], van der Waals complexes,[31–33] and one transition state.[34] However, there remained an open field for a technique that could bridge the gap between the flexibility of conventional anion PES and the high energy resolution of ZEKE. Slow photoelectron velocity-map imaging (SEVI) spectroscopy was developed to fill this niche.[35]

1.1.2 Anion SEVI

Slow photoelectron velocity-map imaging (SEVI) spectroscopy is a high-resolution variant of the pulsed photoelectron imaging experiments described above. Ions are photodetached with a tunable laser at various fixed wavelengths and the kinetic energy distribution of the

resulting photoelectrons is measured with a velocity-map imaging lens. Two experimental conditions, both related to the "slow" part of SEVI's moniker, allow for improved energy resolution:

a. Relatively low extraction voltages are used to magnify the photoelectron image on the position sensitive detector, selectively detecting the slowest electrons and leading to spatially better-resolved features.

b. Photodetachment is carried out very close to threshold for each transition of interest, yielding low-eKE photoelectrons. Because VMI spectrometers have a relatively constant ΔeKE/eKE, the absolute energy resolution is best for small eKE.

Under these conditions, SEVI can easily achieve sub-meV energy resolution. By tuning the detachment laser above each spectral feature of interest, the entire spectrum can be acquired in high-resolution energy windows, as indicated in Fig. 1.1. These windows are then stitched together to create a composite SEVI spectrum; see Chap. 2 for additional details.

SEVI achieves or surpasses the energy resolution of its predecessor, anion ZEKE, while largely avoiding its experimental challenges. Poor threshold cross sections can render certain systems difficult to measure with SEVI, requiring detachment at higher eKE, and hence limiting the effective energy resolution. In the worst cases, SEVI is operated like a conventional photoelectron imaging experiment. The technique therefore maintains both the desired flexibility of anion PES, and the high threshold resolution of ZEKE.

1.1.3 Cryo-SEVI

While SEVI can be used to obtain excellent high-resolution photodetachment spectra of atomic anions, ion temperature is a major limiting factor in the clarity and interpretability of molecular photoelectron spectra. Hot bands, sequence bands, and rotational broadening lead to spectral congestion, especially for systems with low frequency vibrational modes. In SEVI experiments, warm anions demonstrate significantly broadened spectral features compared to instrumental resolution.[36]

Neutral molecules can reliably be prepared at temperatures of a few Kelvin by supersonic gas jet expansion. Producing cold, thermalized anions this way is more difficult. Ion temperature after production in a discharge or filament ionizer source is heavily system-dependent. The ions are often formed after the initial gas expansion, and therefore do not undergo a sufficient number of collisions to fully cool. Strongly bound clusters formed in a laser ablation source are also notoriously difficult to cool in a subsequent jet expansion due to cluster heating during condensation.[37]

Collisional cooling with cold, inert buffer gas is a nearly universal way to thermalize molecules to cryogenic temperatures.[38] Anions are, conveniently, charged and can be controlled by electromagnetic fields. Buffer gas cooling of ions can therefore be carried out in an

ion trap, where the ions are spatially confined and the number of collisions can be controlled through trap residence time and buffer gas pressure. Cryogenic ion cooling in an RF ion trap was first developed by Dieter Gerlich and coworkers,[39] and was subsequently adapted for a variety of applications in chemical physics and spectroscopy.[40] Lai-Sheng Wang and coworkers were the first to report PES of cryo-cooled anions, carried out in a cryo-cooled radiofrequency 3D quadrupole trap.[41,42] The resulting spectra demonstrated considerable improvement in clarity compared to room-temperature studies. Bernd von Issendorff's group also constructed a radiofrequency ion trap for use in cooling cluster anions prior to photodetachment. The construction of this trap is detailed in the thesis of Christian Hock,[43] and was originally used to study PES of water[44] and aluminum clusters[45] with a magnetic bottle spectrometer. Cryo-traps have also proved indispensable for applications in ion vibrational spectroscopy[46–48] as discussed further in Section 1.2.

In 2011-2012, a cryogenically-cooled, radio frequency octupole ion trap was designed and incorporated into the UC Berkeley SEVI machine. This modified "cryo-SEVI" apparatus has been described elsewhere,[49,50] and is discussed in more detail in Chap. 2. The cryogenic ion trap has demonstrated cooling of ions to their ground vibrational and electronic states and dramatically narrowed rotational distributions. We have measured molecular ion temperatures as cold as 10 K,[49] and spectral peak widths as narrow as 2–3 cm^{-1} for molecular systems.[51]

This new cryo-SEVI capability has allowed for exquisite spectral characterization of many systems that were previously not feasible, such as the large aromatic systems discussed in Chaps. 6 and 7, and the metal oxide clusters discussed in Chap. 8 and in the thesis of Jongjin Kim.[50] Additionally, tunable ion temperature can be useful for controlling the population in low-lying vibrational or electronic states of the anion. Temperature-dependent cryo-SEVI studies of CH_2CN^- (Chap. 4), and FeO^-[52] led to more nuanced understandings of vibrational and electronic structure.

Other research groups have developed similar photoelectron imaging experimental capabilities. Lai-Shang Wang's group currently uses a high-resolution VMI spectrometer, coupled to an electrospray ionization (ESI) ion source and a cryogenic ion trap.[53,54] Bernd von Issendorff's group has also coupled their cryogenic trap to a photoelectron imaging setup.[55,56] Chuangang Ning and coworkers developed a high-resolution imaging spectrometer aimed at characterizing transition metal atomic anions[57] and have recently added cryogenic cooling capabilities.[58] Michael Heaven's group has recently reported results from a new SEVI setup,[59] and is working towards incorporating a cryogenic ion trap. Carl Lineberger's group uses velocity-map imaging lenses for photoelectron spectroscopy, sometimes operating in SEVI mode.[60,61] At the time of writing, new SEVI experiments are also in development in the research groups of Etienne Garand at the University of Wisconsin and Duncan Wild at the University of Western Australia.

1.1.4 Photoelectron Spectroscopy Selection Rules

Photoelectron spectroscopy has somewhat relaxed selection rules compared to bound-bound electronic spectroscopy, due to the ability of the photoelectron to carry away whatever kinetic energy and angular momentum is necessary for a given transition.

We can begin with Fermi's Golden Rule for transition intensity I between an initial and final state after absorption of a linearly polarized photon:[62]

$$I \propto \left|\langle \Psi^f | \mu | \Psi^i \rangle\right|^2 \cdot \rho \cdot \delta(\Delta E - h\nu) \tag{1.3}$$

where $|\Psi^i\rangle$ is the initial total wavefunction (here that of the anion), $|\Psi^f\rangle$ is the final total wavefunction, (here that of the neutral plus the nascent photoelectron), μ is the dipole moment, and ρ is the density of final states. The term $\delta(\Delta E - h\nu)$ enforces the conservation of energy upon photon absorption, where ΔE is the difference in energy between initial and final states. For photoelectron spectroscopy, $\Delta E = \text{eKE} + \text{eBE}$.

Because eKE cannot be negative, the energy conservation term in Eqn. 1.3 specifies that photodetachment can only occur when the photon energy $h\nu$ exceeds the electron affinity, the lowest possible eBE. This is analogous to the photoelectric effect in bulk materials, where a photoelectron can be detached only if the photon energy exceeds the workfunction of the material.[63,64]

Within the Born-Oppenheimer approximation, the electronic and nuclear degrees of freedom of the system can be treated as independent, as their respective motion occurs on drastically different time and energy scales. The total molecular wavefunction can therefore be written as a product of electronic (e), spin (s), vibrational (v), and rotational (r) components:

$$\Psi = \psi_e \cdot \psi_s \cdot \psi_v \cdot \psi_r \tag{1.4}$$

ψ_r is generally ignored, as rotational structure is rarely resolved in anion PES experiments. Only in exceptional cases are rotational constants large enough for rotational structure to manifest in SEVI spectra, as in Chap. 4, for the photodetachment of CH_2CN^-. Detail for treating rotational selection rules in these cases is available elsewhere.[65,66]

The dipole moment can also be separated into components due to electronic and nuclear charge distributions, which will interact with the electronic and vibrational wavefunctions, respectively:

$$\mu = \mu_e + \mu_n \tag{1.5}$$

Using Eqns. 1.4 and 1.5, we can rewrite the transition intensity as proportional to:

$$
\begin{aligned}
I &\propto \left|\langle \psi_e^f \cdot \psi_s^f \cdot \psi_v^f | \mu_e + \mu_n | \psi_e^i \cdot \psi_s^i \cdot \psi_v^i \rangle\right|^2 \\
&= \left|\langle \psi_e^f | \mu_e | \psi_e^i \rangle \langle \psi_v^f | \psi_v^i \rangle \langle \psi_s^f | \psi_s^i \rangle + \langle \psi_e^f | \psi_e^i \rangle \langle \psi_s^f | \psi_s^i \rangle \langle \psi_v^f | \mu_n | \psi_v^i \rangle\right|^2
\end{aligned} \tag{1.6}
$$

With fixed nuclear coordinates, different electronic states are orthogonal, so $\langle \psi_e^f | \psi_e^i \rangle = 0$, and the second term of Eqn. 1.6 vanishes. What results is an expression with three factors from which electronic, spin, and vibrational selection rules are derived:[67]

$$
I \propto \left|\langle \psi_e^f | \mu_e | \psi_e^i \rangle\right|^2 \left|\langle \psi_s^f | \psi_s^i \rangle\right|^2 \left|\langle \psi_v^f | \psi_v^i \rangle\right|^2 \tag{1.7}
$$

The first factor of the above expression will specify the electronic symmetry conditions for a given transition, the second specifies the allowed change in electronic spin, and the third term is the Franck-Condon (FC) factor, which determines the relative intensity of transitions between different vibrational states within an electronic band. In order for a transition to occur between given vibrational and electronic states, each of these three factors must be non-zero. We will consider each factor in turn.

The requirement that $\left|\langle \psi_s^f | \psi_s^i \rangle\right|^2 \neq 0$ is simplest: the total electronic spin of the system must be conserved before and after the transition. In bound-to-bound electronic spectroscopy, the initial and final states must have identical electronic spin. In anion PES, a photoelectron with spin 1/2 is detached, leaving behind a neutral core that must have a change in spin of $\pm 1/2$ and a change in spin multiplicity of ± 1 from the anion.

This high number of bright spin states makes PES quite versatile. For instance, both singlet and triplet neutral states are accessible from detachment of a doublet anion. This was first exploited by Jan Hall and coworkers in photodetachment of O_2^- to simultaneously probe the triplet and singlet states of O_2.[68] Since then, anion PES has been used to measure singlet-triplet splittings in a variety of interesting systems.[9,69–72] Similarly, multiple neutral spin states are accessible in detachment of metal oxide cluster anions with high spin multiplicity, as is discussed in Chap. 8 for the SEVI spectra of the Fe_4O^- and Fe_5O^- clusters, and elsewhere.[52,73]

The electronic symmetry condition, $\left|\langle \psi_e^f | \mu_e | \psi_e^i \rangle\right|^2 \neq 0$, also behaves somewhat differently in PES than in conventional electronic spectroscopy. This condition can be reformulated as the requirement that, within the point group of the molecule, the direct product of irreducible representations of the initial state, the final state, and the dipole moment, which transforms as (x, y, z), must include the totally symmetric representation, Γ_A:

$$
\Gamma_A \in \Gamma_e^f \otimes \Gamma_\mu \otimes \Gamma_e^i \tag{1.8}
$$

For a photodetachment transition in particular, one can assume that the wavefunction of the outgoing photoelectron is independent from and orthogonal to the remaining occupied

molecular orbitals (MOs), and its electronic symmetry therefore can be factored out. We can rewrite the above as:

$$\Gamma_A \in \Gamma_e^{neutral} \otimes \Gamma_e^{photoelectron} \otimes \Gamma_\mu \otimes \Gamma_e^{anion} \tag{1.9}$$

For a transition between anion and neutral states of specified symmetry, the outgoing photoelectron can leave with a wavefunction of whatever symmetry and angular momentum is required to yield Γ_A in Eqn. 1.9. In the simplest picture, for detachment from spherical harmonic atomic orbitals with well-defined l, Eqn. 1.9 implies that a photoelectron leaves an orbital with angular momentum l in partial waves of angular momentum $l \pm 1$. The angular momentum of the outgoing photoelectron affects the eKE dependence of the photodetachment cross section and angular distribution, discussed further in Sections 1.1.5 and 1.1.6.

There are no dipole-forbidden transitions in photoelectron spectroscopy as there are in optical electronic spectroscopy. However, photodetachment transitions do typically follow the one-electron rule: provided that the anion and neutral MOs are similar, the electronic configuration of the neutral is identical to that of the anion minus one electron. In other words, no other electrons should be rearranged during photodetachment. Of course, seeming exceptions to this rule can appear in the presence of states with multireference character.[74]

Finally, we consider the Franck-Condon factor, $\left|\langle\psi_v^f|\psi_v^i\rangle\right|^2 \neq 0$, which governs the selection rules for vibrational transitions as well as the relative intensity of vibrational transitions within an electronic band. Stated briefly: excitation occurs to neutral vibrational levels in accordance with their net overlap with the initial anion vibrational wavefunction.

Based on symmetry arguments and the integration properties of harmonic oscillator wavefunctions, the FC factor implies that allowed transitions can exhibit a change in vibrational quantum number of $\Delta v = 0, \pm 1, \pm 2...$ for totally symmetric vibrational modes and $\Delta v = 0, \pm 2, \pm 4...$ for non-totally symmetric modes.

In practice, a large change in geometry between anion and neutral is associated with large Franck-Condon factors for vibrational excited states, particularly for vibrational modes whose motion distorts the molecule along the displacement vector between anion and neutral equilibrium geometries. Excitation in even quanta of non-totally symmetric modes is typically weak, and usually occurs when there is a large change in the harmonic frequency of that mode between anion and neutral. Little change in geometry between the anion and neutral equilibrium geometries results in small Franck-Condon factors for all vibrational levels but the vibrational origin.

The Franck-Condon approximation is frequently violated. Some situations that result in non-FC behavior are discussed below in Section 1.1.7.

1.1.5 Photodetachment Cross Sections

The cross section for photodetachment processes is a function of the angular momentum and kinetic energy of the outgoing photoelectron, and is governed by the symmetry of the

photodetachment transition.

A photoelectron is detached from an atomic orbital with angular momentum l in a superposition of spherical harmonic partial waves with $\Delta l = \pm 1$ (Section 1.1.4). The near-threshold atomic photodetachment cross section, σ for a partial wave with angular momentum l has an eKE dependence governed by the Wigner threshold law:[75]

$$\sigma \propto (\text{eKE})^{l+1/2} \tag{1.10}$$

The eKE-dependence of the cross section is specific to anion photodetachment, as it derives from the weak long-range interactions of the outgoing electron with the neutral core that it leaves behind. During detachment of an an atomic anion, the photoelectron and neutral share a charge-induced dipole interaction, of the form $V(r) \propto -1/r^4$.[76] In contrast, for photoionization of neutrals, the electron leaves behind a cationic core, and experiences a $-1/r$ Coulomb potential.

In addition to the long-range interaction with the molecular core, an outgoing photoelectron with angular momentum l experiences a centrifugal potential $V(r) \propto l(l+1)/r^2$. This angular momentum term is significant compared to the weak attraction between the electron and the neutral core in anion photodetachment. When $l > 0$, the centrifugal contribution to the potential forms a barrier, and slow electrons must tunnel through the barrier in order to be detached. The centrifugal barrier in $V(r)$ is shown schematically in Fig. 1.2(a) for various values of l. In neutral photoionization, the functional form of the Coulomb potential leads

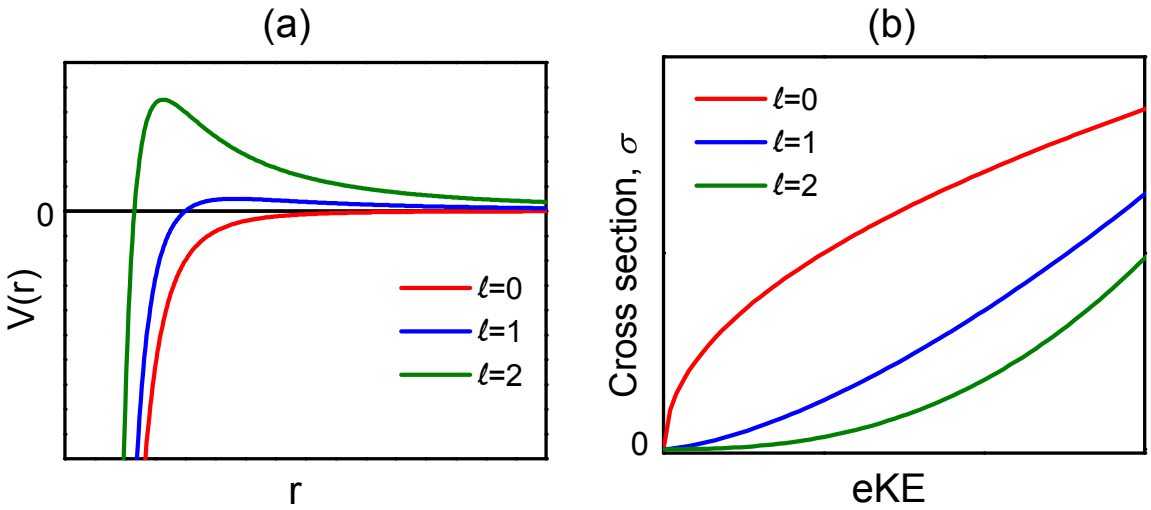

Figure 1.2: (a) Schematic of the potential $V(r)$ felt by the photoelectron during anion photodetachment as a function of its angular momentum, l, and (b) the behavior of the photodetachment cross section σ for various l as a function of eKE, as governed by the Wigner threshold law.

to no centrifugal barrier, and there is therefore no significant l or eKE dependence to the cross section.

The Wigner threshold law for anion photodetachment is intimately tied to the centrifugal barrier, and implies that only photoelectrons detached with $l = 0$ retain significant detachment cross section close to threshold. Fig. 1.2(b) shows the kinetic energy dependence of the photodetachment cross section for three values of l. This eKE relationship is the reason that ZEKE spectroscopy was limited to the study of systems that detached with significant $l = 0$ detachment, and hence had non-vanishing cross sections close to threshold (Section 1.1.2). With typical eKEs of 10–100 cm^{-1} used in SEVI spectroscopy, $l = 0$ detachment dominates, but higher order waves can still be detected.

The Wigner threshold law is derived for detachment of atomic anions, and predicting the threshold behavior of molecular anions requires some additional subtlety. As first discussed by Reed *et al.*,[77] one can use the symmetry of the detachment transition within the molecular point group to determine the dominant partial waves of the outgoing photoelectron, and draw conclusions about the threshold behavior of a given transition.

The s & p model developed by the Sanov group[16,78] is another convenient framework for making these predictions, and is discussed in detail in Section 1.1.6.

1.1.6 Photoelectron Angular Distributions

The distribution of detached photoelectrons varies as a function of angle with respect to the laser polarization axis, and, like the photodetachment cross section, is dictated by the transition symmetry and the angular momentum of the outgoing photoelectron. In photoelectron spectra collected with a VMI spectrometer, the photoelectron angular distribution (PAD) is measured simultaneously with the eKE distribution. For a one-photon photodetachment process with linearly polarized light, the differential cross section for photodetachment at a given solid angle, $d\sigma/d\Omega$, is given by:[79]

$$\frac{d\sigma}{d\Omega} = \frac{\sigma_{\mathrm{tot}}}{4\pi}\left[1 + \beta P_2(\cos\theta)\right], \tag{1.11}$$

where θ is the angle of the photoelectron velocity vector relative to the polarization axis of the laser, P_2 is the second-order Legendre polynomial with $P_2(\cos\theta) = \frac{1}{2}(3\cos^2\theta - 1)$, and β is the anisotropy parameter. At its extremes, the anisotropy parameter varies between $\beta = -1$ giving $d\sigma/d\Omega \sim \cos^2\theta$ and a PAD peaked perpendicular to the laser polarization axis, and $\beta = +2$ giving $d\sigma/d\Omega \sim \sin^2\theta$ for a PAD peaked parallel to the laser polarization axis. $\beta = 0$ yields an isotropic PAD.

As discussed in previously in Sections 1.1.4 and 1.1.5, a photoelectron is detached from an atomic orbital in a superposition of spherical harmonic partial waves with $\Delta l = \pm 1$. The anisotropy parameter, β, can be predicted by the Cooper-Zare formula:[79]

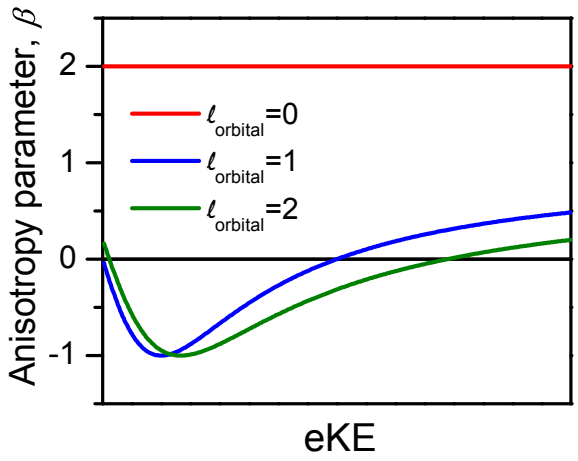

Figure 1.3: The anisotropy parameter, β, for detachment from atomic anions with various orbital angular momenta $l_{orbital}$ as a function of eKE, as governed by the Wigner threshold law and the Cooper-Zare formula.

$$\beta = \frac{l(l-1)\chi_{l,l-1}^2 + (l+1)(l+2)\chi_{l,l+1}^2 - 6l(l+1)\chi_{l,l+1}\chi_{l,l-1}\cos(\delta_{l+1} - \delta_{l-1})}{(2l+1)[l\chi_{l,l-1}^2 + (l+1)\chi_{l,l+1}^2]} \tag{1.12}$$

where l is the angular momentum of the atomic orbital from which detachment occurs, and $\chi_{l,l\pm1}$ and $\delta_{l\pm1}$ are the radial matrix elements and the phase shifts, respectively, for the dipole-allowed outgoing photoelectron partial waves with angular momenta $l \pm 1$.

Hanstorp *et al.*[80] noted that the Cooper-Zare formula depends only on the ratio of partial wave radial matrix elements $\chi_{l,l+1}/\chi_{l,l-1}$, which changes as a function of eKE in accordance with the Wigner threshold law. The partial wave cross section is proportional to the square of the corresponding matrix element $\sigma_{l\pm1} \propto \chi_{l,l\pm1}^2$. Using the Wigner threshold law, we arrive at the ratio $\chi_{l,l+1}/\chi_{l,l-1} = A_l \cdot \text{eKE}$, where A_l is the proportionality constant describing the relative propensity for detachment via the $l+1$ and $l-1$ channels. Eqn. 1.12 can then be expressed as the following explicit function of eKE:[81]

$$\beta = \frac{l(l-1) + (l+1)(l+2)(A_l \cdot \text{eKE})^2 - 6l(l+1)(A_l \cdot \text{eKE})\cos(\delta_{l+1} - \delta_{l-1})}{(2l+1)[l + (l+1)(A_l \cdot \text{eKE})^2]} \tag{1.13}$$

For illustration, in Fig. 1.3, Eqn. 1.13 is used to plot β as a function of eKE for detachment from orbitals with different values of l, taking $A_l = 1$ and neglecting phase shifts.

Detachment from an $l = 0$ s-orbital can only yield p-wave, $l = 1$ photoelectrons, and in the absence of partial wave interference, we get an anisotropy parameter $\beta = 2$ that is independent of eKE. Detachment from orbitals with higher l yield a superposition of partial waves and hence a more complex β parameter that depends on eKE as well as the relative phases and amplitudes of the partial waves.

The discussion of PADs thus far assumes detachment from spherical harmonic atomic orbitals with well-defined l, and as usual, the situation becomes more complicated when considering detachment of molecular anions. Molecular orbitals do not have well-defined orbital angular momentum. Additionally, one must consider the orientation of the molecule's geometrical axes with respect to the laser polarization axis in the lab frame. In detachment of atomic anions, the only defined axis is that imposed by the laser polarization, and orientation is not a consideration. For molecular photodetachment, we will have to average over an ensemble of randomly oriented molecules in the lab frame.

The s & p method developed by the Sanov group,[16,78] is a very simple, yet often effective model to predict the PADs of molecular anion detachment using group theory. We will go through a brief derivation of this model here.

For simplicity, we can consider just three orientations of the molecule with respect to the laser polarization to capture most of the behavior of the ensemble. We can choose these orientations to be with each of the three principal molecular axes aligned along the laser polarization. We will use group theory to determine the allowed symmetry of the outgoing photoelectron wavefunction for each orientation. We can then expand this wavefunction in a basis of symmetry-adapted partial wave spherical harmonics, and consider the major contributing photoelectron partial waves.

With the s & p model, only the partial waves of outgoing angular momentum $l = 0$ or 1 are considered. This choice is motivated by the Wigner threshold law, which dictates that the lowest angular momenta partial waves dominate close to threshold. For slow photoelectrons, we can ignore all contributions from partial waves with $l \geq 2$ and still reproduce much of the behavior of the system. This simplification will break down at higher energies where more partial waves contribute and interfere, but works quite well for the purposes of SEVI.

Following the methodology laid out by Surber *et al.*,[16] we first consider the symmetry of the transition dipole moment for each molecular orientation. We need a way to reference the symmetry of photodetachment in the molecular frame to the lab frame laser polarization axis. As shown for the C_{2v} point group in the top row of Fig. 1.4, we can write down the symmetry species of the laser polarization axis and hence the dipole moment operator in each molecular frame.

Next we consider the selection rule for the dipole-allowed symmetry of the outgoing photoelectron wavefunction. As laid out previously in Eqn. 1.9, the electronic symmetry requirement for photodetachment can be expressed as:

$$\Gamma_{photoelectron} = \Gamma_{neutral} \otimes \Gamma_{anion} \otimes \Gamma_{\mu} \tag{1.14}$$

For each transition symmetry $\Gamma_{neutral} \otimes \Gamma_{anion}$ and each molecular orientation, we can predict the symmetry of the outgoing photoelectron wavefunction and the corresponding spherical harmonics of that symmetry with $l = 0, 1$ in the molecular frame. This is illustrated for all transition symmetries of a C_{2v} molecule in Fig. 1.4. The consistent orientation of the $l = 1$ spherical harmonics in the lab frame for each transition symmetry, even as we average over molecular orientations, is what leads to the PADs measured experimentally.

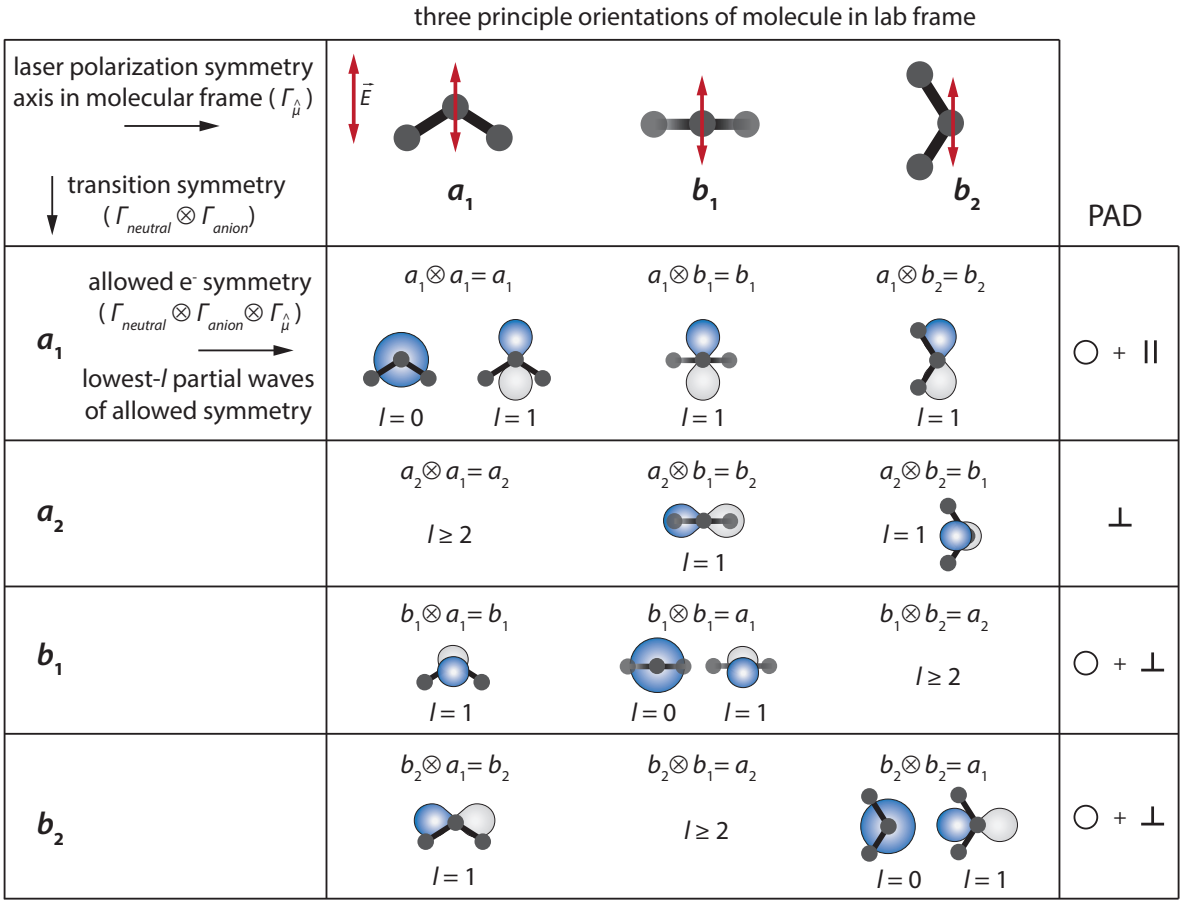

Figure 1.4: The s & p model for predicting photoelectron angular distributions for photodetachment of a C_{2v} molecular anion.

In the C_{2v} point group in particular, we expect partial $l = 0$ detachment for all transition symmetries but A_2, suggesting that most photodetachment transitions would enjoy retained intensity for detachment close to threshold (Section 1.1.5). The perpendicular or parallel character of the PAD and the threshold behavior, when considered together, are a nice signature of the transition symmetry.

A more general trend also emerges from this C_{2v} picture: in any point group, for detachment from a totally symmetric orbital of the anion, the outgoing electron waves will always share the same symmetry as the transition dipole, and therefore will always be detached with a PAD aligned parallel to the laser polarization ($\beta > 0$).

Even within the s & p model, PADs for molecules can be non-intuitive. For detachment of an atomic p orbital, we expect $s + d$-wave detachment, with an isotropic-to-perpendicular PAD, depending on eKE. For the C_{2v} example shown here, detachment from a molecular orbital that looks like a p_z atomic orbital, aligned along the C_2 axis, will have a_1 symmetry,

and therefore give rise to an isotropic-to-parallel PAD. Molecular orbitals with p_x or p_y character, on the other hand, will have b_1 or b_2 symmetry within the C_{2v} framework, and will yield an isotropic-to-perpendicular PAD. The orientation of the MO with respect to the molecular symmetry axes is critical for predicting the PAD.

There are of course situations where the s & p model cannot correctly predict the molecular PAD. This is particularly true in low-symmetry species where group theory is not of much use, or in species where group theory does not fully capture the nodal structure of the MO, as is often the case for transition metal oxide clusters. Luckily, some software packages do exist to simulate the eKE dependence of the photodetachment cross section and photoelectron angular distributions for complex molecular anions, based on *ab initio* calculations of the Dyson transition orbitals.

Work from Anna Krylov's group[82] allows calculation of photodetachment Dyson orbitals for using EOM-IP/EA-CCSD methods in Q-Chem. Cross sections and PADs can then be calculated using the ezDyson code.[83] We use this method to aid in analysis of the SEVI studies of the 2-orthohydroxyphenoxy radical (Chap. 5), the α- and β-naphthyl radicals (Chap. 6), and the 9-, 1-, and 2-anthracenyl radicals (Chap. 7). One limitation of this method is that EOM-IP/EA-CCSD calculations require either the anion or neutral species to be closed-shell, to provide a good reference wavefunction.

More recently, Chuangang Ning and coworkers have developed the PADA code to calculate photodetachment cross sections and PADs using DFT calculations of the anion orbitals within the frozen orbital approximation.[84] This method is promising as a simpler and computationally cheaper alternative to ezDyson, and does not require that one of the involved states be closed shell.

1.1.7 Vibronic Coupling and Anharmonic Effects

SEVI spectra yield rich detail into the geometric, vibrational and electronic structure of exotic neutral molecules. Sometimes the most intriguing aspects of these systems are manifest when the Franck-Condon approximation or the harmonic approximation is violated.

In this section, we highlight common cases where unexpected structure arises, their signatures in SEVI spectra, the information that can be gleaned, and examples of molecular systems.

1.1.7.1 Herzberg-Teller Coupling

Herzberg-Teller (HT) vibronic coupling is perhaps the most common way that the Franck-Condon approximation breaks down. In this case, electronic and vibrational degrees of freedom mix, and cannot be separated as they were in Eqns. 1.4 and 1.5.

Instead, states with the same total vibronic symmetry can mix. For instance, vibrational levels within electronic state B can mix with vibrational levels in electronic state C provided that the following direct product contains the totally symmetric representation, Γ_A,

$$\Gamma_A \in \Gamma_e^B \otimes \Gamma_v^B \otimes \Gamma_e^C \otimes \Gamma_v^C \tag{1.15}$$

where $\Gamma_e^{B,C}$ represents the electronic character of state B or C, and $\Gamma_v^{B,C}$ represents the vibrational character.

In a photoelectron spectrum, HT coupling typically manifests itself as the appearance of non-totally symmetric vibrational levels, which borrow intensity from totally symmetric vibrational levels of a different electronic state. These FC forbidden features demonstrate the anisotropy and threshold behavior of the electronic state from which they borrow intensity, distinct from their neighboring FC allowed peaks. These forbidden features can even dominate the near-threshold spectrum, if they have retained threshold intensity while the allowed peaks do not.[85]

In this thesis, Herzberg-Teller vibronic coupling manifests in the SEVI spectra of C_5^- (Chap. 3), the ortho-hydroxyphenoxy radical (Chap. 5), and the α- and β-naphthyl radicals (Chap. 6).

1.1.7.2 Jahn-Teller and Renner-Teller Coupling

In Jahn-Teller (JT) coupling, or Renner-Teller (RT) coupling in the case of linear molecules, mixing of vibrational levels occurs within a single degenerate electronic state. JT and RT coupling are often accompanied by spin-orbit effects.

As with HT coupling, JT and RT coupling can only occur between states with the same total vibronic symmetry. Two vibrational states v_1 and v_2 in electronic state B can mix provided that

$$\Gamma_A \in \Gamma_e^B \otimes \Gamma_{v_1}^B \otimes \Gamma_e^B \otimes \Gamma_{v_2}^B \tag{1.16}$$

where Γ_A is the totally symmetric representation, Γ_e^B is the electronic character of state B, and Γ_{v_1,v_2}^B are the characters of the two vibrational states in consideration.

In photoelectron spectroscopy, JT and RT coupling primarily manifest as complex shifting and splitting of vibrational structure within a degenerate electronic state. The SEVI spectra of detachment of the methoxide anion to probe the structure of the methoxy radical are a prototypical example of this effect.[86,87]

In more rare cases, RT coupling is invoked as a means of lending intensity to FC forbidden photodetachment transitions. In the C_5^- anion (Chap. 3), RT coupling between vibrational levels in the anion $^2\Pi$ ground electronic state "turns on" photodetachment transitions to non-totally symmetric vibrational levels in the neutral ground state.

1.1.7.3 Anharmonicity

Sometimes the vibrational potential of a given normal mode is so anharmonic that its vibrational energy levels, wavefunctions and Franck-Condon factors are poorly represented by

the harmonic approximation. In these cases, the vibrational potential along the anharmonic normal mode has to be calculated explicitly, and the vibrational wavefunctions and their energies solved for numerically.

Double-well potentials with low barriers are a reasonably common occurrence. In the CH_2CN^- anion (Chap. 4), a double well potential along the ν_5 umbrella mode leads to a low-lying anion vibrational level, and therefore a photoelectron spectrum with a Franck-Condon envelope unusually sensitive to temperature. The neutral Fe_4O cluster (Chap. 8) has a shallow double-well potential along the non-totally symmetric ν_5 mode, which leads to excitation of even quanta of this mode upon photodetachment. The correct FC factors are not captured by the harmonic approximation and have to be calculated explicitly. The $[(TiO_2)_2(D_2O)_2]^-$ anion (Chap. 10) has a double-well potential along a Ti-O-Ti bridge stretching mode, red-shifting the corresponding vibrational feature in the IR spectrum.

Anharmonic terms in the vibrational potential energy can also provide perturbations that allow energy levels associated with different normal modes to mix, lending intensity to otherwise dark transitions. These anharmonic couplings typically occur when vibrational states of the same symmetry within one electronic state lie very close in energy and interact. This leads to mixing of the vibrational wavefunctions and widening of the energy gap as the mixing states repel one another.[65] Within electronic state B, vibrational levels v_1 and v_2 can experience anharmonic coupling if:

$$\Gamma_A \in \Gamma^B_{\nu_1} \otimes \Gamma^B_{\nu_2} \tag{1.17}$$

where Γ_A is the totally symmetric representation. The canonical example of anharmonic vibrational coupling is the Fermi resonance, an accidental degeneracy between the fundamental of a totally symmetric mode and two quanta in another mode (e.g. the ν_1 symmetric stretch fundamental and the $2\nu_2$ bending level in CO_2[65]).

While most commonly observed in infrared spectroscopy, anharmonic couplings also manifest in photoelectron spectra. Vibrational levels that are totally symmetric but weak or non-FC active can borrow intensity from nearby bright modes. These features share the same electronic character as the FC allowed modes, and therefore do not demonstrate distinct anisotropy or threshold behavior, unlike peaks that appear through HT coupling.

In this thesis, anharmonic coupling is invoked in Chap. 7 to assign unexpected vibrational features in the ground electronic states of the 1- and 2-anthracenyl radicals.

1.1.7.4 Vibrational Autodetachment

Resonant mode-specific vibrational autodetachment is another source of unexpected structure in anion photoelectron spectra. In direct photodetachment, excitation is made directly from the ground state of the anion to a neutral state with vibrational quantum numbers $(\nu'_1, \ldots \nu'_n)$:

$$A^- \xrightarrow{h\nu} A(\nu'_1, \ldots \nu'_n) + e^- \tag{1.18}$$

However, if a metastable anion electronic state A^{*-} lies within the manifold of neutral states, excitation to vibrational levels of this state can compete with direct detachment to the neutral. The anion excited state can then undergo autodetachment by converting vibrational (and rotational) internal energy into the electronic energy required to detach an electron:

$$A^- \xrightarrow{h\nu} A^{*-}(\nu_1'', \ldots \nu_n'') \longrightarrow A(\nu_1', \ldots \nu_n') + e^- \tag{1.19}$$

This is a non-Born-Oppenheminer process, as vibrational and electronic degrees of freedom must mix to couple the autodetaching state to the neutral + free electron continuum.[88] The signature of such a process is the appearance of new vibrational structure or significant change in intensity of existing structure at distinct wavelengths where the photon energy is resonant with a transition to the autodetaching anion excited state.

The autodetachment electron signal has a cross section and anisotropy not governed by the direct photodetachment symmetry rules. Vibrational autodetachment can also lead to the appearance of Franck-Condon forbidden peaks, as the neutral vibrational states accessible through autodetachment are no longer governed by the Franck-Condon principle, but rather by the propensity rules first described by Simons.[88]

Resonant mode-specific vibrational autodetachment is particularly common in systems where the neutral has a sufficiently large dipole moment to support a dipole-bound state (DBS) anion, as in the CH_2CN system (Chap. 4). In these cases, the weakly bound DBS has a very similar geometry to the neutral, and for every neutral vibrational level, a corresponding DBS vibrational level lies slightly lower in energy. Vibrational autodetachment also crops up in the first excited state of the 1-anthracenyl radical (Chap. 7).

1.2 Infrared Vibrational Action Spectroscopy

1.2.1 Infrared Photodissociation (IRPD) and Multiple Photon Dissociation (IRMPD) Spectroscopy

As a complement to the UC Berkeley cryo-SEVI experiments, infrared vibrational action spectroscopy experiments are carried out in collaboration with the research group of Prof. Knut Asmis at the Fritz Haber Institute (FHI) in Berlin, Germany. IR action spectroscopy is an excellent characterization tool for the vibrational and geometrical structure of large and complex cluster anions.

In a typical infrared absorption experiment, infrared light passes through a sample, and the amount of light remaining after attenuation through the sample is recorded as a function of wavelength. According to Beer's law, at a given wavelength, the absorbance A of a sample is given by:

$$A = \log(I_0/I) = \sigma \cdot n \cdot l \tag{1.20}$$

where I_0 is the intensity of light striking the sample, I is the intensity of transmitted light, σ is the absorption cross section, n is the number density of the sample, and l is the pathlength of the light through the sample.

In the case of a sample with extremely low n, such as a gas-phase molecular ion beam, a direct absorption measurement is challenging.[89,90] Instead, we turn to action spectroscopy, where we measure an event that occurs as result of absorption of a photon. IR vibrational action spectroscopy of gas-phase ions typically makes use of mass spectrometry techniques to measure a change in mass as a result of absorption of IR light. In the Asmis group, this is typically carried out via IR photodissociation spectroscopy (IRPD) and IR multiple photon dissociation spectroscopy (IRMPD).

In an IRPD experiment, mass-selected anions A^- are first trapped and cryogenically cooled in a radiofrequency ion trap, in principle ensuring both that the clusters are vibrationally cold and that only the energetically most stable isomers are present. The clusters are then complexed with a weakly bound species, or messenger tag, M, and irradiated with IR light. Here, the cryogenic temperatures in the trap aid in complexation of the A^- clusters with the messenger tag, though messenger-tagged vibrational action spectroscopy long predates this capability.[91] The tag is chosen to be sufficiently loosely coordinated that it will not distort the molecular structure of A^-, and will dissociate when A^- becomes vibrationally excited after absorption of a photon.[46,48] The depletion of the tagged parent ion $A^- \cdot M$ and reformation of bare A^- in the mass spectrum is recorded as the IR wavelength is scanned:

$$A^- \cdot M \xrightarrow{h\nu} A^{-*} \cdot M \rightarrow A^- + M \tag{1.21}$$

In IR photodissociation experiments, an intense, tunable, and narrow source of IR light is required. The IRPD experiments detailed in this thesis were performed at the new infrared free electron laser (FEL) facility located at the FHI.[92] The FEL can be optimized for production of wavelengths in the range 400–3000 cm^{-1}. At higher IR frequencies, a tabletop OPO/OPA laser setup is also a reasonable option.

Our previous collaborations with the Asmis group have mainly used IR multiple photon dissociation (IRMPD).[93,94] In IRMPD, A^- is not messenger-tagged. Rather, the IR spectrum of A^- is obtained by measuring its dissociation upon sequential absorption of several IR photons. As the IR wavelength is scanned, the depletion of the parent mass and the formation of smaller fragments is recorded in the mass spectrum. While we do report IRMPD spectra for some clusters in this thesis (Chap. 10), we have mainly opted to use the messenger-tagged IRPD technique instead. IRPD spectra are cleaner and easier to interpret than IRMPD spectra for several reasons. Because IRPD is a single-photon technique, the IR absorption is linear, and the intensities of spectral features can be directly compared to calculated harmonic IR intensities. The linewidths for IRMPD absorption also tend to be much broader than in IRPD, leading to more poorly resolved spectra.

Additionally, some IR active vibrational modes are "transparent" in IRMPD experiments. The weakly associated messenger tag in an IRPD experiment is more sensitive to general

vibrational excitation, and all IR active modes should appear, including low-frequency fingerprint modes.[95] IRPD spectra are therefore more reliable for comparison to simulations and structure determination. An important caveat, of course, is that even with IRPD, the messenger tag may slightly alter the ion structures and shift or split vibrational frequencies.[96] In extreme cases, the tag could even chemically react rather than coordinate weakly with the parent ion.[97]

1.2.2 IR Selection Rules

The features observed in an IRPD experiment are governed by selection rules for vibrational transitions and their linear IR absorption intensities.

According to Fermi's Golden Rule (Eqn. 1.3), the probability of absorption of a linearly polarized photon goes like the square of the transition dipole moment integral. Considering only vibrational transitions, and therefore only the nuclear dipole moment μ, the intensity I of a vibrational transition from initial state ψ_v^i to final state ψ_v^f can be expressed as:

$$I \propto \left|\langle \psi_v^f | \mu | \psi_v^i \rangle\right|^2 \tag{1.22}$$

The nuclear dipole moment μ is a function of the molecular bond lengths, and therefore changes as the molecule vibrates. As the molecule vibrates along one of its n vibrational normal coordinates q_j, we can express μ as a Taylor expansion around its value at the molecule's equilibrium geometry, $\mu(0)$:

$$\mu = \mu(0) \; + \; \sum_j^n \left(\frac{d\mu}{dq_j}\right)_0 q_j \; + \; \cdots \tag{1.23}$$

The transition moment integral can therefore be written as:

$$\begin{aligned} \langle \psi_v^f | \mu | \psi_v^i \rangle &= \langle \psi_v^f | \left[\mu(0) + \sum_j^n \left(\frac{d\mu}{dq_j}\right)_0 q_j + \cdots \right] | \psi_v^i \rangle \\ &= \mu(0) \, \langle \psi_v^f | \psi_v^i \rangle \; + \; \sum_j^n \left(\frac{d\mu}{dq_j}\right)_0 \langle \psi_v^f | q_j | \psi_v^i \rangle \; + \; \cdots \end{aligned} \tag{1.24}$$

Distinct vibrational states within the same electronic state are orthogonal, so $\langle \psi_v^f | \psi_v^i \rangle = \delta_{fi}$. For a transition that leaves the system in a new vibrational state ($f \neq i$), we are therefore left with the leading first order terms:

$$\langle \psi_v^f | \mu | \psi_v^i \rangle = \sum_j^n \left(\frac{d\mu}{dq_j}\right)_0 \langle \psi_v^f | q_j | \psi_v^i \rangle \tag{1.25}$$

Considering now just the term for the k^{th} vibrational normal mode, and writing out our vibrational initial and final states more explicitly in terms of their quantum numbers v:

$$\begin{aligned}
&\left(\frac{d\mu}{dq_k}\right)_0 \langle \psi_v^f | q_k | \psi_v^i \rangle \\
=&\left(\frac{d\mu}{dq_k}\right)_0 \langle v_1^f,\, v_2^f,\, \ldots,\, v_k^f,\, \ldots,\, v_n^f | q_k | v_1^i,\, v_2^i,\, \ldots,\, v_k^i,\, \ldots,\, v_n^i \rangle \\
=&\left(\frac{d\mu}{dq_k}\right)_0 \langle v_k^f | q_k | v_k^i \rangle \prod_{j \neq k}^{n} \langle v_j^f | v_j^i \rangle
\end{aligned} \tag{1.26}$$

In order for a vibrational transition involving normal mode q_k to be IR active, Eqn. 1.26 must be non-zero. From this condition, we derive the important selection rules of IR spectroscopy:

(a) $$\left(\frac{d\mu}{dq_k}\right)_0 \neq 0,$$

which implies that if mode k is IR active, displacement along its normal coordinate must alter the dipole moment of the molecule.

(b) $$\langle v_k^f | q_k | v_k^i \rangle \neq 0$$

If v_k^f and v_k^i are harmonic oscillator wavefunctions, this integral will only be non-zero for transitions with $\Delta v_k = \pm 1$.[98]

(c) $$\langle v_j^f | v_j^i \rangle \neq 0 \text{ for all } j \neq k$$

As distinct vibrational wavefunctions are orthogonal, this term will only be non-zero if all quantum numbers $v_{j \neq k}$ remain unchanged during the transition.

In combination, conditions (b) and (c) imply that overtone and combination band transitions are forbidden to first order. Anharmonicity can relax condition (b) and weakly allow overtones with $\Delta v_k = \pm 2, \pm 3$, etc. The appearance of combination bands is more subtle, and requires coupling between normal modes.

1.2.3 IRPD and Cryo-SEVI

IRPD spectroscopy is complementary to cryo-SEVI on a number of counts. Both techniques start with anions, allowing mass selection of the species of interest, and both rely

on cryogenic ion traps to produce anions in their lowest-energy structures and vibrational states. The energy resolution of the two techniques is similar as well, sufficient for clear distinction of vibrational features. Cryo-SEVI spectra demonstrate 3–5 cm^{-1} fwhm peak widths, typically limited by unresolved molecular rotational structure. In IRPD, resolution can be limited by rotational structure, or by the FHI free electron laser bandwidth, which lies between 2–7 cm^{-1} fwhm over the 450–1200 cm^{-1} range.

IRPD has proved to be more tenable than cryo-SEVI for the spectroscopy of large clusters. For species with a large change in geometry between anion and neutral, the Frank-Condon envelope of the photoelectron spectrum can become very congested, especially for systems with many vibrational modes. With IR spectroscopy however, there is typically only one peak per IR active mode, leading to simpler, more easily simulated and interpreted spectra. Characteristic OH, CH, and NH stretches are also often IR active but not FC active. Additionally, because our IRPD experiments probe only the anion vibrations, there are fewer electronic states to consider, and no need to worry about, for instance, autodetachment processes, which can out-compete direct detachment in photoelectron spectroscopy of large clusters.

In short, while SEVI spectra may contain more information and also reflect on the vibronic structure of the neutral, IRPD spectra of the corresponding anion are simpler and more interpretable for large cluster systems. As the selection rules for the two types of spectroscopies are quite different, the two methods in combination can be an extremely powerful structural probe of clusters.

1.3 Applications

We have investigated a diversity of systems with the cryo-SEVI and IRPD spectroscopy techniques. This section briefly summarizes the molecular species that are detailed in the following chapters of this thesis. Broadly, the systems discussed herein can be classified either as molecular clusters or radicals.

Radicals are exotic molecules quite amenable to study with anion PES. As open-shell species, radicals are difficult to produce cleanly and with high number density, and are therefore difficult to study with most spectroscopic methods. However, radicals typically have positive electron affinities, and using anion PES, their vibronic structure is easily probed through detachment of the corresponding mass-selected closed-shell anion. With the enhanced ion cooling and high resolution afforded by cryo-SEVI, we can report accurate electron affinities, fundamental vibrational frequencies, and term energies of low-lying electronic states of organic radicals.

With the ability to mass-select anions prior to spectroscopic interrogation, both cryo-SEVI and IRPD are excellent methods for size-dependent cluster studies. The evolution of geometries, bonding motifs, electronic structure, energetics, and other properties can be tracked as a function of cluster size as one approaches the bulk limit.

1.3.1 Interstellar Species

Interstellar space is a strange environment characterized by an extremely low density of atoms and molecules, low temperatures, and constant UV radiation. A rich complexity of clusters and radicals abounds in space, though the exact identities of many of these species are unknown. Diffuse interstellar bands (DIBs) are ubiquitous absorption features in interstellar spectra, caused by unknown absorbing species present in the interstellar medium. The assignment of DIBs to particular molecules is a major unsolved problem in astrochemistry. Accurate spectroscopic characterization of these species in the laboratory with techniques like cryo-SEVI is crucial to their identification in astrochemical data.

A cryo-SEVI study of the linear cumulene carbon cluster, C_5, is discussed in Chap. 3. Carbon clusters are structurally complex and of great interest in interstellar, plasma, and combustion chemistry. Small C_n carbon clusters are predominantly linear, while cyclic structures become important beginning around $n = 10$, and at larger n still, spheroidal fullerene cages dominate.[99] Even for the small linear C_5 cluster and its corresponding anion, the vibrational and electronic structure is quite complicated. The cryo-cooling capabilities of the new ion trap in the SEVI instrument were first tested with this system, as the C_5^- anion has a spin-orbit (SO) excited state lying only $25\,cm^{-1}$ above the ground state. Depopulation of this excited state upon cooling served as a sensitive thermometer for measuring the cryogenic temperatures of our ions after extraction from the trap. The improved spectral clarity afforded by cryo-cooling allowed us to measure new vibrational fine structure and subtle vibronic coupling effects in the C_5 system.

Chap. 4 presents a cryo-SEVI study of the cyanomethyl radical, CH_2CN. CH_2CN is important astrochemically as an open-shell carbon-containing species, and the transition from the electronic ground state of the CH_2CN^- anion to its excited dipole bound state is a plausible candidate for the 803.79 nm DIB.[100] We reported improved electron affinities for CH_2CN and CD_2CN, and new vibrational structure involving activity of the ν_5 hydrogen umbrella modes and the ν_6 out-of-plane bending modes. CH_2CN was a system studied early after the installation of the ion trap, as temperature control was incredibly important for spectral clarity and interpretation. Temperature-dependent SEVI spectra showed effects ascribed to controlled population of low-lying anion vibrational levels. We directly measured the inversion splitting between the first two eigenstates of the anion ν_5 umbrella mode in both species. Additionally, CH_2CN and CD_2CN are two of the few systems where observation of rotational structure is possible with SEVI, due to one large rotational constant and nuclear spin state statistics. The resolution and interpretation of this rotational structure was also only possible because of cryogenic ion temperatures.

1.3.2 Aromatic Radicals

The addition of cryo-cooling expanded the purview of SEVI to larger, more complex molecules, with many low-frequency vibrational modes and congested Franck-Condon envelopes. For all the aromatic systems discussed here, we demonstrated the efficacy of high-

resolution photoelectron imaging in combination with cryo-cooling for untangling the vibronic structure of complex radicals.

Chap. 5 discusses cryo-SEVI spectroscopy of the *ortho*-hydroxyphenoxy radical (*o*-HOC_6H_4O). As a deprotonated derivative of catechol, *o*-HOC_6H_4O is a useful model for the photochemistry of larger bio-molecules. Characterizing excited state surfaces and the dynamics of non-radiative relaxation pathways in these species can elucidate the chemistry subsequent to photoexcitation of biological systems. We obtained vibrationally resolved spectra of the first three electronic states of the ortho-hydroxyphenoxy radical, newly resolving the energetics and vibrational frequencies of these states.

Chaps. 6 and 7 discuss SEVI studies of the deprotonated polycyclic aromatic hydrocarbon (PAH) radicals α- and β-naphthyl ($C_{10}H_7$) and 9-, 1-, and 2-anthracenyl ($C_{14}H_9$). PAHs are important combustion intermediates, bridging the gap between molecular-scale combustion chemistry, and the nucleation and aggregation of soot particles.[101] Larger PAHs are also likely constituents of the interstellar medium. In both combustion and astrochemistry environments, PAHs likely exist in some equilibrium of neutral and ionic, and hydrogenated and dehydrogenated states. The naphthyl and anthracenyl radicals and anions serve as tractable models for the chemistry of these important aromatic systems. The use of trimethylsilyl-substituted gas phase synthesis precursors allowed for the acquisition of isomer-specific SEVI spectra for these species. We reported spectra of the ground and first excited states of the naphthyl and anthracenyl radical isomers, with electron affinities, term energies, and vibrational structure sharply resolved and assigned for the first time. These results demonstrate how subtle structural differences between isomers can be characterized spectroscopically.

1.3.3 Transition Metal Oxide Clusters

Catalysts based on transition metal oxides catalyze many reactions fundamental to chemistry. There is considerable interest in developing a molecular-level understanding of what underlies this chemistry. Much of the interesting chemistry on surfaces happens at defect sites, where the local stoichiometry and bonding motifs differ from the bulk crystal structure. In addition to being tractable for both experimental and computational study, small clusters have a high proportion of surface atoms that can be highly reactive, in analogy to surface defects.[102] Clusters display dramatically different structures and reactivity as a function of size; their study can therefore elucidate the evolution of properties and emergence of macroscopic phenomena as one moves towards the bulk. By determining how the size and composition of a cluster governs its reactivity, one can gain insights into the workings of bulk catalysts.

Early cryo-SEVI studies of small metal oxide clusters are detailed in the thesis of Jongjin Kim.[50] More recent SEVI and IRPD work has pushed towards spectroscopic studies of larger clusters and their reactive complexes with substrates, as more explicit models of catalysis.

A cryo-SEVI study of the Fe_4O and Fe_5O iron monoxide clusters is discussed in Chap. 8. Iron oxide materials are used in a variety of catalysts and catalyst supports; iron monoxide clusters can serve as model systems for oxygen-deficient reactive sites on the bulk surface.

Our spectra illuminate the structural isomers, electronic and spin states, and vibrational frequencies of these species. This work demonstrated that even clusters involving four or five metal centers, with complicated electronic structure and competing low-energy structural isomers, can be characterized in high resolution with good agreement between spectroscopic and theoretical methods.

Chaps. 9 and 10 focus on IRPD studies of $(TiO_2)_n^-$ clusters and their complexes after adsorption of water, $[(TiO_2)_n(D_2O)_m]^-$. TiO_2 is an important, extensively-studied semiconducting material, with applications as a catalyst, photocatalyst, catalyst support, and pigment.[103] Most importantly, TiO_2 has been shown to be a viable photocatalyst for water splitting and CO_2 reduction. While we were able to carry out successful SEVI studies of $(TiO_2)_n^-$ with n=1,2, the photoelectron spectra of clusters with $n \geq 3$ contained broad, unresolved structure, likely due to the floppy, delocalized structures xhibited by these larger clusters. IRPD spectroscopy proved a more tractable method for the study of these clusters. The IRPD spectra of $(TiO_2)_n^-$ (n=3-8) were well-resolved, and through comparison with simulated spectra, allowed us to interpret and assign cluster structures and vibrations. We subsequently studied the complexes formed after reaction of $(TiO_2)_n^-$ (n=2-4) with one, two and three water molecules, allowing conclusive assignment of the post-reaction cluster structures through their vibrational signatures. This work illuminates the size- and site-specific reactivity of $(TiO_2)_n^-$ anions, and aids in understanding their utility as model systems for catalysis on the point defects of a bulk TiO_2 surface.

1.3.4 Transition State Spectroscopy

Direct observation of the reaction transition state has been proclaimed one of the "holy grails" of chemistry.[104] Characterization of this unstable species - its geometry, energy relative to the product and reactant asymptotes, and vibrational frequencies - can provide a wealth of information about the reactive potential energy surface and how it governs chemical behavior.

Anion PES is one of the few ways to spectroscopically access neutral transition states on unimolecular and bimolecular reactive surfaces.[10,105] Here, photodetachment of a bound anion similar in geometry to the desired neutral transition state can yield a spectrum showing structure very sensitive to the shape of the neutral potential energy surface. It is possible to observe Franck-Condon structure in modes perpendicular to the reaction coordinate and, often more interestingly, sharper features corresponding to discrete quantum states that are quasibound along the reaction coordinate.[105] Such resonances along the reaction coordinate are very sensitive probes of the surface near the transition state, and are an exceptional point of comparison between theory and experiment.

The first anion PES transition state spectroscopy experiments were carried out in the Lineberger group beginning in the 1980s, and probed unimolecular isomerization surfaces.[9,10,106] The transition state spectroscopy of bimolecular reactions was developed in the Neumark group, and took off in the late 1980s and early 1990s with studies of hydrogen abstraction reactions and heavy-light-heavy systems.[107]

The contribution of anion PES to the search for experimental proof of reactive resonances and transition state structure is best demonstrated through a brief history of the benchmark and much-beloved $F + H_2$ reaction. Molecular beam scattering experiments in the 1980s by Y.T. Lee's group raised questions about reactive resonances in $F + H_2$,[108] but the first definitive sign of reactive resonances didn't come until 2000, where Kopin Liu's group saw a distinct feature in the energy dependence of the integral cross section of $F + HD$.[109]

The first anion photoelectron spectrum of $F + H_2$, via detachment of FH_2^-, was reported by the Neumark group in 1993.[110] The FH_2^- anion has similar bond lengths to the neutral transition state, but is linear while the transition state is bent. As a result, the photoelectron spectrum is dominated by a Franck-Condon progression in the H−H hindered rotor or bending motion. The early anion PES studies could resolve this progression, but saw no hints of reactive resonances. These studies still served as a good benchmark for the state-of-the-art potential energy surfaces of the time. A call to action came in 1996, when improved simulations indicated that sharp features corresponding to resonances in the $F + H_2$ reactant and product wells should be visible in a photoelectron spectrum with 1 meV resolution.[111] Traditional photoelectron spectroscopy lacked the resolution to see these features. The FH_2^- anion has very poor photodetachment cross section close to threshold, making it impossible to study with ZEKE. It took until 2012 for a SEVI study to be published showing a hint of a predicted product resonance.[112]

We revisited the $F + H_2$ reaction with cryo-SEVI in 2014, and finally resolved the long-predicted reactive resonances in the $F+H_2$ product and reactant wells, and near the transition state (Chap. 11). Updates to the SEVI machine since 2012 drastically improved our ability to resolve these resonances (Chap. 2). Theoretical support from David Manolopoulos, Millard Alexander, and Jacek Kłos and new high-quality potential energy surfaces[113] lead to unprecedented agreement between experiment and simulation.

With the $F + H_2$ study, theory was a few decades ahead of experiment in terms of predicting these resonances. We are now moving on to larger reactive systems that are more challenging to model computationally. Most recently, we have extended the cryo-SEVI transition state spectroscopy technique to $F + CH_3OH$, a hydrogen abstraction reaction with 15 degrees of freedom (Chap. 12). The cryo-SEVI spectrum shows a manifold of finely spaced quasibound vibrational states in the CH_3OHF product van der Waals well. These progressions have contributions from high-frequency H−F stretching in the product van der Waals complex and low-frequency stretching of the two product fragments with respect to one another along the reaction coordinate. Our collaborators Hua Guo, Jun Li, Lifen Guo, and Jianyi Ma have constructed a state-of-the-art full-dimensional potential energy surface for this reaction in order to perform quantum dynamics trajectories and simulate the photoelectron spectrum. The level of agreement between theory and experiment is astonishing considering the size and complexity of the system. This work shows the utility of cryo-SEVI as a benchmark for increasingly intricate models of bimolecular reactions.

Chapter 2

Experimental Methods

2.1 Slow Photoelectron Velocity-Map Imaging (SEVI)

2.1.1 Experimental Overview

The SEVI method and apparatus have been described in detail previously in the literature,[35,49,114] and in the Ph.D. theses of several previous graduate students.[50,93,94,115,116] A schematic of the current configuration of the cryo-SEVI machine is shown in Fig. 2.1.

The individual components of this apparatus are detailed systematically in the following sections. Anions are generated using either a filament ionizer or a laser ablation source (Section 2.1.2), and are directed with radiofrequency ion guides to the cryogenic ion trap (Section 2.1.3). Inside the trap, the ions are thermalized to their ground vibrational and electronic states before extraction into a time-of-flight mass spectrometer (Section 2.1.4). Anions of the desired mass are photodetached and the kinetic energies of the resulting photoelectrons are imaged with a velocity-map imaging (VMI) spectrometer (Section 2.1.5). The ions are photodetached just above transition thresholds and the VMI is operated with low extraction voltages, so the slowest electrons are preferentially detected and magnified

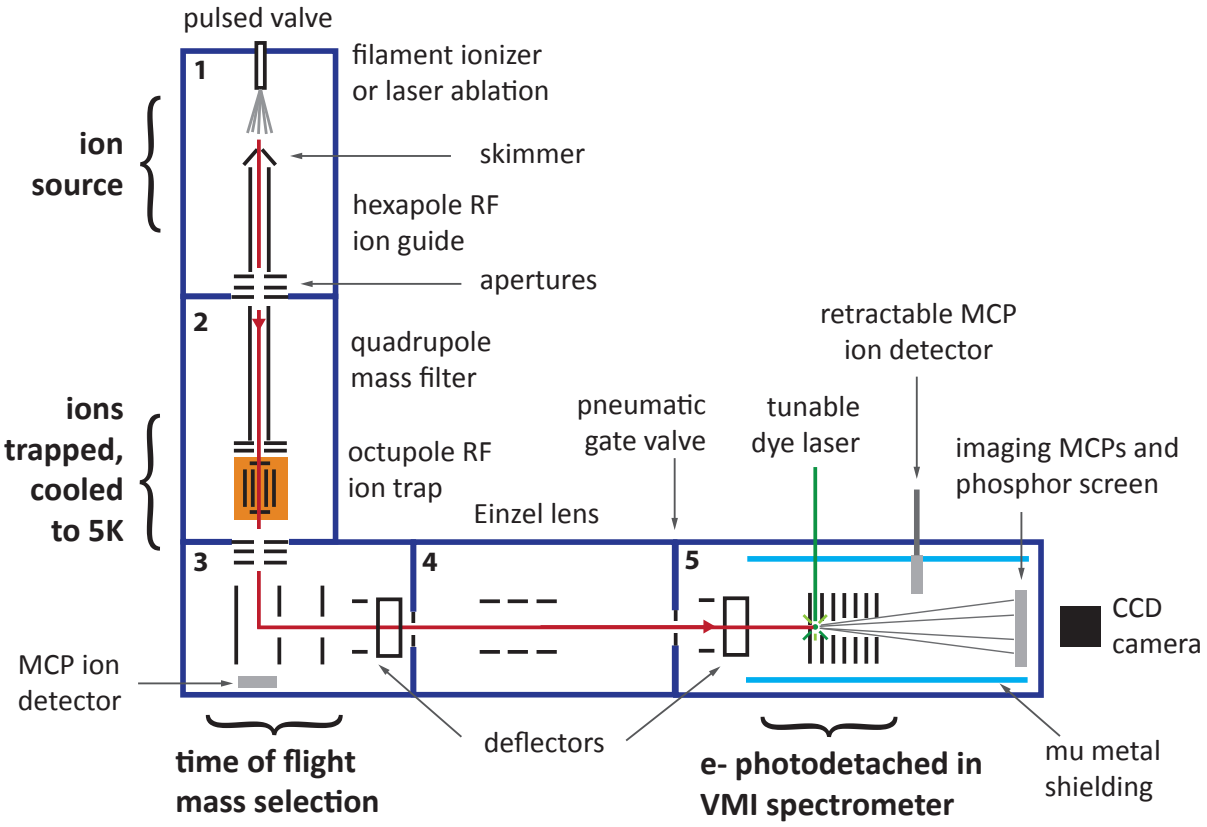

Figure 2.1: Schematic of the cryo-SEVI apparatus.

on the imaging detector, resulting in high energy resolution. Individual electron events are recorded and binned (Section 2.1.6) to form a 2D image from which the 3D distribution of electron velocity vectors is reconstructed (Section 2.1.7). The spectrometer is calibrated using images of well-known photodetachment transitions (Section 2.1.8). Detachment is carried out using a tunable-wavelength laser system spanning the mid-IR to the near-UV (Section 2.1.9).

The SEVI machine consists of five differentially pumped vacuum regions, numbered 1-5 in Fig. 2.1. Each region is evacuated by a separate magnetically levitated turbomolecular pump backed by a mechanical pump. The pumps used for each region are listed in Table 2.1, and typical chamber and foreline pressures for each region are listed in Table 2.2.

The timing triggers for all pulsed components of the apparatus are generated by a Quantum Composers model 9520 pulse generator and three Stanford Research System DG535 digital delay generators. Typical timings used are detailed in Table 2.3.

Table 2.1: Pumping configuration for cryo-SEVI vacuum chambers.

Region	Turbo pump	Pumping speed for N_2 (L/s)	Mech. pump
1	Seiko Seiki STP-A2203C	2200	Welch DuoSeal 1397
2	Boc Edwards STP-H2001K	2200	Edwards E2M40
3	Shimadzu TMP-803M	800	Edwards E2M18
4	Shimadzu TMP-303M	320	Edwards E2M18
5	Seiko Seiki STP-400	420	Varian SD-300

Table 2.2: Typical operating pressures for cryo-SEVI vacuum chambers. Pressures are listed for when the machine is not in use (off), and when the source and trap valves are in use (running).

Region	Chamber pressure (torr)		Foreline pressure (torr)	
	off	running	off	running
1	5×10^{-8}	2×10^{-5}	5×10^{-3}	2×10^{-2}
2	5×10^{-8}	3×10^{-6}	5×10^{-3}	8×10^{-3}
3	5×10^{-8}	1×10^{-7}	5×10^{-3}	5×10^{-3}
4	5×10^{-8}	5×10^{-8}	5×10^{-3}	5×10^{-3}
5	1×10^{-8}	1×10^{-8}	1.5×10^{-2}	1.5×10^{-2}

Table 2.3: Typical timings used for triggering various components of the cryo-SEVI apparatus. The Wiley-McLaren plate timings are optimized for transmission of species of different masses. The spectroscopy Nd:YAG Q-switch, mass gate, and imaging gate timings are changed according to the time-of-flight of the anion of interest.

	Component	Timing		Trigger width
A	source valve (Even-Lavie)	T_0+	5 ms	rising edge
	ionizer	A+	200 µs	100 µs
B	ablation Nd:YAG Q-switch	A+	180 µs	10 µs
	ablation Nd:YAG flashlamp	B−	280 µs	10 µs
	trap valve (Parker)	A−	2 ms	rising edge
C	trap exit electrode	A+	38 ms	1 ms
D	Wiley-McLaren plate 1	C+	20–80 µs	4 µs
	Wiley-McLaren plate 2	D+	200–800 ns	3 µs
E	spectroscopy Nd:YAG Q-switch	D+	10–100 µs	10 µs
	spectroscopy Nd:YAG flashlamp	E−	250 µs	10 µs
	mass gate	D+	10–100 µs	800 ns
	MCP imaging gate	D+	10–100 µs	300 ns
	CCD camera	D−	300 µs	rising edge

2.1.2 Anion Source

Two methods of anion production can be used in the SEVI anion source: a circular filament ionizer to produce molecular anions and a laser ablation cluster source. Both methods are built around a low repetition rate Even-Lavie (EL) valve[117] valve pulsed at 20 Hz. The valve is typically open for 40–80 µs, and backed with 150 psi helium carrier gas containing trace molecular precursors and reactants as needed.

2.1.2.1 Filament Ionizer and Source Chemistry

The filament ionizer allows us to produce a variety of organic molecular anions. We use a commercial filament ionizer made by the same Israeli company as the EL valve (LAMID Ltd.), though their ionizers are no longer in active production. The ionizer consists of a 1" diameter loop of thoriated tungsten filament mounted 1/4" after the valve nozzle, such that the pulse of gas will pass through its center. A constant DC current of 3–4 A runs through the filament, resulting in thermionic emission of electrons. The filament is concentrically surrounded by a metal anode, and itself surrounds a cylinder of grounded wire mesh. Both the anode and the filament are pulsed to −300 V for ∼150 µs to bombard the pulse of gas from the EL valve with electrons.

The primary electrons from the ionizer collide with the carrier gas, producing secondary electrons. The secondary electrons go on to react with the entrained molecular precursors,

with chemistry usually initiated by dissociative electron attachment. The fact that the desired species are charged and will be mass-selected at a later stage means that the source conditions are forgiving, and the synthesis techniques need not be particularly clean. One caveat is that the filament ionizer produces relatively hot anions. Before the addition of the cryogenic ion trap to the SEVI apparatus (Section 2.1.3), a grid discharge source was used instead, to produce ions that were vibrationally and rotionally colder.[93]

There are a variety of ways to entrain a molecular precursor in the helium carrier gas. For gas phase precursors, we use a manifold to make a mixture of ∼0.1–1 % precursor in helium. For volatile liquid precursors, we pull some vapor pressure off the liquid sample and mix it with helium. For nonvolatile liquids and solid precursors, the EL valve has a built-in cartridge that can be packed with a sample and heated. A water-cooling jacket can also be mounted around the EL valve to more carefully control the valve temperature and prevent degradation of more sensitive molecular samples in the cartridge.

Some molecular anions of interest can be synthesized directly through dissociative electron attachment to a precursor. For instance, to prepare the CH_2CN^- anion studied in Chap. 4, we put trace acetonitrile in the source mixture:

$$CH_3CN + e^- \longrightarrow CH_2CN^- + H \tag{2.1}$$

Depending on the desired source chemistry, trace NF_3 or N_2O are often added to the source mixture to make F^- and O^- respectively, through dissociative electron attachment:

$$NF_3 + e^- \longrightarrow F^- + NF_2 \tag{2.2}$$
$$N_2O + e^- \longrightarrow O^- + NO \tag{2.3}$$
$$\tag{2.4}$$

These atomic F^- and O^- anions are often used in anion synthesis as proton scavengers to yield deprotonated species of interest like the o-$HOC_6H_4O^-$ anion studied in Chap. 5

$$o - HOC_6H_4OH + F^- \longrightarrow HOC_6H_4O^- + HF \tag{2.5}$$

or the vinylidene anion:

$$H_2C{=}CH_2 + O^- \longrightarrow H_2C{=}C^- + H_2O \tag{2.6}$$

Isomer-specific source chemistry can be carried out using custom synthetic precursors. A synthetic pathway we often use involves the reaction of a trimethylsilyl-substituted precursor with F^-. Due to the strength of the fluorine-silicon bond,[118] this reaction leads to an anion product that is deprotonated at a specific site. We used this method to prepare the 1- and 2-naphthyl and 9-, 1-, and 2-anthracenyl radicals in Chaps. 6 and 7.

Finally, we can produce weakly bound clusters with the ionizer, like the CH_3OHF^- anion used to carry out transition state spectrocopy on the $F + CH_3OH$ reactive surface in Chap. 12:

$$F^- + CH_3OH \longrightarrow CH_3OHF^- \tag{2.7}$$

Some clusters can also be synthesized directly in the ion trap, as discussed below in Section 2.1.3.

2.1.2.2 Laser Ablation

The laser ablation source is a versatile way to produce clusters of various sizes from materials with low vapor pressure, giving us access to a range of species that cannot be made with the filament ionizer. Laser ablation cluster sources were first developed in the 1980s by the Smalley group,[119,120] and former Smalley student Michael Duncan has written an excellent review article detailing their history and design considerations.[37]

The current configuration of the SEVI machine laser ablation source was designed and implemented in 2013 by Jongjin Kim, and is discussed in detail in his thesis.[50] The ablation source is mounted so that its gas channel connects directly to the output of the EL valve. A 2–10 mJ/pulse pulse of light from the 532 nm second harmonic of a Q-switched Nd:YAG laser (Continuum NY60B-2) is focused onto a solid disk sample target. The target which is rotated and translated by two motors so each laser pulse hits a fresh point on the sample, ablating the surface in an even spiral pattern. The motors are mounted inside vacuum and are fitted with water cooling jackets to prevent overheating.

Each laser pulse vaporizes the surface, creating a plasma of atomic cations and electrons. A pulse of buffer gas then quenches the plasma, initiating collisional cooling and condensation of the atoms into clusters. These clusters, now entrained in the buffer gas, then pass through a confined clustering channel, allowing further cluster growth and collisional cooling before expansion into vacuum. While ablation sources predominantly form cations and neutrals, anions are produced through electron attachment to neutral clusters in sufficient quantities for our purposes.

Laser ablation does produce very warm clusters. The initial plasma can create species in excited electronic states and cluster condensation is a significant heating process, especially for strongly bound species like metal oxide clusters.[37] During aggregation, the binding energy of each additional atom is deposited into the cluster. Because growth events can occur very late in the clustering channel, there is insufficient time for all clusters to be collisionally cooled, leading to a poorly thermalized population. Due to these considerations, laser ablation was not used successfully in conjunction with the SEVI machine until the addition of the cryogenic ion trap (Section 2.1.3).

While ablation sources with rod targets are most widely used, the SEVI ablation source was designed to use disk targets for a number of reasons. Commercial sputtering targets are sold as disks that fit our specifications (1" diameter, 1/4" thick) and are available for a wide

variety of metals, metal oxides, and semiconductor materials. It is also straightforward to press custom disk targets using a hydraulic press, if desired. Disk targets are easier to align than rod targets and they are less likely to jam while rotating. After heavy usage, a rod target can have a noticeably smaller radius, complicating alignment, while slow consumption of the flat side of a disk target presents no problems if the target is kept pushed in place with a spring.

In this thesis, the disk laser ablation source was used for cryo-SEVI studies of the C_5^- carbon cluster (Chap. 3) and the Fe_4O and Fe_5O iron monoxide clusters (Chap. 8). Carbon clusters are generated by ablation of a graphite target, while metal oxide clusters are generated using pure metal targets. We have found that it is not necessary to add oxygen to the buffer gas mixture in order to generate metal oxide clusters from metal targets as there is plenty of trace oxygen in the gas lines and residual oxides on the target surface.

Very recently, a second pulsed valve has been added to our ablation source in order to produce reactive adducts of metal oxide clusters; this modification will be detailed in the thesis of Jessalyn DeVine. The cluster reactor source design is based on early work from the Smalley group,[121] as well as more recent implementations in the Jarrold group[122] and the Asmis group[123] (see also Section 2.2 below).

2.1.3 Radiofrequency Ion Guides and Cryogenic Ion Trap

In 2011-2012, a major rebuild to the SEVI machine added a new source chamber, radiofrequency (RF) ion guides, and a cryogenic ion trap (regions 1 and 2 in Fig. 2.1). Previously, the ion source had been coupled directly into the time-of-flight mass spectrometer. These changes and characterization of the new capabilities of the instrument were reported by Hock *et al.*[49], and details regarding the design and construction of these new components can be found in the thesis of Jongjin Kim.[50] Fig. 2.2 shows the ion optics that now couple the ion source to the time-of-flight mass spectrometer and typical operating voltages are laid out in Table 2.4.

After formation in the source chamber, the ions pass through a skimmer and an aperture (ap1), which collimate the output from the pulsed valve and optimize coupling from the source into the RF guides. Ion transmission and temporal focusing of the ion packet are very sensitive to the voltages on these two components. The ions then pass into a hexapole RF ion guide, which robustly directs the ions into the subsequent regions of the machine, and improves collimation of the ion packet. Ion transmission is not overly sensitive to the amplitude of the RF voltages applied to the hexapole guide rods. However, the bias voltage applied to all six hexapole rods is quite important, and must be tuned significantly depending on source chemistry.

The ions then pass through a set of three apertures set up like an Einzel lens (ap2, ap3) and into a quadrupole ion guide, which can either be used as an RF-only ion guide or as a quadrupole mass filter (QMF). There are two RF oscillator heads for use in different QMF mass ranges: one that operates at 1.25 MHz for mass selection up to 300 m/z, and one at 0.63 MHz for mass selection up to 1000 m/z. The QMF is often used to fill the ion trap down

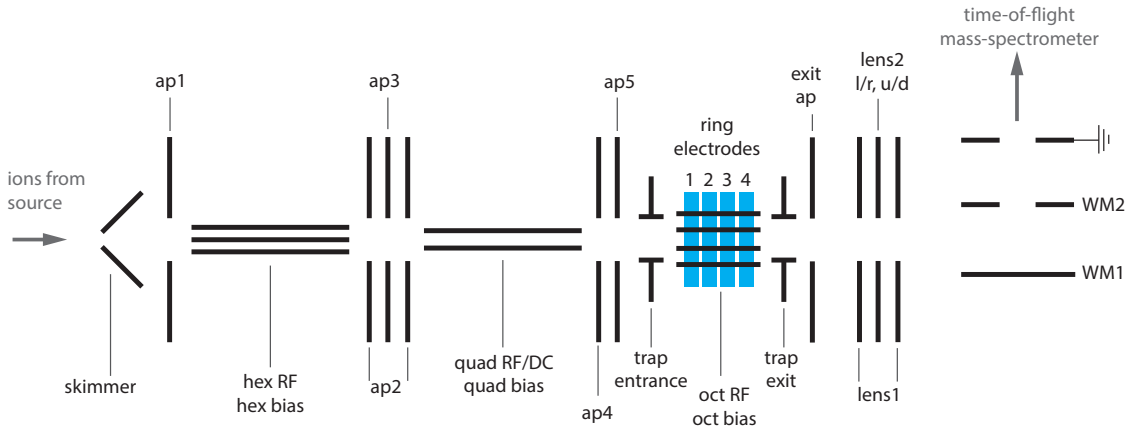

Figure 2.2: Schematic of ion optics in the cryo-SEVI machine.

Table 2.4: Typical voltages applied to ion optics in the cryo-SEVI machine, see Fig. 2.2.

Optic	Voltage
EL valve	0 V
skimmer	−20 V to −40 V
ap1	−10 V to −50 V
hex RF	100–300 Vpp, f=3 MHz
hex bias	−5 V to −20 V
ap2	20 V
ap3	80 V
quad RF/DC	mass dependent, f=0.63 MHz or 1.25 MHz
quad bias	−10 V to 10 V
ap4	20 V
ap5	60 V
trap entrance	−5 V to −10 V
oct RF	300–600 Vpp, f=3 MHz
oct bias	0 V to 1 V
ring electrodes 1, 2, 3, 4	−100 V, −10 V, 10 V, 100 V
trap exit	−16 V pulsed to 16 V for extraction
exit ap	−3 V to −10 V
lens1	15 V to 30 V
lens2	50 V to 80 V
lens2 l/r	−5 V to 5 V
lens2 u/d	−5 V to 5 V
WM1	1.80 kV
WM2	1.65 kV

the line with ions of a specific mass, improving number density of the desired species. Use of the QMF can be difficult in conjunction with the filament ionizer, as the desired anions are sometimes not produced until the reactive precursors undergo further collisions in the ion trap. The quadrupole bias voltage applied to all four rods can be somewhat important for ion transmission, especially when tuned in conjunction with the hexapole bias.

Leaving the quadrupole, the ions pass through two apertures (ap4, ap5) and approach the ion trap and surrounding ion optics. A cutaway view of this part of the instrument is shown in Fig. 2.3. The ion trap is a linear RF octupole trap,[49,50] motivated by the large body of work in the literature on the design and use of linear multipole ion traps for ion cooling and spectroscopy.[39,40,42,43,124] The ions are trapped radially by alternating RF voltages applied to the octupole rods and axially by trap entrance, exit and ring electrodes held at low DC voltages.

The effective radial trapping potential in a multipole trap goes like $V_{eff}(r) \propto r^{n-2}$, where n is the number of rods. For traps with large n, like the popular 22-pole trap, the radial pseudopotential is deep and quite flat in the center, leading to relatively poor radial confinement of the anions. This is acceptable when measurements are made directly inside the trap, but is not optimal when efficient extraction of the ions is required, as in our experiment. A quadrupole trap, on the other hand, has a pseudopotential with greater curvature at small r, leading to better radial confinement of the anions, but can also cause severe RF heating of the anions that experience buffer gas collisions in the wings of the radial potential.[39,124] An octupole trap was chosen for the cryo-SEVI apparatus as a compromise between anion confinement and RF heating concerns, allowing for both the production of cold ions and reasonable extraction efficiency from the trap.

The axial trap voltages are also designed to enhance ion transmission and extraction efficiency, as shown schematically in Fig. 2.4. The voltage on the entrance electrode is tuned to a small negative (repulsive) voltage to allow fast-moving ions from the source to enter the trap and prevent them from leaving after they have slowed through collisions with buffer gas. The exit electrode is set to a small negative voltage during trapping, and is pulsed to a positive voltage for ion extraction. Four ring electrodes (shown in black in Fig. 2.3) surround the octupole rods, creating a sloped potential that pools ions near the exit electrode in preparation for extraction. Different trap electrodes are kept electrically isolated using sapphire plates, which at cryogenic temperatures are simultaneously excellent electrical insulators and thermal conductors.

A microchannel plate ion detector is mounted after the trap, collinearly with the ion trap axis (Fig. 2.1). This allows the source, guiding, and trapping conditions to be tuned in order to optimize ion formation and transmission independent from the downstream components of the machine.

We use collisional cooling with cryogenic buffer gas inside the ion trap to thermalize molecular anions to low internal and translational temperatures. The trap itself is held at cryogenic temperatures to allow thermalization of the buffer gas through collisions with the trap surfaces. The octupole rods are encased by a copper box (shown in brown in Fig. 2.3) in contact with the 4 K second stage of a closed-cycle helium refrigerator (Sumitomo

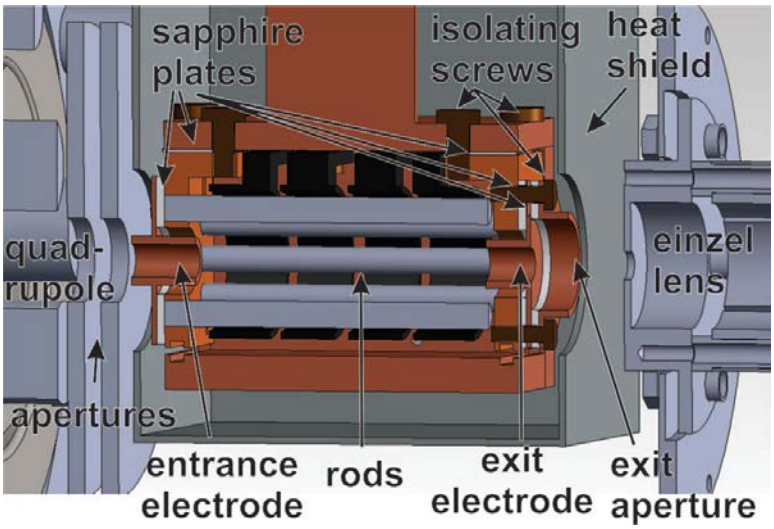

Figure 2.3: Cutaway view of the ion trap and nearby ion optics, adapted from Ref. [49].

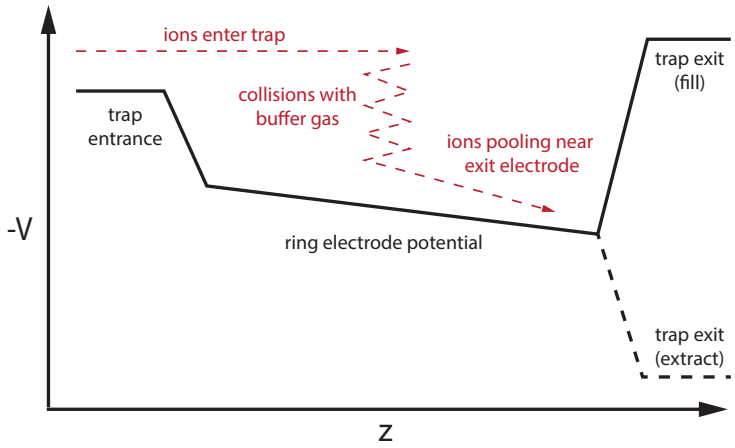

Figure 2.4: Schematic of axial trapping potentials in the ion trap.

RDK-408D2). This inner box is in turn enclosed by heat shielding in thermal contact with the 40 K first stage of the same helium refrigerator, which prevents radiative heating of the trap from the surrounding environment. Two silicon diodes (Lakeshore DT-670C-ET) mounted on either end of the inner trap enclosure measure the temperature in the 4–300 K range. A cartridge heater mounted on the inner trap enclosure allows the trap to be held at any temperature in this range and is controlled via a Stanford Research Systems CTC100 cryogenic temperature controller.

Slightly before the ions reach the trapping region, the trap is filled with a burst of buffer gas from a pulsed valve (Parker General Valve, Series 9) open for 300–400 µs. The valve is backed by ∼3 psi of an 80:20 He:H_2 buffer gas mixture via a vacuum regulator. The buffer gas is precooled to 40 K through thermal contact between the stainless steel tubing that backs the

valve and the first stage of the helium refrigerator. During operation, the vacuum chamber pressure surrounding the trap (region 2 of Fig. 2.1) is typically 3×10^{-6} torr, and pressure within the trap enclosure is estimated to be $\sim 1 \times 10^{-3}$ torr, accounting for conductance of gas out of the trap apertures. The ions are stored in the trap for up to 40 ms, the majority of our 20 Hz repetition rate cycle, and are expected to undergo 10^3–10^4 collisions given the trap pressure.[49]

The translational temperature of the anions is expected to be thermalized within roughly 100 collisions with helium buffer gas, or 0.1–10 µs.[38] The vibrational and rotational degrees of freedom of the warm anions take somewhat longer to thermalize, as rotations and vibrations are inefficiently coupled to translations via collisional energy transfer.[125] The addition of 20% H_2 in the buffer gas dramatically improves thermalization of vibrational degrees of freedom through energy transfer to the rotational and perhaps vibrational states of H_2.[36,52] In the event that the 20 Hz experimental repetition rate does not allow for adequate cooling, it is possible to run the experiment at 10 Hz and double the trap residence time, though this has not yet proved necessary.

Ion temperature is also quite sensitive to the buffer gas pressure inside the trap, with higher pressures generally leading to better cooling.[52] The use of a pulsed valve in the trap rather than a continuous leak valve is therefore important to achieve low ion temperatures. The initial pulse of buffer gas leads to higher pressures and more collisions when the warm ions first enter the trap. The buffer gas is then evacuated from the trap throughout the ion residence time, so the trap is nearly empty by the time the ions are extracted. The ions therefore undergo few collisions during extraction, which can lead to unwanted heating. It is expected that the ions remain slightly warmer than the buffer gas, due to RF heating and warming during extraction. We have measured ion temperatures as low as 10 K at the time of photodetachment, after thermalization with the trap held at 5 K.[49]

The cryogenic ion trap has allowed us to probe anions in their ground vibrational and electronic states and with considerably narrowed rotational distributions. This has facilitated high-resolution SEVI studies of molecular anions with low-lying vibrational and electronic states like C_5^- (Chap. 3) and CH_2CN (Chap. 4) and of large, complex species like polycyclic aromatic hydrocarbons (Chaps. 6 and 7) and polymetal oxide clusters (Chap. 8). The trap has also on occasion proved useful for synthesis of weakly bound clusters, like the FH_2^- anions used to probe the benchmark $F + H_2$ reactive surface (Chap. 11). FH_2^-(FD_2-) anions were formed by sending a beam of atomic F^- into the trap filled with pure H_2(D_2) buffer gas, dramatically improving the experimental signal compared to the use of a grid discharge or filament ionizer source.

2.1.4 Ion Packet Focusing and Mass Selection

Anions are extracted from the ion trap into an orthogonal Wiley-McLaren time-of-flight mass spectrometer (TOFMS).[126] The TOFMS is optimized to (a) spatially and temporally separate ions of different masses, and (b) to spatially and temporally focus the ion packet of the desired mass into the laser interaction region of the velocity-map imaging spectrometer.

A single-stage TOFMS achieves mass separation by accelerating all ions through a homogeneous electric field between two charged plates.[127] If the ions experience a voltage difference of ΔV in this field, an ion of charge q acquires a kinetic energy $E = \Delta V q$. We know $E = 1/2mv^2$ for an ion with mass m, so acceleration through this field leads to a final velocity of:

$$v = \sqrt{\frac{2q\Delta V}{m}} \tag{2.8}$$

After the ions fly through a field-free flight tube of distance d, ions of mass m therefore arrive at the detector at time $t = d/v \propto \sqrt{m}$.

A TOFMS also focuses ions in space and time along the TOF axis,[127] correcting for the spatial and velocity distribution of the initial ion packet as it enters the TOF extraction region. Again, let's consider an ion packet in the homogeneous electric field between the two plates of a single-stage TOFMS, being accelerated towards a detector. Ions that start farther from the detector spend more time accelerating through the electric field and therefore reach a faster velocity than ions that start closer to the detector. At a certain position in the flight path, these faster ions will catch up to the slower ones, and we achieve first-order spatial focusing. The location of this focus is fixed by the geometry of the TOF plates. In a Wiley-McLaren TOFMS, a second acceleration region (i.e. a third TOF plate) is added, providing an additional degree of freedom that can be used to tune the location of the first-order spatial focus, or to create a second-order spatial focus at a fixed location.

The focusing capabilities of our Wiley-McLaren TOFMS rely heavily on the quality of the ion packet as it enters the TOFMS extraction region. Great care must therefore be taken to optimize the focus and steering of the ions as they leave the trap. After the ions are extracted from the trap by a voltage pulse applied to the trap exit electrode, they pass through an additional aperture (exit ap in Fig. 2.2), and a homebuilt ion optic that combines both an Einzel lens and deflectors, described in detail in the thesis of Jongjin Kim.[50] This optic is an Einzel lens whose center electrode is split into four elements, allowing up/down and left/right deflection of the ion packet in addition to spatial focusing. The compact design is necessitated by the confined space between the ion trap and TOFMS plates.

The lens/deflector combination has proved essential to optimize coupling of the ions from the trap into the TOFMS. The ion transmission and the shape of the ion packet in time are incredibly sensitive to the voltages applied to this optic, as well as to the voltage applied to the exit aperture. Ions confined in RF linear multipole traps are known to form a donut-shaped spatial distribution around the central trap axis,[50,124] and the Einzel lens following the trap is essential to refocus this donut into a spherical packet. The orthogonal orientation of the TOF axis relative to the trap extraction axis is also important to minimize initial ion velocity spread along the TOF axis.

The first two TOF plates (WM1 and WM2 in Fig. 2.2) are initially held at low DC voltages ($\sim$3 V) as the ions are extracted from the trap, and are then pulsed to 1.8 kV and 1.6 kV for acceleration of the ions. The third plate is grounded. The apertures in the

second two TOF plates are covered by mesh grids to ensure that the acceleration fields are homogeneous. The timing with which the first two TOFMS plates are switched on is very sensitive to the mass of the desired anions. We also find that a slight delay between switching on the first and second plates is required for optimal ion transmission, and is also quite sensitive to mass (see Table 2.3).

In the TOFMS, the ions fly through a field-free region of ∼2 m before reaching the laser interaction region. Along the flight path are two sets of up/down and left/right ion deflectors. Each deflector consists of a pair of plates lying parallel to the ion trajectory (Fig. 2.5); the voltage between the two plates deflects the ions as they fly between the plates. The first set of deflectors is located shortly after the Wiley-McLaren plates, while the second set of deflectors is shortly before the velocity-map imaging lens. The two sets of deflectors are tuned in combination to steer the ion packet through three 3 mm apertures into the interaction region (see Section 2.1.5). If the steering is slightly off, the ion packet can glance off an aperture and scatter electrons into the interaction region, resulting in background noise. The second set of deflectors is also used as a mass gate to ensure that only anions of the desired mass enter the interaction region. A voltage of −50 V is applied to the left/right deflectors, and is pulsed to the correct voltage to transmit ions for a window of a few hundred microseconds.

Each set of deflectors is followed by an Einzel lens (Fig. 2.5) to improve the spatial focus of the ion packet along the axes normal to its trajectory. The central electrode of the Einzel lens after the first set of deflectors is set to 2.2–2.4 kV. The Einzel lens following the second set of deflectors was found to be superfluous and is not typically used.

The TOF mass spectrum is recorded on a retractable detector mounted after the velocity-map imaging lens (Fig. 2.1), consisting of a chevron stack of two 1" microchannel plates and a current collection anode.[116] A pneumatic gate valve separates the source and trapping

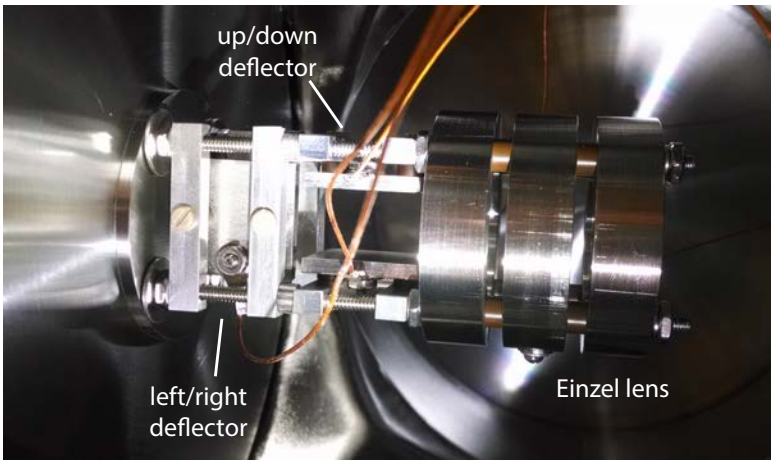

Figure 2.5: The second set of ion deflectors and out-of-use Einzel lens in the machine chamber just before the velocity-map imaging stack.

vacuum chambers from the detector region of the apparatus, so the former can be serviced without venting the detector region.

2.1.5 Velocity-Map Imaging Spectrometer

From the TOFMS, the anions fly into the interaction region of a velocity-map imaging (VMI) spectrometer, with which we measure the velocity distribution of the nascent photoelectrons after detachment. The VMI spectrometer is the key component of the SEVI apparatus that allows us to acquire spectra with energy resolution down to $1\,\mathrm{cm}^{-1}$.

Historically, high-resolution photoelectron imaging has its roots in ion imaging. The seminal work in this field was reported by Chandler and Houston in 1987.[13] The authors resonantly ionized molecular fragments formed after photodissociation and used a homogenous electric field between two electrodes to project the 3D spatial distribution of the fragments onto a 2D imaging detector. The radial and angular distributions of the resulting image reported on the kinetic energy release and anisotropy of the photodissociation process. Another significant development came a decade later, when Eppink and Parker[14] reported that the electric field used to extract the ions could be tuned to significantly improve the image focus at the detector. The Eppink-Parker VMI lens design consists of two acceleration regions between three electrodes with open apertures rather than mesh grids. Lensing of the electric field around the apertures allows focusing of charged particles with different initial positions but identical velocity vectors to the same point on the detector screen, as shown in Fig. 2.6. This counteracts the blurring caused by projection of the interaction region volume onto the detector.

In the SEVI apparatus, the ions enter the VMI collinearly from the TOFMS, so any spread in ion velocities along the TOF axis does not translate into spread in photoelectron velocities

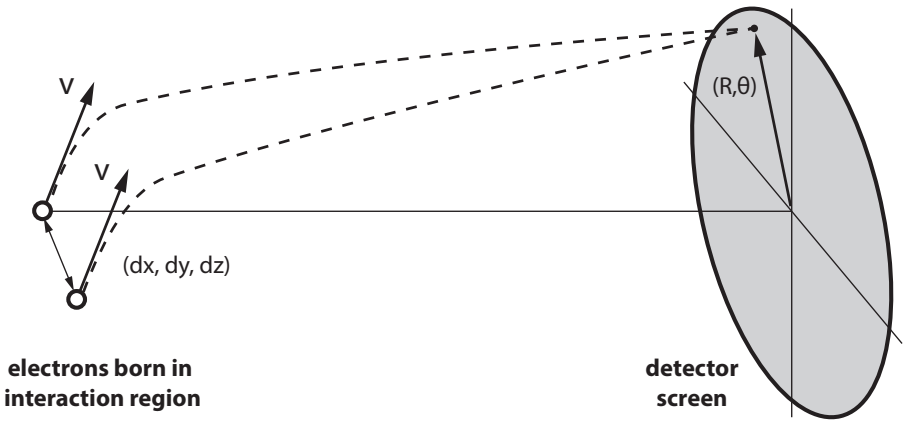

Figure 2.6: A VMI lens focuses two electrons with identical velocity vectors born at different locations in the interaction region to the same point on the detector screen.

in the plane of the detector, which would blur the resulting image.[55] Before reaching the interaction region, the ions fly through three 3 mm diameter apertures. The third aperture is in the repeller plate. The first two apertures are inside a metal tube, on which the VMI stack is mounted. This tube was formerly designed for a pulsed scheme to rereference the anions to the repeller voltage.[115] The referencing tube is now simply held at the DC repeller voltage and used as a convenient means to mount the VMI lens and the apertures preceding it.

The basic Eppink-Parker VMI design is shown in Fig. 2.7a, and a photograph of its implementation in our machine is shown in Fig. 2.8a. We used this lens design in the cryo-SEVI machine until late 2014. The first two electrodes of this design are called the repeller and extractor; the third plate is grounded. The repeller voltage (V_R) is tuned to change the size of the image on the detector, while the extractor voltage (V_E) is tuned with respect to V_R to bring the image into focus.

The ions are intersected at 90° by the photodetachment laser between the first two VMI plates (Fig. 2.7a). Photoelectrons are detached and accelerated into the VMI flight tube, which is approximately 50 cm long and shielded from external magnetic fields by two layers of mu metal shielding. As it flies, the cloud of electrons expands until it hits a 75 mm diameter imaging detector consisting of two chevron-stacked imaging-quality micro-channel plates (MCPs) coupled to a phosphor screen. The front of the first MCP is grounded, while the back of the second MCP is pulsed from 1 kV to 2 kV during the window when electrons arrive, to reduce background noise from dark counts. The phosphor screen is held at 6 kV. The MCP/phosphor assembly was purchased as a unit from Burle (now Photonis). The MCPs have 25 µm pore diameter, 32 µm center-to-center pore spacing, 8° pore bias angle relative to the plate surface, and a 40:1 pore length:diameter aspect ratio. See Sections 2.1.6 and 2.1.7 for details on how the VMI images are acquired, accumulated, and reconstructed.

The VMI stack was one of the only components of the machine that had not been changed during the 2011-2012 cryo-SEVI rebuild. We became inspired by the burgeoning developments in VMI lens design in the ion and photoelectron imaging literature. Several groups reported improved resolution compared to the Eppink-Parker lens. We therefore set about designing a new lens, as detailed in the next section.

2.1.5.1 Modification of the VMI Lens

In late 2014, we modified the original three-electrode Eppink-Parker VMI design[14] to improve the energy resolution of our cryo-SEVI spectra. The new VMI lens configuration is shown in Fig. 2.7b and a photograph of its implementation in our lab is shown in Fig. 2.8b. The major goal of this modification was to improve the energy resolution for eKEs in the range of a few hundred to a few thousand wavenumbers. This is the regime in which SEVI is forced to operate for anions with poor threshold photodetachment cross sections. Additionally, a SEVI spectrum over a particular energy range can now be obtained with fewer high-resolution windows. This lens has been used for all our work published after 2015. The cryo-SEVI studies reported in this thesis for C_5^- (Chap. 3), CH_2CN^- (Chap. 4),

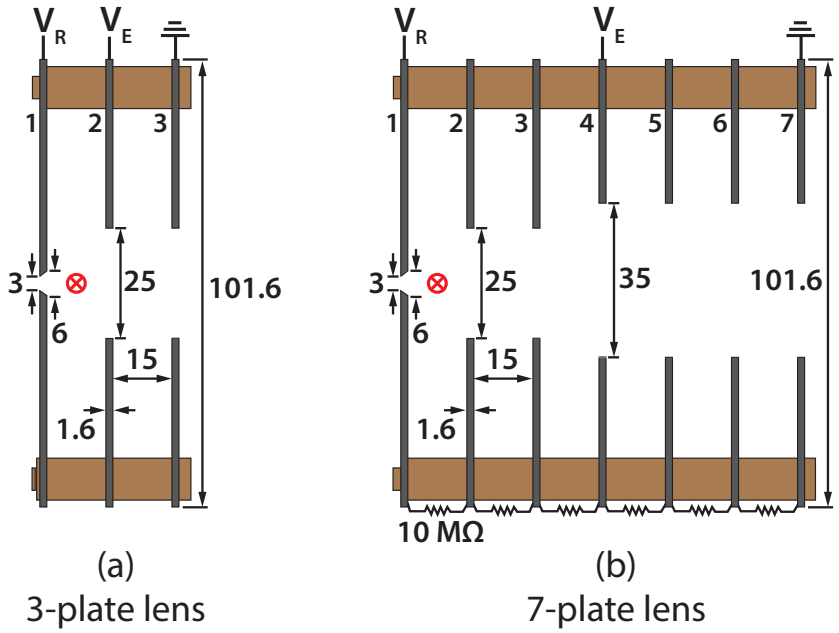

Figure 2.7: Configuration of (a) the 3-plate Eppink-Parker VMI lens and (b) the redesigned 7-plate VMI lens, with electrodes in gray and Vespel spacers in brown. In both designs, ions enter the lens from the left and interact with the laser halfway between plates 1 and 2, indicated in red. All lengths are in millimeters.

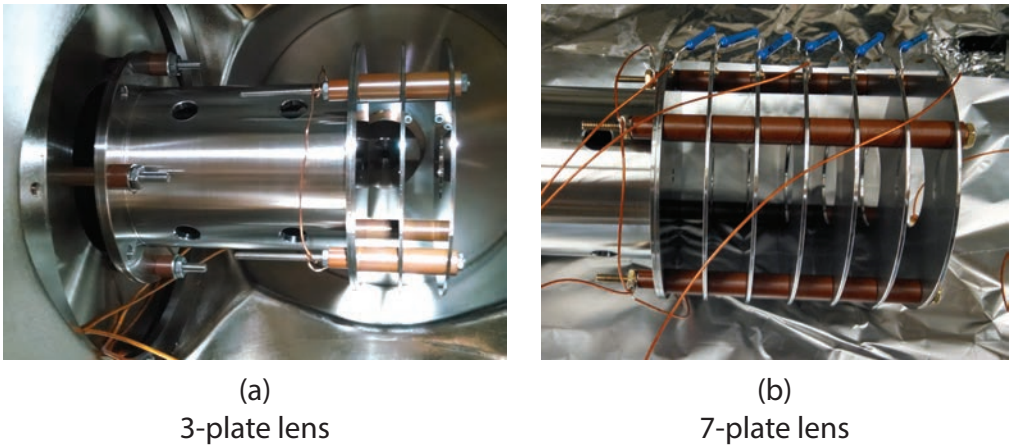

Figure 2.8: Photos of (a) the 3-plate Eppink-Parker VMI lens mounted inside the SEVI machine and (b) the redesigned 7-plate VMI lens. In both cases the VMI stacks are mounted on the former rereferencing tube.

ortho-hydroxyphenoxide (Chap. 5), 1- and 2-naphthyl (Chap. 6), and FH_2^- (Chap. 11) made use of the old Eppink-Parker lens, while the 9-, 1-, and 2-anthracenyl (Chap. 7), Fe_nO^- (Chap. 8), and CH_3OHF^- (Chap. 12) studies use the new lens.

Several alternative VMI designs with excellent focusing capability for photoelectrons have been reported in the literature.[53,55,128–131] In 2003, Arthur Suits' group reported on the first post-Eppink-Parker VMI lens design optimized for sliced ion imaging.[128] This design incorporated a third acceleration region (or equivalently, a fourth electrode), providing an additional degree of freedom to tune the focusing properties of the lens. This configuration is excellent for slice imaging, as it results in an ion packet that is spatially and temporally stretched along the time-of-flight axis. An added bonus of this slicing lens is that by sacrificing the temporal focusing at the detector, the velocity focusing can be dramatically improved. (Slicing is unfortunately not viable for imaging photoelectrons, as they move too quickly to gate just a central slice.)

Similar lenses with three acceleration regions have subsequently been developed for high-resolution velocity-map imaging of photoelectrons, in the research groups of Bernd von Issendorff[55] and Lai-Sheng Wang.[53] Both of these designs, in addition to adding a fourth electrode, also increase the total length of the VMI lens along the photoelectron flight axis, which can significantly improve focusing. VMI lens designs by Cavanagh *et al.*,[129] Ogi *et al.*,[130] and another project here in the Neumark group[131] have also achieved excellent focusing by retaining the two acceleration regions of the Eppink-Parker lens, but extending its length.

The improvement of VMI focusing power with increasing length can be rationalized quite simply: the larger the lens, the more the interaction region looks like a point source and the better its spatial spread can be corrected. The interaction region also looks more like a point source when the apertures in the VMI electrodes are larger, which allows for smoother curvature of the electric field and less distortion of electron trajectories. However, if the plate apertures are too large compared to the spacing between electrodes, we no longer have a clear transition in electric field strength from one acceleration to the next, and the plates must be moved further apart. Hence, the best focusing can be achieved with both increased stack length and electrode apertures. However, adding distance between electrodes allows fringe fields from grounded neighboring parts of the machine to penetrate into the lens and distort electron trajectories. This effect can be corrected either by adding guard rings to the existing electrodes[129] or by adding additional guarding plates to maintain a smooth voltage gradient in each acceleration region.[53,55,130,131]

We chose to implement a design with two acceleration regions for simplicity and ease of optimization; the extra degree of freedom afforded by a third acceleration region can be difficult to optimize. The 7-plate lens configuration shown in Fig. 2.7b keeps the repeller (plate 1), extractor (plate 4) and grounding (plate 7) electrodes of the Eppink-Parker design, and adds four guarding electrodes (plates 2, 3, 5, and 6). The guarding plates are held at voltages linearly interpolated between the repeller, extractor, and ground electrodes using 10 MΩ resistors wired in series.

The plate aperture sizes and voltages were optimized using electron trajectory simulations

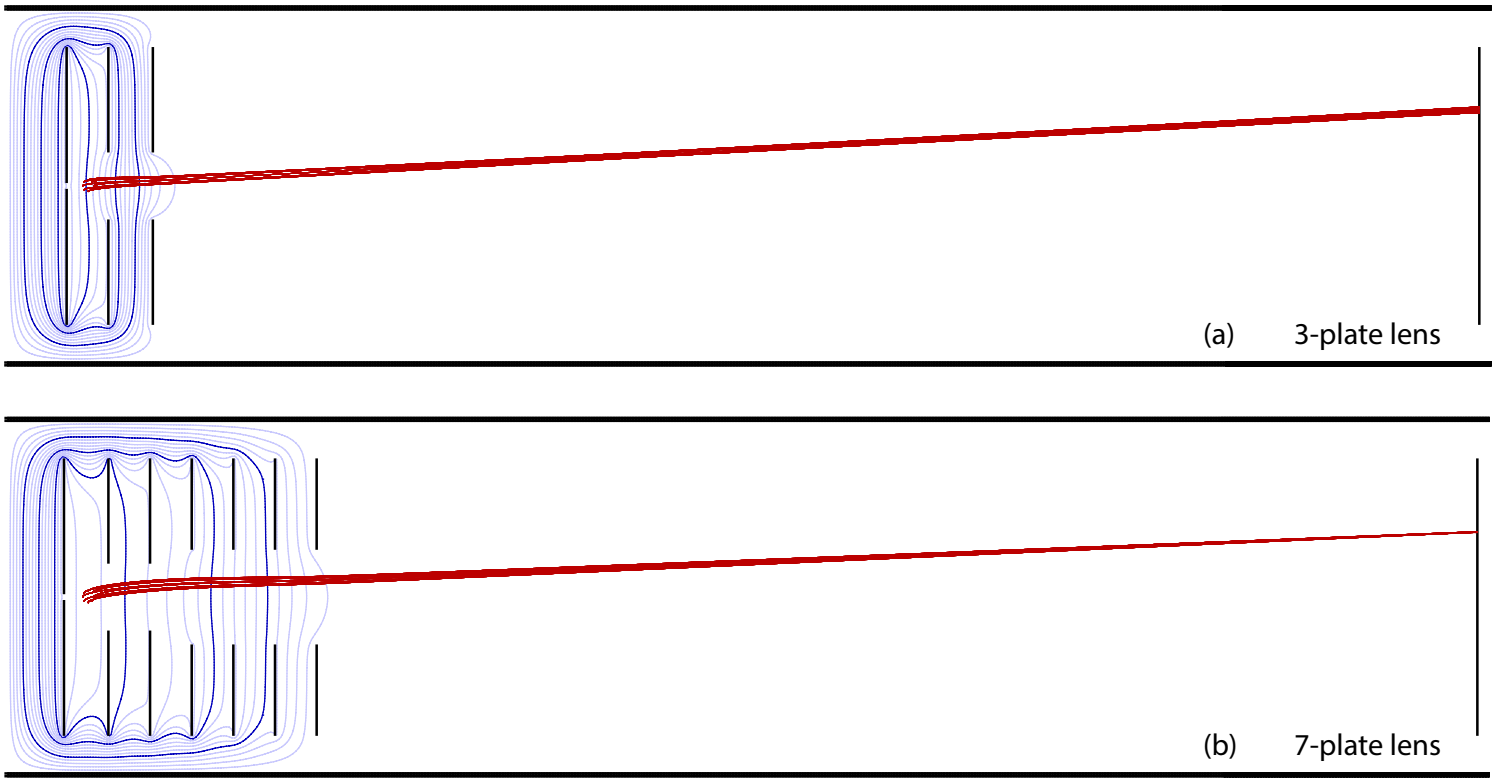

Figure 2.9: SIMION electron trajectory calculations for (a) the 3-plate Eppink-Parker VMI lens and (b) the new 7-plate VMI lens. The plates and mu metal walls are shown in black. Both lenses are shown with a repeller voltage of $V_R = -350\,V$ (plate 1) and optimized extractor voltages of $V_E = -255.0\,V$ (plate 2) for the Eppink-Parker lens, and $V_E = -243.3\,V$ (plate 4) for the 7-plate lens. Electric field lines are shown in dark blue (-300, -200, and $-100\,V$) and light blue (20 V increments).

in SIMION 8.0.[132] We considered different plate spacings as well, but decided to keep the 15 mm spacing between the first two plates so the VMI assembly could be mounted the same way as the previous Eppink-Parker lens with respect to the interaction region. Given this constraint, it proved optimal for all plate spacings to be 15 mm. The parameters were tuned to minimize the simulated spatial spread of photoelectrons with equivalent velocity vectors on the detector.

Figs. 2.9a and b show SIMION simulations of our original 3-plate Eppink-Parker lens and the new 7-plate lens. The focusing power of these lenses was compared by running photoelectron trajectories beginning from a 1 mm radius spherical shell initial spatial distribution, with a range of eKEs from 0.05–0.5 eV and velocity vectors spanning all angles. Under these conditions, the Eppink-Parker lens had an optimized simulated ΔeKE of 3.6 %, while the new lens demonstrated a ΔeKE of 0.7 %. In Figs. 2.9a and b we show the trajectory of electrons starting in a 2 mm radius spherical shell to better illustrate the difference in focusing capability of the two lenses. These electrons have eKE = 0.43 eV and initial velocity vectors transverse to the flight axis.

It is worth noting some of the troubleshooting steps we went through *en route* to a functional new VMI lens. The most important aspects of building and implementing the new VMI stack proved to be dealing with stray electric and magnetic fields. All VMI plates were machined from non-magnetizeable stainless steel 316. Four sets of Vespel spacers maintain the gap between neighboring plates. All hardware used to mount the VMI stack (6-32 rods, washers, and nuts) is made of non-magnetizeable brass.

During the first implementation of the new stack, we tried putting the four mounting rods in contact with the repeller, in hopes that this might lead to less distortion of the electron trajectories in the interaction and acceleration regions. Instead, it lead to significant distortion of the VMI image as the electrons bent away from the rods in the field-free region. We returned to grounding the mounting rods. We also found that coating the VMI plates with colloidal graphite (e.g. Aerodag) was essential to remove patch potentials on the surface of the plates, which caused blurring and distortion of the resulting image. Finally, we had a lingering problem with slight non-circularity and astigmatism of the images. In particular, when the extractor voltage was optimized, one axis of the image would go out of focus while the perpendicular axis came into focus. These problems were symptoms of inhomogeneous magnetic fields. We realized that the old stainless steel rereferencing tube had become magnetized over years of use and accumulated magnetic field gradients on the order of differences of $\pm$200 milligauss over a few centimeters. The rereferencing tube was subsequently replaced with an identical one made of non-magnetizeable aluminum.

2.1.5.2 VMI Resolution and Performance

Velocity-map imaging spectrometers yield images with roughly constant absolute velocity space resolution Δv. Upon conversion from velocity space to kinetic energy space using

$$\mathrm{eKE} = 1/2mv^2 \tag{2.9}$$

the absolute energy resolution ΔeKE correspondingly increases with increasing velocity:

$$\Delta\mathrm{eKE} = mv\Delta v \tag{2.10}$$

Equivalently, by dividing each side of Eqn. 2.10 by eKE, we can consider the relative energy resolution:

$$\frac{\Delta\mathrm{eKE}}{\mathrm{eKE}} = 2\frac{\Delta v}{v} \tag{2.11}$$

Based on these relationships, it is clear that we achieve the best absolute energy resolution ΔeKE for threshold transitions that detach photoelectrons with very low eKE. This is illustrated in Fig. 2.10 for photodetachment of F^-. In order to construct a high-resolution SEVI spectrum covering an entire band, we first obtain a low-resolution overview spectrum at a single photon energy. We then obtain high-resolution photodetachment spectra over relatively narrow eKE windows by measuring spectra at a series of photodetachment energies lying just above features of interest. These windows are combined to create a composite high-resolution spectrum of the entire band.

Using detachment of atomic O^- and F^- to characterize the new lens, we obtain our narrowest feature with a $1.2\,\mathrm{cm}^{-1}$ fwhm at eKE = $5\,\mathrm{cm}^{-1}$ and $V_R = -170\,V$. Farther from threshold, $V_R = -340\,V$ provides the best compromise between image magnification on the detector and invulnerability to stray fields, and yields typical resolution of $6\,\mathrm{cm}^{-1}$ fwhm at eKE = $190\,\mathrm{cm}^{-1}$ and $20\,\mathrm{cm}^{-1}$ fwhm at eKE = $1350\,\mathrm{cm}^{-1}$, comparable to the

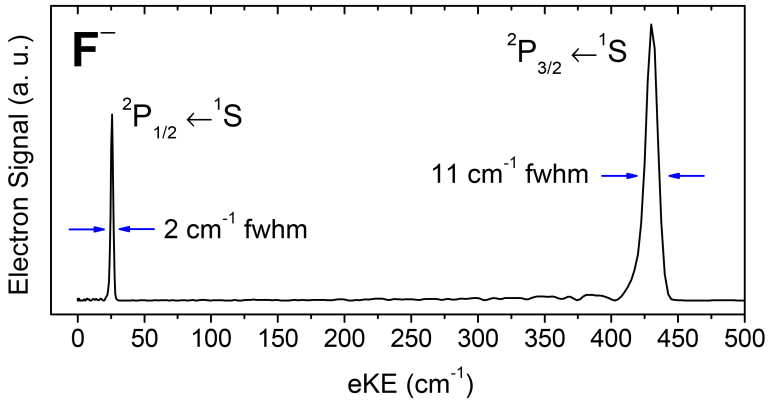

Figure 2.10: A SEVI photodetachment spectrum of F^- demonstrating how energy-space peak widths broaden with increasing eKE.

performance reported by Wang and coworkers.[53] Our resolution with the original Eppink-Parker design with a comparable V_R was $14\,cm^{-1}$ fwhm at eKE = $180\,cm^{-1}$ and $36\,cm^{-1}$ fwhm at eKE = $1000\,cm^{-1}$. With $V_R = -670\,V$, we can achieve $\Delta eKE/eKE \sim 1.4\,\%$ for faster electrons, compared to an optimal resolution of $\sim 3\,\%$ with the Eppink-Parker lens.

The $\Delta eKE/eKE$ that we achieve with the new lens is unfortunately still around twice what was predicted for this design in our SIMION simulations. This discrepancy is likely due to stray electric and magnetic fields lingering around the interaction region and flight tube, and imperfect alignment of the VMI plates relative to one another and the detector screen. Additionally, if our images are not perfectly round, the resolution can be hampered during the image centering and quadrant-symmetrization steps during data workup (see Section 2.1.7 below).

Ultimately, we have improved the resolution of our spectrometer by at least a factor of 2 in the critical eKE = 100–500 cm^{-1} regime. For molecular systems very close to threshold, we are never limited by our $1\,cm^{-1}$ instrumental resolution, but rather by unresolved rotational structure.

2.1.6 Data Acquisition and Event Counting

Following the 2011-2012 rebuild of the cryo-SEVI machine, the imaging camera, data acquisition software, and data processing methods were overhauled to make the best use of the improved spectral clarity afforded by cryo-cooled anions. An overview of the current data acquisition setup is given here, with some additional focus on the details of the acquisition software in use since 2012.

Every experimental cycle, we take an image of the electron spots on the phosphor screen using a monochrome 1024×768 pixel IDS UI-2230SE-M CCD camera fitted with a Schneider Optics Cinegon 21-1001951 lens. Images are typically taken with an exposure time of 100 µs. The camera communicates with our central lab computer via USB 2.0, and was chosen for its compatibility with the NuACQ software provided by Arthur Suits' research group.[133] The IDS camera replaced a considerably more expensive camera (Dalsa Dalstar 1M30P). The low video noise and wide dynamic range afforded by expensive cameras are not particularly important for our application, as we are imaging very bright electron spots on a high-gain detector and ignore the relative brightness of different electron spots. In fact, the NuACQ software was adopted primarily to make use of event counting[134] and centroiding,[130,135] allowing the detection and accumulation of individual electron counts rather than electron spots of varying intensity and size.

Centroiding, which has its origins in astronomy[136] and super-resolution microscopy,[137] makes use of the fact that our electron spots are typically brightest in the center, with roughly Gaussian intensity distributions. The central point of electron impact on the detector can be extracted from this distribution with considerably better precision than the size of the spot. The NuACQ event counting software analyzes each image acquired by the CCD camera in real time, flags regions of interconnected lit pixels as individual electron spots and calculates the centroid, or center of mass (COM), of each spot. A representative example of

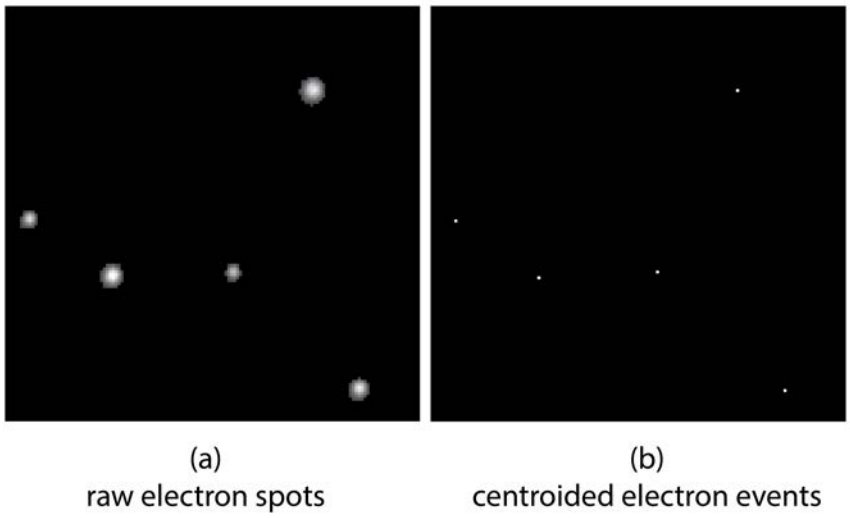

Figure 2.11: (a) Portion of CCD camera frame showing the typical shape and size of raw electron spots and (b) the computed centroids of these spots.

raw electron spots and their calculated centroids are shown in Fig. 2.11. For a spot of n lit pixels, the Cartesian COMs x_{COM} and y_{COM} are calculated as

$$x_{\mathrm{COM}} = \frac{\sum_i^n x_i I_i}{\sum_i^n I_i},\ y_{\mathrm{COM}} = \frac{\sum_i^n y_i I_i}{\sum_i^n I_i} \tag{2.12}$$

where x_i, y_i are the coordinates and I_i the intensity of the i^{th} pixel. This intensity-weighted COM calculation is considered one of the best super-resolution imaging algorithms and should not introduce any artifacts into our images.[130] The COM algorithm is computationally cheap, allowing us to calculate up to hundreds of centroids per frame in real time at our 20 Hz repetition rate. As they are calculated, the (x_{COM}, y_{COM}) coordinates of these centroids are added to an accumulating 2D histogram of the position centers of all electron events and saved as an ASCII image. We typically collect 10^5–10^6 electron events per accumulated image over 10^4–10^5 experimental cycles, depending on the signal level and the extent to which the electron image fills the detector screen.

Implementation of event counting and centroiding have proved incredibly helpful for improving the ultimate resolution of our spectrometer and correcting for spatial inhomogeneity in the MCP detector and CCD array.

The raw electron spots are a few hundred microns in diameter on the phosphor screen or ∼10 pixels in diameter on the CCD array (Fig. 2.11a). If we construct a VMI image by accumulating all lit pixels in each camera frame, we are essentially blurring the resulting image with a 10 pixel Gaussian filter. The achievable image resolution will thus be limited by

the raw electron spot size rather than the focusing capability of the VMI lens. Centroiding, on the other hand, reduces each spot to a single pixel. The center of mass calculations interpolate between pixels, so the grid into which the centroids are binned need not be the same dimensions as the CCD array. The grid size is chosen to be fine enough not to limit the spectrometer resolution. As a result, VMI experiments quite commonly harness centroiding to achieve subpixel resolution. Several groups have demonstrated an imaging resolution ultimately limited by the MCP pore size.[130,131,136]

Event counting and centroiding treat each electron spot as one event, no matter its size or brightness, making the accumulated images much less sensitive to spatial nonuniformity in the response of the detector. Our imaging MCPs are quite old at this point, and produce electron spots significantly larger and brighter near the screen edges compared to the center, which has seen the most use over time. In the raw accumulated image, this would lead to under-representation of signal intensity in the center of the screen, but centroiding completely eliminates this problem.

Centroiding can also correct for problems with the CCD array. CCDs have both hot pixels, which are erroneously always lit, and fixed pattern noise (FPN), a consistent difference in gain between pixels upon uniform illumination. In a non-centroided raw image, hot pixels and FPN can lead to sharp artifacts in the resulting energy spectra that are easily confused with real structure[50] and difficult to work around.[94] Before event counting and centroiding were implemented, we used low-gain, high-threshold acquisition settings to make the electron spots artificially smaller, which also served to amplify the CCD inhomogeneity, particularly for systems with broad spectral structure and poor signal-to-noise.[94] Hot pixels are easily discounted using event counting, as we discard spots that are smaller than a few pixels in area. FPN is also largely dealt with, as the COM calculations effectively average the response of several neighboring pixels.

Event counting and centroiding do come with a few downsides. Centroiding necessitates that we run with few enough detached electrons per shot that we don't have overlapping electron spots, which would lead to under-counted intensity at the crowded parts of the image, as well as wrongly calculated COMs that could blur spectral features. This typically limits us to work with less than 50 events per shot. When imaging a transition very close to threshold, as we often are, we obtain a very small, bright ring of signal in the center of the image and we must be particularly careful about signal levels under these conditions.

Centroiding also produces relatively sparse, grainy images compared to accumulation of raw electron spots. The data is even more sparse when binning centroids into a fine grid to achieve high resolution images. We therefore need to accumulate our images for longer periods of time. When we first implemented centroiding, we would Gaussian blur our images before reconstruction with a numerical inverse-Abel transform in order to combat graininess; after switching to a maximum entropy reconstruction method (Section 2.1.7) smoothing no longer proved necessary.

Since the Suits group provided us with the NuACQ source code to implement event counting and centroiding, we have made several changes to the software functionality. Much of our initial work upon first receiving the software was to fix problems with identifying

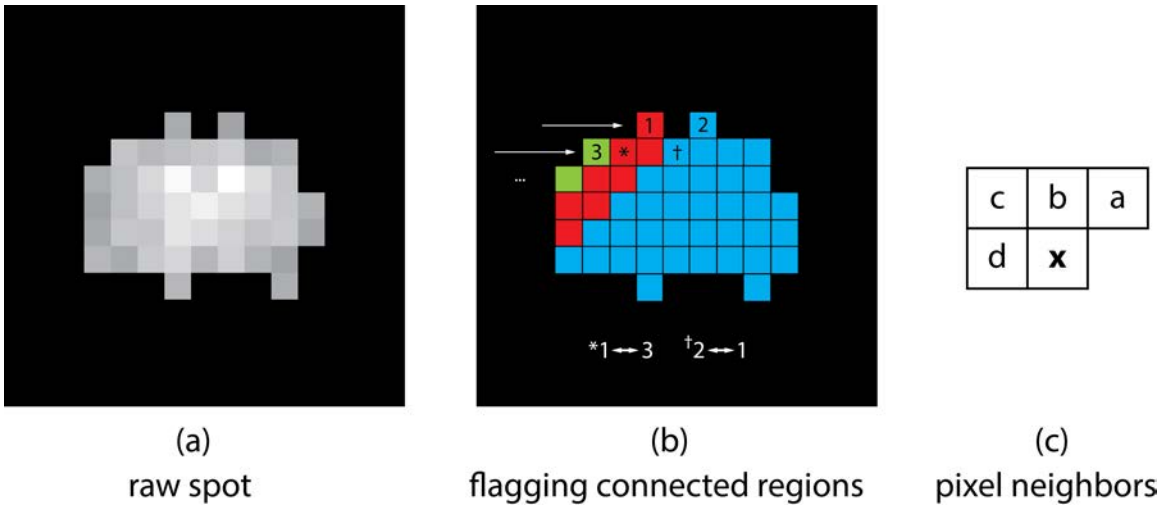

Figure 2.12: Schematic of the two-pass connected component labeling algorithm. (a) Representative raw spot that we would like to identify as a single connected region. (b) The first pass flags three initial regions, marked in red (1), blue (2), and green (3); all other pixels in the spot are then assigned to one of these regions according to the connectivity priorities shown in panel (c) (see text for details). Regions 1 and 3 are marked as equivalent while evaluating the pixel marked with a *; regions 2 and 1 are marked as equivalent while evaluating the pixel marked with a †.

electron spot connectivity; a few bugs and minor oversights had made the implemented algorithm prone to double counting certain oddly shaped spots.

The NuACQ code identifies individual electron events using a connected component labeling algorithm borrowed from the field of computer vision.[138] There are two simple classes of algorithms that can be used to identify connected regions of pixels. In the one-pass method, the image is rastered and once a lit pixel is identified, all other connected lit pixels are recursively identified. In the two-pass method, the image is rastered twice, first to assign temporary region labels to lit pixels and to keep track of which temporary regions are in fact connected, and secondly to relabel the final connected regions. While the recursive one-pass algorithm is perhaps more elegant, the NuACQ code implements the two-pass algorithm. We consider the 8-connectivity of the pixels: pixels can be considered connected to their four up/down/left/right neighbors as well as their four diagonal neighbors

Fig. 2.12 shows an example of how the two-pass algorithm determines pixel connectivity. We demonstrate here how a single spot (Fig. 2.12a) is evaluated, but this treatment is easily extended to an image with many spots, and thus many separate connected regions. Each camera frame is rastered pixel-by-pixel, and left-right/up-down (Fig. 2.12b). If our current pixel **x** is above some threshold intensity, we look at its four neighbors labeled a-d in Fig. 2.12c. If none of these neighbors has been previously assigned a region, we give pixel **x** a new region label. If pixel **x** has one or more labeled neighbors, it is given the region label

of one of its neighbors, with neighbor a taking first priority, then neighbor b, then c, then d. If pixel **x** touches two or more neighbors in different regions, we make a note that these different regions should be considered equivalent; this occurs twice in Fig. 2.12b, at the pixels marked with a * and a †. On the second pass through the image, we know that regions 1-3 are in fact all equivalent, and the spot is relabeled as a single region. The centroid is then easily calculated. At this stage we also throw out regions that are too small (< 3 pixels in area) to discriminate against hot pixels, or too large (> 120 pixels in area) to discriminate against overlapping electron spots.

Since 2012, we have also added capabilities to NuACQ in order to:

- accommodate multiple computer monitors.
- save a snapshot of a single frame of raw electron events and their centroids on command.
- display a readout of the average number of events per frame that updates once per second (every 20 frames).
- display a readout of the running total of accumulated electron events.
- save centroided data binned into both the default 1024×1024 pixel grid and a second grid of a size set by the user.

2.1.7 Image Reconstruction

A velocity-map image represents a two-dimensional projection of a three-dimensional electron velocity distribution. In order to arrive at our desired goal of a spectrum in electron kinetic energy space, we first need to reconstruct the original velocity distribution from the measured projection.

Such a reconstruction is mathematically made possible by the cylindrical symmetry of the 3D photoelectron Newton spheres, which is imparted upon the isotropic ion packet by photodetachment with a linearly polarized photon. The cylindrical symmetry axis is defined by the laser polarization axis, z. An illustration of the 3D photoelectron Newton sphere is shown in Fig. 2.13a. The cylindrical symmetry means that this 3D distribution can be parametrized with just two coordinates, z and $r = \sqrt{x^2 + y^2}$. In other words, a slice through the 3D distribution in the x-z plane (Fig. 2.13b), contains all the information we need: it need only be rotated about the z axis to recover the initial distribution. Let us call this distribution the velocity map, $F(z, r)$. $F(z, r)$ is what we would like to obtain in our experiment. $A(z, x)$, the 2D projection of $F(z, r)$ (Fig. 2.13c), is the image that we measure at the detector screen and is also a function of just two coordinates, z and x. Conveniently, $A(z, x)$ has an exact, one-to-one mapping to the velocity map $F(z, r)$ via the Abel transform:[139,140]

$$A(z, x) = 2 \int_x^\infty F(z, r) \frac{r}{\sqrt{r^2 - x^2}} dr \tag{2.13}$$

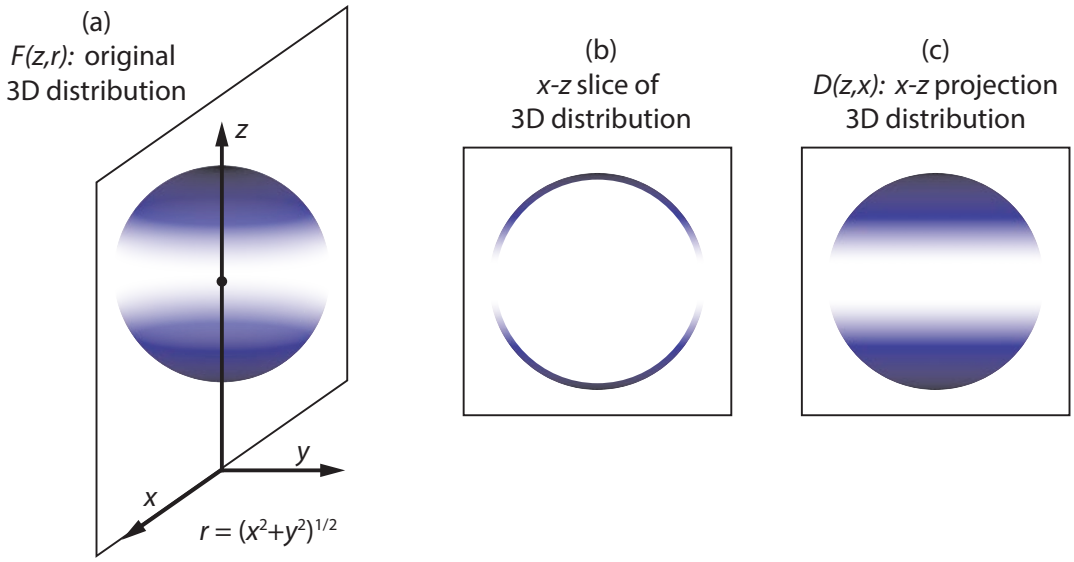

Figure 2.13: Illustration of (a) an initial 3D Newton sphere, (b) a slice of the 3D distribution taken in the x-z plane, which we would like to reconstruct, and (c) the 2D projection of the 3D distribution in the x-z plane, which we might measure on the detector screen.

Meanwhile, $F(z,r)$ can be reconstructed from a measured $A(z,x)$ projection using the inverse-Abel transform:[139,140]

$$F(z,r) = -\frac{1}{\pi}\int_r^\infty \frac{\partial A(z,x)}{\partial x}\frac{dx}{\sqrt{x^2-r^2}} \tag{2.14}$$

Unfortunately, real experimental VMI images cannot simply be inverted with Eqn. 2.14 as the differentiation of $A(z,x)$ greatly amplifies experimental noise. Attempts to circumvent this problem include Hansen and Law's recursive implementation of the inverse-Abel transform which is less sensitive to noise,[139] and the BASEX[141] and pBASEX[142] methods, which fit the experimental data to linear combinations of well-behaved basis functions before inversion. In ion imaging experiments, slicing techniques have been developed to only image a central x-z slice of the Newton sphere, so image reconstruction is no longer necessary.[128,143,144]

Until 2013, we used the Hansen-Law numerical inverse-Abel transform and occasionally the BASEX method for image reconstruction. More recently, maximum entropy reconstruction methods have come to the foreground[140,144] and have proved to be the best option for our purposes.[50] We now exclusively use the Maximum Entropy Velocity Legendre Reconstruction (MEVELER) method reported by Bernhard Dick in 2014.[140]

Maximum entropy reconstruction methods circumvent direct inversion of the experimental data. MEVELER iteratively finds the best velocity map $F(z,r)$ that when projected onto the x-z plane gives an image $A(z,x)$ that is most likely to account for the experimental

measurement $D(z, x)$. The determination of what constitutes this "most likely" velocity map is governed by Bayesian statistics, and the assumption that the experimental data follows a Poissonian distribution of event counts at each pixel. This correctly accounts for the fact that the measured $D(z, x)$ image is a grainy sampling of the projection of the true distribution. MEVELER assumes that $F(z, r)$ is rotationally symmetric about the z axis, and also that the angular dependence of the velocity distribution can be expanded in a basis of Legendre polynomials, as should be true for our photoelectron angular distribution as discussed in Chap. 1. The built-in use of Legendre polynomials makes it very convenient to extract anisotropy parameters from MEVELER output.

Thorough comparisons of various inversion methods and their suitability for use with SEVI have been made previously.[50,115] Here we briefly compare MEVELER to the Hansen-Law, BASEX, and pBASEX inverse-Abel reconstruction methods for analysis of real cryo-SEVI data. Reconstruction of a representative cryo-SEVI image of CH_2CN^- and the resulting energy-space photodetachment spectrum processed with these methods are presented in Figs. 2.14 and 2.15. The pBASEX reconstructed image is not shown in Fig. 2.14, but looks very similar to the BASEX image.

For all methods, the centroided experimental image is centered and quadrant-symmetrized before reconstruction. For the BASEX and pBASEX methods, the image is Gaussian blurred with a 2 pixel standard deviation before reconstruction, so the widths of experimental features are more comparable to those of the BASEX and pBASEX basis functions. For the Hansen-Law inverse-Abel reconstruction, each data point in the raw image is averaged with its nearest neighbors to reduce noise in the numerical transformation. This smoothing of experimental data for the inverse-Abel, BASEX and pBASEX methods essentially sacrifices resolution in favor of cleaner baselines and reduced noise. The spectrum processed with MEVELER is smoothed only in Fig. 2.15 after reconstruction and angular integration; each data point in a resulting trace is averaged with its nearest neighbors. For images with good signal, even this post-reconstruction smoothing often does not prove necessary. MEVELER also has an option to use "hidden layers" which add correlation between neighboring pixels, resulting in a smoother reconstruction albeit with slightly sacrificed resolution.[50] We typically use one hidden layer.

MEVELER clearly reduces the baseline and noise of our spectra compared to the Hansen-Law inverse-Abel method. This improved baseline is particularly important for resolving weak features that lie between much stronger features. The spectra processed with BASEX and pBASEX are less noisy than inverse-Abel spectrum, but both introduce oscillations in the baseline that are easily mistaken for real features, and do not accurately reproduce narrow structure (see inset of Fig. 2.15). Baseline oscillations are much worse for BASEX and pBASEX if the raw images are not Gaussian blurred before reconstruction. It is also clear from Fig. 2.14 that the images obtained from the Hansen-Law and BASEX algorithms demonstrate inversion artifacts along the vertical cylindrical axis of symmetry.

Similar conclusions about the superior performance of the MEVELER algorithm were reached using simulated SEVI images, where the reconstructions can be compared directly to the initial distribution.[50] With simulated data, MEVELER outperforms the other re-

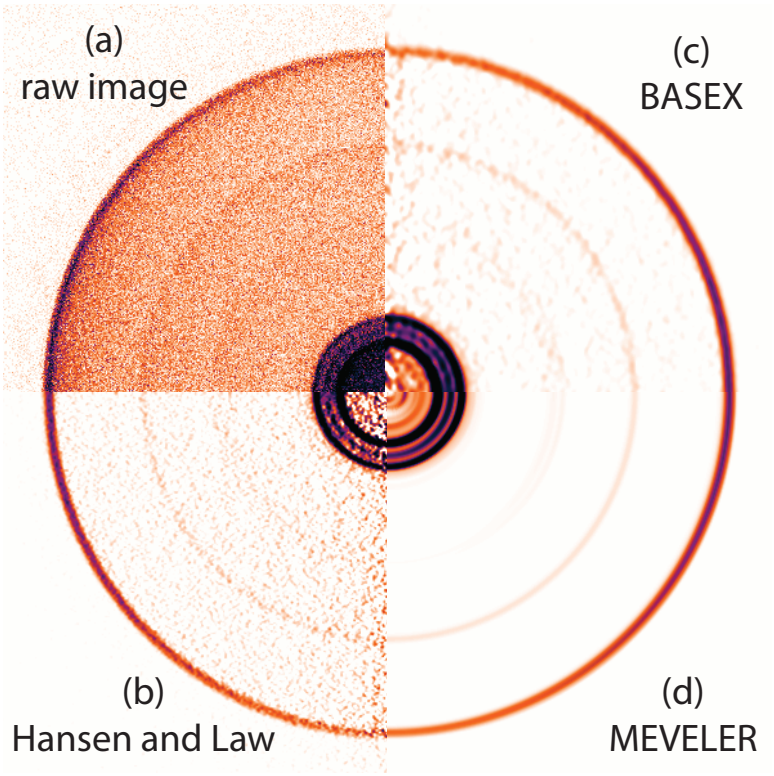

Figure 2.14: Comparison of different reconstruction algorithms for one CH_2CN^- cryo-SEVI image. (a) The centroided cryo-SEVI image and its reconstructed distributions using (b) the Hansen-Law inverse-Abel transform, (c) the BASEX method, and (d) the MEVELER method.

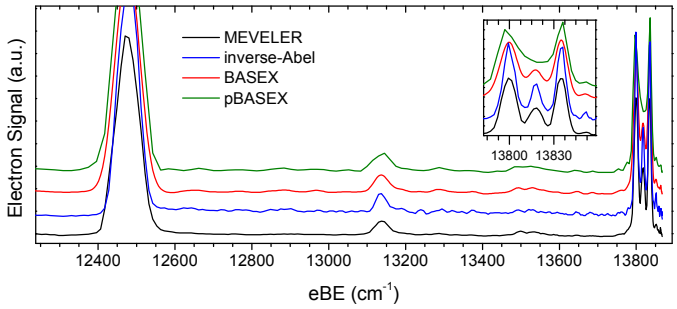

Figure 2.15: Comparison of different reconstruction algorithms on the final cryo-SEVI photodetachment spectrum of CH_2CN^-. The MEVELER method (black trace) is compared to the Hansen-Law inverse-Abel (blue), BASEX (red), and pBASEX (green) methods. Traces are offset vertically for clarity.

construction methods in a variety of scenarios, accurately reproducing peak widths and anisotropies, capturing sharp features superimposed on broad features, and introducing the fewest artifacts. In this thesis, the Hansen and Law inverse-Abel transform was used for the study of C_5^- (Chap. 3), while all subsequent studies make use of the MEVELER algorithm.

2.1.8 Energy Calibration

Whenever the path of the laser beam through the machine changes, the position and size of the interaction region may also be affected, and we must reoptimize the VMI focusing conditions and recalibrate the energy scale for our VMI images. Calibration and VMI optimization are carried out using SEVI spectra of well-known atomic anion photodetachment transitions. Atomic systems are convenient for this purpose because the energetic positions of their transitions are known to high precision. Additionally, atomic lines are not broadened by rotational or vibrational structure, and thus provide us with a good measure of our instrumental energy resolution. The atomic systems used to calibrate SEVI images in various spectral ranges are shown in Table 2.5.

Before calibrating, the VMI focus is optimized by tuning the voltage applied to the extractor electrode relative to that of the repeller via a potentiometer. VMI images are acquired at stepped potentiometer settings until a setting is identified that yields the sharpest rings (in pixels). It is important that these focusing conditions be set before carrying out an energy calibration, as different extractor voltages will slightly change the diameter of the rings in the VMI image. This is also best done at eKEs similar to what would be used experimentally for each repeller voltage. So, for a repeller voltage of $-350\,\mathrm{V}$ that we use flexibly for high-resolution and mid-level resolution images, the focus should be optimized $\sim$20–500 cm^{-1} above the atomic calibration transition threshold. For a repeller voltage of $-657\,\mathrm{V}$, which we use for overview images, the focus should be optimized $\sim$500–2000 cm^{-1} above threshold.

We then take images of the same atomic transitions at several different photon energies, and extract the radial displacement, R, of each transition from each image. The photon energy and the eBE of each transition are known, so we can calculate $\mathrm{eKE} = h\nu - \mathrm{eBE}$ for each transition. We then perform a least-squares fit to relate the measured values of R to eKE, and obtain our calibration parameters.

With the original 3-plate Eppink-Parker VMI lens, the distance of an electron spot from the center of the image is linearly proportional to the electron velocity, and the calibration was derived from fitting $\mathrm{eKE} = a \cdot R^2$. With the modified VMI lens, the added length and lensing properties slightly distort the electron velocities, so an additional polynomial term is needed; we now calibrate by fitting $\mathrm{eKE} = a \cdot R^2 + b \cdot R^4$.

The energy calibration of the system when using mid-IR or 1064 nm photodetachment light (see Section 2.1.9.2 below) warrants additional mention. We had difficulty finding a well-characterized atomic anion with an electron affinity in the range 0.3–0.9 eV that was easily generated in our source. Instead, we have found the simplest way to proceed under

Table 2.5: Atomic calibrant species, the precursors used to make them with the filament ionizer, and the atomic levels and photodetachment transitions used to calibrate the SEVI spectrometer. Also noted are the operating laser regions for which each calibrant is useful; more information about laser configurations can be found in Section 2.1.9.

	O^-	S^-	F^-	Cl^-
Precursor	N_2O	CS_2	NF_3	CH_2Cl_2
Laser region	532-pumping	355-pumping	doubling, BBO1	doubling, BBO2
EA (cm^{-1})	11784.676(7)[a]	16752.974(5)[a]	27432.446(19)[b]	29138.59(22)[c]
Anion levels (cm^{-1})	$^2P_{3/2}$: 0.00 $^2P_{1/2}$: 177.13(5)[d]	$^2P_{3/2}$: 0.0000 $^2P_{1/2}$: 483.5352(34)[e]	^1S: 0.00	^1S: 0.0000
Neutral levels (cm^{-1})	$^3P_2$: 0.000 $^3P_1$: 158.265[f] $^3P_0$: 226.977[f]	$^3P_2$: 0.000 $^3P_1$: 396.055[g] $^3P_0$: 573.640[g]	$^2P_{3/2}$: 0.00 $^2P_{1/2}$: 404.10[h]	$^2P_{3/2}$: 0.0000 $^2P_{1/2}$: 882.3515[i]

[a]Ref. [145]. [b]Ref. [146]. [c]Ref. [147]. [d]Ref. [148]. [e]Ref. [149]. [f]Ref. [150]. [g]Ref. [151]. [h]Ref. [152]. [i]Ref. [153].

these conditions is to align red dye laser light along a beam path through the machine identical to the IR light, and then acquire SEVI images of O^- to calibrate.

2.1.9 Photodetachment Laser Configuration

A key requirement of the SEVI technique is a tunable, narrow-bandwidth photodetachment laser source spanning the near-IR, visible, and near-UV wavelengths. We achieve this using the output of an Nd:YAG pumped dye laser and subsequent nonlinear frequency doubling and mixing processes. A summary of the configurations and operating ranges of our laser setup is shown in Fig. 2.16. We can produce tunable light from 0.3 eV to nearly 5 eV, though there is a gap in our tuning range from ∼0.9–1.3 eV.

Our photodetachment laser setup is based on a Continuum Powerlite 9020 Nd:YAG laser dating from 1995, which pumps a Radiant Dyes Narrowscan dye laser. The Radiant dye laser was installed in 2012 to replace an older Continuum model.

The Powerlite 9020 is operated at 20 Hz and produces pulses 10–20 ns in duration. Our model is also set up for injection seeding with a built-in diode laser, which narrows the Nd:YAG bandwidth from a few wavenumbers to a few thousandths of a wavenumber. The seeding capability has proved useful for IR difference frequency generation, as discussed in Section 2.1.9.2. We control the laser power output by tuning the Q-switch trigger timing, while the timing of the laser with respect to the rest of the cryo-SEVI apparatus is controlled via the flashlamp trigger timing. We use either the second (532 nm) or third (355 nm) Nd:YAG harmonic to pump the dye laser. When the Nd:YAG is in reasonable working order, we can expect power outputs of ∼6 W of 532 nm light, and ∼3 W of 355 nm light.

The dye laser produces fundamental light from 955–420 nm using various commercial

dyes. The fundamental light can be frequency doubled to access the near-UV region (Section 2.1.9.1) or mixed with the 1064 nm Nd:YAG fundamental to access the near-IR in an IR difference frequency generation process (Section 2.1.9.2). The dyes we commonly use and their operating ranges are listed in Table 2.6. We mix dyes in methanol, using the concentrations listed in Table 2.6 for the oscillator dye cell, and diluted by 3–4 times for the amplifier dye cell. Many dyes with neighboring wavelength regions can be mixed together to access regions between gain curves.

Care must be taken not to stray too close to the edge of the dye gain curve, where amplified spontaneous emission (ASE) can be significant, leading to unnecessary spectral congestion in the VMI images. ASE is less of a problem when the dye light is used for frequency conversion in a nonlinear crystal (Sections 2.1.9.1 and 2.1.9.2). In these cases, the crystal angle is tuned for the phase matching condition of the fundamental dye light, and the ASE is not frequency converted.

The efficiency of the dye laser power relative to the Nd:YAG pump power is 10–20 %, depending on the dye. We use a Bethune amplifier cell geometry,[154] slightly sacrificing efficiency in favor of a homogenenous spatial beam profile, which is important for effective nonlinear frequency conversion of the dye laser light. Photodetachment typically requires 20–100 mW of light (1–5 mJ/pulse at 20 Hz), depending on the ion signal and photodetachment cross section.

The fundamental dye laser light is produced with a vertical linear polarization. The frequency doubling and IR difference frequency generation schemes produce horizontal and vertically polarized light, respectively. The light is aligned through the cryo-SEVI detector

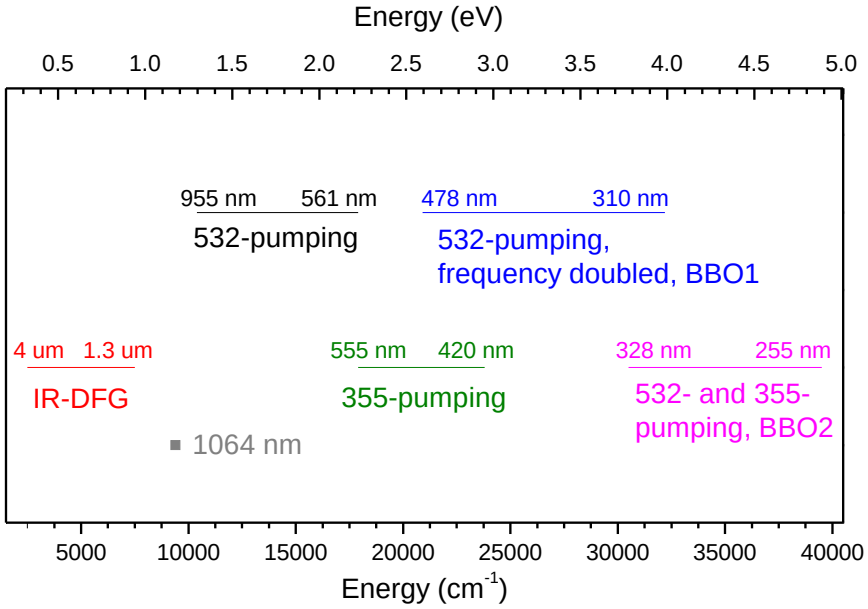

Figure 2.16: Operating regions accessible with different laser table configurations.

Table 2.6: Laser dyes used in the Radiant NarrowScan dye laser, the concentrations for dilution in methanol used in the oscillator dye cell, and typical operating wavelength regions. The operating ranges of each dye can be somewhat dependent on the dye laser alignment and the oscillator grating setting used.

532 nm pumping				
Dye	Conc. (g/L)	Fundamental (nm)	Doubled (nm)	DFG (μm)
LDS 925 (Styryl 13)	1.00	928–955	464–478	
LDS 925/867 mix		875–930	438–465	
LDS 867	0.15	856–872	428–436	
LDS 867/821 mix		841–870	420–435	
LDS 821 (Styryl 9)	0.14	803–826	401–413	3.27–3.69
LDS 798 (Styryl 11)	0.15	785–808	392–404	2.99–3.36
LDS 765	0.15	749–776	374–388	2.53–2.87
LDS 751 (Styryl 8)	0.15	735–759	367–380	2.37–2.65
LDS 722 (Pyridine 2)	0.26	705–740	352–370	2.09–2.43
LDS 698 (Pyridine 1)	0.30	675–710	337–355	1.85–2.13
LDS 698/DCM mix		655–680	327–340	1.70–1.88
DCM	0.35	620–655	310–328	1.49–1.70
R 640 (Rhodamine 101)	0.14	611–618	305–309	1.44–1.47
R 640/610 mix		605–612	302–306	1.40–1.44
R 610 (Rhodamine B)	0.20	587–602	293–301	1.31–1.39
R 610/590 mix		570–590	285–295	
R 590 (Rhodamine 6G)	0.14	561–575	280–288	
355 nm pumping				
Dye	Conc. (g/L)	Fundamental (nm)	Doubled (nm)	
C 540a (Coumarin 153)	2.50	536–555	268–278	
C 503 (Coumarin 307)	0.40	490–523	245–262	
C 480 (Coumarin 102)	0.40	480–490		
C 460 (Coumarin 47)	0.25	448–476		
C 440 (Coumarin 120)	0.20	432–449		
S 420 (Stilbene 3)	0.20	420–425		

chamber via windows mounted at Brewster's angle and a series of light baffles and apertures on either side of the interaction region. The light is directed through the machine using three prisms for the vertically polarized light, and two prisms for the horizontally polarized light. These prism configurations ensure that the light polarization axis is vertical at the interaction region: it is important that the laser polarization axis lie in the plane of the imaging detector, so cylindrical symmetry is preserved during photodetachment and the photoelectron images can be reconstructed. The light is focused into the interaction region using a cylindrical lens with a 50 cm focal length, so that the laser beam profile is a narrow vertical line at the interaction region. The interaction region should be as narrow as possible along the ion TOF axis, as the VMI lens is less adept at correcting for spread in the initial position of photoelectrons born along this axis compared to spread in the plane of the detector.

We use a Coherent Wavemaster to measure the dye laser wavelength to within a few thousandths of a nanometer, while an Ocean Optics USB4000 spectrometer is used to characterize the gain curve and ASE of a given dye.

2.1.9.1 Frequency Doubling

The dye laser output can be frequency doubled for all 532 nm-pumped dyes and for the redder 355 nm-pumped dyes. Doubling is carried out in one of two BBO crystals provided by Radiant Dyes and cut at different angles for different wavelength regions. The BBO1 crystal is used for frequency-doubled wavelengths longer than 300 nm while the BBO2 crystal can be used to produce wavelengths between 220–320 nm (Fig. 2.16).

Each crystal can be placed in a rotation mount built into the dye laser housing, which rotates the crystal around an axis normal to the laser table. A BBO compensating crystal is mounted after the frequency doubling crystal and is rotated in the opposite direction so the downstream beam path is unchanged for different wavelength-dependent phase matching conditions. An Inrad UV harmonic separator box mounted after the BBO crystals is used to separate the doubled light from the fundamental.

While the BBO2 crystal can produce light as high in energy as 220 nm, the UV becomes increasingly difficult to work with at shorter wavelengths. We've found it untenable to take spectra with wavelengths shorter than ∼255 nm. Photons with energies above ∼4 eV (300 nm) begin to surpass the workfunctions of steel and aluminum. Scattered UV light can therefore detach electrons from the VMI plates, vacuum chamber walls, and other metal components, creating a laser noise background in our VMI images that gets progressively worse at shorter wavelengths. To combat this background, we have used lens assemblies to telescope the beam spot to one-half or one-third of its original size to reduce scattering. Another helpful approach is to focus the beam through a 100 µm pinhole. The pinhole acts as a spatial filter to block the divergent higher-order modes of the beam, and leads to considerably less laser noise in our images.

2.1.9.2 Infrared Difference Frequency Generation

In 2016, we greatly extended the wavelength range of the photodetachment laser system with the addition of IR difference frequency generation (IR-DFG). This setup covers the mid-IR (1.3–4 µm, 0.3–0.9 eV), and is similar in design to a setup described by Lineberger and coworkers.[60] This development was motivated by the desire to acquire high-resolution photodetachment spectra of the ground state of vinylidene, H_2CC, which has an electron affinity around 0.5 eV.[9] These results will be described in a forthcoming publication[155] and in the thesis of Jessalyn DeVine.

The IR-DFG setup is shown schematically in Fig. 2.17. The dye laser is pumped by the 532 nm second harmonic of the Nd:YAG and produces 590–840 nm red light. Residual 1064 nm Nd:YAG fundamental light is mixed with the red light in a nonlinear $LiNbO_3$ DFG crystal, producing mid-IR light with a frequency corresponding to the difference between the 1064 nm and red light frequencies. The mid-IR wavelength is tuned via the dye laser wavelength.

Two $LiNbO_3$ DFG crystals were purchased from Sirah Lasertechnik, both $16 \times 11 \times 30$ mm^3 in size. The DFM-2400-T crystal, cut at 56°, can produce 1.3–2.5 µm IR light using 590–750 nm dye light; the DFM-3800-T crystal, cut at 48°, can produce longer IR wavelengths from 1.8–4 µm using 670–840 nm dye light. The DFG crystal of choice is placed in a motorized rotating mount with its optical axis in the 16×30 mm^2 lying parallel to the laser table. Sirah Lasertechnik also provided a 3 mm long $LiNbO_3$ compensating crystal to be rotated in the opposite direction as the DFG crystal. DFG output at a given wavelength is optimized by slowly rotating the $LiNbO_3$ DFG crystal angle while monitoring the IR light output on a sensitive, fast-responding pyroelectric detector (Thorlabs ES111C).

As the crystals are designed for a type-I nonlinear process, the bluest light involved in

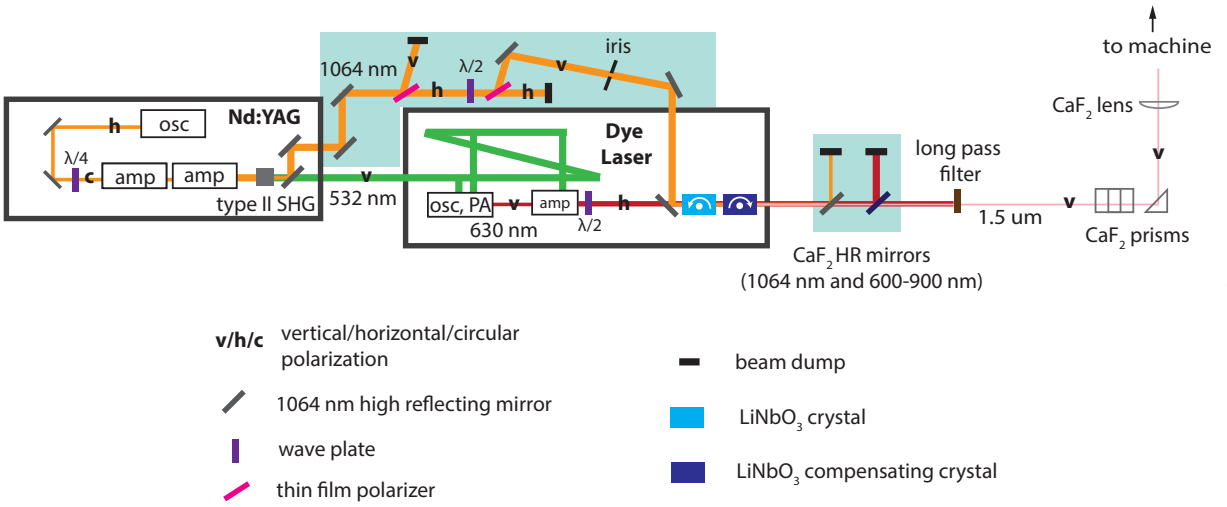

Figure 2.17: IR-DFG laser table configuration.

the mixing process (the 590–840 nm dye laser light), must be polarized extraordinary to the crystal's optical axis, while the two redder colors of light (the 1064 nm Nd:YAG fundamental and the 1.3–4 µm DFG light) must be polarized ordinary to the crystal optical axis. Since the crystal is mounted with its optical axis parallel to the laser table, the dye laser light must be be horizontally polarized and the 1064 nm light and resulting DFG light vertically polarized. Since the dye laser light is by default vertically polarized, we use a 400–800 nm achromatic half wave plate (Thorlabs AQWP05M-600) to rotate the dye laser light polarization by 90° before entering the DFG crystal.

The 1064 nm beam path is more complicated. The 1064 nm light leaves the Nd:YAG laser with a poorly defined elliptical polarization. In order to ultimately have a vertically polarized 1064 nm beam with tunable power distinct from the 532 nm power used to pump the dye laser, we use a combination of two thin film polarizers and a half wave plate, as shown in Fig. 2.17. We use CVI thin film polarizers coated for 1064 nm (TFP-1064-PW), which operate at 56° and are rated for high power. The first thin film polarizer transmits only the horizontal component of the elliptical 1064 nm light, and reflects the vertical component into a beam dump. The half wave plate in combination with the second thin film polarizer acts as a tunable beam splitter, transmitting the horizontal component to a second beam dump, and reflecting the vertical component for use in DFG.

The 1064 nm beam then hits two high-reflecting 1064 nm mirrors (CVI Y1-1025-45), which direct it through the dye laser enclosure. These mirrors are tuned to align the 1064 nm beam perfectly collinearly with the dye laser beam at the crystal position as well as ∼2 m further down the laser table. The dye laser light passes through the back of this last 1064 nm mirror (Fig. 2.17). Good spatial overlap between the two beams is critical for efficient production of DFG light. The dye laser spot is ∼4 mm in diameter coming out of the dye laser Bethune cell amplifier, while the 1064 nm Nd:YAG spot is ∼11 mm in diameter. The amount of DFG light produced is limited by the dye laser power and there is ample leftover 1064 nm power, so we found no reason to telescope the Nd:YAG spot down to match the dye laser spot. An iris before the last two 1064 nm mirrors is used to clean up the edges of the Nd:YAG beam and make it easier to align without clipping.

Good time overlap between the 1064 nm and dye laser beams is also critical for optimizing the DFG signal. We tweaked the beam path of the 1064 nm light until both beams arrived within 1 ns of one another. As we are working with pulses 15 ns long, achieving time overlap is not a very difficult task. We didn't bother to set up a delay stage, as the beam path need not be altered once the proper time overlap is found.

All optics downstream of the DFG crystal are made of CaF_2 or MgF_2 to minimize absorption of mid-IR light. CaF_2 mirrors coated for 1064 nm and 600–900 nm (custom ordered from Eksma Optics) dump the initial wavelengths and transmit the DFG light. Several downstream optics formerly made of fused silica also had to be replaced: the DFG light is aligned through the SEVI machine using CaF_2 prisms, and is focused into the interaction region using a cylindrical CaF_2 lens. The vacuum chamber windows are MgF_2.

Because there can be slight leakage through the 1064 nm and 600–900 nm CaF_2 mirrors, we also use a long-pass filter to ensure only DFG light enters the machine. A filter with a

cut-on wavelength of 1100 nm (Thorlabs FEL1100) is used for DFG light down to ∼2.5 µm, and a Spectrogon cut-on 1900 nm filter on a germanium substrate can be used for DFG light down to 4 µm.

We are able to achieve 50 mW (2.5 mJ/pulse) of 1.55 µm DFG light from mixing 500 mW (25 mJ/pulse) of 630 nm dye laser light (DCM dye) and a comparable power of 1064 nm light. While the efficiency of laser dyes decreases at longer wavlengths, we can still make 20 mW of 2–2.5 µm DFG light from 700–750 nm dye laser light (LDS 722 or LDS 751 dye). Injection seeding the Nd:YAG laser slightly improves the DFG power output compared to unseeded operation and also yields substantially narrower bandwidth light, which can be important for high-resolution SEVI images taken close to threshold.

2.2 Cryogenic Vibrational Action Spectroscopy

IR photodissociation (IRPD) and multiple photon dissociation (IRMPD) experiments were carried out with an ion trap tandem mass spectrometer[156,157] located at the Fritz Haber Institute (FHI) in Berlin, Germany, using tunable, intense IR radiation from the FHI free electron laser (FEL).[92]

A schematic of the FHI instrument is shown in Fig. 2.18.

2.2.1 Apparatus

The main elements of the FHI ion trap-tandem mass spectrometer apparatus are not so dissimilar from those of the cryo-SEVI apparatus. Here we detail the anion source, ion guides and quadrupole mass filter, cryogenic ion trap, and time-of-flight mass spectrometer.

For the IRPD and IRMPD studies of $(TiO_2)_n^-$ and $(TiO_2)_n^-(D_2O)_m$ reported in this thesis (Chaps. 9 and 10), metal oxide clusters and their reactive adducts are prepared in a pulsed laser vaporization source.[158] A frequency-doubled Nd:YAG laser operated at 50 Hz is focused onto a rotating rod target, with a 15–20 mJ pulse energy. The resulting plasma is entrained in a pulse of trace O_2 in 70 psi He from a General Valve. Metal oxide clusters are formed during expansion through a clustering channel downstream of the rod which is held at 270 K by a compressed helium refrigerator. The reactive adduct clusters are prepared in a modified dual gas-channel source (Fig. 2.19),[123] based on the fast flow cluster reactor pioneered by Smalley and coworkers.[121] After a short time delay from the firing of the main valve, a second General Valve pulses 30 psi of He containing the desired reactive substrate (e.g. D_2O from a bubbler or trace CO_2) into the clustering channel to form the desired reactive adducts.

After the source, the ion beam passes through a skimmer and into a linear RF decapole ion guide, filled with He to aid in collimation of the beam and collisional thermalization to room temperature. The ions then enter a linear quadrupole mass filter, which transmits only ions of the desired mass. The quadrupole can also be scanned to acquire a mass spectrum of the clusters produced by the source. Such mass spectra are recorded using a channeltron

detector mounted on-axis with the ion trap after the TOFMS electrodes; the trapping and TOFMS ion optics are not in use during accumulation of these mass spectra.

After the quadrupole mass filter, the beam is deflected by 90° with an electrostatic quadrupole ion deflector, and focused into a 24-pole RF ring electrode ion trap.[156] The trap is filled continuously with a buffer gas consisting of either pure D_2 or a mixture of D_2 in He, and is held at cryogenic temperatures in the range of 14–25 K. Ions are accumulated in the trap over 10 laser vaporization source cycles, where they are thermalized and messenger-tagged[46] through collisions with the buffer gas. For each cluster of interest, the trap temperature and the composition of the buffer gas are optimized for tagging around 10% of clusters with a single D_2 molecule.

Optimally, a less polarizeable (and therefore less perturbing) tag, like a rare gas atom, would be used instead of a "sticky" molecular tag like D_2. However, particularly for anions, it is simply too difficult to get effective tagging with rare gas atoms. D_2 and H_2 have been used successfully for various spectroscopic studies without significant distortion of the vibrational frequencies or native isomer populations,[96,157] though agreement with simulation is occasionally improved if the tag is included in the calculations.[123] D_2 is used in the exper-

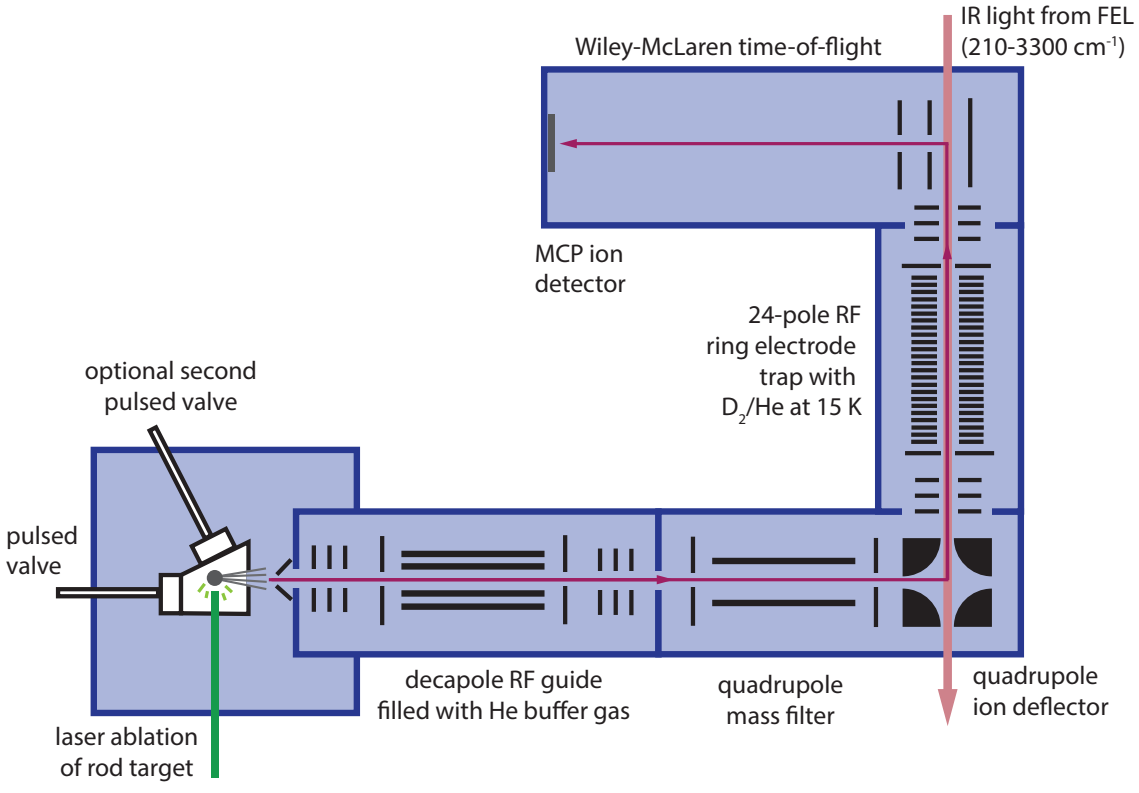

Figure 2.18: Schematic of the FHI ion trap-tandem mass spectrometer apparatus used for IRPD and IRMPD experiments.

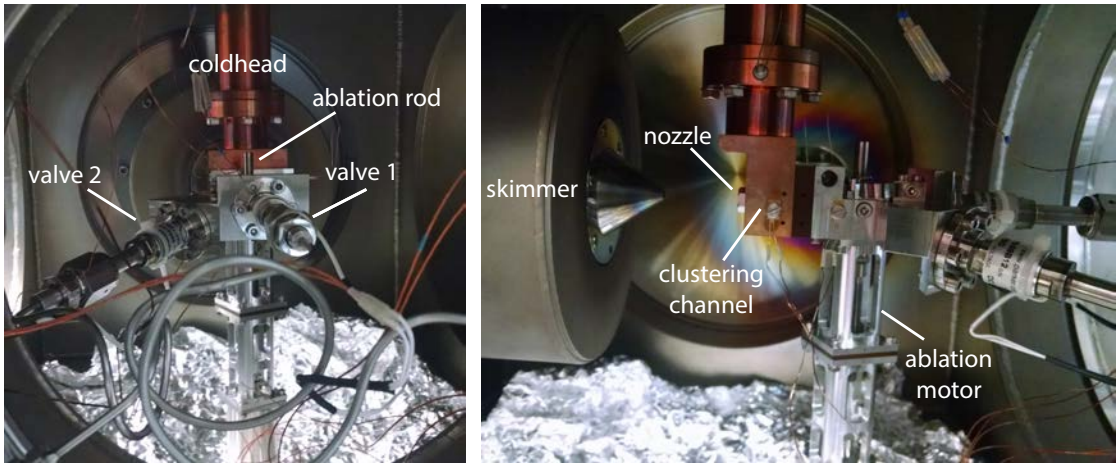

Figure 2.19: The dual-valve ablation source used to produce metal oxide clusters and their reactive adducts for IRPD and IRMPD experiments.

iments discussed here rather here than H_2 because it leads to better separation of the bare and tagged clusters in the mass spectrum.

Ions are extracted from the trap at 5 Hz and are spatially and temporally focused into the extraction region of an orthogonal time-of-flight mass spectrometer, where they are irradiated by a counter-propagating IR macropulse from the FHI FEL. All resulting tagged, bare, and fragmented clusters are then accelerated towards an MCP detector, and their TOF intensities are monitored as the FEL wavelength is scanned.

2.2.2 Free Electron Laser

Construction of the Fritz Haber Institute free electron laser began in 2011 and the system was available for users beginning in 2013.[92] The design of the FHI facility was based in large part on the FELX free electron laser facility in the Netherlands, where the Asmis group previously carried out vibrational action spectroscopy experiments.[93,94,157]

Free electron lasers make use of the coherent light emitted from an oscillating beam of electrons; the wavelength of the emitted light can be tuned by changing the speed of the electron beam and the period and amplitude of their oscillation.[159] The beam of electrons is produced with an electron gun and accelerated to relativistic speeds. This beam is then sent into an undulator made of alternating permanent magnets, which cause the electrons to "wiggle," releasing radiation with each oscillation, much like a radio antenna. The light emission occurs inside an optical cavity, allowing build-up of an intense pulse of light as electron beams are repeatedly sent through the undulator. The resulting FEL light output has an interesting structure, consisting of a macro-pulse of 5–10 µs in duration, made up of thousands of 1 ps long micropulses spaced in time by 1 ns.[92]

The FHI FEL produces 210–3300 cm^{-1} radiation with a relative spectral bandwidth better than $\sim$ 0.5% fwhm.[92] In the experiments discussed here, we use two operating regions of the FEL: the 440–1200 cm^{-1} range produced with a 26 MeV electron beam and the 2600–3000 cm^{-1} range produced with a 43.5 MeV electron beam. In the lower energy region, the FHI-FEL has a spectral bandwidth ranging from $\sim$2 cm^{-1} fwhm at 450 cm^{-1} to $\sim$7 cm^{-1} fwhm at 1200 cm^{-1}. In the higher energy region, the bandwidth is 20–30 cm^{-1}. Typical macropulse energies are 30–40 mJ in both regions. The FEL power output has significant wavelength dependence within a given operating region, which must be taken into account when calculating IRPD and IRMPD cross sections.

2.2.3 Data Acquisition and Workup

For each IRPD spectrum, the photon energy is stepped in 3 cm^{-1} increments, though in some cases, a 5 cm^{-1} step is used in the higher energy region where the FEL bandwidth is larger. For each step, 50–100 TOF traces are acquired and averaged, depending on the signal-to-noise level for a given system. Attenuated laser pulses using 2–50 % of the full FEL power are employed as necessary to ensure operation within a linear absorption regime and to avoid saturating the spectrum through complete depletion of the D_2-tagged clusters. Different levels of attenuation may be required to observe all features linearly in the spectrum of a given species; spectral windows taken with different laser pulse energies are stitched together after processing.

IRMPD processes are also observed for some clusters when irradiated with the full FEL power (Chap. 10). These dissociation channels require multiple photons and are thus negligible with the attenuated laser pulses used to acquire the D_2-tagged IRPD spectra. The spectral structure is considerably broader with IRMPD than IRPD, but also has better signal-to-noise. As a result, the full power spectra are taken with the photon energy stepped in 7 cm^{-1} increments, and only averaging 15 TOF traces per point.

IRPD and IRMPD spectra are processed using the Asmis group Saphir Plot v.3.5 software. The raw data can be plotted as 2D plots of TOF delay versus wavelength, as shown in Fig. 2.20a for the D_2-tagged IRPD spectrum of $(TiO_2)_3^-$. Tagged, bare, and fragmented clusters of different masses are identified by their TOF delays, and line-outs of the 2D plot are taken, integrating over each relevant TOF peak, in order to track the relative intensities of these species as the wavelength is scanned. As shown in Fig. 2.20b, at the IR wavelengths at which $(TiO_2)_3^-$ absorbs, the tagged $(TiO_2)_3^-D_2$ species is depleted and the bare $(TiO_2)_3^-$ cluster is reformed. The wavelength scale is calibrated every few hours during beamtime.

The raw wavelength-dependent TOF intensities are then converted into photodissociation cross sections. The IRPD cross section (σ_{IRPD}) is calculated from the TOF spectra by normalizing the relative abundance of the tagged parent ($I_P(\nu)$) and bare fragment ions ($I_F(\nu)$) to the total ion signal and the laser fluence ($F(\nu)$) at each photon energy:

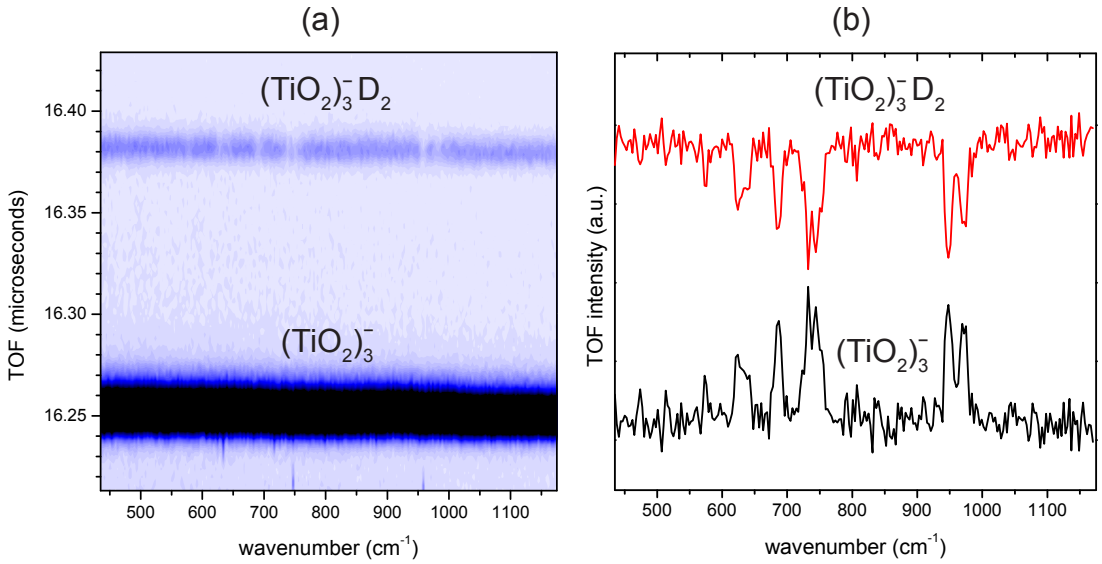

Figure 2.20: Data processing for the D_2-tagged IRPD spectrum of $(TiO_2)_3^-$ showing (a) time-of-flight mass spectra for $(TiO_2)_3^-$ and $(TiO_2)_3^-D_2$ versus FEL wavelength in the 400–1200 cm^{-1} fingerprint region and (b) integrated TOF intensity of the $(TiO_2)_3^-$ and $(TiO_2)_3^-D_2$ mass peaks versus FEL wavelength.

$$\sigma_{\mathrm{IRPD}} = -\ln\left[\frac{I_P(\nu)}{I_P(\nu)+I_F(\nu)}\right]/F(\nu) \tag{2.15}$$

To normalize the IRMPD cross section, the laser power $P(\nu)$ is used instead of the laser fluence, where $P(\nu) \propto F(\nu)\cdot\nu$. This accounts for the fact that IRMPD dissociation processes require the absorption of multiple photons, and at redder photon energies, a larger number of photons is required to reach the dissociation limit. Scaling by laser power serves to enhance the calculated IRMPD cross section of features at the red end of the IR spectrum.

Part II

Interstellar Species

The contemplation of celestial things will make a man both speak and think more sublimely and magnificently when he descends to human affairs.

Marcus Tullius Cicero,
c. 30 BCE

Chapter 3

Vibrational fine structure of C_5

The content and figures of this chapter are reprinted or adapted with permission from M. L. Weichman, J. B. Kim, and D. M. Neumark, "Vibrational fine structure of C_5 via anion slow photoelectron velocity-map imaging" *J. Chem. Phys.* **139**, 144314 (2013).

Abstract

High-resolution anion photoelectron spectra of cryogenically cooled C_5^- clusters are reported using slow photoelectron velocity-map imaging spectroscopy. We resolve vibronic transitions to the ν_2 stretching mode and multiply excited ν_5, ν_6, and ν_7 bending modes of neutral C_5 with significantly higher accuracy than previous experiments. Weak transitions to Franck-Condon (FC) forbidden singly excited bending modes are made possible by Herzberg-Teller coupling between electronic states of the neutral cluster. In addition, we resolve vibrational fine structure corresponding to different angular momentum states of multiply excited bending modes. The observation of this multiplet structure, some of which is FC forbidden, is attributed to Renner-Teller coupling between vibrational levels in the C_5^- ground electronic state.

3.1 Introduction

Carbon clusters (C_n) have been of great interest in interstellar, plasma, and combustion chemistry for over three decades.[99,160–163] They represent one of the most important families of clusters owing to their relevance and structural complexity. Many state-of-the-art experimental and theoretical methods were developed with carbon clusters as their primary target and were subsequently extended to other systems. Following this paradigm, we recently reported a study of the neutral C_5 cluster via high-resolution slow photoelectron velocity-map imaging spectroscopy of cryo-cooled C_5^- anions in order to demonstrate the power of this combination of techniques.[36,49] Here we present a more complete spectroscopic study of C_5 and C_5^- using the same method.

Small carbon clusters with an odd number of atoms tend to have linear geometries, while even-numbered clusters also have low-energy ring structures.[164–166]. Larger clusters can preferentially form rings and fullerenes.[167,168] The neutral C_5 cluster is a linear cumulene with a $^1\Sigma_g^+$ ground electronic state.[165,169,170] C_5 was first detected experimentally by its ν_3 antisymmetric stretching mode in cold neon and argon matrices.[171] Soon afterwards, the same ν_3 mode was identified in the gas phase from the absorption spectrum of the circumstellar shell of a carbon star[172] and in the laboratory using infrared diode laser absorption spectroscopy.[89,173] Electronic and vibrational levels of C_5 have since been investigated with further rare gas matrix studies,[174–176] cavity ringdown spectroscopy,[177] resonant two-photon ionization spectroscopy,[178] and electronic structure calculations.[166,179–184] The C_5^- anion is also linear, with a $^2\Pi_u$ ground state.[185,186] While not as well-characterized as its neutral counterpart, its electronic and vibrational structure has been investigated with multiphoton electron detachment,[187–189], matrix IR absorption,[190–192] and various theoretical methods.[193–195]

Anion photoelectron spectroscopy (PES) is an attractive technique for clusters in general[196,197] as a means of probing the electron affinity and vibronic structure of size-selected neutral species. The vibrational structure in a PE spectrum is sensitive to the change in geometry of a cluster upon photodetachment, and is often complementary to IR spectroscopy

because it is dominated by progressions in totally symmetric vibrational modes. Previous PES studies of C_5^- have been reported by Yang *et al.*[198] at a resolution of $\sim$1000 cm^{-1}, by Arnold *et al.*[199] with a resolution of $\sim$100 cm^{-1}, and by Kitsopoulos *et al.*[25] with zero electron kinetic energy (ZEKE) spectroscopy, at a resolution of 10–30 cm^{-1}. The ZEKE study resolved transitions to the ν_2 (779 cm^{-1}), $2\nu_5$ (432 cm^{-1}), $2\nu_6$ (1070 cm^{-1}), and $2\nu_7$ (212 cm^{-1}) vibrational states of neutral C_5, as well as a spin-orbit (SO) splitting of 22 cm^{-1} between the $^2\Pi_{1/2u}$ and $^2\Pi_{3/2u}$ levels of the C_5^- ground electronic state.

In the present work, we report high-resolution slow photoelectron velocity-map imaging (SEVI) vibronic spectra of C_5^-, cooled in our cryogenic ion trap. We previously focused on the spin-orbit levels of the $\widetilde{X}^1\Sigma_g^+ \leftarrow \widetilde{X}^2\Pi_u$ (neutral $\leftarrow$ anion) vibrational origin to demonstrate the cooling ability of the ion trap, finding an SO splitting of 25 cm^{-1} and an internal ion temperature as low as 10 K.[49] Here, the entire $\widetilde{X}^1\Sigma_g^+ \leftarrow \widetilde{X}^2\Pi_u$ photodetachment band is considered. The combination of cryogenic cooling with the inherent high instrumental resolution of SEVI (<4 cm^{-1}) reveals considerably more vibrational structure of neutral C_5 than was seen in previous studies. We find ν_2 (780 cm^{-1}), $2\nu_5$ (408 cm^{-1}), $2\nu_6$ (1069 cm^{-1}), and $2\nu_7$ (208 cm^{-1}), and assign newly observed combination bands. We resolve vibrational fine structure with splittings as small as 6 cm^{-1} corresponding to doubly excited levels of the ν_5, ν_6, and ν_7 bending modes with different values of vibrational angular momentum. Additionally, a number of Franck-Condon forbidden peaks are seen that provide evidence of subtle vibronic coupling effects in both the neutral and anion clusters. Coupled cluster electronic structure theory calculations and Franck-Condon simulations aid in interpreting the experimental spectra.

3.2 Experimental Methods

The SEVI method and apparatus have been described in detail in Chap. 2.

C_5^- clusters were generated with a laser vaporization cluster source. A frequency-doubled Nd:YAG laser was focused onto a 1" disc of graphite, producing a carbon plasma that was entrained within a pulse of He buffer gas from an Even-Lavie solenoid valve.[117]

The apparatus was calibrated with SEVI images of well-known photodetachment transitions[146] of atomic F^- at a variety of photon energies. The 3D distribution of electron velocity vectors was reconstructed from the 2D accumulated image using an inverse-Abel method.[139]

3.3 Calculations

Electronic structure theory calculations for C_5 and C_5^- were carried out at the RCCSD(T)/aug-cc-pVTZ level of theory[200–202] in order to determine the geometries, normal modes, and harmonic frequencies of both species. All calculations were carried out using the Molpro 2010.1 software package.[203] Clusters were restricted to linear geometries, as recommended

by prior theoretical and experimental work.[25,165,170,199] Calculated electronic term energies were zero-point energy corrected.

The photoelectron spectrum for the $\widetilde{X}^1\Sigma_g^+ \leftarrow \widetilde{X}^2\Pi_u$ photodetachment of C_5^- was simulated using the ezSpectrum v3.0 software package.[204] All modes were treated in the harmonic approximation and Franck-Condon (FC) overlap factors were calculated using full Duschinsky mixing of all normal modes.[205] The vibrational origin was fixed to the experimentally determined value of 23018 cm^{-1} (2.8538 eV).[49] Those frequencies of neutral C_5 that were observed in the SEVI spectra (ν_2, $2\nu_5$, $2\nu_6$, and $2\nu_7$) were scaled to their experimental values; the others were left at their calculated RCCSD(T)/aug-cc-pVTZ values.

As C_5^- has a $^2\Pi_u$ electronic ground state, Renner-Teller and spin-orbit effects must be taken into account when considering the anion bending vibrational modes. In this work, the bending frequencies of C_5^- were taken from taken from Perić *et al.*,[195] in which the authors included these effects in modeling the C_5^- anion bending potentials to obtain better values for the ν_5, ν_6, and ν_7 frequencies. The anion stretch frequencies were left at their calculated RCCSD(T)/aug-cc-pVTZ values.

3.4 Results

The SEVI spectra of the $\widetilde{X}^1\Sigma_g^+ \leftarrow \widetilde{X}^2\Pi_u$ photodetachment of C_5^-, taken at an ion trap temperature of 5 K, are presented in Fig. 3.1. A low-resolution overview spectrum at photon energy $h\nu$ =24728 cm^{-1} is shown in blue. The black traces constitute the high-resolution composite spectrum constructed as described in Experimental Methods. The high-resolution traces are scaled to fit the intensity profile of the overview and are vertically offset for comparison. A FC simulation stick spectrum is shown in red, scaled to match the intensity of peak A.

The spectra are dominated by a single peak at low eBE (peak A), above which we resolve narrow vibrational features covering ∼1500 cm^{-1}. A much weaker peak (peak A′) lies 25 cm^{-1} below peak A. No spectroscopic features are visible below peaks A′/A, indicating that they represent the $\widetilde{X}^1\Sigma_g^+ \leftarrow \widetilde{X}^2\Pi_u$ vibrational origin, with peak A′ originating from the $^2\Pi_{3/2u}$ upper spin-orbit level of the anion, in agreement with previous findings.[25,49] Typical experimental peak linewidths are 5–9 cm^{-1} fwhm, far narrower than previous photodetachment experiments. Additionally, at high resolution, some features (peaks C, D, L, M, and P) resolve into previously unseen multiplets with splittings as small as 6 cm^{-1}.

Most observed peaks in the accumulated images have isotropic photoelectron angular distributions (PADs). This is consistent with the PAD expected of a $^1\Sigma_g^+ \leftarrow {}^2\Pi_u$ photodetachment process.[16,78] Only peaks B and F appear to have anisotropic PADs, aligned parallel to the laser polarization axis. Peaks B and F are only weakly visible in the overview spectrum, and are not seen in the higher resolution composite spectrum.

Positions and assignments for the peaks labeled in Fig. 3.1 are summarized in Table 3.1. Calculated and experimental parameters for C_5^- and C_5 obtained in this work are summarized in Table 3.2 and generally found to be in good agreement with literature values.[99,182,193–195]

Table 3.1: Peak positions, offsets, and assignments for the SEVI spectra of C_5^-.

Peak		eBE (cm^{-1})	Offset (cm^{-1})	Assignment	Electronic Band
A′		22993	-25	0_0^0	$^1\Sigma_g^+ \leftarrow ^2\Pi_{3/2u}$
A		23018	0	0_0^0	$^1\Sigma_g^+ \leftarrow ^2\Pi_{1/2u}$
B		23137	119	7_0^1	$^1\Sigma_g^+ \leftarrow ^2\Pi_{1/2u}$
C	c_1	23226	208	$7_0^2\,(l_7=0)$	$^1\Sigma_g^+ \leftarrow ^2\Pi_{1/2u}$
	c_2	23240	222	$7_0^2\,(l_7=\pm2)$	$^1\Sigma_g^+ \leftarrow ^2\Pi_{1/2u}$
D′		23403	385	5_0^2	$^1\Sigma_g^+ \leftarrow ^2\Pi_{3/2u}$
D	d_1	23426	408	$5_0^2\,(l_5=0)$	$^1\Sigma_g^+ \leftarrow ^2\Pi_{1/2u}$
	d_2	23432	414	$5_0^2\,(l_5=\pm2)$	$^1\Sigma_g^+ \leftarrow ^2\Pi_{1/2u}$
E		23483	465	7_0^4	$^1\Sigma_g^+ \leftarrow ^2\Pi_{1/2u}$
F		23553	535	6_0^1	$^1\Sigma_g^+ \leftarrow ^2\Pi_{1/2u}$
H′	h_1'	23628	610	$5_0^2 7_0^2$	$^1\Sigma_g^+ \leftarrow ^2\Pi_{1/2u}$
	h_2'	23636	618	$6_0^1 7_0^1$	$^1\Sigma_g^+ \leftarrow ^2\Pi_{3/2u}$
H		23662	644	$6_0^1 7_0^1$	$^1\Sigma_g^+ \leftarrow ^2\Pi_{1/2u}$
I′		23773	755	2_0^1	$^1\Sigma_g^+ \leftarrow ^2\Pi_{3/2u}$
I		23798	780	2_0^1	$^1\Sigma_g^+ \leftarrow ^2\Pi_{1/2u}$
J		23835	817	5_0^4	$^1\Sigma_g^+ \leftarrow ^2\Pi_{1/2u}$
K		23876	858	$6_0^1 7_0^3$	$^1\Sigma_g^+ \leftarrow ^2\Pi_{1/2u}$
L′		23989	971	$2_0^1 7_0^2$	$^1\Sigma_g^+ \leftarrow ^2\Pi_{3/2u}$
L	l_1	24012	994	$2_0^1 7_0^2\,(l_7=0)$	$^1\Sigma_g^+ \leftarrow ^2\Pi_{1/2u}$
	l_2	24026	1008	$2_0^1 7_0^2\,(l_7=\pm2)$	$^1\Sigma_g^+ \leftarrow ^2\Pi_{1/2u}$
M′	m_1'	24061	1043	$6_0^2\,(l_6=0)$	$^1\Sigma_g^+ \leftarrow ^2\Pi_{3/2u}$
	m_2'	24068	1050	$6_0^2\,(l_6=\pm2)$	$^1\Sigma_g^+ \leftarrow ^2\Pi_{3/2u}$
M	m_1	24087	1069	$6_0^2\,(l_6=0)$	$^1\Sigma_g^+ \leftarrow ^2\Pi_{1/2u}$
	m_2	24093	1075	$6_0^2\,(l_6=\pm2)$	$^1\Sigma_g^+ \leftarrow ^2\Pi_{1/2u}$
N		24212	1194	$2_0^1 5_0^2$	$^1\Sigma_g^+ \leftarrow ^2\Pi_{1/2u}$
O		24225	1207	$2_0^1 7_0^4$	$^1\Sigma_g^+ \leftarrow ^2\Pi_{1/2u}$
P′		24272	1254	$6_0^2 7_0^2$	$^1\Sigma_g^+ \leftarrow ^2\Pi_{3/2u}$
P	p_1	24291	1273	$6_0^2 7_0^2\,(l_6, l_7 =?)$	$^1\Sigma_g^+ \leftarrow ^2\Pi_{1/2u}$
	p_2	24301	1283	$6_0^2 7_0^2\,(l_6, l_7 =?)$	$^1\Sigma_g^+ \leftarrow ^2\Pi_{1/2u}$

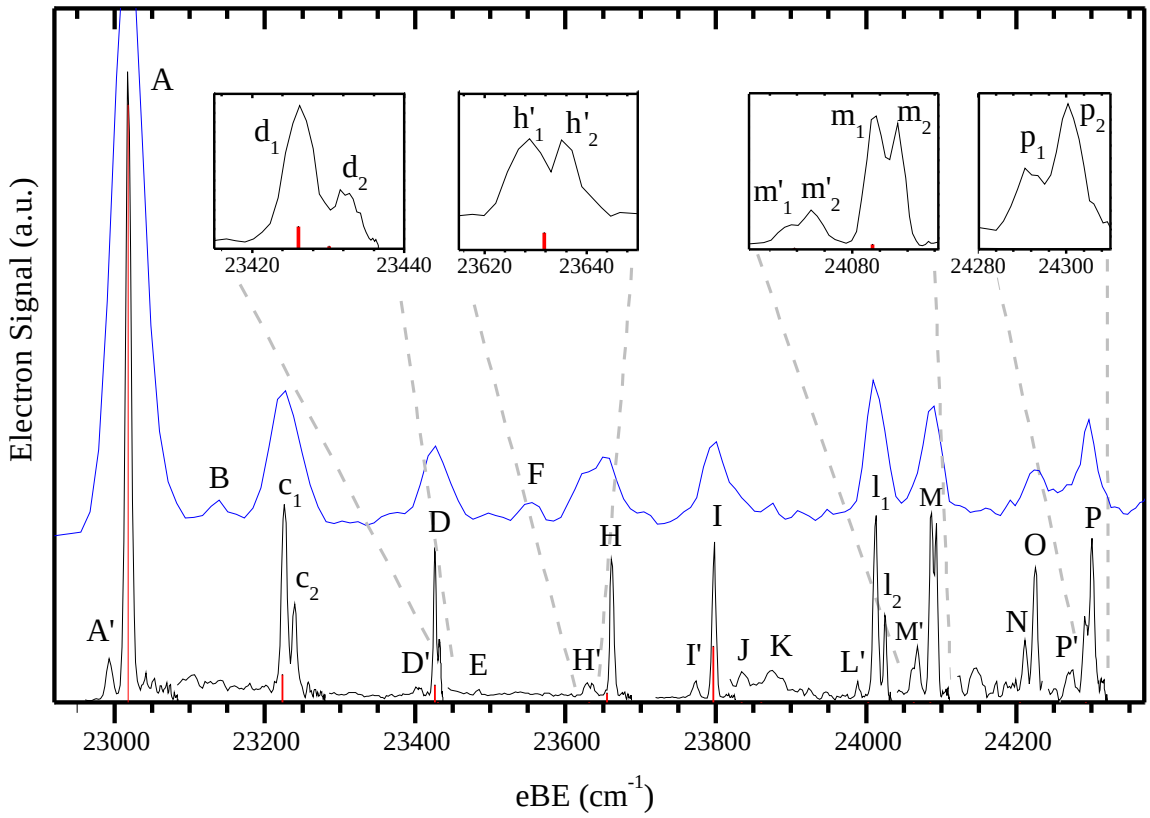

Figure 3.1: SEVI spectra of the $\widetilde{X}^1\Sigma_g^+ \leftarrow \widetilde{X}^2\Pi_u$ photodetachment of C_5^-, taken with the ion trap held at 5 K. A low-resolution overview spectrum is shown in blue. The black trace is a high-resolution composite spectrum taken at many laser frequencies. A FC simulation stick spectrum is shown in red.

3.5 Discussion

The C_5^- SEVI spectra presented in Fig. 3.1 are a significant improvement over the ZEKE spectrum obtained by Kitsopoulos *et al.* in 1991.[25] The experimental resolution is substantially better (2–4 cm^{-1} in the current work as compared to 10–30 cm^{-1} in the ZEKE experiment), enabling better separation of well-defined doublets (A′/A, D′/D, etc.) from the two spin-orbit components of the anion. In addition, even finer multiplet structure of many vibrational modes is seen that was not resolved in the ZEKE spectrum. As these multiplets occur in bending modes with more than one quantum of vibrational excitation, it is likely that they arise from closely spaced vibrational angular momentum states with the same principal quantum number.

Table 3.2: Calculated and experimental parameters for C_5^- and C_5 found in this work. Frequencies are in wavenumbers (cm^{-1}) and bond lengths are in Ångströms (Å). The given uncertainties are one standard deviation of a Gaussian fit to the experimentally observed peak. All calculated parameters were obtained at the RCCSD(T)/aug-cc-pVTZ level of theory, with the exception of the values taken from Ref. [195].

Parameter	C_5^- calculated	C_5 calculated	C_5 experimental	
$R_{C\text{-}C,inner}$	1.307	1.289		
$R_{C\text{-}C,outer}$	1.293	1.297		
$\nu_1\,(\sigma_g^+)$	1976	1977		
$\nu_2\,(\sigma_g^+)$	748	772	$\nu_2 = 780(3)$	
$\nu_3\,(\sigma_u^+)$	1986	2213		
$\nu_4\,(\sigma_u^+)$	1417	1442		
$\nu_5\,(\pi_g)$	(255, 351) 334[a]	196	$2\nu_5 = 408(2)$	$4g_{55} = 6$
$\nu_6\,(\pi_u)$	(333, 545) 521[a]	517	$\nu_6 = 535(13)$; $2\nu_6 = 1069(3)$	$4g_{66} = 7$
$\nu_7\,(\pi_u)$	(123,135) 158[a]	109	$\nu_7 = 119(9)$; $2\nu_7 = 208(4)$	$4g_{77} = 14$
EA		22428	$^1\Sigma_g^+ \leftarrow {}^2\Pi_{1/2u}$: 23018(3) $^1\Sigma_g^+ \leftarrow {}^2\Pi_{3/2u}$: 22993(3)	

The improved resolution of the C_5^- spectra presented here results from several improvements to the SEVI apparatus. The addition of event counting to our data acquisition process increases our sensitivity and enhances VMI spatial resolution. Cryogenic cooling of anions in our trap prior to photodetachment eliminates vibrational hot bands and dramatically narrows rotational envelopes. As described previously,[49] the internal anion temperature can be quantified by comparing the relative intensity of peaks corresponding to photodetachment from the $^2\Pi_{1/2u}$ and $^2\Pi_{3/2u}$ spin-orbit levels of the C_5^- electronic ground state. Assuming that the anions are thermalized in the ion trap, the relative populations of these two states should be governed by Maxwell-Boltzmann statistics. The ZEKE study measured a spin-orbit temperature of 30 K under optimal conditions. Previously, we were able to optimize the cooling conditions in our ion trap to achieve an ion temperature of 10 K at the time of photodetachment.[49] The spectra presented here have a slightly higher SO temperature of 13 K as the system was tuned to optimize both ion temperature and signal.

The spectra are dominated by the vibrational origin (peak A), which indicates that the geometry change between anion and neutral is minimal. The calculated geometries outlined in Table 3.2 correspondingly predict changes in C-C bond lengths of at most ∼1% upon photodetachment. The peak assignments in Table 3.1 were informed by the results of *ab initio* calculations and assignments from previous studies.[25,199] Experimental and simulated peak

positions are generally in good agreement, but the simulation systematically underestimates the intensities for transitions to vibrationally excited states, especially those involving multiply excited bending modes. Peaks designated prime correspond to transitions originating from the $^2\Pi_{3/2u}$ SO level of C_5^-, with the exception of peak h_1', which originates from the $^2\Pi_{1/2u}$ anion ground state but overlaps with an SO peak.

Our assignments of the vibrational origin 0_0^0 (peak A), symmetric stretch 2_0^1 (peak I), and doubly excited bending modes 5_0^2 (peaks d_1 and d_2), 6_0^2 (peaks m_1 and m_2), and 7_0^2 (peaks c_1 and c_2) agree with those of Kitsopoulos *et al.* The ZEKE spectrum also showed a combination band assigned as $5_0^2 7_0^2$. In the analysis presented here, this transition (peak H) is reassigned as $6_0^1 7_0^1$, and a weak feature (peak h_1') overlapping the $6_0^1 7_0^1$ SO peak (peak h_2') is assigned to $5_0^2 7_0^2$, in better agreement with the location and strength of the transitions predicted by the FC simulation. We also observe the $2_0^1 7_0^2$ (peaks l_1 and l_2) and $6_0^2 7_0^2$ (peaks p_1 and p_2) combination bands, as well as the more tentatively assigned features: 5_0^4 (peak J), $6_0^1 7_0^3$ (peak K), $2_0^1 5_0^2$ (peak N), and $2_0^1 7_0^4$ (peak O). The assignment of peaks N and O is especially uncertain, as both lie close to the expected energies of the $2_0^1 5_0^2$ and $2_0^1 7_0^4$ transitions. The simulation predicts $2_0^1 5_0^2$ to be the more intense of the two transitions, but the predicted energy of this feature is closer to peak N, the less intense peak.

There are two weak features (peaks B and F) in the low-resolution SEVI spectrum that do not appear in the high-resolution spectrum. Both peaks are assigned to transitions to a neutral state with a single quantum of excitation in a π_u bending mode: peak B to 7_0^1 and peak F to 6_0^1. These peaks can only appear through a vibronic coupling process, as discussed in more detail below.

The high-resolution traces presented in Fig. 3.1 also show closely-spaced splittings of the vibrational states of C_5 with multiple quanta in doubly degenerate bending modes. These splittings are most reasonably assigned to states with the same vibrational quantum number but different vibrational angular momenta. Our spectra represent the first resolution of vibrational angular momentum structure in C_5, though such structure has been seen in similar systems like C_3[206,207] and carbon suboxide (C_3O_2).[208–210] An approximate energy formula for the excitation of doubly degenerate vibrations in a molecule is given by[65]

$$G(n_1, n_2, \cdots) = \sum_i \nu_i (n_i + d_i/2) + \sum_i \sum_{k \geq i} x_{ik} (n_i + d_i/2)(n_k + d_k/2) + \sum_i \sum_{k \geq i} g_{ik} l_i l_k + \cdots \tag{3.1}$$

where ν_i is the harmonic frequency of the i$^{\text{th}}$ mode, n_i is the vibrational quantum number of the i$^{\text{th}}$ mode, d_i is the degeneracy of the i$^{\text{th}}$ mode, x_{ik} and g_{ik} are small constants giving corrections to account for anharmonicity, and $l_i = \{-n_i, -n_i + 2, \ldots, n_i - 2, n_i\}$ is the vibrational angular momentum of the i$^{\text{th}}$ mode.

The most straightforward case of vibrational angular momentum structure in the C_5 spectra occurs for transitions to a doubly degenerate bending mode ν_i with $n_i = 2$, where $i = \{5, 6, 7\}$. In this case $l_i = \{0, \pm 2\}$; the $l_i = 0$ state has σ_g^+ vibrational symmetry and

the $l_i = \pm 2$ states have δ_g symmetry. In a perfectly harmonic potential, all three levels with $n_i = 2$ would be degenerate in energy, but to the order of accuracy given in Eqn. (3.1), anharmonicity causes a splitting of $4g_{ii}$ between the $l_i = 0$ and $l_i = \pm 2$ states. Splittings observed for the 5_0^2, 6_0^2, and 7_0^2 transitions in the SEVI spectra of C_5^- are reported in Table 3.2. The SO-excited peak of 6_0^2 is intense enough to reveal a splitting as well (peaks m_1' and m_2' in inset of Fig. 3.1). The splitting of the doubly excited ν_7 mode is also seen for $2_0^1 7_0^2$ (peak L); ν_2 is a σ_g^+ stretching mode and therefore does not appear to alter the vibrational angular momentum structure of the 7_0^2 transition when observed in combination. In all cases mentioned above, the peak at lower eBE is more intense, and is assigned to the $l_i = 0$ state since this transition is nominally FC allowed, whereas transitions to the $l_i = \pm 2$ levels are not (see below).

The $6_0^2 7_0^2$ transition (peaks p_1 and p_2) has a complicated multiplet structure not fully resolved in the SEVI spectra. This is befitting of a state involving two quanta of excitation in each of two doubly degenerate vibrational modes, which within the approximation of Eqn. (3.1) should result in a quintuplet. We expect 5_0^4 (peak J), 7_0^4 (peak E), and $6_0^1 7_0^3$ (peak K) to show similar multiplet structure, but they are too weak to resolve any splittings. It is also possible that peaks N and O, tentatively assigned to $2_0^1 5_0^2$ and $2_0^1 7_0^4$, are in fact the angular momentum multiplet of a single vibrational transition.

Eqn. (3.1) predicts the $6_0^1 7_0^1$ transition (peak H) to appear as a doublet split by $2g_{67}$. We resolve peak H as a singlet with a $7\,\mathrm{cm}^{-1}$ fwhm. High-resolution IR spectroscopy studies of the closely related carbon suboxide (C_3O_2) molecule have observed vibrational angular momentum splittings of less than $3\,\mathrm{cm}^{-1}$ for the analogous $\nu_6 + \nu_7$ mode.[208,210] Splittings of this magnitude cannot be resolved with our SEVI spectrometer, so we expect $6_0^1 7_0^1$ to appear as a singlet.

There are several features in the SEVI spectra that are not reproduced in the FC simulations. In addition, the simulated intensities for many of the transitions that are reproduced are systematically lower than the experimental intensities. Some of these discrepancies can be addressed by varying the geometries obtained from the electronic structure calculations. For example, increasing the calculated outer C-C bond length of the anion by 0.01 Å boosts the simulated intensity of the 2_0^1 transition (peak I) by nearly 50%. However, so long as the anion and neutral are linear, odd Δn transitions in the bending modes are FC forbidden.[67] Moreover, one cannot significantly affect the intensities of FC allowed (even Δn) transitions involving the bending vibrations without drastic alteration of the anion and neutral bend frequencies listed in Table 3.2. It is more likely that these systematic intensity discrepancies are caused by vibronic coupling effects in the neutral and anion.

We first consider peaks B and F, which are assigned to the 7_0^1 and 6_0^1 transitions, respectively. These transitions are FC forbidden. However, the neutral levels have overall Π_u vibronic symmetry. Transitions to these levels can occur if they are mixed by Herzberg-Teller (HT) coupling with totally symmetric vibrational levels of a low-lying $^1\Pi_u$ excited electronic state of C_5. Such a state has been predicted by theory to lie ∼2.6 eV above the $^1\Sigma_g^+$ electronic ground state[184] and has been observed for C_5 in a neon matrix and in the gas phase with a term energy of ∼2.43 eV.[176–178]

A photodetachment transition from a $^2\Pi_u$ anion electronic state that is allowed by HT coupling with a $^1\Pi_u$ state would yield an outgoing photoelectron wavefunction with π_u symmetry.[16,78] Indeed, peaks B and F have parallel PADs corresponding to p-wave detachment. Additionally, the near-threshold cross section for photodetachment (σ) is governed by the Wigner threshold law,[75] $\sigma \propto (\mathrm{eKE})^{l+1/2}$, where l is the angular momentum of the outgoing photoelectron. As a result, the photodetachment cross section falls off more sharply close to threshold for p-wave ($l = 1$) electrons than for s-wave ($l = 0$) electrons. Peaks B and F are therefore expected to vanish close to threshold, as they do in the high-resolution SEVI spectra. More detailed discussions of vibronic coupling among neutral electronic states in photoelectron spectra and SEVI experiments are presented elsewhere.[6,85,211]

The appearance of the FC forbidden $l_i = \pm 2$ components of the i_0^2 transitions and the unexpected strength of their $l_i = 0$ components is attributed to a different vibronic coupling scheme: Renner-Teller (RT) coupling between the vibrational levels of the anion within its $^2\Pi_u$ electronic ground state. Renner-Teller coupling between vibrational levels in Π electronic states of linear molecules is well-understood.[195,212,213] It is usually invoked to explain complex shifting and splitting of vibrational and rotational structure within a Π state. In the case of the SEVI spectra of C_5^-, however, RT coupling appears in a somewhat novel way, as a means of providing intensity to weak or forbidden vibronic transitions.

RT coupling in the C_5^- anion has been discussed in detail by Perić *et al.*[195] If the anion electronic orbital angular momentum (Λ) and the vibrational angular momenta of the bend-

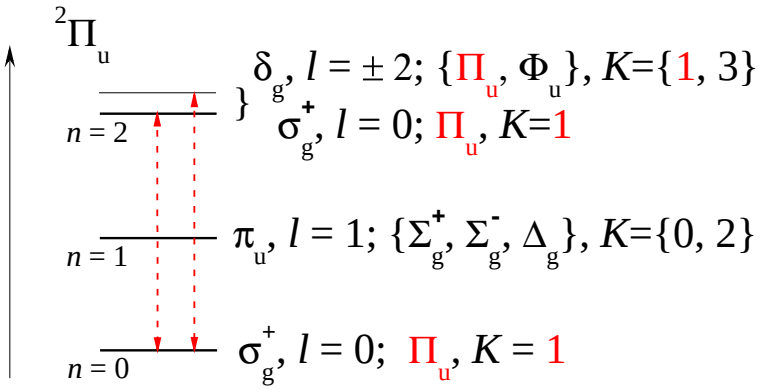

Figure 3.2: Schematic of π_u bending mode levels in the C_5^- anion $^2\Pi_u$ electronic ground state, neglecting spin-orbit splittings and Renner-Teller splitting of the $n = 1$ level for the purpose of illustration. Labels indicate vibrational symmetry and angular momentum quantum number l for each level as well as the overall vibronic symmetry and K value. The ground vibrational state interacts with the $n = 2$, $l = \{0, \pm 2\}$ levels through RT coupling (marked in red), as those levels have components with the same overall Π_u vibronic symmetry and $K = 1$.

ing modes are allowed to mix, Λ and l_i are no longer good quantum numbers. Instead one must consider the vibronic angular momentum $K = |l_5 + l_6 + l_7 + \Lambda|$. The anion ground vibrational state can couple to both the $l_i = 0$ and $l_i = \pm 2$ states for anion bending modes with $n_i = 2$, as all have components with Π_u overall vibronic symmetry and $K = 1$. The matrix elements $\langle n_i = 0, l_i = 0| \widehat{H} |n_i = 2, l_i = 0, \pm 2\rangle$ of the anion Hamiltonian can therefore be non-zero for modes ν_5, ν_6, and ν_7. This coupling scheme is laid out in Fig. 2 for the case of a π_u bending mode. Such a scheme enables transitions from the anion vibrational ground state to the doubly excited bending modes of the neutral with $l_i = \pm 2$. Transitions to neutral bending modes with $n_i = 2$, $l_i = 0$ would also appear more intense than predicted by FC simulation as a result of this coupling, as seen in our spectra.

The situation is very similar for a single quantum of excitation in each of two distinct π_u modes such as the $6_0^1 7_0^1$ transition (peak H). This combination results in three states with vibrational symmetry σ_g^+, σ_g^-, and δ_g, and since $l_6, l_7 = \pm 1$, we have $l_{tot} = l_6 + l_7 = 0, \pm 2$.[65] All three states are of the correct symmetry to couple vibronically with the anion ground vibrational state, and may therefore appear in the neutral spectra through RT coupling, as in the $n_i = 2$ case. As discussed previously, the energy splitting between the various l_{tot} states is too narrow to resolve with SEVI, and as a result, the $6_0^1 7_0^1$ peak appears as a singlet in the spectra. RT coupling is only possible in this case because the ν_6 and ν_7 bending modes are both of cis (i.e. π_u) symmetry.[195] The combination of a single excitation in both a trans mode and a cis mode (e.g. ν_5 and ν_6) would not result in states with the correct symmetry to RT couple with the anion ground vibrational state.

The FC forbidden δ_g peaks could conceivably be attributed to Herzberg-Teller coupling with totally symmetric vibrational levels of a $^1\Delta_g$ excited state of C_5. However, the lowest lying $^1\Delta_g$ state of C_5 has been calculated to lie $\sim$4.5 eV above the C_5 ground state.[184] Such a state would seem too far removed to support what would need to be a strong vibronic coupling with the ground state, since the forbidden $n_i = 2$, $l_i = \pm 2$ bending mode peaks appear nearly as intense as the $n_i = 2$, $l_i = 0$ peaks. Additionally, unlike the proposed Renner-Teller scheme, HT coupling would not explain why all multiply excited bending mode features appear more strongly than predicted by the FC simulation.

3.6 Conclusions

High-resolution SEVI spectra of cryogenically cooled C_5^- clusters are reported. We identify the ν_2 symmetric stretching mode, doubly excited ν_5, ν_6, and ν_7 bending modes, and various combination bands of the neutral C_5 cluster. Coupled cluster electronic structure theory calculations and Franck-Condon simulations are in sufficient agreement with the experimental spectrum to enable assignment of most of the observed features. Additionally, we resolve vibrational angular momentum structure of various multiply excited bending modes which can only appear through Renner-Teller coupling between vibrational levels of the anion electronic ground state, and two FC forbidden π_u vibrational modes which must appear through Herzberg-Teller coupling between electronic levels of the neutral cluster.

The ability to resolve vibrational fine structure in size-selected clusters shows that slow photoelectron velocity-map imaging has considerable potential for cluster spectroscopy, as demonstrated here and, very recently, by Wang and coworkers for Au_4^-.[214] This capability is dramatically enhanced by the cryo-cooling method described in this work.

Chapter 4

Rovibronic structure of CH_2CN and CD_2CN

The content and figures of this chapter are reprinted or adapted with permission from
M. L. Weichman, J. B. Kim, and D. M. Neumark, "Rovibronic structure in slow photoelectron velocity-map imaging spectroscopy of CH_2CN^- and CD_2CN^-"
J. Chem. Phys. **140**, 104305 (2014).

Abstract

We report high-resolution anion photoelectron spectra of the cryogenically cooled cyanomethide anion, CH_2CN^-, and its isotopologue, CD_2CN^-, using slow photoelectron velocity-map imaging (SEVI) spectroscopy. Electron affinities of 12468(2) cm^{-1} for CH_2CN and 12402(2) cm^{-1} for CD_2CN are obtained, demonstrating greater precision than previous experiments. New vibrational structure is resolved for both neutral species, especially activity of the ν_5 hydrogen umbrella modes. The ν_6 out-of-plane bending mode fundamental frequency is measured for the first time in both systems, and found to be 420(10) cm^{-1} for CH_2CN and 389(8) cm^{-1} for CD_2CN. Some rotational structure is resolved, allowing for accurate extraction of vibrational frequencies. Temperature-dependent SEVI spectra show marked effects ascribed to controlled population of low-lying anion vibrational levels. We directly measure the inversion splitting between the first two vibrational levels of the anion ν_5 umbrella mode in both species, finding a splitting of 130(20) cm^{-1} for CH_2CN^- and 81(20) cm^{-1} for CD_2CN^-. Franck-Condon forbidden activity is observed and attributed to mode-specific vibrational autodetachment from the CH_2CN^- and CD_2CN^- dipole bound excited states. We also refine the binding energy of the anion dipole bound states to 39 and 42 cm^{-1} respectively for CH_2CN and CD_2CN^-.

4.1 Introduction

The cyanomethyl radical, CH_2CN, is important astrochemically as an open-shell carbon-containing species.[215,216] It is also an intermediate in hydrocarbon combustion,[217] and is involved in thermal decomposition[218] and atmospheric reactions[219,220] of acetonitrile. The CH_2CN^- anion has been a benchmark system for ion thermochemistry studies,[221,222] and the transition from its electronic ground state to its excited dipole bound state is a plausible candidate for the 803.79 nm diffuse interstellar band.[100,223] Ground state CH_2CN^- has yet to be detected in space, though electronically analogous species like ketenimine (CH_2CNH)[224] and propadienylidene (CH_2CC)[225] have been found in the interstellar medium. Correlating astronomical microwave or IR detection of CH_2CN^- with the 803.79 nm DIB would make the case much more compelling.[226] Accurate spectroscopic characterization of CH_2CN and

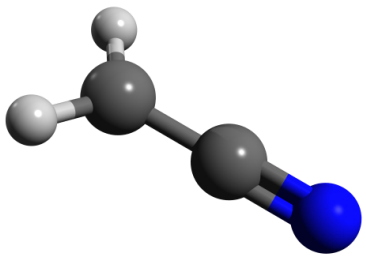

Figure 4.1: Structure of the CH_2CN radical.

CH_2CN^- is crucial to their identification in astrochemical data. In the current work, we report newly resolved rovibronic structure of CH_2CN, CD_2CN, and the corresponding anions via slow photoelectron velocity-map imaging.

The cyanomethyl radical has a planar C_{2v} geometry (Fig. 4.1) and a $^2B_1$ ground electronic state.[227–229] The earliest studies of CH_2CN were electron spin resonance experiments carried out in a cold matrix.[230–232] In 1979, Jacox assigned IR absorption bands to the CH_2CN radical in an argon matrix.[233] The microwave spectrum of CH_2CN was observed in the laboratory in 1988 by Saito *et al.*,[227] which led to its identification in interstellar dust clouds.[215,234] More recently, it has been observed in the circumstellar shell of a carbon-rich star.[216] CH2CN has been further characterized with high-resolution laboratory microwave spectroscopy,[228,235] and argon matrix IR absorption measurements have been made for both CH_2CN and CD_2CN.[236] The rotational structure of the ν_5 hydrogen umbrella mode of CH_2CN was studied in high resolution with IR diode laser spectroscopy.[237] Several theoretical studies have also been carried out to model the radical geometry and vibrational structure.[229,238–241]

Zimmerman and Brauman[242] found the electron affinity of CH_2CN via measurement of the total photodetachment cross section of CH_2CN^- in 1977. The CH_2CN^- anion is closed-shell, and has a slightly non-planar C_s geometry with $^1A'$ electronic symmetry.[223,226,229,240,241,243,244] The potential along the anion ν_5 umbrella coordinate is a shallow double well. *Ab initio* calculations by Gutsev and Adamowicz[240] predict a barrier of $\sim$150 cm^{-1} while Moran *et al.*[229] fit experimental data to yield a barrier height of 100 cm^{-1}. As the barrier is small, the anion geometry can be considered quasi-planar.[240,245,246] Schematic ν_5 bending potentials for anionic and neutral CH_2CN are illustrated in Fig. 4.2.

CH_2CN has a permanent dipole of at least 3.5 Debye,[235,240] allowing an excess electron to bind weakly to form a $^1B_1$ anionic dipole bound state (DBS).[247] The DBS has a planar C_{2v} structure like the neutral species,[223,240,245] as the dipole bound electron only weakly perturbs the molecular core. The DBSs of CH_2CN^- and CD_2CN^- have been studied with rotational autodetachment spectroscopy, first by Marks *et al.*[247] and then at considerably higher resolution by Lykke *et al.*,[245,248] who were able to extract rotational constants and energetics of the valence and DBS anions of both species. Lykke *et al.* placed an upper bound of 67 cm^{-1} on the binding energy of the CH_2CN^- DBS and 66 cm^{-1} on the CD_2CN^- DBS. Wetzel *et al.*[246] later studied the rotational structure of the ν_5 mode of the CH_2CN^- DBS with vibrational autodetachment spectroscopy.

Anion photoelectron spectroscopy (PES) is an attractive technique for studying neutral radicals through photodetachment of a stable closed-shell anion.[17] CH_2CN^- has been studied in several PES experiments at a resolution of $\sim$100 cm^{-1}.[229,244,249] Moran *et al.*[229] found an electron affinity of around 1.54 eV for both CH_2CN and CD_2CN, and observed that both spectra were dominated by a progression in the ν_5 umbrella mode, reflecting transitions from an anion with a small barrier to planarity to a flat neutral. In all of these experiments, the anions were at room temperature or warmer. The $v_5 = 1$ anion level has significant population at 300 K, leading to hot bands and congestion of the photoelectron spectra.

In the present work, we report high-resolution slow photoelectron velocity-map imaging (SEVI) spectra of the $\tilde{X}^2B + 1 \leftarrow \tilde{X}^1A'$ transition for cryogenically cooled CH_2CN^- and

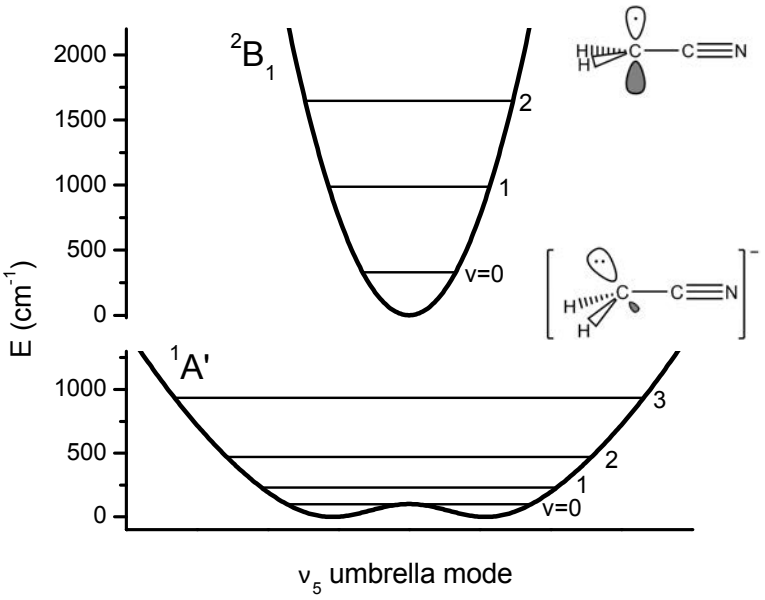

Figure 4.2: Schematic of ν_5 umbrella potentials and vibrational energy levels for the anion and neutral surfaces of CH_2CN.

CD_2CN^-. The combination of cooling with the inherent high instrumental resolution of SEVI reveals considerably more vibrational structure than was seen in previous PES studies, as well as newly resolved rotational structure. The ν_6 fundamentals of both species and the $2\nu_9$ overtone of CH_2CN are observed for the first time experimentally. The inversion splittings between the $v_5 = 0$ and 1 levels in both CH_2CN^- and CD_2CN^- are measured directly in temperature-dependent studies. Weak Franck-Condon (FC) forbidden modes are observed in the spectra of both isotopologues and their appearance is attributed to mode-specific autodetachment from vibrationally excited states of the anion DBSs.

4.2 Experimental Methods

The SEVI method and apparatus has been described in detail in Chap. 2.

CH_2CN^- anions are prepared by expanding a dilute gas mixture of acetonitrile in He buffer gas through a pulsed Even-Lavie solenoid valve[117] fitted with a circular ionizer. CD_2CN^- anions are prepared similarly, using acetonitrile-d_3 as a precursor. Electrons from the ionizer produce slow secondary electrons that undergo dissociative attachment to acetonitrile and acetonitrile-d_3 to form the anions of interest.[250]

The spectrometer is calibrated with spectra of well-characterized photodetachment transitions[145] of atomic O. Electron kinetic energy (eKE) distributions are reconstructed from the accumulated image using the Maximum Entropy Velocity Legendre Reconstruction (MEVELER) method.[140]

4.3 Calculations

Electronic structure theory calculations for CH_2CN^-, CH_2CN, CD_2CN^-, and CD_2CN were carried out at the RCCSD(T)/aug-cc-pVTZ level of theory[200–202] in order to determine the geometries, normal modes, and harmonic frequencies of all species. Time-dependent density functional theory (TDDFT)[251,252] was used at the B3LYP/aug-cc-pVTZ level of theory to find the energies of excited electronic states of neutral CH2CN. Coupled-cluster calculations were carried out using the Molpro 2010.1 software package[203] and TDDFT calculations were carried out in Q Chem 4.0.[253,254] The geometries of the neutral species were fixed at C_{2v} symmetry in keeping with the literature,[228,229] while calculations for the anions were carried out with C_{2v} and C_s geometries. Parameters calculated for CH_2CN, CD_2CN, and their anions are summarized in Table 4.1.

Rotational envelopes for the vibrational features of both isotopologues were modeled

Table 4.1: Energies, geometries, and harmonic frequencies for CH_2CN, CD_2CN, and their respective anions calculated at the CCSD(T)/aug-cc-pVTZ level of theory. Calculated electron affinities are given with respect to the C_s anion and are not corrected for vibrational zero-point energy. Energies are given in wavenumbers (cm^{-1}), bond lengths in Ånströms (Å), and angles in degrees.

	CH_2CN^- (C_s)	CH_2CN^- (C_{2v})	CD_2CN^- (C_{2v})	CH_2CN	CD_2CN
EA	–	–		12010	
$R_{H\text{-}C}$	1.087	1.082		1.080	
$R_{C\text{-}C}$	1.402	1.389		1.396	
$R_{C\text{-}N}$	1.187	1.190		1.174	
$\angle_{HCH,\ in\text{-}plane}$	115.48	119.75		120.44	
$\angle_{HCC,\ in\text{-}plane}$	116.01	120.13		119.73	
$\angle_{HCC,\ out\text{-}of\text{-}plane}$	34.77	–		–	
ω_1 (a_1)		3148	2283	3177	2302
ω_2 (a_1)		2087	2082	2117	2115
ω_3 (a_1)		1419	1157	1453	1155
ω_4 (a_1)		1061	922	1023	913
ω_5 (b_1)		–	–	640	527
barrier[a]		102	102	–	–
ω_6 (b_1)		552	543	410	384
ω_7 (b_2)		3232	2407	3289	2453
ω_8 (b_2)		1015	841	1032	841
ω_9 (b_2)		418	373	361	327

[a]The barrier is calculated as the difference in energy between the optimized C_s and C_{2v} anion structures.

using the PGOPHER program.[255] The rotational constants for neutral CH_2CN and CD_2CN were taken from Saito *et al.*[228] while those for the corresponding anions were taken from Lykke *et al.*[245] The simulation was fit to each experimental rotational contour, with fixed rotational constants and varying band origin, temperature, and Gaussian linewidth.

4.4 Results

Overview SEVI spectra of the $\tilde{X}^2B_1 \leftarrow \tilde{X}^1A'$ photodetachment of CH_2CN^- and CD_2CN^- are presented in Figs. 4.3a and 4.3b, respectively. Spectra of both species were taken at 5 K (black traces) and at 300 K (red traces). The temperature dependence for the low-eBE region of the spectra is examined in higher resolution in Fig. 4.4a for CH_2CN^- and Fig. 4.4b for CD_2CN^-. Both sets of spectra in Figs. 4.3 and 4.4 are highly temperature dependent. For CH_2CN^-, peaks C′ and J′, which are significant at room temperature, vanish at 5 K, while the much weaker peaks C and J become visible. The CD_2CN^- spectrum has more structure: peaks B′, C′, F′, X, Y, and Z, present at higher temperatures, are observed to vanish at 5 K, while peaks B and C become visible.

Cold, high-resolution SEVI spectra for the entire $\tilde{X}^2B_1 \leftarrow \tilde{X}^1A'$ band are shown in Figs. 4.5a and 4.5b for CH_2CN^- and CD_2CN^-, respectively. The high-resolution traces (black) are scaled to the intensity profile of the overview (blue) and are vertically offset for comparison. Both sets of spectra are dominated by intense peaks A at low eBE, with vibrational structure continuing for another $\sim 3000\,cm^{-1}$. For both systems, no spectroscopic features are visible below the peaks labeled A, indicating that peak A represents the vibrational origin in both cases. Positions and assignments for the peaks labeled in Figs. 4.3, 4.4, and 4.5 are summarized in Tables 4.2 and 4.3 for CH_2CN^- and CD_2CN^-. For peaks with rotational multiplet structure resolved in Fig. 4.5, peak positions represent the band origin found by fitting the features rotational contour in PGOPHER as discussed in Section 4.3. Positions for peaks with unresolved rotational structure (hot bands and FC forbidden features) represent the peak center found with a Gaussian fit. While SEVIs instrumental resolution is limited in this system by unusual rotational envelopes, features as narrow as $8\,cm^{-1}$ fwhm were observed in the high-resolution spectra. Peak assignments, discussed in detail in Section 4.5, were informed by the results of *ab initio* harmonic frequency calculations and values from previous studies.[229,233,236,239]

The vibrational features in the spectra of both species have distinctive rotational envelopes, discussed in more detail in Section 4.5.3. The vibrational origins are shown in Fig. 4.6, with experimental contours in black and simulations in red. In the CH_2CN^- spectrum, most vibrational modes have a characteristic three-peak rotational envelope at 5 K. The rotational contours of the CD_2CN^- spectrum have a more complex multiplet structure and are not fully resolved. The CH_2CN^- origin was fit in PGOPHER with a Gaussian linewidth of $4\,cm^{-1}$ and an anion rotational temperature of ∼10 K, in line with previous measurements of ion temperature after extraction from our trap.[49] The CD_2CN^- contours are too poorly resolved for optimal fitting; the fit of the vibrational origin yielded a $6\,cm^{-1}$ linewidth and

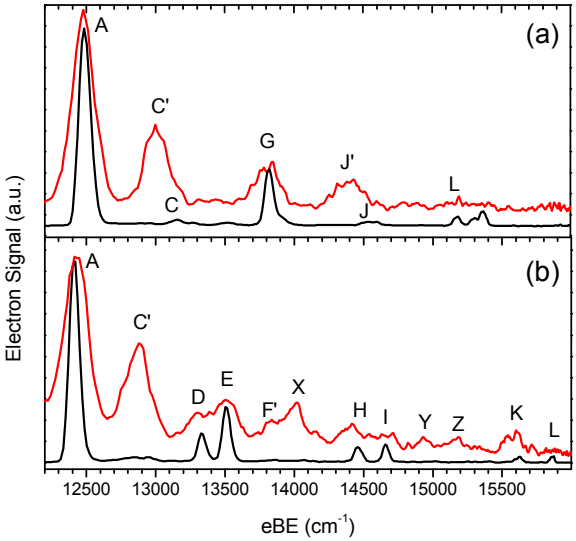

Figure 4.3: Overview SEVI spectra of (a) CH_2CN^- and (b) CD_2CN^-. The black traces were taken with the ion trap held at 5 K, and with photon energies of 16076 cm^{-1} for CH_2CN^- and 16128 cm^{-1} for CD_2CN^-. The red traces were taken with the trap at 300 K and photon energies of 16102 cm^{-1} for CH_2CN^- and 16128 cm^{-1} for CD_2CN^-.

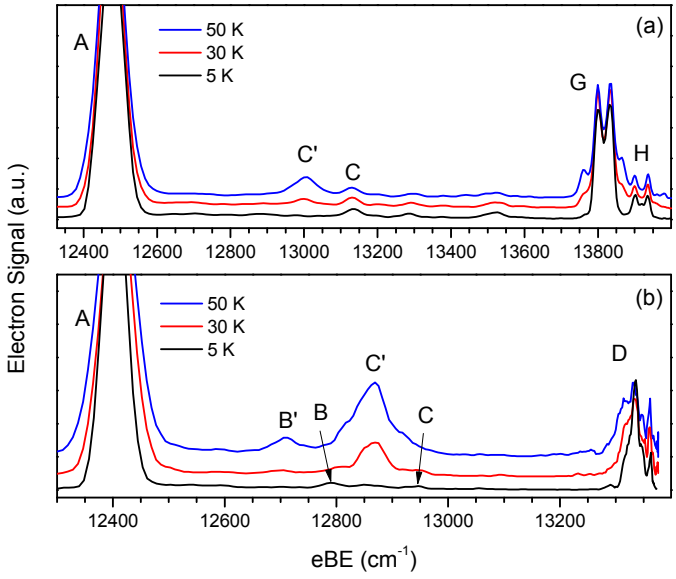

Figure 4.4: Low-eBE regions of the SEVI spectra of (a) CH_2CN^- and (b) CD_2CN^- illustrating the temperature dependence of some vibrational features. The photon energy was tuned to 14028 cm^{-1} for CH_2CN^- and to 13376 cm^{-1} for CD_2CN^-. The ion trap temperature was set to 50 K (blue traces), 30 K (red traces), and 5 K (black traces). Traces are vertically offset for clarity.

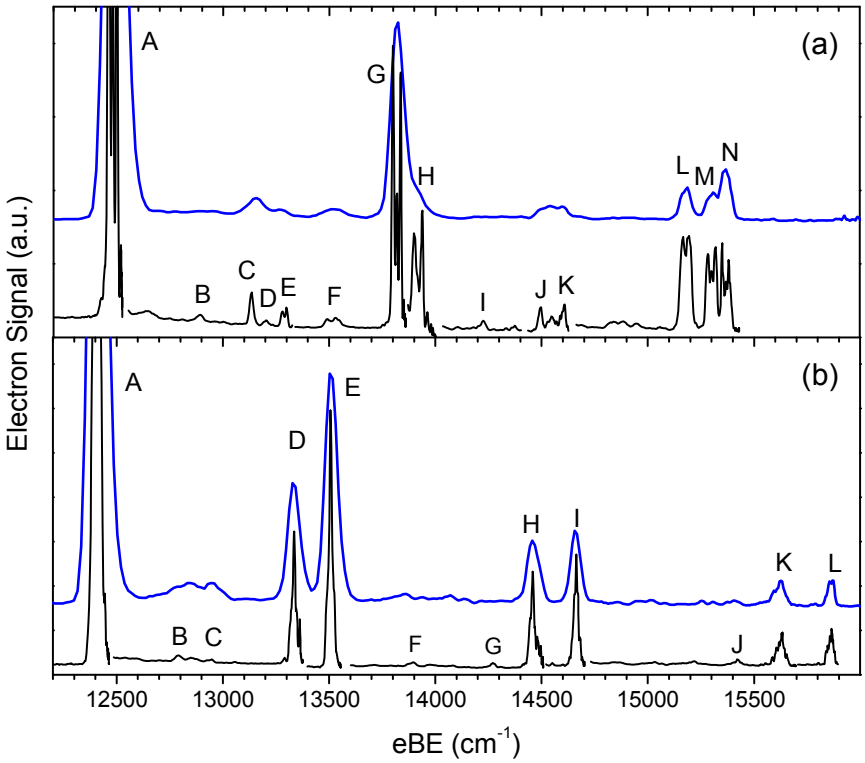

Figure 4.5: SEVI spectra of (a) CH_2CN^- and (b) CD_2CN^-, taken with the ion trap held at 5 K. The blue traces are the cold low-resolution overview spectra from Fig. 4.3. The black traces are high-resolution composite spectra taken at many laser frequencies.

an ion temperature of ∼35 K.

The relative intensities of some peaks are observed to vary dramatically as a function of photon energy. Fig. 4.7 shows the wavelength-dependent intensity of peak C in the SEVI spectra of both isotopologues. A dramatic increase in the relative intensity of peak C is observed with the photon energy tuned just below peak E for CD_2CN^-, and above peak G for CH_2CN^-.

Nearly all peaks in the accumulated images for both isotopologues have photoelectron angular distributions (PADs) aligned perpendicular to the laser polarization axis that shift to isotropic closer to threshold, as is expected for a $\tilde{X}^2B_1 \leftarrow \tilde{X}^1A'$ transition.[16,256] The exceptions are peaks B and C in the CH_2CN^- spectra and peak C in the CD_2CN^- spectra, which appear isotropic regardless of eKE. Peaks I, J, and K for CH_2CN^-, and peaks B and F for CD_2CN^- are too weak to accurately measure anisotropies.

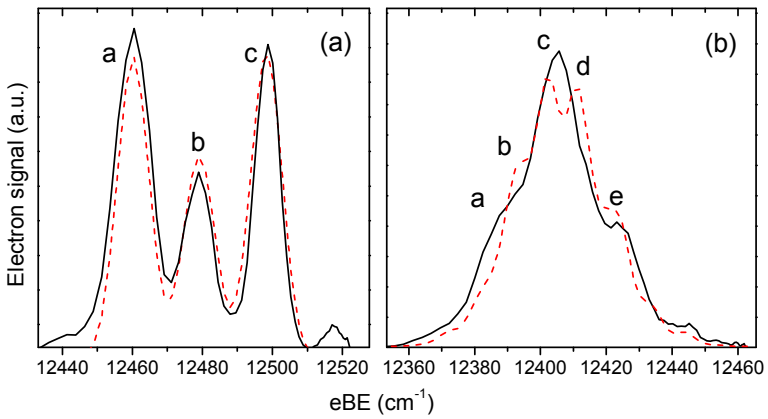

Figure 4.6: Vibrational origins of the (a) CH_2CN^- and (b) CD_2CN^- high-resolution SEVI spectra, taken at 5 K. Experimental spectra are plotted in solid black lines, while simulated spectra are plotted in red dashed lines.

4.5 Discussion

The SEVI spectra of CH_2CN^- and CD_2CN^- demonstrate the utility of cryogenically cooling anions prior to photodetachment. With the ion trap held at 5 K, the hot bands which dominated previously reported photoelectron spectra vanish entirely.[229,244,249] This effect is demonstrated for both species in Fig. 4.3. In the absence of hot bands, we resolve other weak vibrational features. SEVI also provides excellent instrumental resolution (5–7 cm^{-1} in the current work) which, when combined with cooling, elucidates rotational structure and allows for more accurate extraction of vibrational frequencies through fitting of rotational contours. The spectroscopic information extracted from our experiment is summarized in Table 4.4, along with key results from prior work in other laboratories. Error values reported for the current work represent instrumental resolution at a given eKE, determined by one standard deviation of a Gaussian fit to a peak of atomic O^-. The exceptions are the ν_5 inversion splittings, where the reported error is one standard deviation of a Gaussian fit to the 5_1^1 hot band of each species.

4.5.1 Vibrational assignments for CH_2CN

The CH_2CN^- SEVI spectra are dominated by the vibrational origin (peak A in Figs. 4.3a, 4.4a, and 4.5a) at 12468 cm^{-1} (1.546 eV). The room-temperature spectrum (red) in Fig. 4.3a is in excellent agreement with the previously reported photoelectron spectra of CH_2CN^-.[229,244,249] At 300 K, all that is resolved is the vibrational origin (peak A), followed by a progression in the ν_5 mode (peaks C′, G, J′, and L). An intense vibrational origin indicates minimal change in geometry between anion and neutral. Extended progressions in the ν_5 umbrella mode indicate that the anion and neutral geometries differ primarily with regards to planarity.[229,244] The calculated geometries laid out in Table 4.1 support this

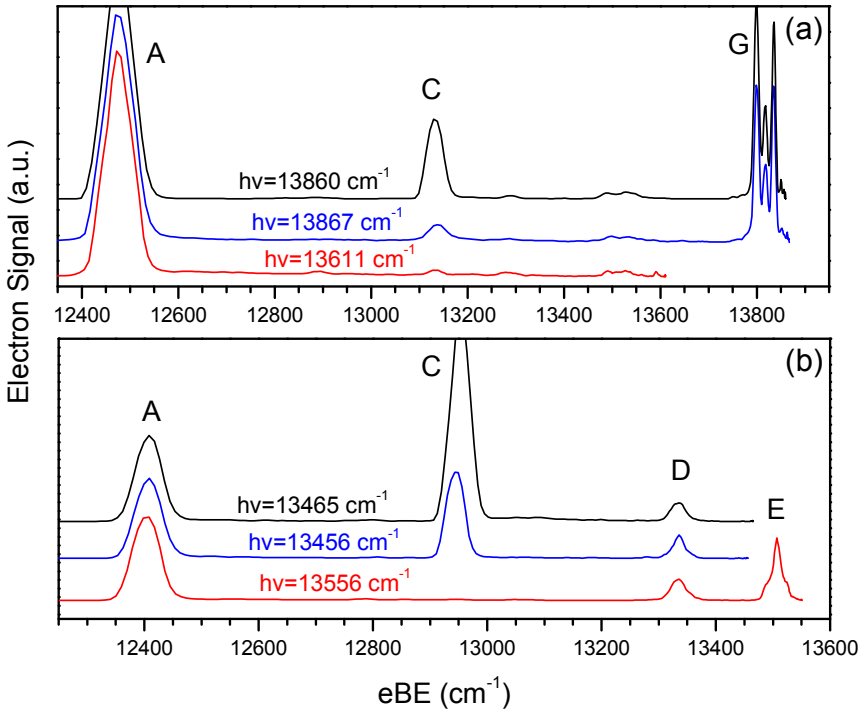

Figure 4.7: SEVI spectra of (a) CH_2CN^- and (b) CD_2CN^- taken at 5 K and various photon energies, illustrating wavelength dependence of relative peak intensities.

conclusion. The optimized anion geometry is a C_s bent structure, while the planar C_{2v} structure lies on top of a barrier, calculated to be 102 cm^{-1}, along the ν_5 coordinate. As this barrier is expected to be comparable to the ν_5 vibrational zero-point energy (see Fig. 4.2),[229] the anion structure is effectively planar, but "floppy." The ν_5 progression in the SEVI spectrum is therefore poorly represented by a harmonic FC simulation.

The progression observed at 300 K is not regularly spaced, because transitions to neutral levels with even and odd quanta in ν_5 originate from different anion vibrational levels. The shallow double well structure of the anion ν_5 potential pushes the two lowest vibrational states closer in energy, creating a small enough gap to have a significant $v_5 = 1$ population at room temperature. Only transitions to neutral states with even quanta in the ν_5 mode can originate from the ground vibrational state of the anion: 5_0^2 (peak G) and 5_0^4 (peak L). Allowed transitions to neutral states with odd ν_5 quanta must originate from the anion $v_5 = 1$ state: 5_1^1 (peak C′) and 5_1^3 (peak J′).

The hot band nature of the odd-quanta states is made clear by the 5 K spectrum shown in black in Fig. 4.3a. Here, the intensities of peaks G and L are unchanged relative to A from the 300 K trace, but peaks C′ and J′ disappear entirely, as there is no significant population in the $v_5 = 1$ anion level at 5 K. The much weaker features C and J, visible in the absence of peaks C′ and J′, are assigned to the FC forbidden transitions 5_0^1 and 5_0^3 based on agreement with IR absorption measurements of the ν_5 fundamental in gas phase[236] and

Table 4.2: Peak positions, shifts, and assignments for the SEVI spectra of CH_2CN^- given in Figs. 4.3a, 4.4a, and 4.5a.

Peak	Position (cm^{-1})	Shift (cm^{-1})	Assignment
A	12468	0	0_0^0
B	12888	420	6_0^1
C′	12997	529	5_1^1
C	13127	659	5_0^1
D	13200	732	9_0^2
E	13279	811	6_0^2
F	13495	1027	4_0^1
G	13808	1340	5_0^2
H	13907	1439	3_0^1
I	14224	1756	$5_0^2 6_0^1$
J′	14386	1918	5_1^3
J	14483	2015	5_0^3
K	14600	2132	$3_0^1 5_0^1$
L	15171	2703	5_0^4
M	15291	2823	$3_0^1 5_0^2$
N	15360	2892	3_0^2

argon matrices.[233,237]

Fig. 4.4a demonstrates more clearly the temperature dependence of 5_1^1 (peak C′). The spacing between peaks C and C′ is well-resolved at temperatures of 30–50 K, giving an inversion splitting of $\sim$130 cm^{-1} between the $v_5 = 0$ and 1 levels of CH_2CN^-, close to the value of 152 cm^{-1} predicted by Moran *et al.*[229] This work is the first direct experimental determination of the splitting between these two levels.

The high-resolution composite spectrum of CH_2CN^- shown in Fig. 4.5a shows additional vibrational structure. In addition to the progression in ν_5 (peaks C, G, J, and L), we observe transitions involving the C-C-N out-of-plane bending mode 6_0^1 (peak B) and 6_0^2 (peak E), the symmetric C-C stretching mode 4_0^1 (peak F), the symmetric CH_2 scissoring mode 3_0^1 (peak H) and 3_0^2 (peak N), and, tentatively, the C-C-N in-plane bending mode 9_0^2 (peak D). We also observe combination bands $5_0^2 6_0^1$ (peak I), $3_0^1 5_0^1$ (peak K), and $3_0^1 5_0^2$ (peak M). Features involving ν_3 and ν_4 were assigned by excellent agreement with matrix IR absorption measurements by Cho and Andrews,[236] while the ν_6 and ν_9 peaks were assigned by comparison with CCSD(T)/aug-cc-pVTZ harmonic frequencies (see Table 4.1).

Several of the observed features have b_1 vibrational symmetry (peaks B, C, I, J, and

Table 4.3: Peak positions, shifts, and assignments for the SEVI spectra of CD_2CN^- given in Figs. 4.3b, 4.4b, and 4.5b.

Peak	Position (cm^{-1})	Shift (cm^{-1})	Assignment
A	12402	0	0_0^0
B′	12710	308	$5_1^0 6_0^1$
B	12791	389	6_0^1
C′	12865	463	5_1^1
C	12946	544	5_0^1
D	13331	929	$5_0^1 6_0^1$
E	13504	1102	5_0^2
F′	13839	1437	$5_1^2 6_0^1$
F	13889	1487	$5_0^2 6_0^1$
X	13998	1596	5_1^3
G	14268	1866	$5_0^2 6_0^2$
H	14455	2053	$5_0^3 6_0^1$
I	14661	2259	5_0^4
Y	14937	2535	$5_1^4 6_0^1$
Z	15167	2765	5_1^5
J	15420	3018	$5_0^4 6_0^2$
K	15630	3228	$5_0^5 6_0^1$
L	15865	3463	5_0^6

K), and are thus FC forbidden. The appearance of these peaks is ascribed to mode-specific vibrational autodetachment from the dipole bound state of CH_2CN^-, and will be discussed in detail in Section 4.5.4.

4.5.2 Vibrational assignments for CD_2CN

The CD_2CN^- SEVI spectra have an intense vibrational origin (peak A in Figs. 4.3b, 4.4b, and 4.5b) at 12402 cm^{-1}(1.538 eV). While the photoelectron spectrum of CD_2CN^- taken by Moran *et al.*[229] resolved only a progression in the ν_5 mode, the SEVI overview spectra of CD_2CN^- in Fig. 4.3b reveal additional structure. The ν_5 progression (peaks C′, E, X, I, Z, and L) is accompanied by combination bands of ν_5 and the ν_6 b_1 bending mode (peaks D, F′, H, Y, and K). In the photodetachment of CH_2CN^-, analysis of our *ab initio* normal mode coordinates indicates that ν_6 primarily involves C-C-N out-of-plane bending in the anion

Table 4.4: Experimental values from previous studies and the current work, all given in wavenumbers (cm^{-1}).

	CH_2CN^-	CH_2CN	CD_2CN^-	CD_2CN
Previous results				
EA		12486(40)[a], 12445(113)[b]		12405(97)[b]
DBS term energy	12428.665[c]		12360.434[c]	
A	9.29431(14)[c]	9.506(4)[d]	4.69517(15)[c]	4.7685(1)[d]
B	0.338427(20)[c]	0.347799(2)[d]	0.300372(11)[c]	0.3029755(3)[d]
C	0.32761(21)[c]	0.329429(2)[d]	0.283102(11)[c]	0.2843613(3)[d]
ν_3		1432.3[e]		
ν_4		1026.0[e], 1028.5[g]		910.6[e]
ν_5		680[b], 664.6[e], 663.794[f], 666.4[g]		538[b], 544.4[e]
barrier	100(50)[h]		100(50)[h]	
inversion splitting	152[h]		101[h]	
This work				
EA		12468(2)		12402(2)
ν_3		1439(3)		
ν_4		1027(8)		
ν_5		659(5) $2\nu_5 = 1340(2)$		544(5) $2\nu_5 = 1105(2)$
inversion splitting	130(20)		81(20)	
ν_6		420(10)		389(8)
ν_9		$2\nu_9 = 732(5)$		

[a]PES, Ref. [249] [b]PES, Ref. [229] [c]Autodetachment spectroscopy, Ref. [245] [d]Microwave spectroscopy, Ref. [228] [e]IR in argon matrix, Ref. [236] [f]IR in gas phase, Ref. [237] [g]IR in argon matrix, Ref. [233] [h]Estimated from fitting of PES, Ref. [229]

and neutral, and does not have significant Duschinsky mixing[205] with ν_5. For CD_2CN^-, calculations indicate that the ν_6 mode involves significant motion of the deuterium atoms. Duschinsky mixing of ν_5 and ν_6 between the anion and neutral normal modes therefore leads to coupled activity of ν_5 and ν_6 in the CD_2CN^- spectra.

The CD_2CN^- overview spectra exhibit numerous temperature-dependent features. In Fig. 4.3b, peaks C′, F′, X, Y, and Z are present at room temperature, and vanish at 5 K, while the intensities of peaks D, E, H, I, K, and L are temperature-independent. As was true for CH_2CN^-, only transitions to neutral states with an even total number of quanta in b_1 modes are FC allowed from the ground vibrational state of the anion. Here, we assign $5_0^1 6_0^1$ (peak D), 5_0^2 (peak E), $5_0^3 6_0^1$ (peak H), 5_0^4 (peak I), $5_0^5 6_0^1$ (peak K), and 5_0^6 (peak L). The transitions to neutral states with odd quanta in b_1 modes originate from the $v_5 = 1$ anion state: peak C′ is assigned to 5_1^1, peak F′ to $5_1^2 6_0^1$, peak X to 5_1^3, peak Y to $5_1^4 6_0^1$, and peak Z to 5_1^5.

Fig. 4.4b gives a higher-resolution picture of the low-eBE region of the spectrum. At 5 K, two weak FC forbidden features are apparent: 6_0^1 (peak B) and 5_0^1 (peak C). At 30–50 K, two hot bands originating from the anion $v_5 = 1$ level are seen: peak C′, already assigned to 5_1^1, and the newly resolved peak B′, assigned to $5_1^0 6_0^1$. The gaps between peaks B and B′, and peaks C and C′ are both $\sim$81 cm^{-1}, yielding the inversion splitting between the first two ν_5 levels of CD_2CN^-, close to the value of 101 cm^{-1} estimated by Moran *et al.*[229]

The high-resolution SEVI spectrum of CD_2CN^- shown in Fig. 4.5b shows additional combination bands of ν_5 and ν_6: $5_0^2 6_0^1$ (peak F), $5_0^2 6_0^2$ (peak G), and $5_0^4 6_0^2$ (peak J). While these three features lie only barely above baseline noise, they are reproduced at many photon energies and are thus considered real structure. As was true for the CH_2CN^- spectra, the presence of FC forbidden vibrational features with b_1 symmetry (peaks B, C, and F) is ascribed to resonant autodetachment from the anion DBS, and will be discussed in Section 4.5.4.

4.5.3 Rotational structure of CH_2CN and CD_2CN

Fig. 4.6 shows high-resolution spectra of the vibrational origins for cold CH_2CN^- and CD_2CN^- (black traces), highlighting partially resolved rotational structure in both cases. These contours are representative of the rovibrational structure of all strong features in the spectra of each species. CH_2CN and CD_2CN are near-prolate asymmetric tops with large rotational constants around their C_2 axes: $A = 9.5\,cm^{-1}$ for CH_2CN and $4.8\,cm^{-1}$ for CD_2CN.[228] Both species have two equivalent hydrogens, yielding para and ortho nuclear spin isomers. Rovibrational structure very similar to that in Fig. 4.6 has been observed for jet-cooled CH_2CO and CD_2CO with ZEKE and MATI photoionization techniques.[257,258] SEVI has also revealed partially resolved rotational structure in the past for the 1-propynyl radical.[259]

The selection rules that govern rovibronic transitions for the nuclear spin isomers of CH_2CN, CD_2CN, and analogous systems have been described elsewhere,[245,258] but we summarize them here for reference. The energy levels of a slightly asymmetric prolate top can

be estimated by[65]

$$E_{prolate}(J,K) = \frac{1}{2}(B+C)J(J+1) + (A - \frac{1}{2}(B+C))K^2 \tag{4.1}$$

where J and K are rotational quantum numbers, and A, B, and C are the rotational constants for the three principal axes of the molecule, with $A > B \sim C$. As B and C for both systems are much smaller than the resolution of SEVI, we cannot distinguish transitions in J, but the A values are large enough to resolve transitions in K.

The allowed values of $\Delta K = K_{neutral} - K_{anion}$ are determined by the requirement that the direct product of the total internal wavefunctions of the initial and final states be antisymmetric with respect to inversion:[66]

$$\Gamma_{rve}^{anion} \otimes \Gamma_{ns}^{anion} \otimes \Gamma_{es}^{anion} \otimes \Gamma_{rve}^{neutral} \otimes \Gamma_{ns}^{neutral} \otimes \Gamma_{es}^{neutral} \otimes \Gamma_{photoelectron} \supset \Gamma^*$$

where Γ_{rve} is the rovibronic character of a given state, Γ_{ns} is the nuclear spin symmetry, Γ_{es} is the electron spin symmetry, and $\Gamma_{photoelectron}$ is the electronic character of the outgoing photoelectron. The nuclear spin and electron spin will remain unchanged during the process, and $\Gamma^* = A_2$ in the C_{2v} point group, so:

$$\Gamma_{rve}^{anion} \otimes \Gamma_{rve}^{neutral} \otimes \Gamma_{photoelectron} \supset A_2$$

Assuming independent rotational, vibrational, and electronic degrees of freedom, $\Gamma_{rve} = \Gamma_{rot} \otimes \Gamma_{vib} \otimes \Gamma_{elec}$, where Γ_{elec} is a states electronic character, Γ_{vib} is its vibrational character, and Γ_{rot} is its rotational character. For the photodetachment process under consideration, the photoelectron distributions are observed to be predominantly isotropic close to threshold and are thus attributed to s-wave ($l = 0$) electrons, so $\Gamma_{photoelectron} = A_1$. For the FC allowed peaks of both CH_2CN^- and CD_2CN^-, we are therefore left with

$$\Gamma_{rot}^{anion} \otimes \Gamma_{rot}^{neutral} \supset B_2$$

Based on the symmetries of rotational states of C_{2v} species,[66] the allowed transitions correspond to $\Delta K =$ odd.

Nuclear spin statistics directly analogous to those of diatomic H_2 and D_2 determine the allowed rotational states for CH_2CN^- or CD_2CN^- before photodetachment. For CH_2CN^- the total internal wavefunction must be antisymmetric with respect to exchange of hydrogen atoms. Anions in ortho nuclear spin states must have odd K_{anion}, while para anions must be in rotational states with even K_{anion}.[66] The statistical ratio of ortho to para states is 3 : 1, so transitions originating from odd K_{anion} states of CH_2CN^- will be three times stronger than those originating from even K_{anion} states. In a SEVI experiment with anions at 5 K, we expect to see only transitions from $K_{anion} = 0$ and $K_{anion} = 1$ in a 1 : 3 intensity ratio.

For CD_2CN^-, the total internal wavefunction must be symmetric with respect to the exchange of deuterium atoms, yielding ortho anions with even K_{anion}, and para anions with

Table 4.5: Rotational assignments for the SEVI spectra of the vibrational origins of CH_2CN^- and CD_2CN^- given in Figs. 4.6a and 4.6b.

	Peak	Nuclear Spin	Transition ($K_{neutral} \leftarrow K_{anion}$)
CH_2CN^-	a	ortho	$0 \leftarrow 1$
	b	para	$1 \leftarrow 0$
	c	ortho	$2 \leftarrow 1$
CD_2CN^-	a	ortho	$1 \leftarrow 2$
	b	para	$0 \leftarrow 1$
	c	ortho	$1 \leftarrow 0$
	d	para	$2 \leftarrow 1$
	e	ortho	$3 \leftarrow 2$

odd K_{anion}. The statistical ratio of ortho to para states is 2 : 1 for CD_2CN^-. Transitions originating from $K_{anion} = 0$ states of cold CD_2CN^- will be twice as strong as those from $K_{anion} = 1$ states. Additionally, as the A constant for CD_2CN^- is small ($\sim$4.7 cm^{-1}),[245] we may see weak transitions originating from $K_{anion} = 2$ states.

The $K_{neutral} \leftarrow K_{anion}$ rotational assignments for the CH_2CN^- and CD_2CN^- vibrational origins are laid out in Table 4.5. For CH_2CN^-, peaks a and c in Fig. 4.6a are the $0 \leftarrow 1$ and $2 \leftarrow 1$ transitions of the ortho isomer. Peak b, the $1 \leftarrow 0$ transition of the para isomer, has roughly one-third the intensity of peaks a and c, based on the nuclear spin statistics described above. These transitions are spaced by approximately $2A$, according to Eqn. 4.1, and assuming $A_{anion} \sim A_{neutral}$ within the resolution of SEVI. Underlying the CD_2CN^- rotational envelope are the $1 \leftarrow 2$, $1 \leftarrow 0$, and $3 \leftarrow 2$ transitions of the ortho isomer (peaks a, c, and e in Fig. 4.6b), and the $0 \leftarrow 1$ and $2 \leftarrow 1$ transitions of the para isomer (peaks b and d). Peak c is roughly twice as strong as peaks b and d, in accordance with nuclear spin statistics, while peaks a and e are much weaker, originating from rotationally excited ortho states. The rotational features for CD_2CN^- are also expected to be spaced by $2A$, but are not well resolved due to the smaller rotational constant. The rotational envelopes simulated in PGOPHER (red traces in Fig. 4.6) reproduce the observed features, though the fit is much better for CH_2CN than for CD_2CN.

4.5.4 Vibrational Autodetachment

The CH_2CN^- and CD_2CN^- SEVI spectra show FC forbidden transitions involving odd changes in vibrational quantum number in the non-totally symmetric ν_5 and ν_6 vibrational modes. The weak appearance of such features is often ascribed to Herzberg-Teller (HT) coupling through excited states of the neutral with the same overall vibronic symmetry as the forbidden feature.[260,261] Both CH_2CN and CD_2CN have a $^2B_1$ ground electronic state, so b_1 vibrational modes like ν_5 and ν_6 would have to undergo HT coupling through an A_1

neutral excited state. TDDFT calculations carried out as described in Section 4.3 indicate that the lowest-lying excited state with A_1 symmetry has a term energy of 5.9 eV. It is therefore unlikely for the b_1 peaks to gain intensity through HT coupling.

The strong dependence of forbidden peak intensities on photon energy suggests an alternate mechanism. Fig. 4.7 shows that the intensity of the 5_0^1 transition in the CH_2CN^- and CD_2CN^- spectra (peak C in both cases) is highly dependent on photon energy. When the photon energy lies just below the 5_0^2 photodetachment transition of CD_2CN^- (peak E in Fig. 4.7b), there is a dramatic spike in the relative intensity of peak C. A weaker resonance is observed for CH_2CN^- when the photon energy lies above 5_0^2 (peak G in Fig. 4.7a). In both cases, it is likely that the anion transitions to a vibrationally excited dipole bound state, and undergoes mode-specific vibrational autodetachment to the neutral $v_5 = 1$ state, dramatically increasing the intensity of the 5_0^1 feature in the SEVI spectrum. This mechanism is analogous to resonant autodetachment from the DBS of phenoxide recently reported by Liu *et al.*[262]

Vibrational autodetachment is a non-Born-Oppenheimer process, wherein vibrational and rotational degrees of freedom couple the autodetaching anion state to the (neutral + free electron) continuum.[88,263] The propensity rules of vibrational autodetachment parallel those of autoionization from Rydberg states.[264] Threshold autodetachment spectroscopy has been used in the past to study the CH_2CN^- and CD_2CN^- DBSs, so the electronic surfaces involved support the coupling of electronic and vibrational degrees of freedom required for vibrational autodetachment. Lykke *et al.* measured rotational spectra of the vibrational origins of both species DBSs with resolved J transitions,[245] while Brauman and co-workers were able to resolve K transitions in the DBS vibrational origins of both species[247] and in the 5_1^1 band of the CH_2CN^- DBS.[246] All three studies found DBS rotational structure covering extensive ranges of energy as detachment from very warm precursor ions allowed for transitions to highly excited DBS J states. As we detach from cryogenically cooled ions, we expect much sparser DBS structure. Therefore, direct detachment to the neutral is the dominant process in our experiment while autodetaching resonances occur at narrow ranges of photon energy.

Vibrational autodetachment preferentially occurs by loss of one vibrational quantum ($\Delta v = -1$) in a coupling mode whose normal coordinate changes the character of the anion orbital from which the electron is autodetached.[88,265] Brauman and co-workers[246] suggested that vibrational autodetachment from the CH_2CN^- DBS was accompanied by the loss of one quantum in ν_5. As the anion and neutral geometries differ along the ν_5 normal coordinate, displacement along ν_5 must affect the electronic character of the DBS, so it is reasonable that the ν_5 mode would couple with autodetachment.

The CH_2CN^- DBS lies 12429 cm^{-1} above the anion ground state, and the CD_2CN^- DBS lies at 12360 cm^{-1}.[245] By comparison to the electron affinities of CH_2CN and CD_2CN reported in this work (see Table 4.4), we obtain binding energies of 39 and 42 cm^{-1} respectively for the DBSs of CH_2CN^- and CD_2CN^-, refining the previous upper bounds of 67 and 66 cm^{-1}.[245] The vibrational frequencies of the DBSs should be quite close to those of the neutrals, as the dipole bound electron only weakly perturbs the neutral geometry.[245] The DBS vibrational

levels should therefore lie $\sim$40 cm^{-1} below their neutral counterparts in both isotopologues. This spacing is consistent with the results shown for CD_2CN^- in Fig. 4.7b, where there is an enormous enhancement of 5_0^1 (peak C) when the photon energy lies $\sim$40 cm^{-1} below 5_0^2 (peak E). Fig. 4.7b thus represents a clear instance of vibrational autodetachment from the $2\nu_5$ level of the CD_2CN^- DBS, accompanied by the loss of one quantum in ν_5. While the region just below the corresponding CH_2CN^- 5_0^2 feature (peak G in Fig. 4.7a) was not scanned for resonances, a resonance in the relative intensity of 5_0^1 (peak C) was noted with the photon energy tuned just above 5_0^2. The appearance of the other b_1 forbidden modes observed in both spectra can be ascribed to autodetachment from FC accessible DBS states by $\Delta v = -1$ processes in ν_5 or ν_6.

4.6 Conclusions

We report high-resolution photoelectron spectra for the cyanomethide anion, CH_2CN^-, and its isotopologue, CD_2CN^-. With our cryogenic ion trap, we eliminate the hot bands that dominated previous photoelectron spectra of these species, allowing resolution of new vibrational features and rotational structure. We refine values for the electron affinities of CH_2CN and CD_2CN, and the binding energies of their dipole bound anions. Tunable ion trap temperature allows for control of vibrationally excited anion populations and the measurement of the inversion splitting of the lowest ν_5 levels in the ground state anions of both species. Additionally, we observe mode-specific vibrational autodetachment from the dipole bound anionic states, producing Franck-Condon forbidden features.

Part III

Aromatic Radicals

The universe (which others call the Library) is composed of an indefinite, perhaps infinite number of hexagonal galleries.

Jorge Luis Borges,
The Library of Babel

Chapter 5

Vibronic structure of *ortho*-hydroxyphenoxy

The content and figures of this chapter are reprinted or adapted with permission from
M. L. Weichman, J. B. Kim, and D. M. Neumark, "Slow photoelectron velocity-map imaging spectroscopy of the *ortho*-hydroxyphenoxide anion"
J. Phys. Chem. A **119**, 6140 (2015).

Abstract

We report high-resolution photodetachment spectra of cryogenically cooled *ortho*-hydroxyphenoxide anions (o-$HOC_6H_4O^-$) using slow photoelectron velocity-map imaging spectroscopy (cryo-SEVI). We observe transitions to the three lowest-lying electronic states of the *ortho*-hydroxyphenoxy radical, and resolve detailed vibrational features. Comparison to Franck-Condon simulations allows for clear assignment of vibronic structure. We find an electron affinity of 2.3292(4) eV for the neutral $\tilde{X}^2A''$ ground state, improving upon the accuracy of previous experiments. We measure term energies of 1.4574(7) eV and 1.5922(48) eV for the $\tilde{A}^2A'$ and $\tilde{B}^2A''$ excited states respectively, representing their first resolution and clear assignment. Photodetachment threshold effects are considered to explain the structure of these bands.

5.1 Introduction

Hydroxybenzenes are important ultraviolet (UV) chromophores in key biomolecules. In general, the presence of heteroatoms greatly complicates the electronic structure of aromatic species. Characterizing excited state surfaces and the dynamics of non-radiative relaxation pathways in these species can elucidate the chemistry subsequent to photoexcitation of biological systems.[266–268]

In this work, we focus on derivatives of catechol (1,2-dihydroxybenzene). Catechol moieties are present in antioxidants,[269–271] the hormones dopamine and adrenaline, and the pigment eumelanin,[272,273] which is thought to be involved in photoprotection of human skin through dissipation of energy after UV irradiation.[274] Catechols also have a proclivity to form complexes with metals in solution, as they can bind with a bidentate motif.[275] Here, we report a high-resolution photodetachment study of deprotonated catechol, the

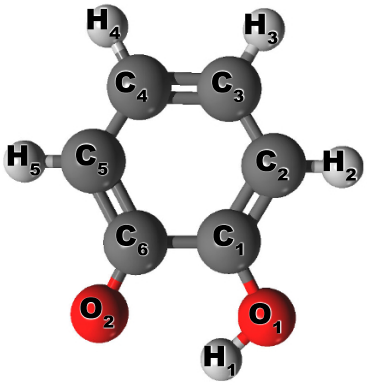

Figure 5.1: Structure of *ortho*-hydroxyphenoxy.

ortho-hydroxyphenoxide (*o*-HPO^-) anion, revealing detailed vibronic structure of the *ortho*-hydroxyphenoxy (*o*-HPO) radical.

The *o*-HPO radical (Fig. 5.1) is of interest as a photodissociation product of catechol, the photochemistry of catechol being a useful model for that of larger biomolecules. In 2012, King *et al.*[276] used H atom Rydberg tagging photofragment translational spectroscopy to study photoexcitation of catechol, probing H-loss and formation of ground state *o*-HPO radicals. The final vibrational states of *o*-HPO were highly dependent on torsional excitation of the free OH moiety in the $^1\pi\pi^*$ (S_1) state of catechol prior to dissociation along the $^1\pi\sigma^*$ (S_2) surface. While internal energies of the *o*-HPO products were measured, no definitive assignment of vibrational modes was made. Soon afterward, Chatterley *et al.*[277] published an ultrafast time-resolved ion imaging study of the photodissociation of catechol. The authors observed formation of ground state *o*-HPO radicals via tunneling from the S_1 state of catechol to the dissociative S_2 state at energies below the S_1/S_2 conical intersection. Livingstone *et al.*[278] and Weiler *et al.*[279] also reported short lifetimes of photoexcited catechol, and ascribed them to dissociation to *o*-HPO + H mediated by this tunneling process.

The *o*-HPO radical itself has been studied experimentally with electron spin resonance spectroscopy,[280,281] and IR spectroscopy in an argon matrix, wherein many IR active vibrational modes were identified.[282] Several studies have reported calculated geometries, energetics, vibrational frequencies and reactivity of *o*-HPO.[283–289] The *o*-HPO^- anion is less well-characterized than its radical counterpart. One theoretical study found a calculated barrier of approximately 2360 cm^{-1} for intramolecular transfer of the proton between the two O atoms in *o*-HPO^-,[290] sufficiently large to make proton tunneling negligible. Experimental work has studied collision-induced fragmentation of *o*-HPO^-,[291] and the kinetics of its reactions with BF_3 and SiF_4.[292] A study by Fattahi *et al.*[293] estimated the electron binding energy and proton affinity of *o*-HPO^- through bracketing with numerous ion-molecule reactions.

Photoelectron spectroscopy (PES) is an attractive technique for gaining spectroscopic access to reactive radicals through photodetachment of a closed-shell anion.[17] The PES spectrum of *o*-HPO^- was measured by Wang *et al.*[289] in 2010, who found an electron affinity (EA) of 2.315(10) eV for the radical ground state, and Franck-Condon (FC) vibrational activity in modes with frequencies of 605(40) cm^{-1} and 1575(40) cm^{-1}. The authors also observed several radical electronic excited states, but could not make definitive assignments.

We report high-resolution slow photoelectron velocity-map imaging (SEVI) spectra of detachment to the ground and two lowest excited electronic states of *o*-HPO , as part of an ongoing effort to characterize complex aromatic radicals.[85,294] More specifically, the present study can be considered an extension of our work on the phenoxy system,[295] with an added hydroxyl group in the ortho position and correspondingly more complex electronic structure. *o* HPO^- anions are buffer-gas cooled in an ion trap at 5 K prior to photodetachment, which in combination with the characteristic SEVI energy resolution of $<4\,cm^{-1}$ reveals detailed vibrational and electronic information. We obtain an accurate EA of the neutral $\tilde{X}$ state, term energies of the $\tilde{A}$ and $\tilde{B}$ electronic bands, and several fundamental vibrational frequencies.

5.2 Experimental Methods

The SEVI method and apparatus has been described in detail in Chap. 2.

o-HPO^- anions are prepared by expanding a dilute gas mixture of catechol through a pulsed Even-Lavie solenoid valve[117] fitted with a circular filament ionizer. The catechol precursor is stored in a cartridge heated to 90 °C. A gas mixture of trace NF_3 in 150 psi of He flows through the cartridge and carries the catechol vapor through the valve into the vacuum chamber. Electrons from the ionizer induce dissociative attachment of NF_3 to form F^-, which deprotonates catechol to form the desired *o*-HPO^- anions.

The spectrometer is calibrated with SEVI images of well-characterized photodetachment transitions of atomic S^- and Cl^-,[147,149,296] in order to relate radial position in the image to electron kinetic energy (eKE). The radial and angular electron distributions are reconstructed from the accumulated image using the Maximum Entropy Velocity Legendre Reconstruction (MEVELER) method.[140]

5.3 Calculations

Electronic structure calculations for the ground state of the *o*-HPO^- anion and the three lowest-lying states of the *o*-HPO radical were carried out with density functional theory (DFT), in order to find the energetics, optimized geometries, normal modes, and harmonic vibrational frequencies of all relevant states. The B3LYP functional was used in combination with the Pople-style 6-311+G* basis set, as this level of theory has proved effective for other aromatic systems studied in our lab.[85,294] The maximum overlap method (MOM)[297] was used for the first two excited states of the radical. In order to avoid root-flipping issues for MOM excited state calculations, an integration grid with 128 radial quadrature points and 302 angular quadrature points was used for the exchange-correlation integrand. Dyson orbitals for photodetachment transitions were calculated with EOM-IP-CCSD/6-311+G*. All *ab initio* calculations were carried out in Q-Chem 4.0.[253,254]

The *o*-HPO^- anion is a closed-shell species, with an electronic molecular orbital (MO) configuration described by $...(4a'')^2(24a')^2(5a'')^2$. Both MOM and EOM-IP-CCSD calculations indicate that detachment from the anion $5a''$ MO yields the $\tilde{X}^2A''$ radical ground state, detachment from the $24a'$ MO yields the $\tilde{A}^2A'$ state, and detachment from the $4a''$ MO gives the $\tilde{B}^2A''$ state. Dyson orbitals for these three detachment transitions are shown in Fig. 5.2. The $5a''$ and $24a'$ orbitals have *p*-like lobes on the oxygen radical site that are out-of-plane and in-plane respectively; they are analogous to the singly occupied MOs in the $\tilde{X}^2B_1$ and $\tilde{A}^2B_2$ states of the phenoxy radical.[295,298,299]

Calculated energetics corrected for vibrational zero-point energy and relevant harmonic vibrational frequencies are summarized in Table 5.1, while full lists of optimized geometries and calculated harmonic frequencies can be found in Tables 5.5 and 5.6 of the Supporting Information. Geometries of all states were restricted to internally H-bonded, planar C_s structures (see Fig. 5.1), as recommended by the literature.[283–286,288,289] The anion ground

state and the neutral $\tilde{X}$ and $\tilde{A}$ states were found to have planar equilibrium geometries. The optimized neutral $\tilde{B}$ state planar structure was found to have a small imaginary out-of-plane frequency (labeled ν_{33} in Table S2). A one-dimensional slice of the $\tilde{B}$ state potential along the ν_{33} normal mode coordinate was calculated with time-dependent DFT (TDDFT).[251] The ν_{33} potential is a shallow double well, with the planar geometry resting on top of a 74 cm^{-1} barrier. The one-dimensional ν_{33} potential was fit to an eighth order polynomial, and energy eigenvalues were solved for numerically. The ν_{33} vibrational zero-point energy was found to lie 63 cm^{-1} above the planar geometry barrier. We therefore treat the radical $\tilde{B}$ state as an effectively planar species.

Photoelectron spectra for detachment to all three neutral states were simulated using the ezSpectrum program.[204] The DFT geometries, normal modes, and harmonic frequencies were given as input, and FC overlap factors were calculated in the harmonic approximation with Duschinsky mixing[205] of all modes. The vibrational origins of the three simulated electronic bands were shifted to the experimentally assigned values, and simulated intensities were scaled to match the first peak in each experimental band. Those frequencies of the neutral $\tilde{X}$ and $\tilde{A}$ states that were observed in the high-resolution SEVI spectra were scaled to their experimental values; the others were left at their calculated B3LYP/6-311+G* values. In the radical $\tilde{B}$ state, the ν_{33} mode, along which the potential is a shallow double well, is not FC active, and its anharmonicity therefore has no significant impact on the simulation.

The photoelectron angular distribution (PAD) of the photodetachment transition to the $\tilde{X}$ state and cross sections for detachment to the $\tilde{A}$ and $\tilde{B}$ states were calculated as functions of eKE with the ezDyson program,[82,83] which uses *ab initio* calculated Dyson orbitals to find the contribution of partial spherical waves with angular momentum $l \leq 4$ to the wavefunction of the outgoing photoelectron.

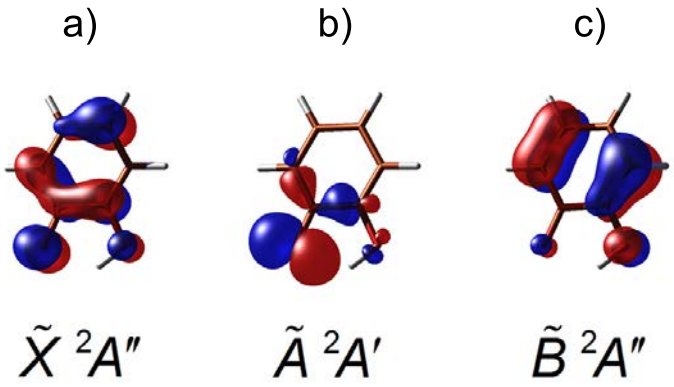

Figure 5.2: Dyson orbitals for detachment from the $\tilde{X}^1A'$ *ortho*-hydroxyphenoxide anion to the a) $\tilde{X}^2A''$, b) $\tilde{A}^2A'$, and c) $\tilde{B}^2A''$ neutral states.

Table 5.1: B3LYP/6-311+G* calculated energetics and relevant harmonic vibrational frequencies for the *ortho*-hydroxyphenoxy radical.

State	Parameter	Calculated
$\tilde{X}^2A''$	EA,[a] eV	2.2317
	ω_8, cm^{-1}	1529
	ω_9, cm^{-1}	1493
	ω_{12}, cm^{-1}	1337
	ω_{13}, cm^{-1}	1265
	ω_{20}, cm^{-1}	579
	ω_{21}, cm^{-1}	566
	ω_{22}, cm^{-1}	450
	ω_{23}, cm^{-1}	331
$\tilde{A}^2A'$	TE,[b] eV	1.4512
	ω_{12}, cm^{-1}	1254
	ω_{13}, cm^{-1}	1214
	ω_{21}, cm^{-1}	523
	ω_{23}, cm^{-1}	289
	ω_{24}, cm^{-1}	927
$\tilde{B}^2A''$	TE, eV	1.5631

[a]Electron affinity. [b]Term energy.

5.4 Results

Overview SEVI spectra of the *o*-HPO^- anion photodetachment are shown in blue in Fig. 5.3 for two regions of binding energy. Accompanying FC simulations, broadened appropriately to match the experimental resolution, are given in grey. High-resolution spectra of photodetachment to the lower energy band are presented in Fig. 5.4, while higher binding energy spectra are shown in Fig. 5.5. In Figs. 5.4 and 5.5, the higher-resolution traces shown in black are scaled to the intensity profile of the overview and vertically offset. FC stick simulations are shown in red and green. All spectra presented here were taken with an ion trap temperature of 5 K.

The photodetachment band in Fig. 5.4 has an intense onset of structure at peak A, with weaker vibrational structure continuing for about 4000 cm^{-1}. Positions and assignments for the peaks labeled in Fig. 5.4 are summarized in Table 5.2, and discussed in detail in Section 5.5. Peak positions represent the center of a Gaussian fit. The narrowest features in this band have a full width at half-maximum (fwhm) of 7–8 cm^{-1}; this is typical of the resolution of SEVI for molecular systems.[85,260]

Fig. 5.5 shows higher-resolution spectra of the features at higher binding energy. The

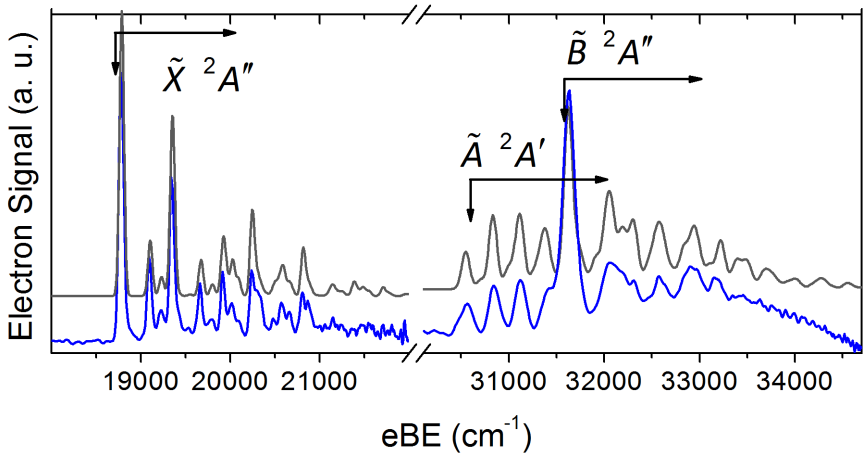

Figure 5.3: Low-resolution SEVI spectra of transitions to the $\tilde{X}$, $\tilde{A}$, and $\tilde{B}$ states of the *ortho*-hydroxyphenoxy radical (blue). The overview of the ground state was taken at a photon energy of 22236 cm^{-1}, while the excited state overview is the average of two traces taken at 34720 cm^{-1} and 34750 cm^{-1}. FC simulations (grey) are broadened by a Gaussian distribution with fwhm 60 cm^{-1} for the $\tilde{X}$ state, and fwhm 100 cm^{-1} for the $\tilde{A}$ and $\tilde{B}$ states.

appearance of the intense peak x in the midst of a weaker progression beginning with peak a suggests two overlapping electronic states. Positions and assignments (see Section 5.5) for the peaks labeled in Fig. 5.5 are summarized in Table 5.3. The best-resolved features in the progression beginning with peak a have a fwhm of ∼13 cm^{-1} with the laser energy ∼100 cm^{-1} above threshold. By contrast, peak x is fit best with a fwhm of 90 cm^{-1} with the laser energy set ∼1800 cm^{-1} above, as its intensity dies away closer to threshold.

SEVI also yields anisotropies of photodetachment transitions. For a one-photon photodetachment process with linearly polarized light, the PAD is given by[79]

$$\frac{d\sigma}{d\Omega} = \frac{\sigma_{tot}}{4\pi}\left[1 + \beta P_2(\cos\theta)\right] \tag{5.1}$$

where θ is the angle relative to the polarization axis of the laser, P_2 is the second-order Legendre polynomial, and β is the anisotropy parameter, which varies between 1 for a PAD aligned perpendicular to the laser polarization and +2 for a PAD parallel to the laser polarization.

The PADs for all peaks in the *o*-HPO $\tilde{X}$ band have negative anisotropy parameters ($-0.5 < \beta < -0.1$) and become more isotropic close to threshold. Representative β values are plotted in Fig. 5.6 as a function of eKE alongside ezDyson simulations. The PADs for the higher energy bands cannot be reported, as high-eKE photoelectrons from detachment to the $\tilde{X}$ state produce overlapping signal that prevents reproduction of excited state anisotropies during image reconstruction.

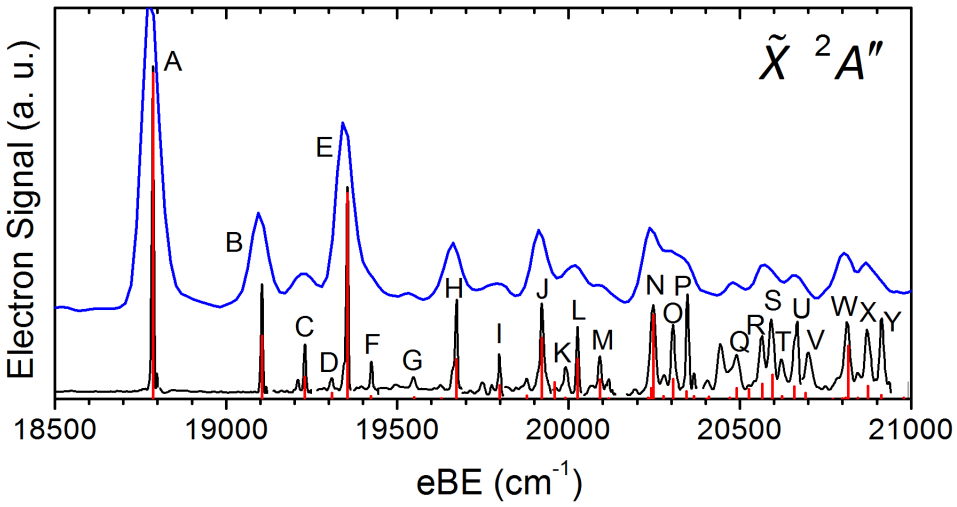

Figure 5.4: SEVI spectra of the $\tilde{X}^2A'' \leftarrow \tilde{X}^1A'$ photodetachment of *ortho*-hydroxyphenoxide. The blue trace is the low-resolution overview spectrum from Fig. 5.3; the black traces are high-resolution spectra taken at many laser frequencies. An FC simulation stick spectrum is shown in red.

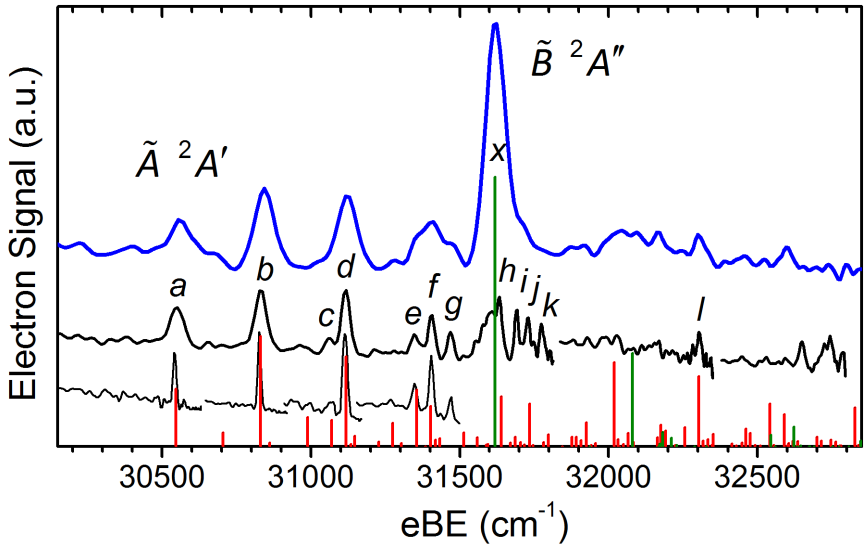

Figure 5.5: SEVI spectra of the $\tilde{A}^2A' \leftarrow \tilde{X}^1A'$ and $\tilde{B}^2A'' \leftarrow \tilde{X}^1A'$ photodetachment transitions of *ortho*-hydroxyphenoxide. A low-resolution spectrum is shown in blue, while black traces are medium- and high-resolution spectra taken at many laser frequencies. FC simulation stick spectra are shown in red for the $\tilde{A}^2A' \leftarrow \tilde{X}^1A'$ band, and in green for the $\tilde{B}^2A'' \leftarrow \tilde{X}^1A'$ band.

Table 5.2: Peak positions, shifts, and assignments for the SEVI spectra of the $\tilde{X}^2A'' \leftarrow \tilde{X}^1A'$ photodetachment of *ortho*-hydroxyphenoxide given in Fig. 5.4.

Peak	Position (cm^{-1})	Shift (cm^{-1})	Assignment
A	18787	0	0_0^0
B	19105	318	23_0^1
C	19230	444	22_0^1
D	19309	523	21_0^1?
E	19354	568	20_0^1
F	19424	638	23_0^2
G	19547	761	$22_0^1 23_0^1$
H	19673	886	$20_0^1 23_0^1$
I	19799	1012	$20_0^1 22_0^1$
J	19923	1136	20_0^2
K	19992	1205	$20_0^1 23_0^2$
L	20026	1240	13_0^1
M	20091	1305	12_0^1
N	20247	1461	9_0^1
O	20305	1519	8_0^1
P	20348	1561	$13_0^1 23_0^1$
Q	20488	1701	20_0^3
R	20564	1777	$9_0^1 23_0^1$
S	20592	1805	$13_0^1 20_0^1$
T	20622	1835	$8_0^1 23_0^1$
U	20664	1877	$12_0^1 20_0^1$
V	20692	1905	$9_0^1 22_0^1$
W	20814	2028	$9_0^1 20_0^1$
X	20873	2087	$8_0^1 20_0^1$
Y	20915	2128	$13_0^1 20_0^1 23_0^1$

Table 5.3: Peak positions, shifts, and assignments for the SEVI spectra of the $\tilde{A}^2A' \leftarrow \tilde{X}^1A'$ and $\tilde{B}^2A'' \leftarrow \tilde{X}^1A'$ photodetachment transitions of *ortho*-hydroxyphenoxide given in Fig. 5.5.

Band	Peak	Position (cm^{-1})	Shift (cm^{-1})	Assignment
$\tilde{A}^2A' \leftarrow \tilde{X}^1A'$	a	30542	0	0_0^0
	b	30827	285	23_0^1
	c	31064	523	21_0^1
	d	31114	573	23_0^2
	e	31347	806	$21_0^123_0^1$
	f	31404	862	23_0^3
	g	31470	928	24_0^1?
	h	31633	1091	$21_0^223_0^1$
	i	31690	1148	23_0^4
	j	31728	1187	13_0^1?
	k	31775	1234	12_0^1?
	l	32304	1762	$13_0^123_0^2$?
$\tilde{B}^2A'' \leftarrow \tilde{X}^1A'$	x	31629	0	0_0^0

5.5 Discussion

The high-resolution *o*-HPO^- spectra presented in Figs. 5.4 and 5.5 are a clear demonstration of the efficacy of cryo-SEVI. The spectral resolution and clarity afforded by this technique allow us to untangle the combination of overlapping electronic states and dense FC structure seen here. We now discuss the assignments of the *o*-HPO^- SEVI spectra, with comparison to simulation and the literature. All spectroscopic information obtained here is summarized and compared to prior work in Table 5.4.

The overview spectra of *o*-HPO^- in Fig. 5.3 exhibit two bands of vibronic structure separated by about $10000\,cm^{-1}$. The lower energy band has a strong onset at low binding energy, while the structure of the higher energy band is not a simple FC envelope. An extended vibrational progression interrupted by one strong feature suggests photodetachment to two overlaid electronic states in the higher energy band. Cryogenic cooling prior to photodetachment ensures that we detach from the ground vibrational and electronic state of the *o*-HPO^- anion. Hence, based on comparison with the electronic structure calculations discussed in Section 5.3, we assign the lower band to the $\tilde{X}^2A'' \leftarrow \tilde{X}^1A'$ photodetachment, and the upper band to the overlapping $\tilde{A}^2A' \leftarrow \tilde{X}^1A'$ and $\tilde{B}^2A'' \leftarrow \tilde{X}^1A'$ transitions.

In Fig. 5.4, peak A is assigned as the vibrational origin of the $\tilde{X}^2A'' \leftarrow \tilde{X}^1A'$ band. This yields an experimental EA of 2.3292(4) eV for the *o*-HPO radical, in good agreement with

the B3LYP calculated EA of 2.2317 eV, and just outside the error bars of the experimental EA of 2.315(10) eV reported by Wang *et al.*[289] The FC envelope of the $\tilde{X}$ band also supports its assignment to detachment to the $\tilde{X}^2A''$ neutral state. The intense vibrational origin and weaker vibrationally excited FC structure suggests a small change in geometry upon photodetachment. Accordingly, there is only a slight displacement between the ground state anion and neutral optimized geometries reported in Table 5.5, and the Dyson orbital for this detachment (Fig. 5.2a) is highly delocalized. Our recent report on the α- and β-naphthyl radicals also demonstrated that detachment from a delocalized π-system yields little FC activity, while detachment from an orbital localized predominantly on one atomic center yields significant disruption in geometry and an extensive FC envelope.[294]

Several fundamental frequencies of the radical ground state are observed (Table 5.4). Both the Gaussian-broadened FC simulation (Fig. 5.3) and the FC stick spectrum (Fig. 5.4) are in good agreement with the experimentally observed features, though the intensities of some overtones and combination bands are underrepresented, perhaps due to anharmonic effects. We report eight in-plane vibrational fundamentals: ν_{23} (peak B) with a frequency of 318 cm^{-1}, ν_{22} (peak C) at 444 cm^{-1}, tentatively ν_{21} (peak D) at 523 cm^{-1}, ν_{20} (peak E) at 568 cm^{-1}, ν_{13} (peak L) at 1240 cm^{-1}, ν_{12} (peak M) at 1305 cm^{-1}, ν_9 (peak N) at 1461 cm^{-1}, and ν_8 (peak O) at 1519 cm^{-1}. Schematics of normal mode displacements for these FC active vibrations are given in Fig. 5.7a. This is the first report of the fundamental frequencies of modes ν_{21}, ν_{22}, and ν_{23}. While modes ν_8, ν_9, ν_{12}, ν_{13}, and ν_{20} have been previously identified with matrix IR spectroscopy[282] and/or PES[289] (see Table 5.4), this work represents their identification in a higher-resolution gas phase experiment.

The $\tilde{X}$ band is also observed to have a PAD polarized perpendicularly to the laser polarization axis ($\beta < 0$). For the detachment of large, low-symmetry molecules like *o*-HPO^-, the PAD cannot be easily predicted with group theory, so we turn to *ab initio* calculation and numerical simulation. The anisotropy parameter for the $\tilde{X}$ state was simulated as a function of eKE using the ezDyson program as described in Section 5.3; the results are shown in Fig. 5.6 and compared with the experimental anisotropy of the $\tilde{X}$ vibrational origin. Simulations reproduce PADs with negative β values over this range of eKE, though anisotropy calculations are very sensitive to the shape of the *ab initio* Dyson orbitals,[82] so the match in the value of β is only qualitative.

Fig. 5.5 shows the high-resolution SEVI spectra of the higher binding energy photodetachment structure. Peak *a* is assigned to the vibrational origin of the $\tilde{A}^2A' \leftarrow \tilde{X}^1A'$ band. The experimental term energy of the $\tilde{A}$ state is therefore 1.4574(7) eV, in good agreement with the MOM-calculated value of 1.4512 eV. The *o*-HPO radical $\tilde{X}$ and $\tilde{A}$ states are more widely spaced than the analogous electronic states in phenoxy, which lie 0.952 eV apart.[299] Favorable interactions between the two O atoms in *o*-HPO stabilize the radical $\tilde{X}$ state with respect to the $\tilde{A}$ state, as evidenced by the nodal structure of the MOs in Figs. 5.2a and 5.2b. The *o*-HPO $\tilde{A}$ state term energy is therefore raised with respect to that of phenoxy. Peak *x* in Fig. 5.5 is assigned to the vibrational origin of the $\tilde{B}^2A'' \leftarrow \tilde{X}^1A'$ band, yielding an experimental $\tilde{B}$ state term energy of 1.5922(48) eV. This value is matched by an MOM calculated term energy of 1.5631 eV, and also lines up with the excited state reported by

Table 5.4: Experimental parameters for the *ortho*-hydroxyphenoxy radical from the current work, with comparison to prior experimental literature values.

State	Parameter	This work	Prior work
$\tilde{X}^2A''$	EA,[a] eV	2.3292[b]	2.315(10)[c]
	ν_8, cm^{-1}	1519(5)	1518[d]
	ν_9, cm^{-1}	1461(7)	1457[d]
	ν_{12}, cm^{-1}	1305(4)	1304[d]
	ν_{13}, cm^{-1}	1240(4)	1240[d]
	ν_{20}, cm^{-1}	568(3)	605(40)[c]
	ν_{21}, cm^{-1}	523(4)	
	ν_{22}, cm^{-1}	444(3)	
	ν_{23}, cm^{-1}	318(3)	
$\tilde{A}^2A'$	TE,[e] eV	1.4574(7)	
	ν_{12}, cm^{-1}	1234(6)	
	ν_{13}, cm^{-1}	1187(7)	
	ν_{21}, cm^{-1}	523(29)	
	ν_{23}, cm^{-1}	285(5)	
	ν_{24}, cm^{-1}	928(5)	
$\tilde{B}^2A''$	TE, eV	1.5922(48)	1.605(10)

[a]Electron affinity. [b]Uncertainties represent one standard deviation of a Gaussian fit to the experimentally observed peak. [c]Photoelectron spectroscopy, Ref. [289]. [d]Matrix IR spectroscopy, Ref. [282]. [e]Term energy.

Wang *et al.*[289] at a term energy of 1.605(10) eV.

The $\tilde{A}$ band is dominated by a progression in the ν_{23} $O_1{-}C_1{-}C_6{-}O_2$ bending mode (peaks *b*, *d*, *f*, and *i*). This extended FC envelope indicates a significant change in geometry between the anion and the neutral $\tilde{A}$ states, as is reflected in the B3LYP optimized geometries (Table 5.5). The anion and $\tilde{A}$ state geometries differ particularly in the $C_6{-}O_2$ bond length and the $C_1{-}O_1{-}H_1$, $C_5{-}C_6{-}O_2$, and $C_5{-}C_6{-}C_1$ bond angles, consistent with localization of the $\tilde{A}$ state Dyson orbital to the $C_6{-}O_2$ bond and neighboring atoms (Fig. 5.2b).

Assignments of all $\tilde{A}$ state vibrational features are detailed in Table 5.3. Schematics of FC active normal modes are given in Fig. 5.7b, and their displacements involve distortions consistent with the change in geometry upon photodetachment. We observe the vibrational fundamentals ν_{23} (peak *b*) at 285 cm^{-1}, ν_{21} (peak *c*) at 523 cm^{-1}, and more tentatively ν_{13} (peak *j*) at 1187 cm^{-1} and ν_{12} (peak *k*) at 1234 cm^{-1}. There is no clear analog in the simulation for peak *g*, which lies at 928 cm^{-1} above the origin; however, it lines up closely with the calculated frequency of the FC forbidden a'' symmetry ν_{24} mode. This mode could gain

intensity through Herzberg-Teller (HT) coupling with totally symmetric vibrational levels of the nearby $\tilde{B}^2A''$ state, which have the same overall vibronic symmetry. We therefore tentatively assign peak *g* to excitation of the ν_{24} fundamental.

As was true for the $\tilde{X}$ band, the FC envelope for the $\tilde{B}$ state is dominated by the vibrational origin, indicating that photodetachment is accompanied by relatively little change in geometry. The optimized geometries of the anion and $\tilde{B}$ state (Table 5.5) and the delocalized nature of the Dyson orbital for detachment to the $\tilde{B}$ state (Fig. 5.2c) support this reasoning. While the vibrational features for the $\tilde{X}$ and $\tilde{A}$ states narrow to $<15\,\mathrm{cm}^{-1}$ fwhm close to threshold, the $\tilde{B}$ state structure is poorly resolved, making assignments intractable beyond identification of the strong vibrational origin. The decaying $\tilde{B}$ state cross section close to threshold allows vibrational features to disappear before they can be narrowly resolved with SEVI.

According to the Wigner threshold law,[75] the near threshold cross section (σ) for photodetachment is a function of both eKE and l, the angular momentum of the outgoing photoelectron:

$$\sigma \propto (\mathrm{eKE})^{l+1/2} \tag{5.2}$$

Treating the *o*-HPO radical as a pseudo-C_{2v} species with the H_1 atom as a symmetry-breaking perturbation, the $\tilde{B}$ state Dyson orbital has approximate a_2 symmetry. Detachment from an a_2 orbital yields outgoing photoelectrons with angular momentum $l \geq 1$, yielding small σ at small eKE.[77,78] The $\tilde{A}$ state, on the other hand, has a localized *p*-like Dyson orbital, allowing for partial $l = 0$ detachment, and retained σ at low eKE. Calculated photodetachment cross sections of the $\tilde{A}$ and $\tilde{B}$ states (Fig. 5.8) reproduce this difference in threshold behavior.

The poor resolution of vibrational features in the $\tilde{B}$ state is therefore due to a combination of factors, including the low photodetachment cross section at low eKE, dense overlapping $\tilde{A}$ state structure with a non-vanishing threshold cross section, and a significant background of high-eKE photoelectrons from detachment to the radical $\tilde{X}$ state. Additionally, as we invoked HT coupling to assign peak *g* to a FC forbidden vibrational state of $\tilde{A}$, there may be added dense structure above the $\tilde{B}$ vibrational origin from similar vibronic coupling processes, further hampering the resolution and assignment of $\tilde{B}$ state features.

5.6 Conclusions

We have acquired slow photoelectron velocity-map imaging spectra of cold *ortho*-hydroxyphenoxide anions. We observe detailed vibronic structure of the neutral radical, measuring a precise electron affinity of the $\tilde{X}^2A''$ state, and reporting experimental $\tilde{A}^2A'$ and $\tilde{B}^2A''$ excited state term energies for the first time. A number of vibrational frequencies of the radical $\tilde{X}$ and $\tilde{A}$ states are also newly assigned. We demonstrate the efficacy of high-resolution photoelectron imaging in combination with cryogenic ion cooling for untangling the vibronic structure of increasingly complex bio-relevant molecules.

5.7 Supporting Information

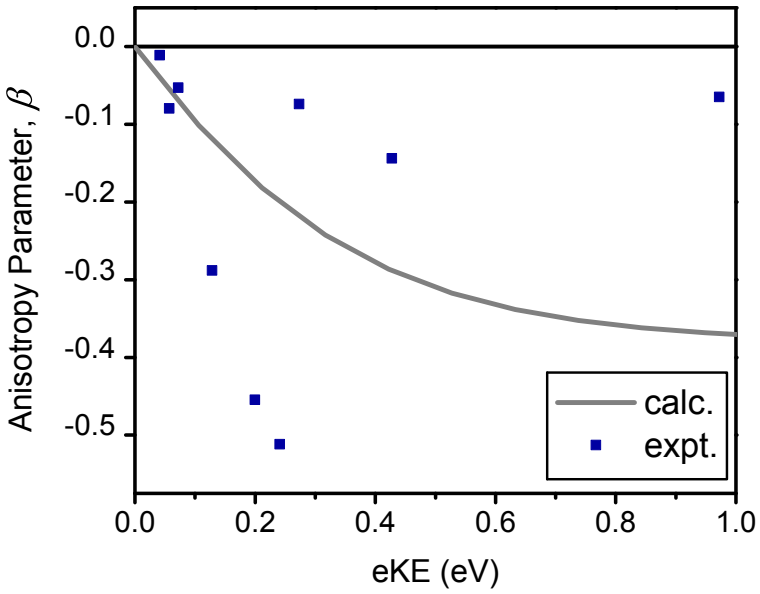

Figure 5.6: Calculated and experimental anisotropy parameters for photodetachment to the *ortho*-hydroxyphenoxy $\tilde{X}$ band vibrational origin as a function of eKE.

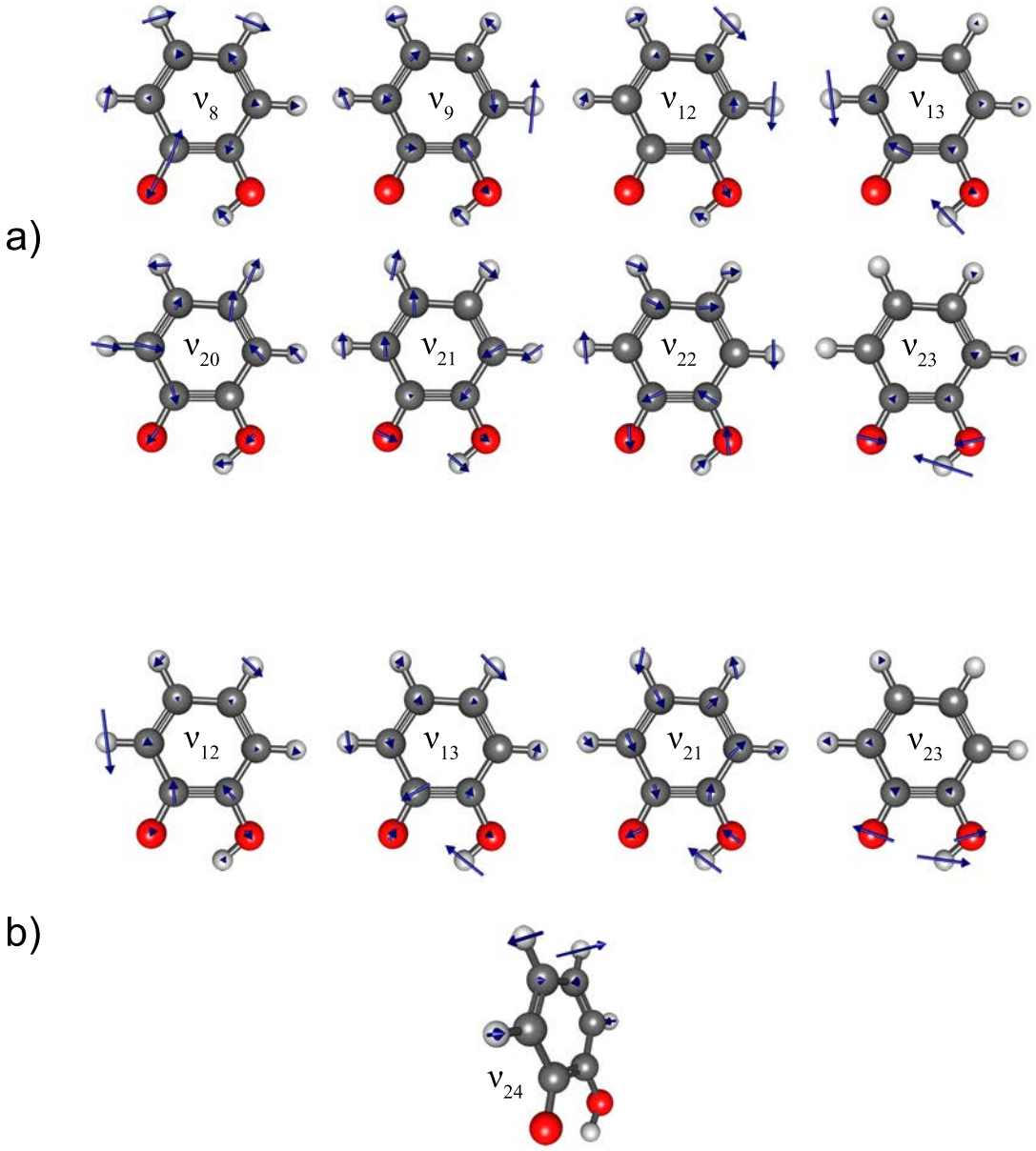

Figure 5.7: Franck-Condon active vibrational modes for detachment to the (a) $\tilde{X}$ and (b) $\tilde{A}$ states of the *ortho*-hydroxyphenoxy radical.

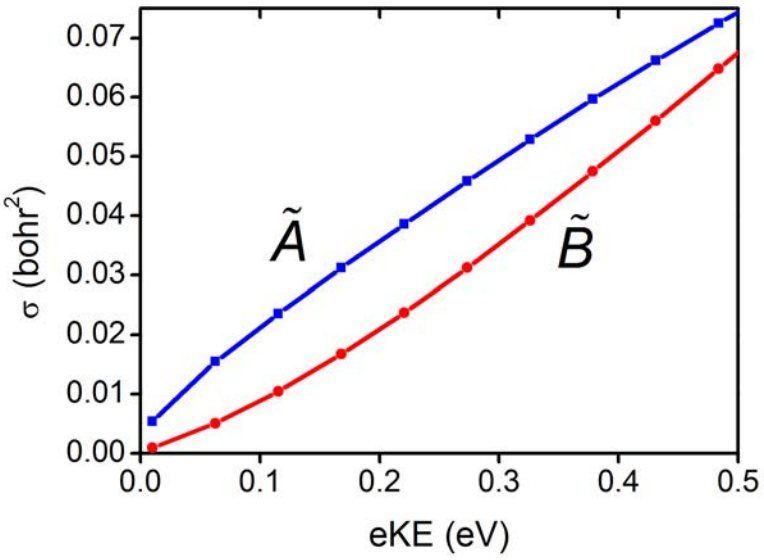

Figure 5.8: Calculated cross sections for photodetachment to the $\tilde{A}$ and $\tilde{B}$ states of the *ortho*-hydroxyphenoxy radical as a function of eKE.

Table 5.5: Optimized geometries for the *ortho*-hydroxyphenoxide anion and the first three electronic states of the radical, calculated at the B3LYP/6-311+G* level of theory. Bond lengths are in Angstroms (Å), and angles are in degrees. Atoms are labeled in Fig. 5.1 of the main text.

	$HOC_6H_4O^-$	HOC_6H_4O		
	$\tilde{X}^1A'$	$\tilde{X}^2A''$	$\tilde{A}^2A'$	$\tilde{B}^2A''$
C_1O_1	1.372	1.332	1.371	1.325
C_6O_2	1.288	1.253	1.335	1.265
O_1H_1	0.987	0.980	0.964	0.996
C_2H_2	1.089	1.084	1.085	1.086
C_3H_3	1.087	1.084	1.084	1.082
C_4H_4	1.090	1.085	1.085	1.085
C_5H_5	1.088	1.084	1.083	1.085
C_1C_2	1.379	1.389	1.388	1.408
C_2C_3	1.412	1.390	1.393	1.426
C_3C_4	1.393	1.421	1.392	1.367
C_4C_5	1.402	1.370	1.392	1.461
C_5C_6	1.418	1.441	1.402	1.409
C_6C_1	1.446	1.468	1.412	1.448
$C_1O_1H_1$	100.98	106.03	111.43	102.87
$O_1C_1C_2$	123.08	122.18	118.76	121.66
$C_1C_2H_2$	119.35	119.76	117.53	118.57
$C_1C_2C_3$	119.74	118.67	120.96	120.24
$C_2C_3H_3$	120.13	119.28	119.76	120.29
$C_2C_3C_4$	119.01	121.61	119.72	117.77
$C_3C_4H_4$	119.55	119.00	120.62	120.19
$C_3C_4C_5$	121.31	120.87	120.59	122.09
$C_4C_5H_5$	120.57	122.25	121.64	119.16
$C_4C_5C_6$	121.56	120.22	119.52	122.05
$C_5C_6O_2$	127.32	125.22	121.12	129.06
$C_5C_6C_1$	115.29	117.06	120.11	113.90
$C_6C_1C_2$	123.10	121.57	119.10	123.96

Table 5.6: Harmonic frequencies for the *ortho*-hydroxyphenoxide anion and radical states, calculated at the B3LYP/6-311+G* level of theory.

	$HOC_6H_4O^-$	HOC_6H_4O		
	$\tilde{X}^1A'$	$\tilde{X}^2A''$	$\tilde{A}^2A'$	$\tilde{B}^2A''$
$\omega_1\,(a')$	3377	3538	3794	3269
$\omega_2\,(a')$	3147	3201	3203	3214
$\omega_3\,(a')$	3134	3196	3196	3196
$\omega_4\,(a')$	3121	3184	3181	3183
$\omega_5\,(a')$	3099	3171	3171	3176
$\omega_6\,(a')$	1633	1614	1629	1730
$\omega_7\,(a')$	1587	1581	1591	1607
$\omega_8\,(a')$	1530	1529	1477	1583
$\omega_9\,(a')$	1499	1493	1462	1500
$\omega_{10}\,(a')$	1460	1445	1360	1419
$\omega_{11}\,(a')$	1342	1387	1278	1375
$\omega_{12}\,(a')$	1291	1337	1254	1317
$\omega_{13}\,(a')$	1253	1265	1214	1301
$\omega_{14}\,(a')$	1203	1197	1200	1227
$\omega_{15}\,(a')$	1159	1172	1180	1188
$\omega_{16}\,(a')$	1099	1132	1107	1056
$\omega_{17}\,(a')$	1029	1011	1053	1004
$\omega_{18}\,(a')$	876	886	849	927
$\omega_{19}\,(a')$	773	756	778	887
$\omega_{20}\,(a')$	583	579	587	866
$\omega_{21}\,(a')$	582	566	523	854
$\omega_{22}\,(a')$	464	450	432	796
$\omega_{23}\,(a')$	337	331	289	772
$\omega_{24}\,(a'')$	876	976	927	699
$\omega_{25}\,(a'')$	851	942	912	606
$\omega_{26}\,(a'')$	804	851	829	591
$\omega_{27}\,(a'')$	748	768	714	563
$\omega_{28}\,(a'')$	701	723	571	462
$\omega_{29}\,(a'')$	684	708	516	374
$\omega_{30}\,(a'')$	558	506	439	317
$\omega_{31}\,(a'')$	438	456	231	274
$\omega_{32}\,(a'')$	292	271	167	218
$\omega_{33}\,(a'')$	186	167	79	$335i$

Chapter 6

Vibronic structure of α- and β-naphthyl

The content and figures of this chapter are reprinted or adapted with permission from
M. L. Weichman, J. B. Kim, J. A. DeVine, D. S. Levine, and D. M. Neumark, "Vibrational and electronic structure of the α- and β-naphthyl radicals via slow photoelectron velocity-map imaging" *J. Am. Chem. Soc.* **137**, 1420 (2015).

Abstract

Slow photoelectron velocity-map imaging (SEVI) spectroscopy has been used to study the vibronic structure of gas-phase α- and β-naphthyl radicals ($C_{10}H_7$). SEVI of cryogenically cooled anions yields spectra with $< 4\,cm^{-1}$ resolution, allowing for the observation and interpretation of congested vibrational structure. Isomer-specific photoelectron spectra of detachment to the radical ground electronic states show detailed structure, allowing assignment of vibrational fundamental frequencies. Transitions to the first excited states of both radical isomers are also observed; vibronic coupling and photodetachment threshold effects are considered to explain the structure of the excited bands.

6.1 Text

Polycyclic aromatic hydrocarbons (PAHs) are of major importance in wide-ranging areas of chemistry. PAHs are involved in the combustion of organic matter[300] and subsequent soot formation,[101,301] while neutral, ionized, hydrogenated, and dehydrogenated PAHs are likely constituents of the interstellar medium (ISM).[302,303] PAHs are possible sources of mid-infrared emission features in the ISM[304–306] and have been considered tentative candidates for carriers of diffuse interstellar bands (DIBs) for many years.[307–309] No conclusive evidence of small PAHs as DIB carriers exists to date, despite much work searching for matches between laboratory spectra and astronomical data.[310,311] Decomposition of large interstellar PAHs may lead to the formation of carbon chains and hydrocarbon radicals in space.[312]

In this communication, we report high-resolution anion photoelectron spectra of α- and β-naphthyl, $C_{10}H_7^-$, whose structures are shown in Fig. 6.1. Naphthalene is the simplest PAH; its derivatives are therefore tractable models for the behavior of larger aromatic systems.

There is a solid body of theoretical work on the electronic structure, geometries, and vibrations of the naphthyl radicals and anions[303,313–318] and some calculations of their reactivity in the context of combustion.[319,320] Experimental characterization is sparser. Reed and Kass[321] and Lardin *et al.*[322] measured the electron affinities (EAs) of the α- and β-naphthyl radicals through kinetic methods and calculated the α and β C-H bond dissociation energies of naphthalene. Both studies found the α anion to be lower in energy than the β anion by several kJ/mol, favoring α formation in deprotonation of naphthalene.

Anion photoelectron spectroscopy (PES) is a powerful technique for probing the vibronic structure of neutral radicals through photodetachment of a closed-shell anion.[35,323] Ervin *et al.*[316] measured the photoelectron spectrum of $C_{10}H_7^-$ at 300 K and with a resolution of $\sim 100\,cm^{-1}$. The authors reported a congested, partially-resolved spectrum of the radical ground state with an EA of 1.403(15) eV. By comparison to Franck-Condon (FC) simulations, the spectrum was assigned to an 11:1 α:β isomer ratio. Substantial enrichment in α-naphthyl is consistent with the authors' use of non-specific deprotonation of naphthalene to generate anions.

Slow photoelectron velocity-map imaging (SEVI) spectroscopy,[35] a high resolution variant of anion PES, is a method apt to tackle the challenges of the naphthyl system in combination with gas-phase synthesis techniques and ion cooling. When anions are cryogenically cooled prior to photodetachment, hot bands and sequence bands vanish and rotational envelopes dramatically narrow, yielding features as narrow as $4\,\mathrm{cm}^{-1}$ full-width at half-maximum (fwhm) for molecular systems.[49] We report vibrationally-resolved, isomer-specific SEVI spectra of the ground and first excited states of the α- and β-naphthyl radicals, providing a wealth of vibronic information on these species.

The SEVI method and apparatus are described in detail elsewhere.[35,49,114] Naphthyl anions were prepared by flowing trace NF_3 in helium gas over a reservoir containing α- or β-trimethylsilyl (TMS) naphthalene, and expanding this mixture through an Even-Lavie pulsed valve[117] fitted with a circular filament ionizer. The TMS-naphthalene precursors were synthesized according to the procedure described by Marcinow *et al.*[324] from the corresponding α- and β-bromonaphthalenes (Sigma-Aldrich, 97%). Dissociative electron attachment to NF_3 produced F^- which reacted with TMS- naphthalene, selectively forming the α- or β-naphthyl anion.[118,321] The anions were collisionally cooled in an ion trap held at 5 K, mass-selected, and then photodetached with the output from a tunable dye laser. The electron kinetic energy (eKE) distribution of the resulting photoelectrons was measured with a velocity-map imaging spectrometer operated using low extraction voltages to preferentially detect low-eKE electrons, which are imaged with the highest resolution.

Energetics, optimized C_s geometries and harmonic frequencies were calculated for the α- and β-naphthyl anionic and neutral states at the B3LYP/6-311+G* level of theory, which has previously worked well for PAH systems.[85] Calculations of excited state geometries and harmonic frequencies were carried out with the maximum overlap method (MOM).[297] Dyson orbitals were calculated with EOM-IP-CCSD/6-311+G*. All calculations were done in Q-Chem 4.0.[253,254] Zero-point corrected energetics and selected vibrational frequencies are reported in Table 6.1. Complete lists of calculated geometries and frequencies are reported in Tables 6.2-6.5 of the Supporting Information (SI), with molecular structures labeled in Fig. 6.4.

FC simulations were carried out using ezSpectrum,[204] with all modes treated in the harmonic approximation and with full Duschinsky mixing. Simulations were shifted in binding energy and scaled to align with the position and intensity of each experimental vibrational origin. Vibrational fundamentals that were observed in the SEVI spectra were scaled to their experimental values; the others were left at their B3LYP calculated values. Photodetachment cross sections were calculated as a function of eKE using the ezDyson program.[82,83] Given *ab initio* Dyson orbitals, ezDyson finds the contribution of partial spherical waves with angular momentum $l \leq 4$ to the wavefunction of the outgoing photoelectron. Photoelectron angular distributions were also considered, as discussed in the SI.

SEVI spectra of photodetachment to the low-eBE edge of the α- and β-naphthyl radical $\tilde{X}^2A'$ bands are shown in Fig. 6.1. Low-resolution spectra are plotted in blue while high-resolution composite traces are in black. Overview spectra of the entire FC profile of the $\tilde{X}$ bands for the two isomers are given in Fig. 6.5. High-resolution peak widths are

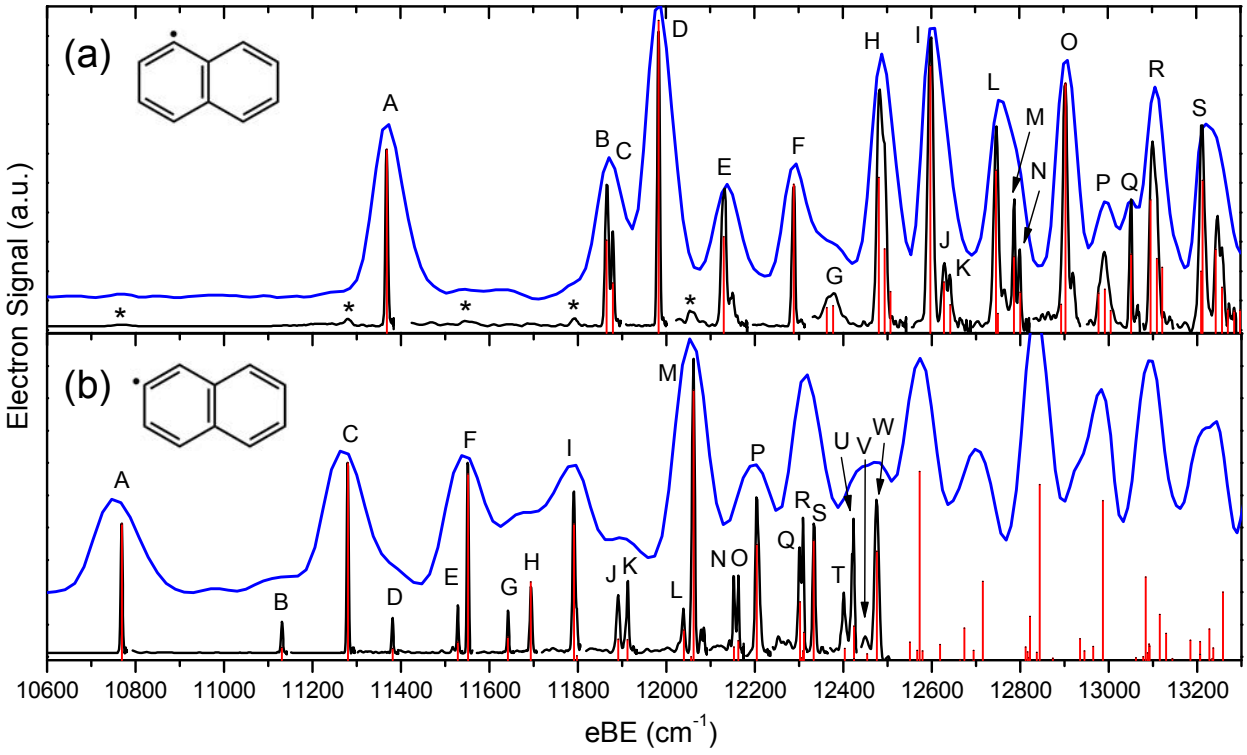

Figure 6.1: SEVI spectra of photodetachment to the $\tilde{X}^2A'$ ground states of (a) α-naphthyl and (b) β-naphthyl, with overview scans in blue, high-resolution traces in black, and FC simulations in red.

$\sim$8 cm^{-1} fwhm, in line with typical SEVI resolution for molecular systems. The ground state spectra of both isomers show congested FC activity that is accurately predicted by FC simulations (red). Peaks indicating a $\sim$ 4% contamination of the β isomer in the α-naphthyl spectrum are marked with asterisks in Fig. 6.1a, and are consistent with the purity of the α-bromonaphthalene starting material and 1 H NMR characterization of the α-TMS-naphthyl precursor.

Spectra of the $\tilde{A}^2A''$ excited states of the two isomers are shown in Fig. 6.2. The $\tilde{A}$ bands of both isomers have strong vibrational origins and weak vibrationally excited FC structure, qualitatively matched by simulation. The $\tilde{A}$ state vibrational origins have vanishing intensities close to threshold. SEVI can only yield narrow features at low eKE, and thus origin peak widths are limited to $\sim$60 cm^{-1} fwhm by the experimental resolution.

Experimental findings are summarized in Table 6.1, and compare well to calculated values. Full spectral assignments can be found in Tables 6.6 and 6.7 of the SI.

The spectra shown in Fig. 6.1 represent the first high-resolution characterization of the α- and β-naphthyl radical ground states, and are a testament to the efficacy of the SEVI method when combined with cryogenic cooling and isomer selection techniques. Our overview

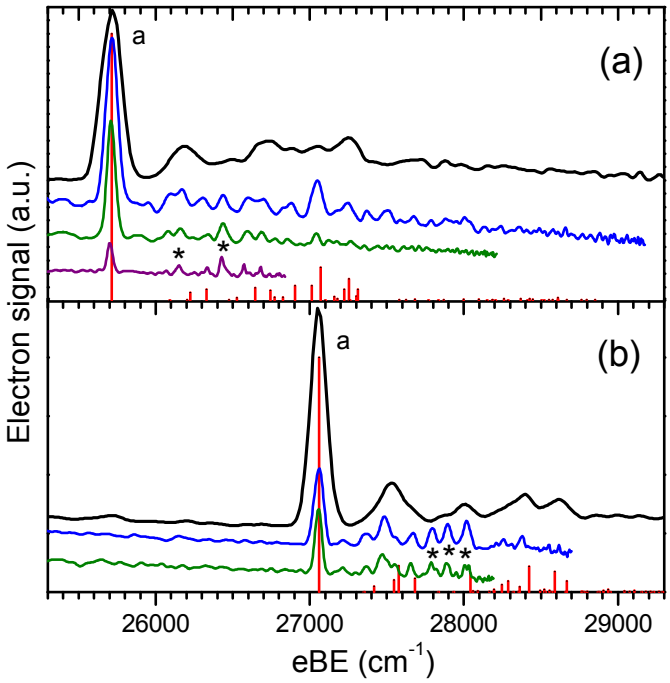

Figure 6.2: SEVI spectra and FC simulation of photodetachment to the $\tilde{A}^2A''$ first excited states of (a) α-naphthyl and (b) β-naphthyl, showing overview spectra in black, FC simulations in red, and colored traces taken at progressively lower photon energies.

spectrum of the α- naphthyl $\tilde{X}$ band (Fig. 6.5) is in excellent agreement with the naphthyl spectrum reported by Ervin *et al.*[316] Our measured EAs for α- and β-naphthyl (Table 6.1) agree with prior work, with much improved precision.[316,321,322]

Both $\tilde{X}$ bands show extensive FC activity, indicative of a large change in geometry upon photodetachment. For these transitions, the electron is detached from an *s*-*p* hybrid orbital localized on the deprotonated site; calculated Dyson orbitals are shown in Fig. 6.3. Correspondingly, geometry optimization calculations indicate that for both anions, the C-C-C interior bond angle at the deprotonated site changes dramatically upon photodetachment, widening by 14 (Tables 6.2 and 6.3 of the SI). The highly FC active vibrational modes are in-plane, as required by the Cs symmetry of the system, and involve distortion at the deprotonated site (Fig. 6.6 in the SI).

The SEVI spectra of the α- and β-naphthyl $\tilde{A}$ bands shown in Fig. 6.2 represent the first experimental report of these states. The observed term energies are well matched by MOM calculations (Table 6.1). The $\tilde{A}$ bands of both species have intense vibrational origins, indicating small changes in geometry upon photodetachment. Accordingly, the calculated excited state geometries show little displacement from the anion geometries (SI Tables 6.2 and 6.3), and the Dyson orbitals for these transitions are highly delocalized (Fig. 6.3).

The poor resolution of the $\tilde{A}$ bands results from transition cross sections decaying close

Table 6.1: Experimental and calculated electron affinities, term energies, and vibrational frequencies for the α- and β naphthyl radicals.

			Experimental	Calculated
α	$\tilde{X}$	EA,[a], eV	1.4095(4)[b]	1.3811
		ν_{25}, cm^{-1}	921(3)	933
		ν_{27}, cm^{-1}	763(5)	773
		ν_{28}, cm^{-1}	615(3)	632
		ν_{29}, cm^{-1}	512(3)	521
		ν_{30}, cm^{-1}	498(4)	508
	$\tilde{A}$	TE,[c], eV	1.7778(32)	1.6269
β	$\tilde{X}$	EA, eV	1.3352(2)	1.3266
		ν_{25}, cm^{-1}	925(3)	937
		ν_{26}, cm^{-1}	782(2)	794
		ν_{27}, cm^{-1}	760(2)	767
		ν_{28}, cm^{-1}	612(2)	629
		ν_{29}, cm^{-1}	511(2)	520
		ν_{31}, cm^{-1}	362(2)	369
	$\tilde{A}$	TE, eV	2.0194(27)	1.8652

[a]Electron affinity. [b]Uncertainties represent one standard deviation of a Gaussian fit to the experimentally observed peak. [c]Term energy.

to threshold. According to the Wigner threshold law,[75] $\sigma \propto (\text{eKE})l + 1/2$, where σ is the near-threshold photodetachment cross section and l is the angular momentum of the nascent photoelectron. Considering the naphthyl isomers as pseudo-D_{2h} species, the $\tilde{A}$ state Dyson orbitals have A_u symmetry. Within the s&p model,[78] an A_u photodetachment transition produces outgoing electrons with $l \geq 2$, yielding vanishing σ at small eKE. The $\tilde{X}$ states, on the other hand, have localized *s-p* hybrid Dyson orbitals, which allows for partial $l = 0$ detachment and retained intensity at small eKE.[325] Calculated photodetachment cross sections, shown in Fig. 6.3, are consistent with this threshold behavior for the $\tilde{X}$ and $\tilde{A}$ states of both species.

Some weak vibrational features (marked with asterisks in Fig. 6.2 maintain intensity close to threshold in the $\tilde{A}$ state spectra of both species, and are not well-represented by simulation. We assign these features as transitions to FC forbidden a'' vibrational modes of the $\tilde{A}\ ^2A''$ state, which can undergo Herzberg-Teller coupling to a' vibrational levels of the $\tilde{X}\ ^2A'$ ground state. This coupling allows otherwise forbidden $\tilde{A}$ state a'' modes to borrow threshold behavior from the $\tilde{X}$ state, explaining both why these features do not appear in simulations, and why they retain intensity at low eKE. More detailed discussion of vibronic

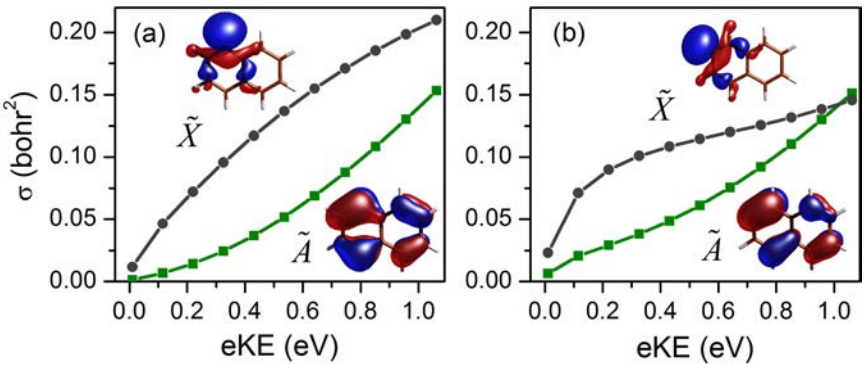

Figure 6.3: Calculated cross sections and visualized Dyson orbitals for photodetachment to the $\tilde{X}$ and $\tilde{A}$ states of (a) α-naphthyl and (b) β-naphthyl as a function of eKE.

coupling among neutral electronic states in SEVI experiments can be found in Ref. [85].

The present work represents the first high-resolution spectroscopic characterization of the ground states of the α- and β-naphthyl radicals, and the first experimental measurement of the lowest excited states of both species. This study demonstrates the utility of SEVI for studying such species, especially when combined with cryogenic cooling and synthetic techniques for isomer selection.

6.2 Supporting Information

Photoelectron Angular Distributions

For a one-photon photodetachment process with linearly polarized light, the photoelectron angular distribution (PAD) is given by[79]

$$\frac{d\sigma}{d\Omega} = \frac{\sigma_{tot}}{4\pi}\left[1 + \beta P_2(\cos\theta)\right] \tag{6.1}$$

where θ is the angle relative to the polarization axis of the laser, P_2 is the second-order Legendre polynomial, and β is the anisotropy parameter, which varies between -1 for a PAD aligned perpendicular to the laser polarization and $+2$ for a PAD parallel to the laser polarization. β generally has a consistent sign over the range of electron kinetic energies (eKEs) probed in SEVI experiments.[85]

The α-naphthyl $\tilde{X}$ band has a slightly parallel PAD ($\beta > 0$), while the β-naphthyl $\tilde{X}$ PAD is slightly perpendicular ($\beta < 0$), as shown with plotted points in Fig. 6.7a. The two PADs differ based on relative s and p contributions to the s-p hybrid Dyson orbitals for the two isomers.[256,325] Detachment from s-like orbitals yields predominantly $l = 1$ photoelectrons, which have PADs with $\beta > 0$, while detachment from p-like orbitals yields both $l = 0$ photoelectrons ($\beta = 0$) and $l = 2$ photoelectrons ($\beta < 0$ for relatively low eKE). The relative

contributions of these detachment channels therefore have great sway over the total PAD, allowing for very different observed anisotropies for the α- and β-naphthyl $\tilde{X}$ states.

The vibrational origins of the $\tilde{A}$ bands of both isomers have slightly perpendicular PADs($\beta < 0$). The β values for these transitions cannot be reported quantitatively, as high-eKE photoelectrons from detachment to the $\tilde{X}$ band create a background that limits accurate reproduction of $\tilde{A}$ state anisotropies during image reconstruction. Additionally, the vibrationally excited features of the $\tilde{A}$ bands are too weak for even qualitative measurement of anisotropies, so the PADs cannot confirm any vibronic coupling to the $\tilde{X}$ state discussed in the main text.

PADs for all states were simulated as a function of eKE using the ezDyson program.[83] As described in the main chapter text, *ab initio* Dyson orbitals were given as input to ezDyson and used to find the contribution of partial spherical waves with angular momentum $l \leq 4$ to the wavefunction of the outgoing photoelectron. The results of these calculations are shown in Fig. 6.7, and compared with experimental anisotropies for the $\tilde{X}$ states. Simulations reproduce the behavior of the experimental β values for the $\tilde{X}$ state over this range of eKEs, though anisotropy calculations are very sensitive to the shape of the *ab initio* Dyson orbitals,[82] so the match is qualitative at best. The $\tilde{A}$ state calculations also predict $\beta < 0$ for most of the eKE range, in agreement with experiment.

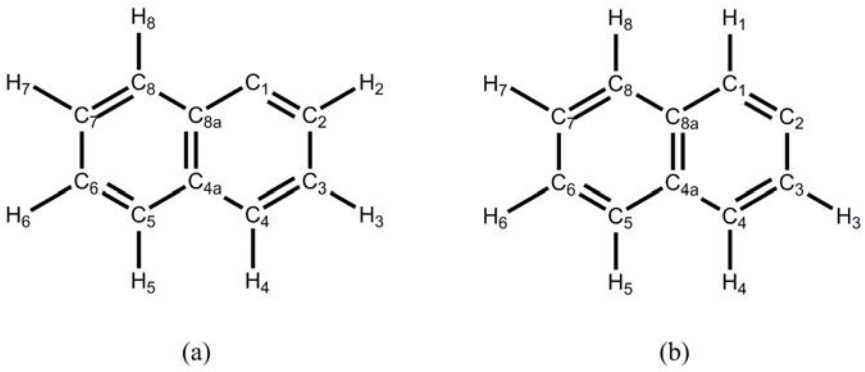

Figure 6.4: Diagrams of (a) α-naphthyl and (b) β-naphthyl.

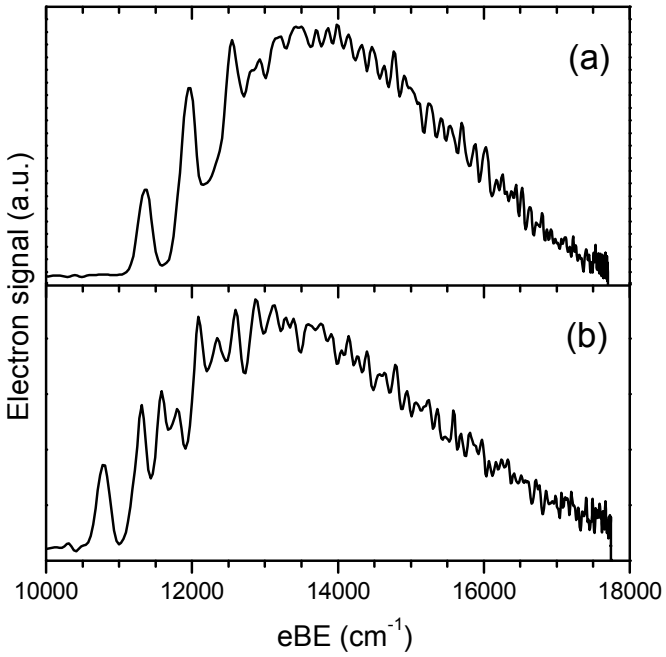

Figure 6.5: Overview SEVI spectra of photodetachment to the $\tilde{X}\ A'$ ground states of (a) α-naphthyl and (b) β-naphthyl.

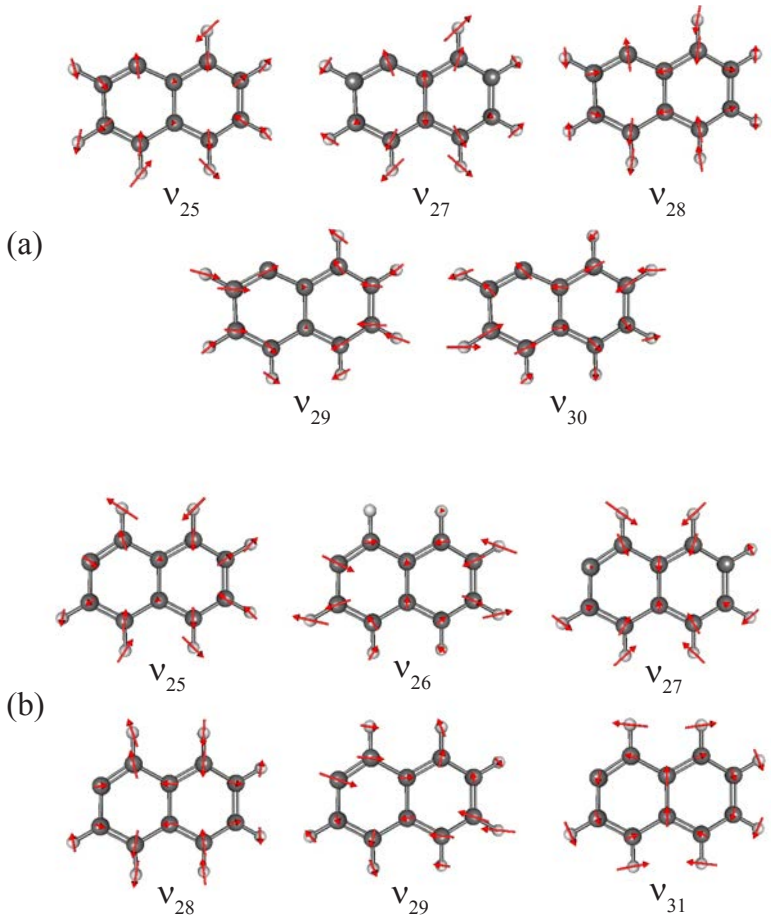

Figure 6.6: Franck-Condon active vibrational modes for the ground state photoelectron spectra of (a) α-naphthyl and (b) β-naphthyl.

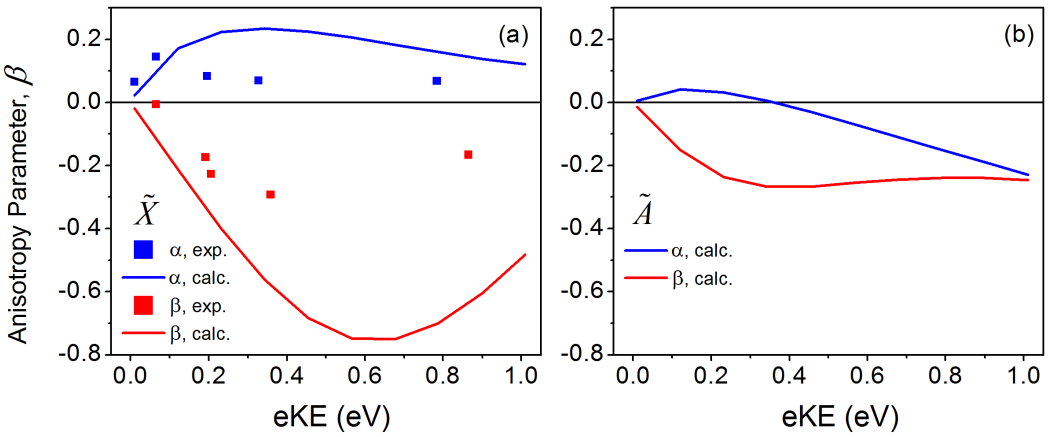

Figure 6.7: Calculated and some experimental anisotropy parameters for photodetachment to (a) the $\tilde{X}$ bands of α- and β-naphthyl and (b) the $\tilde{A}$ bands of α- and β-naphthyl, as functions of eKE.

Table 6.2: Optimized bond lengths (Å) and bond angles (degrees) of the anion and neutral α-naphthyl species calculated with B3LYP/6-311+G*. Atoms are labeled in Fig. 6.4.

	Anion	Ground	Excited
C_2H_2	1.096	1.085	1.089
C_3H_3	1.093	1.086	1.087
C_4H_4	1.090	1.086	1.087
C_5H_5	1.091	1.086	1.087
C_6H_6	1.088	1.085	1.085
C_7H_7	1.088	1.085	1.085
C_8H_8	1.087	1.085	1.085
C_1C_2	1.397	1.355	1.446
C_2C_3	1.420	1.426	1.392
C_3C_4	1.379	1.375	1.397
C_4C_{4a}	1.418	1.421	1.424
$C_{4a}C_5$	1.422	1.419	1.407
$C_{4a}C_8$	1.447	1.441	1.434
C_5C_6	1.377	1.375	1.395
C_6C_7	1.416	1.415	1.395
C_7C_8	1.379	1.374	1.399
C_8C_{8a}	1.425	1.419	1.405
C_1C_{8a}	1.445	1.400	1.451
$C_1C_2H_2$	119.30	122.59	117.79
$C_2C_3H_3$	119.79	119.25	120.74
$C_3C_4H_4$	121.27	119.92	120.32
$C_{4a}C_5H_5$	118.73	118.76	119.70
$C_5C_6H_6$	120.18	119.95	119.81
$C_6C_7H_7$	119.73	119.57	119.97
$C_7C_8H_8$	121.05	120.83	121.04
$C_1C_2C_3$	124.75	116.82	124.83
$C_2C_3C_4$	120.90	120.42	119.99
$C_3C_4C_{4a}$	119.16	121.49	120.42
$C_4C_4aC_5$	121.98	122.78	121.65
$C_4C_{4a}C_{8a}$	118.25	118.98	118.11
$C_{4a}C_5C_6$	121.31	120.96	120.45
$C_5C_6C_7$	119.80	120.51	120.03
$C_6C_7C_8$	119.85	120.46	120.01
$C_7C_8C_{8a}$	122.85	120.39	121.73
$C_8C_{8a}C_1$	119.65	125.02	118.48
$C_8C_{8a}C_{4a}$	116.42	119.44	117.55
$C_{8a}C_1C_2$	113.00	126.74	112.68

Table 6.3: Optimized bond lengths (Å) and bond angles (degrees) of the anion and neutral β-naphthyl species calculated with B3LYP/6-311+G*. Atoms are labeled in Fig. 6.4.

	Anion	Ground	Excited
C_1H_1	1.098	1.086	1.092
C_3H_3	1.096	1.085	1.089
C_4H_4	1.093	1.087	1.089
C_5H_5	1.089	1.086	1.086
C_6H_6	1.088	1.085	1.085
C_7H_7	1.088	1.085	1.085
C_8H_8	1.089	1.086	1.086
C_1C_2	1.396	1.354	1.447
C_2C_3	1.440	1.395	1.433
C_3C_4	1.383	1.381	1.377
C_4C_{4a}	1.419	1.422	1.442
$C_{4a}C_5$	1.419	1.420	1.395
$C_{4a}C_{8a}$	1.437	1.434	1.427
C_5C_6	1.379	1.374	1.401
C_6C_7	1.417	1.415	1.396
C_7C_8	1.379	1.375	1.392
C_8C_{8a}	1.423	1.419	1.411
C_1C_{8a}	1.426	1.430	1.423
$C_2C_3H_3$	118.33	122.01	118.18
$C_3C_4H_4$	120.98	119.93	120.78
$C_{4a}C_5H_5$	118.51	118.78	119.65
$C_5C_6H_6$	120.35	120.10	119.61
$C_6C_7H_7$	119.71	119.63	120.08
$C_7C_8H_8$	120.03	120.35	120.22
$C_{8a}C_1H_1$	114.85	119.82	116.09
$C_1C_2C_3$	112.26	126.31	112.08
$C_2C_3C_4$	125.41	116.81	124.58
$C_3C_4C_{4a}$	120.51	121.12	121.55
$C_4C_{4a}C_5$	123.65	121.83	122.98
$C_4C_{4a}C_{8a}$	117.25	119.55	117.74
$C_{4a}C_5C_6$	121.48	120.99	120.63
$C_5C_6C_7$	119.70	120.23	120.46
$C_6C_7C_8$	120.04	120.39	119.71
$C_7C_8C_{8a}$	121.86	120.75	120.81
$C_8C_{8a}C_1$	123.34	122.22	122.86
$C_8C_{8a}C_{4a}$	117.82	119.01	119.13
$C_{8a}C_1C_2$	125.73	117.45	126.03

Table 6.4: Vibrational frequencies (cm^{-1}) for the anion and neutral α-naphthyl species calculated with B3LYP/6-311+G*.

Symm.	Mode	Anion	Ground	Excited	Symm.	Mode	Anion	Ground	Excited
a'	ν_1	3157	3191	3198	a''	ν_{32}	967	990	1003
	ν_2	3137	3181	3186		ν_{33}	944	968	1000
	ν_3	3117	3180	3172		ν_{34}	921	956	977
	ν_4	3114	3168	3169		ν_{35}	868	887	923
	ν_5	3094	3167	3154		ν_{36}	834	859	891
	ν_6	3067	3157	3147		ν_{37}	774	786	781
	ν_7	3014	3155	3120		ν_{38}	757	769	764
	ν_8	1632	1664	1595		ν_{39}	711	726	746
	ν_9	1602	1638	1587		ν_{40}	621	611	637
	ν_{10}	1547	1584	1540		ν_{41}	489	506	459
	ν_{11}	1517	1524	1506		ν_{42}	454	459	446
	ν_{12}	1462	1487	1463		ν_{43}	394	400	382
	ν_{13}	1439	1456	1444		ν_{44}	165	186	161
	ν_{14}	1380	1392	1382		ν_{45}	160	169	150
	ν_{15}	1348	1382	1355					
	ν_{16}	1313	1361	1297					
	ν_{17}	1255	1275	1279					
	ν_{18}	1225	1238	1238					
	ν_{19}	1199	1201	1189					
	ν_{20}	1157	1180	1180					
	ν_{21}	1150	1171	1130					
	ν_{22}	1123	1140	1111					
	ν_{23}	1035	1047	1055					
	ν_{24}	1022	1034	1028					
	ν_{25}	938	933	928					
	ν_{26}	808	801	810					
	ν_{27}	754	773	762					
	ν_{28}	626	632	613					
	ν_{29}	516	521	510					
	ν_{30}	514	508	486					
	ν_{31}	378	362	371					

Table 6.5: Vibrational frequencies (cm^{-1}) for the anion and neutral β-naphthyl species calculated with B3LYP/6-311+G*.

Symm.	Mode	Anion	Ground	Excited	Symm.	Mode	Anion	Ground	Excited
a'	ν_1	3149	3187	3194	a''	ν_{32}	957	988	1006
	ν_2	3132	3179	3181		ν_{33}	941	963	994
	ν_3	3117	3174	3169		ν_{34}	918	948	965
	ν_4	3110	3162	3165		ν_{35}	891	884	916
	ν_5	3068	3159	3134		ν_{36}	834	839	864
	ν_6	3020	3157	3112		ν_{37}	797	801	840
	ν_7	3000	3153	3099		ν_{38}	766	750	779
	ν_8	1631	1657	1604		ν_{39}	717	739	747
	ν_9	1583	1620	1597		ν_{40}	619	612	610
	ν_{10}	1558	1593	1529		ν_{41}	472	485	450
	ν_{11}	1513	1534	1505		ν_{42}	436	470	417
	ν_{12}	1453	1471	1459		ν_{43}	358	386	329
	ν_{13}	1439	1463	1432		ν_{44}	175	191	159
	ν_{14}	1394	1396	1390		ν_{45}	165	175	144
	ν_{15}	1363	1388	1360					
	ν_{16}	1317	1339	1298					
	ν_{17}	1283	1281	1294					
	ν_{18}	1262	1255	1254					
	ν_{19}	1221	1211	1224					
	ν_{20}	1169	1176	1186					
	ν_{21}	1163	1163	1135					
	ν_{22}	1143	1144	1134					
	ν_{23}	1033	1051	1051					
	ν_{24}	1005	1040	981					
	ν_{25}	935	937	937					
	ν_{26}	795	794	797					
	ν_{27}	770	767	769					
	ν_{28}	639	629	620					
	ν_{29}	521	520	515					
	ν_{30}	511	511	484					
	ν_{31}	360	369	354					

Table 6.6: Peak positions (cm^1), offsets from the origin (cm^1), and assignments for the SEVI spectra of α-naphthyl given in Figs. 6.1a and 6.2a.

Peak	Position	Offset	Assignment	Band
A	11368	0	0_0^0	$\tilde{X}^2A' \leftarrow \tilde{X}^1A'$
B	11867	498	30_0^1	
C	11880	512	29_0^1	
D	11983	615	28_0^1	
E	12131	763	27_0^1	
F	12289	921	25_0^1	
G	12376	1007	$30_0^2,\ 29_0^1 30_0^1$	
H	12487	1119	$28_0^1 30_0^1,\ 28_0^1 29_0^1$	
I	12599	1230	28_0^2	
J	12629	1261	$27_0^1 30_0^1$	
K	12643	1274	$27_0^1 29_0^1$	
L	12747	1379	$27_0^1 28_0^1$	
M	12788	1419	$25_0^1 30_0^1$	
N	12800	1432	$25_0^1 29_0^1$	
O	12903	1535	$25_0^1 28_0^1$	
P	12992	1623	$28_0^1 29_0^1 30_0^1,\ 28_0^1 30_0^2$	
Q	13052	1683	$25_0^1 27_0^1$	
R	13099	1731	$28_0^2 30_0^1$	
S	13110	1741	$28_0^2 29_0^1$	
a	25708	0	0_0^0	$\tilde{A}^2A'' \leftarrow \tilde{X}^1A'$

Table 6.7: Peak positions (cm^1), offsets from the origin (cm^1), and assignments for the SEVI spectra of β-naphthyl given in Figs. 6.1b and 6.2b.

Peak	Position	Offset	Assignment	Band
A	10769	0	0_0^0	$\tilde{X}^2A' \leftarrow \tilde{X}^1A'$
B	11131	362	31_0^1	
C	11280	511	29_0^1	
D	11381	612	28_0^1	
E	11529	760	27_0^1	
F	11551	782	26_0^1	
G	11642	873	$29_0^1 31_0^1$	
H	11694	925	25_0^1	
I	11791	1022	29_0^2	
J	11891	1122	$28_0^1 29_0^1$	
K	11912	1144	$26_0^1 31_0^1$	
L	12038	1269	$27_0^1 29_0^1$	
M	12061	1292	$26_0^1 29_0^1$	
N	12153	1384	$29_0^1 31_0^1$	
O	12162	1394	$26_0^1 28_0^1$	
P	12205	1437	$25_0^1 29_0^1$	
Q	12301	1532	29_0^3	
R	12309	1540	$26_0^1 27_0^1$	
S	12334	1565	26_0^2	
T	12402	1633	$28_0^1 29_0^1$	
U	12422	1654	$26_0^1 29_0^1 31_0^1$	
V	12450	1681	$25_0^1 27_0^1$	
W	12476	1707	$25_0^1 26_0^1$	
a	27056	0	0_0^0	$\tilde{A}^2A'' \leftarrow \tilde{X}^1A'$

Chapter 7

Vibronic structure of 9-, 1-, and 2-anthracenyl

The content and figures of this chapter are reprinted or adapted with permission from
M. L. Weichman, J. A. DeVine, D. S. Levine, J. B. Kim, and D. M. Neumark, "Isomer-specific vibronic structure of the 9-, 1-, and 2-anthracenyl radicals via slow photoelectron velocity-map imaging" *Proc. Natl. Acad. Sci. USA* **113**, 1698 (2016).

Abstract

Polycyclic aromatic hydrocarbons, in various charge and protonation states, are key compounds relevant to combustion chemistry and astrochemistry. Here, we probe the vibrational and electronic spectroscopy of gas-phase 9-, 1-, and 2-anthracenyl radicals ($C_{14}H_9$) by photodetachment of the corresponding cryogenically cooled anions via slow photoelectron velocity-map imaging (cryo-SEVI). The use of a newly designed velocity-map imaging lens in combination with ion cooling yields photoelectron spectra with $<2\,cm^{-1}$ resolution. Isomer selection of the anions is achieved using gas-phase synthesis techniques, resulting in observation and interpretation of detailed vibronic structure of the ground and lowest excited states for the three anthracenyl radical isomers. The ground state bands yield electron affinities of 1.7155(2) eV, 1.5436(2) eV, and 1.4671(2) eV for 9-, 1-, and 2-anthracenyl respectively. Vibrational frequencies for several Franck-Condon active modes are measured and assigned for each isomer. Term energies of the first excited states of the 9-, 1-, and 2-anthracenyl radicals are found to be 1.205(6) eV, 1.515(4) eV, and 1.755(8) eV, respectively. Spectra are interpreted through comparison with *ab initio* quantum chemistry calculations, Franck-Condon simulations, and calculations of threshold photodetachment cross sections and anisotropies. Experimental measures of the subtle differences in energetics and relative stabilities of these radical isomers are of interest from the perspective of fundamental physical organic chemistry, and aid in understanding their behavior and reactivity in interstellar and combustion environments. Additionally, spectroscopic characterization of these species in the laboratory is essential for their potential identification in astrochemical data.

7.1 Introduction

Polycyclic aromatic hydrocarbons (PAHs) are an important class of species in many areas of chemistry. They are major components in coal[326] and in soot formed from combustion of organic matter.[327,328] PAHs are therefore common environmental pollutants, and have well-documented mutagenic and carcinogenic biological activity.[329,330] PAHs are also believed to be abundant in the interstellar medium,[331] and may be carriers of the anomalous IR emission bands.[304–306] Recent molecular beam studies indicate that PAH growth can proceed through cold collisions of smaller hydrocarbons under interstellar conditions.[332,333] Individual PAH molecules can subsequently provide nucleation sites for amorphous graphitic grains.[306] Interstellar PAHs and their clusters therefore bridge the gap between small carbonaceous molecules and larger particles, analogous to their role in soot condensation in combustion environments.[334]

In space, PAH species are likely to exist as an equilibrium of neutral and ionic charge states, with varying degrees of hydrogenation and dehydrogenation.[335–337] Models of dense interstellar clouds find that anionic PAHs are the major carriers of negative charge, rather than free electrons.[338] Closed-shell, singly deprotonated PAH carbanions have large electron affinities compared to radical anionic parent species, and may therefore be reasonably

robust in the interstellar medium.[331,335] We investigate the three dehydrogenated isomers of anthracene, the 9-, 1-, and 2-anthracenyl radicals, via slow photoelectron velocity-map imaging of the corresponding cryogenically cooled, deprotonated anions; structures of the $C_{14}H_9^-$ isomers are shown in Fig. 7.1. This technique, cryo-SEVI, previously yielded highly vibrationally-resolved spectra of α- and β-naphthyl.[294] We demonstrate here that even larger PAH anions are accessible to detailed characterization with cryo-SEVI, and that the three anthracenyl isomers demonstrate strikingly distinct energetics and spectroscopic signatures.

The anthracene molecule has been well characterized experimentally. Its infrared spectrum has been measured in a rare gas matrix[339,340] and in the gas phase,[341] and its vibrational structure has been largely assigned.[342] The $S_1 \leftarrow S_0$ electronic transition in anthracene has been investigated with cavity ring down spectroscopy.[343] The high-temperature oxidation products of anthracene with O_2 and OH have been studied experimentally,[344,345]. In both cases, H atom abstraction to form the anthracenyl radical intermediate competes with direct oxidation of anthracene. These reaction pathways govern the balance between efficient combustion and soot formation; detailed understanding of the intermediates involved is essential for accurately modeling combustion.

The anthracenyl radical and anion isomers are not nearly as well-characterized as the anthracene parent. The 9- and 1-anthracenyl radicals were examined with ESR spectroscopy,[346] which suggested that the unpaired electron resides in a σ orbital localized at the site of dehydrogenation. The reactivity of the 9-anthracenyl radical with naphthalene and toluene has also been measured experimentally.[347] A recent multiple-photon electron detachment study yielded the infrared action spectrum of the 9-anthracenyl anion.[331] Anionic anthracene derivatives in various protonation states are also used in electron transfer dissociation mass spectrometry as an electron source to induce fragmentation of peptide back bones[348]. A fair amount of additional theoretical work has been reported detailing the energetics, electronic structure, geometries, vibrational frequencies, and reactivities of the anthracenyl radicals and anions.[317,318,326,331,349–351] The three C−H bond dissociation energies of anthracene are predicted to be very similar, leading to three anthracenyl radical isomers nearly degenerate in energy.[317,318,326,349] The anionic isomers are calculated to be more separated in energy, with the 9-anthracenyl anion being the most stable, and the 1- and 2-anthracenyl anions lying 0.14 eV and 0.18–0.21 eV higher in energy, respectively.[317,331]

Anion photoelectron spectroscopy (PES) is a technique well-suited for probing the vibronic structure of neutral radicals through photodetachment of a closed-shell anion.[35,323] The cryo-SEVI technique used here is a high-resolution variant of PES and yields spectra of complex anions with sub-meV resolution.[294,352,353] Specific anthracenyl anion isomers are prepared using trimethylsilyl-anthracene precursors and cooled to cryogenic temperatures ($\sim$10 K) prior to photodetachment, eliminating hot spectral features and narrowing the rotational profiles of the observed peaks. Cooling is essential for obtaining interpretable spectra of large molecular species with many low-frequency vibrational modes. We use a newly designed velocity-map imaging (VMI) electrostatic lens with improved energy resolution. This development allows us to observe peaks with 2–3 cm^{-1} fwhm and resolve splittings as small as 3 cm^{-1} for the anthracenyl system. Focusing is also improved at higher electron kinetic

energy (eKE), yielding narrower features farther from threshold and thus facilitating studies of anions with poor threshold photodetachment cross sections.

We present highly vibrationally-resolved, isomer-specific spectra of transitions to the ground and first excited states of the 9-, 1-, and 2-anthracenyl radicals, providing much new spectroscopic information, and demonstrating the new capabilities of the cryo-SEVI instrument. We obtain precise electron affinities for the three anthracenyl radical isomers and term energies for their excited states, and measure Franck-Condon active fundamental vibrational frequencies. Our results illuminate the distinct spectroscopy, energetics, and potential reactivity of these isomers, with far-reaching applications in interpretation of astrochemical data and modeling of combustion chemistry.

7.2 Experimental Methods

The SEVI method and apparatus has been described in detail in Chap. 2.

Specific anthracenyl anion isomers are prepared by flowing trace NF_3 in helium gas over a reservoir containing either 9-, 1-, or 2-(trimethylsilyl)-anthracene heated to 40–60 °C. We expand this mixture through an Even-Lavie pulsed valve[117] operating at 20 Hz, and fitted with a circular filament ionizer. Electrons from the ionizer induce dissociative electron attachment of NF_3 to produce F^-. F^- then reacts with 9-, 1- or 2-(trimethylsilyl)-anthracene, selectively forming the corresponding anthracenyl anion due to the strength of the silicon-fluorine bond.[118]

The three trimethylsilyl-anthracene precursors were synthesized from the corresponding bromoanthracenes according to the procedure described by Marcinow *et al.*[324] 9-bromoanthracene (TCI, > 99%) and 1-bromoanthracene (TCI, > 97%) were obtained commercially, while 2-bromoanthracene was synthesized from 2-aminoanthracene (Sigma-Aldrich, 96%). The details of these syntheses and NMR characterization of products are reported in the Supporting Information.

We calibrate the velocity, and hence eKE of the photoelectrons as a function of radial displacement, R, using SEVI images of atomic O^- and F^-,[145,146] taken at many photon energies. The distance of an electron spot from the center of the reconstructed image is largely linearly proportional to its velocity following photodetachment. However, the added length and lensing properties of the new VMI design slightly distort the electron velocities, so an additional polynomial term is needed; we calibrate by fitting $\text{eKE} = aR^2 + bR^4$. The eKE spectrum can then be converted to eBE using the energy conservation expression $\text{eBE} = h\nu - \text{eKE}$, where $h\nu$ is the photon energy.

7.3 Calculations

Density functional theory calculations were carried out at the B3LYP/6-311+G* level of theory in order to find the energetics, optimized geometries, normal modes, and harmonic

vibrational frequencies for the 9-, 1-, and 2-anthracenyl anions, and the ground and first excited states of the corresponding radicals. The maximum overlap method[297] was used for the radical excited states. Dyson orbitals for photodetachment transitions were calculated with EOM-IP-CCSD/6-311G. All *ab initio* work was done using Q-Chem 4.0.[253,254]

Calculated energetics corrected for vibrational zero-point energy and relevant harmonic vibrational frequencies are summarized in Table 7.1; isomer energetics are summarized in Table 7.2. Full lists of optimized geometries and harmonic frequencies can be found in Tables 7.6-7.11 in the Supporting Information. All states considered were found to have planar equilibrium geometries, in agreement with the literature.[317,318,331]

Photoelectron spectra for detachment to the ground and excited states of the 9-, 1-, and 2-anthracenyl radicals were simulated at 0 K using the ezSpectrum program.[204] The *ab initio* geometries, normal modes, and harmonic frequencies were given as input, and Franck-Condon overlap factors were calculated in the harmonic approximation with Duschinsky mixing of all modes.[205] The vibrational origins of all bands were shifted in eBE to align with their experimental values. Those frequencies of the neutral ground states that were observed in the high-resolution SEVI spectra were scaled to their experimental values; the others were left at their calculated B3LYP/6-311+G* values.

The photoelectron angular distributions and photodetachment cross sections for transitions to the neutral ground and excited states were calculated as functions of eKE with the ezDyson program.[82,83] ezDyson takes as input the *ab initio* Dyson orbitals for the relevant photodetachment transitions, and finds the contribution of partial spherical waves with angular momentum $l \leq 4$ to the wavefunction of the outgoing photoelectron.

7.4 Results and Discussion

7.4.1 Experimental Photodetachment Spectra

The cryo-SEVI spectra of 9-, 1-, and 2-anthracenyl presented in Figs. 7.1 and 7.2 show two well-separated electronic bands, which for each isomer are assigned as transitions from the anion ground state to the ground electronic state ($\tilde{X}$) and the first excited state ($\tilde{A}$) of the neutral radical. Franck-Condon (FC) simulations for all states are plotted as red stick spectra. Experimental energetics and vibrational frequencies for all anthracenyl isomers are summarized in Table 7.1 and compared to calculated values. Positions and assignments for the peaks labeled in Figs. 7.1 and 7.2 are summarized in Tables 7.3-7.5.

Cryo-SEVI spectra of the 9-,1-, and 2-anthracenyl $\tilde{X}$ bands are shown in Fig. 7.1 as a function of electron binding energy (eBE). With SEVI, we first measure a low-resolution overview spectrum at a photon energy well above the eBE of the band of interest, plotted here in blue. We then obtain high-resolution spectra at discrete photon energies tuned above the spectral features of interest, and splice them together to create a composite high-resolution spectrum of the full region, plotted in black. The high-resolution trace for a given feature is

Table 7.1: Experimental and calculated electron affinities, excited state term energies, and vibrational frequencies for the 9-, 1-, and 2-anthracenyl radicals.

Isomer	Parameter	Experimental	Calculated
9 $\tilde{X}$	EA,[a] eV	1.7155(2)[b]	1.6749
	ν_{15}, cm^{-1}	1147(1)	1168
	ν_{17}, cm^{-1}	896(2)	907
	ν_{18}, cm^{-1}	752(4)	759
	ν_{19}, cm^{-1}	648(2)	658
	ν_{20}, cm^{-1}	621(2)	638
	ν_{21}, cm^{-1}	390(2)	398
	ν_{22}, cm^{-1}	228(2)	233
9 $\tilde{A}$	T_0,[c] eV	1.205(6)	1.0382
1 $\tilde{X}$	EA, eV	1.5436(2)	1.5287
	ν_{30}, cm^{-1}	1091(4)	1113
	ν_{34}, cm^{-1}	891(2)	902
	ν_{36}, cm^{-1}	753(2)	762
	ν_{38}, cm^{-1}	621(2)	639
	ν_{39}, cm^{-1}	599(2)	618
	ν_{40}, cm^{-1}	514(2)	526
	ν_{42}, cm^{-1}	388(2)	395
	ν_{43}, cm^{-1}	232(2)	236
1 $\tilde{A}$	T_0, eV	1.515(4)	1.3277
	ν_{56}, cm^{-1}	496(36)	504
	ν_{60}, cm^{-1}	255(33)	256
2 $\tilde{X}$	EA, eV	1.4671(2)	1.4734
	ν_{31}, cm^{-1}	1013(2)	1039
	ν_{34}, cm^{-1}	882(2)	894
	ν_{37}, cm^{-1}	648(1)	658
	ν_{39}, cm^{-1}	591(1)	609
	ν_{40}, cm^{-1}	522(2)	533
	ν_{41}, cm^{-1}	389(1)	398
	ν_{42}, cm^{-1}	392(1)	396
	ν_{43}, cm^{-1}	234(1)	238
2 $\tilde{A}$	T_0, eV	1.755(8)	1.5580

[a]Electron affinity. [b]Uncertainties represent one standard deviation of a Gaussian fit to the experimentally observed peak. [c]Term energy.

then scaled to the intensity of that feature in the overview spectrum to avoid any threshold effects that distort relative peak intensities.

The ground state spectra of all isomers show congested but well-resolved structure that is accurately predicted by FC simulation. High-resolution peak widths are typically 4–5 cm^{-1} fwhm for the ground states of all three anthracenyl radicals, and as narrow as 2–3 cm^{-1} fwhm. This constitutes a notable improvement in instrumental resolution over previous cryo-SEVI studies of aromatic molecules, where the narrowest features were more often 7–8 cm^{-1} fwhm.[294,353] Peaks indicating some contamination of the 1-anthracenyl isomer in the 2-anthracenyl spectrum are plotted in gray in Fig. 7.1c. This contamination is likely due to decomposition of either the 2-trimethylsilyl-anthracene precursor or the 2-anthracenyl anions after formation in the ion source. The contamination worsens with increasing temperature of the ion source, and over time with usage of the same precursor sample.

Spectra of the $\tilde{A}$ bands of 9- and 1-anthracenyl are shown in Figs. 7.2a and b. Due to poor threshold cross sections for these bands, we do not plot composite high-resolution spectra, but rather the full traces at progressively lower photon energies. Though we report its term energy in Table 7.1, the 2-anthracenyl $\tilde{A}$ state spectrum is not presented due to contamination from 1-anthracenyl structure made worse by relative cross section effects. The bands of all isomers have strong vibrational origins and weak vibrationally excited structure. The profiles of these bands are in qualitative agreement with FC simulation, although more vibrational activity is seen in the spectra than the simulations.

Compared to the $\tilde{X}$ bands, the $\tilde{A}$ state vibrational origins are very weak at low eKE, preventing measurements close to threshold where SEVI resolution is best. Hence, peak widths for the $\tilde{A}$ band origins are limited to $\sim$100 cm^{-1} fwhm, even with the improved resolution afforded by the new VMI lens. The remaining features in the $\tilde{A}$ bands largely follow this trend of vanishing intensity close to threshold. However, the intensities of some peaks (most notably *b* and *c*) in the 1-anthracenyl spectrum increase dramatically at certain photon energies as evidenced by the purple trace plotted in Fig. 7.2b, which is an average of spectra taken at photon energies of 27519 cm^{-1} and 27595 cm^{-1}.

SEVI also provides information about the anisotropy of photodetachment transitions. For a photodetachment process with one photon of linearly polarized light, the photoelectron angular distribution (PAD) is given by:[79]

$$\frac{d\sigma}{d\Omega} = \frac{\sigma_{tot}}{4\pi}\left[1 + \beta P_2(\cos\theta)\right] \tag{7.1}$$

where θ is the angle of electron signal relative to the polarization axis of the laser, P_2 is the second-order Legendre polynomial, and β is the anisotropy parameter, which varies between -1 for a PAD aligned perpendicular to the laser polarization and +2 for a PAD parallel to the laser polarization.

Experimental values of β for the vibrational origins of the $\tilde{X}$ bands of all isomers are plotted in Fig. 7.3 as a function of eKE, along with PAD simulations for the $\tilde{X}$ and $\tilde{A}$ bands. We cannot report quantitative anisotropy parameters for the excited states, because high-eKE photoelectrons from detachment to the ground states create a background that distorts the

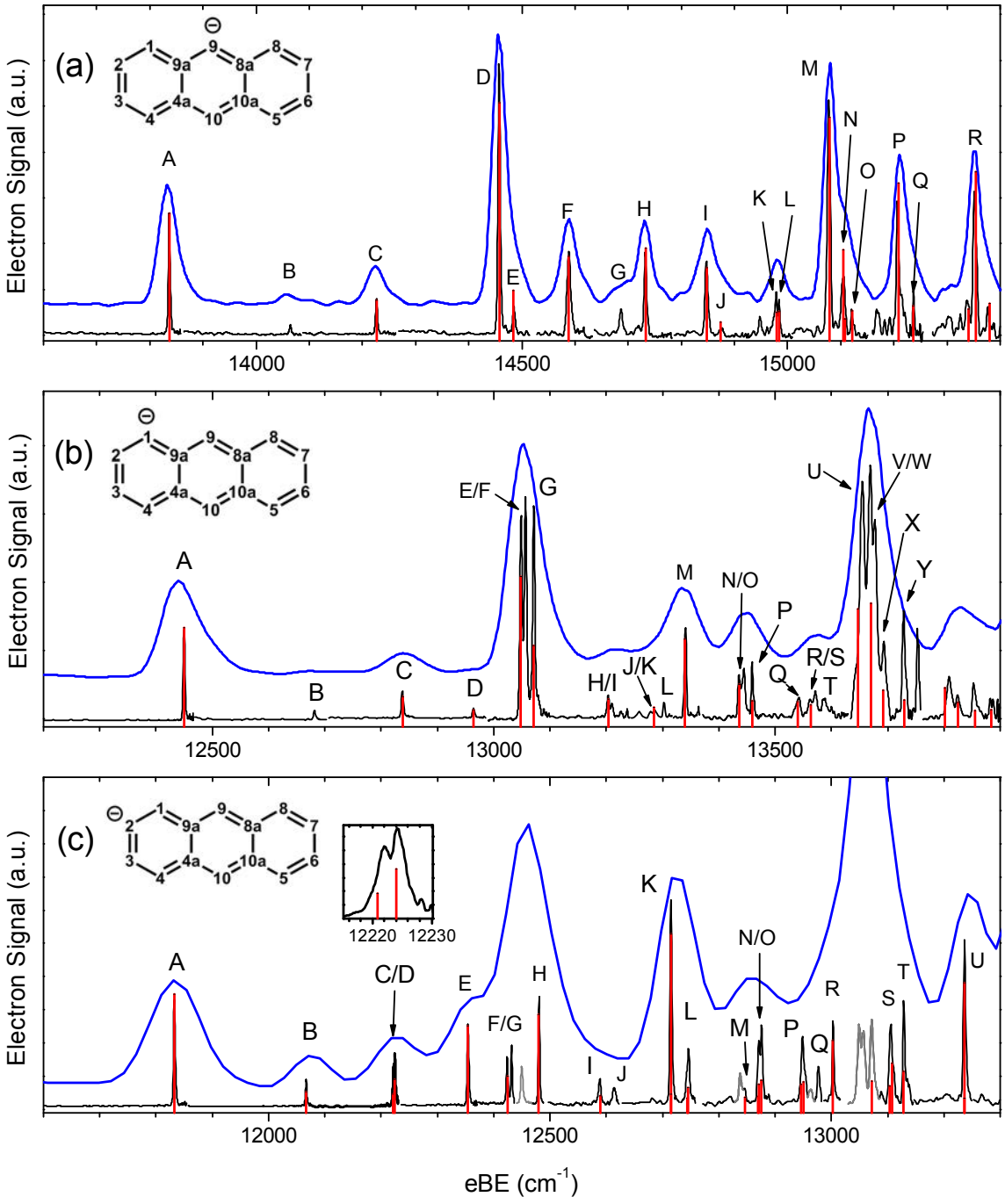

Figure 7.1: SEVI spectra of photodetachment to (a) the $\tilde{X}^2A_1$ ground state of 9-anthracenyl and the $\tilde{X}^2A'$ ground states of (b) 1-anthracenyl and (c) 2-anthracenyl, with low-resolution overview scans in blue and high-resolution traces in black. Features in the spectrum of 2-anthracenyl appearing due to 1-anthracenyl contamination are plotted in gray. FC simulations are shown in red.

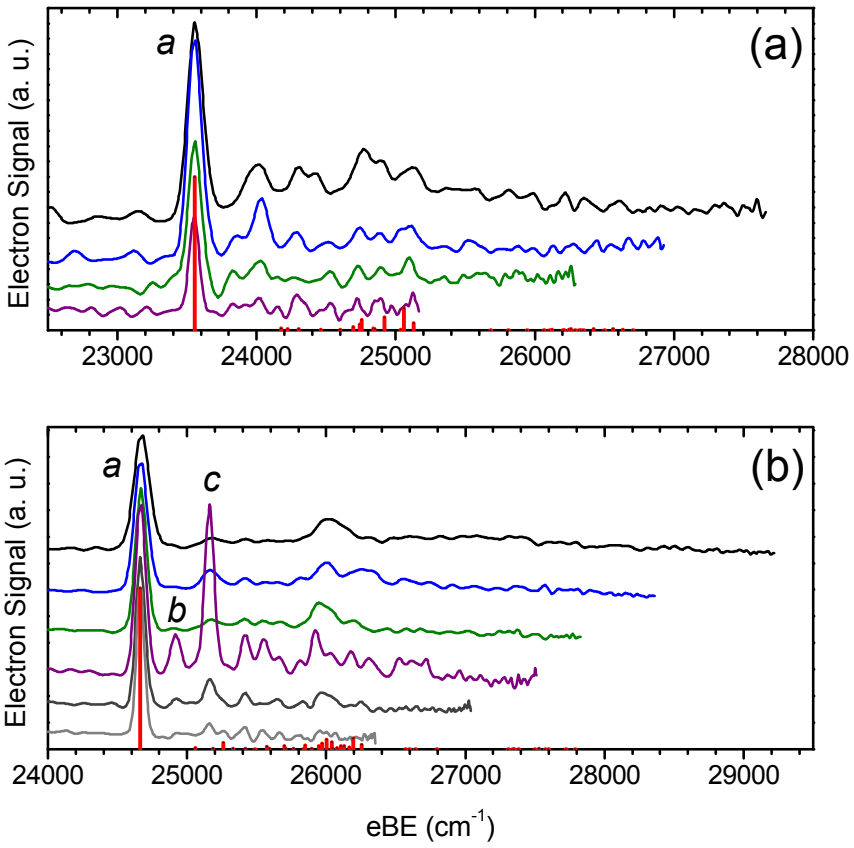

Figure 7.2: SEVI spectra of photodetachment to (a) the $\tilde{A}^2B_1$ excited state of 9-anthracenyl and (b) the $\tilde{A}^2A''$ state of 1-anthracenyl, with colored traces taken at progressively lower photon energies and FC simulations in red.

excited state anisotropies during image reconstruction. However, it is qualitatively clear that all radical isomers have $\tilde{A}$ state vibrational origins with slightly perpendicularly polarized PADs ($\beta < 0$). Intriguingly, in the 1-anthracenyl $\tilde{A}$ state spectrum plotted in purple in Fig. 7.2b, peaks b and c demonstrate positive β values, in contrast to the vibrational origin a.

7.4.2 Assignment of Electronic Structure

Cryogenic cooling ensures, in principle, that we photodetach from the ground vibrational and electronic state of each anthracenyl anion. Our electronic structure calculations indicate that the ground state of each neutral radical is accessed by removing an electron from an in-plane σ molecular orbital (MO) with s-p character localized on the deprotonated site of the closed-shell anion, while the first excited state of each radical is accessed by removal of an electron from a delocalized π MO of the anion. Calculated Dyson orbitals[82] for the photodetachment transitions for each isomer are shown in Fig. 7.4.

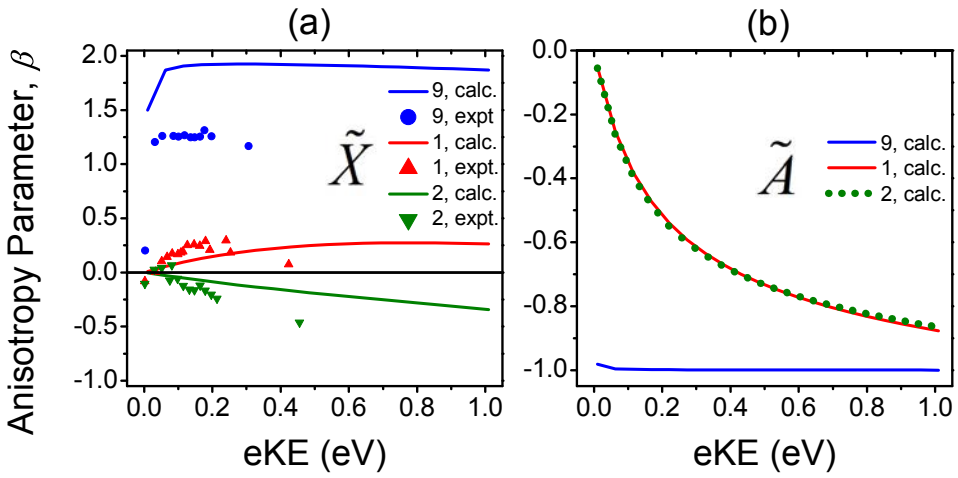

Figure 7.3: Calculated and experimental anisotropy parameters for photodetachment to (a) the $\tilde{X}$ band vibrational origins and (b) the $\tilde{A}$ band vibrational origins of the 9-, 1-, and 2-anthracenyl radicals, as functions of eKE.

We assign the low binding energy bands in Fig. 7.1 to the $\tilde{X}^2A_1 \leftarrow \tilde{X}^1A_1$ detachment transition of 9-anthracenyl and the $\tilde{X}^2A' \leftarrow \tilde{X}^1A'$ transitions of 1- and 2-anthracenyl. The peaks labeled A in Fig. 7.1 represent the vibrational origin of each $\tilde{X} \leftarrow \tilde{X}$ band. The corresponding binding energies yield experimental electron affinities (EAs) of 1.7155(2) eV, 1.5436(2) eV, and 1.4671(2) eV respectively for the 9-, 1-, and 2-anthracenyl radicals, in good agreement with the calculations carried out in the present work (Table 7.1), as well as in the literature.[317] The decrease in EA as the site of deprotonation is moved from C_9 to C_1 to C_2 reflects the energetic ordering of the anions. The isomer energetics calculated in the present work (Table 7.2) are in good agreement with the literature;[317,318,326,331,349]; we find that the 9-anthracenyl anion is lowest in energy with the 1-anthracenyl and 2-anthracenyl anions lying 0.13 eV and 0.18 eV higher in energy, respectively. By contrast, the 9-, 1-, and 2-anthracenyl radicals fall within 0.02 eV of one another.

The higher eBE bands shown in Fig. 7.2 are assigned to the $\tilde{A}^2B_1 \leftarrow \tilde{X}^1A_1$ band of 9-anthracenyl and the $\tilde{A}^2A'' \leftarrow \tilde{X}^1A'$ transition of 1-anthracenyl; the peaks labeled *a* are the vibrational origins of these two bands. The $\tilde{A}$ states lie at term energies (T_0) of 1.205(6) eV, 1.515(4) eV, and 1.755(8) eV respectively for 9-, 1-, and 2-anthracenyl. Calculated energetics (Table 7.1) compare favorably and reproduce the trend of increasing $\tilde{A}$ state term energy from 9- to 1- to 2-anthracenyl. Because the radical ground states are predicted to be nearly degenerate, the differences in T_0 are due to destabilization of the 1- and 2-anthracenyl $\tilde{A}$ states relative to that of 9-anthracenyl. The calculated results in Table 7.2 place the 1-anthracenyl and 2-anthracenyl $\tilde{A}$ states respectively 0.27 eV and 0.50 eV above the 9-anthracenyl $\tilde{A}$ state. Rationalizations for the energetic ordering of the anion and neutral isomers will be discussed in further detail below.

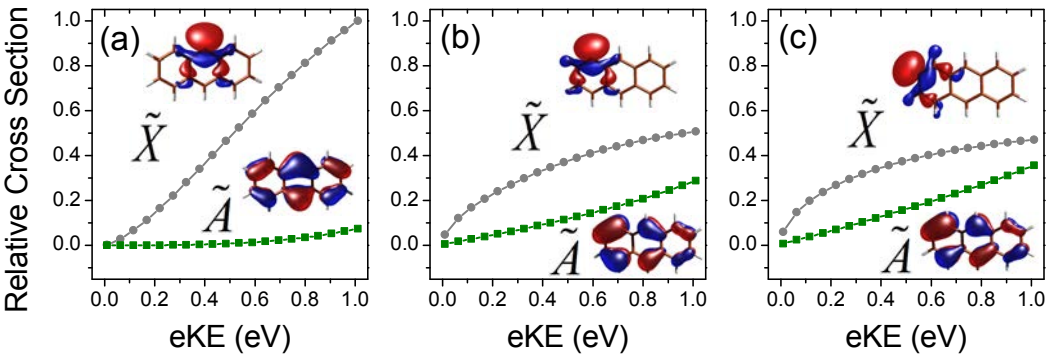

Figure 7.4: Calculated cross sections and visualized Dyson orbitals for photodetachment to the $\tilde{X}$ and $\tilde{A}$ states of (a) 9-anthracenyl, (b) 1-anthracenyl, and (c) 2-anthracenyl as a function of eKE.

Table 7.2: Calculated energies (eV) for all species at the B3LYP/6-311+G* level of theory, given relative to the 9-anthracenyl anion ground state and corrected for vibrational zero point energy.

	9-anthracenyl	1-anthracenyl	2-anthracenyl
Anion	0.0000	0.1309	0.1842
Ground	1.6749	1.6596	1.6576
Excited	2.7130	2.9873	3.2156

7.4.3 Radical Ground States

The $\tilde{X}$ bands of the anthracenyl radicals show extensive FC activity, indicative of a large change in geometry upon photodetachment. This FC structure is consistent with detachment of an electron from a highly localized MO (Fig. 7.4) and with geometry optimization calculations (Tables 7.6-7.8) which indicate that the C−C−C interior bond angle at the deprotonated site widens by $\sim 14^{o}$ in all three systems upon detachment to the radical ground state.

Several fundamental frequencies of each radical ground state are observed (Table 7.1). The FC active vibrational modes should be totally symmetric, and are therefore attributed to a_1 modes for the C_{2v}-symmetric 9-anthracenyl radical and a' modes for the C_s-symmetric 1- and 2 anthracenyl radicals. Schematics for normal mode displacements of all FC active vibrations are given in Fig. 7.5. The most highly FC active modes for each radical involve significant distortion at the deprotonated site, where there is the largest change in geometry upon photodetachment. All assigned experimental frequencies are within a factor of 0.97-0.99 of the corresponding *ab initio* calculated value.

For the 9-anthracenyl radical ground state (Fig. 7.1a), we report seven vibrational fun-

damentals: ν_{22} (peak B) with a frequency of $228(2)\,\mathrm{cm}^{-1}$, ν_{21} (peak C) at $390(2)\,\mathrm{cm}^{-1}$, ν_{20} (peak D) at $621(2)\,\mathrm{cm}^{-1}$, ν_{19} (peak E) at $648(2)\,\mathrm{cm}^{-1}$, ν_{18} (peak F) at $752(4)\,\mathrm{cm}^{-1}$, ν_{17} (peak H) at $896(2)\,\mathrm{cm}^{-1}$, and ν_{15} (peak L) at $1147(1)\,\mathrm{cm}^{-1}$. All other features are progressions or combinations bands of these modes; their assignments are detailed in Table 7.3. The FC stick spectra are in very good agreement with the experimentally observed features. Only peak B does not appear in the simulation but it can be assigned unambiguously to ν_{22} based on comparison with the *ab initio* calculated frequencies of FC allowed a_1 modes. Additionally, the assignment of ν_{15} to peak L is more uncertain than the other fundamentals, given that it appears in a spectrally congested region.

In Fig. 7.1b, the experimental 1-anthracenyl radical $\tilde{X}$ band also largely agrees with the FC simulation. Through comparison with simulation, we report the following vibrational fundamentals: ν_{43} (peak B) at $232(2)\,\mathrm{cm}^{-1}$, ν_{42} (peak C) at $388(2)\,\mathrm{cm}^{-1}$, ν_{40} (peak D) at $514(2)\,\mathrm{cm}^{-1}$, ν_{39} (peak E) at $599(2)\,\mathrm{cm}^{-1}$, ν_{38} (peak G) at $621(2)\,\mathrm{cm}^{-1}$, ν_{36} (peak H) at $753(2)\,\mathrm{cm}^{-1}$, ν_{34} (peak M) at $891(2)\,\mathrm{cm}^{-1}$, and ν_{30} (peak Q) at $1091(4)\,\mathrm{cm}^{-1}$. Only peak B does not appear in the simulation, but again it can be assigned to the fundamental ν_{43} as the only FC allowed a' mode with a sufficiently low calculated frequency. Additionally, we observe a strong feature (peak F) not predicted by the FC simulation. It appears at $607\,\mathrm{cm}^{-1}$ above the origin and only $8\,\mathrm{cm}^{-1}$ above ν_{39} (peak E). Elsewhere in the spectrum, similar doublets (e.g. peaks N/O, V/W) appear where the FC simulation predicts only one peak involving excitation of the 39 mode. The likely source of these features will be discussed below. Nearly all other peaks in the spectrum can be assigned to progressions and combination bands of the observed fundamentals and peak F (Table 7.4).

The 2-anthracenyl radical $\tilde{X}$ band in Fig. 7.1c shows contamination from 1 anthracenyl ground state features; those peaks which derive from 1-anthracenyl are shaded gray. The distinct binding energies and FC profiles of the two bands permit nearly full assignment of the 2-anthracenyl ground state features despite the contamination. We report vibrational fundamentals for ν_{43} (peak B) at $234(1)\,\mathrm{cm}^{-1}$, ν_{42} (peak C) at $392(1)\,\mathrm{cm}^{-1}$, ν_{41} (peak D) at $389(1)\,\mathrm{cm}^{-1}$, ν_{40} (peak E) at $522(2)\,\mathrm{cm}^{-1}$, ν_{39} (peak F) at $591(1)\,\mathrm{cm}^{-1}$, ν_{37} (peak H) at $648(1)\,\mathrm{cm}^{-1}$, ν_{34} (peak K) at $882(2)\,\mathrm{cm}^{-1}$, and ν_{31} (peak M) at $1013(2)\,\mathrm{cm}^{-1}$. Only the ν_{31} fundamental is slightly obscured by an overlapping 1-anthracenyl feature. The instrumental resolution is sufficient to distinguish the ν_{41} and ν_{42} fundamentals (peaks C/D, inset of Fig. 7.1c) which are split by $3\,\mathrm{cm}^{-1}$; this is only now possible with our new VMI electron optics. Nearly all other bands in the 2-anthracenyl $\tilde{X}$ spectrum can be assigned to progressions and combination bands of the observed fundamentals (Table 7.5). As was seen in the 1-anthracenyl $\tilde{X}$ band, we observe a feature not predicted by FC simulation (peak G) at $599\,\mathrm{cm}^{-1}$, again $8\,\mathrm{cm}^{-1}$ above the ν_{39} fundamental (peak F).

The source of peaks F and G in the $\tilde{X}$ state spectra of the 1- and 2-anthracenyl radicals is subtle. The PAD and threshold behavior of these peaks is the same as the neighboring peaks, suggesting that they have the same electronic character as the FC allowed peaks, and thus do not arise through a Herzberg-Teller coupling scheme as we have seen in other systems.[85] However, the locations of peaks F and G with respect to the vibrational origins of 1- and 2-anthracenyl do not align with any calculated a' fundamentals or combinations of FC active

modes. An important clue is that the unexpected features are associated with excitation of the ν_{39} ring distortion modes (Fig. 7.5), lying only $8\,\mathrm{cm}^{-1}$ above the ν_{39} fundamentals in both spectra.

Each of these peaks is most likely a combination band of two a'' modes that together have a' vibrational symmetry, as $a'' \otimes a'' = a'$. Such a combination band is FC allowed by symmetry, and if its frequency is very close to that of the ν_{39} fundamental, it can borrow the intensity of the ν_{39} fundamental through a Fermi resonance. Fermi resonances occur when two vibrational states of the same overall symmetry lie very close together and interact, leading to mixing of the two eigenstates and widening of the energy gap as the mixing states repel one another.[65] Anharmonic terms in the potential energy provide the perturbation that allows energy levels associated with different normal modes to mix.

Based on calculated harmonic frequencies, the most likely a'' modes involved in the combination band in Fermi resonance with ν_{39} are modes ν_{59} and ν_{61} for both isomers (displacements shown in Fig. 7.6). For 1-anthracenyl, the *ab initio* frequencies are $360\,\mathrm{cm}^{-1}$ for ν_{59} and $233\,\mathrm{cm}^{-1}$ for ν_{61}, yielding a combination band at $623\,\mathrm{cm}^{-1}$, just above the calculated frequency of $618\,\mathrm{cm}^{-1}$ for ν_{39} (Table 7.9). For 2-anthracenyl, mode ν_{59} is predicted at $378\,\mathrm{cm}^{-1}$ and ν_{61} at $237\,\mathrm{cm}^{-1}$, and their sum is at $615\,\mathrm{cm}^{-1}$, again lying near the calculated frequency of $609\,\mathrm{cm}^{-1}$ for ν_{39} (Table 7.10).

If we consider 1-anthracenyl and 2-anthracenyl in a pseudo-D_{2h} symmetry framework with the deprotonated sites as small symmetry-breaking perturbations, the in-plane ν_{39} ring distortion is of b_{2u} symmetry, while the out-of-plane modes ν_{59} and ν_{61} transform as b_{3u} and b_{1g} respectively. Since $b_{3u} \otimes b_{1g} = b_{2u}$, the combination band $\nu_{59} + \nu_{61}$ is still of the correct symmetry to mix with ν_{39}; as this Fermi resonance holds in a higher symmetry framework, it may be particularly strong for these vibrational modes.

In 1-anthracenyl, the ν_{39} mode is strongly FC active, and this Fermi resonance manifests several times, with combination bands and progressions of ν_{39} appearing as doublets and multiplets. The ν_{39} mode is less active in 2-anthracenyl and only the fundamental clearly demonstrates this extra feature. No analogous extra peaks appear in the 9-anthracenyl $\tilde{X}$ spectrum, as the ring distortion mode analogous to ν_{39} is of b_2 symmetry (ν_{61} in Table 7.9) and not FC allowed.

At most eKEs, the 9-anthracenyl $\tilde{X}$ band has a strongly parallel PAD ($1 \leq \beta \leq 1.5$), while the 1-anthracenyl $\tilde{X}$ band has slight parallel polarization ($0.1 \leq \beta \leq 0.3$), and the 2-anthracenyl $\tilde{X}$ band has slight perpendicular polarization ($-0.5 \leq \beta \leq -0.1$). The PADs for all three $\tilde{X}$ bands become isotropic close to threshold. Simulations nicely reproduce the behavior of the experimental β values as a function of eKE (Fig. 7.3a). The PADs for detachment to the radical ground states differ based on relative s and p contributions to the s-p hybrid Dyson orbitals of the three isomers.[325] Detachment from s-like orbitals yields predominantly $l = 1$ photoelectrons with parallel PADs, while detachment from p-like orbitals yields both isotropic $l = 0$ photoelectrons and perpendicularly polarized $l = 2$ photoelectrons. The relative contributions of the s and p detachment channels significantly affect the PAD,[354] allowing for very different observed anisotropies for the three isomers.

By these metrics, the 9-anthracenyl $\tilde{X}$ state Dyson MO has the largest contribution of

s character, while 1- and 2-anthracenyl have respectively higher fractions of *p* character. We propose an explanation by considering a model sp^2 hybridized σ bonding network for the anthracenyl anions. In each anion, the deprotonated carbon has three sp^2 orbitals: two participating in C−C σ bonds and one containing the electron lone pair, from which an electron is detached to form the ground state radical. In the 9-anthracenyl anion, the deprotonated C_9 atom is adjacent to two tertiary carbons, C_{9a} and C_{8a} (Fig. 7.1a). The two C_9 sp^2 bonding orbitals therefore have geometric overlap with the other four C−C σ bonds that the tertiary carbons participate in: C_{9a}−C_1, C_{9a}−C_{4a}, C_{8a}−C_8, and C_{8a}−C_{10a}. This overlap delocalizes and stabilizes the longer-range *p* character of the sp^2 bonding orbitals, leaving more *s* character in the lone pair orbital. In the 1-anthracenyl anion, C_1 is bonded to just one tertiary carbon, while in 2-anthracenyl, C_2 adjoins only secondary carbons. In these anions, the deprotonated carbon sp^2 bonding orbitals therefore have less *p* stabilization due to fewer nearby C−C σ bonds with which to overlap. The lone pair orbital thus exhibits more *p* character in the 1-anthracenyl anion and more yet in 2-anthracenyl.

The energetic ordering of the anthracenyl anions is closely related to these effects. Papas *et al.*[317] make the steric argument that the 1- and 2-anthracenyl anions are lifted in energy relative to 9-anthracenyl due to greater repulsion between the excess charge and H atoms bonded to secondary carbons adjacent to the deprotonation site. The repulsion of the lone pair also narrows the CCC interior bond angle at the deprotonated site, and the ability of each isomer structure to accommodate this strain contributes to the energetic ordering of the anions. It is compelling that the radical $\tilde{A}$ states follow the same energetic ordering as the anions, owing to similar hybridization and steric arguments in accommodating the doubly occupied lone pair MO. With no full lone pair to accommodate, the ground state anthracenyl radicals fall much closer together in energy.

7.4.4 Radical Excited States

The anthracenyl radical $\tilde{A}$ bands have very intense vibrational origins and weak FC activity beyond the origins, indicating little change in geometry upon photodetachment from the anion to the radical excited state. The calculated excited state geometries accordingly show little displacement from those of the anions (Tables 7.6-7.8). Dyson MOs for these transitions (Fig. 7.4) are of π symmetry and delocalized over the ring system, consistent with little perturbation in geometry upon removal of an electron.

The $\tilde{A}$ bands are poorly resolved compared to the $\tilde{X}$ bands, making spectral assignments challenging beyond identification of the vibrational origin. The low $\tilde{A}$ state transition cross sections close to threshold cause features to vanish before they can be narrowly resolved with SEVI. According to the Wigner threshold law for photodetachment, the near-threshold cross section (σ) is a function of eKE and *l*, the angular momentum of the nascent photoelectron:[75]

$$\sigma \propto (\text{eKE})^{l+l/2} \tag{7.2}$$

The Dyson MOs for the anthracenyl radical $\tilde{A}$ state, shown in Fig. 7.4, have four nodes: two vertical and one horizontal in-plane nodes and one out-of-plane node. This nodal structure

is analogous to that of an atomic g orbital, in which the orbital angular momentum of the electron is $l = 4$. In a one-photon, one-electron process, a photoelectron is detached from an atomic orbital with $\Delta l = \pm 1$.[78] By extension, after detachment to form the anthracenyl $\tilde{A}$ state, the outgoing photoelectron must have at least $l = 3$, which yields vanishing σ at small eKE according to Eqn. 7.2. The Dyson orbitals for the $\tilde{X}$ states, on the other hand, have localized s-p hybrid character, enabling partial $l = 0$ detachment, and significant intensity at small eKE.[325] Photodetachment cross sections calculated as a function of eKE are shown in Fig. 7.4, and reproduce this difference in threshold behavior for the $\tilde{X}$ and $\tilde{A}$ states of all three isomers.

The 1-anthracenyl $\tilde{A}$ state displays some interesting behavior that warrants additional comment. At photodetachment wavelengths of 27500–27600 cm^{-1}, the $\tilde{A}$ band shows increased cross section and enhanced intensity of vibrational features (e.g. peaks b and c) relative to the origin, as demonstrated by the purple trace in Fig. 7.2b. Additionally, peaks b and c have distinct parallel polarization in contrast to the consistent slightly perpendicular PAD of the vibrational origin. With peak b lying at 255 cm^{-1} and peak c at 496 cm^{-1} above the origin, these features do not appear in the FC simulation, and do not match well with any calculated a' frequencies of the 1-anthracenyl $\tilde{A}$ state. They do however align with the calculated a'' modes ν_{60} and ν_{56} at 256 cm^{-1} and 504 cm^{-1} respectively (Table 7.10).

The strong wavelength-dependent change in photodetachment cross section in combination with the appearance of features with distinct PADs suggests a contributing autodetachment mechanism. If a metastable anion state is embedded in the (neutral + free electron) continuum, resonant transitions to this state can compete with direct photodetachment. The anion excited state can then autodetach, resulting in electron signals whose cross section and anisotropy are not governed by the considerations discussed above. The closed-shell anthracenyl anions should have similar electronic structure to anthracene, whose $S_1 \leftarrow S_0$ band origin lies at 27687 cm^{-1},[343] so the presence of a 1-anthracenyl anion resonance at excitation wavelengths of 27500–27600 cm^{-1} is not surprising.

7.5 Conclusions

We have acquired isomer-specific slow photoelectron velocity-map imaging spectra of cold 9-, 1-, and 2-anthracenyl anions using a newly designed VMI electrostatic lens. We observe detailed vibronic structure of the largely unstudied neutral radicals. The radical ground state spectra are fully vibrationally-resolved, allowing measurement of precise electron affinities and Franck-Condon active vibrational frequencies. Transitions to the radical first excited states are also measured and term energies reported, though poor threshold photodetachment cross sections prevent full vibrational resolution as achieved for the radical ground states.

This work shows how high-resolution photoelectron imaging, in combination with cryogenic ion cooling and techniques for isomer selection, can be used to untangle the vibronic structure of increasingly complex and diverse radical systems. The subtle structural and electronic differences between the 9-, 1-, and 2-anthracenyl radicals are made clear in the

cryo-SEVI spectra and photoelectron angular distributions presented here. These results inform our fundamental understanding of the chemistry of these species, as well as their behavior in the context of astrochemistry and combustion.

7.6 Supporting Information

Synthesis of 2-bromoanthracene

A suspension of 2-aminoanthracene (3.0 g, 11.6mmol) in bromoform (15 mL) was heated to 100 °C. Amyl nitrite (1.89 g, 16.1 mmol) was added portion-wise and the reaction mixture was stirred for 2 h at 100 °C. The volatile materials were removed under vacuum to afford a dark residue, which was dissolved in hexanes and passed through a pad of silica gel to remove most of the colored impurities. The hexanes was removed by rotary evaporation to afford 2-bromoanthracene (15% yield).

2-bromoanthracene: ^{1}H NMR (500 MHz, $CDCl_3$) δ 8.40 (s, 1H), 8.32 (s, 1H), 8.17 (br s, 1H), 8.07–7.96 (m, 2H), 7.88 (d, J = 9.0 Hz, 1H), 7.53–7.45 (m, 3H).

Synthesis of 9-, 1-, and 2-(trimethylsilyl)-anthracene

9-bromoanthracene (2.5 g, 9.72 mmol) was dissolved in dry THF (100 mL) and cooled to −78 °C under a N_2 atmosphere. A solution of *n*-BuLi (1.6 M in hexanes) was added dropwise and the reaction mixture was stirred at −78 °C for 1 h. The previously colorless reaction mixture turned orange and then became cloudy. Trimethylsilylchloride (1.6 mL, 12.6 mmol) was added dropwise at −78 °C and the reaction mixture was stirred for 20 min. The reaction mixture was allowed to warm to room temperature with stirring for 1 h, at which point no orange color remained, then poured into a separatory funnel. Water (100 mL) and diethyl ether (20 mL) were added, and the organic phase was washed with water (2 × 100 mL) and dried over $MgSO_4$. Volatile materials were removed by rotary evaporation to afford the pure solid product (2.25 g, 92% yield). 1- and 2-(trimethylsilyl)-anthracene were prepared by the same method and were both obtained as pure solids.

9-(trimethylsilyl)-anthracene: ^{1}H NMR (600 MHz, $CDCl_3$) δ 8.50–8.45 (m, 3H), 8.05–7.99 (m, 2H), 7.53–7.42 (m, 4H), 0.74 (s, 9H). ^{13}C NMR (151 MHz, $CDCl_3$) δ 137.01, 135.69, 131.34, 129.92, 129.50, 128.70, 124.76, 124.50, 4.57.

1-(trimethylsilyl)-anthracene: ^{1}H NMR (400 MHz, $CDCl_3$) δ 8.64 (s, 1H), 8.44 (d, J = 4.4 Hz, 2H), 8.07–7.92 (m, 3H), 7.69 (dd, J = 6.5, 1.3 Hz, 1H), 7.55–7.37 (m, 2H), 0.55 (s, 9H). ^{13}C NMR (151 MHz, $CDCl_3$) δ 138.33, 134.64, 133.26, 131.85, 131.42, 131.15, 130.06, 128.47, 127.91, 127.35, 126.80, 125.41, 125.36, 124.68, 0.36.

2-(trimethylsilyl)-anthracene: ^{1}H NMR (500 MHz, $CDCl_3$) δ 8.44 (br s, 1H), 8.41 (br s, 1H), 8.19 (br s, 1H), 8.08–7.94 (m, 3H), 7.58 (br d, J = 8.4 Hz, 1H), 7.47 (m, 2H), 0.39 (s, 9H). ^{13}C NMR (151 MHz, $CDCl_3$) δ 137.45, 134.38, 131.97, 131.28, 128.86, 128.35, 128.17, 127.07, 126.44, 126.22, 125.96, 125.41, 125.35, 125.23, −1.11.

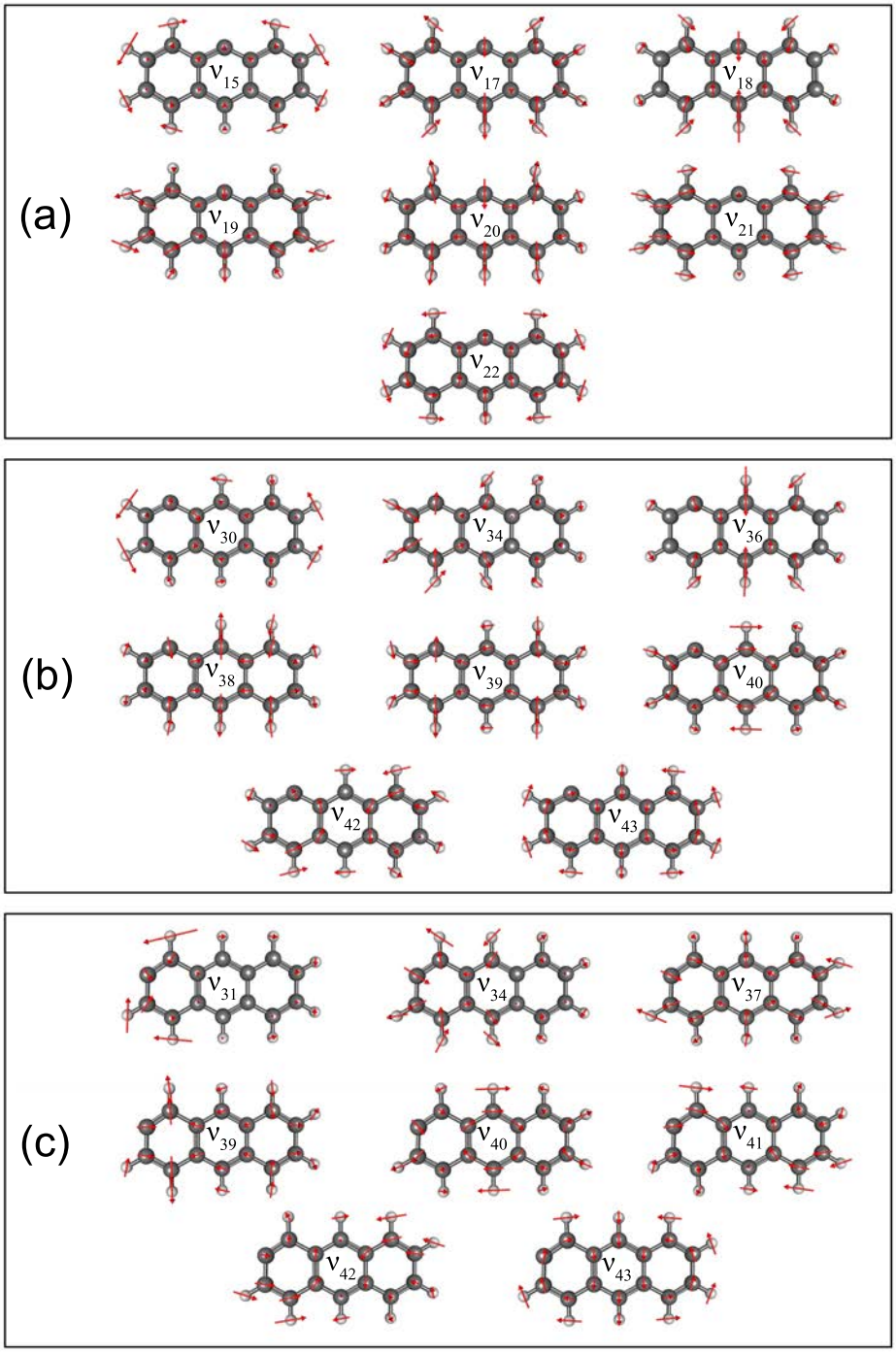

Figure 7.5: Franck-Condon active vibrational modes for the ground state photoelectron spectra of (a) 9-anthracenyl, (b) 1-anthracenyl, and (c) 2-anthracenyl.

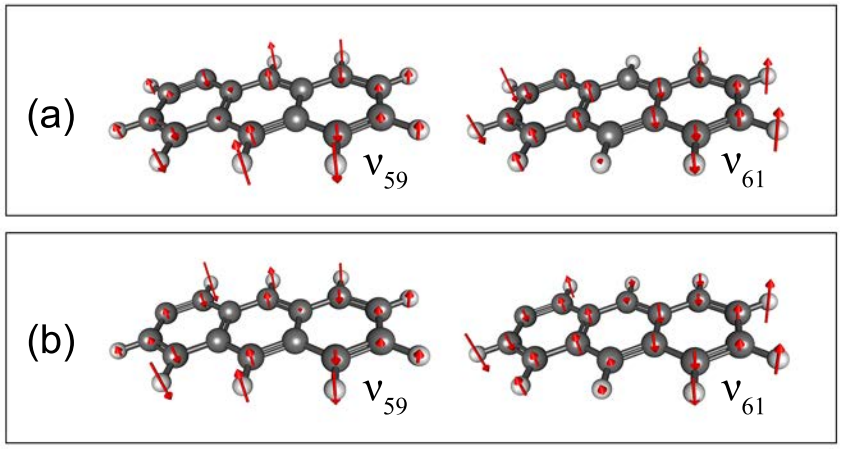

Figure 7.6: Out-of-plane vibrational modes appearing in combination as Fermi resonances in the ground state photoelectron spectra of (a) 1-anthracenyl and (b) 2-anthracenyl.

Table 7.3: Peak positions (cm^{-1}), offsets from the origin (cm^{-1}), and assignments for the SEVI spectra of 9-anthracenyl given in Figs. 7.1a and 7.2a.

Peak	Position	Offset	Assignment	Band
A	13837	0	0_0^0	$\tilde{X}^2A_1 \leftarrow \tilde{X}^1A_1$
B	14064	228	22_0^1	
C	14227	390	21_0^1	
D	14457	621	20_0^1	
E	14485	648	19_0^1	
F	14588	752	18_0^1	
G	14687	850	$20_0^1 22_0^1$	
H	14732	896	17_0^1	
I	14847	1011	$20_0^1 21_0^1$	
J	14875	1039	$19_0^1 21_0^1$	
K	14978	1142	$18_0^1 21_0^1$	
L	14984	1147	15_0^1	
M	15077	1241	20_0^2	
N	15104	1268	$19_0^1 20_0^1$	
O	15121	1284	$17_0^1 21_0^1$	
P	15207	1370	$18_0^1 20_0^1$	
Q	15237	1400	$18_0^1 19_0^1$	
R	15352	1515	$17_0^1 20_0^1$	
a	23555	0	0_0^0	$\tilde{A}^2B_1 \leftarrow \tilde{X}^1A_1$

Table 7.4: Peak positions (cm^{-1}), offsets from the origin (cm^{-1}), and assignments for the SEVI spectra of 1-anthracenyl given in Figs. 7.1b and 7.2b.

Peak	Position	Offset	Assignment	Band
A	12450	0	0_0^0	$\tilde{X}^2A' \leftarrow \tilde{X}^1A'$
B	12682	232	43_0^1	
C	12838	388	42_0^1	
D	12964	514	40_0^1	
E	13049	599	39_0^1	
F	13057	607	$59_0^1 61_0^1$	
G	13071	621	38_0^1	
H	13203	753	36_0^1	
I	13210	760	?	
J	13278	828	$39_0^1 43_0^1$	
K	13286	836	$43_0^1 59_0^1 61_0^1$	
L	13303	853	$38_0^1 43_0^1$	
M	13341	891	34_0^1	
N	13436	986	$39_0^1 42_0^1$	
O	13444	994	$42_0^1 59_0^1 61_0^1$	
P	13459	1010	$38_0^1 42_0^1$	
Q	13541	1091	30_0^1	
R	13562	1113	$39_0^1 40_0^1$	
S	13572	1122	$40_0^1 59_0^1 61_0^1$	
T	13587	1138	$38_0^1 40_0^1$	
U	13655	1205	39_0^2, $39_0^1 59_0^1 61_0^1$	
V	13669	1219	$38_0^1 39_0^1$	
W	13678	1228	$38_0^1 59_0^1 61_0^1$	
X	13693	1243	38_0^2	
Y	13729	1279	$34_0^1 42_0^1$	
a	24665	0	0_0^0	$\tilde{A}^2A'' \leftarrow \tilde{X}^1A'$
b	24920	255	60_0^1	
c	25161	496	56_0^1	

Table 7.5: Peak positions (cm^{-1}), offsets from the origin (cm^{-1}), and assignments for the SEVI spectra of 2-anthracenyl given in Fig. 7.1c.

Peak	Position	Offset	Assignment	Band
A	11833	0	0_0^0	$\tilde{X}^2A' \leftarrow \tilde{X}^1A'$
B	12067	234	43_0^1	
C	12222	389	42_0^1	
D	12224	392	41_0^1	
E	12354	522	40_0^1	
F	12424	591	39_0^1	
G	12432	599	$59_0^1 61_0^1$	
H	12481	648	37_0^1	
I	12588	756	$40_0^1 43_0^1$	
J	12614	781	41_0^2, 42_0^2	
K	12715	882	34_0^1, $37_0^1 43_0^1$	
L	12746	913	$40_0^1 41_0^1$, $40_0^1 42_0^1$	
M	12845	1013	31_0^1	
N	12871	1038	$37_0^1 41_0^1$, $37_0^1 42_0^1$	
O	12876	1044	40_0^2	
P	12949	1116	$34_0^1 43_0^1$, $39_0^1 40_0^1$	
Q	12977	1145	$40_0^1 41_0^1 43_0^1$, $40_0^1 42_0^1 43_0^1$	
R	13003	1170	$37_0^1 40_0^1$	
S	13106	1273	$34_0^1 41_0^1$, $34_0^1 42_0^1$	
T	13129	1296	37_0^2	
U	13237	1404	$34_0^1 40_0^1, 37_0^1 40_0^1 43_0^1$	

Table 7.6: Optimized Cartesian coordinates ($\mathring{A}$) of the anion and neutral 9-anthracenyl states calculated with B3LYP/6-311+G*.

		x	y	z
Anion $\tilde{X}$	C_1	0.0000000000	-2.4620600000	-1.4138759140
	C_2	0.0000000000	-3.6566900000	-0.7343559140
	C_3	0.0000000000	-3.6579300000	0.6888240860
	C_4	0.0000000000	-2.4744600000	1.3814940860
	C_{4a}	0.0000000000	-1.2150500000	0.7017240860
	C_5	0.0000000000	2.4744600000	1.3814940860
	C_6	0.0000000000	3.6579300000	0.6888240860
	C_7	0.0000000000	3.6566900000	-0.7343559140
	C_8	0.0000000000	2.4620600000	-1.4138759140
	C_{8a}	0.0000000000	1.1935700000	-0.7524959140
	C_9	0.0000000000	0.0000000000	-1.5284859140
	C_{9a}	0.0000000000	-1.1935700000	-0.7524959140
	C_{10}	0.0000000000	0.0000000000	1.3964840860
	C_{10a}	0.0000000000	1.2150500000	0.7017240860
	H_1	0.0000000000	-2.4333600000	-2.5001359140
	H_2	0.0000000000	-4.6010500000	-1.2740559140
	H_3	0.0000000000	-4.6035600000	1.2276340860
	H_4	0.0000000000	-2.4796100000	2.4714040860
	H_5	0.0000000000	2.4796100000	2.4714040860
	H_6	0.0000000000	4.6035600000	1.2276340860
	H_7	0.0000000000	4.6010500000	-1.2740559140
	H_8	0.0000000000	2.4333600000	-2.5001359140
	H_{10}	0.0000000000	0.0000000000	2.4865440860
Neutral $\tilde{X}$	C_1	0.0000000000	-2.4903245048	-1.4431914527
	C_2	0.0000000000	-3.6653826971	-0.7440876676
	C_3	0.0000000000	-3.6617710720	0.6808843118
	C_4	0.0000000000	-2.4837968675	1.3760293326
	C_{4a}	0.0000000000	-1.2264868379	0.6974902475
	C_5	0.0000000000	2.4837968675	1.3760293326
	C_6	0.0000000000	3.6617710720	0.6808843118
	C_7	0.0000000000	3.6653826971	-0.7440876676
	C_8	0.0000000000	2.4903245048	-1.4431914527
	C_{8a}	0.0000000000	1.2375428734	-0.7555250468
	C_9	0.0000000000	0.0000000000	-1.3641524660
	C_{9a}	0.0000000000	-1.2375428734	-0.7555250468

continued on next page

Table 7.6 – continued from previous page

		x	y	z
	C_{10}	0.0000000000	0.0000000000	1.3726166406
	C_{10a}	0.0000000000	1.2264868379	0.6974902475
	H_1	0.0000000000	-2.4863326037	-2.5278436424
	H_2	0.0000000000	-4.6124758595	-1.2738202670
	H_3	0.0000000000	-4.6066754977	1.2147008623
	H_4	0.0000000000	-2.4869416435	2.4623671874
	H_5	0.0000000000	2.4869416435	2.4623671874
	H_6	0.0000000000	4.6066754977	1.2147008623
	H_7	0.0000000000	4.6124758595	-1.2738202670
	H_8	0.0000000000	2.4863326037	-2.5278436424
	H_{10}	0.0000000000	0.0000000000	2.4592099737
Neutral $\tilde{A}$	C_1	0.0000000000	-2.4487622124	-1.4143301322
	C_2	0.0000000000	-3.6553967787	-0.7216686326
	C_3	0.0000000000	-3.6602471316	0.6817314098
	C_4	0.0000000000	-2.4656450631	1.3832762666
	C_{4a}	0.0000000000	-1.2294882229	0.6953851477
	C_5	0.0000000000	2.4656450631	1.3832762666
	C_6	0.0000000000	3.6602471316	0.6817314098
	C_7	0.0000000000	3.6553967787	-0.7216686326
	C_8	0.0000000000	2.4487622124	-1.4143301322
	C_{8a}	0.0000000000	1.2089808498	-0.7451534252
	C_9	0.0000000000	0.0000000000	-1.5357106792
	C_{9a}	0.0000000000	-1.2089808498	-0.7451534252
	C_{10}	0.0000000000	0.0000000000	1.3888802971
	C_{10a}	0.0000000000	1.2294882229	0.6953851477
	H_1	0.0000000000	-2.4251695029	-2.4986786282
	H_2	0.0000000000	-4.5953886979	-1.2639732170
	H_3	0.0000000000	-4.6031186222	1.2194076697
	H_4	0.0000000000	-2.4728777445	2.4701378826
	H_5	0.0000000000	2.4728777445	2.4701378826
	H_6	0.0000000000	4.6031186222	1.2194076697
	H_7	0.0000000000	4.5953886979	-1.2639732170
	H_8	0.0000000000	2.4251695029	-2.4986786282
	H_{10}	0.0000000000	0.0000000000	2.4763072681

Table 7.7: Optimized Cartesian coordinates ($\AA$) of the anion and neutral 1-anthracenyl states calculated with B3LYP/6-311+G*.

		x	y	z
Anion $\tilde{X}$	C_1	0.0000000000	-2.4943770380	-1.5558017103
	C_2	0.0000000000	-3.6490852413	-0.7800318218
	C_3	0.0000000000	-3.6717525894	0.6463767173
	C_4	0.0000000000	-2.5100022904	1.3802319334
	C_{4a}	0.0000000000	-1.2585184396	0.6995525986
	C_5	0.0000000000	2.4499581246	1.4009853529
	C_6	0.0000000000	3.6354050113	0.7125020607
	C_7	0.0000000000	3.6385144267	-0.7130688619
	C_8	0.0000000000	2.4521233203	-1.4013998958
	C_{8a}	0.0000000000	1.1945359591	-0.7253430613
	C_9	0.0000000000	-0.0311998399	-1.4056707726
	C_{9a}	0.0000000000	-1.2767856386	-0.7598773381
	C_{10}	0.0000000000	-0.0360322969	1.3882773251
	C_{10a}	0.0000000000	1.1924905998	0.7207667181
	H_2	0.0000000000	-4.6274321081	-1.2726378490
	H_3	0.0000000000	-4.6310147345	1.1698771345
	H_4	0.0000000000	-2.5270849287	2.4689885717
	H_5	0.0000000000	2.4502265439	2.4891581871
	H_6	0.0000000000	4.5794372432	1.2517814573
	H_7	0.0000000000	4.5839205009	-1.2492740271
	H_8	0.0000000000	2.4501790759	-2.4890275581
	H_9	0.0000000000	-0.0478040871	-2.4929299123
	H_{10}	0.0000000000	-0.0420719110	2.4790685300
Neutral $\tilde{X}$	C_1	0.0000000000	-2.4856990474	-1.4068400777
	C_2	0.0000000000	-3.6918630013	-0.8046329559
	C_3	0.0000000000	-3.7022732806	0.6312731707
	C_4	0.0000000000	-2.5295052520	1.3352887214
	C_{4a}	0.0000000000	-1.2592106553	0.6765946911
	C_5	0.0000000000	2.4298332963	1.4118262902
	C_6	0.0000000000	3.6205248108	0.7391505939
	C_7	0.0000000000	3.6451357645	-0.6852698904
	C_8	0.0000000000	2.4780823738	-1.3979720508
	C_{8a}	0.0000000000	1.2116799880	-0.7357574379
	C_9	0.0000000000	0.0033544121	-1.4402905048
	C_{9a}	0.0000000000	-1.2263560011	-0.7751692729

continued on next page

Table 7.7 – continued from previous page

		x	y	z
	C_{10}	0.0000000000	-0.0455470245	1.3705046400
	C_{10a}	0.0000000000	1.1865888059	0.7071916419
	H_2	0.0000000000	-4.6245104726	-1.3600280410
	H_3	0.0000000000	-4.6554109662	1.1513880625
	H_4	0.0000000000	-2.5477190154	2.4209926838
	H_5	0.0000000000	2.4120956322	2.4978443975
	H_6	0.0000000000	4.5564103967	1.2886653350
	H_7	0.0000000000	4.5993715096	-1.2021848008
	H_8	0.0000000000	2.4968021445	-2.4838854669
	H_9	0.0000000000	0.0146046518	-2.5257188760
	H_{10}	0.0000000000	-0.0601150162	2.4575413530
Neutral $\tilde{A}$	C_1	0.0000000000	-2.4673217352	-1.5595502229
	C_2	0.0000000000	-3.6591841922	-0.7622291087
	C_3	0.0000000000	-3.6870046125	0.6371366983
	C_4	0.0000000000	-2.5026285133	1.3693410966
	C_{4a}	0.0000000000	-1.2522948619	0.6954115189
	C_5	0.0000000000	2.4369962807	1.4031965331
	C_6	0.0000000000	3.6296635726	0.7091843285
	C_7	0.0000000000	3.6349778117	-0.7011176195
	C_8	0.0000000000	2.4446372189	-1.4006834368
	C_{8a}	0.0000000000	1.2055708784	-0.7197826387
	C_9	0.0000000000	-0.0347208380	-1.4095870125
	C_{9a}	0.0000000000	-1.2641227547	-0.7562614441
	C_{10}	0.0000000000	-0.0436378592	1.3899007519
	C_{10a}	0.0000000000	1.2004013594	0.7139272229
	H_2	0.0000000000	-4.6202629425	-1.2758419489
	H_3	0.0000000000	-4.6370039095	1.1671767112
	H_4	0.0000000000	-2.5246368702	2.4555817145
	H_5	0.0000000000	2.4369011141	2.4890739406
	H_6	0.0000000000	4.5706034973	1.2494746332
	H_7	0.0000000000	4.5792772513	-1.2351459936
	H_8	0.0000000000	2.4468838067	-2.4862486176
	H_9	0.0000000000	-0.0521726426	-2.4952359560
	H_{10}	0.0000000000	-0.0475798342	2.4778455153

Table 7.8: Optimized Cartesian coordinates ($\AA$) of the anion and neutral 2-anthracenyl states calculated with B3LYP/6-311+G*.

		x	y	z
Anion $\tilde{X}$	C_1	0.0000000000	-2.5390426031	-1.4146391679
	C_2	0.0000000000	-3.7894927876	-0.8089171589
	C_3	0.0000000000	-3.7009158762	0.6380151805
	C_4	0.0000000000	-2.5364171089	1.3705494893
	C_{4a}	0.0000000000	-1.2699623073	0.7147051971
	C_5	0.0000000000	2.4352519339	1.4071578975
	C_6	0.0000000000	3.6239600080	0.7231272470
	C_7	0.0000000000	3.6266995741	-0.7021615720
	C_8	0.0000000000	2.4433233896	-1.3940772055
	C_{8a}	0.0000000000	1.1820315649	-0.7212925638
	C_9	0.0000000000	-0.0416025576	-1.4000290948
	C_{9a}	0.0000000000	-1.2770859969	-0.7347903407
	C_{10}	0.0000000000	-0.0489194016	1.3965074735
	C_{10a}	0.0000000000	1.1810241040	0.7259112829
	H_1	0.0000000000	-2.4678815105	-2.5093837544
	H_3	0.0000000000	-4.6346919462	1.2101730402
	H_4	0.0000000000	-2.5546055100	2.4628442961
	H_5	0.0000000000	2.4314121832	2.4952976751
	H_6	0.0000000000	4.5670515688	1.2633021126
	H_7	0.0000000000	4.5728461730	-1.2372786910
	H_8	0.0000000000	2.4466826109	-2.4819545493
	H_9	0.0000000000	-0.0394575085	-2.4894290231
	H_{10}	0.0000000000	-0.0544676730	2.4860289086
Neutral $\tilde{X}$	C_1	0.0000000000	-2.5114993943	-1.4754104580
	C_2	0.0000000000	-3.6428478473	-0.7432778976
	C_3	0.0000000000	-3.7314770110	0.6578790150
	C_4	0.0000000000	-2.5485753590	1.3563569489
	C_{4a}	0.0000000000	-1.2875621493	0.6800978332
	C_5	0.0000000000	2.4004296428	1.4282576018
	C_6	0.0000000000	3.5919144931	0.7570201941
	C_7	0.0000000000	3.6167987285	-0.6674121456
	C_8	0.0000000000	2.4503861554	-1.3816230510
	C_{8a}	0.0000000000	1.1835384403	-0.7206757801
	C_9	0.0000000000	-0.0265386973	-1.4236809512
	C_{9a}	0.0000000000	-1.2588433658	-0.7649877359

continued on next page

Table 7.8 – continued from previous page

		x	y	z
	C_{10}	0.0000000000	-0.0759347866	1.3796309054
	C_{10a}	0.0000000000	1.1583493081	0.7216210243
	H_1	0.0000000000	-2.5121306369	-2.5617833902
	H_3	0.0000000000	-4.6879259645	1.1698856044
	H_4	0.0000000000	-2.5580205360	2.4430911174
	H_5	0.0000000000	2.3809836289	2.5143159621
	H_6	0.0000000000	4.5274684804	1.3070158211
	H_7	0.0000000000	4.5713755483	-1.1838081325
	H_8	0.0000000000	2.4708363176	-2.4675974322
	H_9	0.0000000000	-0.0070752651	-2.5103461993
	H_{10}	0.0000000000	-0.0943405185	2.4664536287
Neutral $\tilde{A}$	C_1	0.0000000000	-2.5095689598	-1.4174032825
	C_2	0.0000000000	-3.8000183519	-0.7990375270
	C_3	0.0000000000	-3.7160067887	0.6337238796
	C_4	0.0000000000	-2.5415951047	1.3591702723
	C_{4a}	0.0000000000	-1.2659293461	0.7051654263
	C_5	0.0000000000	2.4144903506	1.4128848006
	C_6	0.0000000000	3.6140216751	0.7271641391
	C_7	0.0000000000	3.6296198742	-0.6822813899
	C_8	0.0000000000	2.4451570997	-1.3898609328
	C_{8a}	0.0000000000	1.1996215176	-0.7161784601
	C_9	0.0000000000	-0.0343353224	-1.4087123384
	C_{9a}	0.0000000000	-1.2590341299	-0.7372913468
	C_{10}	0.0000000000	-0.0663905049	1.3926320603
	C_{10a}	0.0000000000	1.1852072249	0.7176179614
	H_1	0.0000000000	-2.4569659549	-2.5082578358
	H_3	0.0000000000	-4.6462809361	1.2020196645
	H_4	0.0000000000	-2.5574226270	2.4484436722
	H_5	0.0000000000	2.4069286016	2.4986228030
	H_6	0.0000000000	4.5507378963	1.2744362714
	H_7	0.0000000000	4.5777957212	-1.2092426425
	H_8	0.0000000000	2.4559588721	-2.4755033776
	H_9	0.0000000000	-0.0302145058	-2.4957404249
	H_{10}	0.0000000000	-0.0719724693	2.4796622968

Table 7.9: Vibrational frequencies (cm^{-1}) for the anion and neutral 9-anthracenyl states calculated with B3LYP/6-311+G*.

Symm.	Mode	Anion	Ground	Excited	Symm.	Mode	Anion	Ground	Excited
a_1	ν_1	3166	3194	3199	b_1	ν_{32}	966	985	1000
	ν_2	3145	3183	3186		ν_{33}	929	960	974
	ν_3	3126	3171	3172		ν_{34}	846	887	903
	ν_4	3111	3163	3158		ν_{35}	798	840	853
	ν_5	3103	3157	3152		ν_{36}	761	765	779
	ν_6	1644	1667	1618		ν_{37}	717	734	755
	ν_7	1549	1566	1575		ν_{38}	600	577	602
	ν_8	1502	1513	1504		ν_{39}	476	499	450
	ν_9	1460	1486	1482		ν_{40}	394	391	393
	ν_{10}	1380	1390	1366		ν_{41}	259	259	284
	ν_{11}	1307	1325	1298		ν_{42}	86	89	83
	ν_{12}	1267	1293	1288					
	ν_{13}	1224	1271	1203	b_2	ν_{43}	3165	3194	3199
	ν_{14}	1173	1193	1187		ν_{44}	3144	3183	3186
	ν_{15}	1146	1168	1143		ν_{45}	3126	3171	3172
	ν_{16}	1025	1029	1046		ν_{46}	3106	3159	3155
	ν_{17}	910	907	909		ν_{47}	1630	1660	1593
	ν_{18}	743	759	750		ν_{48}	1593	1622	1574
	ν_{19}	656	658	669		ν_{49}	1522	1573	1513
	ν_{20}	635	638	624		ν_{50}	1461	1478	1451
	ν_{21}	396	398	391		ν_{51}	1405	1417	1418
	ν_{22}	243	233	241		ν_{52}	1358	1377	1339
						ν_{53}	1304	1364	1303
a_2	ν_{23}	965	984	999		ν_{54}	1230	1238	1261
	ν_{24}	929	958	973		ν_{55}	1178	1200	1197
	ν_{25}	830	854	880		ν_{56}	1153	1170	1175
	ν_{26}	748	759	760		ν_{57}	1107	1125	1114
	ν_{27}	736	739	741		ν_{58}	1021	1025	1046
	ν_{28}	507	498	495		ν_{59}	929	933	929
	ν_{29}	478	470	466		ν_{60}	820	829	837
	ν_{30}	233	232	217		ν_{61}	620	614	620
	ν_{31}	99	114	100		ν_{62}	536	537	529
						ν_{63}	404	384	394

Table 7.10: Vibrational frequencies (cm^{-1}) for the anion and neutral 1-anthracenyl states calculated with B3LYP/6-311+G*.

Symm.	Mode	Anion	Ground	Excited	Symm.	Mode	Anion	Ground	Excited
a'	ν_1	3165	3190	3196	a'	ν_{33}	926	926	926
	ν_2	3153	3183	3185		ν_{34}	911	902	910
	ν_3	3150	3178	3183		ν_{35}	811	822	820
	ν_4	3138	3175	3173		ν_{36}	750	762	756
	ν_5	3128	3171	3170		ν_{37}	661	655	667
	ν_6	3125	3164	3166		ν_{38}	638	639	633
	ν_7	3101	3160	3147		ν_{39}	607	618	596
	ν_8	3075	3159	3145		ν_{40}	536	526	523
	ν_9	3026	3154	3116		ν_{41}	401	400	397
	ν_{10}	1646	1670	1640		ν_{42}	394	395	391
	ν_{11}	1614	1660	1592		ν_{43}	238	236	238
	ν_{12}	1597	1622	1586					
	ν_{13}	1572	1588	1535	a''	ν_{44}	950	985	1000
	ν_{14}	1516	1549	1529		ν_{45}	947	962	993
	ν_{15}	1503	1505	1501		ν_{46}	935	958	970
	ν_{16}	1461	1484	1463		ν_{47}	914	904	944
	ν_{17}	1437	1450	1443		ν_{48}	863	889	919
	ν_{18}	1409	1425	1413		ν_{49}	856	861	890
	ν_{19}	1374	1403	1381		ν_{50}	819	843	860
	ν_{20}	1364	1383	1378		ν_{51}	765	772	768
	ν_{21}	1336	1363	1336		ν_{52}	744	761	756
	ν_{22}	1310	1326	1305		ν_{53}	739	746	750
	ν_{23}	1283	1297	1291		ν_{54}	715	714	748
	ν_{24}	1279	1288	1282		ν_{55}	589	570	597
	ν_{25}	1241	1246	1233		ν_{56}	502	509	504
	ν_{26}	1186	1197	1199		ν_{57}	476	483	478
	ν_{27}	1170	1180	1185		ν_{58}	468	470	441
	ν_{28}	1163	1177	1174		ν_{59}	388	390	385
	ν_{29}	1152	1165	1155		ν_{60}	247	262	256
	ν_{30}	1099	1113	1098		ν_{61}	223	233	210
	ν_{31}	1024	1032	1046		ν_{62}	105	118	107
	ν_{32}	1017	1025	1033		ν_{63}	89	91	83

Table 7.11: Vibrational frequencies (cm^{-1}) for the anion and neutral 2-anthracenyl states calculated with B3LYP/6-311+G*.

Symm.	Mode	Anion	Ground	Excited	Symm.	Mode	Anion	Ground	Excited
a'	ν_1	3165	3190	3197	a'	ν_{33}	923	926	920
	ν_2	3150	3184	3184		ν_{34}	898	894	903
	ν_3	3137	3177	3173		ν_{35}	812	819	821
	ν_4	3130	3164	3168		ν_{36}	760	760	765
	ν_5	3123	3161	3163		ν_{37}	659	658	663
	ν_6	3120	3160	3161		ν_{38}	643	639	634
	ν_7	3081	3158	3134		ν_{39}	620	609	606
	ν_8	3033	3157	3108		ν_{40}	528	533	515
	ν_9	3011	3154	3091		ν_{41}	398	398	395
	ν_{10}	1646	1670	1638		ν_{42}	393	396	388
	ν_{11}	1615	1643	1602		ν_{43}	234	238	233
	ν_{12}	1580	1611	1591					
	ν_{13}	1557	1589	1546	a''	ν_{44}	960	985	999
	ν_{14}	1538	1567	1515		ν_{45}	945	960	993
	ν_{15}	1497	1508	1494		ν_{46}	928	953	964
	ν_{16}	1457	1473	1459		ν_{47}	903	905	932
	ν_{17}	1438	1455	1436		ν_{48}	874	891	915
	ν_{18}	1411	1424	1427		ν_{49}	858	849	888
	ν_{19}	1401	1413	1393		ν_{50}	817	822	856
	ν_{20}	1375	1373	1378		ν_{51}	776	780	819
	ν_{21}	1337	1366	1323		ν_{52}	768	767	768
	ν_{22}	1312	1308	1314		ν_{53}	741	741	755
	ν_{23}	1292	1291	1305		ν_{54}	724	713	744
	ν_{24}	1290	1287	1293		ν_{55}	577	574	568
	ν_{25}	1277	1266	1263		ν_{56}	472	503	480
	ν_{26}	1201	1206	1205		ν_{57}	466	477	446
	ν_{27}	1183	1191	1200		ν_{58}	422	461	407
	ν_{28}	1175	1170	1185		ν_{59}	363	378	357
	ν_{29}	1166	1159	1159		ν_{60}	236	271	216
	ν_{30}	1125	1126	1119		ν_{61}	215	237	189
	ν_{31}	1024	1039	1047		ν_{62}	109	119	99
	ν_{32}	993	1029	999		ν_{63}	92	93	86

Part IV

Transition Metal Oxide Clusters

Ay me! what perils do environ
The man that meddles with
cold iron!

Samuel Butler,
Hudibras

Chapter 8

Vibronic structure of Fe_4O and Fe_5O

The content and figures of this chapter are reprinted or adapted with permission from
M. L. Weichman, J. A. DeVine, D. M. Neumark, "High-resolution photoelectron imaging of cryogenically cooled Fe_4O^- and Fe_5O^-" *J. Chem. Phys.* **145**, 54302 (2016).

Abstract

We report high-resolution photodetachment spectra of the cryogenically cooled iron monoxide clusters Fe_4O^- and Fe_5O^- obtained with slow photoelectron velocity-map imaging (cryo-SEVI). Well-resolved vibrational progressions are observed in both spectra, and transitions to low-lying excited states of both species are seen. In order to identify the structural isomers, electronic states, and vibrational modes that contribute to the cryo-SEVI spectra of these clusters, experimental results are compared with density functional calculations and Franck-Condon simulations. The main bands observed in the SEVI spectra are assigned to the $^{15}A_2 \leftarrow^{16} B_2$ photodetachment transition of Fe_4O^- and the $^{17}A' \leftarrow^{18} A''$ photodetachment transition of Fe_5O^-. We report electron affinities of 1.6980(3) eV for Fe_4O and 1.8616(3) eV for Fe_5O, although there is some uncertainty as to whether the $^{15}A_2$ state is the true ground state of Fe_4O. The iron atoms have a distorted tetrahedral geometry in $Fe_4O^{0/-}$ and a distorted trigonal-bipyramidal arrangement in $Fe_5O^{0/-}$. For both neutral and anionic species, the oxygen atom preferably binds in a μ_2-oxo configuration along the cluster edge. This finding is in contrast to prior predictions that $Fe_5O^{0/-}$ exhibits a μ_3 face-bound structure.

8.1 Introduction

Bulk and nano-structured iron oxide materials have varied uses as catalysts for CO oxidation,[355,356] the water-gas shift reaction,[357,358] Fischer-Tropsch synthesis,[359] and hydrocarbon dehydrogenation[360] and oxidation.[361] They also serve as supports for other catalysts.[362] Interest in the reactivity and chemistry of these materials has spurred investigation of the properties and behavior of molecular-scale iron oxide clusters. Gas-phase clusters can provide insight into the local geometry and behavior of heterogeneous catalysts.[122] The unusual structural motifs and distinct stoichiometry of small clusters can provide useful models for reactive point defects on surfaces.[102,363] Small clusters are also accessible to theoretical as well as experimental study.[364] The ability to mass-select charged clusters allows for experimental investigation of the impact of size and stoichiometry on cluster properties and reactivity.[365–367] It has also been suggested that some clusters demonstrate enhanced reactivity relative to the bulk, due to the wider range of stable stoichiometries, higher densities of reactive sites, and lowered barriers to isomerization.[368]

Spectroscopic and theoretical characterization of the geometries and electronic states of metal oxide clusters is essential for interpretation of their behavior and reactivity,[369] and by extension for understanding the behavior and reactivity of catalytic sites in the bulk. In the current work, we report vibrationally resolved photodetachment spectra of the iron monoxide clusters Fe_4O^- and Fe_5O^- via slow electron velocity-map imaging of cryogenically cold anions (cryo-SEVI). This technique previously yielded detailed structures of the smaller transition metal monoxide clusters Fe_3O^- and Co_3O^-,[73] and was used to identify and order the energies of close-lying structural isomers in $Ti_2O_4^-$ and $Zr_2O_4^-$.[352] We demonstrate here

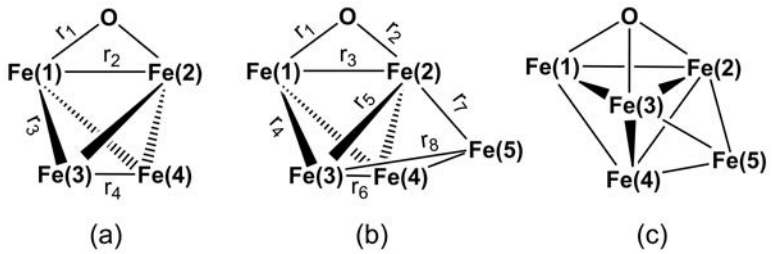

Figure 8.1: Structures of (a) the C_{2v}-symmetric μ_2 structure of $Fe_4O^{0/-}$ and (b) the C_s-symmetric μ_2 and (c) C_1-symmetric μ_3 structures of $Fe_5O^{0/-}$.

that more complex polymetal clusters are also accessible to characterization with cryo-SEVI, and that, with the aid of density functional theory (DFT) calculations, we can confidently assign their geometric, vibrational, and electronic structure, despite many low-lying spin states and structural isomers.

Polymetal iron oxide clusters with varying composition and charge states have been studied previously with a number of experimental methods. In the gas phase, the mass spectra of iron oxide clusters formed by laser ablation have been characterized[370–373] as have their photodissociation[374] and collision-induced dissociation[375] products. Reactions of gas-phase iron oxide clusters with N_2,[376] methanol,[377,378] and CO[379–382] have been investigated. Spectroscopic characterization is more scarce, though some iron oxide clusters have been studied with anion photoelectron spectroscopy (PES)[383] and matrix isolation infrared spectroscopy.[384] There has also been theoretical investigation of the structures of some larger iron oxide species.[385–388]

Among the iron monoxide clusters $Fe_nO^{0/-}$, the diatomic $FeO^{0/-}$ species are by far the most well-studied.[52,263,389–392] Spectroscopic work on larger iron monoxide clusters is limited to photoelectron spectroscopy. Fe_nO^- clusters have been studied with conventional anion PES at fairly low resolution for n up to 16,[393] and at higher resolution for n=2-6.[394] These studies did not resolve any vibrational structure in the spectra of Fe_4O^- and Fe_5O^-, though the authors observed sharp electronic bands, suggesting largely vertical transitions that result in little vibrational excitation of the neutral clusters upon photodetachment. Stern-Gerlach magnetic deflection experiments on neutral Fe_nO for n=2-7 find that these monoxide clusters are ferromagnetic, with magnetic moments that exceed those of the corresponding bare Fe_n clusters.[395]

The theoretical literature suggests that the geometries and electronic spin states of small $Fe_nO^{0/-}$ clusters are similar to those of the bare iron clusters $Fe_n^{0/-}$,[396] with the oxygen atom adsorbed on the cluster surface.[73,393,394,397,398] The oxygen can be accommodated in an edge-bound two-fold coordinated μ_2 site, or a face-bound, three-fold coordinated μ_3 site; structures suggested by the literature for $Fe_4O^{0/-}$ and $Fe_5O^{0/-}$ are shown in Fig. 8.1. Prior work is in agreement that the most stable structures for $Fe_4O^{0/-}$ have the O atom at the μ_2 site (Fig. 8.1a).[393,394,397,398] Gutsev *et al.*[394] report the most thorough DFT study on

small $Fe_nO^{0/-}$ clusters in the literature, using BPW91/6-311+G*, and find an anionic Fe_4O^- ground state with C_{2v} symmetry and $2S+1 = 16$ spin multiplicity. A 13-tet C_{2v}-symmetric structure is identified as the Fe_4O ground state, though a 15-tet state with C_2 symmetry lies only 0.01 eV higher.

There is less agreement in the literature regarding the structures of $Fe_5O^{0/-}$, particularly whether the O atom is preferentially accommodated in the μ_2 or μ_3 site (Figs. 8.1b and c). Early work by Wang *et al.*[393] using a local-spin-density method found that the neutral Fe_5O cluster had a 17-tet ground state, and a μ_2 geometry 0.06 eV more stable than the μ_3 geometry. Shiroishi *et al.*[397] also report a μ_2 ground state geometry for Fe_5O using DFT methods. Gutsev *et al.*,[394] however, report only μ_3 geometries for $Fe_5O^{0/-}$. They find an 18-tet anion ground state, a 17-tet neutral ground state, and a 19-tet neutral excited state lying 0.12 eV above the 17-tet.

Using high-resolution photoelectron imaging of cryogenically-cooled anions in conjunction with DFT calculations, we can gain insight into the electronic and vibrational structure of $Fe_4O^{0/-}$ and $Fe_5O^{0/-}$. The cryo-SEVI technique represents a significant improvement in resolution over conventional anion PES, and is well-suited for the study of complex transition metal oxide clusters.[73,352] Experimental energy resolution down to $\sim$1 cm^{-1} allows for full vibrational resolution of photodetachment bands,[49,51] compared to the more typical resolution of $>$100 cm^{-1} in prior PES work. Spectral clarity is improved by the preparation of cryogenically cold anions, which eradicates vibrational hot bands and dramatically narrows the rotational envelopes of photodetachment features.

Our cryo-SEVI photodetachment spectra of Fe_4O^- and Fe_5O^- yield well-resolved vibrational structure from which we obtain fundamental vibrational frequencies for Fe_4O and Fe_5O. Comparison to electronic structure calculations and Franck-Condon (FC) simulations is essential for interpretation of these results. $Fe_4O^{0/-}$ and $Fe_5O^{0/-}$ are found to take on structures with a μ_2 bridging oxo bound to iron atoms in a distorted tetrahedral configuration for Fe_4O and a distorted trigonal bipyramidal configuration for Fe_5O (Figs. 8.1a and b). We assign a $^{16}B_2$ ground state for Fe_4O^-, and observe a transition to the $^{15}A_2$ state of neutral Fe_4O, the lowest-energy state accessible with one-electron photodetachment. In Fe_5O^-, we report a transition from the $^{18}A''$ anion ground state to the neutral $^{17}A'$ ground state. For both clusters, we also observe photodetachment to a low-lying excited electronic state.

8.2 Experimental Methods

The SEVI method and apparatus has been described in detail in Chap. 2.

Fe_nO^- anions are prepared in a pulsed laser ablation source operating at 20 Hz. During each cycle, a 2–10 mJ pulse of 532 nm light from a frequency doubled Nd:YAG laser is focused onto a steel ablation target. The resulting plasma is quenched in a burst of helium buffer gas from a pulsed Even-Lavie solenoid valve.[117] The presence of trace oxygen in the buffer gas allows for formation of the desired iron oxide clusters.

The maximum-entropy velocity Legendre reconstruction method[140] is used to reconstruct the radial and angular electron distributions from an accumulated image. We calibrate the photoelectron velocity and hence the electron kinetic energy (eKE) as a function of radial displacement from the center of the reconstructed image using SEVI images of well-characterized photodetachment transitions of atomic O^-.[145]

8.3 Experimental Results

The cryo-SEVI spectra of Fe_4O^- and Fe_5O^- are presented in Figs. 8.2 and 8.3 respectively. Low-resolution overview traces are plotted in blue, with high-resolution composite traces plotted in black. The photodetachment bands of the two species are similar in appearance, with strong vibrational origins (peak A in Figs. 8.2 and 8.3) and relatively weak structure continuing for about $1000\,cm^{-1}$. Franck-Condon simulations discussed below demonstrate that this weak structure (peaks B-H in Fig. 8.2 and B-I in Fig. 8.3) corresponds to transitions to vibrationally excited states of neutral Fe_4O and Fe_5O. Both SEVI spectra also demonstrate an additional feature at higher eBE (peak X in Figs. 8.2 and 8.3). Due to the separation in energy between peak X and the main band in each spectrum, peak X is assigned as photodetachment to a second neutral electronic state. Peak positions and assignments for the spectral features in the cryo-SEVI spectra of Fe_4O^- and Fe_5O^- are given in Tables 8.1 and 8.2 respectively. Peak positions represent the center of a Gaussian fit. Typical peak widths in the composite traces are $6\,cm^{-1}$ fwhm.

We can also extract information on the photoelectron angular distribution (PAD) from the SEVI images. For one-photon photodetachment with linearly polarized light, the PAD is given by[79]

$$\frac{d\sigma}{d\Omega} = \frac{\sigma_{tot}}{4\pi}\left[1 + \beta P_2(\cos\theta)\right] \tag{8.1}$$

Here θ is the angle relative to the polarization axis of the laser, P_2 is the second order Legendre polynomial, and β is the anisotropy parameter which varies between -1 and $+2$ for PADs aligned perpendicular and parallel to the laser polarization, respectively.

In the SEVI spectra of Fe_4O^-, peaks A-H demonstrate weakly-negative-to-isotropic anisotropy parameters ($-0.2 < \beta < -0.1$) close to threshold and weakly positive anisotropy parameters ($\beta \sim 0.25$) by $2000\,cm^{-1}$ above threshold. The PAD of peak X is isotropic at small eKE, and grows more negative farther above threshold. For the Fe_5O^- spectra, peaks A-I have consistently negative positive anisotropy parameters starting at $\beta \sim -0.2$ near threshold, and decreasing to $\beta \sim -0.35$ by $1000\,cm^{-1}$ above threshold. The PAD of peak X, on the other hand, remains isotropic over the range of eKE measured here. Hence, for both anions, the PADs further support the assignment of peak X to a different electronic band than the features at lower eBE.

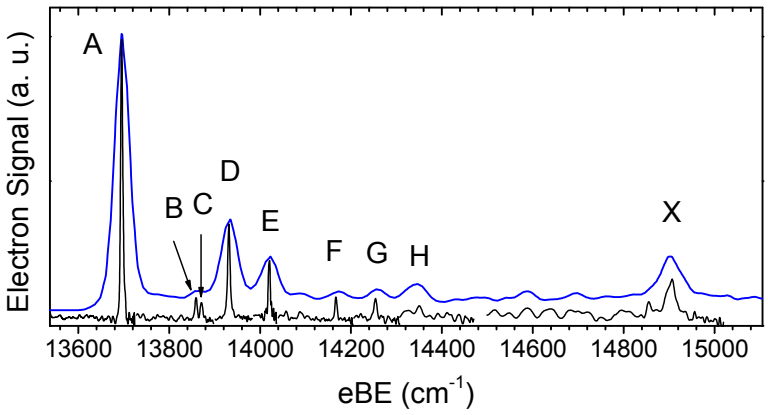

Figure 8.2: Cryo-SEVI spectra of Fe_4O^-. The blue trace is an overview spectrum taken at 16180 cm^{-1} while the black segments are high-resolution portions of scans taken at lower photon energies.

Table 8.1: Peak positions (cm^{-1}), offsets from the origin (cm^{-1}), and assignments for the SEVI spectra of Fe_4O^- given in Fig. 8.2. Uncertainties represent one standard deviation of a Gaussian fit to the experimentally observed peak.

Peak	Position	Offset	Assignment
A	13695(2)	0	0_0^0
B	13859(2)	163	5_0^2
C	13871(3)	175	4_0^1
D	13931(2)	236	3_0^1
E	14020(2)	325	2_0^1
F	14167(2)	472	3_0^2
G	14254(3)	558	$2_0^1 3_0^1$
H	14350(6)	654	2_0^2
X	14904(10)	1208	$\tilde{A}\ 0_0^0$

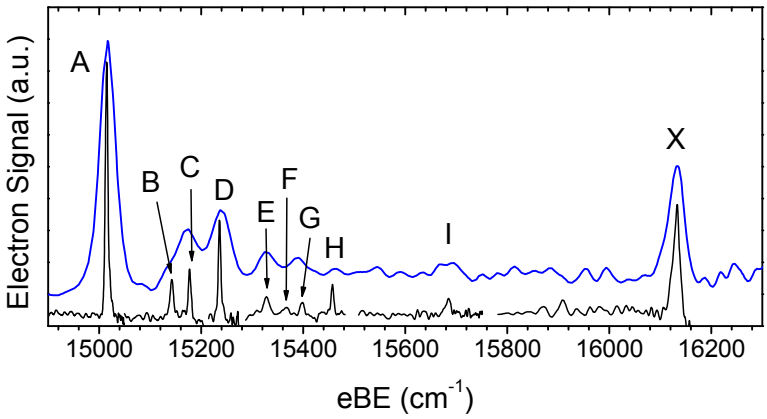

Figure 8.3: Cryo-SEVI spectra of Fe_5O^-. The blue trace is an overview spectrum taken at 16665 cm^{-1} while the black segments are high-resolution portions of scans taken at lower photon energies.

Table 8.2: Peak positions (cm^{-1}), offsets from the origin (cm^{-1}), and assignments for the SEVI spectra of Fe_5O^- given in Fig. 8.3. Uncertainties represent one standard deviation of a Gaussian fit to the experimentally observed peak.

Peak	Position	Offset	Assignment
A	15015(3)	0	0_0^0
B	15142(3)	128	8_0^1
C	15177(3)	163	7_0^1
D	15236(2)	221	5_0^1
E	15328(5)	313	3_0^1
F	15366(6)	351	$5_0^1 8_0^1$
G	15398(4)	383	$5_0^1 7_0^1$
H	15457(2)	443	5_0^2
I	15684(4)	670	1_0^1
X	16131(7)	1117	$\tilde{A}\ 0_0^0$

Over the range of photon energies used to obtain the SEVI spectrum of Fe_5O^-, we observe a background of electrons with an eKE distribution characteristic of thermionic emission.[15] A representative Fe_5O^- spectrum is presented in Fig. 8.10 demonstrating the contributions of both thermionic emission and direct detachment. Gutsev *et al.*[394] observed similar signatures of thermionic emission in the anion photoelectron spectra of Fe_5O^-. The thermionic emission signal increases in intensity relative to the direct detachment signal as the photon energy is increased. The SEVI traces taken at higher photon energies in Fig. 8.3 have therefore been baseline corrected to account for this background. Because we observe thermionic emission signal extending to higher eKE than the vibrational origin of the Fe_5O^- cluster, we ascribe at least some of this signal to weak two-photon absorption.

8.4 Theoretical Methods and Results

8.4.1 Electronic Structure Calculations

To aid in interpreting our spectra, we have carried out DFT calculations to identify the lowest-lying electronic states, optimized geometries, normal modes, and harmonic vibrational frequencies for the $Fe_4O^{0/-}$ and $Fe_5O^{0/-}$ clusters.

For $Fe_4O^{0/-}$, we focus on C_{2v}- and C_2-symmetric μ_2 structures; our attempts to find a μ_3 structure for 16-tet Fe_4O^- also converged to the μ_2 structure. For $Fe_5O^{0/-}$, we searched extensively for μ_2 and μ_3 structures to attempt to resolve the discrepancies in the literature. Calculations were performed with the TPSS, BPW91, and BP86 density functionals in order to assure consistency across the results from each. The BPW91 and BP86 functionals have provided accurate comparisons for prior cryo-SEVI results on polymetal oxide clusters;[73,352] the TPSS functional is also known to perform well for certain transition metal systems.[399] The 6-311+G* basis set was used for both Fe and O atoms with full treatment of all electrons.[400,401] Calculations were carried out in Gaussian 09 with tight geometry optimization criteria and an ultrafine integration grid.[402]

Figs. 8.4 and 8.5 show calculated relative energies for low-lying states of $Fe_4O^{0/-}$ and $Fe_5O^{0/-}$ respectively. In Fig. 8.4 we report only the energies for optimized μ_2 structures of $Fe_4O^{0/-}$ in various spin states, while in Fig. 8.5 we report the energies of the lowest-lying μ_2 and μ_3 structures for each spin state of $Fe_5O^{0/-}$. Full lists of energies, electronic state symmetries, and $\langle S^2 \rangle$ values for all states are given in Tables 8.6-8.7 of the Supporting Information. The values of $\langle S^2 \rangle$ generally fall very close to the expected result of $S(S+1)$, indicating little spin contamination in the DFT calculations. The Supporting Information also contains information on additional higher-lying geometries found for some spin states. Optimized Cartesian coordinates and harmonic vibrational frequencies are reported for all states in Tables 8.8-8.13 and Tables 8.14-8.16 respectively.

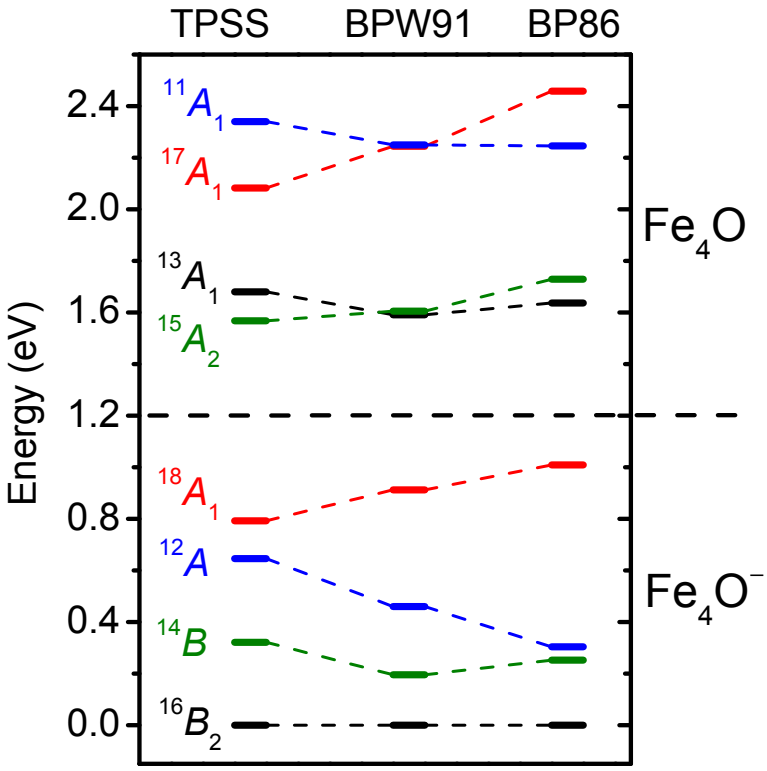

Figure 8.4: Energy level diagram of low-lying $Fe_4O^{0/-}$ electronic spin states; symmetry labels are provided as found with TPSS. Energies are reported for the lowest energy optimized μ_2 structure for each spin state, and are given relative to the anion ground state.

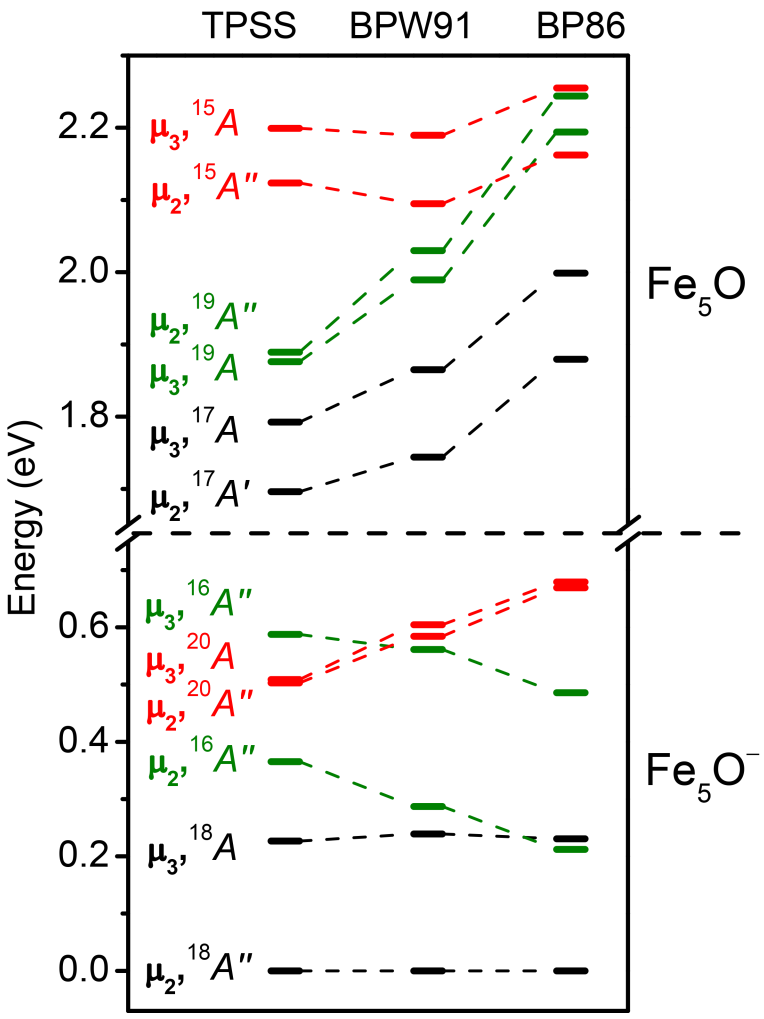

Figure 8.5: Energy level diagram of low-lying $Fe_5O^{0/-}$ electronic spin states; symmetry labels are provided as found with TPSS. Energies are reported for the lowest energy optimized μ_2 and μ_3 structures for each spin state, and are given relative to the anion ground state.

8.4.2 Franck-Condon Simulations

Franck-Condon simulations were carried out at 0 K with the FCFGAUS and PESCAL programs,[316,403], using the harmonic approximation with Duschinsky mixing of totally symmetric modes.[205] FC simulations using TPSS/6-311+G* geometries and frequencies are reported in Fig. 8.6a for the $^{15}A_2 \leftarrow^{16} B_2$ photodetachment transition of $Fe_4O^{0/-}$, and in Fig. 8.7a for the $^{17}A' \leftarrow^{18} A''$ photodetachment transition between μ_2 structures of $Fe_5O^{0/-}$; these are the lowest energy photodetachment transitions from the calculated anion ground states. In both cases they are plotted against high-resolution experimental spectra (black). FC simulations carried out with BPW91 and BP86 yielded essentially identical results.

Since agreement between the experimental and the simulated spectra in Figs. 8.6a and 8.7a is far from perfect, we also used PESCAL to perform nonlinear least-squares fits of the FC simulations to overview SEVI spectra of Fe_4O^- and Fe_5O^-. Fitting parameters included frequencies of totally symmetric FC active neutral vibrational modes, as well as displacements between the anion and neutral geometries along these modes. The frequency and displacement of the ν_1 mode of $Fe_5O^{0/-}$ were not varied during fitting, because the trace

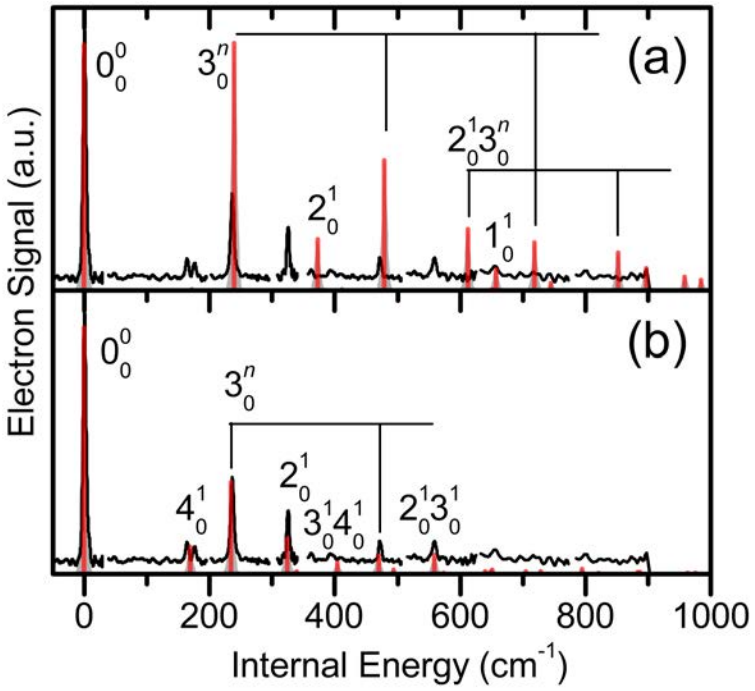

Figure 8.6: (a) FC simulation of the $^{15}A_2 \leftarrow^{16} B_2$ transition of $Fe_4O^{0/-}$ with TPSS/6-311+G* and (b) FC simulation after fitting the simulation parameters to a SEVI overview trace. Simulations are plotted as stick spectra (red) and after convolution with a 10 cm^{-1} fwhm Gaussian line shape function (grey), and compared to the high-resolution SEVI traces (black).

that proved best for fitting most of the band was taken at too low a photon energy to include the ν_1 fundamental. The eBE of the vibrational origin, the overall band intensity, and the width of the stick spectrum Gaussian convolution were also allowed to vary in the fitting routine for both clusters. Simulations fitted to the experimental traces are plotted in Figs. 8.6b and 8.7b. Relevant parameters for the simulations and fits are summarized in Tables 8.3 and 8.4 for Fe_4O^- and Fe_5O^- respectively.

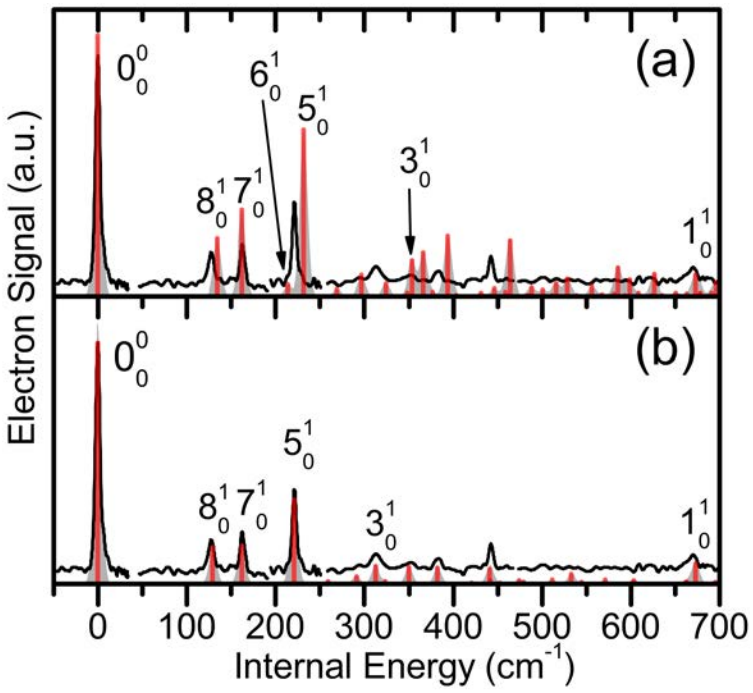

Figure 8.7: (a) FC simulation of the $^{17}A' \leftarrow^{18} A''$ transition between μ_2 structures of $Fe_5O^{0/-}$ with TPSS/6-311+G* and (b) FC simulation after fitting the simulation parameters to a SEVI overview trace. Simulations are plotted as stick spectra (red) and after convolution with a 10 cm^{-1} fwhm Gaussian line shape function (grey), and compared to the high-resolution SEVI traces (black).

Table 8.3: Parameters for the TPSS/6-311+G* FC simulation of Fe_4O^- photodetachment and fit to the SEVI spectrum of Fe_4O^- shown in Fig. 8.6. Parameters optimized in the fitting include the frequencies ω_n of the totally symmetric modes of neutral Fe_4O, and displacements ΔQ_n along these modes between the anion and neutral geometries, given here in the normal mode basis of the anion. Also reported are the anion and neutral DFT bond lengths and neutral bond lengths after displacement fitting, if the anion geometry is kept fixed. Bond labels are given in Fig. 8.1a.

Parameter	TPSS/6-311+G*		after fit
	$^{16}B_2$	$^{15}A_2$	$^{15}A_2$
ω_1 (cm^{-1})	633	657	652
ω_2 (cm^{-1})	352	373	324
ω_3 (cm^{-1})	226	240	235
ω_4 (cm^{-1})	160	172	170
ΔQ_1 ($amu^{1/2}$ Å)	–	-0.091	-0.038
ΔQ_2 ($amu^{1/2}$ Å)	–	-0.109	-0.111
ΔQ_3 ($amu^{1/2}$ Å)	–	-0.587	-0.359
ΔQ_4 ($amu^{1/2}$ Å)	–	-0.073	-0.239
r_1 (Å)	1.835	1.816	1.827
r_2 (Å)	2.414	2.466	2.462
r_3 (Å)	2.356	2.355	2.343
r_4 (Å)	2.279	2.183	2.22

Table 8.4: Parameters for the TPSS/6-311+G* FC simulation of Fe_5O^- photodetachment and fit to the SEVI spectrum of Fe_5O^- shown in Fig. 8.7. Parameters optimized in the fitting include the frequencies ω_n of the totally symmetric modes of neutral Fe_5O, and displacements ΔQ_n along these modes between the anion and neutral geometries, given here in the normal mode basis of the anion. Also reported are the anion and neutral DFT bond lengths and neutral bond lengths after displacement fitting, if the anion geometry is kept fixed. Bond labels are given in Fig. 8.1b.

Parameter	TPSS/6-311+G*		after fit
	$^{18}B''$	$^{17}A'$	$^{17}A'$
ω_1 (cm^{-1})	646	674	–
ω_3 (cm^{-1})	338	354	313
ω_5 (cm^{-1})	225	232	221
ω_6 (cm^{-1})	213	214	214
ω_7 (cm^{-1})	167	162	162
ω_8 (cm^{-1})	128	135	130
ΔQ_1 ($amu^{1/2}$ Å)	–	-0.091	–
ΔQ_3 ($amu^{1/2}$ Å)	–	-0.094	-0.070
ΔQ_5 ($amu^{1/2}$ Å)	–	-0.363	-0.281
ΔQ_6 ($amu^{1/2}$ Å)	–	-0.156	-0.027
ΔQ_7 ($amu^{1/2}$ Å)	–	0.383	0.258
ΔQ_8 ($amu^{1/2}$ Å)	–	-0.489	-0.385
r_1 (Å)	1.811	1.792	1.802
r_2 (Å)	1.848	1.825	1.826
r_3 (Å)	2.332	2.347	2.339
r_4 (Å)	2.381	2.383	2.394
r_5 (Å)	2.435	2.434	2.435
r_6 (Å)	2.383	2.275	2.303
r_7 (Å)	2.355	2.360	2.361
r_8 (Å)	2.346	2.366	2.348

8.5 Discussion

8.5.1 Structural Isomers and Electronic States

For $Fe_4O^{0/-}$, the energetics and μ_2-oxo optimized geometries found here largely reproduce the results reported by Gutsev *et al.*[394] With all three functionals, we find a C_{2v}-symmetric $^{16}B_2$ ground state anion. A C_2-symmetric ^{14}B state lies close above; this state lies slightly lower in energy than the 14-tet C_{2v} structure reported by Gutsev *et al.* The C_{2v}-symmetric 12-tet and 18-tet states lie correspondingly higher in energy. The three functionals used here agree on this state ordering, though for the 12-tet TPSS finds a C_2-symmetric structure rather than the C_{2v} structures found with BPW91 and BP86.

For neutral Fe_4O, our calculations reproduce the two lowest energy, nearly degenerate C_{2v}-symmetric $^{13}A_1$ and C_2-symmetric ^{15}A states identified by Gutsev *et al.*,[394] though the relative ordering of these states is uncertain. Additionally, there is a C_{2v} transition state for the 15-tet that lies only 12–50 cm^{-1} above the C_2 structure, depending on the functional. This structure corresponds to a barrier between the two equivalent C_2 structures that is either comparable to or submerged below vibrational ZPE. We therefore consider the neutral 15-tet to have C_{2v} symmetry with a shallow double-well potential along the a_2-symmetric ν_5 normal coordinate. This anharmonic vibrational potential is discussed in more detail in Section 8.5.2.

Our calculations find that for neutral Fe_4O, the 11-tet state and 17-tet states lie considerably higher in energy and are nearly degenerate with one another. As was the case for the 15-tet, Gutsev *et al.*[394] report a C_2 structure for the 11-tet, while we find this state has functionally C_{2v} symmetry.

Regardless of the exact ordering of the Fe_4O neutral states, since the $^{16}B_2$ state is widely agreed upon as the anion ground state, one electron photodetachment can only access neutral 15-tet and 17-tet states. The assignment for the main photodetachment band in the Fe_4O^- SEVI spectrum is therefore $^{15}A_2 \leftarrow ^{16}B_2$, corresponding to detachment of an electron from the highest-lying molecular orbital (HOMO) of the anion with α spin (visualized in Fig. 8.8a). If we take the Fe_4O $^{15}A_2$ state as the neutral ground state, in agreement with the TPSS results, then the vibrational origin of the main photodetachment band in Fig. 8.2 directly yields the electron affinity (EA) of Fe_4O. However, the Fe_4O $^{13}A_1$ state is predicted to lie nearly degenerate in energy with the $^{15}A_2$ state and cannot be observed in our experiment. We therefore cannot unambiguously rule out the 13-tet as the ground state of Fe_4O.

Our calculations for $Fe_5O^{0/-}$ demonstrate a more significant departure from the work of Gutsev *et al.*,[394] who report only μ_3 geometries for these clusters. While we can largely reproduce their results, we also identify μ_2 geometries that are lower in energy than their μ_3 counterparts for most $Fe_5O^{0/-}$ spin states. Only the 19-tet neutral has a μ_3 structure more stable than the μ_2 structure, and the 20-tet anion has μ_2 and μ_3 structures comparable in energy. In some cases, we also find alternate μ_3 geometries that are lower or comparable in energy to those reported by Gutsev *et al.* All of these states are detailed in the Supporting Information.

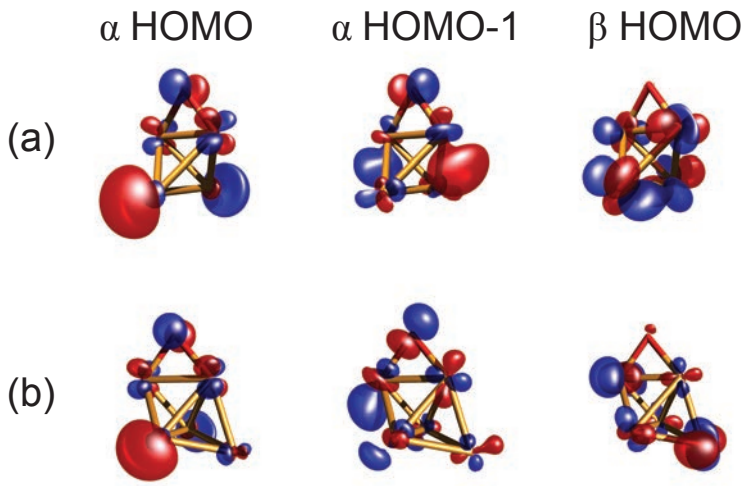

Figure 8.8: Relevant high-lying molecular orbitals of (a) Fe_4O^- and (b) Fe_5O^-.

For Fe_5O^-, all three functionals find an $^{18}A''$ anion ground state with a C_s-symmetric μ_2 geometry. This state is consistently 0.23–0.24 eV lower in energy than the most stable 18-tet μ_3 structure identified by Gutsev *et al.*[394] The 16-tet and 20-tet μ_2 structures lie respectively higher in energy, and are found to be C_1-symmetric with BPW91 and BP86, but have higher C_s symmetry with the TPSS functional. For neutral Fe_5O, we find a $^{17}A'$ ground state with a C_s-symmetric μ_2 geometry that lies 0.10–0.12 eV below the μ_3 17-tet structure. 19-tet and 15-tet states lie higher in energy; the ordering of these states is reasonably consistent between functionals and with the work of Gutsev *et al.* With TPSS, we had difficulty optimizing the 15-tet μ_2 structure, and the state reported here has one small imaginary frequency.

With an $^{18}A''$ μ_2-oxo ground state for Fe_5O^-, only 17-tet and 19-tet neutral states with μ_2 structures should be accessible through photodetachment. The main photodetachment band in the Fe_5O^- SEVI spectrum is therefore assigned to the $^{17}A' \leftarrow ^{18}A''$ transition, between the ground state C_s-symmetric μ_2 anion and neutral structures, and the vibrational origin of this band unambiguously yields the EA of Fe_5O. As was true for Fe_4O^-, this transition corresponds to detachment from the α HOMO (Fig. 8.8b).

In the experimental spectra in Figs. 8.2 and 8.3, peak A is the strong vibrational origin of each main photodetachment band. The eBE of each origin gives an EA of 1.6980(3) eV for Fe_4O and 1.8616(3) eV for Fe_5O, both of which fall within the range of calculated values (Table 8.5). Note that our reported and calculated EAs for Fe_4O assume that its ground state is the $^{15}A_2$ state, as mentioned above. For both species, we assign peak X as the vibrational origin of a second photodetachment band to a neutral excited state with an eBE of 1.8478(12) eV for Fe_4O and 2.0000(9) eV for Fe_5O. The photoelectron spectra reported previously by Gutsev *et al.*[394] demonstrated very sharp bands at vertical detachment energies of 1.70(2) eV and 1.85(2) eV for Fe_4O^- and 1.87(2) eV and 2.00(2) eV for Fe_5O^-, in excellent

agreement with our measurements of peaks A and X for both systems. The sharpness of the features observed by Gutsev *et al.* is also in accord with the intense vibrational origins and comparatively weak vibrational structure observed here.

For both clusters, the assignment of the neutral electronic excited state corresponding to peak X is somewhat speculative. This feature lies at a term energy of 0.1498(12) eV relative to the main photodetachment band for Fe_4O and at 0.1384(9) eV for Fe_5O. One-electron photodetachment from the Fe_4O^- $^{16}B_2$ anion can access both neutral 15-tet and 17-tet states, while 17-tet and 19-tet neutral states are similarly accessible from the $^{18}A''$ state of Fe_5O^-. For Fe_4O, the lowest-lying 17-tet state is calculated to lie 0.52–0.73 eV above the state (Table 8.6), considerably higher than what is observed experimentally. The lowest 19-tet state of neutral Fe_5O is calculated to lie at a term energy of 0.19–0.36 eV above the $^{17}A'$ ground state (Table 8.7), which is within DFT error of the experimental term energy of peak X. These high-spin neutral states are accessible from detachment of the β HOMOs (Fig. 8.8) of Fe_4O^- and Fe_5O^-. Another scenario for both species is that peak X represents a transition to an excited state with the same spin multiplicity as the main photodetachment band, corresponding to detachment from the anion α HOMO-1, also visualized in Fig. 8.8.While we are unable to calculate term energies of excited Fe_4O 15-tets and Fe_5O 17-tets, it is worth noting that our experiment would be sensitive to the plethora of detachment transitions from α HOMO-n orbitals. The fact that we only observe two electronic transitions for each cluster in the energy window considered here suggests that these orbitals are spaced farther apart in energy than one might expect given the high electronic spin in these systems.

For $Fe_4O^{0/-}$, the photoelectron angular distributions of the main detachment band and of peak X are qualitatively consistent with the electronic state assignments discussed above. A model developed by Sanov and coworkers[78] can predict the near-threshold PAD upon photodetachment of a C_{2v} molecular anion. In the $^{15}A_2 \leftarrow ^{16}B_2$ photodetachment transition of Fe_4O^-, an electron is ejected from the b_1-symmetric α HOMO. Within this model, this transition should yield a PAD aligned perpendicular to the laser polarization that grows isotropic at low eKE, as is reasonably consistent with the near-threshold behavior of peaks in the main photodetachment band. Detachment from the β HOMO and α HOMO-1 of Fe_4O^-, both with b_2 symmetry, yields the lowest 17-tet and first excited 15-tet states of Fe_4O. Within the Sanov model, ejection of an electron from a b_2 orbital also yields a perpendicular PAD that grows isotropic close to threshold. This PAD is consistent with that observed experimentally for peak X, and unfortunately does not aid in clarifying the excited band assignment.

The low symmetry C_s point group of $Fe_5O^{0/-}$ makes prediction of PADs more challenging than for $Fe_4O^{0/-}$. However, the a''-symmetric Fe_5O^- α HOMO looks very similar to the b_1-symmetric α HOMO of Fe_4O^-, with electron density largely in s-like antibonding orbitals on the Fe(3) and Fe(4) atoms, and very little participation of the additional Fe(5) atom (atoms labeled in Fig. 8.1). It is therefore reasonable to expect that the main Fe_5O^- photodetachment band also has a PAD aligned perpendicular to the laser polarization axis that grows isotropic close to threshold, and indeed this is what is observed experimentally. The low-lying excited state (peak X) exhibits an isotropic PAD, which does not allow us to

Table 8.5: All assigned states, state energies, and vibrational frequencies for $Fe_4O^{0/-}$ and $Fe_5O^{0/-}$. Calculated energies are corrected for vibrational zero-point energy.

			exptl	TPSS	BPW91	BP86
Fe_4O^-	$^{16}B_2$					
Fe_4O	$^{15}A_2$	EA,[a] eV	1.6980(3)[b]	1.5674[c]	1.6054[c]	1.7290[c]
		ν_2, cm^{-1}	325(2)	373	363	365
		ν_3, cm^{-1}	236(2)	240	248	249
		ν_4, cm^{-1}	175(3)	172	176	177
		ν_5, cm^{-1}	163(2)	149	125	127
	$\tilde{A}$	TE,[d] eV	0.1498(12)			
Fe_5O^-	$^{18}A''$					
Fe_5O	$^{17}A'$	EA, eV	1.8616(3)	1.6961	1.7440	1.8796
		ν_1, cm^{-1}	670(4)	674	660	663
		ν_3, cm^{-1}	313(5)	354	344	346
		ν_5, cm^{-1}	221(2)	232	233	234
		ν_7, cm^{-1}	163(3)	162	156	156
		ν_8m cm^{-1}	128(3)	135	128	128
	$\tilde{A}$	TE, eV	0.1384(9)			

[a]Electron affinity. [b]Uncertainties represent one standard deviation of a Gaussian fit to the experimentally observed peak. [c]Calculated electron affinities for Fe_4O reflect the difference in energy between the $^{16}B_2$ anion and $^{15}A_2$ neutral states. [d]Term energy.

distinguish between detachment from the β HOMO and α HOMO-1 of Fe_5O^-, both of which have a' symmetry.

8.5.2 Vibrational Structure

We use calculated harmonic vibrational frequencies and simulated FC envelopes to assign the vibrational structure of the Fe_4O^- and Fe_5O^- SEVI spectra. The $Fe_4O^{0/-}$ clusters have four totally symmetric a_1 vibrational modes within the C_{2v} point group, while the C_s-symmetric $Fe_5O^{0/-}$ species have eight totally symmetric a' vibrational modes. These modes are shown schematically in Fig. 8.11. The TPSS/6-311+G* frequencies for FC active modes and displacements along these modes for the $^{15}A_2 \leftarrow ^{16}B_2$ photodetachment transition of Fe_4O^- and the $^{17}A' \leftarrow ^{18}A''$ transition of Fe_5O^- are summarized in Tables 8.3 and 8.4. These calculated parameters yield the FC simulations shown in Figs. 8.6a and 8.7a.

For Fe_4O^-, the FC simulation in Fig. 8.6a shows predominant excitation in mode ν_2, some excitation in ν_3, and weaker still activity in ν_1. Qualitatively, moderate excitation in a

few modes matches the experimental spectrum; the largest discrepancies are the simulated overemphasis of FC intensity for the ν_3 progression, and the absence of features lower in energy than the ν_3 fundamental. For Fe_5O^-, the envelope of the FC simulation in Fig. 8.7a is an excellent qualitative match for our experimental results, confirming the preferential μ_2 structures of $Fe_5O^{0/-}$. Modes ν_5, ν_7, and ν_8 demonstrate significant FC intensity, while ν_1, ν_3, and ν_6 appear more weakly. All modes have somewhat exaggerated FC intensity in the simulation compared to experiment, and some calculated fundamental frequencies are higher than experimental frequencies. We plot FC simulations for photodetachment transitions of the alternative C_1- and C_s-symmetric μ_3 structures of $Fe_5O^{0/-}$ in Fig. 8.12 of the SI; both are comparatively very poor matches with the observed experimental structure.

Fitting the FC simulation parameters to the experimental overviews, as described in Section 8.4.2, yields the simulations in Figs. 8.6b and 8.7b and the altered parameters for neutral Fe_4O and Fe_5O in the rightmost columns of Tables 8.3 and 8.4. In fitting the FC activity of totally symmetric modes to the experiment, we arrive at new values for the displacement between anion and neutral structures and, keeping the DFT anion geometries fixed, new neutral bond lengths. These fitted bond lengths represent a fairly minor update in geometry from the DFT results for both neutral clusters; the norm of the geometry difference between the DFT and neutral geometries is 0.04 Å for Fe_4O and 0.03 Å for Fe_5O. The corresponding change in the simulated spectra highlights the sensitivity of FC structure to small changes in displacement, particularly for the three-dimensional structures exhibited by metal oxide clusters.

The results of the FC simulation and fitting inform our interpretation of the high-resolution SEVI spectra; all vibrational frequencies observed experimentally are compared to their calculated values in Table 8.5. In the Fe_4O^- spectrum (Fig. 8.2), we can unambiguously assign peak D at a shift of 236 cm^{-1} from the origin to 3_0^1; the ν_3 fundamental is calculated at 232–236 cm^{-1}. Peak E at 325 cm^{-1} is assigned to 2_0^1. The ν_2 fundamental is calculated higher in frequency at 352–366 cm^{-1}, but falls within the error of DFT vibrational frequencies for species involving transition metals.[399] Peaks F, G, and H are the 3_0^2, $2_0^1 3_0^1$, and 2_0^2 transitions respectively. The ν_1 fundamental, calculated to lie at 644–658 cm^{-1}, may also be underlying peak H, which lies 654 cm^{-1} above the vibrational origin. Mode ν_1 is not predicted to have much FC activity however, so we do not make an assignment.

At low binding energies, two closely spaced peaks B and C are resolved at respective shifts of 163 and 175 cm^{-1} above the Fe_4O^- vibrational origin. We assign peak C as 4_0^1, as the ν_4 fundamental is calculated to lie at 169–175 cm^{-1}. Peak B does not align with the calculated frequency of any totally symmetric vibrational mode, but it could arise from a $\Delta\nu = 2$ transition in a non-totally symmetric mode. The only non-totally symmetric mode of the $^{15}A_2$ state that lies sufficiently low in energy for two quanta of excitation to match the position of peak B is ν_5 (mode shown schematically in Fig. 8.11a). As mentioned in Section 8.5.1, the $^{15}A_2$ state of neutral Fe_4O has a double-well vibrational potential along the ν_5 normal coordinate, which can lead to enhanced FC activity in transitions involving even quanta of excitation in ν_5.

FC factors for transitions to ν_5 vibrational states are calculated by treating this mode

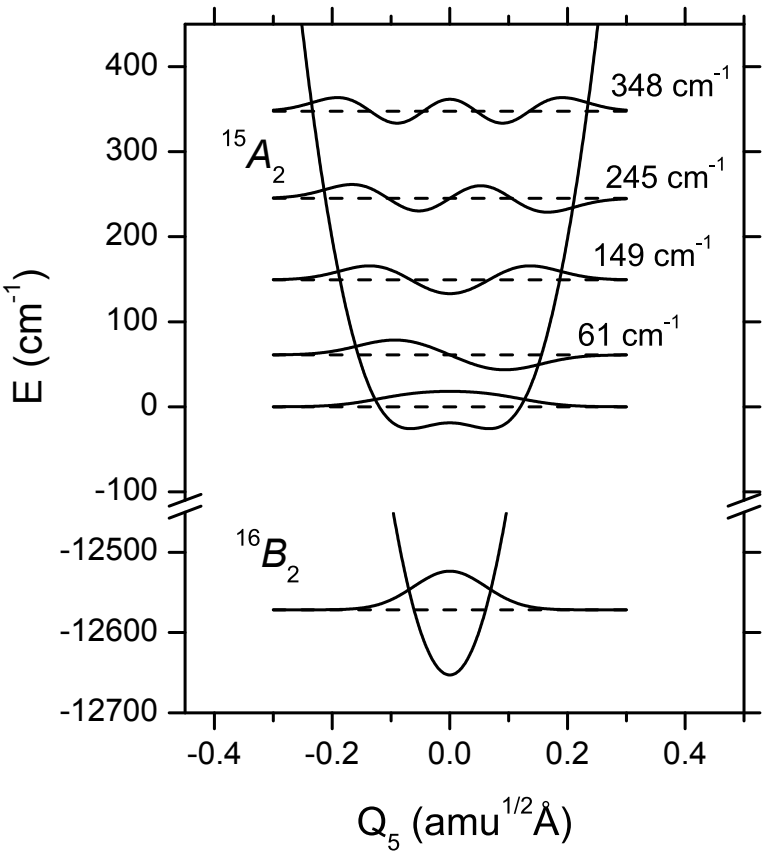

Figure 8.9: Vibrational potential, low-lying eigenenergies, and wavefunctions for the ν_5 mode of the $^{16}B_2$ state of Fe_4O^- and the $^{15}A_2$ state of Fe_4O, calculated with TPSS/6 311+G*.

as an anharmonic oscillator. Single-point calculations were carried out scanning a one-dimensional slice of the vibrational potential along the ν_5 coordinate for the neutral $^{15}A_2$ state and the anionic $^{16}B_2$ state. These points were then fit to a 16^{th} order polynomial for the neutral state and a 4^{th} order polynomial for the anion, and a MATLAB script was used to numerically solve for the vibrational eigenenergies and wavefunctions. These results are shown in Fig. 8.9 using TPSS/6 311+G*. We find $2\nu_5$ =149 cm^{-1}, which compares well to the experimental shift of peak B at 163 cm^{-1}.

We use direct integration of the anion and neutral vibrational wavefunctions to solve for the Franck-Condon factors $|\langle\nu_{neutral}|\nu_{anion}\rangle|^2$ of the 5_0^n transitions. The calculated FC intensity of 5_0^2 relative to the vibrational origin is 0.12 using the TPSS functional; all other 5_0^n FC intensities are negligibly small. This value provides a good match with the experimental intensity of peak B, at about 10% of the origin intensity. We therefore assign peak B to the 5_0^2 transition.

Assigning the vibrational structure of the high-resolution Fe_5O^- SEVI spectrum in Fig.

8.3 is more straightforward. Three fundamentals can be assigned very clearly: peak B to the 8_0^1 transition, peak C to 7_0^1, and peak D to 5_0^1. Peaks F, G, and H then line up as $5_0^1 8_0^1$, $5_0^1 7_0^1$, and 5_0^2. Peak E, lying 313 cm^{-1} from the vibrational origin, cannot be accounted for as part of a progression or a combination band, so it is likely the 3_0^1 fundamental, which is predicted to be FC active with calculated frequencies of 344–354 cm^{-1}. Peak I at 670 cm^{-1} is assigned to the 1_0^1 fundamental, which is calculated at 660–674 cm^{-1} and predicted to have similar FC intensity to what is observed experimentally.

The Franck-Condon structure of the main photodetachment bands of both clusters can also be rationalized in the context of the α HOMOs from which the electron is detached. Both α HOMOs feature s-like lobes of opposite phase localized on the Fe(3) and Fe(4) atoms (Fig. 8.8). Accordingly, the bond between the Fe(3) and Fe(4) atoms shrinks upon photodetachment by 0.10 Å for Fe_4O^- and 0.11 Å for Fe_5O^-, consistent with removal of an electron from an antibonding orbital. The vibrational states of the neutral clusters that are populated after photodetachment correspondingly involve modes with significant distortion of the bond between the Fe(3) and Fe(4) atoms, where the primary change in electron density occurs upon detachment.

8.6 Conclusions

We report a high-resolution photoelectron imaging study of cryogenically cooled Fe_4O^- and Fe_5O^- iron monoxide cluster anions using SEVI spectroscopy. Our results represent the first vibrationally-resolved spectra of these species, providing precise electron affinities and excited state term energies as well as newly observed and assigned vibrational frequencies. Through comparison of our experimental results with DFT calculations and Franck-Condon simulations, we determine the structural isomers and electronic states of these clusters. The experimental and theoretical results point to C_{2v}-symmetric $Fe_4O^{0/-}$ and C_s-symmetric $Fe_5O^{0/-}$ clusters, both of which preferentially bind the O atom in a μ_2 configuration.

This work represents the next step in our extension of the cryo-SEVI technique towards ever-larger transition metal oxide clusters. We demonstrate here that clusters involving four and five metal centers are accessible to detailed characterization with good agreement between spectroscopic and theoretical methods, despite the presence of multiple low-energy electronic states and structural isomers. In future work, it will be of considerable interest to study Fe_nO^- clusters complexed to small molecules such as CO as a model system for CO oxidation by iron oxide catalysts.

8.7 Supporting Information

Table 8.6: Calculated states, energies (eV) relative to the ground state of each anionic or neutral species, and calculated vs. expected spin for the low-lying Fe_4O anion and neutral states with the TPSS, BPW91, and BP86 DFT functionals. Calculated electron affinities are given for the $^{15}A_2 \leftarrow ^{16}B_2$ photodetachment transitions. All energies are corrected for vibrational zero-point energy with the exception of those marked with an asterisk, which have one small imaginary frequency.

	TPSS/6-311+G*					BPW91/6-311+G*					BP86/6-311+G*				
species	state	EA	T_0	$<S^2>$	$S(S+1)$	state	EA	T_0	$<S^2>$	$S(S+1)$	state	EA	T_0	$<S^2>$	$S(S+1)$
Fe_4O^-	^{12}A, C_2	–	0.65	36.21	35.75	$^{12}A_1$, C_{2v}	–	0.46	36.10	35.75	$^{12}A_1$, C_{2v}	–	0.30	36.07	35.75
	^{14}B, C_2	–	0.32	49.03	48.75	^{14}B, C_2	–	0.19	48.98	48.75	^{14}B, C_2	–	0.25	48.75	48.75
	$^{14}B_2$, C_{2v}	–	0.39	49.06	48.75	$^{14}B_2$, C_{2v}	–	0.27	49.00	48.75	$^{14}B_2$, C_{2v}	–	0.33	48.98	48.75
	$^{16}B_2$, C_{2v}	–	0.00	63.86	63.75	$^{16}B_2$, C_{2v}	–	0.00	63.85	63.75	$^{16}B_2$, C_{2v}	–	0.00	63.84	63.75
	$^{18}A_1$, C_{2v}	–	0.79	80.83	80.75	$^{18}A_1$, C_{2v}	–	0.91	80.83	80.75	$^{18}A_1$, C_{2v}	–	1.01	80.82	80.75
Fe_4O	$^{11}A_1$, C_{2v}	–	0.77*	30.49	30.00	$^{11}A_1$, C_{2v}	–	0.63*	30.45	30.00	$^{11}A_1$, C_{2v}	–	0.61	30.42	30.00
	$^{13}A_1$, C_{2v}	–	0.11	42.01	42.00	$^{13}A_1$, C_{2v}	–	0.00	42.25	42.00	$^{13}A_1$, C_{2v}	–	0.00	42.23	42.00
	$^{15}A_2$, C_{2v}	1.57	0.00	56.11	56.00	$^{15}A_2$, C_{2v}	1.61	0.01	56.10	56.00	$^{15}A_2$, C_{2v}	1.73	0.09	56.09	56.00
	$^{17}A_1$, C_{2v}	–	0.52	72.08	72.00	$^{17}A_1$, C_{2v}	–	0.65	72.08	72.00	$^{17}A_1$, C_{2v}	–	0.82	72.07	72.00

Table 8.7: Calculated states, energies (eV) relative to the ground state of each anionic or neutral species, and calculated vs. expected spin for the low-lying Fe_5O anion and neutral states with the TPSS, BPW91, and BP86 DFT functionals. Calculated electron affinities are given for the $^{17}A' \leftarrow ^{18}A''$ photodetachment transitions. All energies are corrected for vibrational zero-point energy with the exception of those marked with an asterisk, which have one small imaginary frequency.

	TPSS/6-311+G*					BPW91/6-311+G*					BP86/6-311+G*				
species	state	EA	T_0	$<S^2>$	$S(S+1)$	state	EA	T_0	$<S^2>$	$S(S+1)$	state	EA	T_0	$<S^2>$	$S(S+1)$
Fe_5O^-, μ_2	$^{16}A''$, C_s	–	0.37	64.00	63.75	^{16}A, C_1	–	0.29	63.97	63.75	^{16}A, C_1	–	0.21	63.95	63.75
	$^{18}A''$, C_s	–	0.00	80.92	80.75	$^{18}A''$, C_s	–	0.00	80.91	80.75	$^{18}A''$, C_s	–	0.00	80.90	80.75
	$^{20}A''$, C_s	–	0.50	99.87	99.75	^{20}A, C_1	–	0.58	99.87	99.75	^{20}A, C_1	–	0.67	99.86	99.75
Fe_5O^-, μ_3	$^{16}A''$, C_s	–	0.59	64.05	63.75	$^{16}A''$, C_s	–	0.56	64.02	63.75	$^{16}A''$, C_s	–	0.49	63.99	63.75
	^{16}A, C_1	–	0.59	64.02	63.75	–	–	–	–	–	–	–	–	–	–
	^{18}A, C_1	–	0.23	80.92	80.75	^{18}A, C_1	–	0.24	80.91	80.75	^{18}A, C_1	–	0.23	80.90	80.75
	$^{18}A'$, C_s	–	0.25	80.91	80.75	$^{18}A'$, C_s	–	0.29	80.90	80.75	$^{18}A'$, C_s	–	0.28	80.89	80.75
	^{20}A, C_1	–	0.51	99.87	99.75	^{20}A, C_1	–	0.60	99.87	99.75	^{20}A, C_1	–	0.68	99.86	99.75
Fe_5O, μ_2	$^{15}A''$, C_s	–	0.43*	56.33	56.00	$^{15}A''$, C_s	–	0.35	56.30	56.00	$^{15}A''$, C_s	–	0.28	56.27	56.00
	$^{17}A'$, C_s	1.70	0.00	72.20	72.00	$^{17}A'$, C_s	1.74	0.00	72.18	72.00	$^{17}A'$, C_s	1.88	0.00	72.12	72.00
	$^{19}A''$, C_s	–	0.19	90.14	90.00	$^{19}A''$, C_s	–	0.29	90.13	90.00	$^{19}A''$, C_s	–	0.36	90.12	0.00
Fe_5O, μ_3	^{15}A, C_1	–	0.52	56.46	56.00	^{15}A, C_1	–	0.45	56.40	56.00	^{15}A, C_1	–	0.38	56.36	56.00
	$^{15}A''$, C_s	–	0.50	56.41	56.00	$^{15}A''$, C_s	–	0.56	56.45	56.00	–	–	–	–	–
	^{17}A, C_1	–	0.10	72.22	72.00	^{17}A, C_1	–	0.12	72.21	72.00	^{17}A, C_1	–	0.12	72.19	72.00
	$^{17}A''$, C_s	–	0.10	72.23	72.00	$^{17}A''$, C_s	–	0.12	72.21	72.00	$^{17}A''$, C_s	–	0.12	72.19	72.00
	^{19}A, C_1	–	0.18	90.12	90.00	^{19}A, C_1	–	0.25	90.12	90.00	^{19}A, C_1	–	0.31	90.11	90.00

Table 8.8: Optimized Cartesian coordinates (Å) for relevant states of Fe_4O^- using the TPSS, BPW91, and BP86 density functionals. Atom labels are given in Fig. 8.1a of the main text.

TPSS/6-311+G*																
	^{12}A, C_2			^{14}B, C_2			$^{14}B_2$, C_{2v}			$^{16}B_2$, C_{2v}			$^{18}A_1$, C_{2v}		
	x	y	z	x	y	z	x	y	z	x	y	z	x	y	z
O	0.0000	0.0000	2.1561	0.0000	0.0000	2.0417	0.0000	0.0000	2.0291	0.0000	0.0000	2.0700	0.0000	0.0000	2.0611
Fe(1)	0.0000	1.0940	0.7065	0.0000	1.1914	0.6579	0.0000	1.2096	0.6583	0.0000	1.2068	0.6882	0.0000	1.2650	0.7317
Fe(2)	0.0000	-1.0940	0.7065	0.0000	-1.1914	0.6579	0.0000	-1.2096	0.6583	0.0000	-1.2068	0.6882	0.0000	-1.2650	0.7317
Fe(3)	-1.1288	-0.0808	-1.0148	-1.1588	-0.1234	-0.9498	-1.1294	0.0000	-0.9485	-1.1396	0.0000	-0.9841	-1.1518	0.0000	-1.0264
Fe(4)	1.1288	0.0808	-1.0148	1.1588	0.1234	-0.9498	1.1294	0.0000	-0.9485	1.1396	0.0000	-0.9841	1.1518	0.0000	-1.0264
BPW91/6-311+G*																
	$^{12}A_1$, C_{2v}			^{14}B, C_2			$^{14}B_2$, C_{2v}			$^{16}B_2$, C_{2v}			$^{18}A_1$, C_{2v}		
	x	y	z	x	y	z	x	y	z	x	y	z	x	y	z
O	0.0000	0.0000	2.1662	0.0000	0.0000	2.0432	0.0000	0.0000	2.0316	0.0000	0.0000	2.0622	0.0000	0.0000	2.0628
Fe(1)	0.0000	1.0942	0.7104	0.0000	1.1989	0.6603	0.0000	1.2155	0.6590	0.0000	1.2232	0.6891	0.0000	1.2756	0.7365
Fe(2)	0.0000	-1.0942	0.7104	0.0000	-1.1989	0.6603	0.0000	-1.2155	0.6590	0.0000	-1.2232	0.6891	0.0000	-1.2756	0.7365
Fe(3)	-1.1356	0.0000	-1.0201	-1.1660	-0.1310	-0.9524	-1.1377	0.0000	-0.9495	-1.1440	0.0000	-0.9839	-1.1559	0.0000	-1.0314
Fe(4)	1.1356	0.0000	-1.0201	1.1660	0.1310	-0.9524	1.1377	0.0000	-0.9495	1.1440	0.0000	-0.9839	1.1559	0.0000	-1.0314
BP86/6-311+G*																
	$^{12}A_1$, C_{2v}			^{14}B, C_2			$^{14}B_2$, C_{2v}			$^{16}B_2$, C_{2v}			$^{18}A_1$, C_{2v}		
	x	y	z	x	y	z	x	y	z	x	y	z	x	y	z
O	0.0000	0.0000	2.1600	0.0000	0.0000	2.0377	0.0000	0.0000	2.0269	0.0000	0.0000	2.0548	0.0000	0.0000	2.0556
Fe(1)	0.0000	1.0928	0.7068	0.0000	1.1990	0.6582	0.0000	1.2147	0.6569	0.0000	1.2255	0.6861	0.0000	1.2778	0.7332
Fe(2)	0.0000	-1.0928	0.7068	0.0000	-1.1990	0.6582	0.0000	-1.2147	0.6569	0.0000	-1.2255	0.6861	0.0000	-1.2778	0.7332
Fe(3)	-1.1336	0.0000	-1.0156	-1.1626	-0.1326	-0.9496	-1.1354	0.0000	-0.9467	-1.1414	0.0000	-0.9798	-1.1539	0.0000	-1.0271
Fe(4)	1.1336	0.0000	-1.0156	1.1626	0.1326	-0.9496	1.1354	0.0000	-0.9467	1.1414	0.0000	-0.9798	1.1539	0.0000	-1.0271

Table 8.9: Optimized Cartesian coordinates (Å) for relevant states of Fe_4O using the TPSS, BPW91, and BP86 density functionals. Atom labels are given in Fig. 8.1a of the main text.

TPSS/6-311+G*												
	$^{11}A_1$, C_{2v}			$^{13}A_1$, C_{2v}			$^{15}A_2$, C_{2v}			$^{17}A_1$, C_{2v}		
	x	y	z	x	y	z	x	y	z	x	y	z
O	0.0000	0.0000	2.0499	0.0000	0.0000	2.0144	0.0000	0.0000	2.0299	0.0000	0.0000	2.0572
Fe(1)	0.0000	1.1259	0.6721	0.0000	1.1967	0.6588	0.0000	1.2330	0.6965	0.0000	1.2201	0.7011
Fe(2)	0.0000	-1.1259	0.6721	0.0000	-1.1967	0.6588	0.0000	-1.2330	0.6965	0.0000	-1.2201	0.7011
Fe(3)	-1.1473	0.0000	-0.9652	-1.1423	0.0000	-0.9468	-1.0914	0.0000	-0.9868	-1.1884	0.0000	-0.9952
Fe(4)	1.1473	0.0000	-0.9652	1.1423	0.0000	-0.9468	1.0914	0.0000	-0.9868	1.1884	0.0000	-0.9952
BPW91/6-311+G*												
	$^{11}A_1$, C_{2v}			$^{13}A_1$, C_{2v}			$^{15}A_2$, C_{2v}			$^{17}A_1$, C_{2v}		
	x	y	z	x	y	z	x	y	z	x	y	z
O	0.0000	0.0000	2.0605	0.0000	0.0000	2.0188	0.0000	0.0000	2.0284	0.0000	0.0000	2.0567
Fe(1)	0.0000	1.1259	0.6779	0.0000	1.2005	0.6623	0.0000	1.2425	0.6988	0.0000	1.2328	0.7057
Fe(2)	0.0000	-1.1259	0.6779	0.0000	-1.2005	0.6623	0.0000	-1.2425	0.6988	0.0000	-1.2328	0.7057
Fe(3)	-1.1490	0.0000	-0.9725	-1.1488	0.0000	-0.9509	-1.0982	0.0000	-0.9888	-1.1893	0.0000	-0.9997
Fe(4)	1.1490	0.0000	-0.9725	1.1488	0.0000	-0.9509	1.0982	0.0000	-0.9888	1.1893	0.0000	-0.9997
BP86/6-311+G*												
	$^{11}A_1$, C_{2v}			$^{13}A_1$, C_{2v}			$^{15}A_2$, C_{2v}			$^{17}A_1$, C_{2v}		
	x	y	z	x	y	z	x	y	z	x	y	z
O	0.0000	0.0000	2.0560	0.0000	0.0000	2.0141	0.0000	0.0000	2.0224	0.0000	0.0000	2.0509
Fe(1)	0.0000	1.1245	0.6752	0.0000	1.1990	0.6598	0.0000	1.2430	0.6959	0.0000	1.2342	0.7031
Fe(2)	0.0000	-1.1245	0.6752	0.0000	-1.1990	0.6598	0.0000	-1.2430	0.6959	0.0000	-1.2342	0.7031
Fe(3)	-1.1465	0.0000	-0.9692	-1.1465	0.0000	-0.9477	-1.0966	0.0000	-0.9851	-1.1866	0.0000	-0.9963
Fe(4)	1.1465	0.0000	-0.9692	1.1465	0.0000	-0.9477	1.0966	0.0000	-0.9851	1.1866	0.0000	-0.9963

Table 8.10: Optimized Cartesian coordinates (Å) for μ_2 geometries of relevant states of Fe_5O^- using the TPSS, BPW91, and BP86 density functionals. Atom labels are given in Fig. 8.1b of the main text.

TPSS/6-311+G*									
	$^{16}A''$, C_s			$^{18}A''$, C_s			$^{20}A''$, C_s		
	x	y	z	x	y	z	x	y	z
O	-1.6975	1.6775	0.0000	-1.6888	1.7632	0.0000	-1.7116	1.6825	0.0000
Fe(1)	-1.8140	-0.1176	0.0000	-1.8070	-0.0440	0.0000	-1.8798	-0.1155	0.0000
Fe(2)	0.1015	1.2728	0.0000	0.1001	1.2981	0.0000	0.1212	1.4132	0.0000
Fe(3)	0.1015	-0.8334	1.1460	0.1001	-0.8254	1.1913	0.1212	-0.8521	1.1511
Fe(4)	0.1015	-0.8334	-1.1460	0.1001	-0.8254	-1.1913	0.1212	-0.8521	-1.1511
Fe(5)	1.9950	0.0318	0.0000	1.9896	-0.1075	0.0000	2.0056	-0.0745	0.0000
BPW91/6-311+G*									
	^{16}A, C_1			$^{18}A''$, C_s			^{20}A, C_1		
	x	y	z	x	y	z	x	y	z
O	-1.9687	1.3657	-0.2312	-1.6973	1.7644	0.0000	-1.9095	1.1986	-0.6183
Fe(1)	-1.7494	-0.4062	0.0051	-1.8076	-0.0446	0.0000	-1.7682	-0.5043	-0.0359
Fe(2)	-0.1209	1.2909	-0.2181	0.1041	1.3197	0.0000	-0.1461	1.5280	-0.1804
Fe(3)	0.2488	-0.4668	1.3166	0.1041	-0.8440	1.1960	0.3698	-1.3403	-0.7354
Fe(4)	0.2548	-1.1286	-0.9116	0.1041	-0.8440	-1.1960	1.8683	0.2961	-0.2468
Fe(5)	1.9296	0.3202	-0.1259	1.9807	-0.0915	0.0000	0.2222	-0.3222	1.3753
BP86/6-311+G*									
	^{16}A, C_1			$^{18}A''$, C_s			^{20}A, C_1		
	x	y	z	x	y	z	x	y	z
O	-1.9610	1.3667	-0.2273	-1.6958	1.7555	0.0000	-1.8883	1.1842	-0.6533
Fe(1)	-1.7458	-0.4042	0.0053	-1.8055	-0.0520	0.0000	-1.7596	-0.5078	-0.0408
Fe(2)	-0.1163	1.2914	-0.2158	0.1045	1.3193	0.0000	-0.1417	1.5410	-0.1839
Fe(3)	0.2480	-0.4699	1.3125	0.1045	-0.8409	1.1929	0.3763	-1.3672	-0.7075
Fe(4)	0.2506	-1.1248	-0.9121	0.1045	-0.8409	-1.1929	1.8533	0.2922	-0.2566
Fe(5)	1.9242	0.3167	-0.1248	1.9770	-0.0875	0.0000	0.2117	-0.2968	1.3756

Table 8.11: Optimized Cartesian coordinates (Å) for μ_3 geometries of relevant Fe_5O^- states using the TPSS, BPW91, and BP86 density functionals. Atom labels are given in Fig. 8.1c of the main text.

TPSS/6-311+G*															
	$^{16}A''$, C_s			^{16}A, C_1			^{18}A, C_1			$^{18}A'$, C_s			^{20}A, C_1		
	x	y	z	x	y	z	x	y	z	x	y	z	x	y	z
O	1.0854	-1.7666	0.0000	1.3832	-1.4233	-0.3458	1.1576	-1.2376	-0.8457	0.9170	-1.7356	0.0000	1.2627	-1.3462	0.5573
Fe(1)	1.7462	0.1833	0.0000	1.8277	0.3384	0.1388	1.8278	0.2079	0.2058	1.7335	0.0892	0.0000	1.7623	0.3344	-0.2566
Fe(2)	-0.0587	-0.7333	-1.1250	-0.1788	-0.7105	-1.1318	-0.2789	-0.1364	-1.3731	-0.0512	-0.6452	-1.2630	-0.0561	-1.2526	-0.8262
Fe(3)	-0.0587	-0.7333	1.1250	-0.0197	-0.7302	1.0755	0.0326	-1.1275	0.8454	-0.0512	-0.6452	1.2630	0.1155	0.0299	1.3923
Fe(4)	-0.0587	1.5360	0.0000	-0.0870	1.4739	-0.1440	-0.0346	1.4518	0.2995	-0.0512	1.5257	0.0000	-0.3210	1.4236	-0.5380
Fe(5)	-1.8805	0.2524	0.0000	-1.9378	0.0354	0.1603	-1.8779	-0.0419	0.2643	-1.8422	0.1719	0.0000	-1.8619	-0.1504	0.0692
BPW91/6-311+G*															
	$^{16}A''$, C_s						^{18}A, C_1			$^{18}A'$, C_s			^{20}A, C_1		
	x	y	z	–	–	–	x	y	z	x	y	z	x	y	z
O	1.0756	-1.7785	0.0000	–	–	–	1.1284	-1.1714	-0.9507	0.8973	-1.7446	0.0000	1.1312	-1.2938	-0.7031
Fe(1)	1.7452	0.1894	0.0000	–	–	–	1.8302	0.1831	0.2075	1.7312	0.1071	0.0000	1.8504	0.2654	0.1271
Fe(2)	-0.0611	-0.7466	-1.1335	–	–	–	-0.3040	-0.0286	-1.3955	-0.0522	-0.6606	-1.2762	-0.3377	-0.2931	-1.4484
Fe(3)	-0.0611	-0.7466	1.1335	–	–	–	0.0382	-1.2011	0.7884	-0.0522	-0.6606	1.2762	0.0869	-1.0657	0.9873
Fe(4)	-0.0611	1.5570	0.0000	–	–	–	-0.0243	1.4434	0.3934	-0.0522	1.5387	0.0000	-0.0763	1.4818	0.2291
Fe(5)	-1.8695	0.2554	0.0000	–	–	–	-1.8628	-0.0618	0.2780	-1.8313	0.1742	0.0000	-1.8467	-0.0185	0.3060
BP86/6-311+G*															
	$^{16}A''$, C_s						^{18}A, C_1			$^{18}A'$, C_s			^{20}A, C_1		
	x	y	z	–	–	–	x	y	z	x	y	z	x	y	z
O	1.0718	-1.7744	0.0000	–	–	–	1.1215	-1.1593	-0.9615	0.8873	-1.7423	0.0000	1.1206	-1.2818	-0.7253
Fe(1)	1.7415	0.1924	0.0000	–	–	–	1.8287	0.1813	0.2068	1.7289	0.1076	0.0000	1.8468	0.2612	0.1287
Fe(2)	-0.0617	-0.7459	-1.1319	–	–	–	-0.3104	-0.0169	-1.3949	-0.0520	-0.6580	-1.2767	-0.3434	-0.2674	-1.4536
Fe(3)	-0.0617	-0.7459	1.1319	–	–	–	0.0415	-1.2058	0.7784	-0.0520	-0.6580	1.2767	0.0888	-1.0816	0.9712
Fe(4)	-0.0617	1.5543	0.0000	–	–	–	-0.0236	1.4369	0.4015	-0.0520	1.5339	0.0000	-0.0728	1.4762	0.2500
Fe(5)	-1.8628	0.2526	0.0000	–	–	–	-1.8570	-0.0641	0.2831	-1.8266	0.1727	0.0000	-1.8400	-0.0218	0.3112

Table 8.12: Optimized Cartesian coordinates (Å) for μ_2 geometries of relevant states of Fe_5O using the TPSS, BPW91, and BP86 density functionals. Atom labels are given in Fig. 8.1b of the main text.

TPSS/6-311+G*									
	$^{15}A''$, C_s			$^{17}A'$, C_s			$^{19}A''$, C_s		
	x	y	z	x	y	z	x	y	z
O	-1.6926	1.6084	0.0000	-1.6725	1.7501	0.0000	-1.7029	1.6772	0.0000
Fe(1)	-1.8732	-0.1225	0.0000	-1.8317	-0.0353	0.0000	-1.8674	-0.1123	0.0000
Fe(2)	0.1046	1.2295	0.0000	0.0972	1.3024	0.0000	0.1068	1.3370	0.0000
Fe(3)	0.1046	-0.7711	1.1606	0.0972	-0.8499	1.1373	0.1068	-0.8019	1.1792
Fe(4)	0.1046	-0.7711	-1.1606	0.0972	-0.8499	-1.1373	0.1068	-0.8019	-1.1792
Fe(5)	2.0432	-0.0248	0.0000	2.0184	-0.0678	0.0000	2.0340	-0.1005	0.0000
BPW91/6-311+G*									
	$^{15}A''$, C_s			$^{17}A'$, C_s			$^{19}A''$, C_s		
	x	y	z	x	y	z	x	y	z
O	-1.7167	1.5733	0.0000	-1.6837	1.7466	0.0000	-1.7103	1.6799	0.0000
Fe(1)	-1.7939	-0.1694	0.0000	-1.8275	-0.0387	0.0000	-1.8586	-0.1132	0.0000
Fe(2)	0.1141	1.2850	0.0000	0.1013	1.3273	0.0000	0.1088	1.3548	0.0000
Fe(3)	0.1141	-0.6909	1.2663	0.1013	-0.8694	1.1420	0.1088	-0.8163	1.1917
Fe(4)	0.1141	-0.6909	-1.2663	0.1013	-0.8694	-1.1420	0.1088	-0.8163	-1.1917
Fe(5)	1.9424	-0.1836	0.0000	2.0049	-0.0493	0.0000	2.0212	-0.0893	0.0000
BP86/6-311+G*									
	$^{15}A''$, C_s			$^{17}A'$, C_s			$^{19}A''$, C_s		
	x	y	z	x	y	z	x	y	z
O	-1.7152	1.5656	0.0000	-1.6819	1.7393	0.0000	-1.7088	1.6743	0.0000
Fe(1)	-1.7867	-0.1752	0.0000	-1.8240	-0.0440	0.0000	-1.8534	-0.1174	0.0000
Fe(2)	0.1141	1.2863	0.0000	0.1018	1.3266	0.0000	0.1091	1.3545	0.0000
Fe(3)	0.1141	-0.6890	1.2641	0.1018	-0.8668	1.1398	0.1091	-0.8143	1.1905
Fe(4)	0.1141	-0.6890	-1.2641	0.1018	-0.8668	-1.1398	0.1091	-0.8143	-1.1905
Fe(5)	1.9349	-0.1808	0.0000	1.9997	-0.0464	0.0000	2.0147	-0.0872	0.0000

Table 8.13: Optimized Cartesian coordinates (Å) for μ_3 geometries of relevant Fe_5O states using the TPSS, BPW91, and BP86 density functionals. Atom labels are given in Fig. 8.1c of the main text.

TPSS/6-311+G*																
	^{15}A, C_1			$^{15}A''$, C_s			^{17}A, C_1			$^{17}A''$, C_s			^{19}A, C_1			
	x	y	z	x	y	z	x	y	z	x	y	z	x	y	z	
O	1.1788	-0.8787	-1.0940	0.9643	-1.5520	0.0000	1.1405	-1.4334	-0.4542	0.9327	-1.7194	0.0000	1.1849	-1.1601	-0.8931	
Fe(1)	1.7931	0.1685	0.2497	1.8337	0.0393	0.0000	1.8569	0.2595	0.0752	1.7438	0.1186	0.0000	1.8352	0.2216	0.2399	
Fe(2)	-0.1933	0.4064	-1.3285	-0.0563	-0.5109	-1.2724	-0.3270	-0.5565	-1.2574	-0.0503	-0.6658	-1.2322	-0.2555	-0.0226	-1.3999	
Fe(3)	0.1225	-1.3073	0.5070	-0.0563	-0.5109	1.2724	0.0830	-0.8143	1.0800	-0.0503	-0.6658	1.2322	0.0444	-1.2167	0.7576	
Fe(4)	-0.1876	1.2315	0.7469	-0.0563	1.4281	0.0000	-0.0277	1.4753	-0.0257	-0.0503	1.5389	0.0000	-0.0758	1.4249	0.3934	
Fe(5)	-1.8717	-0.2479	0.1377	-1.9407	-0.0018	0.0000	-1.9113	0.0460	0.2579	-1.8598	0.1659	0.0000	-1.8872	-0.0755	0.2644	
BPW91/6-311+G*																
	^{15}A, C_1			$^{15}A''$, C_s			^{17}A, C_1			$^{17}A''$, C_s			^{19}A, C_1			
	x	y	z	x	y	z	x	y	z	x	y	z	x	y	z	
O	1.1706	-0.7984	-1.1434	0.7989	-1.6626	0.0000	1.1053	-1.4203	-0.5239	0.9170	-1.7170	0.0000	1.1246	-1.0768	-1.0203	
Fe(1)	1.7858	0.1753	0.2648	1.8364	-0.1906	0.0000	1.8523	0.2526	0.0739	1.7391	0.1510	0.0000	1.8347	0.1743	0.2314	
Fe(2)	-0.2285	0.4576	-1.3303	-0.0393	-0.4657	-1.3140	-0.3649	-0.5199	-1.2935	-0.0522	-0.6819	-1.2478	-0.3012	0.1186	-1.4131	
Fe(3)	0.1573	-1.3547	0.4500	-0.0393	-0.4657	1.3140	0.0992	-0.8670	1.0708	-0.0522	-0.6819	1.2478	0.0431	-1.3046	0.6764	
Fe(4)	-0.2038	1.2337	0.7765	-0.0393	1.4099	0.0000	-0.0204	1.4915	0.0068	-0.0522	1.5508	0.0000	-0.0382	1.4123	0.5112	
Fe(5)	-1.8456	-0.2835	0.1661	-1.9469	0.1875	0.0000	-1.8822	0.0490	0.2919	-1.8447	0.1530	0.0000	-1.8600	-0.0927	0.2858	
BP86/6-311+G*																
	^{15}A, C_1						^{17}A, C_1			$^{17}A''$, C_s			^{19}A, C_1			
	x	y	z	–	–	–	x	y	z	x	y	z	x	y	z	
O	1.1608	-0.7869	-1.1495	–	–	–	1.0980	-1.4148	-0.5325	0.9126	-1.7120	0.0000	1.1156	-1.0646	-1.0326	
Fe(1)	1.7821	0.1725	0.2638	–	–	–	1.8502	0.2504	0.0749	1.7355	0.1551	0.0000	1.8310	0.1703	0.2304	
Fe(2)	-0.2324	0.4703	-1.3248	–	–	–	-0.3701	-0.5123	-1.2947	-0.0525	-0.6802	-1.2478	-0.3073	0.1328	-1.4112	
Fe(3)	0.1586	-1.3570	0.4379	–	–	–	0.0994	-0.8718	1.0649	-0.0525	-0.6802	1.2478	0.0443	-1.3115	0.6648	
Fe(4)	-0.2017	1.2250	0.7844	–	–	–	-0.0179	1.4875	0.0107	-0.0525	1.5465	0.0000	-0.0342	1.4071	0.5210	
Fe(5)	-1.8386	-0.2858	0.1674	–	–	–	-1.8756	0.0508	0.2965	-1.8389	0.1482	0.0000	-1.8528	-0.0943	0.2903	

Table 8.14: Vibrational frequencies (cm^{-1}) for relevant Fe_4O^- and Fe_4O states using the TPSS, BPW91, and BP86 density functionals. Vibrational mode symmetries for states with C_2 geometries are given within a pseudo-C_{2v} framework.

		Fe_4O^-														
		^{12}A, C_2	$^{12}A_1$, C_{2v}	$^{12}A_1$, C_{2v}	^{14}B, C_2			$^{14}B_2$, C_{2v}			$^{16}B_2$, C_{2v}			$^{18}A_1$, C_{2v}		
		TPSS	BPW91	BP86	TPSS	BPW91	BP86	TPSS	BPW91	BP86	TPSS	BPW91	BP86	TPSS	BPW91	BP86
ω_1	a_1	639	627	633	624	612	616	626	612	616	633	618	619	627	611	612
ω_2		360	360	363	351	345	347	364	357	360	352	342	344	315	307	308
ω_3		295	298	299	200	207	208	241	246	247	226	234	235	209	217	220
ω_4		176	180	182	153	159	160	160	170	171	160	168	168	165	168	168
ω_5	a_2	83	100	107	84	125	130	145	214	234	162	160	160	137	123	123
ω_6	b_1	222	227	228	244	247	248	209	219	221	206	201	203	188	171	171
ω_7		142	136	136	88	122	123	109	130	131	103	113	111	136	141	140
ω_8	b_2	376	358	363	413	401	404	381	364	368	409	396	399	474	462	466
ω_9		76	85	111	185	186	187	187	195	200	235	230	231	65	152	146
		Fe_4O														
		$^{11}A_1$, C_{2v}			$^{13}A_1$, C_{2v}			–			$^{15}A_2$, C_{2v}			$^{17}A_1$, C_{2v}		
		TPSS	BPW91	BP86	TPSS	BPW91	BP86	–	–	–	TPSS	BPW91	BP86	TPSS	BPW91	BP86
ω_1	a_1	679	669	674	649	638	642	–	–	–	657	643	646	659	643	644
ω_2		360	362	365	363	356	359	–	–	–	373	363	365	332	323	324
ω_3		299	294	296	244	248	248		–		240	248	249	200	212	214
ω_4		198	192	193	162	171	172	–	–	–	172	176	177	175	176	176
ω_5	a_2	$58i$	$30i$	33	83	129	133	–	–	–	$72i$	$116i$	$113i$	167	154	153
ω_6	b_1	240	240	242	213	226	229	–	–	–	210	206	207	197	186	188
ω_7		136	133	133	80	118	118	–	–	–	129	140	139	125	135	134
ω_8	b_2	385	419	514	449	437	440	–	–	–	449	433	436	449	432	435
ω_9		101	227	250	219	218	220	–	–	–	233	231	232	166	174	174

Table 8.15: Vibrational frequencies (cm^{-1}) for μ_2 geometries of relevant Fe_5O^- and Fe_5O states using the TPSS, BPW91, and BP86 density functionals. Vibrational mode symmetries are given for species with C_s symmetries; modes for C_1 states are listed in order of decreasing frequency.

Fe_5O^-										
		$^{16}A''$, C_s	^{16}A, C_1	^{16}A, C_1	$^{18}A''$, C_s			^{20}A, C_1	^{20}A, C_1	$^{20}A''$, C_s
		TPSS	BPW91	BP86	TPSS	BPW91	BP86	TPSS	BPW91	BP86
ω_1	a'	638	626	630	646	632	635	631	612	613
ω_2		408	395	399	416	404	408	456	476	482
ω_3		355	343	346	338	327	330	326	313	315
ω_4		275	278	278	287	282	282	251	252	254
ω_5		224	230	232	225	225	225	222	237	238
ω_6		207	207	209	213	206	207	211	209	209
ω_7		139	195	195	167	160	159	143	199	199
ω_8		115	186	186	128	123	123	126	173	173
ω_9	a''	217	143	143	207	203	205	212	147	149
ω_{10}		191	114	113	197	184	185	196	129	129
ω_{11}		108	99	100	144	143	143	135	107	109
ω_{12}		41	54	54	70	44	43	46	49	52
Fe_5O										
		$^{15}A''$, C_s			$^{17}A'$, C_s			$^{19}A''$, C_s		
		TPSS	BPW91	BP86	TPSS	BPW91	BP86	TPSS	BPW91	BP86
ω_1	a'	673	658	663	674	660	663	657	644	646
ω_2		442	425	429	444	430	434	459	443	446
ω_3		356	347	350	354	344	346	328	318	320
ω_4		275	285	286	283	280	281	266	262	264
ω_5		222	214	214	232	233	234	223	219	219
ω_6		181	189	191	214	208	209	213	214	215
ω_7		147	157	157	162	156	156	169	155	154
ω_8		93	94	96	135	128	128	128	124	124
ω_9	a''	231	250	252	214	207	207	218	207	208
ω_{10}		164	178	179	187	177	178	203	190	190
ω_{11}		100	125	125	146	145	145	131	132	131
ω_{12}		$12i$	79	76	73	46	44	76	37	30

Table 8.16: Vibrational frequencies (cm^{-1}) for μ_3 geometries of relevant Fe_5O^- and Fe_5O states using the TPSS, BPW91, and BP86 density functionals. Vibrational mode symmetries are given for species with C_s symmetries; modes for C_1 states are listed in order of decreasing frequency.

		Fe_5O^-												
		$^{16}A''$, C_s			$^{16}A''$, C_s	^{18}A, C_1			$^{18}A'$, C_s			^{20}A, C_1		
		TPSS	BPW91	BP86	TPSS	TPSS	BPW91	BP86	TPSS	BPW91	BP86	TPSS	BPW91	BP86
ω_1	a'	564	551	557	559	556	539	542	559	545	548	561	532	534
ω_2		349	337	339	382	386	377	381	335	329	331	357	379	383
ω_3		307	303	304	354	342	334	336	300	297	298	315	311	312
ω_4		273	268	268	289	290	287	287	241	235	236	275	255	258
ω_5		199	190	191	262	247	244	246	211	198	198	268	252	253
ω_6		180	182	183	216	244	230	230	185	189	190	231	233	234
ω_7		166	155	156	193	215	209	210	160	162	163	209	217	218
ω_8		135	136	135	171	196	186	187	103	102	101	190	191	191
ω_9	a''	307	302	305	148	169	172	173	266	263	267	160	155	157
ω_{10}		160	162	165	114	155	158	160	214	207	209	133	142	141
ω_{11}		151	149	151	108	140	142	143	193	178	179	124	130	131
ω_{12}		102	107	107	83	98	105	106	100	99	98	83	87	89
		Fe_5O												
		^{15}A, C_1			$^{15}A''$, C_s		^{17}A, C_1			$^{17}A''$, C_s			^{19}A, C_1	
		TPSS	BPW91	BP86	TPSS	BPW91	TPSS	BPW91	BP86	TPSS	BPW91	BP86	TPSS	BPW91	BP86
ω_1	a'	587	569	572	591	604	569	552	555	584	571	575	566	548	550
ω_2		423	423	427	390	349	403	393	397	331	326	328	384	382	385
ω_3		345	337	339	344	334	341	332	334	297	297	299	335	327	328
ω_4		306	298	300	279	292	287	289	290	249	238	239	276	272	274
ω_5		278	276	278	215	221	282	278	280	217	218	220	262	253	254
ω_6		252	251	252	199	178	231	229	230	176	181	182	244	237	238
ω_7		207	204	205	159	154	222	218	219	150	157	159	220	214	214
ω_8		199	197	197	134	117	204	196	196	95	102	102	205	195	196
ω_9	a''	179	178	179	335	297	154	162	163	367	377	382	177	175	177
ω_{10}		163	167	168	239	224	148	152	152	215	213	214	141	162	162
ω_{11}		139	154	155	159	184	130	130	131	181	165	165	128	146	146
ω_{12}		46	88	88	69	52	83	94	94	90	94	93	87	99	99

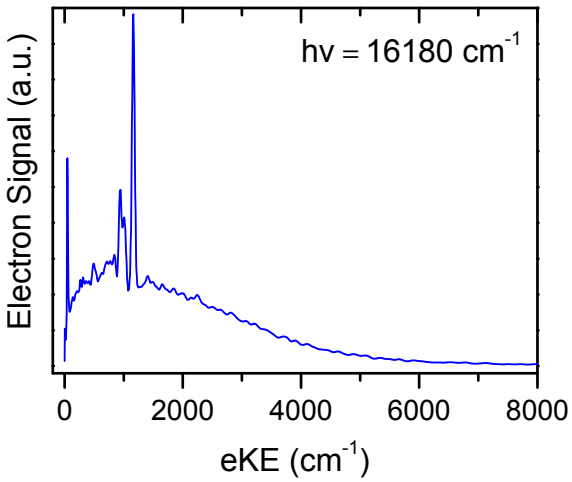

Figure 8.10: Representative trace showing the contributions of both thermionic emission (broad) and direct detachment (sharp) structure in the SEVI spectra of Fe_5O^-.

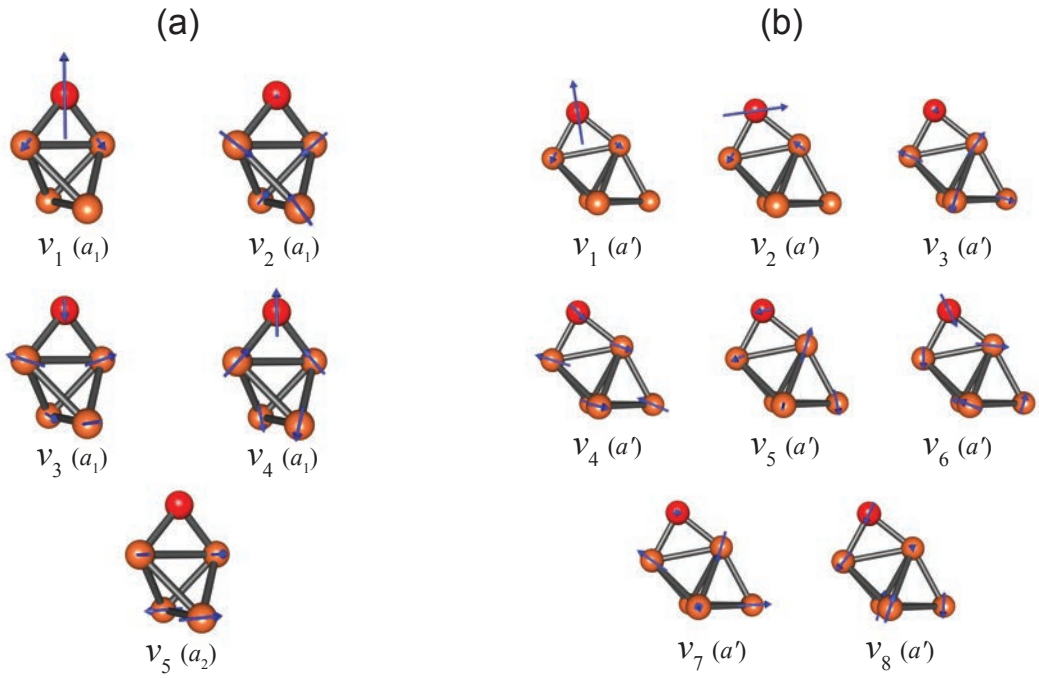

Figure 8.11: Relevant vibrational normal modes of a) $Fe_4O^{0/-}$ and b) $Fe_5O^{0/-}$.

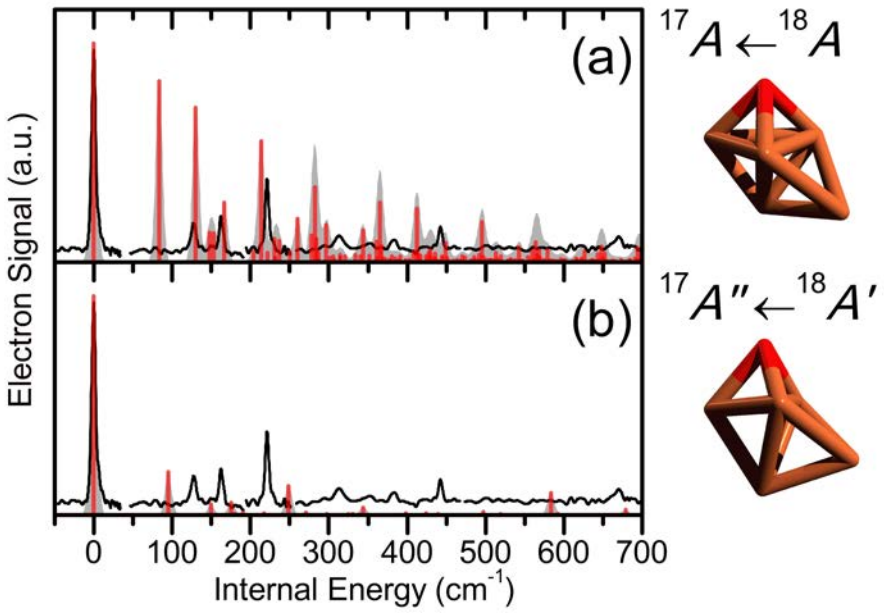

Figure 8.12: TPSS/6-311+G* FC simulations of photodetachment of (a) C_1-symmetric and (b) C_s-symmetric μ_3 geometries of Fe_5O^-. All simulations are plotted as stick spectra (red) and after convolution with a 10 cm^{-1} Gaussian line shape function (grey), and compared to high-resolution SEVI traces (black).

Chapter 9

Vibrational structure of $(TiO_2)_n^-$ (n=3-8) clusters

The content and figures of this chapter are reprinted or adapted with permission from
M. L. Weichman, X. Song, M. R. Fagiani, S. Debnath, S.Gewinner, W. Schöllkopf, D. M. Neumark, and K. R. Asmis, "Gas phase vibrational spectroscopy of cold $(TiO_2)_n^-$ (n=3-8) clusters" *J. Chem. Phys.* **144**, 124308 (2016).

Abstract

We report infrared photodissociation (IRPD) spectra for the D_2-tagged titanium oxide cluster anions $(TiO_2)_n^-$ with n=38 in the spectral region from 450 to 1200 cm^{-1}. The IRPD spectra are interpreted with the aid of harmonic spectra from BP86/6-311+G* density functional theory calculations of energetically low-lying isomers. We conclusively assign the IRPD spectra of the n=3 and n=6 clusters to global minimum energy structures with C_s and C_2 symmetry, respectively. The vibrational spectra of the n=4 and n=7 clusters can be attributed to contributions of at most two low-lying structures. While our calculations indicate that the n=5 and n=8 clusters have many more low-lying isomers than the other clusters, the dominant contributions to their spectra can be assigned to the lowest energy structures. Through agreement between the calculated and experimental spectra, we can draw conclusions about the size-dependent evolution of the properties of $(TiO_2)_n^-$ clusters, and on their potential utility as model systems for catalysis on a bulk TiO_2 surface.

9.1 Introduction

TiO_2 is an important, extensively-studied semiconducting material, with varied applications as a catalyst, photocatalyst, catalyst support, gas sensor, and pigment. TiO_2 was first identified as a photocatalyst for water splitting by Fujishima and Honda in 1972.[404] Since then its photoelectrochemical properties have been studied not only for further applications in water splitting catalysis[405,406] but for use in photovoltaics,[407,408] the degradation of organic pollutants,[409,410] and CO_2 reduction.[411,412] In the bulk, TiO_2 exists in rutile, anatase, and brookite crystal structures;[103] the bulk rutile structure is the thermodynamic ground state under ambient conditions, but anatase is predicted to be the stable phase for nanoparticles smaller than 14 nm.[413]

An optimal photocatalyst should have a band gap tuned for absorption of the solar spectrum. The band gap of TiO_2, 3.05 eV for rutile and 3.15 eV for anatase,[414] allows for absorption of only ∼5 % of sunlight.[415] The use of TiO_2 nanostructures, perhaps in combination with doping, promises more tunable electronic structure for optimization of photocatalytic properties[416,417] and increased surface area for reaction. As such, various nanostructures have been synthesized and tested for wide applications.[418–423] Characterization of the properties of TiO_2 on the nano-scale is therefore of great interest.

Small gas-phase clusters are an insightful window into the study of larger metal oxide systems. In addition to being tractable for both experimental and computational study, small clusters can serve as models for catalytically active point defect sites on surfaces,[102,363,424] which often demonstrate distinct bonding and stoichiometry from the bulk. Clusters display dramatically different structures and reactivity as a function of size;[366,367,392] their study can therefore elucidate the evolution of properties and emergence of macroscopic phenomena as one moves towards the bulk. Negatively-charged $(TiO_2)_n^-$ clusters are particularly interesting models for catalysis, as photocatalytic reduction of CO_2 on bulk titania requires

migration of a photoexcited electron to the surface and subsequent transfer to the adsorbate.[412] We therefore aim to characterize how the presence of an excess negative charge affects the structure and properties of titanium oxide clusters. In the current work we use cryogenic ion trap vibrational spectroscopy of messenger-tagged, mass-selected anions to elucidate the structures of the $(TiO_2)_n^-$ clusters with n=3-8.

Gas-phase titanium oxide clusters have been investigated with several experimental methods. Photoionization mass spectrometry experiments of neutral Ti_nO_m clusters generated with laser ablation showed that Ti_nO_{2n} and Ti_nO_{2n+1} stoichiometries were most prevalent.[425] Infrared resonant multiphoton ionization experiments conducted on large neutral clusters compared the broad IR features observed to the phonon modes of bulk rutile TiO_2.[159,426] The IR multiple photon photodissociation (IRMPD) action spectrum of $Ti_4O_{10}^-$ has also been reported.[427,428] Anion photoelectron spectroscopy (PES) experiments on $(TiO_2)_n^-$ for n=1-10[71,429] yielded the electron affinities and band gaps of the neutral clusters as a function of size, but lacking vibrational resolution could not shed light on cluster geometries. The reactivity of some small neutral and cationic titanium oxide clusters have also been studied experimentally with CO, CO_2, and small hydrocarbons.[430–433] Very recently, Yin and Bernstein[434] reported an experimental study of water oxidation on Ti_2O_4 and Ti_2O_5 neutral clusters under irradiation with visible light.

Higher-resolution spectroscopies have been applied to the smallest titanium dioxide clusters. The rotational, vibrational and electronic structure of triatomic TiO_2 and TiO_2^- have been well studied.[261,435–437] IR spectra have been observed for neutral $(TiO_2)_2$ in a rare gas matrix.[438] A slow photoelectron velocity-map imaging study of cryogenically cooled anions (cryo-SEVI) identified the two lowest energy isomers of $(TiO_2)_2^-$ and elucidated the vibronic structure of the corresponding neutrals.[352]

While there is relatively little experimental work on $(TiO_2)_n$ with $n \geq 3$, a fair number of theoretical studies of neutral, and to a lesser extent, anionic clusters in this size range have been carried out. For the neutral clusters, most of the theoretical work has used density functional theory (DFT) to characterize the lowest-lying $(TiO_2)_n$ isomers in the range n=1-15.[416,439–450] Only Qu and Kroes[441] and Tang *et al.*[448] report on low-lying anionic $(TiO_2)_n^-$ isomers with DFT. Several of these DFT studies made comprehensive searches for the global minimum energy neutral structures, using genetic algorithms,[440,450,451] simulated annealing,[440,451] systematic topological structure generation,[448] and basin hopping algorithms.[449] Of these studies, Tang *et al.*,[448] Marom *et al.*,[449] and Chen and Dixon[450] report the most thorough lists of candidate structures for neutral $(TiO_2)_n$, and are largely in agreement regarding the energetically lowest-lying isomers.

The highest-level theoretical results for $(TiO_2)_n$ and $(TiO_2)_n^-$ with n=1-4 are reported by Li and Dixon,[417] using coupled cluster theory (CCSD(T)) with large basis sets, core-valence correlation, and scalar relativistic corrections. The predictions made in this coupled-cluster study for the most stable $(TiO_2)_2^-$ isomers, as well as the same authors' analogous calculations for $(ZrO_2)_2^-$,[452] are in excellent agreement with recent high-resolution cryo-SEVI experiments.[352] Beyond the coupled cluster study for n=1-4,[417] the structures of the anionic $(TiO_2)_n^-$ clusters with $n \geq 5$ are not well-characterized theoretically, and the existing DFT

reports are not in good agreement for many cluster sizes. The most stable anionic structures are also likely to differ from those of the corresponding neutral clusters.[352,417]

The combination of ion trapping and cooling with vibrational action spectroscopy[453] has emerged as a viable, sensitive method for structural characterization of complex gas-phase ions,[47,48] including mass-selected transition metal oxide cluster ions.[367,454] In this work, we present the first vibrationally-resolved spectra of titanium dioxide cluster anions $(TiO_2)_n^-$, n=3-8, using infrared photodissociation (IRPD) spectroscopy. We also report a thorough DFT investigation of the energetics and vibrational structure of these anionic clusters. The experimental IR action spectra are acquired in the linear absorption regime via messenger-tagging of ions with D_2 in a radiofrequency ion trap, and the measurement of D_2-loss upon irradiation with tunable IR light between 450–1200 cm^{-1}.[46] The positions and intensities of features in these IRPD spectra can be directly compared to simulated DFT results. The clusters are cooled in a clustering channel after production in a laser vaporization source, and thermalized by many collisions with a cold buffer gas to cryogenic temperatures in the ion trap held at 14–25 K. In principle, this preparation ensures both that the clusters are vibrationally cold and that only the energetically most stable isomers are present.

Comparison of these IRPD spectra to calculations allows assignment of the most stable $(TiO_2)_n^-$ isomers for n=3-8. We conclusively identify the C_s-symmetric lowest-lying isomer of $(TiO_2)_3^-$ and the C_2 lowest-lying $(TiO_2)_6^-$ structure, and we can confidently isolate the two low-lying structures that contribute to the experimental spectra of $(TiO_2)_4^-$ and $(TiO_2)_7^-$. The $(TiO_2)_5^-$ and $(TiO_2)_8^-$ clusters exhibit substantially more "glassy" potential energy surfaces, with many distinct, nearly energetically degenerate isomers. Nonetheless, the calculated spectra for the lowest energy isomers agree qualitatively with experiment, and we assign the dominant spectral contributions to these isomers. Through analysis of the calculated and experimental results for $(TiO_2)_n^-$ (n=3-8), we can directly observe evolution of the properties of these titanium oxide clusters with size.

9.2 Experimental Methods

The IRPD method and apparatus have been described in detail in Chap. 2.

$(TiO_2)_n^-$ clusters are prepared in a pulsed laser vaporization source.[158] A frequency-doubled Nd:YAG laser operated at 50 Hz is focused onto a rotating titanium rod, and the resulting plasma is entrained in a pulse of 0.75% O_2 in He from a General Valve.

The desired $(^{48}Ti^{16}O_2)_n^-$ clusters are selected with the quadrupole mass filter. The ion trap is filled continuously with a buffer gas consisting of either pure D_2 or a mixture of 10% D_2 in He, and is held at cryogenic temperatures between 14 and 25 K. For each $(TiO_2)_n^-$ cluster, the trap temperature and the composition of the buffer gas are optimized for tagging with a single D_2 molecule.

Here we use the range 450–1200 cm^{-1} in 3 cm^{-1} steps; for each step, $\sim$ 100 TOF traces are acquired and averaged. Attenuated laser pulses using 2-33% of the full FEL power are employed to ensure operation within the linear absorption regime and avoid saturation.

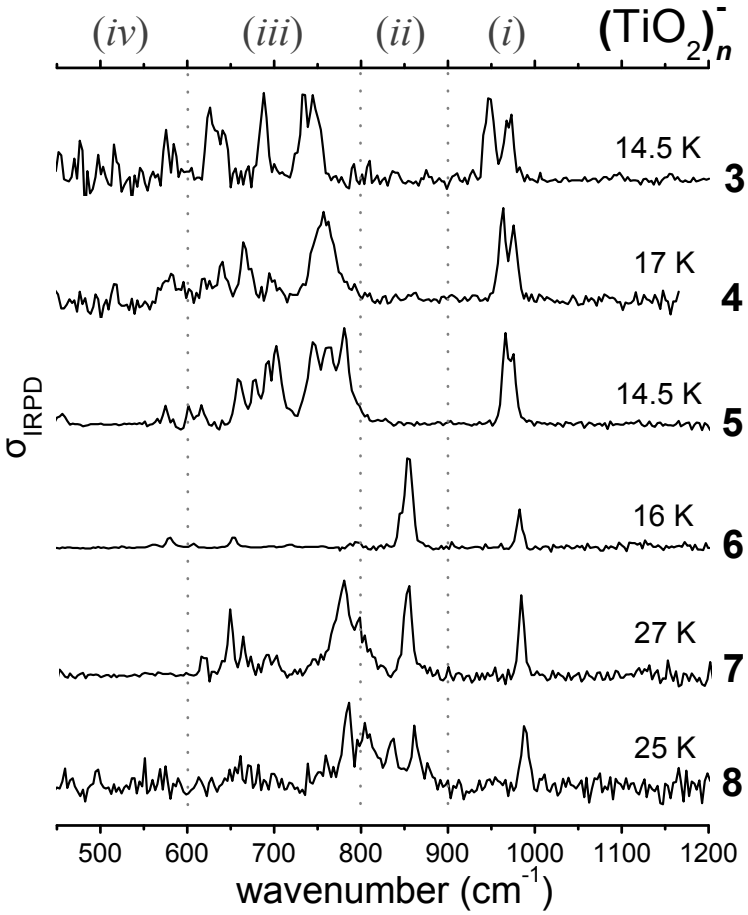

Figure 9.1: Experimental IRPD spectra of D_2-tagged $(TiO_2)_n^-$ (n=3-8). Regions (i)-(iv) of vibrational structure are marked with dashed lines. The trapping temperature for each cluster is also indicated.

9.3 Calculations

DFT calculations were carried out to find the relative energies, optimized geometries, harmonic vibrational frequencies, IR intensities, and vertical detachment energies of the lowest-lying $(TiO_2)_n^-$ isomers. We use the BP86 functional as it has been found to qualitatively reproduce higher-level CCSD(T) results for the energetics and geometries of metal oxide clusters,[417,455] and has provided a good comparison for experimental spectroscopic work on TiO_2^- and $(TiO_2)_2^-$.[261,352] The 6-311+G* basis set was used for both Ti and O atoms, with full treatment of all electrons.[400,401] Transition state optimizations were also carried out with BP86/6-311+G* in order to locate isomerization barriers between $(TiO_2)_4^-$ clusters demonstrating similar bond connectivity. Additionally, we determined the harmonic vibrational frequencies for the lowest-lying $(TiO_2)_3^-$ cluster complexed with D_2. In this case

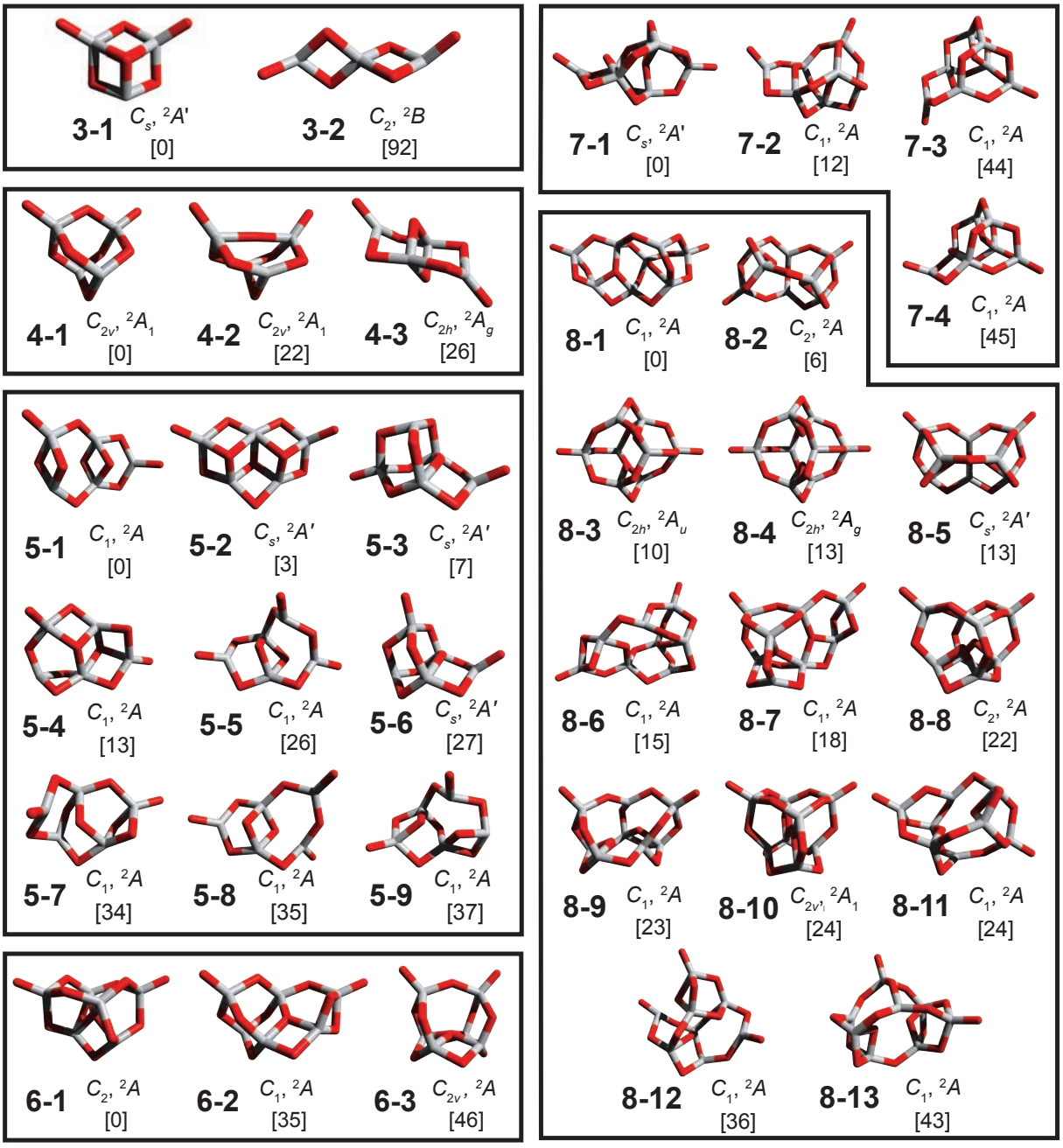

Figure 9.2: BP86/6-311+G* minimum energy structures, point groups, electronic states and relative energies (kJ/mol) of energetically low-lying isomers of $(TiO_2)_n^-$ (n=3-8) clusters.

we use a semiempirical dispersion correction as parametrized by Grimme,[456] in addition to the BP86 functional, hereafter referred to as BP86+D. All *ab initio* calculations were carried out using Gaussian 09.[402]

Potential low-lying $(TiO_2)_n^-$ structures were identified through a comprehensive literature search. Chemical intuition alone is not sufficient to identify the most stable structural candidates, particularly for the larger clusters, owing to the complexity of the potential energy landscapes in question and the wealth of structural isomers. Thorough lists of low-lying anionic and neutral isomers have previously been identified by Li and Dixon[417] for n=3-4 and Tang *et al.*[448] for n=3-6, and by Marom *et al.*[449] for the neutral $(TiO_2)_n^-$ clusters with n=3-10. We considered all reasonably low-lying structures proposed in these works, and reoptimized them with spin-unrestricted BP86/6 311+G* calculations as doublet anions; the literature is in agreement that $(TiO_2)_n^-$ anions have a single unpaired electron.[352,417,441,448] All $< S^2 >$ values calculated for the clusters reported here fall very close to the expected value of 0.75 for doublet states. We report all $(TiO_2)_n^-$ (n=3-8) isomers that were found to lie within 50 kJ/mol of the lowest energy structure after correction for vibrational zero point energies (ZPEs).

Full lists of calculated isomer energetics, electronic states, vertical detachment energies, harmonic vibrational frequencies above 400 cm^{-1}, and optimized geometries for all structures can be found in the Supporting Information (SI), as well as visualizations of the singly occupied molecular orbitals (SOMOs) of relevant clusters (Fig. 9.7).

9.4 Results and Discussion

Experimental IRPD spectra of the $(TiO_2)_n^-$ (n=3-8) clusters in the region of 450–1200 cm^{-1} are shown in Fig. 9.1; the ion trapping temperatures used for each cluster are also indicated. Experimental peak positions and widths are reported in Table 9.1. Structures, relative energies, point groups, and electronic states for all calculated low energy clusters are shown in Fig. 9.2. Simulated IR spectra for these isomers are plotted and compared to experimental results in Figs. 9.3-9.6. For ease of visual comparison, the experimental data in these figures are smoothed by averaging of adjacent data points from Fig. 9.1, reducing noise at the slight cost of resolution. Simulations are derived from unscaled harmonic vibrational frequencies and IR intensities, and are plotted both as stick spectra (red) and as traces convoluted with a 10 cm^{-1} fwhm Gaussian line shape function (blue) to account for rotational band contours as well as the spectral width of the laser pulse.

Based on comparison of the IRPD results with the *ab initio* vibrational normal modes and harmonic spectra, $(TiO_2)_n^-$ clusters exhibit four general types of IR active vibrational modes, with characteristic frequency ranges delineated in Fig. 9.1 (*i*) stretching modes of terminal Ti-O bonds (900–1000 cm^{-1}); (*ii*) stretching modes associated with groups of three Ti-O-Ti bridges tetrahedrally coordinated to a terminal Ti-O moiety (800–900 cm^{-1}); (*iii*) lower-frequency stretching modes of Ti-O-Ti bridges (600–800 cm^{-1}); and (*iv*) more delocalized bending, wagging, rocking, and ring breathing modes (<600 cm^{-1}). Qu and Kroes[441] have

Table 9.1: Experimental vibrational frequencies (cm^1) of $(TiO_2)_n^-$ clusters. Band positions and full widths at half-maximum (in parentheses) are determined by a least squares fit of a Gaussian line function to the experimental data.

Cluster	Region	Band Positions (cm^{-1})
$(TiO_2)_3^-$	(*i*)	970(13), 948(15)
	(*iii*)	746(15), 733(8), 688(9), 640(12), 626(10)
	(*iv*)	576(6)
$(TiO_2)_4^-$	(*i*)	976(9), 963(9)
	(*iii*)	757(27), 697(12), 667(13), 640(9)
	(*iv*)	580(35), 517(8)
$(TiO_2)_5^-$	(*i*)	975(8), 966(7)
	(*iii*)	781(12), 763(15), 745(13), 703(13), 691(6) 678(11), 660(10), 616(11), 602(6)
	(*iv*)	575(6), 455(14)
$(TiO_2)_6^-$	(*i*)	982(8)
	(*ii*)	854(12)
	(*iii*)	794(15), 719(8), 653(8), 607(6)
	(*iv*)	580(8), 562(12)
$(TiO_2)_7^-$	(*i*)	982(7)
	(*ii*)	851(10)
	(*iii*)	795(11), 776(18), 700(6), 689(9), 661(6), 647(7), 616(7)
$(TiO_2)_8^-$	(*i*)	989(10)
	(*ii*)	862(6), 836(9), 806(20)
	(*iii*)	784(9), 760(4)

previously simulated IR absorption spectra for neutral $(TiO_2)_n$ (n=2-9) clusters, and noted similar categories of vibrational structure in these regions. Chen and Dixon[450] have also calculated terminal Ti-O stretching frequencies and IR intensities for the neutral clusters with n=2-13.

In our experimental spectra, all six $(TiO_2)_n^-$ clusters with n=3-8 show vibrational activity in region (*i*), indicating that each has dangling Ti-O bonds. Vibrational activity is seen in region (*ii*) for clusters with $n \geq 6$, while the smaller clusters show a distinctive gap with no absorption in this region. All clusters show structure in region (*iii*) with varying degrees of intensity, and most show weak structure in region (*iv*). Each experimental spectrum compares quite well qualitatively to the simulated spectrum of at least one low-lying predicted structure. The unscaled calculated frequencies of the best-fit simulations are generally lower than those observed experimentally, by factors of 0.99 in region (*i*), 0.97 in region (*ii*), and

a range of 0.93-0.99 in regions (*iii*) and (*iv*).

We now give more detailed analysis of the experimental and theoretical results for each isomer in turn.

9.4.1 $(TiO_2)_3^-$

The experimental IRPD spectrum for $(TiO_2)_3^-$ (Fig. 9.3) exhibits an intense pair of vibrational features in region (*i*) along with a series of strong features spanning region (*iii*) and the high-frequency edge of region (*iv*). Comparison with DFT results supports an unambiguous assignment of the experimental spectrum to the isomer **3-1**, based on calculated energetics and simulated linear IR spectra.

The **3-1** C_s structure has been previously calculated to be the ground state structure for the n=3 anion,[417,441,448] and is widely agreed upon as the global minimum energy structure for the neutral n=3 cluster as well.[416,417,439–451] The next lowest-lying anionic isomer, the C_2 structure **3-2**, is calculated to lie 92 kJ/mol higher in energy with BP86/6-311+G*; with CCSD(T), Li and Dixon[417] find that the **3-2** anion lies 172 kJ/mol above **3-1**. The presence of the **3-2** structure experimentally can be ruled out based on these energetics and the considerably poorer agreement between its simulated spectrum and experiment.

Through comparison with the simulated IR spectrum of isomer **3-1** in Fig. 9.3, we can assign the experimental vibrational features. The two highest-frequency vibrations observed here at 970 cm^{-1} and 948 cm^{-1} correspond respectively to symmetric and antisymmetric stretching modes involving the two terminal Ti-O bonds. At the BP86/6-311+G* level of theory, these modes are calculated to lie at 961 cm^{-1} and 938 cm^{-1} respectively. The series of experimental peaks at 746 cm^{-1}, 733 cm^{-1}, 688 cm^{-1}, 640 cm^{-1}, 626 cm^{-1}, and 576 cm^{-1} are various stretching modes of Ti-O-Ti bridges in the central ring of the cluster. These features are well-matched by calculated frequencies of 724 cm^{-1}, 723 cm^{-1}, 665 cm^{-1}, 611 cm^{-1}, 605 cm^{-1}, and 554 cm^{-1}. The separation of the two highest energy modes (724/723 cm^{-1}) in region (*iii*) increases from 1 cm^{-1} to 6 cm^{-1} when the D_2 tag is considered explicitly in a BP86+D/6 311+G* calculation (see Fig. 9.8 in the SI), in improved agreement with the experimental observation of two maxima separated by 13 cm^{-1}. The experimental features in region (*iii*) show decreasing intensity with decreasing frequency; the calculated spectrum demonstrates qualitatively similar structure.

9.4.2 $(TiO_2)_4^-$

The experimental IRPD spectrum of $(TiO_2)_4^-$ (Fig. 9.3) shows an intense, narrowly spaced pair of peaks in region (*i*), one very intense, broad feature on the high energy side of region (*iii*), and several weaker features spanning regions (*iii*) and (*iv*).

There are three low-lying structures for $(TiO_2)_4^-$. The literature is in reasonable agreement that for the neutral cluster the C_{2v} structure **4-2** yields the lowest energy.[416,417,440,442–444,446,448–451] Previous DFT studies by Qu and Kroes[441] and Tang *et al.*[448] concur with our BP86/6 311+G* results that the C_{2v} structure **4-1** gives the most stable

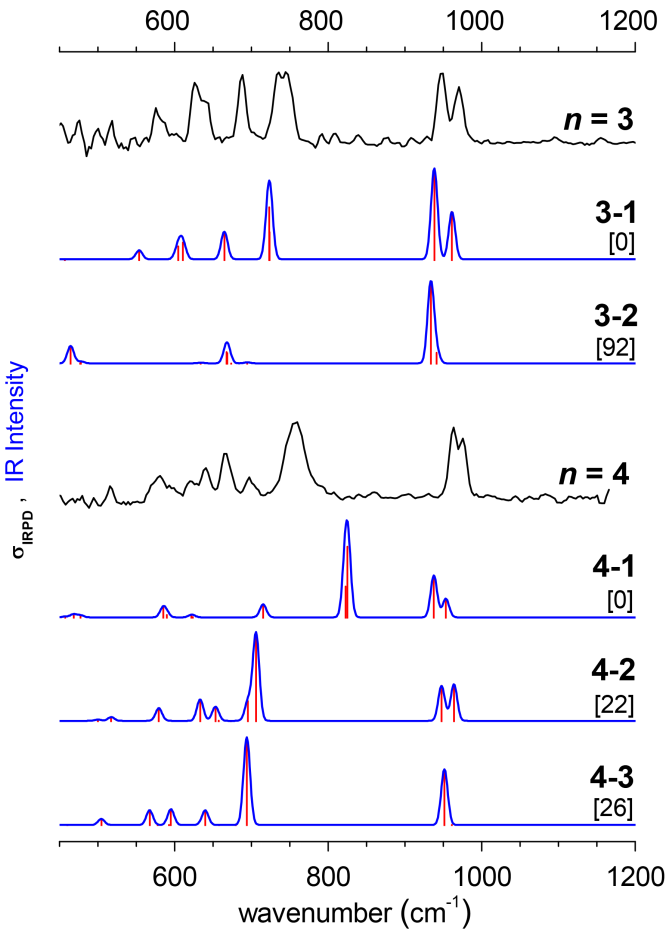

Figure 9.3: Smoothed experimental IRPD spectra (black) of D_2-tagged $(TiO_2)_n^-$ (n=3, 4) and simulated linear IR absorption traces (blue), stick spectra (red), and relative energies (kJ/mol) of the predicted lowest-lying isomers at the BP86/6-311+G* level of theory.

anion. We find that in the anion **4-2** and **4-3** lie 22 kJ/mol and 26 kJ/mol above **4-1**, respectively. CCSD(T) calculations by Li and Dixon[417] find the C_{2h} structure **4-3** lowest in energy for the anion, with **4-2** and **4-1** lying incrementally higher in energy by 1 kJ/mol and 3 kJ/mol respectively. Li and Dixons CCSD(T) results accurately predicted the energetic ordering of anionic isomers observed experimentally in photodetachment of $(TiO_2)_2^-$,[352] where DFT methods had failed.[441,448] The relative energies of the $(TiO_2)_4^-$ isomers given by CCSD(T) may therefore be more trustworthy than the DFT values, in which case the three n=4 isomers are predicted to be nearly isoenergetic.

The experimental n=4 spectrum has a strong feature in region (*iii*) at 757 cm^{-1}, and no structure in region (*ii*). The simulated spectrum of **4-1**(Fig. 9.3) has intense IR absorptions in region (*ii*) at 825 cm^{-1} and 822 cm^{-1}, corresponding to antisymmetric and symmetric Ti-

O-Ti bridge stretching; analogous strongly IR active bridge-stretching modes are shifted to lower frequencies of 706 cm^{-1} and 696 cm^{-1} in **4-2**. The strong region (*ii*) modes of **4-1** have frequencies much higher than experiment, especially given the general trend that calculated frequencies for the best-fit isomers are consistently lower than experimental values. The corresponding IR active transitions in **4-2**, however, are predicted too low to provide a good match with experiment, at factors of 0.92-0.93 lower than the experimental value. It is therefore worth considering that the experiment probes a fluxional cluster encompassing the **4-1** and **4-2** basins, with vibrational frequencies that are not well represented by the harmonic approximation.

Unlike most clusters reported in this work, **4-1** and **4-2** have identical bond connectivity. With BP86/6-311+G*, the transition state between **4-1** and **4-2** is of C_s symmetry, and lies 36 kJ/mol above **4-1** and only 14 kJ/mol above **4-2** without ZPE correction. By comparison, the barrier between structures **4-2** and **4-3** lies much higher in energy: 67 kJ/mol above **4-2** and 63 kJ/mol above **4-3**. Such a small **4-1/4-2** barrier suggests that these isomers are perhaps not separate spectroscopic species, but two shallow local minima of a rather floppy system. The *ab initio* harmonic frequency analysis of **4-1** and **4-2** therefore may not accurately capture the vibrational signature of this particular Ti-O-Ti bridging motif. For comparison, we plot the calculated IR spectrum of the **4-1/4-2** transition state alongside the **4-1** and **4-2** spectra in Fig. 9.9. The **4-1/4-2** TS spectrum looks intermediate to those of the **4-1** and **4-2** isomers, lending further support to an assignment to a fluxional **4-1/4-2** system. Though beyond the scope of the current work, it would be of interest to investigate the isomerization barrier between these two structures at the CCSD(T) level of theory.

A significant contribution from isomer $4-3$ is unlikely based on the vibrational structure in region (*i*). Experimentally, we observe peaks at 976 cm^{-1} and 963 cm^{-1} corresponding to two free Ti-O stretching modes. In structure **4-3**, based on the C_{2h} symmetry of the system, only the antisymmetric Ti-O stretching mode calculated at 952 cm^{-1} is IR active. The C_{2v} **4-1** and **4-2** structures, on the other hand, have two IR active modes in this region, at 953 cm^{-1} and 938 cm^{-1} for **4-1**, and 964 cm^{-1} and 948 cm^{-1} for **4-2**, and can therefore account for all features observed experimentally. We cannot, however, rule out a small contribution from isomer **4-3**. The calculated frequency of the IR active Ti-O stretching mode for **4-3** falls close to the two calculated frequencies for **4-1** and **4-2**, and could contribute to the doublet feature observed in region (*i*).

9.4.3 $(TiO_2)_5^-$

The $(TiO_2)_5^-$ IRPD spectrum (Fig. 9.4) shows a single somewhat broad feature in region (*i*), a series of closely-spaced, intense absorption features in region (*iii*), and weaker features extending into region (*iv*).

Nine $(TiO_2)_5^-$ isomers are calculated to lie within 50 kJ/mol of the lowest energy cluster, many of which are effectively degenerate within the accuracy of DFT. Our calculations find the C_1-symmetric **5-1** structure lowest in energy, with two C_s structures, **5-2** and **5-3**, lying 3 kJ/mol and 7 kJ/mol higher, respectively. Prior DFT work by Tang *et al.*[448] reports **5-2** as

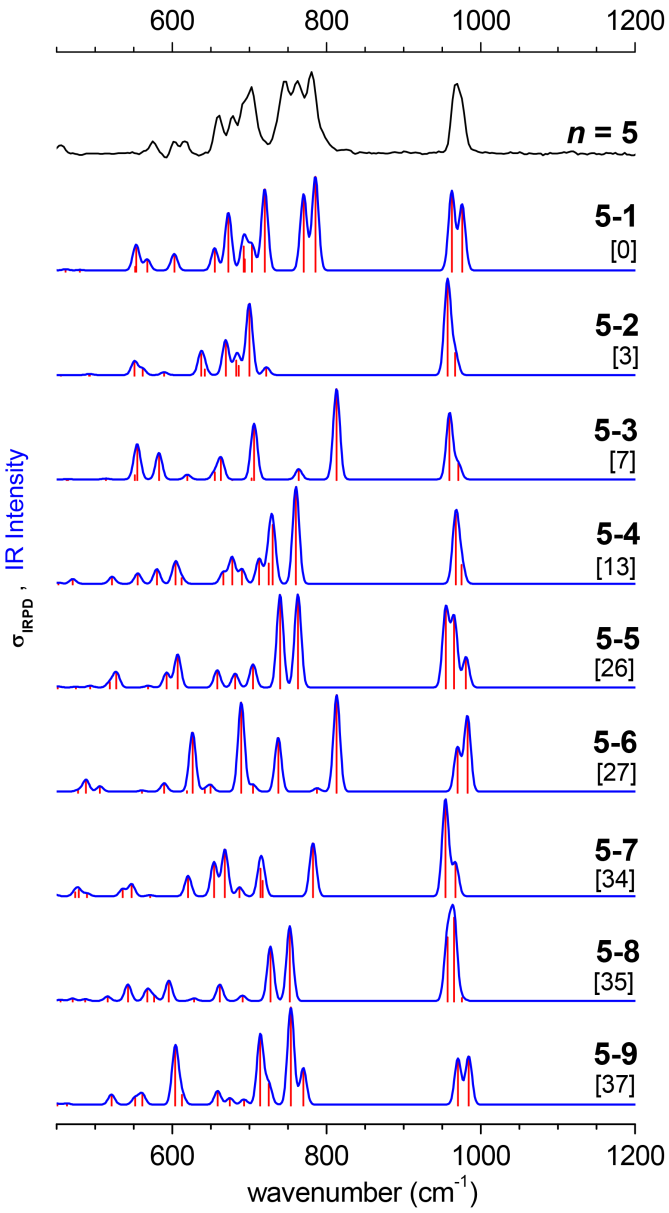

Figure 9.4: Smoothed experimental IRPD spectrum (black) of D_2-tagged $(TiO_2)_n^-$ (n=5) and simulated linear IR absorption traces (blue), stick spectra (red), and relative energies (kJ/mol) of the predicted lowest-lying isomers at the BP86/6-311+G* level of theory.

the anion global minimum energy structure, while Qu and Kroes[441] report **5-3** as the ground state. The neutral n=5 cluster is also observed to have a "glass" potential energy surface with many low-lying structures.[449] Most DFT studies in the literature report either **5-2** or **5-3** as the neutral global minimum energy structure,[440–444,446–451] with both structures often reported to lie within 3 kJ/mol of one another.[448–451]

Among the many calculated low-lying clusters, the simulated IR spectrum of structure **5-1** (Fig. 9.4) best reproduces the observed experimental features, particularly the strong peaks between 700–800 cm^{-1}. Intense experimental peaks in the upper half of region (*iii*) at 781 cm^{-1}, 763 cm^{-1}, and 745 cm^{-1} reasonably match the strongly IR active modes for **5-1** at 785 cm^{-1}, 770 cm^{-1}, and 720 cm^{-1}. Structure **5-1** also exhibits two Ti-O stretching modes in region (*i*) at 976 cm^{-1} and 962 cm^{-1} that are resolved in the unsmoothed spectrum in Fig. 9.1 at 975 cm^{-1} and 966 cm^{-1}.

Other low-lying isomers may well contribute to the observed structure in the experimental spectrum. For instance, structure **5-2** could contribute to the absorption in region (*i*) and the lower frequency side of region (*iii*), but it cannot alone explain the observed experimental features, as it is lacking in intense structure between 700–800 cm^{-1}. Isomer **5-4** similarly may be involved with absorption in the higher frequency side of region (*iii*), but on its own does not have enough distinct IR active modes to match experiment. Structures **5-3** and **5-6** can be ruled out, as they predict absorption in region (*ii*) due to the presence of a free Ti-O moiety bound to three roughly tetrahedrally coordinated Ti-O-Ti bridges in both structures. Structure **5-5** can also most likely be ruled out, as it has three Ti-O dangling bonds, and thus three IR active modes in region (*i*) that should yield broader absorption than what is observed experimentally.

It is remarkable that given the plethora of low-lying calculated structures for $(TiO_2)_5^-$, the simulated IR spectrum of the lowest-lying DFT structure **5-1** is a qualitative match with experiment, and may indicate a dominant contribution from this isomer. It is also possible that as for $n = 4$, the $(TiO_2)_5^-$ anions demonstrate fluxional character, and that nearby local minima on the glassy $n = 5$ potential energy surface contribute to the IR spectrum in a way not captured by our harmonic IR simulations.

9.4.4 $(TiO_2)_6^-$

The IRPD spectrum for $(TiO_2)_6^-$ (Fig. 9.5) is distinct from those of the other clusters in its simplicity. The spectrum is dominated by a single very intense peak in region (*ii*), and shows a single weak feature in region (*i*) along with a handful of very weak features in regions (*iii*) and (*iv*). Using calculated energetics and simulated IR spectra, the experimental spectrum can be assigned unambiguously to the C_2-symmetric **6-1** isomer.

Prior DFT studies for the n=6 anion by Qu and Kroes[441] and Tang *et al.*[448] have reported **6-1** as the most stable isomer; this structure has also been fairly widely identified as the lowest-lying neutral structure.[441,443,446,448–451] We identify two energetically higher-lying isomers, the C_1 structure **6-2** and the C_{2v} structure **6-3**, at 35 kJ/mol and 46 kJ/mol above **6-1**, respectively. **6-2** can be ruled out due to the poor match between the experimental

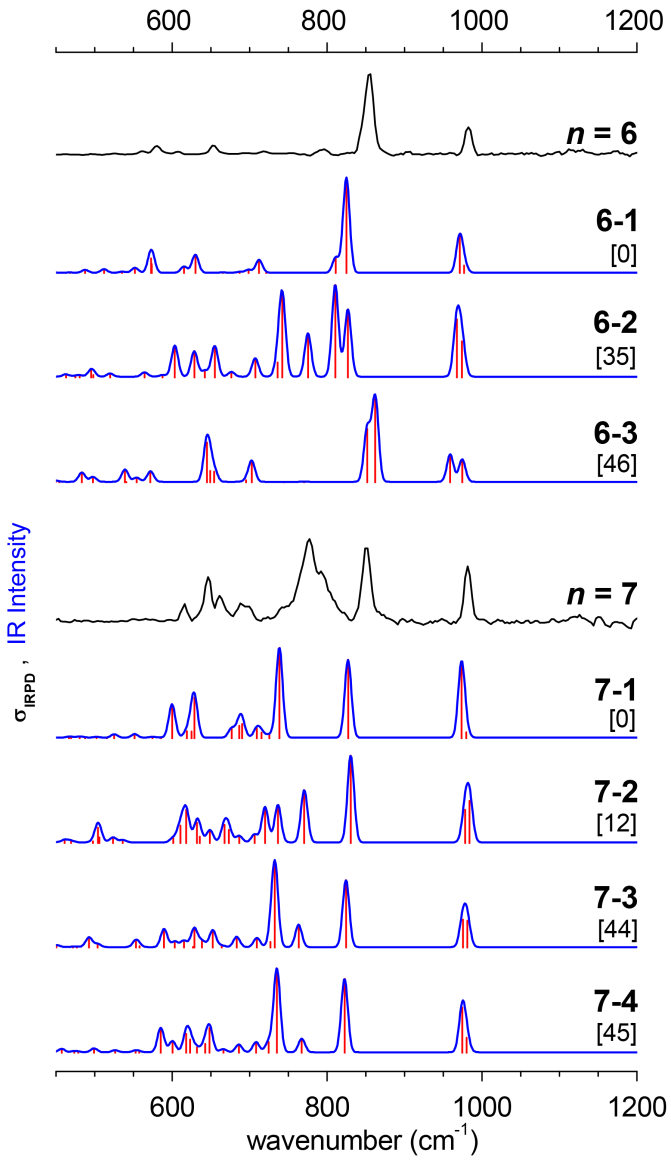

Figure 9.5: Smoothed experimental IRPD spectra (black) of D_2-tagged $(TiO_2)_n^-$ (n=6, 7) and simulated linear IR absorption traces (blue), stick spectra (red), and relative energies (kJ/mol) of the predicted lowest-lying isomers at the BP86/6-311+G* level of theory.

and simulated spectra; **6-3** is a poorer match to the experimental spectrum than **6-1**, and is calculated to lie at a high enough relative energy that it can be safely ruled out as well.

We can assign the observed vibrational features through comparison with the simulated IR spectrum of isomer **6-1** (Fig. 9.5). The peak observed in region (*i*) at 982 cm^{-1} corresponds largely to the antisymmetric Ti-O stretching mode, calculated at 971 cm^{-1}. The

experimental feature in region (*ii*) appears at 854 cm^{-1}, and is matched by a strongly IR active calculated mode at 825 cm^{-1}. This mode corresponds to antisymmetric umbrella-like stretching of the two groups of tetrahedrally coordinated Ti-O-Ti bridges connected to each free Ti-O moiety. Considering the much weaker features in regions (*iii*) and (*iv*), the observed peaks at 719 cm^{-1}, 653 cm^{-1}, and 580 cm^{-1} align with predicted weakly IR active Ti-O-Ti bridge stretching modes at 712 cm^{-1}, 630 cm^{-1}, and 573 cm^{-1}.

9.4.5 $(TiO_2)_7^-$

The IRPD spectrum for $(TiO_2)_7^-$ (Fig. 9.5) has a single sharp peak in region (*i*), a single peak in region (*ii*), a broad, strong peak at the high-frequency edge of region (*iii*), and weaker features extending through region (*iii*) towards lower frequencies.

Four n=7 isomers lie within 50 kJ/mol of the lowest energy structure. The C_s isomer **7-1** is most stable, with the C_1-symmetric **7-2** structure lying 12 kJ/mol above, and additional C_1 isomers **7-3** and **7-4** lying 44 and 45 kJ/mol above. Beginning with n=7, the literature becomes sparse regarding thorough reports for the most stable clusters. Only Qu and Kroes[441] have published DFT structures and energetics for anions with $n \geq 7$, but they did not perform a thorough structure search, and thus do not report the isomers we find to be lowest in energy. Better searches exist for the global minimum structures of the neutral (TiO_2)n clusters. Structures **7-1** and **7-2** have been identified as the two lowest-lying neutral cluster isomers by Chelikowsky[449] and Dixon;[417] Chaudhury[451] also finds **7-1** to be the most stable neutral cluster.

All four n=7 structures reported here have simulated IR spectra that compare reasonably well to experiment (Fig. 9.5). The experimental features at 982 cm^{-1} in region (*i*) and 851 cm^{-1} in region (*ii*) are reproduced by strongly IR active modes in all four isomers, at 974 cm^{-1} and 827 cm^{-1} for **7-1**, 984/978 cm^{-1} and 831 cm^{-1} for **7-2**, 981/975 cm^{-1} and 824 cm^{-1} for **7-3**, and 975 cm^{-1} and 822 cm^{-1} for **7-4**. The features in region (*i*) correspond to symmetric/antisymmetric free Ti-O stretches, while those in region (*ii*) involve stretching of the three tetrahedrally coordinated Ti-O-Ti bridges at the single Ti-O moiety with 4-fold coordination.

More distinctive is the broad, intense structure observed at the high frequency edge of region (*iii*) between 750–810 cm^{-1}. Within this broad feature lie an intense peak at 776 cm^{-1}, and a weaker shoulder at 795 cm^{-1}. This feature cannot be explained by the simulated IR spectrum of a single isomer, however, it could be modeled by the presence of both isomers **7-1** and **7-2**, or perhaps a fluxional cluster encompassing both structures. In particular, the strong absorptions of isomer **7-1** at 738 cm^{-1} and of isomer **7-2** at 771 cm^{-1} match well with the intense peak and shoulder of this broad feature respectively, and additional IR active modes of **7-2** at 720 cm^{-1} and 736 cm^{-1} could also contribute intensity in this region. Isomers **7-3** and **7-4** could also contribute to the experimental spectrum, but lie significantly higher in energy. We therefore assign the experimental spectrum to a combination, perhaps fluxional in nature, of isomers **7-1** and **7-2**.

9.4.6 $(TiO_2)_8^-$

The IRPD spectrum for $(TiO_2)_8^-$ (Fig. 9.6) has a single feature in region (*i*), a dense cluster of features between 770–880 cm^{-1} spanning region (*ii*) and the high frequency edge of region (*iii*), and weaker, unresolved features in the lower frequency span of region (*iii*).

$(TiO_2)_8^-$ has many isomers lying close in energy; with DFT we identify thirteen n=8 anionic structures within 50 kJ/mol of the lowest energy structure. The most stable structure **8-1** is of C_1 symmetry and is quite disordered compared to the C_2, C_{2h}, and C_s structures **8-2** through **8-5** that lie only slightly higher in energy. The only theoretical study for anions with n=8 is presented by Qu and Kroes,[441] who do not report the structures we identify as lowest in energy, and again, considerably more work has been done to search for the lowest energy neutral structures. Marom *et al.*[449] report the most thorough list of neutral isomers found with basin hopping and note that like the n=5 cluster, the n=8 cluster also has a particularly "glassy" potential energy surface. Despite this, there is some agreement in the literature that the most stable neutral n=8 cluster is a C_{2h} species analogous to the isomers **8-3** and **8-4** reported here.[443,446,449–451]

The experimental spectrum shows one peak in region (*i*) at 989 cm^{-1} and four peaks of increasing intensity in regions (*ii*) and (*iii*) at 862 cm^{-1}, 836 cm^{-1}, 806 cm^{-1}, and 784 cm^{-1}, with a weaker shoulder at 760 cm^{-1}. The spectrum of the **8-1** isomer is a good match for the experimental data (Fig. 9.6), with calculated close-lying symmetric and antisymmetric Ti-O stretching modes at 982 cm^{-1} and 976 cm^{-1} in region (*i*), Ti-O-Ti bridge stretching modes in regions (*ii*) and (*iii*) at 831 cm^{-1}, 806 cm^{-1}, 779 cm^{-1}, and 750 cm^{-1}, and a weak feature at 733 cm^{-1}. These calculated frequencies reproduce all features observed experimentally.

While structures **8-2**, **8-3**, **8-4**, and **8-5** can be considered degenerate with **8-1** within the accuracy of DFT, none of their simulated spectra can alone account for the features observed experimentally. Due to their higher levels of symmetry, they exhibit too few distinct IR active modes between 770–880 cm^{-1}. The same can be said for the energetically higher-lying isomers **8-8**, **8-9**, and **8-10**. It is possible that any of these structures could partially contribute to the congested structure we observe, but they cannot alone reproduce experimental features.

Isomers **8-6**, **8-7**, **8-11**, **8-12**, and **8-13**, on the other hand, are of C_1 symmetry with disordered geometries, and demonstrate more IR activity between 770–880 cm^{-1}. Structure **8-12** can perhaps be ruled out as it has three terminal Ti-O bonds and therefore a relatively broad absorption in region (*i*), while the experimental feature in that region is quite narrow. The isomers **8-6**, **8-7**, **8-11**, and **8-13** cannot be ruled out from contributing to the spectrum, but do not appear to match the overall spectral profile of the experimental results as well as isomer **8-1**.

We therefore assign the dominant contribution to the experimental spectrum to **8-1**, but cannot make a concrete statement about whether other isomers are also present. It is noteworthy that, like for n=5, although there are many candidate n=8 clusters, the IR spectrum for the lowest-lying DFT structure is a reasonable match to experiment and that many other low-lying structures can be easily ruled out.

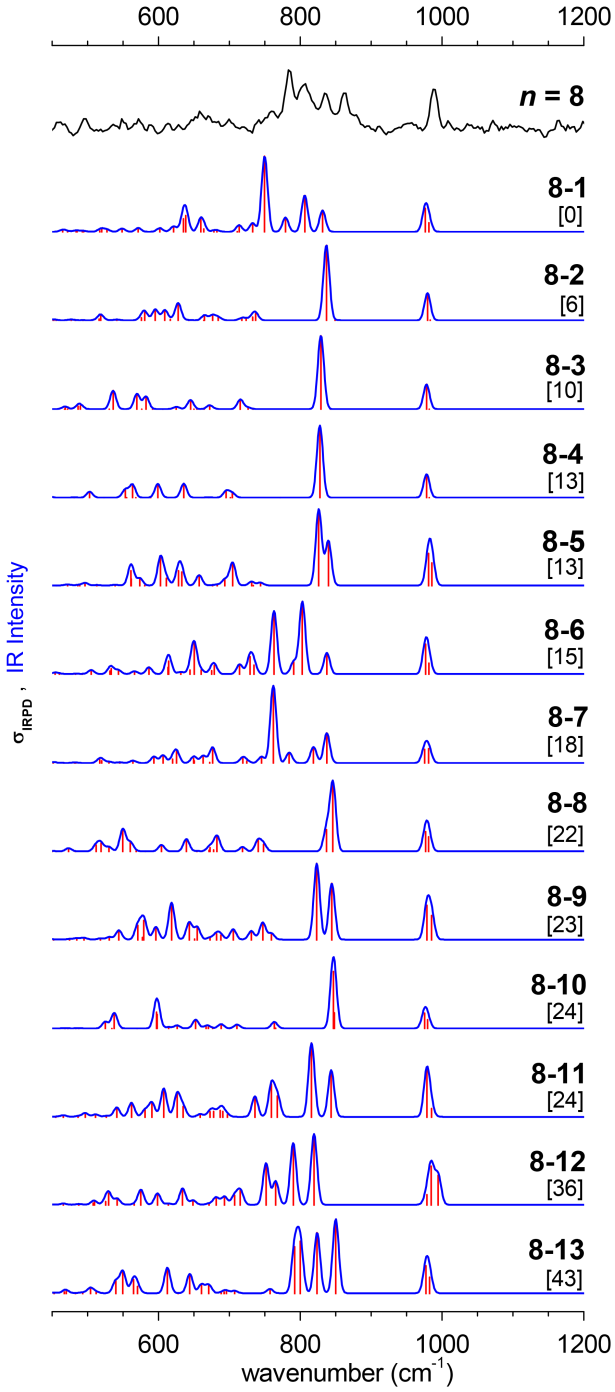

Figure 9.6: Smoothed experimental IRPD spectrum (black) of D_2-tagged $(TiO_2)_n^-$ (n=8) and simulated linear IR absorption traces (blue), stick spectra (red), and relative energies (kJ/mol) of the predicted lowest-lying isomers at the BP86/6-311+G* level of theory.

9.4.7 Structural Trends

The qualitative agreement between calculated and experimental IR spectra indicates that the candidate $(TiO_2)_n^-$ (n=3-8) structures identified here and in the literature are reasonable. The experimental data we report is uniquely suited not only to identify the most likely cluster structures, but also to highlight when the harmonic approximation does not capture the spectroscopic signatures of potentially fluxional clusters, as seen here for $n = 4$ and $n = 7$. However, the predicted global minimum energy DFT structures are satisfactorily good matches for many of the IRPD spectra reported here. It is possible that barriers between low-lying structures are small enough to facilitate population of the global minimum structure for each cluster size under the present experimental conditions. Using the best calculated structures for each $(TiO_2)_n^-$ cluster (**3-1**, **4-1/4-2**, **5-1**, **6-1**, **7-1/7-2**, and **8-1**) we can consider the size-dependent evolution of their properties.

The assigned clusters feature compact structures, with only two terminal Ti-O bonds and many bridging O atoms. Ti atoms have primarily 3- and 4-fold coordination, and O atoms, apart from the free Ti-O moieties, have primarily 2-fold coordination, occasionally 3-fold coordination (structures **3-1**, **7-1**, and **8-1**), and remarkably even 4-fold coordination (structure **6-1**). The level of coordination generally increases with cluster size. Structure **3-1** has an average Ti atom coordination of 3.67 and O coordination of 1.83 and **4-1** and **4-2** share an average Ti coordination of 3.50 and O coordination of 2.00; structures **6-1** and **8-1** meanwhile have respective Ti coordination numbers of 4.00 and 3.88, and O coordination numbers of 2.33 and 2.17. In both rutile and anatase bulk TiO_2, each Ti atom is coordinated with 6 O atoms in a roughly octahedral layout and each O atom has 3 Ti atoms coordinated in a trigonal planar geometry.[103] $(TiO_2)_n^-$ clusters do not reach this average level of coordination within the size range studied here.

In conjunction with lowered coordination relative to the bulk, the average Ti-O bond lengths in the small $(TiO_2)_n^-$ clusters are shorter than those of bulk TiO_2. Room temperature rutile and anatase have average Ti-O bond lengths of 1.96 Å.[457,458] The predicted bond lengths of the $(TiO_2)_n^-$ clusters stay fairly similar over the range of n studied here. The terminal Ti-O bonds are significantly shorter than those with higher coordination, falling consistently in the range of 1.64–1.66 Å for all n=3-8 clusters. The average length of non-terminal Ti-O bonds ranges from 1.88–1.92 Å over n=3-8, consistently shorter than the bulk values. Chen and Dixon[450] also report that both the coordination numbers and the average bond lengths of calculated neutral clusters as large as n=13 fall short of the bulk values.

The IRPD spectra of the $(TiO_2)_n^-$ clusters also show some trends worth noting. All experimental spectra have IR absorption in region (i), due to the excitation of the terminal Ti-O stretching modes ubiquitous in the clusters studied here, though not present in bulk TiO_2. The frequencies of these Ti-O stretching features increase slightly with the size of the cluster, from as low as 948 cm^{-1} for n=3 to as high as 989 cm^{-1} for n=8. Additionally, the spacing between frequencies of the symmetric and antisymmetric terminal Ti-O stretching modes decreases with increasing cluster size. In n=3-5, the experiment resolves a splitting in the region (i) features. For n=6-8, no splittings are observed. The simulated spectra

suggest that both symmetric and antisymmetric modes are IR active in these species, but are too close in frequency to resolve in our experiment. The IR active modes in regions (*ii*) and (*iii*) also tend to shift towards higher frequency with larger cluster size. For n=3-5, the highest frequency absorption in region (*iii*) increases from 746 cm^{-1} to 757 cm^{-1} to 781 cm^{-1}. Beginning with n=6, the structural motif of three Ti-O-Ti bridges tetrahedrally coordinated to a terminal Ti-O moiety appears. This motif yields IR absorption in region (*ii*), and persists for larger n, with the highest frequency absorption in region (*ii*) at 854 cm^{-1} for n=6, 851 cm^{-1} for n=7, and 862 cm^{-1} for n=8. The DFT calculated frequencies for the best predicted structures also follow these general trends (see SI); with larger n, the strong features in regions (*i*)-(*iii*) shift towards higher frequencies and the splitting between the region (*i*) features decreases.

A final size-dependent property worth considering is the localization of the anion SOMO for the assigned $(TiO_2)_n^-$ clusters. The additional electron in the anion SOMO can perturb the cluster enough that the relative energies of specific isomers are drastically different for the anions and neutrals.[417] The SOMOs of relevant clusters are visualized in Fig. 9.7; they are largely of 3*d* character localized on Ti atoms. As has been noted by Li and Dixon,[417] the **3-1** cluster anion SOMO is a $3d_{z^2}$ orbital localized entirely on the least-coordinated Ti atom, while the **4-1** and **4-2** clusters have SOMOs with 3*d* character distributed across two Ti atoms. Like the **3-1** cluster, the **5-1** cluster has a SOMO localized in a $3d_{z^2}$ orbital of a 3-fold coordinated Ti atom; the clusters with $n \geq 6$, however, have more delocalized SOMOs distributed over the 3*d* orbitals of four or more Ti atoms. In all species, the SOMO avoids localization on Ti atoms with terminal Ti-O bonds, to reduce unfavorable repulsion of the excess electron density.

In bulk TiO_2, titanium centers are found as Ti^{4+} cations; oxygen vacancy defect sites on TiO_2 surfaces are therefore accompanied by under-coordinated Ti^{3+} cations. These Ti^{3+} centers are critical to reactive adsorption[459,460] and reduction of organic molecules[461] on TiO_2 surfaces. $(TiO_2)_n^-$ clusters with an excess electron localized on a single Ti atom, like those in the **3-1** and **5-1** structures, are similarly expected to be quite reactive. These clusters may therefore have strong reducing capability, and may be reasonable analogs for Ti^{3+} defect sites on bulk TiO_2 catalytic surfaces. It would be of interest to see if these clusters are particularly reactive toward CO_2 and other electron-accepting species.

9.5 Conclusions

We report IRPD spectra for the messenger-tagged $(TiO_2)_n^-$ clusters with n=3-8 in the 450–1200 cm^{-1} spectral range. DFT calculations are performed to determine the structures, energetics, and harmonic IR spectra of the most stable cluster isomers. Comparison of experimental and calculated spectra does not always allow clear identification of a single lowest energy cluster structure; however, the overall agreement between theory and experiment provides much new information about these species. We unambiguously assign the structures of $(TiO_2)_3^-$ and $(TiO_2)_6^-$, narrow down the contributions to the spectra for $(TiO_2)_4^-$

and $(TiO_2)_7^-$ to two isomers, and find that the $(TiO_2)_5^-$ and $(TiO_2)_8^-$ spectra satisfactorily match simulated spectra for the lowest energy isomer, even though these clusters have complex potential energy surfaces with many low-lying candidate structures.

The information reported here about the likely structures of small anionic titanium oxide clusters will be of great utility in guiding future spectroscopic work. In particular, applying the complementary technique of slow photoelectron velocity-map imaging[352] to these clusters could aid in distinguishing close-lying anion isomers that detach to neutrals more widely spaced in energy. Additionally, the clusters studied in this work have considerable potential as model systems for catalysis on bulk TiO_2. Of particular interest is the reduction of CO_2 on a TiO_2 surface; in forthcoming IRPD work, we aim to characterize the complexes formed after reaction of $(TiO_2)_n^-$ clusters with CO_2.

9.6 Supporting Information

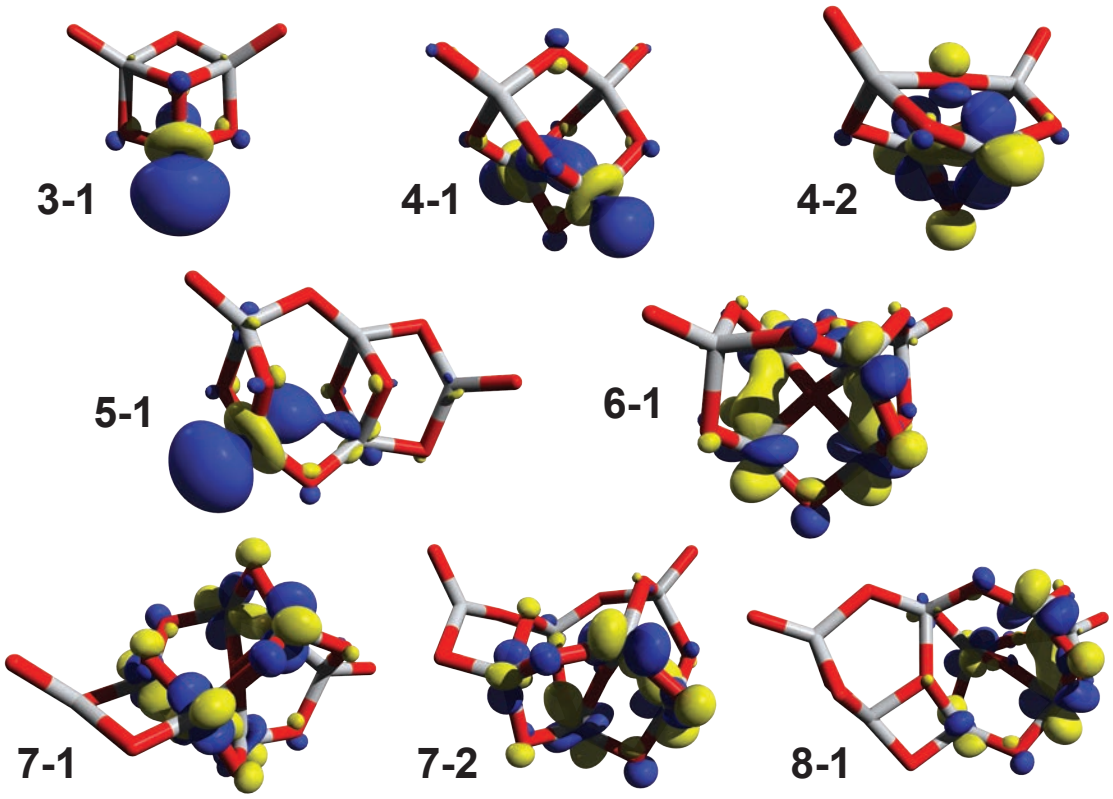

Figure 9.7: Visualized singly occupied molecular orbitals of selected $(TiO_2)_n^-$ clusters.

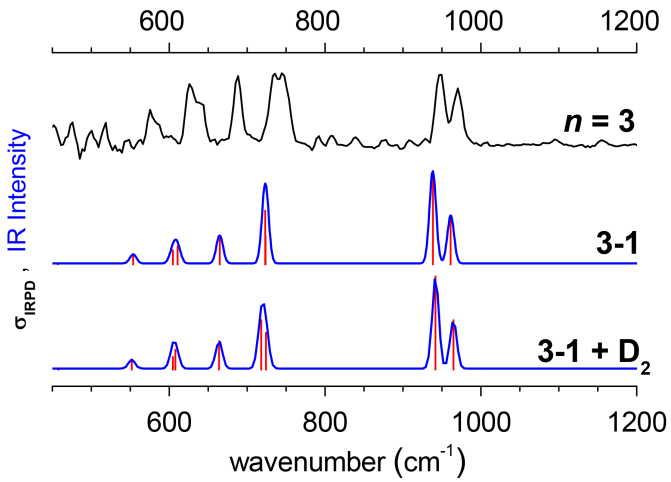

Figure 9.8: Experimental IRPD spectrum (black) of D_2-tagged $(TiO_2)_3^-$ compared with simulated linear IR absorption traces (blue) and stick spectra (red) of the predicted lowest-lying **3-1** isomer at the BP86/6-311+G* level of theory and after inclusion of the D_2 tag using BP86+D/6 311+G*.

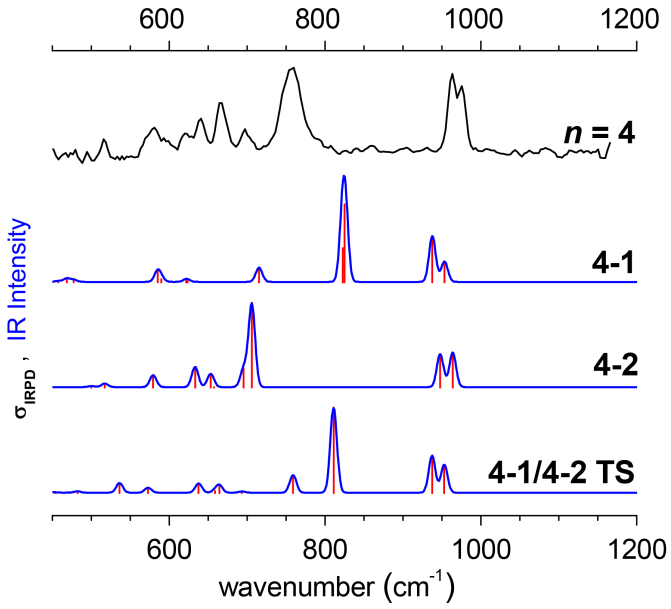

Figure 9.9: Experimental IRPD spectrum (black) of D_2-tagged $(TiO_2)_4^-$ compared with simulated linear IR absorption traces (blue) and stick spectra (red) of the **4-1** and **4-2** isomers and the **4-1/4-2** transition state at the BP86/6-311+G* level of theory.

Calculated electronic states, relative energies (kJ/mol), vertical detachment energies (kJ/mol), harmonic vibrational frequencies (cm^1) above $400\,cm^{-1}$, normal mode symmetries where applicable, and relative IR intensities for low-lying $(TiO_2)_n^-$ cluster isomers at the BP86/6 311+G* level of theory. Values are also reported for **4-1/4-2** and **4-2/4-3** transition states with BP86/6-311+G* and for the D_2 tagged **3-1** cluster with BP86+D/6-311+G*. Vibrational zero point energy corrections are included for relative isomer energies, though are not included in transition state energies. Isomers mostly likely observed in the experimental spectra presented in the main text are marked with asterisks.

Cluster	Isomer	State	Energy	VDE	Harmonic frequencies
$(TiO_2)_3^-$	**3-1***	$^2A'$, C_s	0	305	961 (a', 0.52), 938 (a'', 1.00), 724 (a', 0.30), 723 (a'', 0.57), 665 (a', 0.30), 611 (a', 0.18), 605 (a'', 0.14), 554 (a', 0.10), 457(a'', 0.00), 417 (a', 0.02)
	3-1+D_2	^2A, C_1			965 (0.53), 942 (1.00), 724 (0.39), 718 (0.52), 664 (0.30), 608 (0.20), 604 (0.13), 552 (0.10), 458 (0.00), 414 (0.02)
	3-2	^2B, C_2	92	233	941 (a, 0.13), 934 (b, 1.00), 694 (b, 0.01), 673 (a, 0.00), 669 (a, 0.13), 667 (b, 0.14), 634 (a, 0.01), 478 (b, 0.02), 477 (a, 0.00), 464 (b, 0.22), 406 (b, 0.12)

Cluster	Isomer	State	Energy	VDE	Harmonic frequencies
$(TiO_2)_4^-$	**4-1***	$^2A_1\,C_{2v}$	0	375	953 (a_1, 0.26), 938 (b_2, 0.59), 825 (b_2, 1.00), 822 (a_1, 0.43), 715 (b_1, 0.18), 715 (a_1, 0.00), 624 (b_2, 0.01), 622 (a_1, 0.03), 590 (b_1, 0.04), 585 (a_1, 0.14), 477 (a_1, 0.03), 468 (b_1, 0.04), 457 (b_2, 0.01), 446 (a_2, 0.00)
	4-2*	$^2A_1\,C_{2v}$	22	345	964 (a_1, 0.42), 948 (b_2, 0.40), 706 (b_2, 1.00), 696 (a_1, 0.22), 673 (a_2, 0.00), 657 (a_1, 0.00), 653 (b_2, 0.16), 633 (b_1, 0.24), 579 (a_1, 0.14), 517 (b_1, 0.04), 500 (b_2, 0.01), 438 (a_2, 0.00), 429 (a_1, 0.03), 423 (b_1, 0.01), 401 (b_1, 0.00)
	4-3	$^2A_g\,C_{2h}$	26	354	961 (a_g, 0.00), 952 (b_u, 0.64), 694 (b_u, 1.00), 680 (b_g, 0.00), 658 (a_g, 0.00), 640 (a_u, 0.17), 596 (b_u, 0.18), 593 (a_g, 0.00), 578 (a_g, 0.00), 568 (b_u, 0.17), 505 (a_u, 0.07), 461 (b_g, 0.00), 420 (b_g, 0.00), 407 (a_u, 0.01)

Cluster	Transition State	Energy	Harmonic frequencies
$(TiO_2)_4^-$	**4-1/4-2**, C_s	36 above **4-1**, 14 above **4-2**	953 (a', 0.33), 937 (a'', 0.43), 811 (a'', 1.00), 759 (a', 0.21), 693 (a'', 0.01), 664 (a', 0.09), 659 (a'', 0.02), 638 (a', 0.11), 573 (a', 0.06), 536 (a', 0.11), 482 (a', 0.02), 472 (a'', 0.00), 454 (a', 0.00), 447 (a'', 0.00), 165i (a', 0.02)
	4-2/4-3, C_s	67 above **4-2**, 63 above **4-3**	966 (a', 0.31), 949 (a', 1.00), 689 (a', 0.74), 676 (a'', 0.00), 668 (a', 0.65), 635 (a'', 0.41), 593 (a', 0.03), 586 (a', 0.27), 566 (a', 0.02), 551 (a', 0.11), 521 (a'', 0.05), 446 (a'', 0.00), 436 (a'', 0.01), 419 (a', 0.00), 403 (a'', 0.00), 89i (a', 0.01)

Cluster	Isomer	State	Energy	VDE	Harmonic frequencies
$(TiO_2)_5^-$	**5-1***	^2A, C_1	0	345	976 (0.70), 962 (0.84), 785 (1.00), 770 (0.81), 720 (0.87), 703 (0.27), 694 (0.12), 693 (0.26), 673 (0.62), 655 (0.24), 603 (0.18), 567 (0.12), 553 (0.24), 552 (0.04), 480 (0.01), 462 (0.01), 440 (0.03), 418 (0.02), 402 (0.02)
	5-2*	$^2A'$, C_s	3	307	967 (a', 0.23), 957 (a'', 1.00), 722 (a', 0.08), 700 (a'', 0.75), 686 (a', 0.10), 683 (a'', 0.16), 669 (a', 0.37), 642 (a'', 0.06), 637 (a', 0.22), 589 (a', 0.03), 561 (a', 0.07), 551 (a'', 0.15), 493 (a'', 0.01), 492 (a', 0.00), 455 (a'', 0.00), 432 (a', 0.00), 418 (a'', 0.04), 410 (a', 0.04), 400 (a'', 0.00)
	5-3	$^2A'$, C_s	7	330	971 (a', 0.18), 959 (a', 0.73), 813 (a', 1.00), 764 (a'', 0.11), 706 (a', 0.61), 703 (a'', 0.01), 678 (a'', 0.00), 663 (a', 0.24), 655 (a', 0.08), 620 (a', 0.05), 583 (a'', 0.29), 555 (a'', 0.36), 551 (a', 0.04), 514 (a', 0.01), 465 (a', 0.00), 463 (a'', 0.00), 416 (a', 0.03)
	5-4*	^2A, C_1	13	349	975 (0.20), 968 (0.72), 760 (1.00), 730 (0.61), 725 (0.21), 713 (0.26), 690 (0.15), 678 (0.27), 666 (0.12), 612 (0.06), 604 (0.22), 580 (0.15), 555 (0.11), 522 (0.07), 471 (0.05), 452 (0.01), 430 (0.02), 411 (0.00), 401 (0.01)
	5-5	^2A, C_1	26	374	981 (0.33), 965 (0.75), 955 (0.85), 763 (1.00), 740 (1.00), 705 (0.25), 681 (0.15), 658 (0.18), 607 (0.35), 593 (0.16), 569 (0.02), 527 (0.16), 519 (0.06), 493 (0.02), 475 (0.01), 451 (0.01), 420 (0.01)

Cluster	Isomer	State	Energy	VDE	Harmonic frequencies
$(TiO_2)_5^-$	**5-6**	$^2A'$, C_s	27	370	983 (a', 0.78), 970 (a', 0.45), 813 (a', 1.00), 788 (a'', 0.04), 737 (a', 0.56), 704 (a'', 0.08), 689 (a', 0.92), 650 (a'', 0.07), 642 (a', 0.02), 626 (a'', 0.61), 619 (a', 0.01), 589 (a', 0.09), 561 (a'', 0.01), 506 (a', 0.06), 488 (a'', 0.12), 478 (a', 0.02)
	5-7	^2A, C_1	34	302	967 (0.34), 954 (1.00), 782 (0.55), 717 (0.16), 714 (0.28), 687 (0.09), 668 (0.48), 654 (0.35), 620 (0.21), 571 (0.01), 547 (0.13), 536 (0.08), 490 (0.03), 479 (0.07), 474 (0.04), 448 (0.01), 439 (0.04), 400 (0.01)
	5-8	^2A, C_1	35	342	976 (0.03), 965 (1.00), 957 (0.76), 752 (0.90), 727 (0.65), 691 (0.07), 662 (0.20), 628 (0.03), 595 (0.24), 576 (0.05), 568 (0.14), 542 (0.20), 516 (0.05), 487 (0.02), 471 (0.03), 455 (0.01), 404 (0.03)
	5-9	^2A, C_1	37	335	984 (0.50), 970 (0.47), 770 (0.37), 754 (1.00), 725 (0.22), 714 (0.72), 693 (0.05), 675 (0.07), 659 (0.14), 612 (0.10), 604 (0.60), 561 (0.11), 552 (0.07), 521 (0.10), 463 (0.01), 451 (0.01), 439 (0.02), 404 (0.00)

Cluster	Isomer	State	Energy	VDE	Harmonic frequencies
$(TiO_2)_6^-$	**6-1***	^2A, C_2	0	354	977 (a, 0.08), 971 (b, 0.38), 825 (b, 1.00), 811 (a, 0.16), 721 (a, 0.00), 712 (b, 0.13), 699 (b, 0.03), 687 (a, 0.01), 665 (a, 0.00), 630 (a, 0.19), 615 (b, 0.07), 574 (a, 0.09), 573 (b, 0.15), 552 (b, 0.05), 535 (a, 0.01), 512 (b, 0.04), 488 (b, 0.03), 487 (a, 0.00), 468 (a, 0.00), 446 (b, 0.01), 429 (a, 0.02), 418 (b, 0.01), 403 (b, 0.00)
	6-2	^2A, C_1	35	405	974 (0.39), 968 (0.62), 827 (0.73), 811 (1.00), 775 (0.47), 742 (0.88), 736 (0.15), 707 (0.20), 676 (0.05), 655 (0.33), 642 (0.07), 629 (0.28), 603 (0.34), 588 (0.02), 564 (0.05), 520 (0.03), 498 (0.02), 495 (0.07), 480 (0.01), 475 (0.01), 463 (0.03), 403 (0.01)
	6-3	$^2A_1$, C_{2v}	46	388	974 (a_1, 0.26), 959 (b_2, 0.32), 862 ($a-1$, 1.00), 852 (b_2, 0.62), 770 (b_1, 0.00), 744 (a_2, 0.00), 703 (b_2, 0.25), 696 (a_1, 0.02), 654 (a_1, 0.12), 649 (b_2, 0.13), 645 (b_1, 0.46), 572 (b_1, 0.12), 554 (b_2, 0.05), 541 (a_2, 0.00), 539 (a_1, 0.14), 498 (b_1, 0.06), 483 (b_2, 0.11), 454 (a_2, 0.00), 450 (a_1, 0.01), 422 (b_2, 0.00), 417 (a_1, 0.00), 401 (b_1, 0.04)

Cluster	Isomer	State	Energy	VDE	Harmonic frequencies
$(TiO_2)_7^-$	**7-1***	$^2A'$, C_s	0	363	980 (a', 0.06), 974 (a', 0.83), 827 (a', 0.87), 738 (a', 1.00), 725 (a'', 0.03), 715 (a'', 0.06), 709 (a', 0.10), 690 (a', 0.15), 687 (a'', 0.13), 677 (a', 0.10), 629 (a'', 0.45), 625 (a', 0.07), 619 (a', 0.07), 600 (a', 0.37), 586 (a'', 0.00), 575 (a', 0.01), 552 (a'', 0.04), 525 (a', 0.04), 516 (a'', 0.00), 502 (a', 0.01), 488 (a', 0.01), 480 (a'', 0.01), 469 (a'', 0.01), 467 (a', 0.01), 441 (a'', 0.01), 427 (a', 0.07), 418 (a'', 0.01)
	7-2*	^2A, C_1	12	367	984 (0.48), 978 (0.38), 831 (1.00), 771 (0.60), 736 (0.43), 720 (0.41), 706 (0.09), 686 (0.08), 673 (0.15), 667 (0.20), 649 (0.14), 636 (0.07), 632 (0.23), 618 (0.38), 611 (0.19), 601 (0.05), 536 (0.03), 524 (0.06), 506 (0.06), 504 (0.17), 498 (0.01), 469 (0.02), 461 (0.03), 447 (0.01), 419 (0.00), 415 (0.02), 407 (0.01)
	7-3	^2A, C_1	44	350	981 (0.31), 975 (0.32), 824 (0.79), 763 (0.26), 732 (1.00), 727 (0.06), 709 (0.11), 683 (0.12), 664 (0.02), 652 (0.20), 639 (0.07), 629 (0.22), 627 (0.00), 615 (0.08), 603 (0.07), 589 (0.22), 558 (0.01), 553 (0.08), 504 (0.04), 493 (0.11), 477 (0.01), 472 (0.00), 451 (0.03), 442 (0.01), 435 (0.01), 411 (0.00)
	7-4	^2A, C_1	45	347	980 (0.17), 975 (0.53), 822 (0.88), 767 (0.16), 735 (1.00), 724 (0.12), 708 (0.12), 686 (0.09), 666 (0.04), 648 (0.29), 642 (0.10), 632 (0.06), 623 (0.15), 618 (0.22), 600 (0.13), 585 (0.29), 557 (0.01), 553 (0.02), 526 (0.02), 499 (0.05), 479 (0.00), 474 (0.01), 457 (0.04), 434 (0.01), 427 (0.01), 408 (0.01)

Cluster	Isomer	State	Energy	VDE	Harmonic frequencies
$(TiO_2)_8^-$	**8-1***	^2A, C_1	0	385	982 (0.12), 976 (0.31), 831 (0.28), 806 (0.48), 779 (0.19), 750 (1.00), 733 (0.11), 714 (0.09), 711 (0.00), 682 (0.02), 678 (0.01), 664 (0.04), 660 (0.17), 639 (0.21), 635 (0.17), 621 (0.07), 602 (0.05), 571 (0.05), 549 (0.04), 527 (0.03), 520 (0.03), 517 (0.01), 495 (0.01), 493 (0.00), 485 (0.01), 484 (0.01), 472 (0.01), 465 (0.03), 413 (0.01), 404 (0.00), 401 (0.01)
	8-2	^2A, C_2	6	351	983 (a, 0.00), 979 (b, 0.36), 849 (a, 0.00), 837 (b, 1.00), 737 (b, 0.09), 733 (a, 0.04), 724 (a, 0.02), 718 (b, 0.03), 684 (a, 0.04), 676 (b, 0.07), 665 (b, 0.07), 664 (a, 0.00), 643 (a, 0.00), 628 (b, 0.23), 617 (a, 0.01), 609 (a, 0.13), 596 (b, 0.15), 581 (a, 0.11), 576 (b, 0.03), 541 (a, 0.01), 519 (b, 0.07), 516 (a, 0.02), 494 (b, 0.00), 482 (b, 0.00), 477 (a, 0.01), 456 (b, 0.00), 452 (b, 0.01), 450 (a, 0.00), 409 (b, 0.00), 409 (a, 0.00)
	8-3	^2A_u, C_{2h}	10	320	982 (a_g, 0.00), 978 (b_u, 0.34), 843 (a_g, 0.00), 829 (b_u, 1.00), 733 (b_g, 0.00), 726 (a_u, 0.02), 715 (b_u, 0.13), 715 (a_g, 0.00), 672 (a_u, 0.05), 664 (b_g, 0.00), 654 (a_g, 0.00), 650 (b_g, 0.00), 645 (b_u, 0.12), 625 (a_u, 0.03), 606 (a_g, 0.00), 592 (b_g, 0.00), 582 (b_u, 0.17), 576 (a_g, 0.00), 570 (a_u, 0.21), 536 (b_u, 0.25), 530 (a_g, 0.00), 490 (a_u, 0.04), 487 (b_u, 0.04), 472 (b_g, 0.00), 468 (b_u, 0.03), 468 (a_g, 0.00), 442 (a_g, 0.00), 431 (b_u, 0.05), 424 (b_g, 0.00), 414 (a_u, 0.01)

Cluster	Isomer	State	Energy	VDE	Harmonic frequencies
$(TiO_2)_8^-$	**8-4**	^2A_g, C_{2h}	13	319	982 (a_g, 0.00), 978 (b_u, 0.32), 845 (a_g, 0.00), 828 (b_u, 1.00), 772 (a_g, 0.00), 704 (a_u, 0.06), 701 (b_g, 0.00), 701 (a_g, 0.00), 696 (b_u, 0.09), 671 (a_u, 0.00), 664 (b_g, 0.00), 661 (a_g, 0.00), 636 (b_u, 0.19), 614 (a_g, 0.00), 599 (a_u, 0.19), 589 (b_u, 0.00), 568 (a_g, 0.00), 563 (a_u, 0.18), 555 (b_g, 0.00), 553 (b_u, 0.11), 523 (b_g, 0.00), 503 (b_u, 0.08), 481 (a_u, 0.00), 481 (a_g, 0.00), 447 (b_g, 0.00), 444 (b_u, 0.03), 434 (a_u, 0.05), 427 (a_g, 0.00), 406 (b_g, 0.00), 402 (b_u, 0.01)
	8-5	$^2A'$, C_s	13	375	986 (a', 0.30), 981 (a'', 0.42), 840 (a', 0.58), 826 (a'', 1.00), 744 (a', 0.04), 734 (a'', 0.00), 731 (a', 0.05), 705 (a'', 0.30), 694 (a'', 0.08), 683 (a', 0.01), 676 (a'', 0.00), 657 (a', 0.14), 633 (a'', 0.17), 628 (a', 0.19), 611 (a'', 0.09), 603 (a', 0.38), 581 (a'', 0.00), 574 (a', 0.09), 562 (a', 0.09), 561 (a'', 0.19), 539 (a', 0.01), 513 (a'', 0.01), 496 (a', 0.03), 489 (a'', 0.00), 486 (a', 0.01), 472 (a'', 0.01), 456 (a'', 0.00), 430 (a', 0.02), 424 (a', 0.00), 417 (a'', 0.00), 409 (a', 0.01)
	8-6	^2A, C_1	15	395	981 (0.15), 977 (0.41), 838 (0.29), 803 (1.00), 791 (0.17), 763 (0.87), 735 (0.12), 729 (0.24), 715 (0.14), 679 (0.12), 675 (0.05), 660 (0.05), 650 (0.43), 644 (0.05), 631 (0.03), 614 (0.18), 613 (0.09), 587 (0.09), 566 (0.04), 543 (0.05), 533 (0.07), 531 (0.04), 505 (0.05), 493 (0.00), 483 (0.00), 460 (0.01), 454 (0.02), 437 (0.01), 420 (0.02), 406 (0.00), 406 (0.00)

Cluster	Isomer	State	Energy	VDE	Harmonic frequencies
$(TiO_2)_8^-$	**8-7**	^2A, C_1	18	384	981 (0.18), 975 (0.18), 837 (0.39), 819 (0.21), 784 (0.13), 762 (1.00), 745 (0.08), 725 (0.02), 719 (0.07), 676 (0.20), 672 (0.01), 663 (0.09), 650 (0.03), 650 (0.06), 625 (0.15), 620 (0.05), 606 (0.10), 594 (0.08), 564 (0.03), 545 (0.01), 530 (0.02), 520 (0.03), 517 (0.04), 483 (0.00), 482 (0.00), 466 (0.00), 452 (0.01), 435 (0.01), 424 (0.00), 409 (0.00)
	8-8	^2A, C_2	22	333	981 (a, 0.21), 977 (b, 0.29), 846 (b, 1.00), 837 (a, 0.32), 748 (a, 0.10), 741 (b, 0.16), 719 (b, 0.06), 698 (a, 0.00), 683 (b, 0.22), 678 (a, 0.02), 673 (a, 0.05), 671 (b, 0.02), 654 (a, 0.01), 639 (a, 0.18), 604 (b, 0.09), 582 (a, 0.00), 568 (b, 0.01), 560 (a, 0.13), 550 (b, 0.33), 530 (b, 0.07), 519 (b, 0.12), 512 (a, 0.09), 483 (a, 0.00), 473 (b, 0.05), 456 (a, 0.00), 450 (b, 0.00), 446 (a, 0.01), 426 (b, 0.03), 405 (a, 0.01), 402 (a, 0.00)
	8-9	^2A, C_1	23	360	985 (0.32), 979 (0.45), 845 (0.74), 823 (1.00), 759 (0.08), 747 (0.23), 731 (0.11), 705 (0.14), 688 (0.06), 682 (0.07), 673 (0.03), 655 (0.16), 651 (0.01), 643 (0.22), 618 (0.49), 596 (0.17), 579 (0.25), 577 (0.03), 571 (0.19), 544 (0.12), 531 (0.03), 518 (0.02), 495 (0.02), 485 (0.02), 474 (0.01), 452 (0.00), 441 (0.01), 436 (0.01), 422 (0.01), 413 (0.01)

Cluster	Isomer	State	Energy	VDE	Harmonic frequencies
$(TiO_2)_8^-$	**8-10**	$^2A_1$, C_{2v}	24	336	980 (a_1, 0.15), 975 (b_2, 0.27), 848 (a_1, 0.28), 847 (b_2, 1.00), 765 (a_1, 0.00), 763 (b_1, 0.11), 711 (a_1, 0.07), 700 (a_2, 0.00), 688 (b_2, 0.08), 677 (a_2, 0.00), 670 (b_1, 0.03), 667 (a_1, 0.03), 653 (b_2, 0.15), 626 (b_1, 0.05), 614 (a_1, 0.02), 598 (b_1, 0.25), 597 (a_1, 0.28), 570 (a_1, 0.00), 549 (b_2, 0.00), 538 (b_1, 0.27), 534 (b_1, 0.00), 525 (a_1, 0.12), 487 (b_1, 0.00), 483 (b_2, 0.00), 472 (a_2, 0.00), 468 (a_1, 0.01), 442 (a_2, 0.00), 434 (b_2, 0.00), 420 (b_1, 0.02), 415 (a_2, 0.00), 406 (a_1, 0.00)
	8-11	^2A, C_1	24	357	985 (0.11), 979 (0.64), 844 (0.63), 816 (1.00), 768 (0.28), 759 (0.45), 736 (0.28), 697 (0.03), 691 (0.07), 687 (0.09), 678 (0.07), 673 (0.07), 659 (0.04), 635 (0.14), 626 (0.31), 607 (0.38), 591 (0.20), 581 (0.10), 562 (0.19), 541 (0.13), 526 (0.01), 511 (0.03), 497 (0.05), 487 (0.01), 466 (0.02), 455 (0.00), 431 (0.02), 426 (0.01), 421 (0.00), 414 (0.01), 405 (0.03)
	8-12	^2A, C_1	36	384	995 (0.42), 985 (0.55), 979 (0.14), 819 (1.00), 790 (0.87), 765 (0.33), 752 (0.59), 715 (0.20), 707 (0.13), 693 (0.13), 681 (0.11), 671 (0.02), 649 (0.06), 634 (0.23), 614 (0.02), 599 (0.16), 575 (0.21), 566 (0.01), 542 (0.09), 530 (0.16), 525 (0.04), 510 (0.04), 508 (0.02), 488 (0.01), 466 (0.02), 447 (0.00), 436 (0.00), 427 (0.00), 408 (0.00), 400 (0.01)

Cluster	Isomer	State	Energy	VDE	Harmonic frequencies
$(TiO_2)_8^-$	**8-13**	^2A, C_1	43	376	982 (0.21), 977 (0.37), 850 (1.00), 824 (0.82), 800 (0.70), 792 (0.63), 757 (0.06), 707 (0.03), 696 (0.03), 693 (0.02), 689 (0.00), 671 (0.11), 661 (0.12), 644 (0.26), 628 (0.00), 613 (0.34), 570 (0.09), 565 (0.18), 550 (0.30), 540 (0.17), 512 (0.02), 504 (0.07), 493 (0.01), 483 (0.00), 470 (0.03), 467 (0.02), 453 (0.01), 426 (0.01), 420 (0.01)

Optimized Cartesian coordinates (Å) of the low-lying $(TiO_2)_n^-$ isomers and relevant transition states calculated with BP86/6 311+G*.

Isomer		x	y	z
3-1	Ti	-1.424628	-0.588677	-0.086381
	Ti	0.000014	1.759957	0.206206
	Ti	1.424619	-0.588692	-0.086391
	O	-2.778682	-1.407430	0.424250
	O	-1.526691	1.286211	-0.628949
	O	-0.000013	-1.523927	-0.878018
	O	0.000007	0.164297	1.195461
	O	1.526713	1.286197	-0.628952
	O	2.778653	-1.407463	0.424265
3-1+D_2	Ti	-1.570060	-0.354657	0.180147
	Ti	0.222441	1.683256	-0.364933
	Ti	1.236994	-0.864936	0.016672
	O	-3.076260	-0.948808	-0.191802
	O	-1.298698	1.536779	0.591304
	O	-0.273549	-1.473563	0.953025
	O	-0.122827	0.054580	-1.234699
	O	1.697248	0.993174	0.418817
	O	2.387180	-1.942400	-0.508044
	D	3.666828	1.880269	1.549902
	D	4.262179	2.161027	1.919811
3-2	Ti	-2.716894	0.133400	0.240349
	Ti	0.000000	0.080307	0.000005
	Ti	2.716891	0.133367	-0.240375
	O	-3.958871	-0.688508	-0.506583
	O	-1.390925	1.010166	-0.783022
	O	-1.277420	-0.798899	1.016813
	O	1.277409	-0.799036	-1.016697
	O	1.390938	1.010266	0.782897
	O	3.958878	-0.688442	0.506650

Isomer		x	y	z
4-1	Ti	-1.626493	-0.960071	0.000050
	Ti	-0.000168	1.314021	-1.439644
	Ti	0.000168	1.313595	1.440032
	Ti	1.626493	-0.960071	-0.000332
	O	-2.984225	-1.915156	0.000070
	O	-1.460473	0.318674	-1.500425
	O	-1.460119	0.318227	1.500864
	O	0.000000	-1.880331	-0.000283
	O	0.000000	2.491290	0.000368
	O	1.460120	0.318669	-1.500768
	O	1.460473	0.318232	1.500521
	O	2.984225	-1.915156	-0.000638
4-2	Ti	-2.013520	-0.685025	0.000060
	Ti	0.000000	0.888651	-1.312547
	Ti	0.000000	0.888904	1.312392
	Ti	2.013520	-0.685025	0.000060
	O	-3.020464	-2.005022	0.000187
	O	-1.758348	0.350989	-1.589925
	O	-1.758366	0.351313	1.589838
	O	0.000000	-0.731850	0.000100
	O	0.000000	2.216650	-0.000206
	O	1.758347	0.350989	-1.589925
	O	1.758367	0.351313	1.589838
	O	3.020463	-2.005022	0.000187
4-3	Ti	-2.486221	0.000001	-0.096811
	Ti	0.000000	-1.321899	-0.000002
	Ti	0.000000	1.321900	-0.000002
	Ti	2.486221	-0.000002	0.096813
	O	-4.018743	-0.000005	0.542074
	O	-1.681263	-1.629002	-0.742872
	O	-1.681262	1.629010	-0.742867
	O	-0.865863	0.000000	1.133423
	O	0.865865	0.000000	-1.133425
	O	1.681260	-1.629010	0.742866
	O	1.681262	1.629002	0.742872
	O	4.018745	0.000005	-0.542066

TS		x	y	z
4-1/4-2	Ti	0.65235	1.51876	0.00000
	Ti	-0.81253	-0.17706	1.80416
	Ti	-0.81253	-0.17706	-1.80416
	Ti	1.55470	-1.12603	0.00000
	O	0.00664	1.58233	1.69312
	O	0.00664	1.58233	-1.69312
	O	-1.92458	-0.47888	3.00202
	O	-1.36037	-0.02724	0.00000
	O	2.25397	0.58787	0.00000
	O	-1.92458	-0.47888	-3.00202
	O	0.67090	-1.43687	1.52413
	O	0.67090	-1.43687	-1.52413
4-2/4-3	Ti	-0.51718	0.05504	1.31311
	Ti	0.39469	2.37828	0.00000
	Ti	0.41522	-2.47871	0.00000
	Ti	-0.51718	0.05504	-1.31311
	O	-0.51718	1.88519	1.62757
	O	0.17781	-1.66617	1.67688
	O	1.55370	3.57042	0.00000
	O	0.89174	0.44036	0.00000
	O	-1.79450	-0.35969	0.00000
	O	0.64507	-4.11565	0.00000
	O	-0.51718	1.88519	-1.62757
	O	0.17781	-1.66617	-1.67688

Isomer		x	y	z
5-1	Ti	-2.989244	-0.337759	0.398702
	Ti	-0.948262	1.410006	-0.458312
	Ti	-0.556378	-1.314226	-0.635100
	Ti	2.022794	1.678175	0.306502
	Ti	2.588685	-0.992355	0.204191
	O	-4.047385	-0.560513	1.643577
	O	-2.299705	-1.880152	-0.555565
	O	-2.778374	1.435316	-0.365750
	O	-0.998826	-0.069479	0.755580
	O	-0.463133	0.173153	-1.729840
	O	0.364855	2.594284	-0.013992
	O	1.018432	-2.079588	-0.269622
	O	2.151692	0.377119	1.522317
	O	2.719686	0.589922	-0.926753
	O	4.009370	-1.800623	0.446096
5-2	Ti	-2.938513	-0.742758	0.007867
	Ti	-1.357682	1.494169	-0.004237
	Ti	-0.000007	-1.151588	-0.135316
	Ti	1.357692	1.494172	-0.004247
	Ti	2.938508	-0.742766	0.007869
	O	-4.277207	-1.360166	0.761692
	O	-2.983629	1.063623	-0.729337
	O	-1.556409	-1.911499	-0.665998
	O	-1.442222	0.047049	1.107546
	O	0.000001	0.601755	-1.046324
	O	0.000006	2.754369	0.450682
	O	1.442228	0.047061	1.107542
	O	1.556398	-1.911510	-0.665977
	O	2.983633	1.063606	-0.729352
	O	4.277203	-1.360169	0.761699

Isomer		x	y	z
5-3	Ti	-2.303326	-0.000006	-0.757783
	Ti	-0.695816	0.000044	1.834050
	Ti	0.282098	-1.823238	-0.148029
	Ti	0.282131	1.823227	-0.148077
	Ti	2.553410	-0.000022	-0.561827
	O	-3.785712	0.000004	-1.486545
	O	-2.369953	0.000014	1.164422
	O	-1.154767	-1.536343	-1.154469
	O	-1.154725	1.536300	-1.154510
	O	-0.199721	-1.874674	1.621359
	O	-0.199708	1.874736	1.621312
	O	0.766371	0.000003	0.351920
	O	1.935110	-1.788972	-0.973674
	O	1.935144	1.788916	-0.973730
	O	3.902093	0.000002	0.383494
5-4	Ti	-2.268796	-1.817609	-0.351569
	Ti	-2.041377	1.382824	0.070567
	Ti	0.205233	-1.280031	0.318349
	Ti	0.779742	1.533257	-0.330008
	Ti	2.920016	-0.140925	0.150197
	O	-3.004322	-0.164538	-0.534410
	O	-2.888177	2.310196	1.134527
	O	-1.301991	-1.980518	1.204194
	O	-0.725591	2.402828	-0.925188
	O	-0.687642	-1.921531	-1.236807
	O	-0.341474	0.548724	0.816428
	O	1.371359	-0.010764	-1.100487
	O	1.881134	-1.567074	0.959366
	O	2.383344	1.692848	0.539705
	O	4.427608	-0.423338	-0.465554

Isomer		x	y	z
5-5	Ti	-2.482610	-0.785820	-0.001018
	Ti	-0.760799	1.944278	-0.505765
	Ti	0.163575	-1.539118	-0.428843
	Ti	0.512954	0.404318	1.469868
	Ti	2.691918	-0.317238	-0.243318
	O	-3.951803	-1.382756	0.472020
	O	-2.359905	0.997210	-0.539868
	O	-1.404485	-1.804282	-1.268378
	O	-0.794374	-1.023233	1.223011
	O	-0.653880	3.303951	-1.437239
	O	-0.236029	2.036637	1.357292
	O	0.711279	0.402433	-0.549379
	O	1.929700	-2.013898	-0.666582
	O	2.319246	0.133247	1.575779
	O	4.096398	0.158037	-0.966698
5-6	Ti	-2.557912	0.000000	-0.006051
	Ti	-0.230827	-1.754105	-0.343975
	Ti	-0.230827	1.754105	-0.343975
	Ti	1.328311	0.000000	1.506935
	Ti	1.884365	0.000000	-1.574214
	O	-3.629166	0.000001	1.244517
	O	-2.063455	-1.771132	-0.616838
	O	-2.063455	1.771134	-0.616838
	O	-0.594934	0.000000	0.392102
	O	0.721065	-1.960158	1.128479
	O	0.721065	1.960158	1.128479
	O	0.897511	-1.543391	-1.812148
	O	0.897511	1.543391	-1.812147
	O	1.955126	0.000000	3.021131
	O	2.627681	0.000000	0.036782

Isomer		x	y	z
5-7	Ti	-2.748795	-0.567093	0.234551
	Ti	-0.970403	1.404000	0.653937
	Ti	0.152901	-1.167490	-1.053262
	Ti	1.394665	1.415869	-0.743334
	Ti	2.385692	-0.810542	0.706755
	O	-4.380813	-0.851095	0.195797
	O	-2.038435	1.033130	-0.693527
	O	-2.013591	0.362398	1.765940
	O	-1.496557	-1.779422	-0.650971
	O	0.425033	2.702927	0.130616
	O	0.503732	0.063322	0.458388
	O	0.655383	0.333386	-2.075484
	O	1.622538	-2.080671	-0.566640
	O	3.025708	0.772483	-0.117531
	O	3.108339	-1.312002	2.107130
5-8	Ti	-3.084445	-0.492565	0.011995
	Ti	-1.027166	1.341541	-0.489768
	Ti	-0.392968	-1.101506	0.547154
	Ti	1.696275	1.747685	0.145743
	Ti	2.803150	-1.500126	-0.090708
	O	-4.480319	-1.130468	-0.602160
	O	-2.795472	1.402211	0.036176
	O	-1.998730	-1.452180	1.306643
	O	-1.318636	-0.513537	-1.049464
	O	0.152882	0.717569	0.943075
	O	0.364694	2.340855	-1.128691
	O	1.109217	-2.165167	0.355438
	O	2.324376	2.914450	1.132626
	O	2.874224	0.315005	-0.278040
	O	3.781939	-2.415066	-1.057743

Isomer		x	y	z
5-9	Ti	-2.565301	-0.379268	0.568409
	Ti	-1.025357	1.090178	-1.255784
	Ti	0.042657	-1.388301	-0.235625
	Ti	1.276778	1.397262	0.497642
	Ti	2.722283	-1.063916	0.143185
	O	-3.578250	-0.266931	1.866333
	O	-2.829763	0.806039	-0.916390
	O	-1.578514	-2.037808	0.247032
	O	-0.723347	0.438124	0.516432
	O	-0.275937	-0.460758	-1.842574
	O	0.238624	2.322157	-0.925241
	O	1.334401	-0.644964	1.221860
	O	1.617914	-2.286176	-0.725899
	O	1.671884	2.431518	1.705094
	O	2.882569	0.644923	-0.370673
6-1	Ti	-2.642211	-0.890879	-0.347652
	Ti	-1.199069	1.737042	0.744087
	Ti	-0.238285	-0.629249	1.750100
	Ti	0.238285	-0.629249	-1.750100
	Ti	1.199069	1.737042	-0.744087
	Ti	2.642211	-0.890879	0.347652
	O	-4.142342	-1.546491	-0.509748
	O	-2.663580	1.057800	-0.015909
	O	-1.614489	-1.600639	1.166287
	O	-1.474502	-1.198383	-1.848873
	O	-0.796383	1.030517	2.414424
	O	0.000000	0.332017	0.000000
	O	0.000000	2.989343	0.000000
	O	0.796383	1.030517	-2.414424
	O	1.474502	-1.198383	1.848873
	O	1.614489	-1.600639	-1.166287
	O	2.663580	1.057801	0.015909
	O	4.142342	-1.546491	0.509748

Isomer		x	y	z
6-2	Ti	-2.585382	-0.621873	-1.233813
	Ti	-2.244720	-0.120088	1.815704
	Ti	-0.866460	1.813881	-0.048671
	Ti	0.102983	-1.453722	0.358266
	Ti	1.972052	1.503659	-0.295536
	Ti	3.298814	-0.820819	-0.083879
	O	-3.626865	-1.077245	-2.425923
	O	-3.380433	-0.607960	0.539311
	O	-1.888148	1.204405	-1.373480
	O	-1.729985	1.650529	1.587177
	O	-1.025849	-1.768074	-0.988721
	O	-0.863191	-1.342525	1.946530
	O	0.421970	0.412971	0.082472
	O	0.616071	2.877553	-0.371845
	O	1.825392	-2.012670	0.272419
	O	2.703709	0.426472	-1.504616
	O	2.998590	0.821213	0.988376
	O	4.836200	-1.412523	-0.159898
6-3	Ti	-1.759052	1.799841	0.000001
	Ti	-1.401910	-1.105037	-1.362250
	Ti	-1.401897	-1.105026	1.362273
	Ti	1.401897	-1.105038	-1.362263
	Ti	1.401910	-1.105027	1.362259
	Ti	1.759053	1.799841	-0.000016
	O	-2.859974	3.027325	0.000001
	O	-2.249684	-2.074439	0.000020
	O	-2.010628	0.529053	-1.529057
	O	-2.010614	0.529065	1.529072
	O	-0.000012	-1.732809	-2.446975
	O	0.000000	-0.690720	0.000003
	O	0.000001	2.390537	-0.000008
	O	0.000012	-1.732788	2.446988
	O	2.010613	0.529053	-1.529077
	O	2.010630	0.529065	1.529052
	O	2.249683	-2.074439	-0.000003
	O	2.859975	3.027324	-0.000027

Isomer		x	y	z
7-1	Ti	-3.433303	0.000073	0.376225
	Ti	-1.151358	-1.368889	-1.361966
	Ti	-1.151256	1.368557	-1.362232
	Ti	-0.615467	0.000226	1.882498
	Ti	1.340520	-1.563740	0.269182
	Ti	1.340672	1.563861	0.268863
	Ti	3.725585	-0.000062	-0.033486
	O	-5.061027	0.000149	0.597947
	O	-2.766257	-1.551180	-0.646929
	O	-2.766148	1.551073	-0.647253
	O	-2.416609	0.000248	2.014012
	O	-1.089053	-0.000294	-2.624885
	O	-0.538103	-0.000064	-0.075642
	O	0.297094	-2.496173	-0.969204
	O	0.297176	2.495951	-0.969733
	O	0.409927	-1.501306	1.918122
	O	0.410013	1.501724	1.917758
	O	1.897516	-0.000051	-0.744973
	O	3.103170	-1.737864	0.619617
	O	3.103325	1.737960	0.619244
	O	4.966647	-0.000242	-1.115559
7-2	Ti	-3.435457	0.566202	0.163898
	Ti	-1.459430	-1.442139	0.797228
	Ti	-1.000891	1.100931	-1.272613
	Ti	0.326042	-1.630358	-1.561838
	Ti	1.194462	-0.516299	1.851715
	Ti	1.839408	2.145282	0.180473
	Ti	2.716961	-0.874961	-0.365785
	O	-4.297823	1.544039	1.163433
	O	-3.254729	-1.296834	0.772187
	O	-2.787444	1.415346	-1.458892
	O	-1.477861	0.451480	0.458296
	O	-0.901990	-2.591657	-0.584043
	O	-0.442198	-0.250561	-2.466344
	O	-0.377785	-1.477986	2.302527
	O	0.248877	2.331341	-0.922949
	O	0.797865	-0.584598	-0.044373
	O	1.395082	1.246890	1.879517
	O	2.143024	-2.050112	-1.741279
	O	2.584432	3.586745	0.421171
	O	2.805211	-1.376539	1.436313
	O	3.067329	0.843637	-0.646526

Isomer		x	y	z
7-3	Ti	-1.644667	2.276290	-0.801236
	Ti	-1.559248	-2.269818	0.726134
	Ti	-1.455362	0.347185	1.684386
	Ti	-1.346126	-0.961922	-1.685115
	Ti	1.139762	-1.660113	-0.341830
	Ti	1.189910	1.642063	0.819890
	Ti	3.454835	0.122726	-0.043746
	O	-2.492116	-2.253411	-0.889705
	O	-2.449389	3.596958	-1.355061
	O	-2.443039	1.545147	0.841625
	O	-2.208786	-1.324251	2.192727
	O	-1.764520	0.744319	-2.026543
	O	-0.754842	-0.601240	0.130135
	O	0.145591	2.717290	-0.183890
	O	0.173773	-2.913004	0.708562
	O	0.182577	0.996814	2.249932
	O	0.309300	-1.750658	-2.003334
	O	1.527334	0.262752	-0.411000
	O	2.908692	-1.783727	-0.055547
	O	3.006606	1.628290	1.092715
	O	4.466284	0.519594	-1.276444
7-4	Ti	-3.465498	-0.513374	-0.343507
	Ti	-1.329120	1.425005	-0.697668
	Ti	-1.010664	-1.862354	0.398999
	Ti	0.918902	2.275260	1.059178
	Ti	1.212725	-0.437102	1.814925
	Ti	1.576030	1.268019	-1.382513
	Ti	2.229104	-1.784451	-0.774583
	O	-4.743943	-0.296815	0.665376
	O	-2.983405	1.137464	-1.337703
	O	-2.693933	-2.288186	-0.204444
	O	-1.705346	-0.080278	0.413270
	O	-0.817421	2.732316	0.542406
	O	-0.174788	-1.641951	2.068567
	O	-0.098396	1.546072	-2.102016
	O	0.301557	-2.159544	-0.765151
	O	0.715603	0.552002	0.191289
	O	1.409758	1.308700	2.577281
	O	2.166290	2.683750	-0.252268
	O	2.543793	-0.177505	-1.809561
	O	2.594095	-1.266979	1.081144
	O	3.124571	-3.069306	-1.273976

Isomer		x	y	z
8-1	Ti	-4.399486	-0.930033	-0.030732
	Ti	-3.039939	1.381849	0.018796
	Ti	-1.184434	-1.463679	-0.139366
	Ti	-0.230855	1.947883	0.216785
	Ti	0.994743	-0.219587	1.742118
	Ti	1.679046	-1.214246	-1.489628
	Ti	2.343757	1.368445	-1.191384
	Ti	3.968776	-0.625919	0.649254
	O	-5.922505	-1.531419	0.154169
	O	-4.126101	0.631062	-1.196153
	O	-3.714553	0.359725	1.296376
	O	-2.854502	-2.091772	-0.221115
	O	-1.819104	2.843605	0.278671
	O	-1.413166	0.439423	-0.389540
	O	-0.296644	-1.516154	1.495177
	O	-0.045408	-2.021436	-1.435036
	O	0.331379	1.488924	1.934961
	O	1.047860	2.723727	-0.833599
	O	1.183841	0.176538	-0.140356
	O	2.124610	0.188443	-2.629448
	O	2.703130	-0.569456	2.125909
	O	3.099855	-1.837776	-0.627699
	O	3.843050	1.101555	-0.263460
	O	5.496337	-1.057953	1.067571
8-2	Ti	-3.256524	-1.202801	-0.196837
	Ti	-2.489623	1.908061	-0.231809
	Ti	-1.536639	0.443033	1.884217
	Ti	-0.054111	-1.469508	-1.403153
	Ti	0.054106	1.469531	-1.403144
	Ti	1.536648	-0.443055	1.884216
	Ti	2.489622	-1.908062	-0.231831
	Ti	3.256520	1.202802	-0.196830
	O	-4.593754	-2.148860	-0.290202
	O	-3.610314	0.640346	-0.774594
	O	-2.653356	-0.901674	1.633300
	O	-2.468866	2.071197	1.630822
	O	-1.711687	-2.007671	-1.060666
	O	-1.338877	2.707766	-1.488225
	O	-1.006268	0.699780	0.045063
	O	-0.000001	0.000015	-2.519765
	O	0.000004	-0.000015	2.840516
	O	1.006271	-0.699784	0.045063
	O	1.338869	-2.707746	-1.488254
	O	1.711683	2.007684	-1.060644
	O	2.468874	-2.071216	1.630798
	O	2.653362	0.901656	1.633308
	O	3.610309	-0.640340	-0.774607
	O	4.593751	2.148860	-0.290190

Isomer		x	y	z
8-3	Ti	-3.233460	0.135669	-0.000001
	Ti	-0.931890	-1.318200	-1.802404
	Ti	-0.931891	-1.318200	1.802403
	Ti	-0.729529	2.691320	0.000000
	Ti	0.729529	-2.691320	0.000000
	Ti	0.931891	1.318200	-1.802403
	Ti	0.931890	1.318200	1.802404
	Ti	3.233460	-0.135669	0.000001
	O	-4.859434	0.352659	-0.000001
	O	-2.645355	-0.931134	-1.531951
	O	-2.645357	-0.931137	1.531948
	O	-2.314769	1.863555	0.000001
	O	-0.360627	-1.126585	0.000000
	O	-0.090270	-3.014262	-1.645836
	O	-0.090270	-3.014262	1.645836
	O	0.000002	-0.000001	-2.697894
	O	-0.000002	0.000001	2.697894
	O	0.090269	3.014262	-1.645836
	O	0.090270	3.014262	1.645836
	O	0.360627	1.126585	0.000000
	O	2.314769	-1.863555	-0.000001
	O	2.645357	0.931137	-1.531948
	O	2.645355	0.931134	1.531951
	O	4.859434	-0.352659	0.000001
8-4	Ti	-3.243961	-0.000053	-0.231843
	Ti	-1.051223	-2.368209	0.972173
	Ti	-1.051330	2.368196	0.972150
	Ti	-0.384535	-0.000024	-1.769806
	Ti	0.384534	0.000025	1.769806
	Ti	1.051330	-2.368195	-0.972150
	Ti	1.051223	2.368209	-0.972173
	Ti	3.243961	0.000052	0.231843
	O	-4.853999	-0.000095	-0.549370
	O	-2.660800	-1.690431	0.584647
	O	-2.660887	1.690368	0.584622
	O	-2.150657	-0.000054	-1.820141
	O	-0.360714	-1.569592	2.479051
	O	-0.360778	1.569622	2.479031
	O	0.000073	-3.616249	0.000019
	O	0.000046	-1.106939	0.000007
	O	-0.000045	1.106939	-0.000007
	O	-0.000073	3.616249	-0.000019
	O	0.360779	-1.569621	-2.479031
	O	0.360713	1.569593	-2.479051
	O	2.150657	0.000055	1.820141
	O	2.660887	-1.690370	-0.584620
	O	2.660800	1.690430	-0.584649
	O	4.853999	0.000095	0.549371

Isomer		x	y	z
8-5	Ti	-3.130416	1.605540	-0.234451
	Ti	-2.727774	-1.517401	-0.281550
	Ti	-1.614898	-0.195687	1.859144
	Ti	-0.000012	-1.640823	-1.294679
	Ti	0.000008	1.116314	-1.147826
	Ti	1.614910	-0.195727	1.859129
	Ti	2.727775	-1.517396	-0.281595
	Ti	3.130409	1.605549	-0.234431
	O	-4.302598	2.744678	-0.362401
	O	-3.748787	-0.181786	-0.839448
	O	-2.720557	-1.678932	1.572062
	O	-2.542740	1.286620	1.635591
	O	-1.610607	-2.581088	-1.349418
	O	-1.505219	2.090765	-1.134595
	O	-1.179594	-0.413105	-0.026327
	O	0.000003	-0.249892	-2.451392
	O	0.000010	-0.250425	2.790167
	O	1.179598	-0.413099	-0.026343
	O	1.505207	2.090813	-1.134547
	O	1.610575	-2.581091	-1.349432
	O	2.542753	1.286579	1.635619
	O	2.720566	-1.678977	1.572002
	O	3.748785	-0.181758	-0.839458
	O	4.302596	2.744683	-0.362369
8-6	Ti	-3.067186	-1.393860	-1.157032
	Ti	-2.430153	-0.199469	1.656185
	Ti	-1.572782	1.419972	-1.468868
	Ti	-1.348611	2.297479	1.046242
	Ti	-0.190218	-1.798803	0.568234
	Ti	1.306325	1.411952	-0.313830
	Ti	2.669572	-1.690356	0.320646
	Ti	4.379733	0.268277	-0.327479
	O	-4.089125	-2.428647	-1.917930
	O	-3.719602	-0.822922	0.609320
	O	-2.704638	0.219596	-2.168432
	O	-2.433711	1.534091	2.377968
	O	-2.175051	2.914477	-0.491681
	O	-1.326686	-2.194232	-0.731764
	O	-1.325065	0.502227	0.230587
	O	-1.149765	-1.460931	2.113418
	O	0.254867	1.561905	-1.815552
	O	0.507300	2.451932	0.996378
	O	1.195115	-0.442514	0.171892
	O	1.262381	-2.913774	0.724273
	O	3.048477	1.674642	-0.549751
	O	3.561802	-1.306455	-1.173351
	O	3.801996	-0.702204	1.283675
	O	5.988340	0.546033	-0.550322

Isomer		x	y	z
8-7	Ti	-2.471806	-1.766085	1.108330
	Ti	-2.445432	-0.748366	-1.411678
	Ti	-1.951873	2.424872	-0.942895
	Ti	-1.727624	0.846610	1.732903
	Ti	0.040440	-2.050750	-0.463592
	Ti	1.009170	1.348519	0.469170
	Ti	2.841064	-1.443119	-0.450779
	Ti	4.229767	0.775965	0.142370
	O	-3.666450	-1.693928	-0.311495
	O	-2.689634	0.933174	-1.955391
	O	-2.682410	-0.576212	2.531337
	O	-2.602259	2.126834	0.881122
	O	-2.362098	3.894059	-1.549262
	O	-1.454022	-0.348443	0.208995
	O	-1.022438	-1.824369	-1.951713
	O	-0.978196	-2.860674	0.863380
	O	-0.031646	2.189775	-0.703791
	O	0.048582	1.242416	2.051938
	O	1.187585	-0.517889	-0.075241
	O	1.602057	-2.894738	-0.806269
	O	2.727276	1.891158	0.557185
	O	3.665964	-0.244174	-1.462911
	O	3.792824	-0.974268	0.968929
	O	5.774674	1.341262	0.247660
8-8	Ti	-2.567335	1.656188	-0.693091
	Ti	-2.052973	-1.488161	-0.369375
	Ti	-0.781715	-1.648845	2.090837
	Ti	-0.768621	1.132193	1.906145
	Ti	0.768605	1.132604	-1.905941
	Ti	0.781701	-1.648426	-2.091156
	Ti	2.052977	-1.488214	0.369103
	Ti	2.567341	1.656022	0.693395
	O	-3.673869	2.708083	-1.295287
	O	-3.204453	-0.212892	-0.800234
	O	-2.160177	-2.543812	1.197534
	O	-2.085649	2.069404	1.144841
	O	-1.016835	-0.234836	3.234676
	O	-0.949470	-2.168654	-1.714857
	O	-0.946209	-0.369722	0.698719
	O	-0.900263	1.710334	-1.685612
	O	0.900347	1.709755	1.686068
	O	0.946250	-0.369557	-0.698826
	O	0.949497	-2.168964	1.714428
	O	1.016741	-0.234184	-3.234736
	O	2.085670	2.069608	-1.144473
	O	2.160131	-2.543582	-1.197997
	O	3.204498	-0.213058	0.800204
	O	3.673848	2.707835	1.295782

Isomer		x	y	z
8-9	Ti	-2.703455	-1.269762	1.158719
	Ti	-2.415981	-0.539693	-1.911367
	Ti	-2.268207	1.530536	-0.082504
	Ti	0.476483	-0.419473	-1.701532
	Ti	0.643200	2.208754	1.086325
	Ti	0.670588	-0.493805	1.888191
	Ti	2.552140	1.321989	-0.746350
	Ti	3.001084	-1.653635	0.067274
	O	-3.723108	-2.087913	2.145042
	O	-3.165122	1.161718	-1.699156
	O	-3.085223	0.668684	1.208207
	O	-3.063157	-1.714866	-0.748393
	O	-1.166707	0.090093	-0.626070
	O	-0.989328	2.796513	0.439474
	O	-0.900180	-0.922388	-2.901457
	O	-0.894644	-1.348337	1.833984
	O	0.733962	1.246723	2.650517
	O	1.074860	0.498975	0.193624
	O	1.500384	-1.774925	-1.218741
	O	1.584535	0.935909	-2.301452
	O	2.135642	-1.517271	1.786527
	O	2.215292	2.859688	0.268907
	O	3.778906	0.105323	-0.322713
	O	4.085295	-2.881434	-0.044876
8-10	Ti	-2.430402	0.001998	-1.740324
	Ti	-2.263873	0.001906	1.129257
	Ti	-0.002048	-2.479829	1.731054
	Ti	-0.001296	-1.543467	-1.418780
	Ti	0.001253	1.543464	-1.418782
	Ti	0.002101	2.479833	1.731049
	Ti	2.430348	-0.002002	-1.740392
	Ti	2.263907	-0.001903	1.129192
	O	-3.587301	0.002951	-0.293691
	O	-1.650861	-1.457054	1.933978
	O	-1.648533	1.459952	1.933838
	O	-1.630018	-1.521255	-2.393284
	O	-1.627577	1.523984	-2.393195
	O	-1.102040	0.000876	-0.410124
	O	-0.003222	-3.863824	2.616344
	O	-0.002410	-2.796975	-0.171829
	O	0.002409	2.796975	-0.171835
	O	0.003300	3.863829	2.616336
	O	1.102027	-0.000878	-0.410152
	O	1.627505	-1.523989	-2.393239
	O	1.629946	1.521250	-2.393334
	O	1.648591	-1.459948	1.933796
	O	1.650919	1.457059	1.933929
	O	3.587292	-0.002952	-0.293794

Isomer		x	y	z
8-11	Ti	-3.144219	1.059613	-0.340038
	Ti	-2.274363	-1.971311	-0.831552
	Ti	-1.851675	-0.917687	1.691415
	Ti	0.145729	2.347809	-0.057913
	Ti	0.528018	-1.268859	-1.169851
	Ti	1.032903	0.564111	1.897029
	Ti	2.102576	1.092579	-1.595720
	Ti	3.406714	-0.895088	0.404118
	O	-4.493222	1.969484	-0.525603
	O	-3.313468	-0.637193	-1.374357
	O	-2.999321	0.396910	1.512911
	O	-2.611168	-2.467304	0.938238
	O	-1.572672	2.167513	-0.529361
	O	-1.070491	-0.741637	-0.019561
	O	-0.793383	-2.478509	-1.802933
	O	-0.308287	-0.504112	2.626856
	O	0.674099	2.378391	1.755932
	O	1.002301	0.545468	-0.079752
	O	1.163981	-0.205541	-2.544283
	O	1.423756	2.815657	-1.365163
	O	1.908351	-1.989124	-0.345143
	O	2.714870	-0.040582	2.000229
	O	3.651173	0.524706	-0.913155
	O	4.772852	-1.764835	0.672054
8-12	Ti	-3.070497	1.088156	-0.349565
	Ti	-1.913824	-2.103962	0.144821
	Ti	-0.862992	2.034834	1.145186
	Ti	-0.071639	-1.119900	1.924505
	Ti	0.359421	-2.270383	-1.495503
	Ti	0.516447	0.620521	-1.446408
	Ti	2.024542	2.571991	-0.242531
	Ti	2.624711	-1.281397	0.438205
	O	-4.044901	1.701994	-1.518300
	O	-3.153229	-0.822919	-0.147992
	O	-2.648254	2.306152	1.108195
	O	-1.443985	-2.388919	1.929379
	O	-1.224210	-3.244324	-1.180205
	O	-1.088963	1.261635	-0.604174
	O	-0.484096	0.637189	2.271924
	O	-0.205963	-1.132350	-0.021424
	O	0.373875	-0.788450	-2.625949
	O	0.557215	3.135440	0.867589
	O	1.209823	2.172938	-1.968279
	O	1.646095	-1.601651	2.059864
	O	1.931593	0.549896	-0.126704
	O	1.979675	-2.616013	-0.828644
	O	3.432101	3.417611	-0.197452
	O	4.246265	-1.322842	0.655717

Isomer		x	y	z
8-13	Ti	-2.743217	0.730334	-0.645836
	Ti	-2.655402	-1.095002	1.502024
	Ti	-1.903525	-1.849812	-1.165587
	Ti	-0.257764	2.975394	-0.027544
	Ti	0.108507	0.060945	1.583170
	Ti	1.389789	-1.481695	-1.491330
	Ti	2.222739	1.127316	-1.134961
	Ti	3.166128	-0.904793	1.008255
	O	-3.744383	0.254287	0.927143
	O	-3.056837	-0.606872	-1.946500
	O	-2.719467	-2.580963	0.391497
	O	-1.855013	2.246907	-0.894566
	O	-1.406247	-0.485419	0.146279
	O	-1.316064	-0.718883	2.649022
	O	-0.463446	4.556089	0.366927
	O	-0.269402	-2.285793	-1.886138
	O	-0.028038	1.822067	1.528426
	O	0.951494	-0.059091	-0.333271
	O	1.327572	2.682875	-1.085365
	O	1.671506	-0.540420	2.187476
	O	2.205585	-0.183947	-2.501158
	O	2.548097	-2.210807	-0.372813
	O	3.515030	0.760591	0.033753
	O	4.489663	-1.448010	1.811762

Chapter 10

Vibrational structure of $[(TiO_2)_n(D_2O)_m]^-$ (n=2-4, m=1-3)

The content and figures of this chapter are reprinted or adapted with permission from M. L. Weichman, S. Debnath, J. T. Kelly, S. Gewinner, W. Schöllkopf, D. M. Neumark, and K. R. Asmis, "Dissociative water adsorption on gas-phase titanium dioxide cluster anions probed with vibrational action spectroscopy" *Top. Catal.* (in preparation).

Abstract

Gas-phase complexes of water on small titanium oxide clusters are an excellent model system to illuminate the molecular-scale mechanism of dissociative water adsorption on bulk titania. Here, we report D_2 messenger-tagged infrared photodissociation (IRPD) spectra for cryo-cooled $[(TiO_2)_n(D_2O)_m]^-$ clusters with n=2–4 and m=1–3. Vibrational features are reported in the spectral windows of 400–1200 cm^{-1} and 2600–3000 cm^{-1}, capturing both fingerprint cluster modes and OD stretching modes. The IRPD spectra are interpreted with the aid of ωB97X-D/aug-cc-pVDZ density functional calculations. We see strong evidence for dissociative adsorption of water on the clusters studied here. We conclusively assign the IRPD spectra of the n=2 clusters with one and two water molecules, and the n=3 clusters with up to three water molecules to dissociatively adsorbed global minimum energy structures. We also provide insight into the reactivity of the more complicated n=4 clusters. From this work, we can draw conclusions about the size dependence and site-specificity of $(TiO_2)_n^-$ cluster reactivity, and, by extension, the behavior of defect sites on a bulk titania surface.

10.1 Introduction

Titanium dioxide (TiO_2) is an abundant, inexpensive, non-toxic, stable, and versatile semiconducting material with numerous applications[103,462] in heterogenous catalysis and photocatalysis,[412,463,464] photovoltaic cells,[407,465] environmental pollutant degradation,[409] and as a gas sensor and a white pigment. TiO_2 is perhaps most notable as the worlds most widely studied photocatalyst.[405,466–468] Since Fujishima and Honda's 1972 discovery of photocatalytic water splitting and H_2 evolution on a TiO_2 electrode,[404] extensive work has been done to develop, characterize, and optimize TiO_2-based technologies for sustainable conversion of solar light into chemical hydrogen fuel.[469] This technology has not yet become feasible for widespread deployment due to the mismatch between the solar spectrum and the bandgap of TiO_2[415,469] and slow rates of H_2 evolution. Reaching a detailed understanding of the chemical mechanisms of hydrolysis and H_2 evolution on TiO_2 surfaces and nanostructures remains a complex problem. In this paper, we explore water splitting on TiO_2 in microscopic detail by measuring infrared spectra of $[(TiO_2)_n(D_2O)_m]^-$ cluster anions. This work stands as a follow-up to our prior vibrational characterization of the bare $(TiO_2)_n^-$ anions[470] as we move towards more explicit cluster-based models of catalytic reaction mechanisms.

There is an enormous body of experimental and theoretical work on the interaction of water with titanium dioxide surfaces. Wetting of the TiO_2 surface is necessarily the first step of any water splitting reaction pathway, and yet the extent to which water adsorbs molecularly or dissociatively on TiO_2 is not agreed upon.[471,472] Experimental studies show that water adsorption trends are distinct for different facets of rutile and anatase TiO_2 and depend heavily on water surface coverage and the presence of defect sites.[473–487] Further studies have found that TiO_2 photoexcitation can enhance the initial dissociative adsorption

of water.[487,488] Overall, dissociative water adsorption appears to be a minor pathway on defect-free TiO_2 surfaces, but is more likely to occur at defect sites like steps,[486,489] ridges,[490] and particularly oxygen vacancies.[473–475,478,479,481,483,484,491]

In a bulk experiment, it is challenging to prepare a surface with reproducible, well-characterized defect sites, let alone to probe the reaction mechanism at a specific catalytic center. Small gas-phase clusters can serve as model systems of the local behavior and reactivity of a bulk metal oxide.[424,492–494] Clusters demonstrate varied geometries and stoichiometries, with under-coordinated atoms and dangling moieties that mimic reactive point defects on a bulk surface.[392,495] Specific clusters can be complexed with an exact number of adsorbed substrates, allowing for systematic characterization of how cluster size, stoichiometry, and bonding motifs affect reactivity.[122,123,434] These systems are also tractable for simulation with higher level quantum chemistry calculations, allowing for analysis of geometries and reaction mechanisms with clarity not available in bulk studies.[364]

While there is a growing body of work on the gas-phase spectroscopy of bare titanium dioxide clusters,[71,261,352,429,438,470] studies probing their interactions with water are more sparse. Early work from the Castleman group reported on the mass spectrum of the water-solvated TiO^+ cation.[496] Yin and Bernstein[434] reacted neutral Ti_2O_4 and Ti_2O_5 clusters with water, and saw oxidation of water to hydrogen peroxide on Ti_2O_5 after irradiation with visible light. Zheng and coworkers have reported infrared action spectra of $[TiO(H_2O)_m]^+$ clusters[497] and anion photoelectron spectra of $[TiO_2(H_2O)_m]^-$ clusters,[498] and ascribe both sets of measurements to structures involving dissociatively adsorbed waters.

Several theoretical groups have reported calculations of molecular and dissociative water adsorption and water splitting on small $(TiO_2)_n$ clusters;[499–506] others have studied these interactions on larger TiO_2 nanostructures.[507–510] The most thorough body of work comes from calculations by Dixon and coworkers regarding water adsorption, hydrolysis, and H_2/O_2 evolution on small neutral titanium dioxide clusters.[511–513] Most recently, these authors used a hybrid genetic algorithm to rigorously identify the lowest-energy structures for the neutral $(TiO_2)_n(H_2O)_m$ ($n \leq 4$, $m \leq 2n$) clusters.[513] Structure optimization and single-point energy calculations were then carried out with the B3LYP and CCSD(T) methods respectively.

Dixon and coworkers predict that the bare $(TiO_2)_n$ (n = 2–4) clusters dissociatively adsorb the first two water molecules, forming minimum energy structures with two and four terminal hydroxide groups after the first and second waters react, respectively.[513] $(TiO_2)_3$ can go on to dissociate a third water, forming a structure with six terminal hydroxide groups. Many theoretical studies[501,503,511,513] note that after the initial adsorption of water on a bare $(TiO_2)_n$ cluster, at least two H atom transfer steps are required in order to form the $(TiO_2)_n(H_2O)_m$ global minimum structure. Typically, the reaction proceeds through an intermediate containing a bridging OH before reaching the final structure containing only terminal OH moieties.[503,511] Water dissociation is preferred until all titanium atoms are saturated with coordination numbers of four; subsequent water molecules added beyond these hydrolysis limits adsorb molecularly.[513]

Cryogenic vibrational action spectroscopy has proved to be an excellent method to characterize the vibrational frequencies and geometries of gas-phase ions,[47,48] and has been par-

ticularly illuminating for the study of transition metal oxide clusters, which demonstrate complex electronic structure and many low-lying structural isomers.[367,454,470] Most recently this technique has been adapted to illuminate site-specific water dissociation on $Al_3O_4^+$.[123]

Here, we present vibrationally resolved infrared photodissociation (IRPD) spectra of the cryo-cooled deuterated titanium dioxide-water cluster anions $[(TiO_2)_n(D_2O)_m]^-$ with n=2–4 and m=1–3. We also report a density functional theory (DFT) study of the structural isomers, energetics, and harmonic IR spectra of these anionic clusters. The vibrational action spectra are acquired by measuring changes in the time-of-flight mass spectrum after irradiation with intense light in the fingerprint region (400–1200 cm^{-1}) and in the OD stretching region (2600–3000 cm^{-1}).

We unambiguously assign the $[(TiO_2)_n(D_2O)_m]^-$ clusters with $n = 2, 3$ to the minimum energy calculated structures, demonstrating dissociative adsorption of up to two waters on $(TiO_2)_2^-$ and up to three waters on $(TiO_2)_3^-$. The clusters with $n = 4$ and m=1–2 present a more challenging case, with potential contributions from higher-lying structural isomers. Through agreement between experimental and DFT results, we identify regions of vibrational structure associated with OD stretching (2600–2800 cm^{-1}), terminal TiO stretching (900–1000 cm^{-1}), Ti-O-Ti bridge stretching (700–900 cm^{-1}), and Ti-O-D bending and stretching as well as more delocalized cluster modes (700 cm^{-1} and below). As D_2O molecules adsorb sequentially, Ti atoms become fully coordinated and dangling TiO moieties react to form Ti-O-D moieties; the loss of vibrational structure in the TiO stretching region therefore serves as the most conclusive signature of dissociative water adsorption on $(TiO_2)_n^-$. From these results, we draw conclusions about the size- and site-dependent reactivity of $(TiO_2)_n^-$ and comment on the relevance of this work to understanding water splitting on bulk TiO_2 defect sites.

10.2 Experimental Methods

The IRPD methods and apparatus have been described in detail in Chap. 2. TiO_2-water cluster anions are cryo-cooled and messenger-tagged with D_2. The depletion of the tagged species after irradiation with light is monitored as a function of wavelength in order to construct an infrared action spectrum. It was convenient to use D_2O rather than H_2O clusters in order to (a) mitigate congestion in the mass spectrum and (b) have access to the OD stretching region with the free electron laser.

$[(TiO_2)_n(D_2O)_m]^-$ clusters are prepared in a dual gas-channel pulsed laser vaporization source,[123] based on the fast flow cluster reactor pioneered by Smalley and coworkers.[121] A frequency-doubled Nd:YAG laser operated at 50 Hz is focused onto a rotating titanium rod, with a pulse energy of 15–20 mJ. The resulting plasma is quenched with a pulse of 0.25% O_2 in helium from a General Valve. $(TiO_2)_n$ clusters are formed during expansion through a clustering channel downstream from the rod. After a short time delay, a second General Valve backed by 2 bar of helium passed through a D_2O bubbler sends a pulse of gas into the final stage of the clustering channel to form the desired $[(TiO_2)_n(D_2O)_m]^-$ clusters.

A quadrupole mass filter is tuned to transmit only the desired $[(^{48}Ti^{16}O_2)_n(D_2{}^{16}O)_m]^-$ clusters for a given experiment. The quadrupole can also be scanned to acquire a mass spectrum of the clusters produced by the source; quadrupole mass spectra of the $(TiO_2)_n$ clusters before and after addition of D_2O are shown in Fig. 10.8.

For all systems discussed in the current work, the ring-electrode ion trap is filled continuously with pure D_2 buffer gas and is held at 15 K. The trap temperature and buffer gas concentration were chosen to tag around 10% of clusters with a single D_2 molecule.

In this experiment, we use two operating regions of the FEL: the 440–1200 cm^{-1} range produced with a 26 MeV electron beam, and the 2600–3000 cm^{-1} range produced with a 43.5 MeV electron beam. In the lower energy region, the FHI-FEL has a spectral bandwidth ranging from $\sim$2 cm^{-1} fwhm at 450 cm^{-1} to $\sim$7 cm^{-1} fwhm at 1200 cm^{-1}. In the higher energy region, the bandwidth is 15–20 cm^{-1}. Typical macropulse energies are 30–40 mJ in both regions. For each spectrum, the photon energy is stepped in 3 cm^{-1} increments, though in some cases, a 5 cm^{-1} step was used in the higher energy region where the FEL bandwidth is larger.

D_2O loss is also observed for some clusters when irradiated with the full FEL power. These dissociation channels are infrared multiple photon dissociation (IRMPD) processes and are negligible with the attenuated laser pulses used to acquire the D_2-tagged IRPD spectra.

10.3 Calculations

The relative energies, optimized geometries, harmonic vibrational frequencies, and IR intensities of the lowest-lying $[(TiO_2)_n(D_2O)_m]^-$ isomers were investigated using DFT. We use the range-separated hybrid ωB97X-D functional[514] which includes dispersion interactions and has been shown to perform well for geometry optimization of transition metal compounds.[515] The aug-cc-pVDZ (aVDZ) basis set is used for all atoms, with full treatment of all electrons. All DFT calculations were carried out using Gaussian 09, revision C01.[402]

Low-lying $[(TiO_2)_n(D_2O)_m]^-$ structures were adapted largely from the recent theoretical work by Dixon and coworkers[513] who used a genetic algorithm to identify the most stable neutral $(TiO_2)_n(H_2O)_m$ cluster structures. We considered all low-lying structures these authors proposed as well as additional $n = 4$ cluster structures involving bridging OH moieties,[503,511] The literature geometries were reoptimized with spin-unrestricted ωB97X-D/aVDZ calculations as doublet anions. All optimizations were carried out without symmetry restrictions. We report all calculated $[(TiO_2)_n(D_2O)_m]^-$ cluster structures lying within 150 kJ/mol of the lowest energy isomer, as well as some higher-lying molecularly adsorbed $n = 4$ structures. Complete lists of calculated isomer energetics, harmonic vibrational frequencies above 400 cm^{-1}, and optimized geometries can be found in the Supporting Information (SI). We also list the binding energy of the last D_2O molecule to each cluster by comparing the energy of $[(TiO_2)_n(D_2O)_m]^-$ to that of the lowest energy $[(TiO_2)_n(D_2O)_{m\text{-}1}]^-$ cluster plus a free D_2O molecule.

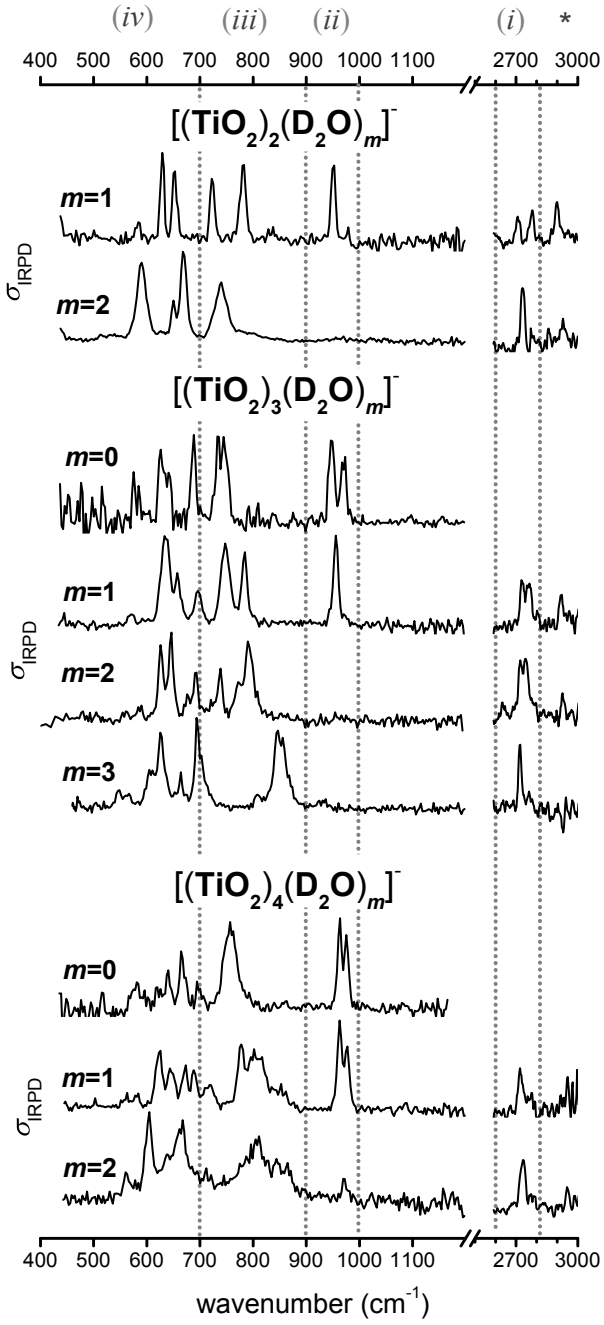

Figure 10.1: Experimental D_2-tagged IRPD spectra of $[(TiO_2)_n(D_2O)_m]^-$ (n=2–4, m=0–3) clusters. Regions (i)-(iv) of vibrational structure are marked with gray dashed lines. The region marked with an asterisk contains the D_2 tag stretching. The m=0 spectra are reproduced from our prior work.[470]

Table 10.1: Experimental vibrational frequencies (cm^{-1}) from the D_2-tagged IRPD spectra of $[(TiO_2)_n(D_2O)_m]^-$ clusters. Band positions and full widths at half-maximum (in parentheses) are determined by fitting a Gaussian line function to the experimental data.

n	m	Region	Band Positions (cm^{-1})					
2	1	(*i*)	**A**	2776(25)	**B**	2709(23)		
		(*ii*)	**C**	951(9)				
		(*iii*)	**D**	781(13)	**E**	723(10)		
		(*iv*)	**F**	652(10)	**G**	629(9)	**H**	584(10)
		tag	*	2900(33)				
2	2	(*i*)	**A**	2732(23)				
		(*iii*)	**B**	740(27)				
		(*iv*)	**C**	669(14)	**D**	650(9)	**E**	590(20)
		tag	*	2929(33)				
3	1	(*i*)	**A**	2761(34)	**B**	2728(20)		
		(*ii*)	**C**	955(11)				
		(*iii*)	**D**	784(13)	**E**	748(21)		
		(*iv*)	**F**	696(16)				
			I	571(11)	**G**	659(14)	**H**	635(20)
		tag	*	2920(22)				
3	2	(*i*)	**A**	2746(31)	**B**	2719(17)		
		(*iii*)	**C**	792(19)	**D**	771(12)	**E**	738(9)
		(*iv*)	**F**	692(9)	**G**	645(10)	**H**	626(10)
			I	586(14)	**J**	561(14)		
		tag	*	2928(38)				
3	3	(*i*)	**A**	2719(17)				
		(*iii*)	**B**	855(17)	**C**	844(10)		
		(*iv*)	**D**	700(23)	**E**	694(5)	**F**	664(5)
			G	627(16)	**H**	606(15)	**I**	564(18)
			J	546(11)				
4	1	(*i*)	**A**	2723(30)				
		(*ii*)	**B**	977(11)	**C**	963(10)		
		(*iii*)	**D**	853(21)	**E**	805(42)	**F**	776(12)
			G	716(23)				
		(*iv*)	**H**	689(11)	**I**	672(13)	**J**	646(17)
			K	623(14)	**L**	582(11)	**M**	562(17)
4	2	(*i*)	**A**	2732(29)				
		(*ii*)	**B**	972(9)				
		(*iii*)	**C**	849(93)	**D**	806(36)		
		(*iv*)	**E**	663(20)	**F**	604(15)	**G**	562(13)
		tag	*	2950(20)				

10.4 Results and Discussion

Experimental D_2-tagged IRPD spectra of the $[(TiO_2)_n(D_2O)_m]^-$ clusters are shown in Fig. 10.1; experimental peak positions and widths from these spectra are reported in Table 10.1. D_2-tagged spectra for the bare $(TiO_2)_n^-$ ($n = 3, 4$) clusters in the 400–1200 cm^{-1} fingerprint region are also plotted in Fig. 10.1 from our earlier IRPD study,[470] though no IRPD spectrum could be acquired for the bare $n = 2$ cluster, which is known to react with molecular hydrogen rather than tagging.[97,352] The lowest-energy structures for the bare clusters identified in previous work[352,417,470] are reproduced in Fig. 10.2. The structures and relative energies (kJ/mol) are shown for the calculated low energy $[(TiO_2)_n(D_2O)_m]^-$ ($m \geq 1$) structures in Fig. 10.3.

D_2O-loss IRMPD spectra taken with the full FEL power are shown in Fig. 10.9 for some clusters. IRMPD spectra are generally more difficult to interpret than their IRPD counterparts; because IRMPD involves the sequential absorption of multiple photons, the intensities of spectral features are not directly comparable to calculated harmonic IR intensities. Some IR active vibrational modes may also be transparent in IRMPD experiments.[95] Despite these caveats, the D_2-tagged and D_2O-loss spectra are in good agreement for the clusters with $n = 2, 3$, but do show some interesting differences for the $n = 4$ cluster spectra, as will be discussed further below.

Simulated IR spectra derived from unscaled DFT harmonic vibrational frequencies and IR intensities are compared to the experimental IRPD results in Figs. 10.4-10.7. Simulations are plotted both as stick spectra (red) and as traces convoluted with a 10 cm^{-1} Gaussian lineshape function (blue). Based on comparison of the IRPD and DFT simulated spectra, we can classify four general frequency regions of IR-active vibrational structure, which are

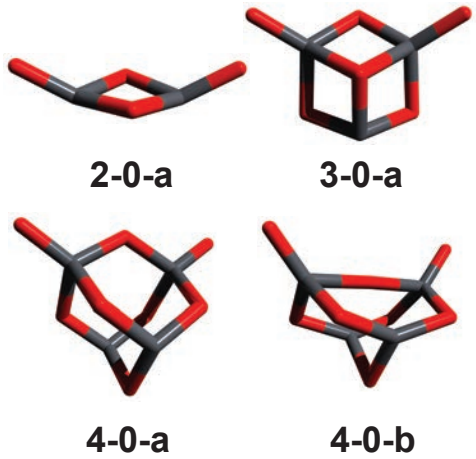

Figure 10.2: Low-lying isomers of $(TiO_2)_n^-$, n=2–4 clusters identified in prior work.[352,417,470] Atoms in dark gray represent Ti, atoms in red represent O.

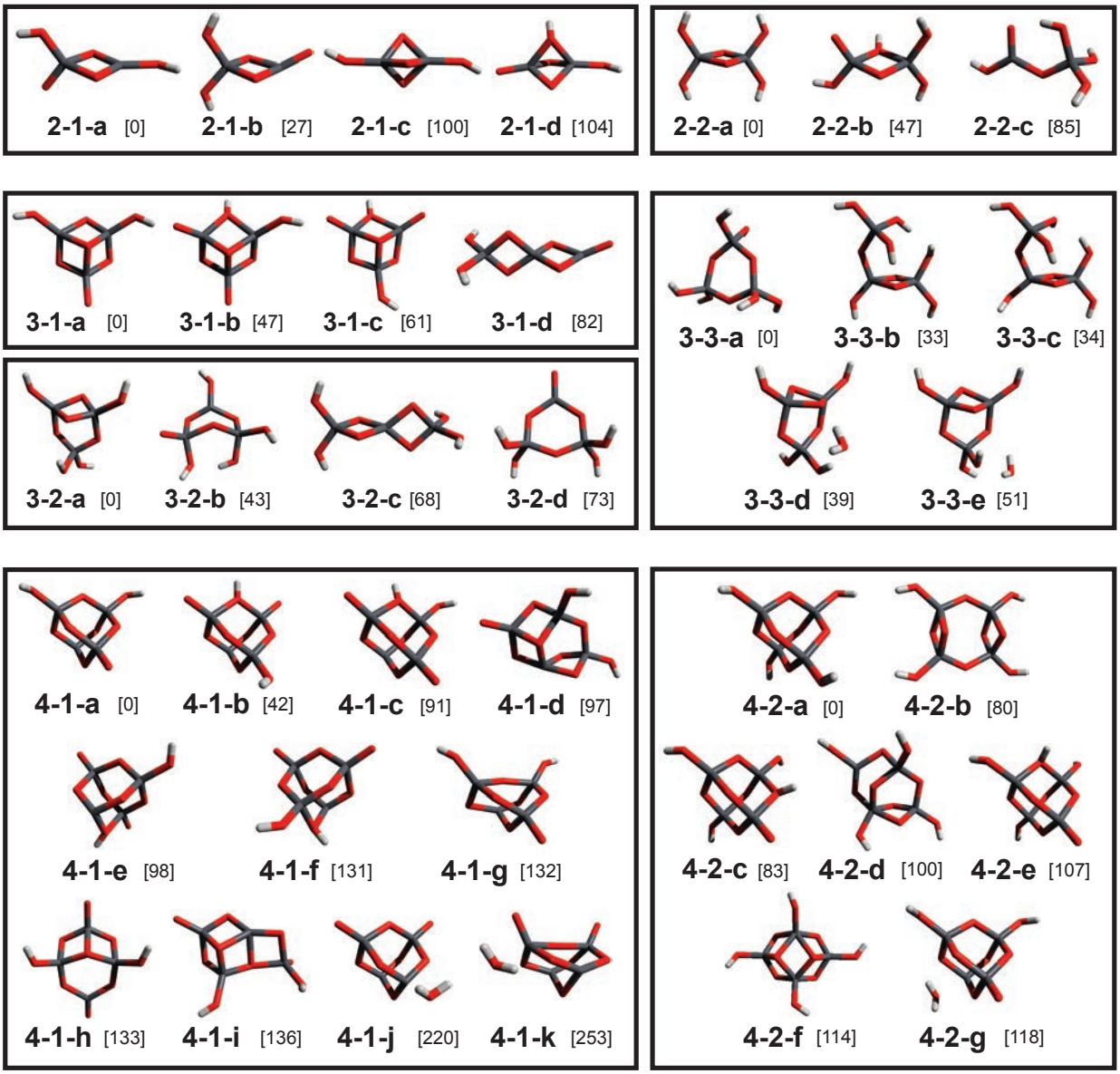

Figure 10.3: ωB97X-D/aVDZ minimum energy structures and relative energies (kJ/mol) of energetically low-lying isomers of doublet $[(TiO_2)_n(D_2O)_m]^-$ cluster anions. Atoms in dark gray represent Ti, atoms in red represent O, and atoms in light gray represent H.

laid out in Fig. 10.1. Region (*i*) from 2600–2800 cm^{-1} and region (*ii*) from 900–1000 cm^{-1} are uniquely associated with OD stretching and terminal TiO stretching modes, respectively. Region (*iii*) from 700–900 cm^{-1} is largely associated with Ti-O-Ti bridge stretching. Ti-O-Ti bridge motion also couples with Ti-O-D bending and stretching modes, which tend to fall below 700 cm^{-1} in region (*iv*), along with more delocalized wagging, bending, rocking, and ring breathing modes. Dixon and coworkers[511,513] have also reported simulated IR spectra and described similar frequency regions and vibrational motions for the neutral $(TiO_2)_n(H_2O)_m$ clusters.

For $n = 2, 3$, the simulated IR spectra of the minimum energy calculated structures are in reasonably good agreement with the experimental spectra; the assignments for the $n = 4$ structures prove more complex, as discussed in more detail below. The ωB97X-D/aVDZ frequencies of the best-fit simulations are generally higher than those observed experimentally, yielding scaling factors of 0.94–0.95 in regions (*i*) and (*ii*) and a range of 0.95–1.02 in regions (*iii*) and (*iv*). Note that this is in contrast to the BP86/6-311+G* calculations in our prior work,[470] which produced frequencies typically lower than the experimental values. These results are in reasonable accordance with the literature-recommended scale factors for these functionals.[516]

Most of the spectra of the tagged clusters studied here also exhibit a D_2 stretching feature in the 2900–2950 cm^{-1} range of the IRPD spectrum, as marked with an asterisk in Fig. 10.1. While the D_2 stretch is IR forbidden in free D_2, it appears weakly here due to polarizing interactions with $[(TiO_2)_n(D_2O)_m]^-$. The adsorbed tag stretching frequencies are also red-shifted from the free D_2 stretching fundamental frequency at 2994 cm^{-1}.[517] The observation of these tag stretching features also provides some confirmation that the tag molecules are weakly molecularly adsorbed, rather than dissociated or chemisorbed on the $[(TiO_2)_n(D_2O)_m]^-$ cluster surface.

We now provide more thorough analyses of the experimental and theoretical results for each of the $[(TiO_2)_n(D_2O)_m]^-$ clusters.

10.4.1 $[(TiO_2)_2(D_2O)_m]^-$

The experimental IRPD spectrum for $[(TiO_2)_2(D_2O)]^-$ (Fig. 10.1) shows a pair of vibrational features in the OD stretching region (*i*), one strong peak in the TiO stretching region (*ii*), and four strong features spanning regions (*iii*) and (*iv*). The spectrum simplifies with the addition of a second D_2O, with only one vibrational feature in region (*i*) and no features in region (*ii*).

The bare $(TiO_2)_2^-$ cluster structure **2-0-a** is shown in Fig. 10.2.[352,417] The two lowest energy calculated structures upon addition of one D_2O, **2-1-a** and **2-1-b** (Fig. 10.3), correspond to dissociative water adsorption on **2-0-a**. Structure **2-1-b**, with two terminal OD groups on the same Ti atom, has been reported as the lowest energy neutral structure,[501,513] while we find the **2-1-a** anion to lie 27 kJ/mol lower in energy. The second water also dissociatively adsorbs to form the **2-2-a** structure, with two terminal OD moieties on each Ti atom, leaving both Ti atoms four-fold coordinated. Structures with **2-2-a** connectivity are

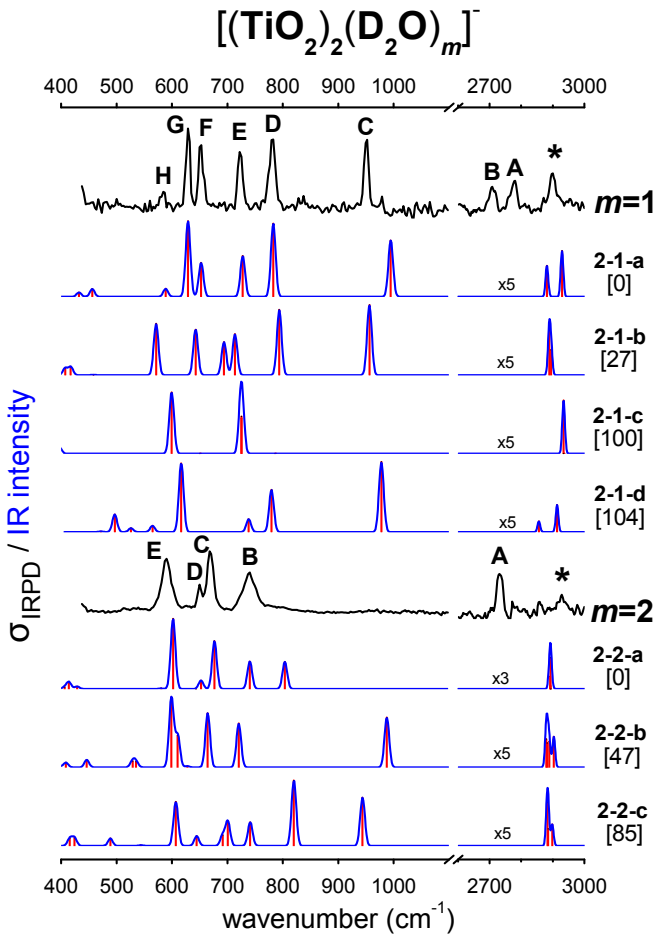

Figure 10.4: Experimental D_2-tagged IRPD spectra (black) of $[(TiO_2)_2(D_2O)_m]^-$, simulated unscaled linear IR absorption traces (blue), stick spectra (red), and relative energies (kJ/mol) of the predicted lowest-lying isomers at the ωB97X-D/aVDZ level of theory.

widely predicted to be the neutral lowest-lying isomer as well.[500,501,504,505,511,513] Dixon and coworkers[513] report a C_{2v} structure for the **2-2-a** neutral only slightly distorted from D_{2d} symmetry. With our ωB97X-D/aVDZ calculations, we find a C_1-symmetry local minimum for the **2-2-a** anion with the two bridging O atoms shifted significantly closer to one of the two Ti atoms.

We assign the experimental $[(TiO_2)_2(D_2O)_m]^-$ vibrational features through comparison with the simulated IR spectra (Fig. 10.4). The agreement between the **2-1-a** simulated spectrum and the IRPD $[(TiO_2)_2(D_2O)]^-$ spectrum is unambiguous, as all experimental features are closely reproduced. The two experimental OD stretching features in region (i) at 2776 and 2709 cm^{-1} (peaks A and B) are predicted to lie at 2930 and 2882 cm^{-1}. The higher frequency of these two modes corresponds to the stretching of the OD bonded to

the undercoordinated Ti atom. Stretching of the single terminal TiO moiety yields peak C in region (*ii*) measured at 951 cm^{-1} and calculated to lie at 996 cm^{-1}. Peaks D and E in region (*iii*) at 781 and 723 cm^{-1} correspond respectively to symmetric and antisymmetric stretching of the two Ti-O-Ti bridges, calculated at 783 and 728 cm^{-1}, while peaks F, G, and H at 652, 629, and 584 cm^{-1} correspond closely to Ti-O-D bending motions calculated at 653, 629, and 589 cm^{-1}.

For $[(TiO_2)_2(D_2O)_2]^-$, **2-2-a** is clearly a better match for the experimental IRPD spectrum than **2-2-b** or **2-2-c**, as it reproduces the complete absence of features in region (*ii*). We observe a single sharp feature (peak A) in region (*i*), experimentally observed at 2732 cm^{-1} and reproduced by four calculated **2-2-a** OD stretching modes with nearly degenerate frequencies around 2893 cm^{-1}. In region (*iv*), peaks C, D, and E at 669, 650, and 590 cm^{-1} are closely reproduced by DFT features at 677, 653, and 602 cm^{-1}, and correspond to Ti-O-D stretching and bending motions. However, in region (*iii*), where the DFT **2-2-a** spectrum shows two distinct Ti-O-Ti symmetric and antisymmetric bridge stretching features at 804 cm^{-1} and 740 cm^{-1}, the experimental spectrum shows only a single broad feature (peak B) centered at 741 cm^{-1}.

This discrepancy results from significant anharmonicity of the 804 cm^{-1} symmetric Ti-O-Ti bridge stretching mode of **2-2-a**. This mode has a double well vibrational potential that connects two equivalent C_1-symmetric local minima via a C_2-symmetric transition state (TS) structure lying 25 kJ/mol (2100 cm^{-1}) higher; the vibrational displacement of the imaginary mode at the C_2 geometry is shown in Fig. 10.10a. This barrier causes inversion splitting of each vibrational level and a significant red shift of the fundamental transition, likely resulting in an experimental vibrational feature that contributes to the broad experimental peak B, rather than at the 804 cm^{-1} location originally predicted by the harmonic simulation. Fig. 10.10b compares the simulated harmonic IR spectrum at the **2-2-a** TS geometry to that of the **2-2-a** minima and the experimental IRPD spectrum.

10.4.2 $[(TiO_2)_3(D_2O)_m]^-$

The $[(TiO_2)_3(D_2O)]^-$ D_2-tagged IRPD spectrum shows two closely spaced OD features in region (*i*), one strong TiO feature in region (*ii*), and intense features in region (*iii*) continuing into region (*iv*) (Fig. 10.1). With the addition of a second water molecule in $[(TiO_2)_3(D_2O)_2]^-$ and a third in $[(TiO_2)_3(D_2O)_3]^-$, the IRPD spectra show the structure in region (*i*) merging into a single feature, a complete absence of features in region (*ii*), and intense structure in regions (*iii*) and (*iv*) blue-shifting with additional water molecules.

The comparison between experimental and calculated vibrational structure is reasonably straightforward for all three $[(TiO_2)_3(D_2O)_m]^-$ structures (Fig. 10.5). In previous work, we assigned the lowest energy isomer of the bare $(TiO_2)_3^-$ cluster to the **3-0-a** structure (Fig. 10.2).[470] For $[(TiO_2)_3(D_2O)]^-$, the lowest-lying **3-1-a** structure corresponds to dissociative adsorption of D_2O on **3-0-a**, with two terminal OD groups on neighboring Ti atoms and one remaining terminal TiO group (Fig. 10.3). This structure has also been predicted to be the global minimum for the corresponding neutral cluster.[503,513]

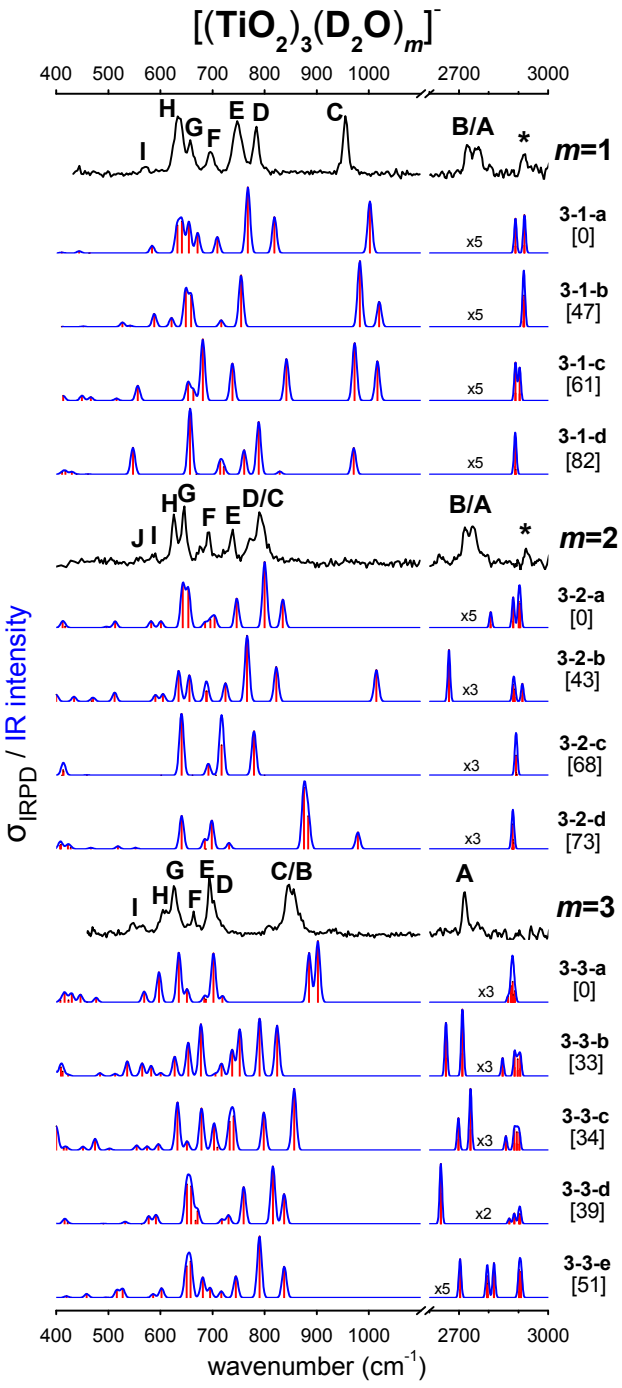

Figure 10.5: Experimental D_2-tagged IRPD spectra (black) of $[(TiO_2)_3(D_2O)_m]^-$, simulated unscaled linear IR absorption traces (blue), stick spectra (red), and relative energies (kJ/mol) of the predicted lowest-lying isomers at the ωB97X-D/aVDZ level of theory.

The simulated **3-1-a** IR spectrum reproduces all experimental vibrational features. The two experimental OD stretching features in region (*i*) at 2761 and 2728 cm^{-1} (peaks A and B) are matched by DFT peaks at 2920 and 2890 cm^{-1}. The sole terminal TiO stretching frequency in region (*ii*) at 955 cm^{-1} (peak C) is calculated to lie at 1002 cm^{-1}. The two strong peaks in region (*iii*) at 784 and 748 cm^{-1} (peaks D and E) are matched by intense calculated Ti-O-Ti bridge stretching features at 819 and 768 cm^{-1}. Weaker peaks F and G in region (*iv*) at 696 and 659 cm^{-1} correspond to Ti-O-Ti bridge stretching and Ti-O-D stretching modes, respectively. Three calculated modes at 655, 641 and 633 cm^{-1} underlie experimental peak H, at 635 cm^{-1}, and correspond to delocalized stretching modes involving the Ti-O-Ti bridges, Ti-O-D moieties, and the central triply coordinated O atom. Even the tiny experimental peak I at 571 cm^{-1} is reproduced with a weak calculated Ti-O-Ti bridge stretching feature at 584 cm^{-1}.

Interpretation of the $[(TiO_2)_3(D_2O)_2]^-$ spectrum proceeds through similarly reasonable agreement with the simulated spectrum of the global minimum **3-2-a** structure (Fig. 10.5). The **3-2-a** structure (Fig. 10.3) follows directly from addition of a second D_2O on **3-1-a**, forming two terminal OD groups at the previous site of the terminal TiO group, and releasing the strain of the central triply coordinated O atom. As for **3-1-a**, this structure was also predicted to be preferred by the corresponding neutral cluster.[504,513] Peaks A and B in region (*i*) at 2746 and 2719 cm^{-1} are reproduced by calculated OD stretching modes at 2906/2901 cm^{-1} and 2883 cm^{-1}; the higher frequency modes correspond to stretching of the two OD moieties on separate Ti atoms, while the lower frequency mode corresponds to stretching of one of the two OD groups that share the remaining Ti atom. In region (*iii*), overlapping experimental peaks C and D at 792/771 cm^{-1} are reasonably matched by DFT features at 835 and 800 cm^{-1} and correspond to Ti-O-Ti bridge stretching modes. Leading into region (*iv*), weak peaks E and F at 738 and 692 cm^{-1} are reproduced respectively by a calculated Ti-O-Ti bridge stretching mode at 746 cm^{-1} and a cluster of delocalized ring stretching modes at 704, 695, and 685 cm^{-1}. Intense peaks G and H at 645 and 626 cm^{-1} match up with closely spaced DFT features at 654 and 643 cm^{-1} and correspond to stretching of the Ti-O-D moieties that do not share a Ti atom. Weak features I and J at 586 and 561 cm^{-1} line up with DFT peaks at 601 and 582 cm^{-1}, and involve Ti-O-Ti bridge stretching and Ti-O-D bending and stretching motion.

For $[(TiO_2)_3(D_2O)_3]^-$, the minimum energy structure **3-3-a** is formed through addition of a third D_2O to **3-2-a**, and results in two terminal OD groups on each of the three Ti centers, all of which remain 4-coordinate as one of the Ti-O-Ti bridges is released. The same structure has been widely predicted for the neutral $(TiO_2)_3(H_2O)_3$ clusters.[503,504,513] The assignment of $[(TiO_2)_3(D_2O)_3]^-$ IRPD spectrum to the **3-3-a** minimum energy structure is quite clear, as no higher-lying candidates demonstrate the required intense structure on the high energy side of region (*iii*) and a gap between 700–800 cm^{-1}. Additionally, only structure **3-3-a** has a single sharp feature in region (*i*), due to the six terminal OD groups having become nearly equivalent.

The experimental peak A in region (*i*) measured at 2719 cm^{-1} is matched by the DFT frequencies tightly clustered around 2880 cm^{-1}. Overlapping peaks B/C at 855/844 cm^{-1}

near the high energy edge of region (*iii*) are reproduced by calculated modes at 902/885 cm^{-1} and correspond to coordinated motion of all three roughly equivalent Ti-O-Ti bridges. In region (*iv*), overlapping peaks D/E at 700/694 cm^{-1} correspond closely to a cluster of DFT features at 719/702/688/684 cm^{-1}, corresponding to Ti-O-D motion, with the central peak at 702 cm^{-1} being the most intense. Peak F at 664 cm^{-1} and the overlapping peaks G and H at 627/606 cm^{-1} correspond to calculated coupled Ti-O-D stretching and ring breathing peaks at 651 cm^{-1} and 635/597 cm^{-1}. The weak peak I at 564 cm^{-1} is matched by a delocalized bridge stretching mode at 569 cm^{-1}.

10.4.3 $[(TiO_2)_4(D_2O)_m]^-$

The D_2-tagged IRPD spectrum of $[(TiO_2)_4(D_2O)]^-$ shows a single OD stretching feature in region (*i*), two strong TiO stretching features in region (*ii*), broad structure spanning region (*iii*), and several weaker features in region (*iv*) (Fig. 10.1). With the addition of a second D_2O molecule, the $[(TiO_2)_4(D_2O)_2]^-$ D_2-tagged IRPD spectrum shows one OD feature in region (*i*), a single weak TiO feature in region (*ii*), further amorphous broad structure spanning region (*iii*), and more intense, broadened structure in region (*iv*). The persistent region (*ii*) TiO features in the $[(TiO_2)_4(D_2O)_m]^-$ spectra represent a departure from the $n = 2$ and $n = 3$ clusters discussed above, where complete loss of TiO structure with increasing addition of water was a clear indicator of dissociative adsorption. Interestingly, the analogous D_2O-loss IRMPD spectra shown in Fig. 10.9 are also quite distinct from the IRPD spectra for both $n = 4$ clusters.

The $[(TiO_2)_4(D_2O)_m]^-$ IRPD spectra are compared to harmonic DFT spectra of low-lying isomers in Figs. 10.6 and 10.7. For $[(TiO_2)_4(D_2O)]^-$, the lowest-energy calculated **4-1-a** structure (Fig. 10.3) is also predicted to be the lowest energy structure of neutral $(TiO_2)_4(H_2O)$ by Dixon and coworkers[513] and by Du *et al.*[503] However, the IRPD spectrum distinctly shows two TiO stretching features in region (*ii*), while the simulated **4-1-a** structure, with its single TiO moiety, demonstrates only one. For $[(TiO_2)_4(D_2O)_2]^-$, **4-2-a** is by far the lowest energy calculated anionic structure, and was also found by Dixon and coworkers to be the preferred neutral structure.[513] The $[(TiO_2)_4(D_2O)_2]^-$ IRPD spectrum shows one TiO feature in region (*ii*), indicating at least partial dissociative adsorption of D_2O after the addition of a second water. However, the lowest-lying **4-2-a** structure has no remaining TiO moieties and thus no features in region (*ii*).

In $[(TiO_2)_4(D_2O)]^-$, the presence of **4-1-b**, the next lowest-lying cluster 42 kJ/mol above **4-1-a**, could account for the extra terminal TiO stretching spectral feature. **4-1-b** has the same core cluster structure as **4-1-a**, but with one terminal OD group and one bridging OD group; clusters with this kind of structure have also been considered in the literature as hydrolysis intermediates.[503,511] It is also possible that the bridging OD structure **4-1-c** could contribute. Though **4-1-c** lies considerably higher in energy, at 91 kJ/mol above **4-1-a**, it represents an intermediate structure on the pathway to form **4-1-a** after initial molecular adsorption of D_2O on $(TiO_2)_4^-$,[503,511] and could be present if there was a high final barrier to form **4-1-a**.

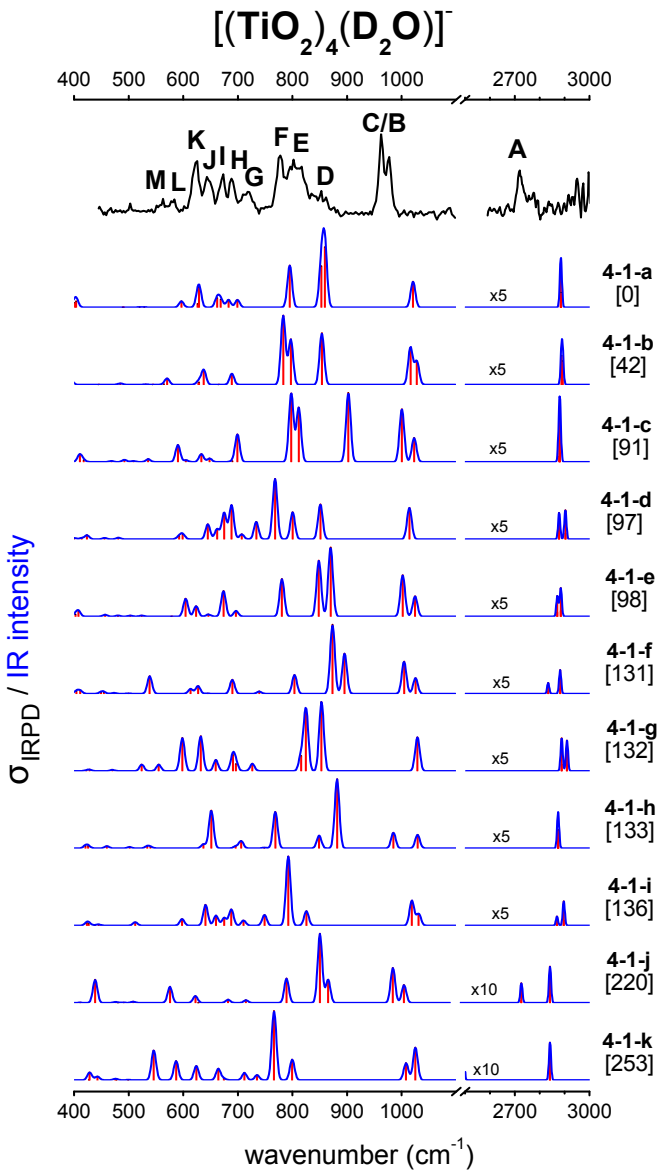

Figure 10.6: Experimental D_2-tagged IRPD spectra (black) of $[(TiO_2)_4(D_2O)]^-$, simulated unscaled linear IR absorption traces (blue), stick spectra (red), and relative energies (kJ/mol) of the predicted lowest-lying isomers at the ωB97X-D/aVDZ level of theory.

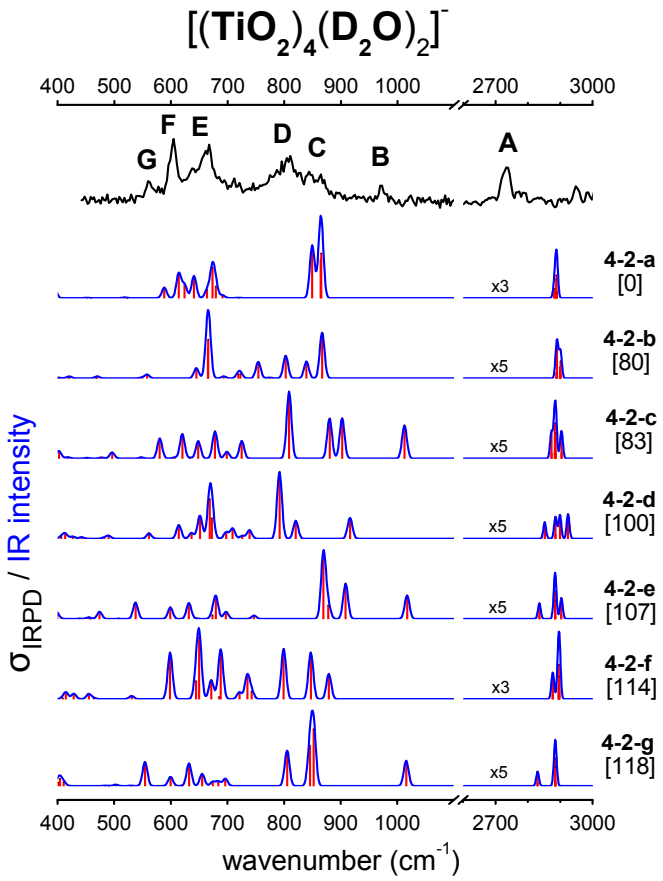

Figure 10.7: Experimental D_2-tagged IRPD spectra (black) of $[(TiO_2)_4(D_2O)_2]^-$, simulated unscaled linear IR absorption traces (blue), stick spectra (red), and relative energies (kJ/mol) of the predicted lowest-lying isomers at the ωB97X-D/aVDZ level of theory.

Experimentally, we observe one region (*i*) feature at 2723 cm^{-1} (peak A), which is consistent with the potential presence of both **4-1-a** and **4-1-b** clusters, which have close-lying OD stretching modes at 2885 cm^{-1} and 2892/2888 cm^{-1}, respectively. In region (*ii*), **4-1-b** has two TiO stretching frequencies derived from its two remaining terminal TiO moieties, narrowly spaced by 12 cm^{-1} at 1028 and 1016 cm^{-1}, which straddle the single **4-1-a** TiO stretching frequency at 1021 cm^{-1}. These three overlapping features could explain the experimental peaks B and C at 977 and 963 cm^{-1} in region (*ii*). The broad experimental structure in region (*iii*) can be ascribed to overlapping peaks at 859/853 and 795 cm^{-1} from **4-1-a** and at 854, 797, and 783 cm^{-1} from **4-1-b**, all corresponding to stretching modes involving all four nearly equivalent Ti-O-Ti bridges.

For $[(TiO_2)_4(D_2O)_2]^-$, structure **4-2-c**, lying at 83 kJ/mol above **4-2-a**, is the lowest-lying structure with a bridging OD group that reproduces the TiO stretching peak. Between structures **4-2-a** and **4-2-c**, the $[(TiO_2)_4(D_2O)_2]^-$ IRPD spectrum can largely be

explained. In region (*i*), we observe a single experimental OD stretching feature (peak A) at 2732 cm^{-1}, which is matched by calculated modes spanning 2881–2889 cm^{-1} in **4-2-a** and 2873–2904 cm^{-1} in **4-2-c**. Peak B in region (*ii*) at 972 cm^{-1} corresponds to the TiO stretching feature in **4-2-c** at 1012 cm^{-1}. In region (*iii*), Ti-O-Ti bridge stretching peaks at 865/864 and 850 cm^{-1} from **4-2-a** and 902, 880, and 809 cm^{-1} from **4-2-c** could underlie the broad experimental structure.

Finally, the fact that the $[(TiO_2)_4(D_2O)_m]^-$ D_2O-loss IRMPD spectra in Fig. 10.9 look quite distinct from the messenger-tagged IRPD spectra suggests that there may be a small population of molecularly adsorbed clusters that readily dissociate D_2O and thereby dominate the IRMPD spectra. Structures **4-1-j** and **4-2-g** correspond to the lowest-lying molecularly adsorbed $[(TiO_2)_4(D_2O)_m]^-$ structures, with D_2O adsorbed on **4-0-a** and **4-1-a**, respectively. The simulated IR spectrum of **4-1-b** (Fig. 10.6) is in particularly compelling agreement with the $[(TiO_2)_4(D_2O)]^-$ D_2O-loss IRMPD spectrum.

Ultimately, while we are unable to make definitive spectral and structural assignments for the $[(TiO_2)_4(D_2O)_m]^-$ clusters, it is reasonable to ascribe the observed structure to contributions from nultiple isomers. Experimentally, the presence of structures with bridging OD groups and the potential presence of molecularly adsorbed structures suggests that there may be significant isomerization barriers to form the lowest-energy $n = 4$ clusters, leading to kinetic trapping of the partially dissociated species.

10.4.4 Structural Trends

The agreement between the experimental $[(TiO_2)_n(D_2O)_m]^-$ IRPD spectra and the simulated IR spectra for the minimum-energy calculated structures are unambiguous for $n = 2, 3$ and within reason for $n = 4$. We confirm that the theoretical predictions made by Dixon and coworkers[513] for the neutral $(TiO_2)_n(H_2O)_m$ clusters hold for their deuterated anionic analogs: dissociative adsorption proceeds spontaneously on $(TiO_2)_n^{-/0}$ for the first two water molecules with $n = 2$ and for the first three water molecules with $n = 3$. Our DFT calculations for all $n = 2-4$ anions reproduce the same minimum-energy structures that Dixon and coworkers found for the neutral clusters,[513] with the exception of the $[(TiO_2)_2(D_2O)]^-$ cluster, for which a different structure is favored between anion and neutral. Taken together, these results indicate that the excess electron present in the $(TiO_2)_n^-$ clusters does not drastically affect the structural aspects of water dissociation.

Using the minimum-energy structures for each $[(TiO_2)_n(D_2O)_m]^-$ cluster, we can consider the size-dependent evolution of their geometries, vibrational structure, and reactivity. For the clusters considered here, dissociative adsorption proceeds preferentially at the undercoordinated Ti sites, and continues with the addition of subsequent water molecules until all Ti sites have coordination numbers of four, and all terminal TiO moieties have been converted to Ti-O-D. The hydrolysis limit of each bare $(TiO_2)_n^-$ cluster is therefore closely related to the initial number of unsaturated Ti atoms. The $(TiO_2)_3^-$ cluster is a special case, as the **3-0-a** structure begins both with one coordinatively unsaturated Ti atom and a triply coordinated central O atom. All Ti atoms in this cluster already have coordination numbers

of 4 after reaction with one water to form **3-1-a**, but it remains favorable for the cluster to go on to dissociate a second and third water molecule in order to reduce the strain of the central O atom in **3-1-a** and the two Ti-O-Ti bridges that share Ti atoms in **3-2-a**.[513]

Site-specific reactivity is also closely related to the localization of the singly occupied molecular orbital (SOMO) for each doublet anion cluster. Li and Dixon report the SOMOs for the bare $(TiO_2)_n^-$ clusters with n =2–4,[417] while we plot the SOMOs for relevant $[(TiO_2)_n(D_2O)_m]^-$ isomers in Fig. 10.11. In the bare clusters, the SOMO is always localized to the undercoordinated Ti atoms. In all cases, after reaction with the first D_2O, one of these SOMO-localized undercoordinated reactive sites becomes 4-coordinated with the addition of a dangling TiO moiety. **2-1-a**, **4-1-a**, and **4-1-b** have SOMOs localized to the last remaining undercoordinated Ti atom, while the **3-1-a** SOMO is more delocalized as all Ti atoms are already fully coordinated. The SOMOs grow more delocalized with the addition of subsequent waters molecules. This is in good agreement with bulk titania surface studies, which find that dissociative water adsorption occurs preferentially at defect sites, and particularly at oxygen vacancies on undercoordinated Ti atoms.[473–475,478,479,481,483,484,491] Our work reiterates the validity of these small clusters as models for reactive point defects.

The vibrational trends observed as a function of cluster size and increasing water adsorption are also of interest; the spectral signatures of water dissociation seen here may help inform vibrational spectroscopic studies of water dissociation and oxidation intermediates on bulk TiO_2 surfaces.[518–523]. The clearest indicator of dissociative water adsorption is the disappearance of structure in the TiO stretching regime from 900–1000 cm^{-1}, as terminal TiO moieties react to form Ti-O-D groups with sequential addition of D_2O. These Ti-O-D groups have lower-frequency stretching, bending, and wagging vibrational modes than terminal TiO groups, leading to increased intense structure below 700 cm^{-1} in region (*iv*) with the addition of water. Splitting between features in the OD stretching region (*i*) from 2600–3000 cm^{-1} decreases with increasing water adsorption, while structure in the Ti-O-Ti bridge stretching region (*iii*) tends to blue-shift with increasing water adsorption.

Our IRPD results are consistent with prior vibrational studies of hydrated bulk TiO_2. Spectral assignments associated with dissociative water adsorption on TiO_2 surfaces in the literature have largely been based on OH stretching frequencies. Many groups assign vibrational structure in the 3650–3750 cm^{-1} window to surface-bound hydroxyl groups.[476,518–522] Finnie *et al.*[520] reported two distinct OH vibrational features at 3730 and 3670 cm^{-1} that remained on a TiO_2 film after dehydration at high temperatures and assigned them to terminal and bridging OH group stretches, respectively. Henderson[476], on the other hand, studied the vibrational features of a hydrated TiO_2 surface with electron energy loss spectroscopy and saw only one feature in this region at 3690 cm^{-1}. In this work, we report OD stretches in a fairly narrow 2709–2776 cm^{-1} range, which can be scaled by a factor of 1.36[123,524] to yield comparable OH stretching frequencies in the 3684–3775 cm^{-1} range, in good agreement with the bulk surface assignments. In our DFT calculations, we see no major distinction in stretching frequencies between terminal and bridging hydroxyl groups; compare for instance the harmonic IR spectra of structures **4-1-a** and **4-1-b** in Fig. 10.6. Rather, we find that hydroxyl stretching frequencies are affected by the extent to which they couple with other

cluster modes as well as the coordination numbers of neighboring Ti atoms. More bulk spectroscopic work is needed to fully characterize the vibrational signatures of surface hydroxyl groups in different bonding sites and environments.

10.4.5 Summary and Conclusions

We have reported vibrational action spectra of the cryo-cooled $[(TiO_2)_n(D_2O)_m]^-$ (n=2–4, m=1–3) clusters, messenger-tagged with D_2, in the 400–1200 cm^{-1} fingerprint range and the 2600–3000 cm^{-1} OD stretching range. DFT calculations performed at the ωB97X-D/aVDZ level of theory allow for unambiguous structural and spectral assignment of the $n = 2, 3$ clusters with up to two and three adsorbed waters, respectively. We also comment on the contributions to the spectra of the $n = 4$ clusters.

We find conclusive evidence that all clusters studied in this work have structures corresponding to dissociative adsorption of the water molecules on the $(TiO_2)_n^-$ core. The clearest spectral indicator of this process is the disappearance of terminal TiO stretching vibrational structure in the 900–1000 cm^{-1} region that accompanies water adsorption. The $[(TiO_2)_n(D_2O)_m]^-$ clusters studied here are of considerable interest as model systems for photocatalytic water splitting on bulk TiO_2. The ready dissociative adsorption of water on undercoordinated Ti atoms illuminates at the molecular level how hydrolysis reactions may be initiated at reactive TiO_2 defect sites.

10.5 Supporting Information

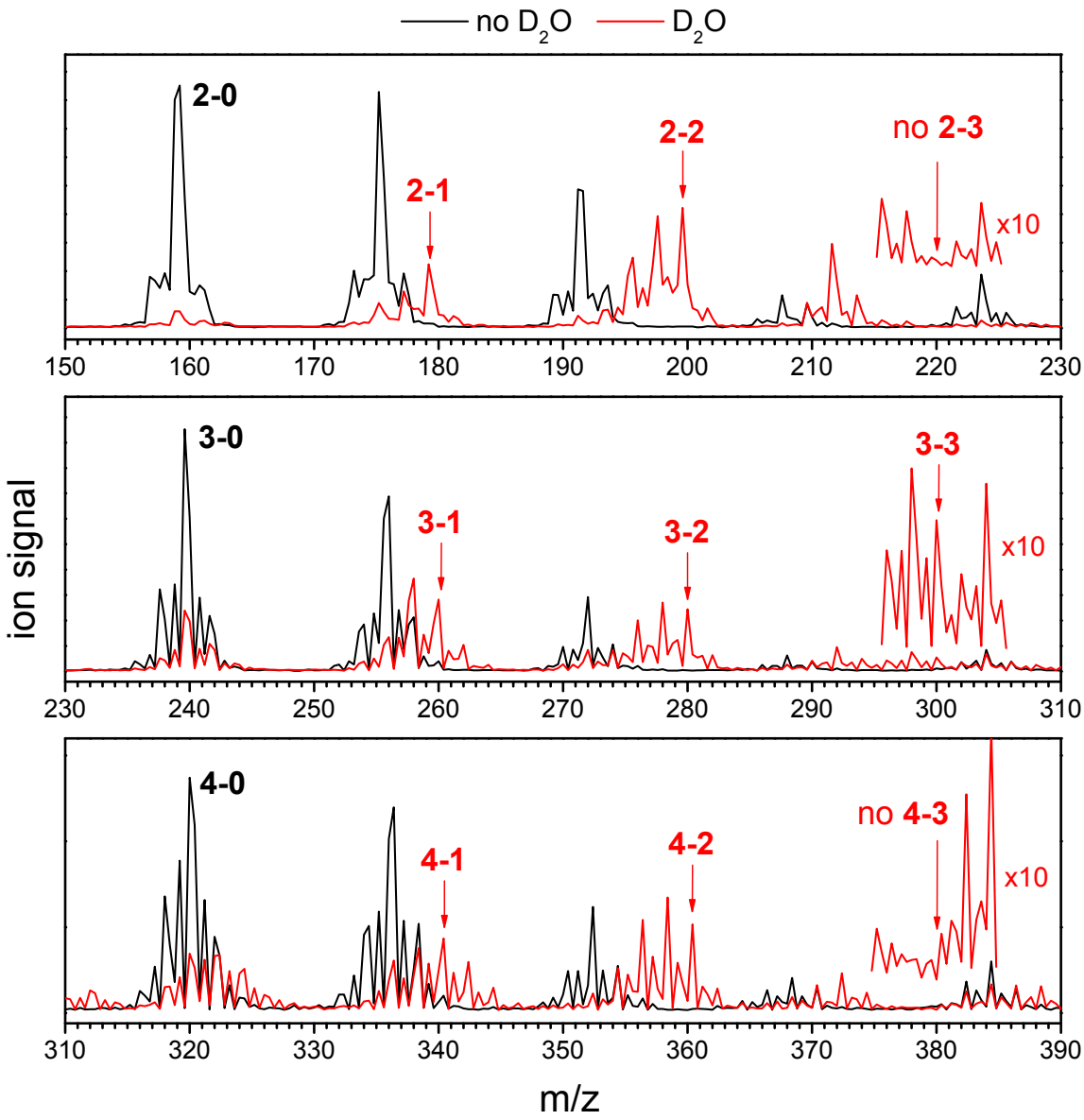

Figure 10.8: Quadrupole mass spectra of $(TiO_2)_n^-$ clusters before and after addition of D_2O.

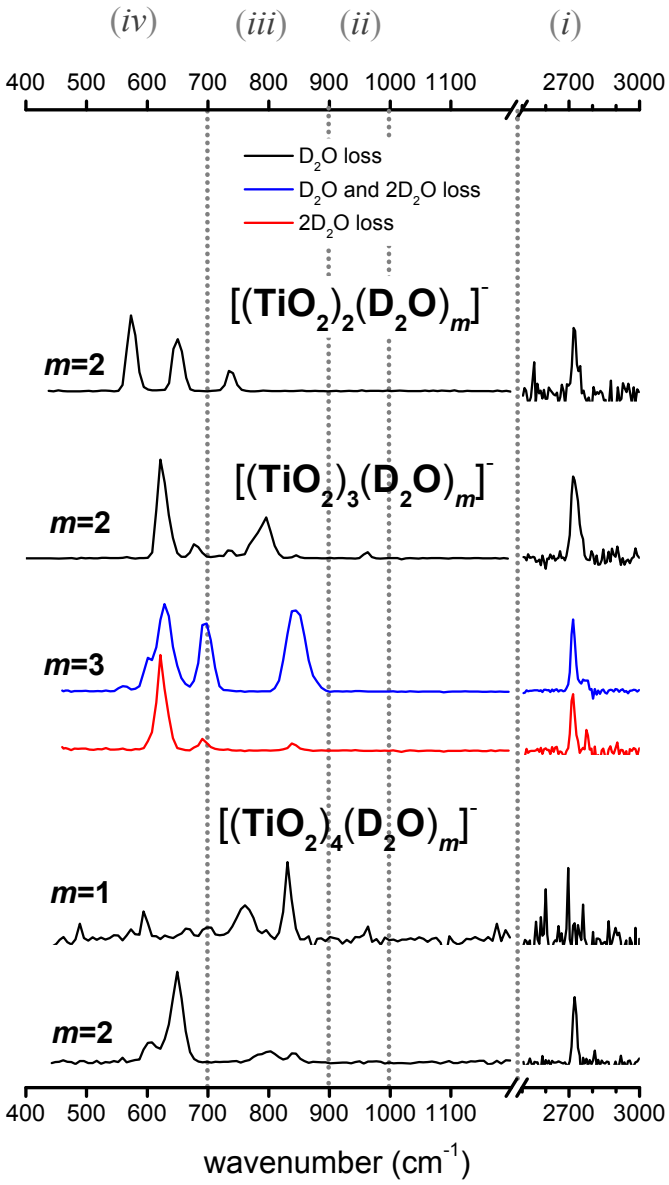

Figure 10.9: Full-power D_2O-loss IRMPD spectra of some $[(TiO_2)_n(D_2O)_m]^-$ clusters. Loss of up to two D_2O fragments is observed for $[(TiO_2)_3(D_2O)_3]^-$.

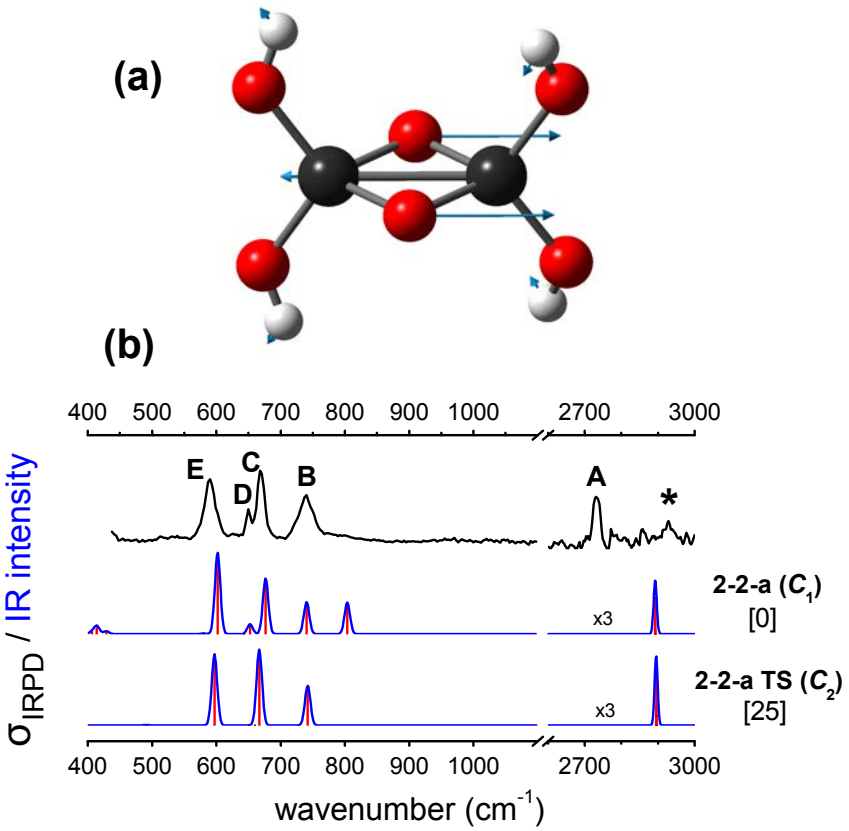

Figure 10.10: (a) 869i cm^{-1} vibrational normal mode of the C_2-symmetric **2-2-a** transition state of $[(TiO_2)_2(D_2O)_2]^-$ and (b) experimental IRPD spectrum (black) of D_2-tagged $[(TiO_2)_2(D_2O)_2]^-$ compared with simulated linear IR absorption traces (blue) and stick spectra (red) of the C_1-symmetric **2-2-a** minimum energy structure and the C_2-symmetric **2-2-a** transition state at the ωB97X-D/aVDZ level of theory. Energies are given in kJ/mol and are not corrected for vibrational zero-point energy.

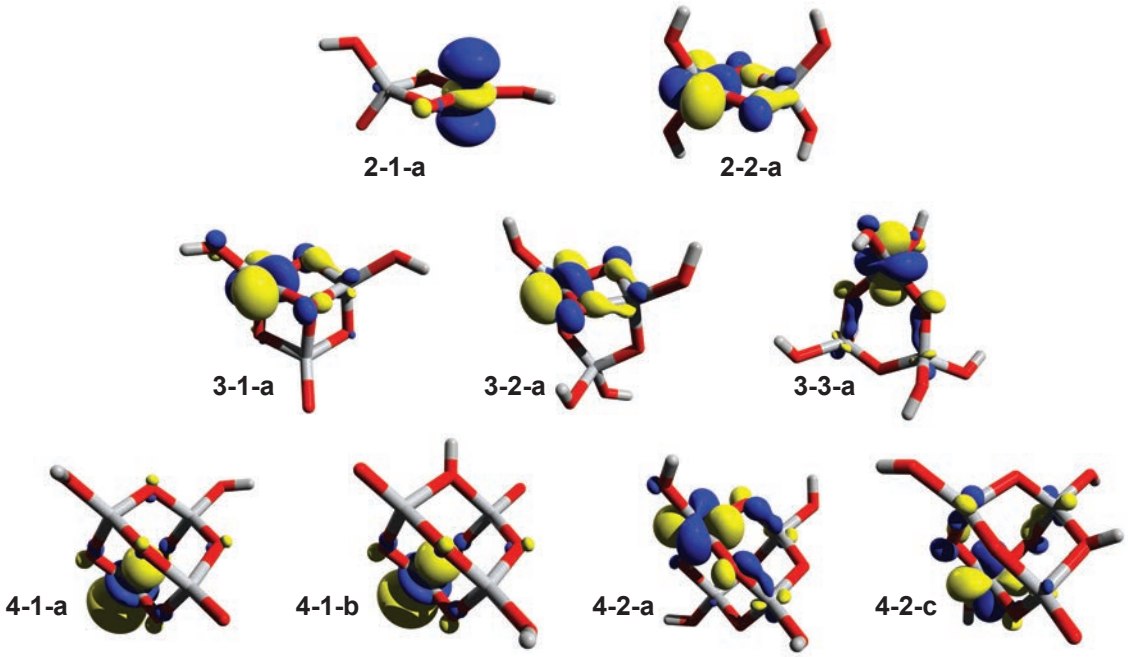

Figure 10.11: Visualized singly occupied molecular orbitals of relevant low-lying $[(TiO_2)_n(D_2O)_m]^-$ clusters.

Calculated relative energies (kJ/mol), binding energies (BE) of the last D_2O (kJ/mol), harmonic vibrational frequencies (cm^{-1}) above 400 cm^{-1}, and IR intensities (in parenthesis, km/mol) for low-lying $[(TiO_2)_n(D_2O)_m]^-$ cluster isomers at the ωB97X-D/aug-cc-pVDZ level of theory. Vibrational zero point energy corrections are included for relative isomer energies and D_2O binding energies.

Cluster	Isomer	Energy	D_2O BE	Harmonic frequencies and intensities
$[(TiO_2)_2(D_2O)]^-$	**2-1-a**	0	293	2930 (58), 2882 (39), 996 (356), 783 (461), 728 (257), 653 (214), 629 (477), 589 (50), 456 (49), 432 (27)
	2-1-b	27	266	2895 (34), 2889 (60), 956 (475), 794 (443), 714 (278), 694 (225), 643 (309), 571 (349), 459 (3), 417 (57), 407 (48)
	2-1-c	100	193	2934 (0), 2934 (92), 786 (0), 726 (325), 725 (308), 650 (0), 599 (534)
	2-1-d	104	190	2914 (46), 2856 (18), 978 (596), 780 (359), 738 (109), 617 (585), 565 (52), 526 (33), 497 (150), 472 (5)
$[(TiO_2)_2(D_2O)_2]^-$	**2-2-a**	0	169	2894 (0), 2893 (102), 2893 (10), 2892 (41), 804 (267), 741 (270), 677 (470), 653 (82), 644 (0), 602 (689), 581 (5), 429 (24), 414 (68), 407 (18)
	2-2-a TS	25[a]	–	2896 (0), 2895 (23), 2895 (140), 2895 (5), 742 (286), 728 (0), 667 (548), 660 (0), 650 (0), 597 (514), 491 (3), 869*i* (685)
	2-2-b	47	123	2903 (46), 2889 (39), 2882 (37), 2879 (43), 988 (377), 721 (333), 665 (410), 628 (9), 610 (241), 599 (530), 535 (42), 529 (48), 446 (57), 409 (36)
	2-2-c	85	84	2898 (35), 2885 (28), 2883 (73), 2525 (339), 944 (400), 820 (544), 741 (196), 701 (204), 692 (89), 645 (83), 607 (365), 544 (5), 489 (61), 424 (67), 416 (61)

[a]Not corrected for vibrational zero-point energy.

Cluster	Isomer	Energy	D_2O BE	Harmonic frequencies and intensities
$[(TiO_2)_3(D_2O)]^-$	**3-1-a**	0	213	2920 (74), 2890 (67), 1002 (500), 819 (349), 768 (637), 709 (156), 672 (197), 655 (306), 641 (307), 633 (270), 584 (72), 463 (1), 444 (20), 411 (7)
	3-1-b	47	184	2919 (75), 2917 (64), 1020 (299), 983 (784), 755 (614), 717 (81), 659 (377), 649 (446), 621 (109), 588 (156), 542 (15), 527 (54), 452 (7), 411 (2)
	3-1-c	61	170	2904 (64), 2890 (74), 1017 (382), 973 (558), 842 (403), 738 (360), 681 (594), 663 (104), 653 (179), 557 (145), 516 (21), 466 (34), 450 (50), 414 (48)
	3-1-d	82	148	2891 (15), 2889 (125), 971 (438), 829 (51), 789 (868), 761 (403), 722 (125), 715 (212), 669 (6), 657 (1088), 547 (445), 461 (6), 439 (4), 430 (44), 418 (57), 411 (34)

Cluster	Isomer	Energy	D_2O BE	Harmonic frequencies and intensities
$[(TiO_2)_3(D_2O)_2]^-$	**3-2-a**	0	148	2906 (57), 2901 (63), 2883 (73), 2807 (38), 835 (337), 800 (785), 747 (350), 704 (135), 696 (97), 686 (68), 654 (461), 643 (522), 601 (78), 582 (79), 513 (77), 497 (15), 417 (17), 412 (73)
	3-2-b	43	105	2913 (72), 2887 (49), 2883 (69), 2666 (207), 1015 (378), 822 (415), 766 (793), 725 (222), 689 (123), 688 (124), 656 (317), 635 (369), 605 (91), 591 (81), 512 (109), 471 (43), 468 (8), 434 (59), 400 (83)
	3-2-c	68	80	2894 (4), 2893 (13), 2892 (106), 2892 (106), 800 (0), 780 (708), 717 (483), 717 (483), 707 (2), 707 (2), 692 (185), 661 (0), 641 (985), 602 (0), 459 (2), 459 (2), 414 (60), 414 (60), 413 (83), 411 (1)
	3-2-d	73	75	2883 (38), 2883 (57), 2880 (156), 2880 (6), 979 (315), 884 (622), 876 (1155), 732 (114), 699 (537), 687 (0), 685 (188), 641 (626), 552 (26), 519 (54), 467 (24), 428 (27), 422 (81), 409 (84), 407 (65)

Cluster	Isomer	Energy	D_2O BE	Harmonic frequencies and intensities
$[(TiO_2)_3(D_2O)_3]^-$	**3-3-a**	0	94	2888 (49), 2883 (32), 2881 (87), 2879 (40), 2875 (70), 2865 (26), 902 (782), 885 (629), 719 (82), 702 (625), 688 (39), 684 (56), 651 (171), 635 (634), 597 (385), 569 (140), 477 (60), 459 (4), 446 (99), 430 (107), 424 (27), 416 (121), 408 (27)
	3-3-b	33	61	2906 (64), 2897 (51), 2887 (74), 2846 (55), 2711 (200), 2656 (160), 824 (455), 790 (518), 752 (420), 738 (238), 717 (112), 706 (24), 678 (466), 653 (302), 627 (175), 601 (29), 582 (93), 565 (117), 536 (133), 513 (22), 484 (27), 423 (15), 412 (43), 409 (79)
	3-3-c	34	61	2903 (56), 2895 (58), 2886 (67), 2858 (45), 2739 (196), 2698 (103), 857 (587), 799 (360), 740 (327), 733 (272), 709 (27), 703 (250), 679 (399), 651 (85), 633 (456), 596 (59), 575 (36), 554 (45), 502 (17), 475 (110), 452 (34), 420 (26), 415 (18), 400 (230)
	3-3-d	39	56	2906 (62), 2902 (65), 2886 (68), 2869 (37), 2639 (387), 2420 (449), 1228 (25), 837 (385), 816 (742), 760 (476), 731 (114), 718 (60), 671 (164), 668 (42), 659 (485), 651 (512), 592 (120), 578 (100), 564 (1), 532 (30), 491 (4), 422 (14), 416 (61)
	3-3-e	51	43	2909 (65), 2902 (70), 2818 (87), 2797 (35), 2794 (55), 2703 (97), 1232 (89), 838 (390), 790 (770), 745 (269), 717 (80), 695 (125), 681 (255), 658 (455), 650 (397), 602 (119), 586 (47), 527 (113), 517 (97), 496 (4), 459 (48), 420 (20)

Cluster	Isomer	Energy	D_2O BE	Harmonic frequencies and intensities
$[(TiO_2)_4(D_2O)_1]^-$	**4-1-a**	0	323	2885 (53), 2885 (123), 1021 (453), 859 (1062), 853 (726), 795 (738), 699 (132), 683 (131), 669 (137), 662 (164), 629 (353), 626 (64), 597 (110), 529 (5), 520 (5), 490 (1), 489 (1), 404 (107), 402 (85)
	4-1-b	42	282	2892 (75), 2888 (92), 1028 (370), 1016 (592), 854 (817), 797 (718), 783 (1095), 689 (173), 665 (1), 638 (234), 629 (36), 628 (27), 571 (97), 565 (7), 544 (0), 531 (7), 485 (20), 445 (1)
	4-1-c	91	232	2882 (106), 2878 (66), 1023 (293), 1001 (644), 903 (844), 812 (665), 798 (839), 699 (337), 690 (13), 648 (42), 633 (96), 605 (22), 590 (207), 536 (34), 509 (11), 492 (27), 468 (11), 418 (22), 411 (93)
	4-1-d	97	227	2903 (83), 2878 (76), 1014 (452), 851 (500), 800 (389), 768 (868), 734 (249), 707 (71), 688 (490), 675 (380), 662 (147), 645 (214), 599 (69), 593 (45), 481 (22), 456 (17), 424 (57), 414 (16), 400 (19)
	4-1-e	98	223	2885 (84), 2871 (61), 1025 (297), 1002 (609), 870 (1016), 848 (822), 781 (553), 697 (82), 674 (373), 646 (30), 624 (153), 605 (261), 578 (1), 524 (13), 503 (13), 481 (15), 457 (25), 408 (81), 403 (30)
	4-1-f	131	192	2882 (86), 2834 (40), 1025 (285), 1005 (586), 896 (731), 873 (1259), 804 (343), 739 (40), 690 (255), 645 (4), 627 (141), 613 (88), 539 (318), 500 (7), 474 (16), 455 (29), 449 (28), 411 (56), 404 (47)

Cluster	Isomer	Energy	D_2O BE	Harmonic frequencies and intensities
$[(TiO_2)_4(D_2O)_1]^-$	**4-1-g**	132	191	2910 (76), 2888 (81), 1029 (418), 853 (854), 825 (763), 816 (190), 727 (89), 697 (86), 691 (199), 660 (137), 632 (431), 598 (411), 555 (80), 524 (80), 470 (14), 428 (17), 423 (5)
	4-1-h	133	190	2874 (81), 2874 (78), 1029 (294), 985 (338), 882 (1500), 849 (276), 769 (788), 749 (14), 706 (159), 696 (43), 651 (818), 637 (88), 540 (29), 534 (45), 502 (29), 460 (46), 426 (52), 421 (50)
	4-1-i	136	188	2897 (105), 2869 (39), 1031 (251), 1019 (536), 826 (310), 792 (1480), 749 (226), 710 (110), 688 (348), 675 (167), 660 (216), 641 (444), 598 (138), 512 (72), 445 (22), 438 (7), 427 (37), 424 (57)
	4-1-j	220	104	2848 (66), 2737 (36), 1193 (45), 1013 (324), 992 (634), 872 (423), 857 (1260), 795 (443), 719 (48), 686 (58), 630 (0), 625 (125), 578 (294), 510 (21), 493 (4), 481 (0), 478 (15), 439 (421), 411 (4)
	4-1-k	253	71	2841 (64), 2491 (175), 1180 (29), 1025 (554), 1008 (288), 800 (351), 766 (1176), 735 (87), 712 (124), 674 (28), 664 (195), 624 (241), 587 (325), 546 (506), 499 (4), 478 (6), 475 (18), 443 (61), 429 (129), 428 (4)

Cluster	Isomer	Energy	D_2O BE	Harmonic frequencies and intensities
$[(TiO_2)_4(D_2O)_2]^-$	**4-2-a**	0	178	2889 (28), 2888 (95), 2888 (120), 2881 (49), 865 (702), 864 (601), 850 (828), 720 (7), 691 (44), 679 (180), 673 (482), 664 (128), 641 (347), 624 (209), 614 (391), 588 (165), 523 (2), 518 (9), 458 (0), 452 (5)
	4-2-b	80	98	2901 (72), 2899 (47), 2890 (140), 2888 (22), 867 (970), 839 (356), 803 (479), 774 (16), 754 (351), 723 (89), 719 (85), 693 (39), 666 (818), 666 (647), 645 (216), 558 (79), 549 (17), 470 (42), 468 (0), 421 (28), 419 (13), 402 (10)
	4-2-c	83	95	2904 (72), 2886 (68), 2883 (94), 2873 (69), 1012 (438), 902 (532), 880 (532), 809 (888), 725 (232), 699 (88), 678 (359), 648 (230), 633 (9), 620 (324), 606 (13), 580 (266), 548 (15), 496 (80), 477 (13), 452 (7), 418 (17), 402 (96)
	4-2-d	100	78	2924 (81), 2899 (78), 2885 (72), 2852 (54), 916 (344), 820 (295), 792 (1105), 739 (140), 726 (48), 709 (170), 698 (107), 672 (339), 669 (652), 651 (381), 636 (95), 614 (225), 561 (88), 490 (48), 482 (18), 442 (26), 427 (36), 413 (86), 406 (33)

Cluster	Isomer	Energy	D_2O BE	Harmonic frequencies and intensities
$[(TiO_2)_4(D_2O)_2]^-$	**4-2-e**	107	71	2903 (70), 2884 (62), 2884 (94), 2835 (52), 1017 (396), 908 (594), 878 (226), 869 (1127), 747 (55), 697 (120), 679 (372), 673 (62), 646 (6), 632 (268), 599 (193), 538 (275), 508 (3), 474 (120), 459 (1), 455 (24), 438 (4)
	4-2-f	114	64	2897 (72), 2896 (41), 2895 (110), 2877 (86), 879 (245), 847 (450), 799 (486), 743 (74), 735 (229), 721 (66), 688 (468), 685 (20), 671 (183), 650 (601), 645 (173), 599 (449), 531 (31), 464 (11), 455 (49), 429 (51), 415 (66), 409 (8)
	4-2-g	118	60	2885 (66), 2885 (97), 2830 (51), 2535 (145), 1188 (22), 1016 (444), 852 (997), 846 (704), 805 (620), 696 (129), 684 (80), 674 (72), 655 (212), 632 (395), 620 (3), 599 (160), 554 (423), 530 (6), 503 (21), 491 (3), 484 (5), 411 (63), 404 (124), 401 (60)

Optimized Cartesian coordinates (Å) of the low-lying $[(TiO_2)_n(D_2O)_m]^-$ isomers calculated with ωB97X-D/aug-cc-pVDZ.

Isomer		x	y	z
2-1-a	Ti	-1.2544	-0.0822	0.0015
	Ti	1.4713	-0.0016	-0.0039
	O	-2.3689	1.4489	-0.0066
	O	-2.1206	-1.4751	0.0208
	O	0.2026	-0.0514	-1.2744
	O	0.2177	-0.0239	1.2717
	O	3.3724	0.1390	-0.0694
	D	-3.3176	1.3139	0.0016
	D	4.1208	0.2303	0.5149
2-1-b	Ti	-1.1029	0.0426	0.0000
	Ti	1.6182	-0.2611	0.0002
	O	-2.3805	-1.3254	-0.0008
	O	-1.9637	1.7025	0.0002
	O	0.1245	-0.1249	1.2725
	O	0.1252	-0.1244	-1.2720
	O	3.1325	0.4382	-0.0005
	D	-2.1560	-2.2561	0.0008
	D	-1.4859	2.5326	0.0000
2-1-c	Ti	-1.1375	0.0537	0.0007
	Ti	1.1376	-0.0538	0.0008
	O	-3.0450	0.0326	-0.0004
	O	-0.0523	-1.2778	0.7617
	O	-0.0008	-0.0204	-1.4872
	O	0.0527	1.2980	0.7265
	O	3.0451	-0.0321	-0.0004
	D	-3.8888	-0.4095	-0.0179
	D	3.8895	0.4089	-0.0183
2-1-d	Ti	-1.1974	-0.0631	0.0708
	Ti	1.3133	-0.0365	-0.0120
	O	-3.1031	-0.1853	-0.0502
	O	0.0105	-0.4992	1.3617
	O	0.0970	1.6515	-0.2066
	O	0.1723	-0.6999	-1.2327
	O	2.9623	-0.2622	-0.0052
	D	-3.7605	-0.1339	-0.7409
	D	0.0986	2.2880	0.5115

Isomer		x	y	z
2-2-a	Ti	-1.3248	0.0000	0.0000
	Ti	1.4112	0.0000	0.0000
	O	-2.4099	-1.5402	-0.0004
	O	-2.4099	1.5402	0.0004
	O	-0.1096	-0.0356	-1.2785
	O	-0.1096	0.0356	1.2785
	O	2.4063	-1.5962	0.0658
	O	2.4063	1.5962	-0.0658
	D	-2.1073	-2.3717	-0.3659
	D	-2.1073	2.3717	0.3659
	D	2.0632	-2.4846	0.1597
	D	2.0632	2.4846	-0.1597
2-2-a TS	Ti	0.0000	-1.3024	0.0000
	Ti	0.0000	1.3024	0.0000
	O	-1.3226	0.0000	0.0002
	O	-0.0405	-2.3510	1.5594
	O	-0.0405	2.3505	-1.5597
	O	0.0405	-2.3505	-1.5597
	O	0.0405	2.3510	1.5594
	O	1.3226	0.0000	0.0002
	D	-0.2914	-2.0369	2.4279
	D	-0.2924	2.0363	-2.4278
	D	0.2924	-2.0363	-2.4278
	D	0.2914	2.0369	2.4279
2-2-b	Ti	-1.4602	-0.0459	-0.0377
	Ti	1.4514	0.0808	-0.0538
	O	-2.4961	-1.6148	0.0167
	O	-2.3917	1.5934	-0.0752
	O	0.0374	0.0162	-1.2201
	O	0.0582	-0.1278	1.3849
	O	2.2206	1.5321	0.0581
	O	2.6610	-1.3797	-0.1277
	D	-2.1869	-2.4956	-0.1966
	D	-1.9610	2.4308	-0.2539
	D	0.0270	0.3384	2.2188
	D	3.5982	-1.1962	-0.0502
2-2-c	Ti	-1.8150	-0.0705	-0.0086
	Ti	1.4993	-0.0733	0.0001
	O	-3.5006	-0.9625	-0.1248
	O	-1.7098	1.5861	0.1930
	O	-0.0419	-0.8883	-0.0888
	O	1.1065	1.6745	0.2729
	O	2.4639	-0.2554	-1.5808
	O	2.5373	-0.7686	1.3751
	D	-4.3583	-0.5412	-0.0773
	D	0.1470	1.8926	0.2869
	D	2.1413	0.1160	-2.4033
	D	2.1744	-1.3906	2.0074

Isomer		x	y	z
3-1-a	Ti	-1.1260	-1.0633	-0.0802
	Ti	-0.4422	1.6162	-0.0338
	Ti	1.6117	-0.3512	-0.0714
	O	-2.3699	-2.3136	0.5625
	O	-1.7171	0.4529	-0.8625
	O	-0.8873	3.0590	0.6098
	O	-0.1101	-0.0020	1.0790
	O	0.3098	-1.6654	-0.8798
	O	1.2965	1.3307	-0.7166
	O	3.2551	-1.0661	0.5148
	D	-3.2647	-2.1016	0.8302
	D	4.0937	-0.7007	0.7887
3-1-b	Ti	-1.1422	-1.2360	-0.0107
	Ti	-0.6701	1.5052	0.0708
	Ti	1.6573	-0.1157	0.0473
	O	-2.1364	-2.3700	-0.6570
	O	-1.8765	0.2449	0.7995
	O	-1.2156	2.9119	-0.5727
	O	-0.0624	-0.0244	-1.0528
	O	0.6130	-1.7455	0.8408
	O	1.0918	1.3998	0.8364
	O	3.3803	-0.5389	-0.5885
	D	0.8689	-2.3449	1.5382
	D	4.1887	-0.0550	-0.7453
3-1-c	Ti	-1.3091	-0.8064	-0.0996
	Ti	-0.1154	1.6693	0.0057
	Ti	1.5702	-0.8830	-0.0186
	O	-2.8127	-1.7092	0.5541
	O	-1.5255	0.8262	-0.9020
	O	-0.3371	3.1410	0.6828
	O	-0.0963	0.0522	1.0540
	O	-0.0958	-1.7396	-0.9036
	O	1.6086	1.1686	-0.8079
	O	2.9187	-1.5627	0.6635
	D	-2.8901	-2.6615	0.6197
	D	2.4059	1.6930	-0.8720
3-1-d	Ti	-3.0321	0.0000	-0.1502
	Ti	-0.2979	0.0000	-0.0672
	Ti	2.4239	0.0000	0.0449
	O	-4.5335	0.0000	0.5601
	O	-1.4997	-1.2882	-0.1326
	O	-1.4997	1.2882	-0.1326
	O	1.0989	0.0000	1.2389
	O	1.1911	0.0000	-1.2534
	O	3.4749	-1.5219	0.0842
	O	3.4749	1.5219	0.0842
	D	3.1398	-2.4192	0.1030
	D	3.1398	2.4192	0.1030

Isomer		x	y	z
3-2-a	Ti	-1.8125	-0.1122	0.0185
	Ti	0.9172	1.3447	0.0582
	Ti	1.0759	-1.3383	0.1008
	O	-3.4246	-0.1752	0.9236
	O	-2.1519	-0.1273	-1.7939
	O	-0.9389	1.3939	0.4417
	O	-0.7627	-1.5252	0.4355
	O	0.9301	0.1293	-1.2409
	O	1.6026	0.2374	1.2245
	O	1.8169	2.9738	-0.2127
	O	2.3206	-2.7323	-0.1274
	D	-3.7061	0.5502	1.4835
	D	-1.3324	-0.0611	-2.3000
	D	2.6915	3.1959	0.1049
	D	3.2375	-2.7528	-0.3964
3-2-b	Ti	0.0067	1.6641	-0.2404
	Ti	1.6443	-0.6651	0.0482
	O	-2.9362	-0.7405	1.3047
	O	-1.6473	1.0601	-0.6912
	O	-1.6044	-2.1196	-0.9538
	O	0.0604	-0.2161	0.8531
	O	0.1979	3.4905	0.1475
	O	1.2736	-2.1145	-0.9988
	O	1.7207	0.8578	-0.8138
	O	3.0983	-0.9498	1.1762
	D	-2.1629	-2.8880	-0.8308
	D	-0.4209	4.1413	0.4740
	D	0.3423	-2.3142	-1.2033
	D	3.2962	-1.8108	1.5483
3-2-c	Ti	0.0000	0.0000	-2.7261
	Ti	0.0000	0.0000	0.0000
	Ti	0.0000	0.0000	2.7261
	O	-1.5264	0.0000	-3.7880
	O	-1.2675	0.0000	1.4700
	O	0.0000	-1.5264	3.7880
	O	0.0000	-1.2676	-1.4700
	O	0.0000	1.2676	-1.4700
	O	0.0000	1.5264	3.7880
	O	1.2675	0.0000	1.4700
	O	1.5264	0.0000	-3.7880
	D	-2.4215	-0.0001	-3.4473
	D	0.0000	-2.4214	3.4474
	D	0.0000	2.4214	3.4474
	D	2.4215	0.0001	-3.4473

Isomer		x	y	z
3-2-d	Ti	-1.7049	-0.7365	0.0208
	Ti	0.0001	2.1028	-0.1761
	Ti	1.7049	-0.7366	0.0208
	O	-2.5991	-1.4907	-1.4181
	O	-2.5827	-1.1613	1.5944
	O	-1.6326	0.9843	-0.1774
	O	0.0000	-1.3946	0.1016
	O	0.0001	3.7281	0.1061
	O	1.6327	0.9842	-0.1771
	O	2.5828	-1.1617	1.5943
	O	2.5988	-1.4908	-1.4183
	D	-2.8970	-0.4769	2.1875
	D	-2.6690	-2.4403	-1.5300
	D	2.6673	-2.4404	-1.5312
	D	2.8969	-0.4774	2.1876
3-3-a	Ti	-1.4566	-1.2904	0.0270
	Ti	-0.3973	1.8888	0.0242
	Ti	1.9182	-0.6257	-0.0274
	O	-2.3311	-1.9620	-1.4673
	O	-2.1854	-2.0404	1.5592
	O	-1.6171	0.5387	0.0788
	O	-0.6629	2.8639	-1.5406
	O	-0.6074	2.9876	1.5080
	O	0.2257	-1.6576	-0.0621
	O	1.1949	1.2070	0.0264
	O	2.7815	-0.8571	-1.6769
	O	2.8586	-0.9616	1.5713
	D	-1.8329	-2.3504	-2.1883
	D	-1.6154	-2.3879	2.2474
	D	-1.5480	2.9610	-1.8969
	D	0.0562	2.9878	2.2000
	D	2.4607	-0.4960	-2.5056
	D	3.8080	-1.0602	1.6478

Isomer		x	y	z
3-3-b	Ti	-2.2324	-0.2358	-0.0129
	Ti	0.5479	1.5288	0.1191
	Ti	1.8418	-0.8740	0.0090
	O	-4.0512	0.0854	-0.0680
	O	-1.8696	-1.5057	1.2421
	O	-1.6070	-0.8403	-1.6186
	O	-1.3137	1.2371	0.3407
	O	0.7819	-2.4076	0.2901
	O	1.0555	0.1437	-1.2197
	O	1.2546	3.2507	-0.0585
	O	1.6020	0.3137	1.2783
	O	3.6411	-1.2718	-0.3297
	D	-4.4229	0.9685	-0.0515
	D	-0.9685	-1.8681	1.2686
	D	-0.6883	-0.5680	-1.8007
	D	0.1731	-2.6842	-0.4009
	D	2.1296	3.5729	-0.2694
	D	4.3672	-0.6794	-0.1350
3-3-c	Ti	-1.9429	-0.8184	0.0004
	Ti	-0.5053	1.5315	-0.1212
	Ti	2.2228	-0.3421	0.0536
	O	-3.7296	-1.0666	0.4751
	O	-1.6615	0.4693	-1.2114
	O	-1.1290	-2.4031	-0.4418
	O	-0.9643	0.1145	1.1609
	O	-0.8241	3.3897	-0.0500
	O	1.4232	1.1537	-0.2847
	O	1.6344	-1.5762	-1.2260
	O	1.6808	-0.9515	1.6856
	O	4.0661	-0.1428	0.0120
	D	-4.3365	-0.3616	0.7013
	D	-0.8854	4.0085	0.6759
	D	-0.1720	-2.4257	-0.5942
	D	0.7469	-0.7417	1.8588
	D	1.1559	-1.2471	-1.9913
	D	4.4793	0.7103	-0.1284

Isomer		x	y	z
3-3-d	Ti	-1.8491	-0.1159	-0.3097
	Ti	1.0324	1.2590	-0.3979
	Ti	1.0953	-1.4013	-0.0549
	O	-3.1938	-0.3101	-1.5633
	O	-2.6049	0.0819	1.3261
	O	-0.8149	1.3270	-0.6732
	O	-0.7565	-1.5534	-0.3236
	O	-0.5061	0.6489	3.1589
	O	1.1530	0.2399	1.0828
	O	1.6150	-0.0306	-1.4220
	O	1.9706	2.8841	-0.4250
	O	2.2857	-2.8094	0.3012
	D	-3.0295	-0.6371	-2.4490
	D	-2.0206	0.2435	2.0914
	D	-0.5036	1.6066	3.2230
	D	0.1628	0.4613	2.4522
	D	2.8601	3.0225	-0.7487
	D	3.2176	-2.8431	0.5111
3-3-e	Ti	-1.3683	-0.8025	0.1925
	Ti	0.6707	1.5739	0.1765
	Ti	1.6976	-0.9110	-0.0378
	O	-3.7917	1.1336	-0.5211
	O	-2.8143	-1.4423	1.1240
	O	-1.8579	-0.7856	-1.6051
	O	-1.0460	0.9305	0.6399
	O	0.0969	-1.7916	0.4644
	O	1.0264	0.2215	-1.2400
	O	1.1548	3.3727	-0.0441
	O	1.9273	0.3542	1.1464
	O	3.1903	-1.9474	-0.5023
	D	-3.5976	-0.8837	1.0565
	D	-3.3760	0.5698	-1.1919
	D	-3.0237	1.4891	-0.0516
	D	-1.1128	-0.5003	-2.1496
	D	1.9223	3.8241	-0.3911
	D	4.1011	-1.7906	-0.2553

Isomer		x	y	z
4-1-a	Ti	-1.5995	-0.9149	-0.3536
	Ti	0.0000	0.1787	2.0101
	Ti	0.0000	1.8692	-0.5605
	Ti	1.5995	-0.9149	-0.3536
	O	-3.0917	-1.8383	-0.9490
	O	-1.5083	-0.7393	1.4733
	O	-1.4971	0.7185	-1.0006
	O	0.0000	-1.6995	-0.7981
	O	0.0000	1.8432	1.3536
	O	0.0000	3.3415	-1.2525
	O	1.4971	0.7185	-1.0006
	O	1.5083	-0.7393	1.4733
	O	3.0917	-1.8383	-0.9490
	D	-3.7212	-1.4660	-1.5682
	D	3.7212	-1.4660	-1.5682
4-1-b	Ti	-1.4790	-1.2467	-0.4783
	Ti	-0.1794	1.9194	-0.4577
	Ti	-0.1643	0.0498	2.0048
	Ti	1.7027	-0.7039	-0.3160
	O	-2.6331	-2.2075	-1.1045
	O	-1.6044	0.6631	-1.1549
	O	-1.5070	-1.0004	1.3895
	O	-0.3713	1.7516	1.4032
	O	-0.3110	3.4219	-1.0663
	O	0.3066	-1.6670	-0.9191
	O	1.3950	0.9593	-0.8998
	O	1.4805	-0.6228	1.5073
	O	3.3552	-1.3619	-0.8403
	D	-2.2614	0.9343	-1.7965
	D	4.0177	-0.8333	-1.2872
4-1-c	Ti	-1.3935	-1.3643	-0.4543
	Ti	-0.6394	1.7902	-0.5140
	Ti	-0.1317	0.0624	2.0118
	Ti	1.8719	-0.3138	-0.2980
	O	-2.3444	-2.5569	-1.0403
	O	-1.6430	0.3312	-1.1152
	O	-1.2160	-1.2551	1.4384
	O	-1.0407	3.2414	-1.1365
	O	-0.6148	1.6702	1.4054
	O	0.5954	-1.6805	-0.9633
	O	1.2160	1.1413	-0.9248
	O	1.6458	-0.3363	1.4759
	O	3.5926	-0.6881	-0.8480
	D	0.8617	-2.5713	-1.1969
	D	4.0500	-0.2042	-1.5379

Isomer		x	y	z
4-1-d	Ti	-2.3048	-0.5663	-0.2784
	Ti	-0.4837	1.5641	-0.0467
	Ti	0.2556	-1.5784	0.4560
	Ti	2.3400	-0.0045	-0.1542
	O	-3.8643	-0.6123	0.2006
	O	-1.6691	1.0050	-1.2427
	O	-1.3363	-2.1712	-0.2627
	O	-0.9486	3.1883	0.7087
	O	-0.9082	0.0721	0.9881
	O	1.2725	1.5034	-0.4825
	O	1.4598	-1.3280	-0.9893
	O	1.7642	-0.6132	1.3797
	O	4.1875	0.1339	-0.3902
	D	-0.2958	3.7511	1.1291
	D	4.8774	-0.3047	0.1066
4-1-e	Ti	-1.3732	-1.2802	-0.6014
	Ti	-0.4295	1.8265	-0.5550
	Ti	-0.0729	0.1388	2.0477
	Ti	1.7712	-0.5439	-0.3425
	O	-2.4883	-2.3348	-1.1605
	O	-1.6416	0.4817	-1.0324
	O	-1.4386	-1.2021	1.4894
	O	-0.7109	3.2980	-1.1934
	O	-0.4617	1.7184	1.4201
	O	0.4706	-1.6814	-0.8233
	O	1.3150	1.0491	-0.9263
	O	1.5517	-0.4304	1.5258
	O	3.4712	-1.0606	-0.8740
	D	-2.3181	-1.3441	1.8451
	D	4.0753	-0.4674	-1.3231
4-1-f	Ti	-1.0493	1.5976	-0.5084
	Ti	-0.9337	-1.6323	-0.5706
	Ti	-0.2735	-0.0324	2.0465
	Ti	1.8591	0.0635	-0.4227
	O	-1.7731	2.9246	-1.1185
	O	-1.6749	-0.0277	-1.1340
	O	-1.5888	-2.9812	-1.2081
	O	-1.0334	1.4348	1.4398
	O	-0.9264	-1.5268	1.3908
	O	0.9213	1.4686	-0.7823
	O	1.0107	-1.3833	-0.8787
	O	1.7215	-0.0177	1.6245
	O	3.6432	0.1008	-0.9275
	D	2.2390	-0.7537	1.9670
	D	4.1019	0.8967	-1.2019

Isomer		x	y	z
4-1-g	Ti	-1.9014	-0.5909	-0.4420
	Ti	0.0739	1.8875	-0.1630
	Ti	0.0117	-0.6968	1.5834
	Ti	1.8964	-0.7277	-0.5019
	O	-3.0651	-1.4490	-1.5347
	O	-1.9010	-0.9200	1.3285
	O	-1.5404	1.1706	-0.7808
	O	-0.0667	-1.0937	-0.3603
	O	0.1072	1.0784	1.5603
	O	0.1255	3.6986	-0.1453
	O	1.5302	1.1423	-0.8753
	O	1.7291	-1.1843	1.3994
	O	2.8516	-1.5944	-1.4997
	D	-3.7104	-2.1654	-1.5508
	D	3.7763	-1.8081	-1.6708
4-1-h	Ti	-2.6811	0.0000	-0.3048
	Ti	0.1320	-1.7325	0.3619
	Ti	0.1320	1.7325	0.3619
	Ti	2.0633	0.0000	-0.7764
	O	-4.2515	0.0000	-0.8004
	O	-1.5563	-1.6080	-0.0112
	O	-1.5563	1.6080	-0.0112
	O	0.5134	-3.0670	1.5793
	O	0.5134	3.0670	1.5793
	O	0.8363	0.0000	0.8503
	O	1.2291	-1.6823	-1.0591
	O	1.2291	1.6823	-1.0591
	O	3.6662	0.0000	-0.5082
	D	1.3983	-3.4206	1.6907
	D	1.3983	3.4206	1.6907
4-1-i	Ti	-2.5574	-0.5711	0.2040
	Ti	-0.6711	1.4787	0.0920
	Ti	0.1272	-1.2404	-0.5030
	Ti	2.7255	-0.2040	0.2078
	O	-4.1217	-0.8271	-0.1817
	O	-1.9632	1.0263	1.1906
	O	-1.3676	-1.9934	0.3223
	O	-1.2660	0.2235	-1.1202
	O	-0.5514	3.2448	-0.4274
	O	0.8574	0.5157	0.4130
	O	1.8827	-1.6647	-0.6797
	O	3.4588	-0.5707	1.6094
	O	3.8105	0.8900	-0.8687
	D	-1.1858	3.9529	-0.3140
	D	3.5345	1.1023	-1.7628

Isomer		x	y	z
4-1-j	Ti	-1.7609	-0.0001	0.0886
	Ti	0.5043	0.0000	2.0058
	Ti	0.8947	-1.6237	-0.6284
	Ti	0.8946	1.6238	-0.6283
	O	-3.6954	-0.0001	-0.9311
	O	-1.3992	-0.0001	1.8518
	O	-1.1029	-1.4206	-0.6689
	O	-1.1030	1.4205	-0.6689
	O	1.1737	-1.4869	1.2776
	O	1.1736	1.4870	1.2776
	O	1.4748	-2.9663	-1.3601
	O	1.4425	0.0000	-1.3438
	O	1.4747	2.9664	-1.3601
	D	-3.6154	-0.7707	-1.5099
	D	-3.6154	0.7705	-1.5099
4-1-k	Ti	-2.2633	-0.0490	0.5760
	Ti	-0.2809	-1.1589	-1.0969
	Ti	-0.1553	1.5915	-0.5244
	Ti	1.7906	-0.3038	0.6374
	O	-3.2021	-0.2692	1.8934
	O	-2.0362	-1.4776	-0.7000
	O	-1.9716	1.6960	-0.0613
	O	-0.2497	-0.1510	0.5925
	O	-0.1236	0.2960	-2.0586
	O	1.3601	-1.7476	-0.5729
	O	1.6039	1.5935	0.0991
	O	2.3856	-0.6576	2.1113
	O	3.7805	0.3065	-0.2179
	D	3.3059	1.1690	-0.2925
	D	4.3161	0.3630	0.5806

Isomer		x	y	z
4-2-a	Ti	-0.2715	1.5872	1.0901
	Ti	-0.4799	0.0000	1.9882
	Ti	-0.5478	3.1045	2.1270
	Ti	-0.2715	-1.5872	1.0901
	O	-0.5478	-3.1046	2.1270
	O	-1.3392	-1.4955	-0.2834
	O	-1.3392	1.4955	-0.2834
	O	0.6174	0.0000	-1.9657
	O	1.8394	0.0000	-0.6739
	O	1.4267	-1.4314	0.3743
	O	1.4267	1.4314	0.3743
	O	3.5794	0.0000	-1.3199
	O	-1.2543	0.0000	-1.5681
	O	-2.6403	0.0000	-2.8307
	D	-1.1939	-3.7751	1.9014
	D	-3.5811	0.0000	-2.6502
	D	3.7938	0.0000	-2.2536
	D	-1.1939	3.7750	1.9015
4-2-b	Ti	-1.6698	1.3564	0.0096
	Ti	-1.6628	-1.3432	-0.0065
	Ti	1.6725	-1.3211	-0.0131
	Ti	1.6928	1.4028	-0.0031
	O	-3.0892	2.5496	0.0232
	O	-3.0777	-2.5415	-0.0068
	O	-1.7828	0.0153	-1.2305
	O	-1.7716	0.0004	1.2349
	O	-0.0825	2.1281	0.0110
	O	-0.0762	-2.1086	-0.0152
	O	1.7654	-0.0950	-1.2777
	O	1.7902	-0.1309	1.2626
	O	3.0572	-2.5824	-0.0147
	O	3.1846	2.5277	-0.0039
	D	-4.0133	2.2973	0.0211
	D	-4.0020	-2.2898	-0.0063
	D	3.8437	-2.5278	0.5277
	D	4.1134	2.3302	-0.1176

Isomer		x	y	z
4-2-c	Ti	-1.4269	-1.4058	-0.3890
	Ti	-0.4778	0.7244	1.8722
	Ti	-0.1323	1.5084	-1.2300
	Ti	1.8252	-0.7703	-0.1385
	O	-2.5240	-2.7549	-1.1078
	O	-1.5487	-0.6784	1.2975
	O	-1.2187	0.1999	-1.5548
	O	-0.7404	1.3060	3.3753
	O	-0.4004	1.9977	0.4886
	O	-0.2516	2.8935	-2.4671
	O	0.5497	-1.8694	-0.4101
	O	1.4029	-0.1063	1.6994
	O	1.5687	0.6792	-1.1449
	O	3.5254	-1.4990	-0.2396
	D	-3.2491	-3.2365	-0.7117
	D	-0.7753	2.8227	-3.2663
	D	2.0861	0.2578	2.2657
	D	3.6964	-2.4399	-0.3040
4-2-d	Ti	-2.2681	-0.4671	-0.3933
	Ti	-0.5254	1.7133	0.1957
	Ti	0.3499	-1.5296	0.2578
	Ti	2.2778	0.3487	-0.3401
	O	-4.1167	-0.7289	-0.3471
	O	-1.8063	1.3743	-0.9554
	O	-1.1992	-1.9869	-0.5706
	O	-0.9628	3.1051	1.3402
	O	-0.7692	0.0032	0.9063
	O	0.8510	-3.0182	1.2290
	O	1.1517	1.8354	-0.4823
	O	1.3489	-1.0057	-1.1764
	O	1.8949	-0.3456	1.1688
	O	4.0908	0.5694	-0.7342
	D	-4.8657	-0.5842	0.2262
	D	-1.8620	3.4201	1.4430
	D	1.6875	-2.9103	1.6907
	D	4.8238	0.2189	-0.2286

Isomer		x	y	z
4-2-e	Ti	-1.6937	0.8789	-0.5902
	Ti	0.0001	-1.9849	-0.5246
	Ti	0.0000	0.0148	2.0293
	Ti	1.6937	0.8790	-0.5902
	O	-3.2073	1.7505	-1.2287
	O	-1.4897	0.9219	1.1541
	O	-1.4290	-0.7083	-1.1732
	O	0.0001	-3.6646	-1.3782
	O	0.0000	-1.7044	1.2721
	O	0.0000	0.0610	3.6582
	O	0.0000	1.8255	-1.2060
	O	1.4290	-0.7082	-1.1732
	O	1.4896	0.9220	1.1541
	O	3.2072	1.7506	-1.2287
	D	-3.7191	1.4403	-1.9773
	D	0.0001	-4.5420	-0.9976
	D	-0.0001	2.7619	-0.9835
	D	3.7190	1.4405	-1.9773
4-2-f	Ti	-2.2676	0.0080	-0.4293
	Ti	-0.0089	-1.5167	0.2910
	Ti	-0.0029	1.5543	0.3692
	Ti	2.2675	-0.0064	-0.4241
	O	-4.1409	0.0475	-0.3196
	O	-1.4588	1.4242	-1.0345
	O	-1.4065	-1.5483	-0.9073
	O	-1.2228	-0.0287	1.0556
	O	-0.0097	3.1605	1.2982
	O	-0.0036	-3.0167	1.3495
	O	1.2088	-0.0280	1.0549
	O	1.3728	-1.5721	-0.8930
	O	1.4967	1.4015	-1.0462
	O	4.1365	-0.0152	-0.2805
	D	-4.6964	-0.6584	0.0115
	D	-0.3306	4.0046	0.9805
	D	0.7922	-3.5416	1.4561
	D	4.7154	0.7353	-0.4139

Isomer		x	y	z
4-2-g	Ti	-0.8390	-0.5350	-1.5611
	Ti	-0.7775	1.5106	0.7720
	O	-1.5331	2.9821	1.6179
	Ti	0.0548	-1.5725	1.2093
	Ti	1.9163	0.3923	-0.5274
	O	-3.0897	-0.6346	-2.0471
	O	-1.6459	1.0402	-0.7514
	O	-0.8751	-1.9278	-0.4321
	O	-0.7578	0.0730	1.8048
	O	0.0609	-2.7921	2.2894
	O	0.9051	-0.0649	-1.9841
	O	0.9710	1.7538	0.2526
	O	1.7852	-0.9591	0.6002
	O	3.6750	0.8224	-0.9380
	D	-3.3751	-1.3636	-1.4843
	D	-3.0885	0.1609	-1.4675
	D	-1.7215	2.9932	2.5574
	D	4.4219	0.3679	-0.5457

Part V

Transition State Spectroscopy

> Nature, it seems, is the popular name for milliards and milliards and milliards of particles playing their infinite game of billiards and billiards and billiards.
>
> — Piet Hein

Chapter 11

Reactive resonances in $F + H_2$

The content and figures of this chapter are reprinted or adapted with permission from
J. B. Kim, M. L. Weichman, T. F. Sjolander, D. M. Neumark, J. Kłos, M. H. Alexander, and D. E. Manolopoulos, "Spectroscopic observation of resonances in the $F + H_2$ reaction" *Science* **349**, 510 (2015).

Abstract

Photodetachment spectroscopy of the FH_2^- and FD_2^- anions allows for the direct observation of reactive resonances in the benchmark reaction F + H_2 ⟶ HF + H. Using cooled anion precursors and a high-resolution electron spectrometer, we observe several narrow peaks not seen in previous experiments. Theoretical calculations, based on a highly accurate F + H_2 potential energy surface, convincingly assign these peaks to resonances associated with quasibound states in the HF + H and DF + D product arrangements and with a quasibound state in the transition state region of the F + H_2 reaction. The calculations also reveal quasibound states in the reactant arrangement, which have yet to be resolved experimentally.

11.1 Text

Much of our understanding of the structures of stable molecules has come from spectroscopy. The analysis of bound-bound transitions yields molecular geometries and frequencies, fingerprints of the molecular potential energy surface (PES). The observation of similar sharp structures during a chemical reaction would give comparable insight into the reactive PES, in particular in the all important transition state region.[104] The fleeting nature of the transition state makes this task much more challenging, however. Here, we report the spectroscopic observation of sharp resonance structures associated with the transition state and product valley regions of the F + H_2 ⟶ HF + H reaction, a benchmark reaction in the field of chemical reaction dynamics.[525]

The rapid variation of a scattering cross section with energy or angle has long guided physicists in the investigation of nuclear and subnuclear structure. These so-called resonances are signs of metastable excited states or previously unknown particles. In chemistry, the experimental and theoretical search for these quantum features in reactive scattering experiments has been intense.[526–530] Although tentative experimental evidence for resonances in the F + H_2 reaction was first reported in the 1980s,[108] it took until 2000 for a resonance to be unambiguously identified in a crossed molecular beam experiment, as a step-like feature in the energy dependence of the integral cross section of F + HD ⟶ HF + D.[109,531] The same resonance a quasibound state in the FHD transition state region with three quanta of excitation in the H−F stretch and none in either the H−D stretch or the bend - has since been found under higher resolution to give rise to undulations in individual state-to-state differential cross sections of the reaction as a function of the collision energy.[532] More recent molecular beam experiments combined with theoretical simulations have also provided some evidence for a resonance[533] (or perhaps two resonances[534]) in F + H_2.

Anion photoelectron spectroscopy provides an alternative experimental approach to the study of chemical reactions.[105] Because the geometry of the FH_2^- anion is close to that of the neutral F + H_2 transition state, photodetachment of the electron from the anion provides a direct spectroscopic probe of the transition state dynamics,[34] as illustrated in Fig. 11.1. If the

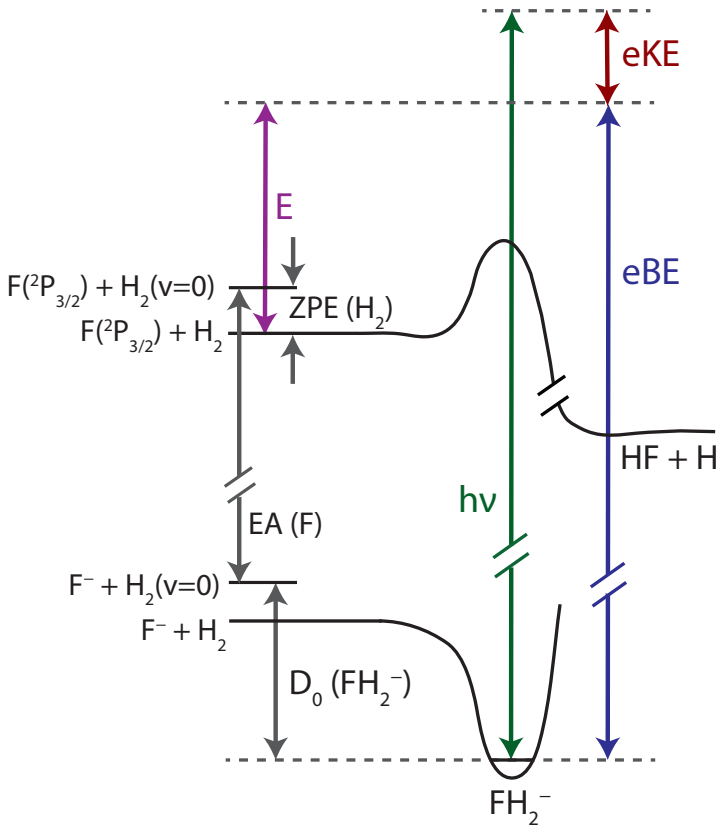

Figure 11.1: Schematic of the energetics of the photodetachment process. Arrows show the relationship between the experimental electron binding energy (eBE) and the scattering energy (E).

precursor anion is rotationally cold, this probe avoids the averaging over angular momentum that tends to obscure resonances in a crossed molecular beam experiment. Previous spectra of FH_2^- have revealed broad peaks associated with the bending levels of the FH_2 transition state complex, which correspond to the "quantized bottlenecks" of the reaction rather than reactive scattering resonances.[110] Calculations based on the best potential energy surface then available reproduced the positions and intensities of these broad peaks, as well as predicting a number of narrower peaks, which were assigned to resonances.[111] Unfortunately, the experimental resolution available at the time (∼20 meV) was not high enough to permit the detection of these features.

The development of slow-electron velocity-map imaging (SEVI) with cryogenic ion cooling has enabled the acquisition of photoelectron spectra of complex species with sub-millielectron volt (sub-meV) resolution.[49] Much improved signal-to-noise ratio compared to that of a previous SEVI report[112] has allowed the detection of sharp peaks in the spectra of both FH_2^- and FD_2^-, which we report here.

The experimental apparatus has been described in detail previously,[49,114] with relevant features highlighted in the Supporting Information (SI). The FH_2^- and FD_2^- ions are created by introducing F^- anions into a cryogenically cooled ion trap containing H_2 or D_2 buffer gas at low pressure; the resulting ion yield is substantially higher than in previous work, where FH_2^- was generated in a molecular beam ion source. The ions are extracted from the trap, mass-selected, and photodetached at various photon energies. The photoelectron kinetic energy (eKE) distribution is obtained with SEVI, in which a velocity-map imaging electron spectrometer[14] operated at comparatively low extraction voltages produces high-resolution (sub-meV) photoelectron spectra at low eKE. The electron binding energy (eBE) gives the energy difference between the anion and neutral states and is obtained by subtracting the measured eKE from the photon energy. As previous simulations suggested more obvious signatures of resonances with *para*-H_2 than *ortho*-H_2,[111] the FH_2^- ions were enriched in *p*-H_2. However, the FD_2^- ions were formed by trapping F^- in a buffer gas of *normal* deuterium (*n*-D_2).

Several earlier publications outline the calculation of the photodetachment spectrum of the FH_2^- anion.[111,535] Photodetachment projects the vibrational wave function of the anion onto the F + H_2 potential energy surface, where it evolves under the influence of the neutral FH_2 Hamiltonian. In the Condon approximation, the photodetachment spectrum P(E) is the Fourier transform of the overlap between this evolving wave function and the initial anion vibrational wave function.[111] We use here the very high quality LWAL F + H_2 potential energy surface,[113] which is based on multireference, configuration-interaction calculations. The relation between the experimentally measured binding energy of the electron (eBE) and the energy E in the theoretical simulation, which refers to the bottom of the F + H_2 reactant valley with the F atom in its ground ($^2P_{3/2}$) spin-orbit state, is

$$\mathrm{eBE} = \mathrm{E} - \mathrm{ZPE}(\mathrm{H_2}) + \mathrm{EA}(\mathrm{F}) + \mathrm{D_0}(\mathrm{FH_2^-}) \tag{11.1}$$

where ZPE is the zero-point energy of H_2, EA is the electron affinity of F, and D_0 is the dissociation energy of the FH_2^- anion. These energetics are illustrated schematically in Fig. 11.1. In the theoretical simulations, we use the experimental E of F (3.4012 eV[146]) and the ZPEs for H_2 and D_2 as predicted by the LWAL PES (0.2705 and 0.1918 eV, respectively). To determine D_0, we have performed new *ab initio* and vibrational bound state calculations described in the SI, obtaining D_0 = 0.2005 eV for FH_2^- and 0.2219 eV for FD_2^-.

The experimental and simulated SEVI spectra of *p*-FH_2^- and *n*-FD_2^- are presented in Figs. 11.2 and 11.3, respectively. Spectra at additional photon energies are shown in Figs. 11.5 and 11.6. Figs. 11.7 and 11.8 show a comparison of the *p*-FH_2^- photodetachment spectra obtained with two different anion wave functions (Fig. 11.7) and two different potential energy surfaces (Fig. 11.8).

The overview *p*-FH_2^- photodetachment spectrum is dominated by three broad peaks, labeled *A*, *B*, and *C* in Fig. 11.2. These had been previously assigned to hindered H_2 rotor (or bending) states of the transient FH_2 complex.[110,536] The equilibrium geometry of

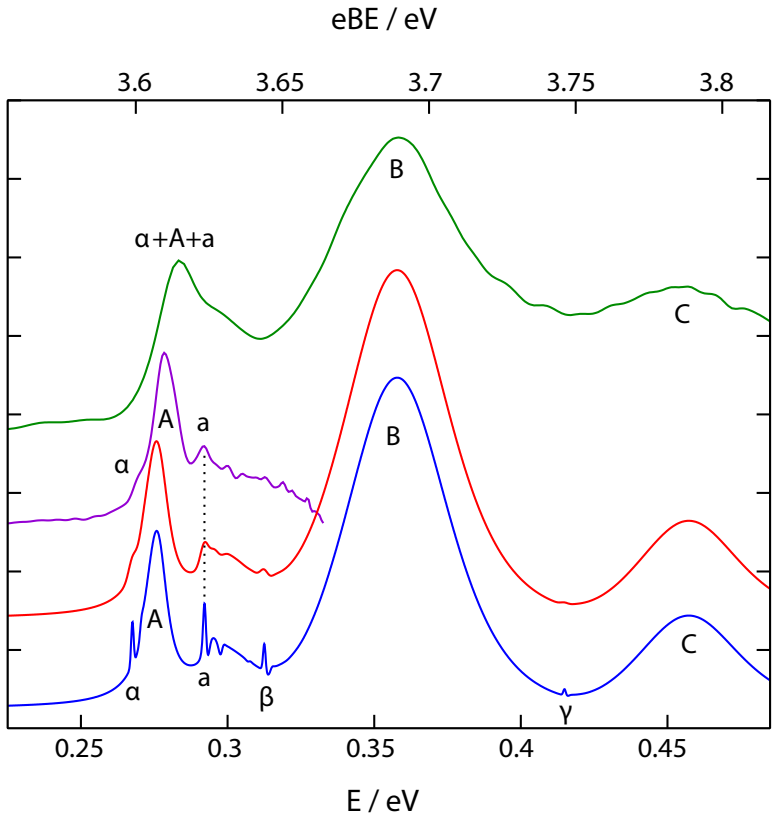

Figure 11.2: Photodetachment spectra of p-FH_2^-. Green: experimental overview spectrum ($\sim$10 meV resolution). Purple: highest-resolution experimental spectrum (2 to 3 meV) over a narrower energy window. Blue: theoretical simulation at 1 meV energy resolution. Red: convolution of the theoretical simulation over a Gaussian function with full width at half maximum (fwhm) of 3 meV. The calculated spectra have not been shifted to match experiment. The relation between the experimental electron binding energy eBE and the energy E relative to $F(^2P_{3/2}) + H_2(r_e)$ is given by Eqn. 11.1 as eBE = E + 3.3312 eV.

the linear FH_2^- anion is just on the reactant side of the neutral transition state. Because the minimum $F + H_2$ barrier on the neutral potential energy surface has a bent geometry, photodetachment of the electron excites a bending progression in the neutral FH_2 complex. We also observe a smaller peak in the high-resolution p-FH_2^- spectrum (purple), labeled a, just above the first broad peak A. This peak has not been resolved in any previous experiment. It also occurs in the simulated spectra, along with two smaller peaks (labeled β and γ) at higher energy, and a pronounced peak (labeled α, seen experimentally as a slight shoulder) on the low-energy side of peak A.

The situation for n-FD_2^- is similar. The experimental overview spectrum in Fig. 11.3 is dominated by two broad peaks, labeled D and E. The high-resolution spectrum shows

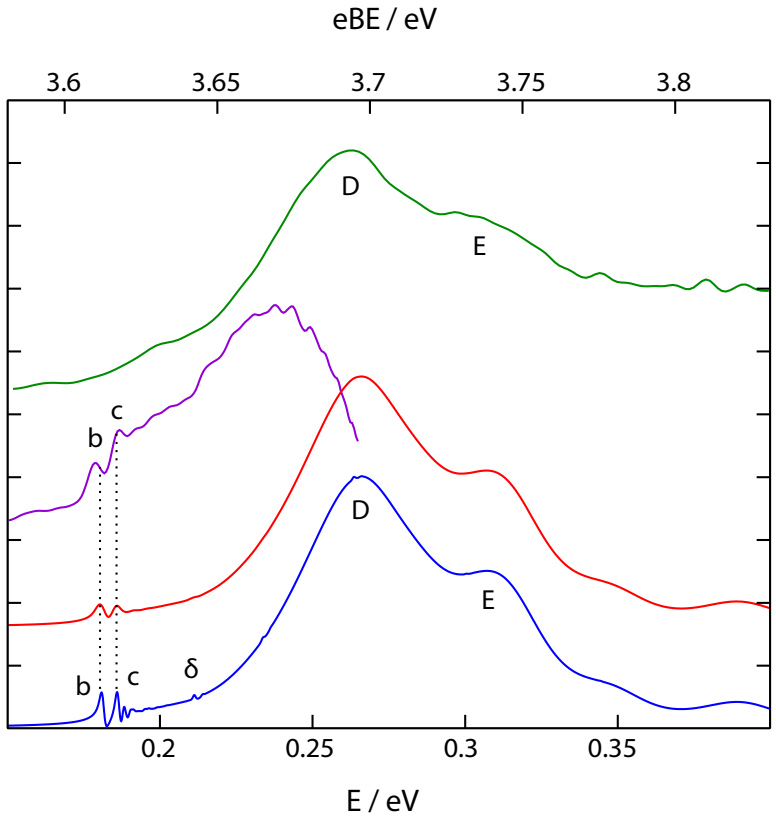

Figure 11.3: Photodetachment spectra of n-FD_2^-. Green: experimental overview spectrum (∼10 meV resolution). Purple: highest-resolution experimental spectrum (2 to 3 meV) over a narrower energy window. Blue: theoretical simulation at 1 meV energy resolution. Red: convolution of the theoretical simulation over a Gaussian function with fwhm of 3 meV. The calculated spectra have not been shifted to match experiment. The relation between the experimental electron binding energy eBE and the energy E relative to $F(^2P_{3/2}) + D_2(r_e)$ is given by Eqn. 11.1 as eBE = E + 3.4313 eV.

two smaller peaks at lower energy, labeled b and c. These smaller peaks are also seen in the theoretical spectra, along with an additional small peak labeled δ, which is not resolved in the experimental spectrum. In both cases (p-FH_2^- and n-FD_2^-), the agreement between the positions of the calculated and the observed high-resolution peaks (peak a in Fig. 11.2 and peaks b and c in Fig. 11.3) is excellent, suggesting that an analysis of the theoretical calculations will provide a reliable guide to the origin of these experimental peaks. What makes this comparison especially compelling is that no arbitrary shift was introduced to align the experimental and theoretical spectra in Figs. 11.2 and 11.3; use of the *ab initio* values of D_0 for FH_2^- and FD_2^- in the relationship between E and eBE in Eqn. 11.1 locates the theoretical spectra.

Calculating the scattering wave function $\Psi(E)$ at the energy E of each peak allows us

to characterize the peaks in the theoretical spectra in Figs. 11.2 and 11.3. This is the same procedure used previously by Russell and Manolopoulos.[111] The details of the present, more accurate calculations of the wave functions Ψ(E) are given in the SI.

Fig. 11.4 shows plots of the wave functions corresponding to the low-energy resonance peaks α, A, and a in Fig. 11.2 and peaks b, c, and δ in Fig. 11.3, in collinear F−H−H (F−D−D) geometry. This figure unambiguously reveals the nature of the peaks in the photodetachment spectra: peaks α and δ are reactant resonances, peak A is a transition state resonance, and peaks a, b, and c are product resonances. The quasibound states that give rise to these resonances are localized in the reactant F + H_2 (F + D_2) van der Waals well, the FH_2 transition state, and the product HF + H (DF + D) van der Waals well, respectively. The green contours in Fig. 11.4 depict the anion wave functions.

It is possible to assign quantum numbers to the resonance wave functions on the basis of their nodal structure. The reactant resonances have quantum numbers v, j, and t, where v enumerates the number of quanta in the H−H stretch; j, in the hindered H_2 rotation; and t, in the F−H_2 stretch of the F + H_2 van der Waals complex. For the product resonances, v', j', and t' refer, similarly, to the H−F stretch, the hindered HF rotation, and the H−HF van der Waals stretch. The quantum numbers of the reactant resonances in Fig. 11.4 are $(v, j, t) = (0, 0, 0)$ for both α (p-FH_2^-) and δ (n-FD_2^-), whereas the quantum numbers of the product resonances are $(v', j', t') = (3, 0, 0)$ for a and $(v', j', t') = (4, 0, 0)$ and $(4, 0, 1)$ for b and c, respectively. Finally, the transition state resonance that gives rise to peak A in the p-FH_2^- spectrum has three quanta in the H−F stretch (ν_1) and none in either the F−H−H bend (ν_2) or the H−H stretch (ν_3).

The resonances a, b, and c that have been detected as narrow peaks in the present high-resolution SEVI spectra of p-FH_2^- and n-FD_2^- are thus all product resonances: quasibound states localized in the van der Waals well region in the product valley. For additional clarification, Fig. 11.9 shows how well the positions of the FH−H and FD−D product state resonances are captured by an adiabatic-bender model.[537–539] Because the energies of these resonances are below the thresholds for production of HF($v' = 3$) + H and DF($v' = 4$) + D, they cannot decay into these channels and must decay instead into HF($v' = 2$) + H and DF($v' = 3$) + D by vibrational predissociation (the hallmark of a Feshbach resonance). The reason why there are two resonances for FD_2 and only one for FH_2 can be traced to the larger mass of D, which leads to two quasibound states in the D−DF($v' = 4, j' = 0$) van der Waals stretching coordinate rather than just one (see the SI for a more detailed analysis). The emergence of peak a at high resolution was predicted by Russell and Manolopoulos in their earlier theoretical study of the p-FH_2^- spectrum,[111] but peaks b and c in the n-FD_2^- spectrum have been neither predicted nor measured until now.

The broader low-energy peak A in the p-FH_2^- spectrum was previously assigned to a "direct scattering" or "quantized bottleneck" state associated with the opening of the F + H_2($v = 0, j = 0$) channel at the transition state.[111] However, it is clear from the present calculations that the wave function Ψ(E) at the energy of this peak is localized in the transition state region rather than delocalized along the reaction coordinate. This localization is the characteristic feature of a resonance wave function.[540] This resonance has precisely the

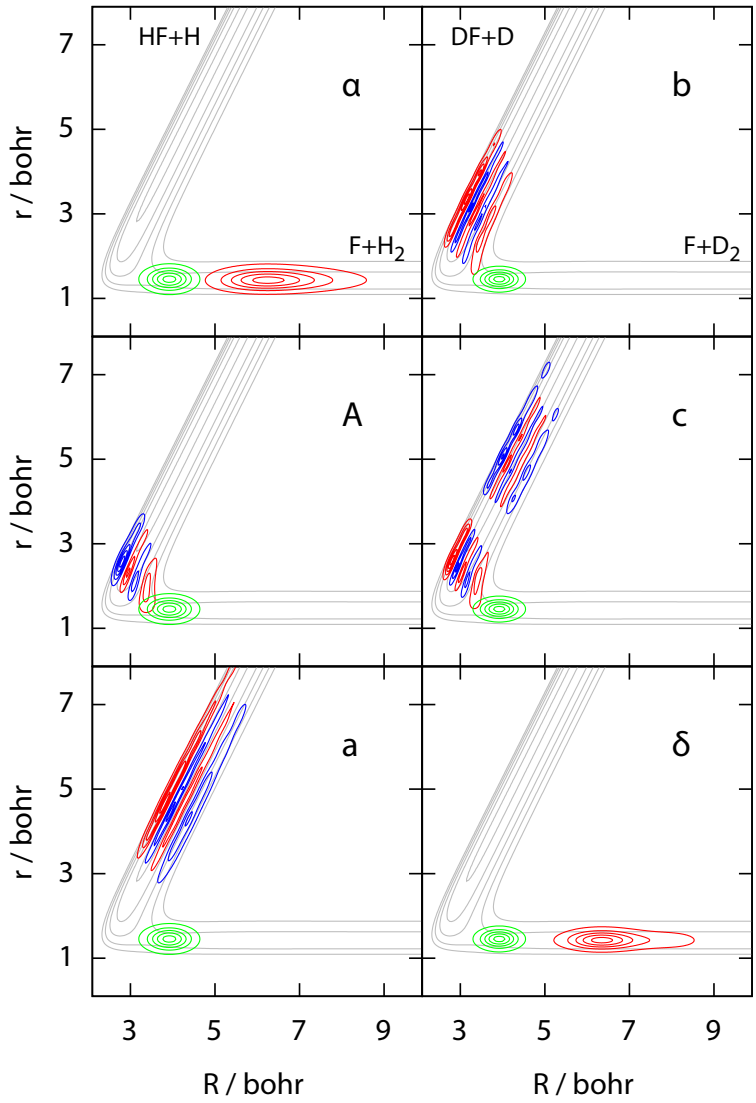

Figure 11.4: Resonance wave functions. The wave functions $\Psi(\mathrm{E})$ at the energies E of the first three peaks in the p-FH_2^- spectrum in Fig. 11.2 (α, A, and a; left), and the first three peaks in the n-FD_2^- spectrum in Fig. 11.3 (b, c, and d; right), plotted in collinear geometry, as red ($\Psi(\mathrm{E}) > 0$) and blue ($\Psi(\mathrm{E}) < 0$) contours, as a function of the distance R between F and the center-of- mass of H_2 (D_2) and the bond length r of H_2 (D_2). Superimposed in gray are contours of the LWAL potential energy surface.[113] Contours of the FH_2^- and FD_2^- anion wave functions are shown in green for comparison. The contoured regions of all wave functions encompass probability density values greater than 10% of their maxima; the apparent lack of overlap between the anion wave functions and some of the resonance wave functions arises because the overlap is in the tail ($< 10\%$) of the probability distribution.

Table 11.1: Assignment of the peaks in the *p*-FH_2^- and *n*-FD_2^- photodetachment spectra in Figs. 11.2 and 11.3. The quantum numbers given for the quantized bottlenecks (see Fig. 11.10) are those of the reactant channel that becomes energetically accessible as a hindered rotor (bending) state at the transition state at the energy of the peak in the photodetachment spectrum.

Spectrum	Peak	E/eV	Assignment	Quantum numbers
p-FH_2^-	α	0.2676	Reactant resonance	$(v, j, t) = (0, 0, 0)$
	A	0.2758	Transition state resonance	$(\nu_1, \nu_2, \nu_3) = (3, 0, 0)$
	a	0.2921	Product resonance	$(v', j', t') = (3, 0, 0)$
	β	0.3125	Reactant resonance	$(v, j, t) = (0, 2, 0)$
	B	0.3578	Quantized bottleneck[a]	$F + H_2(v = 0, j = 2)$
	γ	0.4149	Reactant resonance	$(v, j, t) = (0, 4, 0)$
	C	0.4573	Quantized bottleneck[a]	$F + H_2(v = 0, j = 4)$
n-FD_2^-	b	0.1809	Product resonance	$(v', j', t') = (4, 0, 0)$
	c	0.1860	Product resonance	$(v', j', t') = (4, 0, 1)$
	δ	0.2112	Reactant resonance	$(v, j, t) = (0, 0, 0)$
	D	0.2661	Quantized bottleneck[a]	$F + D_2(v = 0, j = 2)$
	E	0.3071	Quantized bottleneck[a]	$F + D_2(v = 0, j = 4)$

[a] For quantized bottlenecks, the quantum numbers given are those of the reactant channel that becomes energetically accessible as a hindered rotor (bending) state at the transition state at the energy of the peak in the photodetachment spectrum. Examples of quantized bottleneck wave functions are given in the SI.

same form and quantum numbers as the transition state resonance found by Skodje *et al.* in the F + HD reaction.[109,531] It is thus simply an analytic continuation of this resonance in the mass of one of the two hydrogen atoms. It is the broad peaks B and C in Fig. 11.2 and D and E in Fig. 11.3 that are due to quantized bottlenecks, with wave functions that are delocalized along the reaction coordinate;[540] the associated wave functions are shown in Fig. 11.10.

All of the other peaks in Figs. 11.2 and 11.3 can be assigned in the same way by examining the scattering wave functions at the peak energies. The results of these assignments are summarized in Table 11.1. The narrow peaks β and γ in Fig. 11.2 are reactant resonances with quantum numbers $(v, j, t) = (0, 2, 0)$ and $(0, 4, 0)$, respectively. Like peak δ in Fig. 11.3, the theoretical calculations predict only low intensity for these peaks. They have yet to be resolved experimentally. As shown in Fig. 11.8, the agreement between the experimental and theoretical resonance positions is noticeably poorer with the use of another recently developed F + H_2 surface,[541] illustrating that the resonances are indeed a sensitive and experimentally accessible probe of the neutral reactive surface.

We have shown that high-resolution SEVI photodetachment spectra of *p*-FH_2^- and *n*-FD_2^- anions reveal previously unresolved peaks in the low-energy region that can unambiguously be attributed to reactive scattering resonances. The signatures of these resonances in the SEVI spectra are far clearer than they would be in a crossed molecular beam experiment, where angular momentum averaging washes out resonance features in both integral and differential cross sections. Thanks to recent experimental developments (including SEVI and, crucially for the present study, the use of a cryogenically cooled ion trap to produce large amounts of *p*-FH_2^- and *n*-FD_2^-), high-resolution anion photodetachment spectroscopy does indeed provide an effective way to observe the elusive resonances in F + H_2 reactive scattering, as was predicted by Russell and Manolopoulos almost 20 years ago.[111]

11.2 Supporting Information

11.2.1 Experimental Details

The SEVI method and apparatus has been described in detail in Chap. 2. The most significant differences from our previous report on SEVI spectra of FH_2^-[112] are in ion production and cooling, along with image acquisition and processing. Instead of forming FH_2^- ions in a gas jet expansion, they were created in an ion trap. F^- ions were generated by dissociative electron attachment of trace NF_3 in a helium gas expansion. The ions were transferred by ion guides and a quadrupole mass filter to a cryogenic ion trap filled with a burst of pure hydrogen buffer gas. The H_2/D_2 gas clustered with the fluoride anion and cooled the resulting FH_2^- and FD_2^- complexes, allowing for ion yields several times that in the previous experiment. *p*-H_2 was prepared by flowing *n*-H_2 over an iron oxide catalyst at 30 K;[542] the spin-isomer-enriched products were stored in an aluminum gas cylinder prior to injection in the ion trap. The expected spin isomer purity is $\sim$ 95% *p*-H_2.

Temperatures in the ion trap depended on the system of interest. The ion trap was held at 20 K with *n*-D_2 buffer gas due to its tendency to freeze at lower temperatures. The ion trap was held at 40 K with *p*-H_2 to maximize production of *p*-FH_2^-; at very low temperatures, the equilibrium constants for the formation of the FH_2^- complexes are expected to favor *o*-H_2 over *p*-H_2, counteracting the initial spin isomer enrichment.[543]

We obtain highest resolution at lowest eKE as $\Delta\text{eKE} \propto \text{eKE}^{1/2}$, but the cross-sections for these systems roughly follow $\sigma \propto \text{eKE}^{3/2}$, with a rapidly vanishing signal with increasing resolution.[112] We obtained overview lower-resolution spectra at high eKE to minimize the effects of near-threshold intensity variations and obtain meaningful relative intensities. We also obtained higher-resolution, lower-eKE spectra in an attempt to resolve possible resonance features. With improved signal-to-noise, we record spectra at photon energies down to $\sim$500–1000 cm^{-1} above all features of interest, with an instrumental resolution of 20–30 cm^{-1} (2.5–3.7 meV) fwhm. This should be compared to the previous report prior to installation of the cryogenic ion trap in which spectra were obtained $\sim$1000–1500 cm^{-1} above the features of interest, with a resolution of 30–40 cm^{-1} (3.7–5.0 meV) fwhm[112] and, more importantly,

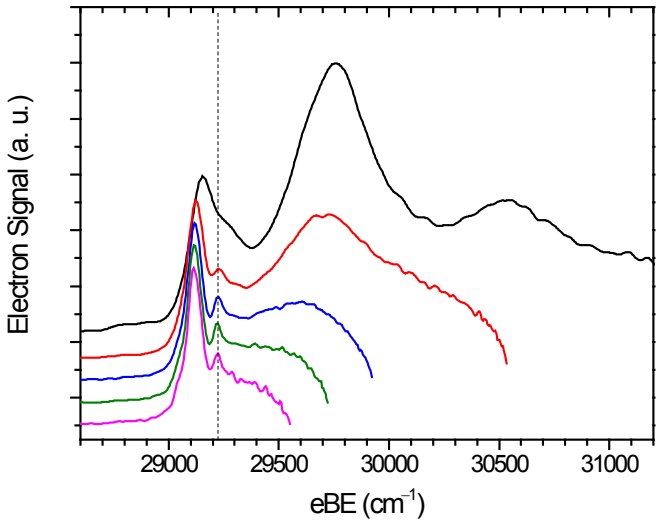

Figure 11.5: Experimental SEVI spectra of p-FH_2^- over more photon energies than shown in Fig. 11.2. Spectra are offset vertically for clarity. The weak peak at 29224 cm^{-1} (peak a in Fig. 11.2) is present in several different spectra, but is most evident in the highest-resolution spectra corresponding to the lowest photon energies.

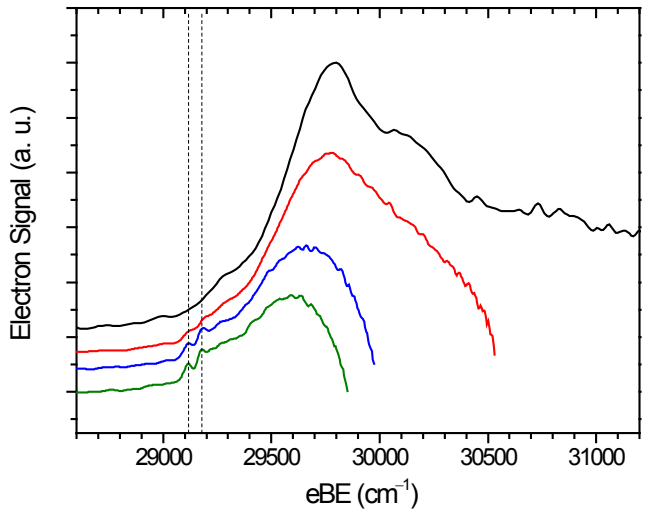

Figure 11.6: Experimental SEVI spectra of n-FD_2^- over more photon energies than shown in Fig. 11.3. Spectra are offset vertically for clarity. The weak peaks at 29110 and 29179 cm^{-1} (peaks b and c in Fig. 11.3) are present in the higher-resolution spectra.

considerably poorer signal-to-noise.

We have found that the MEVELER method,[140] which relies on maximum entropy methods, reproduces the original distributions from simulated photoelectron images more faithfully, particularly for the difficult case of a weak sharp resonance superimposed on a strong broad signal, as we expect to see for FH_2^- spectra.[111]

The photoelectron angular distribution (PAD) for all observed features is aligned parallel to the laser polarization axis. There is a near-isotropic unstructured photoelectron signal coming from detachment to the higher-lying repulsive $^2\Pi$ surface.[535] Detachment to the $^2\Pi$ nonreactive surface has largely s-wave ($l = 0$) character, while detachment to the reactive $^2\Sigma$ surface is largely p-wave ($l = 1$); according to the Wigner threshold law for photodetachment,[75] the cross section is proportional to $\mathrm{eKE}^{l+1/2}$ and thus the isotropic component contributes more to the photoelectron spectra at low eKE. Earlier reports have roughly separated these two components by only recording the photoelectron signal parallel to the detachment laser,[110,536,544] or by subtracting the perpendicular component of the signal from the parallel component.[112] The anisotropy of a given photodetachment transition varies with eKE,[79,545] and we record spectra at several different photon energies, so there is no clear way to separate the two detachment components for all spectra. We present the spectra integrated over all angles, noting simply that there is a broad isotropic component on all spectra that contributes most at low eKE. Figs. 11.5 and 11.6 show experimental spectra of p-FH_2^- and n-FD_2^- over a wider range of photon energies than are displayed in Figs. 11.2 and 11.3.

11.2.2 Theoretical Details

11.2.2.1 Photodetachment calculations

The present simulations of the p-FH_2^- and n-FD_2^- photodetachment spectra were performed using the method described by Russell and Manolopoulos.[111] Under the assumption that the anion is sufficiently rotationally cold to be modeled by total angular momentum $J = 0$, and that the electronic dipole matrix element for the bound-continuum electronic transition is a constant function of both the nuclear coordinates in the Franck-Condon region and the energy of the ejected photoelectron, the spectrum P(E) is given by a simple vibrational Franck-Condon factor[111,535]

$$\mathrm{P(E)} = \langle \Psi | \Psi(\mathrm{E}) \rangle \tag{11.2}$$

where $|\Psi\rangle$ is the ground state wave function of the FH_2^- (FD_2^-) anion and

$$|\Psi(\mathrm{E})\rangle = \frac{1}{\pi\hbar}\,\mathrm{Re}\int_0^\infty \exp[-i(H - i\varepsilon - \mathrm{E})t/\hbar]|\Psi\rangle dt \tag{11.3}$$

Here H is the Hamiltonian of the FH_2 (FD_2) neutral, and ε is a positive infinitesimal that is needed to ensure the convergence of the time integral.

In practice, $|\Psi(\mathrm{E})\rangle$ is calculated by propagating the time-dependent wave packet

$$|\Psi(t)\rangle = \exp[-i(H - i\varepsilon)t/\hbar]|\Psi\rangle \tag{11.4}$$

by means of the symmetric split operator method.[546] The initial wave function $|\Psi\rangle$ and the neutral Hamiltonian H are both represented in the Jacobi coordinates R, r, γ of the $F + H_2$ ($F + D_2$) reactant arrangement, where $R = |\mathbf{R}|$ is the distance from F to the center-of-mass of H_2 (D_2), $r = |\mathbf{r}|$ is the H_2 (D_2) bond length, and γ is the angle between the vectors $\mathbf{R}$ and $\mathbf{r}$. The formal convergence factor $-i\varepsilon$ is replaced in this method by a negative imaginary absorbing potential $V(R, r) = -i\varepsilon(R, r)$ at the edges of the grids in R and r.

In the present calculations we used Colbert-Miller[547] sine discrete variable representation grids in $0 < R < 24$ bohr and $0 < r < 24$ bohr, with 205 (278) grid points in R and 107 (152) in r for FH_2 (FD_2). A transmission-free absorbing potential[548] was placed on the last half of each of these grids, from 12 to 24 bohr. The angular coordinate γ was discretized using a basis of 151 even Legendre polynomials for p-H_2, 212 even Legendre polynomials for o-D_2, and 211 odd Legendre polynomials for p-D_2; the n-FD_2^- photoelectron spectrum was then calculated as a 2:1 weighted average of the o-FD_2^- and p-FD_2^- spectra. The time step of the symmetric split operator evolution was 0.11 fs and the wave packet was propagated for 5.76 ps to calculate P(E) with 1 meV (Gaussian fwhm) energy resolution. All of these numerical parameters are far better converged than those used by Russell and Manolopoulos in 1996.[111]

The key inputs to the photodetachment calculation are the vibrational wave function of the anion and its dissociation energy D_0 (see Eqn. 11.1 in the main text), and the potential energy surface of the neutral FH_2 system. We shall now describe each of these in turn.

11.2.2.2 FH_2^- wavefunction and dissociation energy

For the calculations reported in Figs. 11.2 and 11.3, we have used the anion wave function of Zhang and Miller.[535] This is a simple harmonic normal mode approximation to the ground state anion wave function constructed from the equilibrium geometry and harmonic normal mode frequencies obtained in the early *ab initio* calculation of Simons and co-workers.[549]

For comparison with this simple anion wave function, and in particular to calculate a more accurate dissociation energy D_0 for the anion, we have also performed some new *ab initio* and vibrational bound state calculations on FH_2^-. To determine a 3-dimensional *ab initio* FH_2^- potential energy surface, we chose the explicitly-correlated coupled-cluster method with single, double and non-iterative triple excitations (CCSD(T)-F12a)[550,551] and, in addition, the scaled triples correction.[551] We used an augmented correlation-consistent triple-zeta basis (aug-ccpVTZ) with a density-fitting basis (JKFIT) tailored for the F12a calculations.[552–554]

Calculations, done with the MOLPRO program suite,[555] were carried out on a grid of 3720 $F + H_2$ Jacobi coordinates. The interaction energy was calculated in the standard supermolecular approach in which basis set superposition error is removed by computing all the energies with the triatomic basis set:

$$V_{\rm int}(R,r,\gamma) = E_{\rm FH_2^-}(R,r,\gamma) - E_{\rm F^-}(R,r,\gamma) - E_{\rm H_2}(R,r,\gamma) \tag{11.5}$$

To determine the vibrational wave function for this anion PES we used a basis consisting of 20 distributed Gaussian functions in R, 10 distributed Gaussian functions in r, and body-frame rotational functions of the H_2 moiety up to $j = 12$ (only even or odd functions depending on the nuclear-spin species).

Table 11.2 lists the resulting equilibrium geometry of the anion, its zero-point energy, and the zero-point corrected dissociation energy ($FH_2^-(000) \longrightarrow F^- + H_2(v = 0, j = 0)$). We compare with values from the earlier calculations of Simons and co-workers,[549] and those of Stark,[556] as reported by Hartke and Werner.[557] In general, for a CCSD(T) calculation, the larger the basis set, the higher the accuracy. The calculations of Simons *et al.* used a triple-zeta basis set, those of Stark were somewhat better than a quadruple zeta basis.[556] The present calculation, based on the new explicitly correlated (F12) methodology, is comparable to using a fully converged atomic orbital basis.

We see from Table 11.2 that our presumably more accurate calculations predict an anion geometry which is slightly more expanded than that of Simons *et al.*[549] but almost identical to the earlier calculation of Stark.[556,557] The zero-point energy is slightly lower than the estimates based on the harmonic frequencies, as one might expect for a weakly-bound, anharmonic system.

Table 11.2: Properties of the FH_2^- anion.

Calculation	r_e(FH)*	r_e(HH)*	ε_0†	D_0‡
Simons *et al.*§	3.194	1.455	2990‖	0.204
Stark¶	3.290	1.482	2997‖	0.1950
Present	3.302	1.480	2831#	0.2005
				0.2219**

* Bond distance in bohr. The minimum corresponds to collinear FHH.
† Zero-point energy in cm^-1, with respect to the bottom of the $F^- \cdots HH$ well.
‡ Dissociation energy in eV; $FH_2^-(0,0,0) \longrightarrow F^- + H_2(v = 0, j = 0)$.
§ Ref. [549].
‖ Sum of symmetric stretch, antisymmetric stretch and doubly-degenerate bend harmonic zero-point energies: $(\hbar\omega_{\rm s} + \hbar\omega_{\rm a} + 2\hbar\omega_{\rm b})/2$.
¶ Refs. [556, 557] and private communication from H.-J. Werner.
# Energy of the lowest $(0,0,0)$ vibrational level of the anion with respect to the potential minimum.
** The second entry corresponds to FD_2^-.

11.2.2.3 FH_2 potential energy surface

Several high-quality *ab initio* FH_2 PESs are now available.[113,541,558–560] Here, we used the Li-Werner-Alexander-Lique (LWAL) PES.[113] Li, Werner, and Alexander described fits to two *ab initio* multi-reference, configuration-interaction calculations, in which the external correlation energy was additionally scaled by factors of 1.05 (LWA-5) and 1.078 (LWA-78). Subsequent, benchmark calculations[561] in the region of the barrier showed that the LWA-5 PES gave a better estimate of the barrier height but that the exoergicity[562] was predicted better by the LWA-78 PES. The LWAL PES merges the LWA-5 and LWA-78 potentials to allow the best description of both these key properties.

Table 11.3 compares some key features of the LWAL PES with those of the early Hartke-Stark-Werner (HSW) surface,[556,557] the Werner-Kallay-Gauss (WKG) calculation,[561] and two recent potential energy surfaces (FXZ and CSZ) from the Dalian group.[541,560]

Of the properties considered in this table, the endoergicity $\Delta E(3)$ of the HF($v' = 3, j' = 0$) + H channel relative to $F(^2P_{3/2}) + H_2(v = 0, j = 0)$ is the most relevant to the present problem, as it will have a direct impact on the relative energies of the reactant and product resonances in the photodetachment of p-FH_2^-. Since the FXZ potential of the Dalian group

Table 11.3: Barrier heights and exoergicities of the $F(^2P_{3/2}) + H_2$ reaction on various potential energy surfaces.

PES	E_a/meV†	Exoergicity*	
		$\Delta E(0)$/eV	$\Delta E(3)$/eV
HSW‡	83.2	-1.356	51.6
FXZ§	76.8	-1.3885	22.5
CSZ‖	72.9	-1.3903	20.1
LWAL¶	71.2	-1.3895	22.2
WKG#	71.3	-1.3875	
experiment		-1.3872(6)**	22.3(6)††

* $F(^2P_{3/2})^+H_2(v = 0, j = 0) \longrightarrow HF(v', j' = 0) + H$, where $v' = 0$ and 3.
† Bent barrier height relative to $F(^2P_{3/2}) + H_2(r_e)$.
‡ Refs. [556, 557].
§ Ref. (31).
‖ Ref. (54).
¶ Ref. (24).
# Ref. (55).
** Ref. (56).
†† $\Delta E(0)$ from column 3 plus the difference between the experimental $v = 0$ and $v = 3$ HF band origins, taken from http://webbook.nist.gov.

has an endoergicity that is comparable to that of the LWAL surface, and in equally good agreement with the experimental value, we shall compare the predictions of these two surfaces for the photodetachment spectrum of *p*-FH_2^- below.

11.2.2.4 Assumption of electronic adiabaticity

In the complete treatment of the scattering of F by H_2, six electronic states are coupled by the electronic and spin-orbit Hamiltonians (see Eqns. (20) and (25) of Ref. [563]). Instead of a single PES, the system is described by four electronic PESs, which we designate V_Σ, V_Π, V_1, and V_2, as well as two spin-orbit coupling terms, which we designate A and B.[563] Each of these depends on the three internal coordinates. At each value of the coordinates, diagonalization, of the 6×6 matrix of the full Hamiltonian gives rise to three electronically-adiabatic states, each of which is doubly-degenerate.

In the region where the anion vibrational wave function is localized, two of the three pairs of states lie at much higher energy.[563] We accordingly assume that after photodetachment of the electron, the neutral FH_2 evolves on a potential energy surface defined by the coordinate-dependent energy of this lowest electronically-adiabatic state. In addition, we ignore the electronic spin ($S = 1/2$) of this state. These assumptions are entirely reasonable for the photodetachment of FH_2^- and FD_2^-. (In the case of ClH_2^-, for which the spin-orbit interaction is stronger and the Franck-Condon region coincides with the van der Waals well in the reactant valley where the electronic states of ClH_2 are closer in energy, a fully non-adiabatic treatment is required to give quantitative agreement with the experimental SEVI spectrum.[564] Our results here show that this is not necessary for FH_2^-.)

11.2.3 Additional Theoretical Results

11.2.3.1 Comparison of anion vibrational wave functions

Fig. 11.7 shows a comparison of the *p*-FH_2^- photodetachment spectra obtained from simulations on the LWAL FH_2 PES with two different choices of the anion vibrational wave function: the Zhang-Miller fit to the earlier calculation of Simons and co-workers and the more sophisticated calculation described above.

We observe that there is very little difference between the spectra simulated with the two anion wave functions, even at 1 meV resolution (the difference is even less at 3 meV resolution). The calculated photodetachment peak positions are in the same places in both simulations, as they must be because these positions are determined by the dynamics of the FH_2 neutral. The simulation based on the Zhang-Miller vibrational wave function gives a slightly better fit to the experimental spectrum in terms of the relative intensities of peaks α, , a, and β (compare also with Fig. 11.2). This better agreement likely reflects a fortuitous cancellation of errors: inaccuracies introduced by the Condon approximation, in which we assume a constant electronic transition moment, are compensated by the use of a less-accurate vibrational wave function for the negative ion.

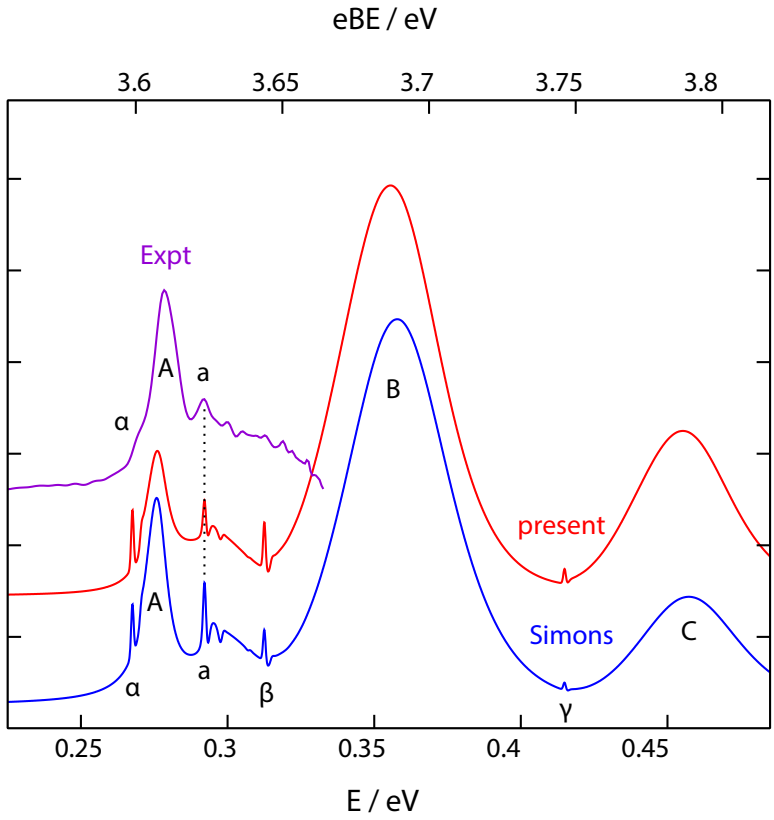

Figure 11.7: Photodetachment spectra of *p*-FH_2^-. Purple: highest resolution experimental scan. Red and blue: theoretical simulations at 1 meV energy resolution using the LWAL potential energy surface for the FH_2 neutral and (red) the present anion wave function or (blue) the anion wave function based on the earlier *ab initio* calculations of Simons and coworkers.[549]

11.2.3.2 Comparison of neutral potential energy surfaces

Fig. 11.8 compares the *p*-FH_2^- photodetachment spectra obtained using two recent neutral potential energy surfaces the LWAL surface of Lique *et al.*[113] and the FXZ surface from the Dalian group.[541] The Simons anion vibrational wave function was used in both cases.

There is a bigger difference between these results than between the calculations using different anion wave functions in Fig. 11.7. The reactant resonances α and β are in the same positions on both neutral surfaces, but the product resonance a is shifted away from its correct position in the calculation on the FXZ surface, worsening the agreement with the high resolution *p*-FH_2^- experiment. This clearly shows that experiment is capable of differentiating between the best available neutral $F + H_2$ potential energy surfaces. We have chosen the FXZ surface for this comparison because Sun and Zhang have recently argued that it is the best available surface for accounting for reactive resonances in the $F + H_2$

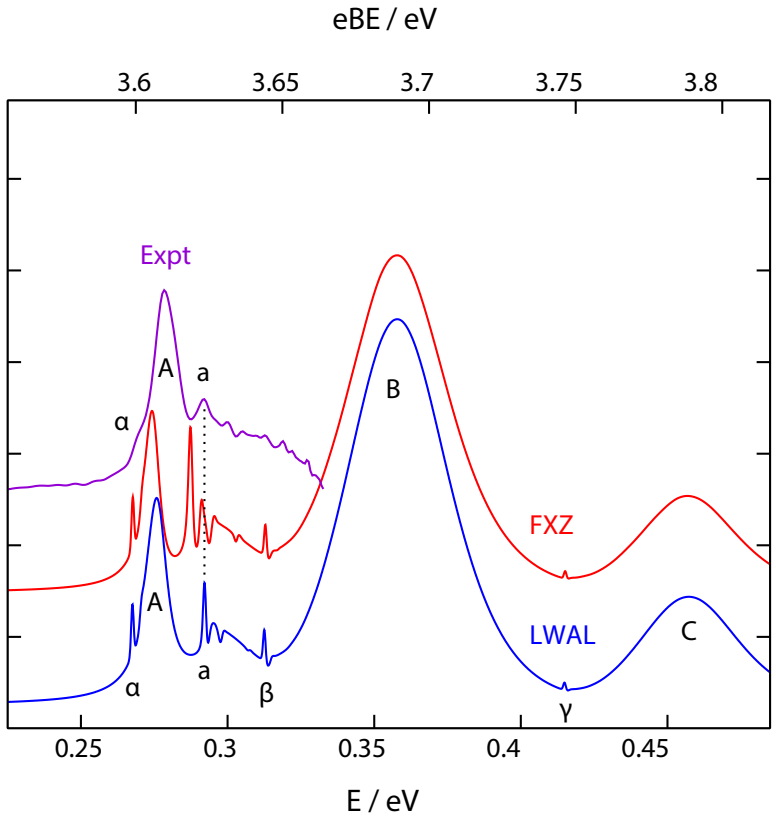

Figure 11.8: Photodetachment spectra of p-FH_2. Purple: highest resolution experimental scan. Red and blue: theoretical simulations at 1 meV energy resolution using (blue) the LWAL potential energy surface for the FH_2 neutral[113] or (red) the FXZ potential energy surface.[541] In both cases the Simons anion wave function was used.

and F + HD reactions.[565] The comparison in Fig. 11.8 clearly shows that the LWAL surface predicts the position of the product resonance a in F + H_2 more accurately than the FXZ surface. Given the assignment of the resonance wave function of peak a in Fig. 11.4, this suggests that, although they predict similar energetic positions of the HF($v' = 3, j' = 0$) asymptotes (see Table 11.3), the LWAL surface provides a more accurate description of the FH_2 potential energy surface in the region of the product van der Waals well.

11.2.3.3 Quantized bottleneck wave functions

We did not have enough space in the article to give an example of a wave function Ψ(E) at the energy of a quantized bottleneck. Fig. 11.9 gives two such examples, at the energies of peak B in the p-FH_2^- spectrum and peak D in the n-FD_2^- spectrum.

One sees that these quantized bottleneck states are delocalized along the reaction coordinate, and that they therefore have an entirely different structure (and physical origin the

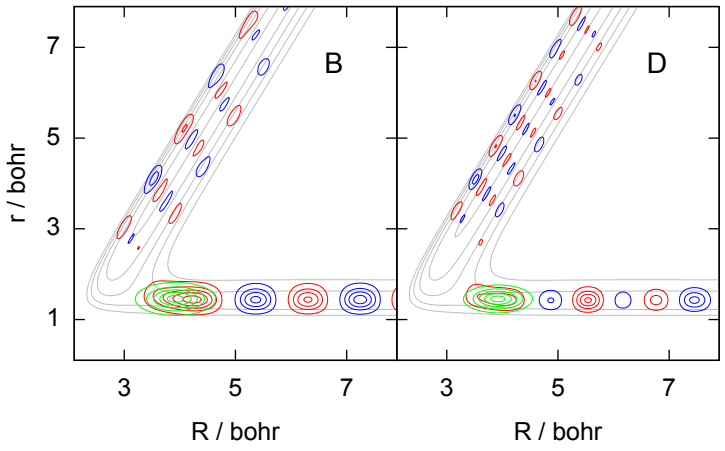

Figure 11.9: Quantized bottlenecks: The wave functions Ψ(E) at the energies of peak *B* in the *p*-FH_2^- spectrum in Fig. 11.2 and peak *D* in the *n*-FD_2^- spectrum in Fig. 11.3, plotted in the same way (and with the same contours, which highlight regions of > 10% probability density) as the resonance wave functions in Fig. 11.4. The contours of the FH_2^- and FD_2^- anion wave functions are again shown in green.

slowing down of the reactants as they approach the top of an adiabatic reaction barrier[540]) from the resonance wave functions in Fig. 11.4. Both quantized bottleneck states clearly have a good Franck-Condon overlap with their respective anion wave functions, which is why they lead to such pronounced peaks in the photodetachment spectra.

11.2.3.4 Why there are two product resonances in the *n*-FD_2^- spectrum

The high resolution experimental photodetachment spectrum of *p*-FH_2^- in Fig. 11.2 shows just one product resonance peak (*a*), whereas the high-resolution spectrum of *n*-FD_2^- in Fig. 11.3 shows two (*b* and *c*). This has nothing to do with the fact that *n*-FD_2^- is composed of a 2:1 mixture of *o*-FD_2^- and *p*-FD_2^-, because the resonances that give rise to peaks *b* and *c* are localized in the DF + D product region, and therefore occur at the same energy for both nuclear spin species of the reactant. Instead it is simply a reduced mass effect: because D has twice the mass of H, deuteration leads to more quasi-bound states.

This is illustrated in Fig. 11.10, which shows the adiabatic bending curves[537–539] that correlate with the HF($v' = 3, j' = 0$) + H and DF($v' = 4, j' = 0$) + D channels on the LWAL potential energy surface. The first of these curves has a shallow well in the van der Waals region that supports one bound state (*a*) in the H−HF stretching coordinate, whereas the second has a slightly deeper well that supports two bound states (*b* and *c*) in the D−DF stretching coordinate. The energies of all three of these bound states are within ∼2 meV of the energies of the corresponding scattering resonances in Table 11.1. In a fully-coupled calculation, the states are quasi-bound because they can decay by vibrational predissociation

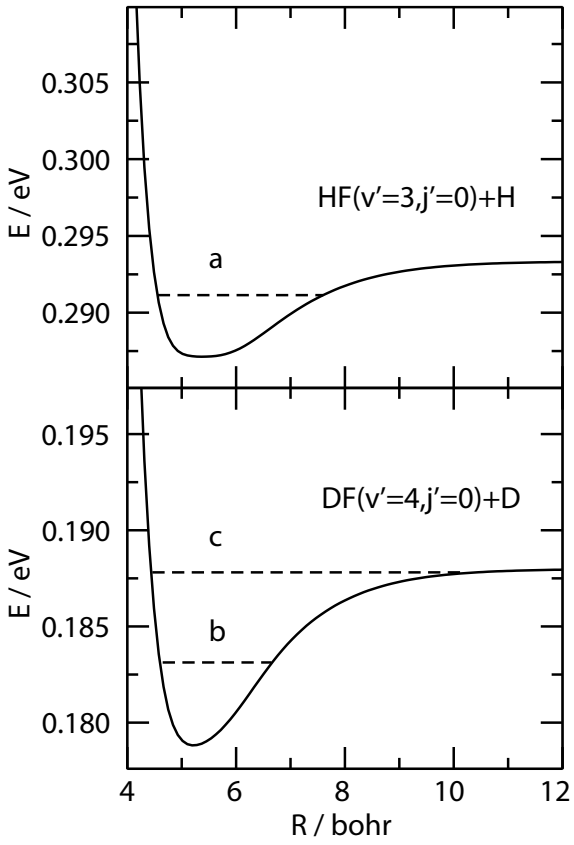

Figure 11.10: Adiabatic potential energy curves correlating with the $v' = 3, j' = 0$ level of HF and the $v' = 4, j' = 0$ level of DF, as a function of the Jacobi distance R from H (D) to the center-of-mass of HF (DF), as calculated on the LWAL potential energy surface. The bound states supported by these curves provide an approximation to the resonances a, b, and c seen in the fully coupled calculation.

to HF($v' < 3$) + H and DF($v' < 4$) + D product channels, which is not possible within the adiabatic bending approximation.

11.2.3.5 Contribution of resonances to reactive scattering

The wavefunctions corresponding to the reactant, product and transition state resonances, along with the scattering wavefunctions at the quantized bottlenecks shown in Fig. 11.9 are localized in the region of the negative ion (shown by the green contours in Figs. 11.4 and 11.9) to a slightly greater extent than the unbound (scattering) $F + H_2$ wavefunction at other energies. This larger overlap gives rise to the peaks in the photodetachment spectra presented in Figs. 11.2 and 11.3. These peaks and their intensities are direct spectroscopic manifestations of the elusive resonances associated with the FH_2 potential energy surface.

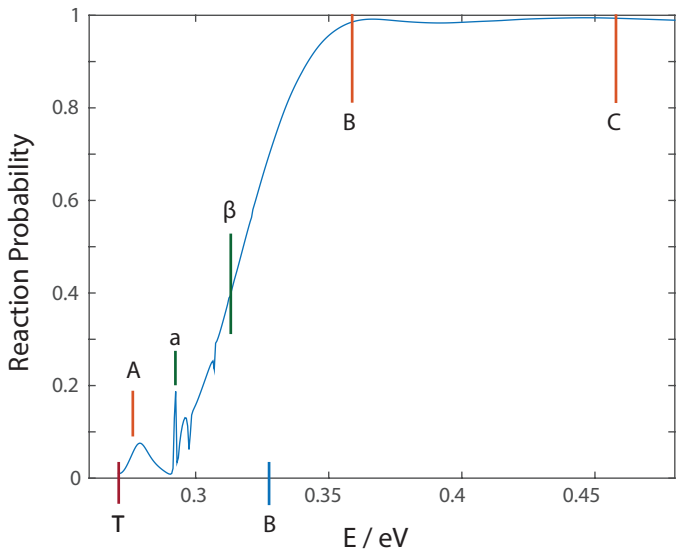

Figure 11.11: $F + H_2(v = 0, j = 0) \longrightarrow FH + H$ $J = 0$ reaction probability as a function of energy as predicted by the LWAL PES. The heavy vertical lines on the abscissa marked "T" and "B" correspond, respectively, to the threshold for reaction (which is the energy of the reactants, with respect of the same zero of energy used in the main text) and the energy of the zero-point-corrected barrier to reaction. The positions of the features A, a, β, B, and C of Fig. 11.2 are indicated. The lowest reactant resonance, α, lies below the energy of $F + H_2(v = 0, j = 0)$ and hence is not shown.

They are not, as we reemphasize here, a measure of the energy dependence of the integral or differential cross sections for the reaction of F with the isotopologues of H_2.

The $F + H_2(v, j)$ reaction cross section is given by the following sum of reaction probabilities over all total angular momenta:

$$\sigma_{vj}(E) = \frac{\pi}{(2j+1){k_{vj}}^2} \sum_J (2J+1) P^J_{vj}(E) \tag{11.6}$$

where the reaction probability is a sum over all energetically accessible HF final states $(v'j')$ as well as over all projection quantum numbers of the initial and final rotational angular momenta of the diatomic moiety of the absolute values squared of the corresponding scattering S-matrix elements. Here, also, k_{vj} is the wavevector associated with the reactant channel. For the lowest $(v = 0, j = 0)$ state of p-H_2, and for $J = 0$, the reaction probability predicted by the LWAL PES is shown in Fig. 11.11. Superimposed are the positions of the peaks A, a, β, B, and C labeled in Fig. 11.2.

The prominent features in the p-FH_2^- photodetachment spectrum contribute in only a minor way to the $J = 0$ reaction probability. In addition, this $J = 0$ probability will make only a small contribution to the overall reaction cross section, because the $(2J+1)$ degeneracy

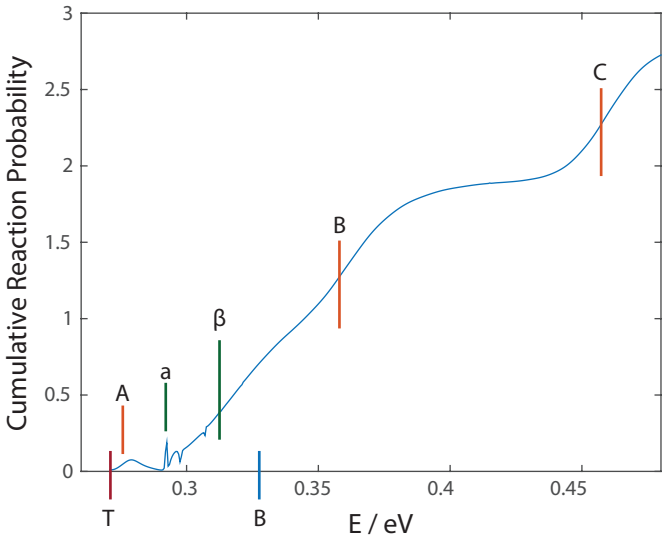

Figure 11.12: $F + p{-}H_2 \longrightarrow FH + H$ $J = 0$ cumulative reaction probability as a function of energy as predicted by the LWAL PES. The heavy vertical lines on the abscissa marked "T" and "B" as well as the features A, a, β, B and C are unchanged from Fig. 11.11.

factor in Eqn. 11.6 amplifies the importance of higher partial waves. As discussed in the main text, the footprint of resonances in the integral and differential cross sections for the reaction of F with the isotopologues of H_2, particularly HD, have been intensively explored previously.[109,531–534]

The overall rate of the $F + H_2$ reaction is proportional to the cumulative reaction probability, which, when restricted to $J = 0$, is given by

$$N^{J=0}(E) = \sum_{vj} P_{vj}^{J=0}(E) \tag{11.7}$$

where the reaction probability is defined in Eqn. 11.6. This is plotted in Fig. 11.12. At low energy, only the $v = 0, j = 0$ state of p-H_2 contributes to $N(E)$. As the energy increases, the $v = 0, j = 2$, and, then, the $v = 0, j = 4$ states contribute. This is manifested in the two distinct steps in $N(E)$. The edges of the steps are softened by tunneling.

Peaks B and C in the photodetachment spectrum of Fig. 11.2, the reaction bottlenecks, correspond to the onset of additional contributions to the reactivity of the $j = 2$, and, then, the $j = 4$ states of H_2. In fact, peaks B and C correspond to relative maxima in the slope of $N(E)$.

Chapter 12

Resonances in the exit channel of $F + CH_3OH \longrightarrow HF + CH_3O$

The content and figures of this chapter are reprinted or adapted with permission from M. L. Weichman, J. A. DeVine, M. C. Babin, J. Li, L. Guo, J. Ma, H. Guo, and D. M. Neumark "Feshbach resonances in the exit channel of the $F + CH_3OH \rightarrow HF + CH_3O$ reaction via transition state spectroscopy" *Nat. Chem.* (under review).

Abstract

The transition state governs how chemical bonds form and cleave during a chemical reaction. Direct characterization of the reactive transition state is a long-standing challenge in physical chemistry. Transition state spectroscopy experiments based on negative ion photodetachment provide a direct probe of vibrational structure and metastable resonances characteristic of the reactive surface. Dynamical resonances are extremely sensitive to the reactive surface topography and are an exceptional point of comparison with theory. Here, we study the seven-atom $F + CH_3OH \longrightarrow HF + CH_3O$ reaction via slow photoelectron velocity-map imaging spectroscopy of cryo-cooled CH_3OHF^- anions. This measurement reveals structure associated with a manifold of vibrational Feshbach resonances and bound states supported by the post-transition-state potential well. Quantum dynamical calculations yield excellent agreement with experimental results, allow assignment of structure, and demonstrate that the key dynamics of complex bimolecular reactions can be captured with a relatively simple theoretical framework.

12.1 Introduction

Since the development of crossed molecular beam experiments in the 1960s,[566,567] studies of reaction dynamics via reactive scattering experiments and accompanying theoretical advances have led to major insights into the fundamental interactions that govern chemical reactivity.[125] A key concept in chemistry is that during the course of a reactive collision, chemical bond formation and cleavage occur in the transition state region of the potential energy surface (PES).[568–570] Hence, there is much interest in characterizing reaction transition states experimentally and theoretically.[104]

Increasingly sophisticated scattering experiments involving state-selective reactant preparation and state-resolved product detection provide new windows into properties of the transition state, such as the reaction barrier height and geometry, that dictate mode specificity and the most favorable reactant orientation for promoting a reactive collision.[571–573] However, such experiments do not probe the transition state region of the PES directly. Complementary experiments based on negative ion photodetachment yield vibrationally resolved structure characteristic of the transition state,[105] and have been applied with considerable success to benchmark bimolecular[574] and unimolecular[9,10] reactions.

In this publication, we report a joint high-resolution photoelectron imaging and theoretical quantum dynamics study of the $F + CH_3OH \longrightarrow HF + CH_3O$ hydrogen abstraction reaction, based on photodetachment of the stable CH_3OHF^- anion. The spectra are obtained via slow photoelectron velocity-map imaging of cryogenically cooled anions (cryo-SEVI),[35,49,114] which yields photoelectron spectra of complex species with kinetic energy resolution as high as $1\,cm^{-1}$.[51,575] The resolution of the cryo-SEVI spectra of CH_3OHF^- and CH_3ODF^- is substantially improved over previous photodetachment experiments,[576,577] revealing low-frequency progressions assigned to exit channel bound states and Feshbach res-

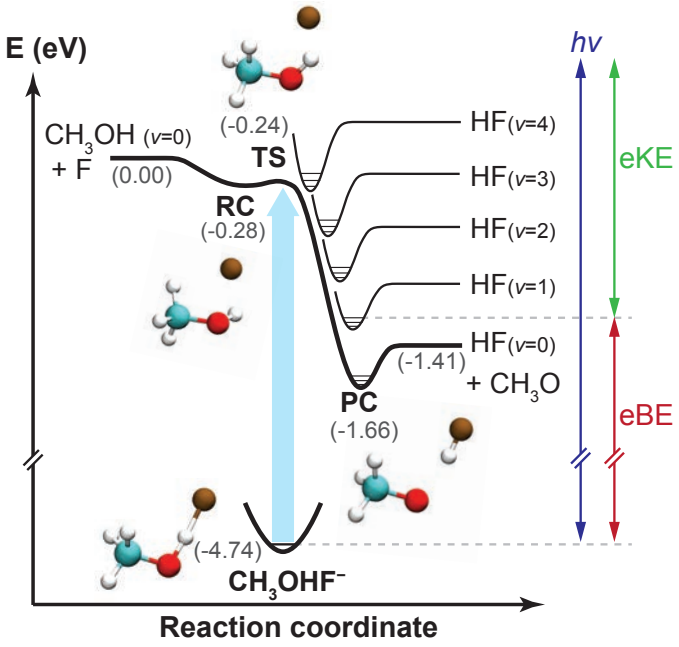

Figure 12.1: Schematic energy diagram for photodetachment of the CH_3OHF^- anion to the neutral $F + CH_3OH \longrightarrow HF + CH_3O$ reactive PES. The bold line is the zero-point energy corrected surface connecting reactants and products in their ground vibrational states. Geometries are shown for the anion, reactant complex (RC), transition state (TS) and product complex (PC) stationary points. Energies derived from the fitted PIP-NN surface, shown in gray text, are given in eV relative to the reactant asymptote.

onances and providing new insights into the transition state region of this polyatomic reaction. The experimental spectrum is assigned with the help of reduced-dimensional quantum dynamical calculations on a global PES determined by fitting a large number of high-level *ab initio* points in full dimensionality.

Dynamical Feshbach resonances of the type probed here are transient metastable states supported by the reactive PES. These resonances have sufficient vibrational energy to dissociate, but decay slowly because of the inefficient energy flow from the excited modes to the reaction coordinate. Quantum scattering calculations indicate that the energies and widths of these resonances are exquisitely sensitive to the topography of the reactive PES.[572,574,578] Dynamical resonances can strongly mediate reactivity and can manifest as peaks in the integral or differential cross section as a function of collision energy.[526,530,579,580] These effects have been sought out and, in some cases, clearly observed in molecular beam reactive scattering experiments.[108,109,530,534,572,581]

Anion photoelectron transition state spectroscopy offers an alternative and often more direct means to detect dynamical resonances.[105,574] In such an experiment, a bound anion similar in geometry to the neutral transition state is photodetached. The vibrational wave-

function of the anion is vertically projected onto the neutral PES, and the kinetic energy of the nascent photoelectron reports on the wave packet evolution under the influence of the neutral Hamiltonian. The resulting photoelectron spectrum may show broad structure if photodetachment accesses a repulsive Franck-Condon region of the neutral PES. On the other hand, direct detachment to discrete bound or quasi-bound neutral states will manifest as sharp, well-defined features in the photoelectron spectrum.[111] These features provide valuable information on the neutral PES in strongly interacting regions such as reactive intermediate wells and transition states. Resonances identified in transition state spectroscopy studies offer an exceptional point of comparison with quantum theory, which can provide assignments based on the nodal structure of the resonance wavefunctions. Thus far such comparisons have been limited to triatomic[34,564,574] and tetratomic systems,[582] and the somewhat irregular structure in the entrance channel of the $F + CH_4$ reaction.[583]

Here, we exploit the high resolution of cryo-SEVI to observe and identify dynamical resonances in the more complex, seven-atom $F + CH_3OH$ hydrogen atom abstraction reaction. This reaction can proceed either at the hydroxyl or the methyl site, leading to methoxy (CH_3O) or hydroxymethyl (CH_2OH) radical products, respectively. The methoxy and hydroxymethyl pathways are exothermic by 1.357(4) and 1.767(4) eV respectively[584] and both are predicted to proceed without a barrier.[585–587] The $F + CH_3OH$ branching ratio for abstraction from the hydroxyl group is considerably higher than the value of 25% expected if the branching were statistical.[586–592] This is attributed to the fact that hydroxyl group abstraction proceeds through a reactant complex and transition state stabilized by hydrogen bonding interactions.[585] The H-bonded CH_3OHF^- anion is similar in geometry to the hydroxyl abstraction transition state,[576,577,593–595] as shown schematically in Fig. 12.1 (further details on the calculated reactive surface are given in Section 12.3). This system is an ideal case for transition state spectroscopy, where the accessible part of the neutral reactive PES is constrained by the anion geometry. At the same time, this system poses a challenge, particularly to theory, with fifteen degrees of freedom potentially involved in the dynamics.

12.2 Methods

The SEVI method and apparatus has been described in detail in Chap. 2.

CH_3OHF^- and CH_3ODF^- anions are prepared by expanding trace NF_3 and either methanol or methanol-d_1 vapor in helium gas through an Even-Lavie pulsed valve[117] fitted with a circular filament ionizer. Dissociative electron attachment to NF_3 produces F^- atomic ions which then cluster with methanol(-d_1).

The quantum dynamical calculations are performed with a reduced-dimensional model, in which the methyl moiety is fixed at the geometry associated with the PC well. This is a reasonable approximation as the methyl group behaves largely as a spectator in the $F + CH_3OH \longrightarrow HF + CH_3O$ channel. The remaining six coordinates are represented by the diatom-diatom Jacobi coordinates, in the same fashion as our recent work on $F^-(H_2O)$ photodetachment.[596] The photodetachment process is simulated within the Condon approx-

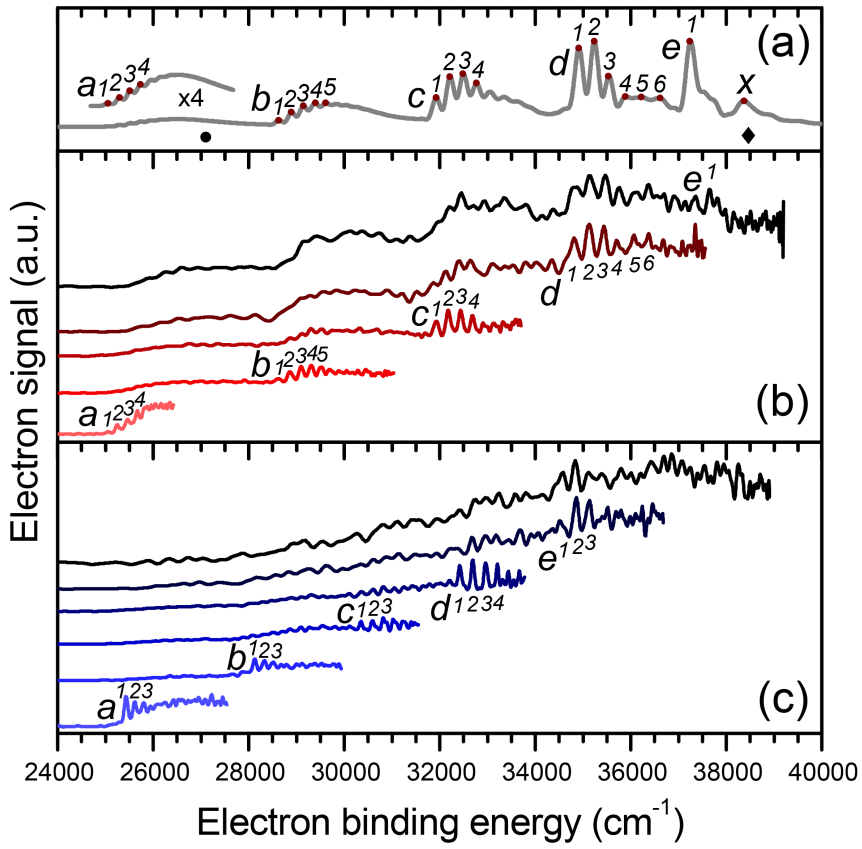

Figure 12.2: Experimental and theoretical photodetachment spectra of CH_3OHF^- and CH_3ODF^-. (a) Theoretical simulation of the CH_3OHF^- photoelectron spectrum obtained with a 200 fs propagation time (gray), and experimental cryo-SEVI spectra of (b) CH_3OHF^- and (c) CH_3ODF^- detachment. Experimental overview spectra are plotted in black and high-resolution traces taken at progressively lower photon energies are plotted in color. The ● and ♦ symbols represent the zero-point energy corrected PIP-NN product and reactant asymptotes, respectively.

imation, in which the anion wavefunction is placed on the neutral PES in a vertical transition. The subsequent dynamics are followed by propagating the initial wave packet in the Chebyshev order domain and the photoelectron spectrum is computed by a discrete cosine transform of the Chebyshev auto-correlation function.[597] Additional theoretical details, including descriptions of the benchmark calculations and the construction of the PESs, can be found in the Supporting Information.

12.3 Results

Experimental cryo-SEVI spectra of CH_3OHF^- and CH_3ODF^- are shown in Figs. 12.2b and 12.2c. The spectra are dominated by broad steps (labeled *a*, *b*, *c*, *d*, *e*), with an *a*-*b* spacing of $\sim$3600 cm^{-1} in the CH_3OHF^- spectrum and $\sim$2700 cm^{-1} for CH_3ODF^-. These features were also seen in lower resolution photoelectron spectroscopy results by Bradforth *et al.*[576] and in a recent photoelectron-photofragment coincidence study by Ray *et al.*[577] Both prior studies assigned this stepped structure to an HF stretching progression of the CH_3O-HF product complex. The considerably higher spectral resolution afforded by cryo-SEVI reveals an additional layer of vibrational structure not seen previously. We now resolve much finer structure spaced by $\sim$200 cm^{-1} superimposed on the broad steps with typical peak widths of 75–125 cm^{-1} full-width at half maximum (fwhm). Peak positions and spacings are listed in Tables 12.1 and 12.2. A key trend is that the spacing of resonances within each step increases with increasing HF stretching excitation. For example, the *a1*-*a2*, *b1*-*b2*, *c1*-*c2*, and *d1*-*d2* gaps are measured experimentally as 192, 248, 255, and 315 cm^{-1}, respectively.

Accurate quantum dynamical studies on a reactive PES are necessary to interpret the experimental spectra. We model the $F + CH_3OH$ reaction using a full 15-dimensional PES constructed with $\sim$121,000 points calculated at the explicitly correlated unrestricted coupled cluster level with singles, doubles, and perturbative triples[551] with the augmented correlation-consistent polarized valence double zeta basis set and core electrons frozen (FC-UCCSD(T)-F12a/AVDZ). The CCSD(T)-F12/AVDZ method is expected to yield results of quality comparable to the conventional CCSD(T)/AVQZ level. The PES is fit using the permutation invariant polynomial-neural network (PIP-NN) method.[598]

Fig. 12.1 shows a schematic of the $F + CH_3OH \longrightarrow HF + CH_3O$ reaction path. The bold line is the zero-point energy (ZPE) corrected minimum energy path connecting reactants and products in their ground vibrational states. The reported stationary point energies derived from the PIP-NN PES are in good agreement with prior work (see a detailed comparison in Fig. 12.4).[577,585] The transition state (TS), reactant complex (RC), and product complex (PC) all lie below the energy of free reactants. The RC is a covalent three-electron two-center hemi-bonded complex, similar to that between F and H_2O,[599] which is bound by 0.28 eV relative to free reactants but lies only slightly lower in energy than the TS. The PC is a hydrogen-bonded complex between HF and the methoxy radical bound by 0.25 eV relative to the free products. The stationary point geometries are consistent across different levels of theory and agree well with available experimental results (Figs. 12.5 and 12.6). The corresponding harmonic frequencies of these stationary points are compared in Table 12.3.

To simulate the photoelectron spectrum, wave packet based quantum dynamics were carried out with a reduced six-dimensional model with a frozen methyl moiety. The CH_3OHF^- detachment spectrum simulated with a $\sim$200 fs wave packet propagation is given in Fig. 12.2a and compares favorable with experimental results. The electron binding energy (eBE) of the bottom of the PC well is calculated to lie at 24810 cm^{-1}, close to the experimental onset of structure at 25058(25) cm^{-1} (peak *a1*) and with previos measurements.[576,577] The simulated spectrum has therefore been shifted to higher eBE by 250 cm^{-1} so that the onset

of structure at low eBE matches that observed experimentally. Experimental and theoretical peak positions are compared for CH_3OHF^- detachment in Table 12.1; note that theory reproduces the trend of increasing resonance peak spacings mentioned above.

The product asymptote for the $F + CH_3OH \longrightarrow HF + CH_3O$ reaction lies at 26800 cm^{-1} while the reactant asymptote lies at 38200 cm^{-1} on the ZPE-corrected PIP-NN surface. These asymptotes are marked in Fig. 12.2a with ● and ♦ symbols, respectively, and have also been shifted to higher eBE by 250 cm^{-1} for comparison with experiment. The energies of these asymptotes indicates that much of the observed structure can lie only in the PC well. The peaks in the *a* manifold fall below the product asymptote and are thus bound with respect to free $HF + CH_3O$ products. Ray *et al.*[577] accordingly found that the *a* manifold was associated with production of non-dissociating neutral complexes, while higher-lying peaks were correlated largely with dissociated fragments. The agreement of experiment and theory unambiguously identifies the newly resolved low frequency progressions as derived from discrete bound states and Feshbach resonances on the product side of the transition state.

12.4 Discussion

The presence of the low frequency progressions and the trend of their increasing spacing within steps *a*-*d* can be explained intuitively with reference to the vibrational adiabatic potentials (VAPs) shown in Fig. 12.1. These VAPs correspond to the HF vibrational levels plotted along the reaction coordinate and correlate to vibrationally excited free HF(v) + CH_3O products. The HF vibrational adiabaticity is expected to be strong due to its high vibrational frequency, which couples weakly with the dissociation coordinate. Each spectral step *a*-*e* represents detachme to an HF(v=0–4) VAP. The finely spaced progressions within each step are resonances supported in the wells of the VAPs and reflect increasing quanta of excitation in the low-frequency CH_3O−HF stretching mode. The VAP wells deepen as the HF excitation is increased, resulting in more widely spaced states within each well. The deepening of the PC VAPs can be explained by dynamical vibrational bonding. It is a well-known phenomenon in heavy-light-heavy[600–602] and other triatomic[572,603] systems that VAPs can support increasingly stabilized wells as the vibrationally excited light atom is more delocalized between the two outer fragments.

To better understand the vibrational character of the observed spectral features, the simulated wavefunctions of all peaks are extracted. Relevant examples are shown in Fig. 12.3. From the localized character of these wavefunctions, it is clear that they are stable bound states or metastable resonances supported by the PC well. The ∼100 cm^{-1} fwhm peak widths of the observed spectral features allow us to place a lower bound of 50 fs on the lifetimes of the Feshbach resonance states that lie above the $HF + CH_3O$ dissociation limit, although theoretical results suggest much longer lifetimes. The final dissociation of these resonance states is expected to proceed via vibrational predissociation facilitated by energy flow from the HF stretching coordinate to translational motion along the dissociation

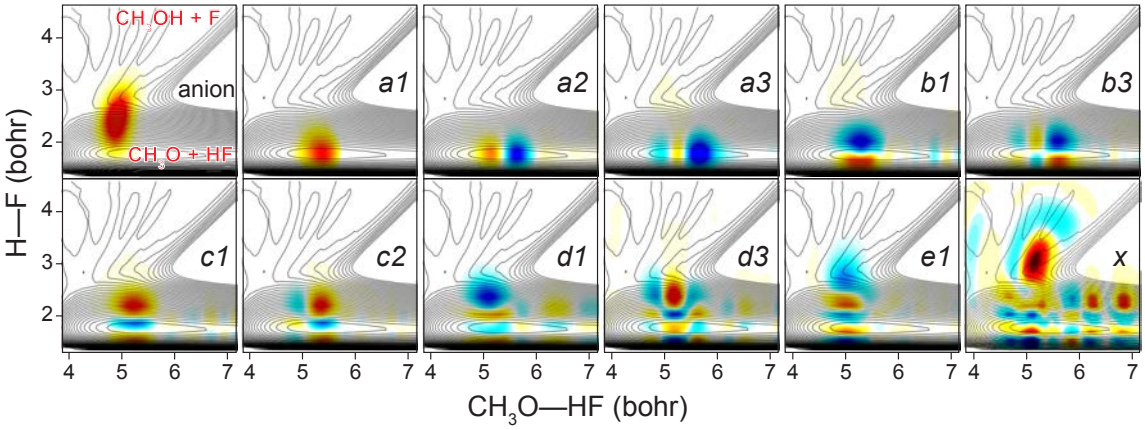

Figure 12.3: Cuts of the CH_3OHF^- anion vibrational ground state wavefunction and representative $F + CH_3OH \longrightarrow HF + CH_3O$ resonance wavefunctions. The labels correspond to the related peaks in the simulated photodetachment spectrum of CH_3OHF^- (Fig. 12.1a). Wavefunctions are superimposed on the neutral PES contours, in which the other four coordinates are relaxed. The locations of the entrance and exit channels are labeled in red in the upper-left plot.

coordinate. Because of the large frequency mismatch, such energy flow is expected to be slow, resulting in long lifetimes for these resonances. Similar long-lived Feshbach resonance states were observed in $F + H_2O$[582] and this picture holds even in the presence of many degrees of freedom for the $F + CH_3OH$ system.

Vibrational assignments can be confirmed by examining the resonance wavefunction nodal structure. Peaks in the *a1-b1-c1-d1-e1* progression show an increasing integer number of nodes along the HF stretching coordinate (vertical axis in Fig. 12.3). The broad shelves in the spectrum therefore indeed correspond to a progression of HF stretching vibrational states of the product complex. The isotope effect observed in the CH_3ODF^- cryo-SEVI spectrum (Fig. 12.2c) further validates this assignment. The increasing number of nodes in the *a1-a2-a3* progression along the CH_3O-HF coordinate (horizontal axis in Fig. 12.3) confirms that the finely spaced progressions are Feshbach resonances with increasing quanta of excitation in the stretching mode between the product fragments. The experimental and theoretical Franck-Condon factors increase along with HF stretching excitation, as the PC vibrational states with higher quanta of excitation in the HF stretch have more wavefunction density at larger HF displacement. Compare, for instance, the vibrational wavefunctions for peaks *a1* and *d1*: the latter has substantially better Franck-Condon overlap with the anion wavefunction, leading to increased intensity in the photoelectron spectrum.

To further illustrate the evolution of these resonances, the simulated photoelectron spectrum is shown in Fig. 12.7 for three different propagation times. The low-resolution spectrum obtained in the first 40 fs of propagation suggests that the short-time dynamics on the neu-

tral PES are along the HF vibrational coordinate, as the spectrum clearly resolves peaks related to the HF vibrational frequency. By 200 fs, the fine structure peaks emerge due to the recursion of the wave packet along the CH_3O-HF dissociation coordinate. By 800 fs, the fine structure peaks split further into sharper peaks related to $H_3C-O-HF$ bending excitation, though these are not resolved experimentally.

The vibrational assignments made here are also sensible in the context of the Franck-Condon principle. Comparison of the anion and PC geometries (Figs. 12.5 and 12.6) indicates that photodetachment to the PC well should be accompanied by vibrational excitation in HF stretching and CH_3O-HF stretching and bending modes. Indeed, the HF bond length in the anion (1.32 Å) is considerably longer than that of free HF (0.92 Å). The geometry of the methyl moiety is largely unchanged by detachment, so freezing its internal degrees of freedom during the quantum dynamical calculations does not have an adverse impact on the accuracy of the simulation. In this regard, the transition state spectrum of $F + CH_3OH$ is analogous to that predicted and observed for the $F + H_2O$ system.[582,596] In $F + H_2O$, photodetachment predominantly accesses the OH + HF product well and is accompanied by considerable HF vibrational excitation, with the OH fragment acting as a spectator, as CH_3O does here.

We do not find evidence of resonances supported by the RC well. All sharp features that fall below the reactant asymptote (marked with ♦ in Fig. 12.2a) have wavefunctions localized on the product side of the transition state (Fig. 12.3). Ray *et al.*[577] tentatively assigned a spectral feature lying below the reactant asymptote to an RC resonance, as it appeared to have a longer lifetime than neighboring peaks. In the cryo-SEVI spectra this feature is resolved as peaks *d4*, *d5*, and *d6*, which are well-reproduced by theory as resonances in the PC well. On the other hand, the long-lived feature observed by Ray *et al.*[577] represents a sufficiently small fraction of the total dissociative signal that there may not be a reasonable expectation of resolving it in our present experiment. Furthermore, such a state may not be accurately captured by our simulations as the reduced-dimensional model, which is ideal for the $HF + CH_3O$ product channel, might not be sufficient for the $F + CH_3OH$ reactant channel.

The resonances we report here are non-reactive as they are submerged below the energy of free reactants. These states cannot, for instance, be accessed in an $F + CH_3OH$ scattering experiment and are therefore uniquely accessible with anion photoelectron spectroscopy. It is expected that reactive resonances also exist at higher energies, similar to what was predicted for $F+H_2O$.[582,596] The lowest-lying reactive resonance that is predicted theoretically underlies the feature labeled *x* in Fig. 12.2a. The wavefunction for this feature is shown in Fig. 12.3 and clearly has intensity extending into the reactant channel. Unfortunately, no unambiguous evidence of this feature is resolved experimentally, as the spectrum becomes congested at higher photon energies.

The poor agreement between the experimental and theoretical results for the position and intensity of peak *e1* could also be due to experimental congestion. The laser noise background becomes a limiting factor at high photon energies. It is also possible that detachment to excited $F + CH_3OH$ surfaces, analogous to those predicted in $F + H_2O$,[596]

contributes at higher eBE, leading to the increased baseline of the experimental spectra compared to theory. Additionally, the Wigner threshold law[75] can distort relative peak intensities close to threshold, which may further hamper our ability to resolve peaks *e1* and x at the relatively low eKEs accessible here.

In conclusion, we have investigated the photodetachment of CH_3OHF^- and its singly deuterated isotopologue using slow photoelectron velocity-map imaging spectroscopy and quantum dynamical calculations on a new *ab initio* based potential energy surface. The cryo-SEVI spectrum is dominated by Feshbach resonances supported in the product well of the $F + CH_3OH \longrightarrow HF + CH_3O$ reaction. These resonances are fully reproduced by theory, allowing their unambiguous assignment to vibrational HF and CH_3O-HF stretching states of the product complex. This work demonstrates the utility of cryo-SEVI transition state spectroscopy experiments for probing detailed multi-dimensional dynamical features near the transition state as well as the theoretical advances in modeling the dynamics of increasingly complex bimolecular reactions. It also illustrates that despite much increased complexity, the key dynamical features of this seven-atom reaction remain largely local and can still be captured by a relatively simple physical picture.

12.5 Supporting Information

Supplementary Theoretical Details

Ab Initio Calculations

All *ab initio* calculations were performed using the MOLPRO 2015.1 package.[203] Specifically, the Hartree-Fock (HF) wavefunctions were used in explicitly correlated (F12)[551] coupled cluster singles, doubles, and perturbative triples (CCSD(T)) calculations. The F12 version of CCSD(T) offers much faster convergence with respect to the size of the basis set. The frozen-core (FC) treatment was used in the post-Hartree-Fock calculations. Augmented correlation-consistent polarized valence double-zeta basis sets (aug-cc-pVDZ or AVDZ) were chosen. For some simple species, such as CH_3OH, CH_3O, CH_2OH, HF, and CH_3OHF^-, additional calculations with the larger AVTZ basis set were performed for geometry optimizations and frequency analysis. The dependence on the basis size was found to be small. As a compromise between efficiency and cost, the FC-CCSD(T)-F12a/AVDZ level of theory was selected for calculating the energies of the potential energy surface (PES) points.

PES Construction

The construction of a PES consists of two steps: sampling and calculations of the data points in the relevant configuration space and fitting them with a specific function. Here, our PESs for both the neutral and anionic species are developed in full 15 dimensions. Following our strategy,[598] possible reaction paths were first surveyed to determine the ranges of configurations and energies. For the neutral system, only abstraction channels for the hydrogens of different CH_3OH sites were considered. Next, we used grids with appropriate coordinates in various regions to sample relevant configurations. In the reactant region, for instance, the internal coordinates of CH_3OH were sampled in a fine grid while the coordinates involving the attaching F atom were sampled in a relative sparse grid. In addition, a small set of data points around the reaction path was selected by running direct dynamics trajectories at a low level of theory. Such a strategy allows for the selection of points into all product channels. Indeed, the global PES includes both the $F + CH_3OH \longrightarrow HF + CH_3O$ and $F + CH_3OH \longrightarrow HF + CH_2OH$ reaction channels. For the anion, the points are mostly selected near the equilibrium geometry.

With the initial set of points, *ab initio* calculations were performed at the FC-UCCSD(T)-F12a/AVDZ level and a primitive PES was fit. Trajectories with various initial conditions were then dispatched on this primitive PES to further explore the configuration space and to generate new points. New points were then added to patch up these regions if they were not too close to the existing data sets based on the Euclidean distance between the new point $\{\vec{r_i}\}$ and a data point $\{\vec{r_i}'\}$ in the existing data set, $\chi(\{\vec{r_i}\}) = \sqrt{\sum_i^{21} |\vec{r_i} - \vec{r_i}'|} < 0.2\,\text{Å}$. Note that all permutation equivalent points were included in such screening. The resulting PES was examined by key *ab initio* properties of the system, such as geometries, frequencies, and

energies of the stationary points, as well as the reaction paths. The procedure mentioned above was repeated, and the PES was improved gradually until convergence. In addition, a very small percentage of points with T_1 values larger than 0.05 were discarded if their energy was higher than 50.0 kcal/mol (2.2 eV). Finally, a total of *ca.* 121,000 points were calculated at the FC-CCSD(T)-F12a/AVDZ level, and employed to fit the PES.

The permutation invariant polynomial-neural network (PIP-NN) method[604,605] has been successfully applied to several reactive systems for fitting PESs, as it combines the advantages of both the PIP[606] and NN[607] approaches: the non-linear nature of NNs provides a flexible means to approximate any unknown real-valued multi-dimensional function accurately;[607] the choice of PIPs[606] as the input vector enforces permutation symmetry in the NN fitting. In practice, all PIPs up to a specific maximum order were used to circumvent the problem. In this work, the following feed-forward NN functional form with two hidden layers was used:

$$V = b_1^{(3)} + \sum_{k=1}^{K} \left(\omega_{1,k}^{(3)} \cdot f_2 \left(b_k^{(2)} + \sum_{j=1}^{J} \left(\omega_{k,j}^{(2)} \cdot f_1 \left(b_j^{(1)} + \sum_{i=1}^{I} \omega_{j,i}^{(1)} \cdot G_i \right) \right) \right) \right), \tag{12.1}$$

where I denotes the number of PIPs G_i of the input layer; J and K are the number of the neurons of the two hidden layers, respectively; f_i (i=1, 2), transfer functions for the two hidden layers, are taken as the hyperbolic tangent function; $\omega_{j,i}^{(l)}$ are weights that connect the ith neuron of the $(l-1)$th layer and the jth neuron of the lth layer; $b_j^{(l)}$ are biases of the jth neurons of the lth layer. The parameters ω and b are determined by non-linear fitting of NN. The explicit form of PIPs G_i is[606]

$$\mathbf{G} = \hat{\mathbf{S}} \prod_{i<j}^{N} p_{ij}^{l_{ij}} \tag{12.2}$$

where $p_{ij} = \exp(-\alpha r_{ij})$ are the Morse-like variables with α as an adjustable constant and r_{ij} the $N(N-1)/2$ internuclear distances. l_{ij} is the degree of p_{ij} and $MAX = \sum_{i<j}^{N} l_{ij}$ is the total degree of each monomial. In this work, MAX is selected to be 4. $\hat{\mathbf{S}}$ is the symmetrization operator, including all 4! = 24 nuclear permutation operations in the title system.

For each NN fitting, the data were divided randomly into three sets, namely the training (90%), validation (5%), and test (5%) sets, to avoid overfitting. To avoid false extrapolation due to edge points in the randomly selected validation and test sets, only fits with similar RMSEs (defined as RMSE=$\sqrt{\sum_{i=1}^{N_{data}} \left(E_{output}^{i} - E_{target}^{i}\right)^2 / N_{data}}$) for all three sets were accepted. In addition, the maximum deviation was also used as an important criterion in selecting the final PIP-NN PES. Different NN architectures with two hidden layers were tested. For each architecture, 100 different NN training calculations were performed. The final NN has two hidden layers with 5 and 100 neurons, resulting in 6226 parameters including weights

and biases. Its RMSEs for the train/validation/test/total sets and maximum deviation are 0.021/0.020/0.025/0.024 and 0.4575 eV, respectively. Fig. 12.8 shows the distribution of the fitting errors.

The properties of the stationary points on the PIP-NN PESs are compared in Table 12.3 and Figs. 12.4 and 12.5. In Fig. 12.9, the PES is plotted as a function of the bond lengths of the breaking OH and forming HF bonds, with all other coordinates fixed at the transition state values. The PES is very similar to that of the F + H_2O system.[608] Note that the spin-orbit corrections are not included here, but can be readily added.[609]

For the anion PES, ∼48,000 points were sampled and calculated at the level of FC-CCSD(T)-F12a/AVDZ level, and fit using the PIP method.[606] All polynomials with the maximum order up to five were employed, resulting in 4672 linear coefficients. The total RMSE is 0.017 eV. The geometry of the stationary anion is shown in Fig. 12.6, compared to available data in the literature.[594] Its harmonic frequencies from various sources are compared in Table 12.3.

Quantum Dynamics

The quantum dynamics calculations of the photodetachment of CH_3OHF^- anion were carried out using the diatom-diatom Jacobi coordinates (r_0, r_1, r_2, θ_1, θ_2, ϕ),[596] as shown in Fig. 12.10. In the reduced-dimensional coordinate system, the center of mass of the CH_3 group is replaced by a combined atom (X), and the orientation of the CH_3 group is fixed at the equilibrium structure of the PC complex. r_1 and r_2 are the F−H and O−X bond lengths and r_0 is the distance between the two diatomic centers of mass, where θ_1, θ_2, and ϕ denote the polar and dihedral angles. The rotationless Hamiltonian has the following form ($\hbar$=1):

$$\hat{H} = -\frac{1}{2\mu_0}\frac{\partial^2}{\partial r_0^2} - \frac{1}{2\mu_1}\frac{\partial^2}{\partial r_1^2} - \frac{1}{2\mu_2}\frac{\partial^2}{\partial r_2^2} + \frac{\hat{j}_1^2}{2\mu_1 r_1^2} + \frac{\hat{j}_2^2}{2\mu_2 r_2^2} + \frac{\hat{j}_0^2}{2\mu_0 r_0^2} + V(r_0, r_1, r_2, \theta_1, \theta_2, \phi) \tag{12.3}$$

where μ_0, μ_1, and μ_2 are the corresponding reduced masses of r_0, r_1, and r_2. $\hat{j}_1$ and $\hat{j}_2$ are the angular momentum operators for r_1 and r_2, respectively, and $\hat{j}_0{}^2 = (\hat{j}_1 + \hat{j}_2)^2$. V is the reduced 6-dimensional PIP-NN PES. Some calculations have also been performed using the (2+1) Radau-Jacobi coordinates, which are designed for the reactant channel. The corresponding Hamiltonian has a similar form as that in Eqn. 12.3.

As in our previous work,[596] the Hamiltonian is discretized using a mixed grid-basis representation, and a non-direct product strategy was used.[610] The photodetachment is considered within the Condon approximation, in which the initial wave packet on the neutral PES was chosen as the ground vibrational eigenstate on the corresponding anion PES. The wave packet on the neutral state PES is propagated using the Chebyshev propagator,[611] and the photoelectron spectra are obtained from the cosine Fourier transform of the autocorrelation functions C_k:[597]

$$S(E) = \frac{1}{\pi H^{-} \sin\vartheta} \sum_{k=0} (2 - \delta_{k,0}) \cos(k\vartheta) C_k \tag{12.4}$$

where H^{-} is the half width of the spectral of the Hamiltonian, $\vartheta = \arccos(E)$ is the Chebyshev angle, and k is the Chebyshev order.[611]

All of the numerical parameters used in the dynamics calculations are collected in Table 12.4. Due to the strong long range interaction between the HF and CH_3O species, a large diatom-diatom distance must be used in the simulations. To reduce the size of the basis set, the L-shape grids and the vibrational basis are adopted. A similar treatment was used for the Radau-Jacobi coordinates to describe the $F + CH_3OH$ channel.

Table 12.1: Experimental and theoretical peak positions (cm^{-1}), HF stretching spacings between the first peaks of each manifold labeled with *a1-e1* (cm^{-1}), and $CH_3O{-}HF$ peak spacings between peaks within each *a-e* grouping (cm^{-1}) in the photoelectron spectra of CH_3OHF^- shown in Figs. 12.2a and 12.2b.

Peak	eBE		HF spacings		$CH_3O{-}HF$ spacings	
	expt	calc	expt	calc	expt	calc
a1	25058	25058				
a2	25250	25297			192	239
a3	25470	25523			220	227
a4	25672	25741			202	218
b1	28619	28634	3561	3577		
b2	28867	28898			248	264
b3	29102	29146			235	248
b4	29310	29385			208	239
b5	29517	29618			207	233
c1	31925	31923	3306	3289		
c2	32181	32217			255	294
c3	32440	32496			259	279
c4	32687	32769			248	273
d1	34816	34914	2890	2991		
d2	35131	35233			315	319
d3	35433	35543			302	310
d4	35714	35895			281	352
d5	36068	36217			354	322
d6	36370	36585			302	368
e1	37651	37250	2836	2335		

Table 12.2: Experimental and theoretical peak positions (cm^{-1}), DF stretching spacings between the first peaks of each manifold labeled with *a1*-*e1* (cm^{-1}), and $CH_3O{-}DF$ peak spacings between peaks within each *a*-*e* grouping (cm^{-1}) in the photoelectron spectra of CH_3ODF^- shown in Fig. 12.2c.

Peak	eBE	DF spacings	$CH_3O{-}DF$ spacings
a1	25434		
a2	25614		179
a3	25804		190
b1	28128	2694	
b2	28321		193
b3	28516		195
c1	30351	2223	
c2	30598		247
c3	30835		237
d1	32421	2071	
d2	32692		270
d3	32966		274
d4	33206		241
e1	34527	2106	
e2	34855		327
e3	35125		271

Table 12.3: Comparison of harmonic frequencies (cm^{-1}) of the $F + CH_3OH \longrightarrow HF + CH_3O$ reaction stationary points and the CH_3OHF^- anion.

Species	Method	Frequencies (cm^{-1})														
		1	2	3	4	5	6	7	8	9	10	11	12	13	14	15
$F + CH_3OH$	PES[a]	243	1078	1085	1168	1367	1484	1503	1521	3025	3078	3151	3866			
	CCSD(T)[b]	291	1063	1089	1179	1379	1481	1505	1515	3013	3072	3134	3860			
	CCSD(T)[c]	288	1061	1089	1181	1381	1485	1511	1521	3016	3076	3137	3864			
	CCSDT(Q)[d]	286	1054	1082	1176	1379	1484	1512	1523	3011	3069	3128	3844			
	Expt.[e]	200	1033	1060	1165	1345	1455	1477	1477	2844	2960	3000	3681			
$HF + CH_3O$	PES[a]	4166	701	701	1108	1239	1405	1405	3027	3093	3093					
	CCSD(T)[b]	4141	754	970	1119	1377	1383	1514	2933	3015	3063					
	CCSD(T)[c]	4139	762	960	1115	1384	1388	1519	2936	3021	3065					
	CCSDT(Q)[d]	4125	760	961	1107	1391	1393	1522	2936	3018	3061					
	Expt.[e]	4138	652	652	914	914	1047	1412	2758	2758	2840					
RC	PES[a]	101	189	357	506	1035	1096	1166	1346	1430	1469	1496	3026	3128	3172	3819
	CCSD(T)[b]	120	193	361	475	1039	1072	1167	1356	1459	1498	1504	3041	3123	3166	3809
	CCSDT(Q)[d]	117	187	349	468	1029	1067	1166	1356	1465	1504	1511	3037	3117	3159	3798
PC	PES[a]	76	80	246	580	727	741	879	1077	1409	1438	1476	2972	3043	3128	3770
	CCSD(T)[b]	i111	75	240	580	740	926	1052	1117	1363	1384	1512	2924	3034	3095	3762
	CCSDT(Q)[d]	72	84	241	603	751	940	1059	1108	1383	1399	1517	2932	3036	3096	3751
TS	PES[a]	i732	63	221	451	1027	1108	1144	1345	1464	1493	1517	3077	3141	3157	3298
	CCSD(T)[b]	i644	i172	186	426	1020	1079	1135	1304	1452	1475	1490	3037	3122	3152	3294
	CCSDT(Q)[d]	i800	73	197	422	1013	1095	1155	1312	1457	1481	1510	3042	3116	3139	3157
CH_3OHF^-	PES[a]	66	152	410	1115	1147	1167	1180	1405	1455	1490	1703	2009	2883	2984	2989
	CCSD(T)[b]	90	164	407	1134	1153	1168	1205	1449	1482	1505	1632	2076	2916	2933	2977
	CCSD(T)[c]	i35	164	404	1129	1154	1172	1207	1454	1484	1508	1636	2095	2920	2938	2981
	CCSDT(Q)[d]	66	166	407	1120	1152	1169	1224	1452	1488	1510	1641	2065	2913	2928	2971
	MP2[f]	65	170	447	1141	1162	1181	1287	1451	1493	1519	1655	1875	2960	2988	3031

[a]This work, fitted PIP-NN PES; [b]This work, UCCSD(T)-F12a/AVDZ; [c]This work, UCCSD(T)-F12a/AVTZ; [d]CCSD(T)/AVTZ, from Ray *et al.*[577]; [e]Experimental vibrational frequencies from NIST.[612] Values represent fundamental vibrational frequencies for all species, with the exception of HF, for which ω_e is given instead; [f]MP2/6-311++G(2df, 2pd), from Sun *et al.*[594] If two species are involved, frequencies are shown in the order the species are listed.

Table 12.4: Numerical parameters (a.u.) used in wave packet calculations with the HF+OX Jacobi coordinate and the F + HOX Radau-Jacobi coordinate (X=CH_3).

	HF + OX	F + HOX
Grid/basis ranges and sizes	$r_0 \in (3.2, 10.0)$, $N_0 = 140$	$r_0 \in (3.5, 10.0)$, $N_0 = 80$
	when $1 \leq i_0 \leq 90$, $r_1 \in (1.2, 5.7)$, $N_1 = 30$	when $1 \leq i_0 \leq 55$, $r_1 \in (1.5, 6.0)$, $N_1 = 25$
	when $91 \leq i_0 \leq 140$, 8 vibrational basis for r_1	when $56 \leq i_0 \leq 80$, 3 vibrational basis for r_1
	6 PODVR for r_2	when $1 \leq i_0 \leq 55$, $r_1 \in (1.7, 3.0)$, $N_1 = 30$
		when $56 \leq i_0 \leq 80$, 3 vibrational basis for r_1
Largest values of j_1, j_2 and m	32, 50, 32	24, 50, 24
Absorption potential for r_0 [a]	$\alpha_{abs} = 0.08$, $r_{0,abs} = 8.5$	$\alpha_{abs} = 0.1$, $r_{0,abs} = 8.3$
Absorption potential for r_1 [a]	$\alpha_{abs} = 0.08$, $r_{1,abs} = 3.8$	$\alpha_{abs} = 0.1$, $r_{1,abs} = 5.0$
Propagation steps	8000	400

[a]The damping function is defined as $D = \exp[-\alpha_{abs}(r - r_{abs})^2]$, $r \geq r_{abs}$]

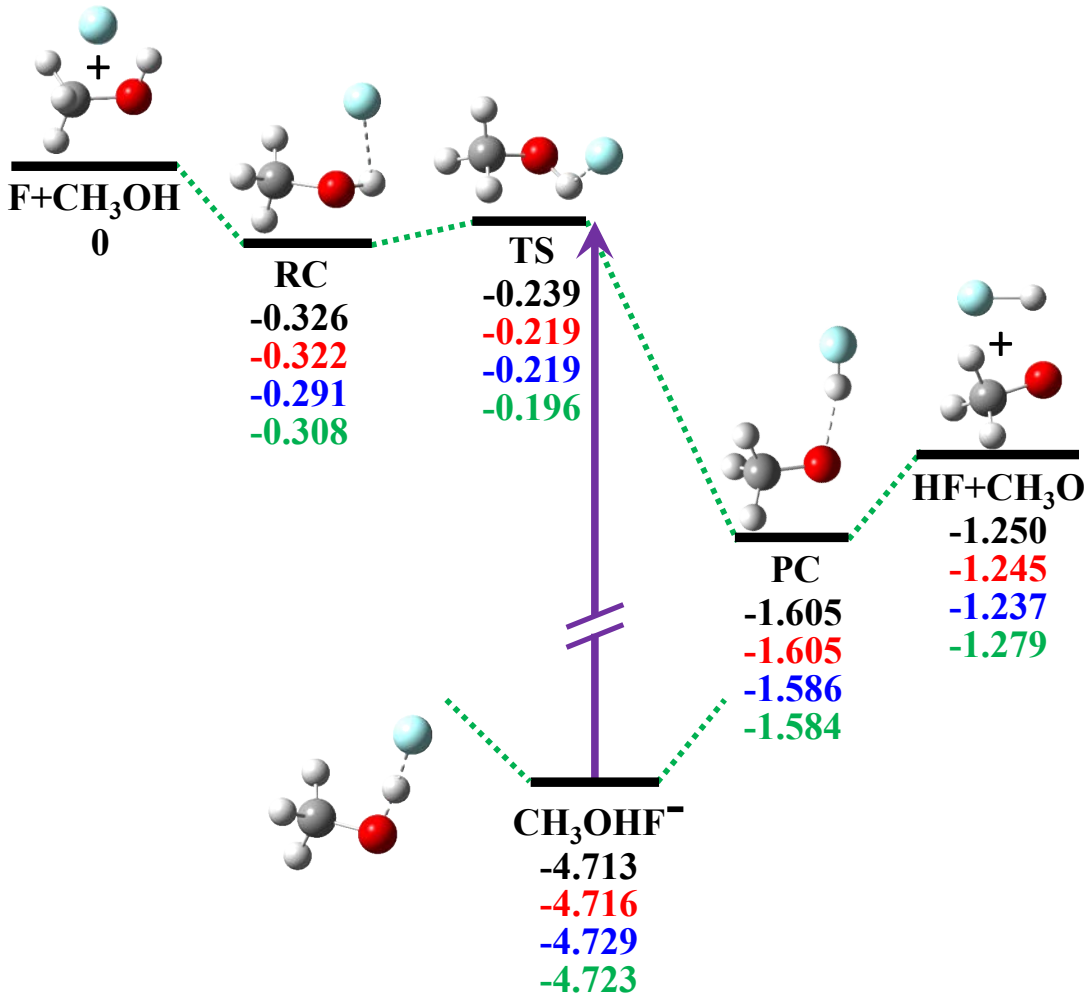

Figure 12.4: Schematic of the energetics for the $F + CH_3OH \longrightarrow HF + CH_3O$ reaction and the CH_3OHF^- anion. All energies are in eV and relative to the $F + CH_3OH$ asymptote at various levels: PIP-NN PES (black), CCSD(T)-F12a/AVDZ (red), CCSD(T)-F12a/AVTZ (blue), and CCSDT(Q)/CBS (green, from Ray *et al.*[577]). Energies are not corrected for vibrational zero-point energy.

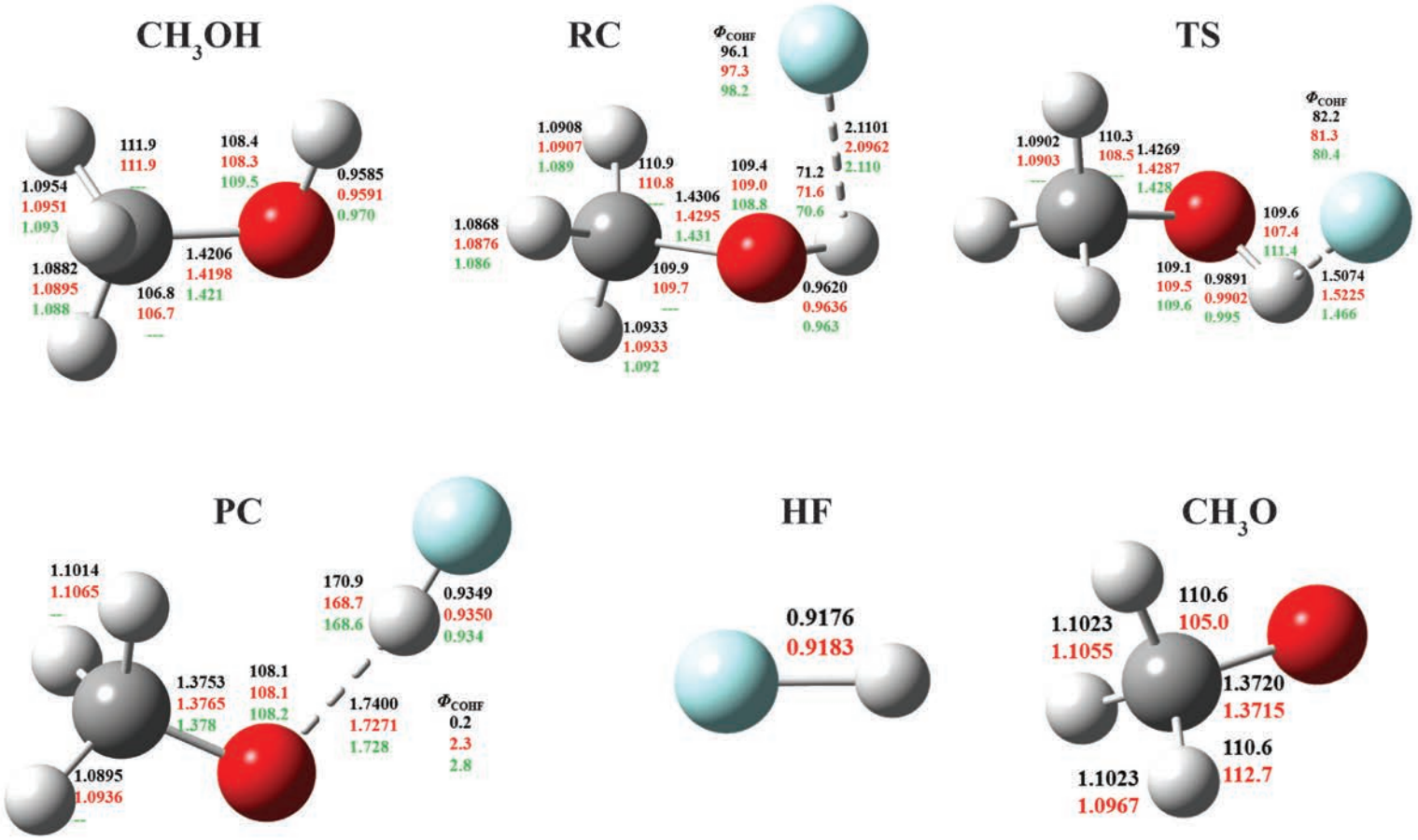

Figure 12.5: Optimized geometries (lengths in Å, angles in °) of CH_3OH, the reactant complex (RC), the transition state (TS), the product complex (PC), HF, and CH_3O at various levels of theory: PIP-NN PES (black), CCSD(T)-F12a/AVDZ (red), and CCSD(T)/AVQZ (green, from Feng *et al.*[585]).

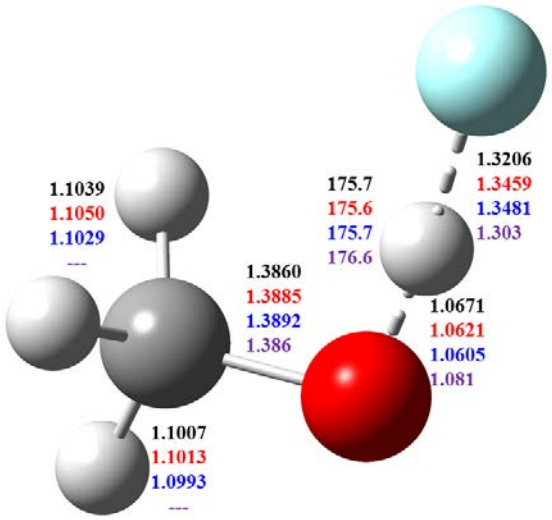

Figure 12.6: Optimized geometries (lengths in Å, angles in °) of the CH_3OHF^- anion at various levels of theory: PIP PES (black), CCSD(T)-F12a/AVDZ (red), CCSD(T)-F12a/AVTZ (blue), and MP2/6-311++G(2df,2pd) (purple, from Sun *et al.*[594]).

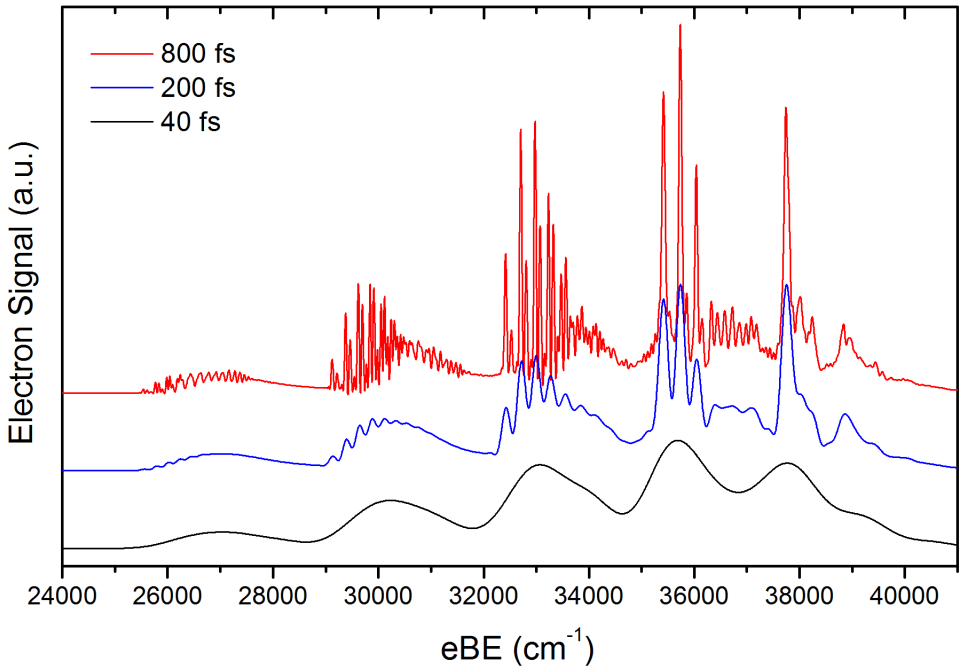

Figure 12.7: Photoelectron spectrum of CH_3OHF^- simulated with short (black, 400 steps or 40 fs), medium (blue, 2000 steps or 200 fs), and long (red, 8000 steps or 800 fs) propagation times.

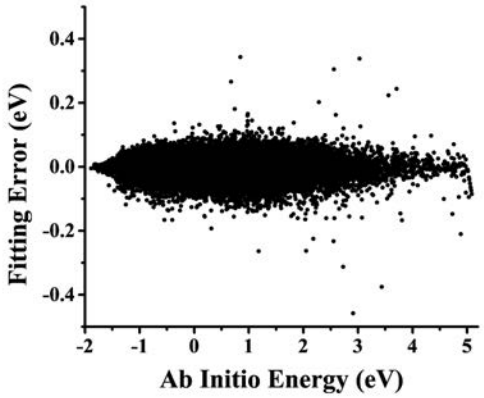

Figure 12.8: Fitting errors ($E_{fit} - E_{ab\ initio}$, in eV) of the neutral PES as a function of the *ab initio* energy (eV) relative to the F + CH_3OH reactant asymptote.

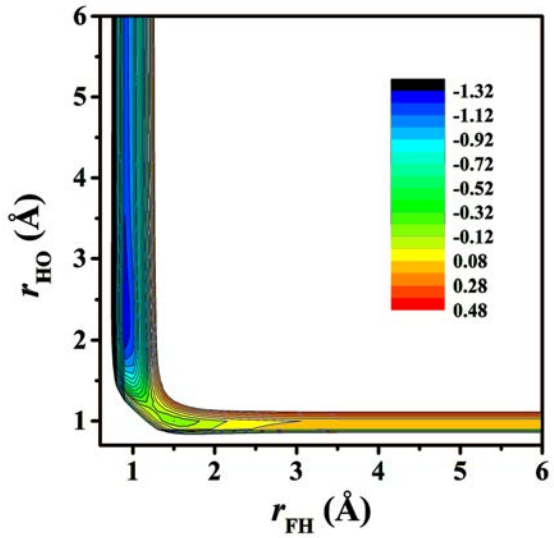

Figure 12.9: Contour plot of the neutral potential energy surface in the F + $CH_3OH \longrightarrow$ HF + CH_3O reaction channel as a function of the OH and HF bond lengths. All other coordinates are fixed at the transition state geometry. The colored energy scale is in units of eV.

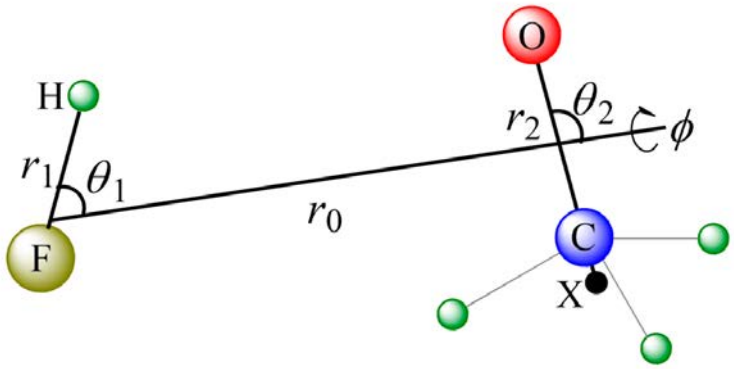

Figure 12.10: The reduced dimension HF + OX (X=CH_3) Jacobi coordinates.

Part VI

Appendix

Bibliography

[1]D. W. Turner, *Molecular Photoelectron Spectroscopy* (Wiley, London, 1970).

[2]B. Brehm, M. A. Gusinow, and J. I. Hall, *Phys. Rev. Lett.* **19**, 737 (1967).

[3]A. Kasdan and W. C. Lineberger, *Phys. Rev. A* **10**, 1658 (1974).

[4]C. S. Feigerle, R. R. Corderman, S. V. Bobashev, and W. C. Lineberger, *J. Chem. Phys.* **74**, 1580 (1981).

[5]J. M. Oakes and G. B. Ellison, *J. Am. Chem. Soc.* **105**, 2969 (1983).

[6]K. M. Ervin and W. C. Lineberger, *J. Phys. Chem.* **95**, 1167 (1991).

[7]J. T. Snodgrass, J. V. Coe, C. B. Freidhoff, K. M. McHugh, and K. H. Bowen, *Faraday Discuss. Chem. Soc.* **86**, 241 (1988).

[8]A. A. Bengali, S. M. Casey, C. L. Cheng, J. P. Dick, P. T. Fenn, P. W. Villalta, and D. G. Leopold, *J. Am. Chem. Soc.* **114**, 5257 (1992).

[9]K. M. Ervin, J. Ho, and W. C. Lineberger, *J. Chem. Phys.* **91**, 5974 (1989).

[10]P. G. Wenthold, D. A. Hrovat, W. T. Borden, and W. C. Lineberger, *Science* **272**, 1456 (1996).

[11]L. A. Posey, M. J. Deluca, and M. A. Johnson, *Chem. Phys. Lett.* **131**, 170 (1986).

[12]P. Kruit and F. H. Read, *J. Phys. E* **16**, 313 (1983).

[13]D. W. Chandler and P. L. Houston, *J. Chem. Phys.* **87**, 1445 (1987).

[14]A. T. J. B. Eppink and D. H. Parker, *Rev. Sci. Instrum.* **68**, 3477 (1997).

[15]B. Baguenard, J. C. Pinaré, C. Bordas, and M. Broyer, *Phys. Rev. A* **63**, 023204 (2001).

[16]E. Surber, R. Mabbs, and A. Sanov, *J. Phys. Chem. A* **107**, 8215 (2003).

[17]J. C. Rienstra-Kiracofe, G. S. Tschumper, H. F. Schaefer, S. Nandi, and G. B. Ellison, *Chem. Rev.* **102**, 231 (2002).

[18]R. B. Metz, A. Weaver, S. E. Bradforth, T. N. Kitsopoulos, and D. M. Neumark, *J. Phys. Chem.* **94**, 1377 (1990).

[19]L. Wang, H. Cheng, and J. Fan, *J. Chem. Phys.* **102**, 9480 (1995).

[20]K. Müller-Dethlefs and E. W. Schlag, *Annu. Rev. Phys. Chem.* **42**, 109 (1991).

[21]T. Kitsopoulos, I. Waller, J. Loeser, and D. Neumark, *Chem. Phys. Lett.* **159**, 4 (1989).

[22]T. Lenzer, I. Yourshaw, M. R. Furlanetto, G. Reiser, and D. M. Neumark, *J. Chem. Phys.* **110**, 9578 (1999).

[23]G. Reiser and K. Müller-Dethlefs, *J. Phys. Chem.* **96**, 9 (1992).

[24]C. C. Arnold and D. M. Neumark, *J. Chem. Phys.* **99**, 3353 (1993).

[25]T. N. Kitsopoulos, C. J. Chick, Y. Zhao, and D. M. Neumark, *J. Chem. Phys.* **95**, 5479 (1991).

[26]C. C. Arnold, Y. Zhao, T. N. Kitsopoulos, and D. M. Neumark, *J. Chem. Phys.* **97**, 6121 (1992).

[27]C. C. Arnold, T. N. Kitsopoulos, and D. M. Neumark, *J. Chem. Phys.* **99**, 766 (1993).

[28]C. C. Arnold and D. M. Neumark, *J. Chem. Phys.* **100**, 1797 (1994).

[29]C. C. Arnold, C. Xu, G. R. Burton, and D. M. Neumark, *J. Chem. Phys.* **102**, 6982 (1995).

[30]G. R. Burton, C. Xu, C. C. Arnold, and D. M. Neumark, *J. Chem. Phys.* **104**, 2757 (1996).

[31]Y. Zhao, I. Yourshaw, G. Reiser, C. C. Arnold, and D. M. Neumark, *J. Chem. Phys.* **101**, 6538 (1994).

[32]C. C. Arnold, D. M. Neumark, D. M. Cyr, and M. A. Johnson, *J. Phys. Chem.* **99**, 1633 (1995).

[33]T. Lenzer, M. R. Furlanetto, N. L. Pivonka, and D. M. Neumark, *J. Chem. Phys.* **110**, 6714 (1999).

[34]I. M. Waller, T. N. Kitsopoulos, and D. M. Neumark, *J. Phys. Chem.* **94**, 2240 (1990).

[35]D. M. Neumark, *J. Phys. Chem. A* **112**, 13287 (2008).

[36]J. B. Kim, C. Hock, T. I. Yacovitch, and D. M. Neumark, *J. Phys. Chem. A* **117**, 8126 (2013).

[37]M. A. Duncan, *Rev. Sci. Instrum.* **83**, 041101 (2012).

[38]W. C. Campbell and J. M. Doyle, "Cooling, Trap Loading, and Beam Production Using a Cryogenic Helium Buffer Gas", in *Cold Molecules: Theory, Experiment, Applications*, edited by R. V. Krems, W. C. Stwalley, and B. Friedrich (CRC Press, Boca Raton, FL, 2009) Chap. 13, pp. 473–508.

[39]D. Gerlich, in *Advances in Chemical Physics*, Vol. 82, edited by C.-Y. Ng and M. Baer (Wiley, 1992), pp. 1–176.

[40]R. Wester, *J. Phys. B: At. Mol. Opt. Phys.* **42**, 154001 (2009).

[41]X.-B. Wang, H.-K. Woo, and L.-S. Wang, *J. Chem. Phys.* **123**, 051106 (2005).

[42]X.-B. Wang and L.-S. Wang, *Rev. Sci. Instrum.* **79**, 073108 (2008).

[43]C. Hock, "Nanocalorimetry and angle-resolved photoelectron spectroscopy on sodium, aluminum, and water clusters", PhD thesis (Universität Freiburg, 2010).

[44]L. Ma, K. Majer, F. Chirot, and B. von Issendorff, *J. Chem. Phys.* **131**, 144303 (2009).

[45]L. Ma, B. von Issendorff, and A. Aguado, *J. Chem. Phys.* **132**, 104303 (2010).

[46]M. Brümmer, C. Kaposta, G. Santambrogio, and K. R. Asmis, *J. Chem. Phys.* **119**, 12700 (2003).

[47]T. R. Rizzo, J. A. Stearns, and O. V. Boyarkin, *Int. Rev. Phys. Chem.* **28**, 481 (2009).

[48]A. B. Wolk, C. M. Leavitt, E. Garand, and M. A. Johnson, *Acc. Chem. Res.* **47**, 202 (2014).

[49]C. Hock, J. B. Kim, M. L. Weichman, T. I. Yacovitch, and D. M. Neumark, *J. Chem. Phys.* **137**, 244201 (2012).

[50]J. B. Kim, "Slow photoelectron imaging spectroscopy of cryogenically-cooled anions", PhD thesis (University of California, Berkeley, 2014).

[51]M. L. Weichman, J. A. DeVine, D. S. Levine, J. B. Kim, and D. M. Neumark, *P. Natl. Acad. Sci. U.S.A.* **113**, 1698 (2016).

[52]J. B. Kim, M. L. Weichman, and D. M. Neumark, *Mol. Phys.* **113**, 2105 (2015).

[53]I. León, Z. Yang, H.-T. Liu, and L.-S. Wang, *Rev. Sci. Instrum.* **85**, 083106 (2014).

[54]L.-S. Wang, *J. Chem. Phys.* **143**, 040901 (2015).

[55]C. Bartels, "Angular distributions of photoelectrons from cold, size-selected sodium cluster anions", PhD thesis (Universität Freiburg, 2008).

[56]C. Bartels, C. Hock, R. Kuhnen, and B. von Issendorff, *J. Phys. Chem. A* **118**, 8270 (2014).

[57]Z. Luo, X. Chen, J. Li, and C. Ning, *Phys. Rev. A* **93**, 020501 (2016).

[58]H.-F. Li, Y.-X. Zhao, Z. Yuan, Q.-Y. Liu, Z.-Y. Li, X.-N. Li, C.-G. Ning, and S.-G. He, *J. Phys. Chem. Lett.* **8**, 605 (2017).

[59]K. J. Mascaritolo, A. R. Dermer, M. L. Green, A. M. Gardner, and M. C. Heaven, *J. Chem. Phys.* **146**, 054301 (2017).

[60]A. M. Oliveira, Y.-J. Lu, J. H. Lehman, P. B. Changala, J. H. Baraban, J. F. Stanton, and W. C. Lineberger, *J. Am. Chem. Soc.* **137**, 12939 (2015).

[61]D. J. Nelson, W. K. Gichuhi, E. M. Miller, J. H. Lehman, and W. C. Lineberger, *J. Chem. Phys.* **146**, 074302 (2017).

[62]D. J. Griffiths, *Introduction to Quantum Mechanics* (Pearson Prentice Hall, Upper Saddle River, NJ, 2005).

[63]A. Einstein, *Ann. Phyz.* **322**, 132 (1905).

[64]R. A. Millikan, *Phys. Rev.* **7**, 355 (1916).

[65]G. Herzberg, *Molecular Spectra and Molecular Structure. Vol. 2: Infrared and Raman Spectra of Polyatomic Molecules* (D. Van Nostrand Co., Inc., New York, 1945).

[66]P. R. Bunker and P. Jensen, *Molecular Symmetry and Spectroscopy* (NRC Research Press, Ottawa, 1998).

[67]G. Herzberg, *Molecular Spectra and Molecular Structure. Vol. 3: Electronic Spectra and Electronic Structure of Polyatomic Molecules* (Van Nostrand Reinhold Co., New York, 1966).

[68]R. J. Celotta, R. A. Bennett, J. L. Hall, M. W. Siegel, and J. Levine, *Phys. Rev. A* **6**, 631 (1972).

[69]P. F. Zittel, G. B. Ellison, S. V. O'Neil, E. Herbst, W. C. Lineberger, and W. P. Reinhardt, *J. Am. Chem. Soc.* **98**, 3731 (1976).

[70]P. G. Wenthold, R. R. Squires, and W. C. Lineberger, *J. Am. Chem. Soc.* **120**, 5279 (1998).

[71]H.-J. Zhai and L.-S. Wang, *J. Am. Chem. Soc.* **129**, 3022 (2007).

[72]T. Ichino, S. M. Villano, A. J. Gianola, D. J. Goebbert, L. Velarde, A. Sanov, S. J. Blanksby, X. Zhou, D. A. Hrovat, W. T. Borden, and W. C. Lineberger, *Angew. Chem. Int. Ed.* **48**, 8509 (2009).

[73]J. B. Kim, M. L. Weichman, and D. M. Neumark, *J. Chem. Phys.* **141**, 174307 (2014).

[74]J. B. Kim, M. L. Weichman, and D. M. Neumark, *J. Chem. Phys.* **140**, 034307 (2014).

[75]E. P. Wigner, *Phys. Rev.* **73**, 1002 (1948).

[76]J. Simons, *J. Phys. Chem. A* **112**, 6401 (2008).

[77]K. J. Reed, A. H. Zimmerman, H. C. Andersen, and J. I. Brauman, *J. Chem. Phys.* **64**, 1368 (1976).

[78]R. Mabbs, E. R. Grumbling, K. Pichugin, and A. Sanov, *Chem. Soc. Rev.* **38**, 2169 (2009).

[79]J. Cooper and R. N. Zare, *J. Chem. Phys.* **48**, 942 (1968).

[80]D. Hanstorp, C. Bengtsson, and D. J. Larson, *Phys. Rev. A* **40**, 670 (1989).

[81]E. R. Grumbling and A. Sanov, *J. Chem. Phys.* **135**, 164302 (2011).

[82]C. M. Oana and A. I. Krylov, *J. Chem. Phys.* **131**, 124114 (2009).

[83]S. Gozem and A. I. Krylov, *ezDyson 3.0*, `http://iopenshell.usc.edu/downloads/ezdyson`.

[84]Y. Liu and C. Ning, *J. Chem. Phys.* **143**, 144310 (2015).

[85]J. B. Kim, M. L. Weichman, T. I. Yacovitch, C. Shih, and D. M. Neumark, *J. Chem. Phys.* **139**, 104301 (2013).

[86]M. J. Nee, A. Osterwalder, J. Zhou, and D. M. Neumark, *J. Chem. Phys.* **125**, 014306 (2006).

[87]M. L. Weichman, L. Cheng, J. B. Kim, D. M. Neumark, and J. F. Stanton, *J. Chem. Phys.* (submitted).

[88]J. Simons, *J. Am. Chem. Soc.* **103**, 3971 (1981).

[89]J. R. Heath, A. L. Cooksy, M. H. Gruebele, C. A. Schmuttenmaer, and R. J. Saykally, *Science* **244**, 564 (1989).

[90]G. Hilpert, H. Linnartz, M. Havenith, J. ter Meulen, and W. Meerts, *Chem. Phys. Lett.* **219**, 384 (1994).

[91]M. Okumura, L. I. Yeh, J. D. Myers, and Y. T. Lee, *J. Chem. Phys.* **85**, 2328 (1986).

[92]W. Schöllkopf, S. Gewinner, H. Junkes, A. Paarmann, G. von Helden, H. Bluem, and A. M. M. Todd, *Proc. SPIE* **9512**, 95121L (2015).

[93]E. Garand, "Slow photoelectron imaging and infrared dissociation spectroscopy of ionic clusters", PhD thesis (University of California, Berkeley, 2010).

[94]T. I. Yacovitch, "Slow photoelectron velocity-map imaging of transient species and infrared multiple photon dissociation of atmospherically relevant anion clusters", PhD thesis (University of California, Berkeley, 2012).

[95]T. I. Yacovitch, N. Heine, C. Brieger, T. Wende, C. Hock, D. M. Neumark, and K. R. Asmis, *J. Phys. Chem. A* **117**, 7081 (2013).

[96]K. Mizuse and A. Fujii, *Phys. Chem. Chem. Phys.* **13**, 7129 (2011).

[97]X. Song, M. R. Fagiani, S. Debnath, M. Gao, S. Maeda, T. Taketsugu, S. Gewinner, W. Schöllkopf, K. R. Asmis, and A. Lyalin, (in preparation).

[98]C. Cohen-Tannoudji, B. Diu, and F. Laloe, *Quantum Mechanics, Vol. 1* (Wiley, Paris, 1977).

[99]A. Van Orden and R. J. Saykally, *Chem. Rev.* **98**, 2313 (1998).

[100]P. J. Sarre, *Mon. Not. R. Astron. Soc.* **313**, L14 (2000).

[101]H. Richter and J. B. Howard, *Prog. Energy Combust. Sci.* **26**, 565 (2000).

[102]K. A. Zemski, D. R. Justes, and A. W. Castleman, *J. Phys. Chem. B* **106**, 6136 (2002).

[103]U. Diebold, *Surf. Sci. Rep.* **48**, 53 (2003).

[104]J. C. Polanyi and A. H. Zewail, *Acc. Chem. Res.* **28**, 119 (1995).

[105]D. M. Neumark, *Phys. Chem. Chem. Phys.* **7**, 433 (2005).

[106]S. M. Burnett, A. E. Stevens, C. Feigerle, and W. C. Lineberger, *Chem. Phys. Lett.* **100**, 124 (1983).

[107]R. B. Metz, S. E. Bradforth, and D. M. Neumark, *Adv. Chem. Phys.* **81**, 1 (1992).

[108]D. M. Neumark, A. M. Wodtke, G. N. Robinson, C. C. Hayden, and Y. T. Lee, *J. Chem. Phys.* **82**, 3045 (1985).

[109]R. T. Skodje, D. Skouteris, D. E. Manolopoulos, S.-H. Lee, F. Dong, and K. Liu, *J. Chem. Phys.* **112**, 4536 (2000).

[110]D. E. Manolopoulos, K. Stark, H.-J. Werner, D. W. Arnold, S. E. Bradforth, and D. M. Neumark, *Science* **262**, 1852 (1993).

[111]C. L. Russell and D. E. Manolopoulos, *Chem. Phys. Lett.* **256**, 465 (1996).

[112]T. I. Yacovitch, E. Garand, J. B. Kim, C. Hock, T. Theisa, and D. M. Neumark, *Faraday Discuss.* **157**, 399 (2012).

[113]F. Lique, G. Li, H.-J. Werner, and M. H. Alexander, *J. Chem. Phys.* **134**, 231101 (2011).

[114]A. Osterwalder, M. J. Nee, J. Zhou, and D. M. Neumark, *J. Chem. Phys.* **121**, 6317 (2004).

[115]J. Zhou, "Slow electron velocity-map imaging spectroscopy of small radicals and infrared multiphoton dissociation study of solvated systems", PhD thesis (University of California, Berkeley, 2007).

[116]M. J. Nee, "Chemical dynamics and structure studied with slow electron velocity-map imaging spectroscopy and infrared dissociation", PhD thesis (University of California, Berkeley, 2005).

[117]U. Even, J. Jortner, D. Noy, N. Lavie, and C. Cossart-Magos, *J. Chem. Phys.* **112**, 8068 (2000).

[118]C. H. DePuy, V. M. Bierbaum, L. A. Flippin, J. J. Grabowski, G. K. King, R. J. Schmitt, and S. A. Sullivan, *J. Am. Chem. Soc.* **102**, 5012 (1980).

[119]T. G. Dietz, M. A. Duncan, D. E. Powers, and R. E. Smalley, *J. Chem. Phys.* **74**, 6511 (1981).

[120]D. E. Powers, S. G. Hansen, M. E. Geusic, A. C. Puiu, J. B. Hopkins, T. G. Dietz, M. A. Duncan, P. R. R. Langridge-Smith, and R. E. Smalley, *J. Phys. Chem.* **86**, 2556 (1982).

[121]M. E. Geusic, M. D. Morse, S. C. O'Brien, and R. E. Smalley, *Rev. Sci. Instrum.* **56**, 2123 (1985).

[122]R. O. Ramabhadran, J. E. Mann, S. E. Waller, D. W. Rothgeb, C. C. Jarrold, and K. Raghavachari, *J. Am. Chem. Soc.* **135**, 17039 (2013).

[123]M. R. Fagiani, X. Song, S. Debnath, S. Gewinner, W. Schöllkopf, K. R. Asmis, F. A. Bischoff, F. Müller, and J. Sauer, *J. Phys. Chem. Lett.* **8**, 1272 (2017).

[124]T. Majima, G. Santambrogio, C. Bartels, A. Terasaki, T. Kondow, J. Meinen, and T. Leisner, *Phys. Rev. A* **85**, 053414 (2012).

[125]R. D. Levine, *Molecular Reaction Dynamics* (Cambridge University Press, Cambridge, 2005).

[126]W. C. Wiley and I. H. McLaren, *Rev. Sci. Instrum.* **26**, 1150 (1955).

[127]U. Boesl, *Mass Spectrom. Rev.* **36**, 86 (2017).

[128]D. Townsend, M. P. Minitti, and A. G. Suits, *Rev. Sci. Instrum.* **74**, 2530 (2003).

[129]S. J. Cavanagh, S. T Gibson, M. N. Gale, C. J. Dedman, E. H. Roberts, and B. R. Lewis, *Phys. Rev. A* **76**, 052708 (2007).

[130]Y. Ogi, H. Kohguchi, D. Niu, K. Ohshimo, and T. Suzuki, **113**, 14536 (J. Phys. Chem. A).

[131]A. W. Harrison, M. Ryazanov, E. N. Sullivan, and D. M. Neumark, *J. Chem. Phys.* **145**, 024305 (2016).

[132]*SIMION 8.0*, `http://simion.com`.

[133]M. B. Doyle, C. Abeyasera, and A. G. Suits, *NuACQ*, `http://chem.wayne.edu/suitsgroup/NuACQ.html`.

[134]B.-Y. Chang, R. C. Hoetzlein, J. A. Mueller, J. D. Geiser, and P. L. Houston, *Rev. Sci. Instrum.* **69**, 1665 (1998).

[135]W. Li, S. D. Chambreau, S. A. Lahankar, and A. G. Suits, *Rev. Sci. Instrum.* **76**, 063106 (2005).

[136]M. K. Carter, B. E. Patchett, P. D. Read, and N. Waltham, *Nucl. Instr. Meth. Phys. Res.* **A310**, 305 (1991).

[137]E. Betzig, G. H. Patterson, R. Sougrat, W. Lindwasser, S. Olenych, J. S. Bonifacino, M. W. Davidson, J. Lippincott-Schwartz, and H. F. Hess, *Science* **313**, 1642 (2006).

[138]L. G. Shapiro and G. C. Stockman, *Computer Vision* (Prentice Hall, Upper Saddle River, NJ, 2001).

[139]E. W. Hansen and P. L. Law, *J. Opt. Soc. Am. A* **2**, 510 (1985).

[140]B. Dick, *Phys. Chem. Chem. Phys.* **16**, 570 (2014).

[141]V. Dribinksi, A. Ossadtchi, V. A. Mandelshtam, and H. Reisler, *Rev. Sci. Instrum.* **73**, 2634 (2002).

[142]G. A. Garcia, L. Nahon, and I. Powis, *Rev. Sci. Instrum.* **75**, 4989 (2004).

[143]C. R. Gebhardt, T. P. Rakitzis, P. C. Samartzis, V. Ladopoulos, and T. N. Kitsopoulos, *Rev. Sci. Instrum.* **72**, 3848 (2001).

[144]M. Ryazanov, "Development and implementation of methods for sliced velocity map imaging. studies of overtone-induced dissociation and isomerization dynamics of hydroxymethyl radical (CH_2OH and CD_2OH)", PhD thesis (University of Southern California, 2012).

[145]C. Blondel, W. Chaibi, C. Delsart, C. Drag, F. Goldfarb, and S. Kröger, *Eur. Phys. J. D* **33**, 335 (2005).

[146]C. Blondel, C. Delsart, and F. Goldfarb, *J. Phys. B: At. Mol. Opt. Phys.* **34**, 2757 (2001).

[147]U. Berzinsh, M. Gustafsson, D. Hanstorp, A. Klinkmüller, U. Ljungblad, and A.-M. Møartensson-Pendrill, *Phys. Rev. A* **51**, 231 (1995).

[148]D. M. Neumark, K. R. Lykke, T. Andersen, and W. C. Lineberger, *Phys. Rev. A* **32**, 1890 (1985).

[149]C. Blondel, W. Chaibi, C. Delsart, and C. Drag, *J. Phys. B: At. Mol. Opt. Phys.* **39**, 1409 (2006).

[150]C. E. Moore, "Tables of Spectra of Hydrogen, Carbon, Nitrogen, and Oxygen Atoms and Ions", in *CRC Series in Evaluated Data in Atomic Physics*, edited by J. W. Gallagher (CRC Press, Boca Raton, FL, 1993).

[151]W. C. Martin, R. Zalubas, and A. Musgrove, *J. Phys. Chem. Ref. Data* **19**, 821 (1990).

[152]C. E. Moore, "Atomic Energy Levels as Derived from the Analysis of Optical Spectra Hydrogen through Vanadium", in *Nat. Stand. Ref. Data Ser., NSRDS-NBS 35 Vol. I* (Nat. Bur. Stand., U.S., 1971).

[153]L. J. Radziemski and V. Kaufman, *J. Opt. Soc. Am.* **59**, 424 (1969).

[154]D. S. Bethune, *Appl. Opt.* **20**, 1897 (1981).

[155]J. A. DeVine, M. L. Weichman, M. C. Babin, G. B. Villaneuva, S. T. Gibson, R. W. Field, J. Ma, H. Guo, and D. M. Neumark, (in preparation).

[156]D. J. Goebbert, G. Meijer, and K. R. Asmis, *AIP Conf. Proc.* **1104**, 22 (2009).

[157]N. Heine, "Vibrational spectroscopy of gaseous hydrogen-bonded clusters: on the role of isomer-specificity and anharmonicity", PhD thesis (Freie Universität Berlin, 2014).

[158]T. M. Maier, A. D. Boese, J. Sauer, T. Wende, M. Fagiani, and K. R. Asmis, *J. Chem. Phys.* **140**, 204315 (2014).

[159]G. von Helden, D. van Heijnsbergen, and G. Meijer, *J. Phys. Chem. A* **107**, 1671 (2003).

[160]W. Weltner and R. J. Van Zee, *Chem. Rev.* **89**, 1713 (1989).

[161]R. P. A. Bettens and E. Herbst, *Astrophys. J.* **478**, 585 (1997).

[162]E. B. Jochnowitz and J. P. Maier, *Annu. Rev. Phys. Chem.* **59**, 519 (2008).

[163]A. G. G. M. Tielens, *Rev. Mod. Phys.* **85**, 1021 (2013).

[164]K. S. Pitzer and E. Clementi, *J. Am. Chem. Soc.* **81**, 4477 (1959).

[165]K. Raghavachari and J. S. Binkley, *J. Chem. Phys.* **87**, 2191 (1987).

[166]J. M. L. Martin and P. R. Taylor, *J. Phys. Chem.* **100**, 6047 (1996).

[167]R. E. Smalley, *Accts. Chem. Res.* **25** (1992).

[168]G. von Helden, M. T. Hsu, N. Gotts, and M. T. Bowers, *J. Phys. Chem.* **97**, 8182 (1993).

[169]G. Pacchioni and J. Koutecký, *J. Chem. Phys.* **88**, 1066 (1988).

[170]J. Kurtz and L. Adamowicz, *Astrophys. J.* **370**, 784 (1991).

[171]M. Vala, T. M. Chandrasekhar, J. Szczepanski, R. Van Zee, and W. Weltner, Jr., *J. Chem. Phys.* **90**, 595 (1989).

[172]P. F. Bernath, K. H. Hinkle, and J. J. Keady, *Science* **244**, 562 (1989).

[173]N. Moazzen-Ahmadi, A. R. W. McKellar, and T. Amano, *J. Chem. Phys.* **91**, 2140 (1989).

[174]R. H. Kranze and W. R. M. Graham, *J. Chem. Phys.* **96**, 2517 (1992).

[175]J. Szczepanski, S. Ekern, C. Chapo, and M. Vala, *Chem. Phys.* **211**, 359 (1996).

[176]D. Forney, P. Freivogel, M. Grutter, and J. P. Maier, *J. Chem. Phys.* **104**, 4954 (1996).

[177]T. Motylewski, O. Vaizert, T. F. Giesen, H. Linnartz, and J. P. Maier, *J. Chem. Phys.* **111**, 6161 (1999).

[178]A. E. Boguslavskiy and J. P. Maier, *J. Chem. Phys.* **125**, 094308 (2006).

[179]P. Botschwina and P. Sebald, *Chem. Phys. Lett.* **160**, 485 (1989).

[180]P. Botschwina, *J. Chem. Phys.* **101**, 853 (1994).

[181]M. Kolbuszewski, *J. Chem. Phys.* **102**, 3679 (1995).

[182]P. Botschwina, *Theor. Chem. Acc.* **104**, 160 (2000).

[183]M. Hanrath and S. D. Peyerimhoff, *Chem. Phys. Lett.* **337**, 368 (2001).

[184]H. Massó, V. Veryazov, P. Å. Malmqvist, B. O. Roos, and M. L. Senent, *J. Chem. Phys.* **127**, 154318 (2007).

[185]L. Adamowicz, *Chem. Phys. Lett.* **180**, 466 (1991).

[186]J. D. Watts and R. J. Bartlett, *J. Chem. Phys.* **97**, 3445 (1992).

[187]M. Ohara, H. Shiromaru, Y. Achiba, K. Aoki, K. Hashimoto, and S. Ikuta, *J. Chem. Phys.* **103**, 10393 (1995).

[188]M. Tulej, D. A. Kirkwood, G. Maccaferri, O. Dopfer, and J. P. Maier, *Chem. Phys.* **228**, 293 (1998).

[189]N. M. Lakin, F. Güthe, M. Tulej, M. Pachkov, and J. P. Maier, *Faraday Discuss.* **115**, 383 (2000).

[190]J. Szczepanski, S. Ekern, and M. Vala, *J. Phys. Chem. A* **101**, 1841 (1997).

[191]P. Freivogel, M. Grutter, D. Forney, and J. P. Maier, *Chem. Phys.* **216**, 401 (1997).

[192]D. Forney, M. Grutter, P. Freivogel, and J. P. Maier, *J. Phys. Chem. A* **101**, 5292 (1997).

[193]M. G. Giuffreda, M. S. Deleuze, and J.-P. François, *J. Phys. Chem. A* **106**, 8569 (2002).

[194]Z. Cao, S. D. Peyerimhoff, F. Grein, and Q. Zhang, *J. Chem. Phys.* **115**, 2062 (2001).

[195]M. Perić, M. Petković, and S. Jerosimić, *Chem. Phys.* **343**, 141 (2008).

[196]D. G. Leopold, J. Ho, and W. C. Lineberger, *J. Chem. Phys.* **86**, 1715 (1987).

[197]A. W. Castleman, Jr. and K. H. Bowen, Jr., *J. Phys. Chem.* **100**, 12911 (1996).

[198]S. Yang, K. J. Taylor, M. J. Craycraft, J. Conceicao, C. L. Pettiette, O. Cheshnovsky, and R. E. Smalley, *Chem. Phys. Lett.* **144**, 431 (1988).

[199]D. W. Arnold, S. E. Bradforth, T. N. Kitsopoulos, and D. M. Neumark, *J. Chem. Phys.* **95**, 8753 (1991).

[200]P. J. Knowles, C. Hampel, and H. J. Werner, *J. Chem. Phys.* **99**, 5219 (1993).

[201]J. D. Watts, J. Gauss, and R. J. Bartlett, *J. Chem. Phys.* **98**, 8718 (1993).

[202]R. A. Kendall, T. H. Dunning, and R. J. Harrison, *J. Chem. Phys.* **96**, 6796 (1992).

[203]H.-J. Werner, P. J. Knowles, G. Knizia, F. R. Manby, M. Schütz, P. Celani, T. Korona, R. Lindh, A. Mitrushenkov, G. Rauhut, K. R. Shamasundar, T. B. Adler, R. D. Amos, A. Bernhardsson, A. Berning, D. L. Cooper, M. J. O. Deegan, A. J. Dobbyn, F. Eckert, E. Goll, C. Hampel, A. Hesselmann, G. Hetzer, T. Hrenar, G. Jansen, Y. L. C. Köppl, A. W. Lloyd, R. A. Mata, A. J. May, S. J. McNicholas, W. Meyer, M. E. Mura, A. Nicklass, D. P. ONeill, P. Palmieri, K. Püger, R. Pitzer, M. Reiher, T. Shiozaki, H. Stoll, A. J. Stone, R. Tarroni, T. Thorsteinsson, M. Wang, and A. Wolf, *MOLPRO, version 2010.1, a package of ab initio programs*, `http://www.molpro.net`.

[204]V. A. Mozhayskiy and A. I. Krylov, *ezSpectrum 3.0*, `http://iopenshell.usc.edu/downloads`.

[205]F. Duschinsky, *Acta Physicochim. URSS* **7**, 551 (1937).

[206]E. A. Rohlfing and J. E. M. Goldsmith, *J. Opt. Soc. Am. B* **7**, 1915 (1990).

[207]F. J. Northrup and T. J. Sears, *J. Opt. Soc. Am. B* **7**, 1924 (1990).

[208]P. Jensen and J. W. C. Johns, *J. Mol. Spectrosc.* **118**, 248 (1986).

[209]J. Vander Auwera, J. W. C. Johns, and O. L. Polyansky, *J. Chem. Phys.* **95**, 2299 (1991).

[210]J. Vander Auwera, J. K. Holland, P. Jensen, and J. W. C. Johns, *J. Mol. Spectrosc.* **163**, 529 (1994).

[211]K. Klein, E. Garand, T. Ichino, D. M. Neumark, J. Gauss, and J. F. Stanton, *Theor. Chem. Acc.* **129**, 527 (2011).

[212]C. Jungen and A. J. Merer, *Mol. Phys.* **40**, 1 (1980).

[213]S. G. He and D. J. Clouthier, *J. Chem. Phys.* **123**, 014316 (2005).

[214]Z. Yang, I. Leon, and L.-S. Wang, *J. Chem. Phys.* **139**, 021106 (2013).

[215]W. M. Irvine, P. Friberg, Å. Hjalmarson, S. Ishikawa, N. Kaifu, K. Kawaguchi, and S. C. Madden, *Astrophys. J.* **334**, L107 (1988).

[216]M. Agúndez, J. P. Fonfría, J. Cernicharo, J. R. Pardo, and M. Guélin, *Astron. Astrophys.* **479**, 493 (2008).

[217]K. Hoyermann and J. Seeba, *Z. Phys. Chem.* **188**, 215 (1995).

[218]A. Lifshitz, A. Moran, and S. Bidani, *Int. J. Chem. Kinet.* **19**, 61 (1987).

[219]M. J. Kurylo and G. L. Knable, *J. Phys. Chem.* **88**, 3305 (1984).

[220]G. Poulet, G. Laverdet, J. L. Jourdain, and G. L. Bras, *J. Phys. Chem.* **88**, 6259 (1984).

[221]D. A. Shea, R. J. J. M. Steenvoorden, and P. Chen, *J. Phys. Chem. A* **101**, 9728 (1997).

[222]R. P. Thorn, P. S. Monks, L. J. Stief, S.-C. Kuo, Z. Zhang, S. K. Ross, and R. B. Klemm, *J. Phys. Chem. A* **102**, 846 (1998).

[223]M. A. Cordiner and P. J. Sarre, *Astron. Astrophys.* **472**, 537 (2007).

[224]F. J. Lovas, J. M. Hollis, A. J. Remijan, and P. R. Jewell, *Astrophys. J.* **645**, L137 (2006).

[225]J. Cernicharo, C. A. Gottlieb, M. Guélin, T. C. Killian, G. Paubert, P. Thaddeus, and J. M. Vrtilek, *Astrophys. J.* **368**, L39 (1991).

[226]R. C. Fortenberry, T. D. Crawford, and T. J. Lee, *Astrophys. J.* **762**, 121 (2013).

[227]S. Saito, S. Yamamoto, W. M. Irvine, L. M. Ziurys, H. Suzuki, M. Ohishi, and N. Kaifu, *Astrophys. J.* **334**, L113 (1988).

[228]S. Saito and S. Yamamoto, *J. Chem. Phys.* **107**, 1732 (1997).

[229]S. Moran, H. B. Ellis, D. J. DeFrees, A. D. McLean, and G. B. Ellison, *J. Am. Chem. Soc.* **109**, 5996 (1987).

[230]P. B. Ayscough, R. G. Collins, and T. J. Kemp, *J. Phys. Chem.* **70**, 2220 (1966).

[231]R. J. Egland and M. C. R. Symons, *J. Chem. Soc. A*, 1326 (1970).

[232]P. Svejda and D. H. Volman, *J. Phys. Chem.* **74**, 1872 (1970).

[233]M. E. Jacox, *Chem. Phys.* **43**, 157 (1979).

[234]B. E. Turner, P. Friberg, W. M. Irvine, S. Saito, and S. Yamamoto, *Astrophys. J.* **355**, 546 (1990).

[235]H. Ozeki, T. Hirao, S. Saito, and S. Yamamoto, *Astrophys. J.* **617**, 680 (2004).

[236]H.-G. Cho and L. Andrews, *J. Phys. Chem. A* **115**, 8638 (2011).

[237]Y. Sumiyoshi, K. Tanaka, and T. Tanaka, *J. Chem. Phys.* **104**, 1839 (1996).

[238]F. Delbecq, *Chem. Phys. Lett.* **99**, 21 (1983).

[239]M. Horn, M. Oswald, R. Oswald, and P. Botschwina, *Ber. Bunsenges. Phys. Chem.* **99**, 323 (1995).

[240]G. L. Gutsev and L. Adamowicz, *Chem. Phys. Lett.* **246**, 245 (1995).

[241]P. M. Mayer, M. S. Taylor, M. W. Wong, and L. Radom, *J. Phys. Chem. A* **102**, 7074 (1998).

[242]A. H. Zimmerman and J. I. Brauman, *J. Am. Chem. Soc.* **99**, 3565 (1977).

[243]P. G. Mezey, M. A. Robb, K. Yates, and I. G. Csizmadia, *Theor. Chim. Acta* **49**, 277 (1978).

[244]D. J. Goebbert, L. Velarde, D. Khuseynov, and A. Sanov, *J. Phys. Chem. Lett.* **1**, 792 (2010).

[245]K. R. Lykke, D. M. Neumark, T. Anderson, V. J. Trapa, and W. C. Lineberger, *J. Chem. Phys.* **87**, 6842 (1987).

[246]D. M. Wetzel and J. I. Brauman, *J. Chem. Phys.* **90**, 68 (1989).

[247]J. Marks, D. M. Wetzel, P. B. Comita, and J. I. Brauman, *J. Chem. Phys.* **84**, 5284 (1986).

[248]K. R. Lykke, K. K. Murray, D. M. Neumark, and W. C. Lineberger, *Phil. Trans. R. Soc. Lond. A* **324**, 179 (1988).

[249]T. Ichino, D. H. Andrews, G. J. Rathbone, F. Misaizu, R. M. D. Calvi, S. W. Wren, S. Kato, V. M. Bierbaum, and W. C. Lineberger, *J. Phys. Chem. B* **112**, 545 (2008).

[250]W. Sailer, A. Pelc, P. Limão-Vieira, N. J. Mason, J. Limtrakul, P. Scheier, M. Probst, and T. D. Märk, *Chem. Phys. Lett.* **381**, 216 (2003).

[251]E. Runge and E. K. U. Gross, *Phys. Rev. Lett.* **52**, 997 (1984).

[252]M. E. Casida, in *Recent Advances in Density Functional Methods*, edited by D. P. Chong (World Scientific, Singapore, 1995), p. 155.

[253]Y. Shao, L. F. Molnar, Y. Jung, J. Kussmann, C. Ochsenfeld, S. T. Brown, A. T. B. Gilbert, L. V. Slipchenko, S. V. Levchenko, D. P. O'Neill, R. A. DiStasio, R. C. Lochan, T. Wang, G. J. O. Beran, N. A. Besley, J. M. Herbert, C. Y. Lin, T. V. Voorhis, S. H. Chien, A. Sodt, R. P. Steele, V. A. Rassolov, P. E. Maslen, P. P. Korambath, R. D. Adamson, B. Austin, J. Baker, E. F. C. Byrd, H. Dachsel, R. J. Doerksen, A. Dreuw, B. D. Dunietz, A. D. Dutoi, T. R. Furlani, S. R. Gwaltney, A. Heyden, S. Hirata, C.-P. Hsu, G. Kedziora, R. Z. Khalliulin, P. Klunzinger, A. M. Lee, M. S. Lee, W. Liang, I. Lotan, N. Nair, B. Peters, E. I. Proynov, P. A. Pieniazek, Y. M. Rhee, J. Ritchie, E. Rosta, C. D. Sherrill, A. C. Simmonett, J. E. Subotnik, H. L. Woodcock, W. Zhang, A. T. Bell, A. K. Chakraborty, D. M. Chipman, F. J. Keil, A. Warshel, W. J. Hehre, H. F. Schaefer, J. Kong, A. I. Krylov, P. M. W. Gill, and M. Head-Gordon, *Phys. Chem. Chem. Phys.* **8**, 3172 (2006).

[254]A. I. Krylov and P. M. W. Gill, *WIREs Comput. Mol. Sci.* **3**, 217 (2013).

[255]C. M. Western, *PGOPHER, a Program for Simulating Rotational Structure*, `http://pgopher.chm.bris.ac.uk`.

[256]A. Sanov, *Annu. Rev. Phys. Chem.* **65**, 341 (2014).

[257]S. Willitsch, A. Haldi, and F. Merkt, *Chem. Phys. Lett.* **353**, 167 (2002).

[258]S. Wang, Y. Shi, Z. J. Jakubek, M. Barnett, B. Simard, K. Müller-Dethlefs, C.-P. Liu, and Y.-P. Lee, *J. Chem. Phys.* **117**, 6546 (2002).

[259]J. Zhou, E. Garand, W. Eisfeld, and D. M. Neumark, *J. Chem. Phys.* **127**, 034304 (2007).

[260]M. L. Weichman, J. B. Kim, and D. M. Neumark, *J. Chem. Phys.* **139**, 144314 (2013).

[261]J. B. Kim, M. L. Weichman, and D. M. Neumark, *Phys. Chem. Chem. Phys.* **15**, 20973 (2013).

[262]H.-T. Liu, C.-G. Ning, D.-L. Huang, P. D. Dau, and L.-S. Wang, *Angew. Chem. Int. Ed.* **52**, 8976 (2013).

[263]T. Anderson, K. R. Lykke, D. M. Neumark, and W. C. Lineberger, *J. Chem. Phys.* **86**, 1858 (1987).

[264]R. S. Berry, *J. Chem. Phys.* **45**, 1228 (1966).

[265]J. Simons, in *Photoionization and Photodetachment*, edited by C. Y. Ng (World Scientific, Singapore, 1999), p. 958.

[266]A. L. Sobolewski, W. Domcke, C. Dedonder-Lardeux, and C. Jouvet, *Phys. Chem. Chem. Phys.* **4**, 1093 (2002).

[267]M. N. R. Ashfold, B. Cronin, A. L. Devine, R. N. Dixon, and M. G. D. Nix, *Science* **312**, 1637 (2006).

[268]M. N. R. Ashfold, G. A. King, D. Murdock, M. G. D. Nix, T. A. A. Oliver, and A. G. Sage, *Phys. Chem. Chem. Phys.* **12**, 1218 (2010).

[269]J. S. Wright, E. R. Johnson, and G. A. DiLabio, *J. Am. Chem. Soc.* **123**, 1173 (2001).

[270]H. H. Hussain, G. Babic, T. Durst, J. S. Wright, M. Flueraru, A. Chichirau, and L. L. Chepelev, *J. Org. Chem.* **68**, 7023 (2003).

[271]H.-Y. Zhang, Y.-M. Sung, and X.-L. Wang, *Chem. – Eur. J.* **9**, 502 (2003).

[272]P. Meredith, B. J. Powell, J. Riesz, S. P. Nighswander-Rempel, M. R. Pederson, and E. G. Moore, *Soft Matter* **2**, 37 (2006).

[273]P. Meredith and T. Sarna, *Pigment Cell Res.* **19**, 572 (2006).

[274]A. Huijser, A. Pezzella, and V. Sundström, *Phys. Chem. Chem. Phys.* **13**, 9119 (2011).

[275]C. G. Pierpont and C. W. Lange, in *Progress in Inorganic Chemistry*, Vol. 41, edited by K. D. Karlin (Wiley, Hoboken, NJ, 1994), p. 331.

[276]G. A. King, T. A. A. Oliver, R. N. Dixon, and M. N. R. Ashfold, *Phys. Chem. Chem. Phys.* **14**, 3338 (2012).

[277]A. S. Chatterley, J. D. Young, D. Townsend, J. M. Żurek, M. J. Paterson, G. M. Roberts, and V. G. Stavros, *Phys. Chem. Chem. Phys.* **15**, 6879 (2013).

[278]R. A. Livingstone, J. O. F. Thompson, M. Iljina, R. J. Donaldson, B. J. Sussman, M. J. Paterson, and D. Townsend, *J. Chem. Phys.* **137**, 18304 (2012).

[279]M. Weiler, M. Miyazaki, G. F/'eraud, S. Ishiuchi, C. Dedonder, C. Jouvet, and M. Fujii, *J. Phys. Chem. Lett.* **4**, 3819 (2013).

[280]K. Loth, M. Andrist, F. Graf, and H. H. Günthard, *Chem. Phys. Lett.* **29**, 163 (1974).

[281]K. Loth, F. Graf, and H. H. Günthard, *Chem. Phys.* **13**, 95 (1976).

[282]M. Nagaya, S. Kudoh, and M. Nakata, *Chem. Phys. Lett.* **432**, 446 (2006).

[283]A. M. Mebel and M. C. Lin, *J. Am. Chem. Soc.* **116**, 9577 (1994).

[284]M. C. Lin and A. M. Mebel, *J. Phys. Org. Chem.* **8**, 407 (1995).

[285]I. Vedernikova, E. Proynov, D. Salahub, and A. Haemers, *Int. J. Quantum Chem.* **77**, 161 (2000).

[286]S. G. Estácio, P. C. do Couto, B. J. C. Cabral, M. E. M. da Piedade, and J. A. M. Simões, *J. Phys. Chem. A* **108**, 10834 (2004).

[287]C. A. McFerrin, R. W. Hall, and B. Dellinger, *J. Mol. Struct. (THEOCHEM)* **848**, 16 (2008).

[288]M. Altarawneh, B. Z. Dlugogorski, E. M. Kennedy, and J. C. Mackie, *J. Phys. Chem. A* **114**, 1098 (2010).

[289]X.-B. Wang, Q. Fu, and J. Yang, *J. Phys. Chem. A* **114**, 9083 (2010).

[290]R. D. Parra and I. Dukarevich, *J. Chem. Phys.* **122**, 124316 (2005).

[291]R. W. Binkley, G. W. Dillow, T. W. Flechtner, W. Winnik, and M. J. S. Tevesz, *Org. Mass. Spectrom.* **29**, 491 (1994).

[292]W. S. Taylor and L. M. Babcock, *J. Am. Chem. Soc.* **117**, 6497 (1995).

[293]A. Fattahi, S. R. Kass, J. F. Liebman, M. A. R. Matos, M. S. Miranda, and V. M. F. Morais, *J. Am. Chem. Soc.* **127**, 6116 (2005).

[294]M. L. Weichman, J. B. Kim, J. A. DeVine, D. S. Levine, and D. M. Neumark, *J. Am. Chem. Soc.* **137**, 1420 (2015).

[295]J. B. Kim, T. I. Yacovitch, C. Hock, and D. M. Neumark, *Phys. Chem. Chem. Phys.* **13**, 17378 (2011).

[296]E. Garand and D. M. Neumark, *J. Chem. Phys.* **135**, 024302 (2011).

[297]A. T. B. Gilbert, N. A. Besley, and P. M. W. Gill, *J. Phys. Chem. A* **112**, 13164 (2008).

[298]R. F. Gunion, M. K. Gilles, M. L. Polak, and W. C. Lineberger, *Int. J. Mass Spectrom. Ion Processes* **117**, 601 (1992).

[299]C. W. g, H. Witek, and Y. P. Lee, *J. Chem. Phys.* **129**, 154307 (2008).

[300]A. B. Fialkov, J. Dennebaum, and K.-H. Homann, *Combust. Flame* **125**, 763 (2001).

[301]M. Frenklach, *Phys. Chem. Chem. Phys.* **4**, 2028 (2002).

[302]A. Omont, *Astron. Astrophys.* **164**, 159 (1986).

[303]C. Falvo, H. Friha, T. Pino, Z. Dhaouadi, P. Parneix, F. Calvo, and P. Bréchignac, *Phys. Chem. Chem. Phys.* **15**, 10241 (2013).

[304]J. L. Puget and A. Léger, *Annu. Rev. Astron. Astrophys.* **27**, 161 (1989).

[305]L. J. Allamandola, A. G. G. M. Tielens, and J. R. Barker, *Astrophys. J. Suppl. S.* **71**, 733 (1989).

[306]A. G. G. M. Tielens, *Annu. Rev. Astron. Astrophys.* **46**, 289 (2008).

[307]A. Léger and L. d'Hendecourt, *Astron. Astrophys.* **146**, 81 (1985).

[308]R. Ruiterkamp, T. Halasinski, F. Salama, B. H. Foing, L. J. Allamandola, W. Schmidt, and P. Ehrenfreund, *Astron. Astrophys.* **390**, 1153 (2002).

[309]F. Salama, G. A. Galazutdinov, J. Krełowski, L. Biennier, Y. Beletsky, and I.-O. Song, *Astrophys. J.* **728**, 154 (2011).

[310]G. Galazutdinov, B.-C. Lee, I.-O. Song, M. Kazmierczak, and J. Krełowski, *J. Mon. Not. R. Astron. Soc.* **412**, 1259 (2011).

[311]J. M. Searles, J. D. Destree, T. P. Snow, F. Salama, D. G. York, and J. Dahlstrom, *Astrophys. J.* **732**, 50 (2011).

[312]J. Pety, D. Teyssier, D. Fossé, M. Gerin, E. Roueff, A. Abergel, E. Habart, and J. Cernicharo, *Astron. Astrophys.* **435**, 885 (2005).

[313]F. Pauzat, D. Talbi, and Y. Ellinger, *Astron. Astrophys.* **293**, 263 (1995).

[314]P. Du, F. Salama, and G. H. Loew, *Chem. Phys.* **173**, 421 (1993).

[315]H. Curran, C. Wu, N. Marinov, W. J. Pitz, C. K. Westbrook, and A. Burcat, *J. Phys. Chem. Ref. Data* **29**, 463 (2000).

[316]K. M. Ervin, T. M. Ramond, G. E. Davico, R. L. Schwartz, S. M. Casey, and W. C. Lineberger, *J. Phys. Chem. A* **105**, 10822 (2001).

[317]B. N. Papas, S. Wang, N. J. DeYonker, H. L. Woodcock, and H. F. Schaefer, *J. Phys. Chem. A* **107**, 6311 (2003).

[318]D. L. Kokkin and T. W. Schmidt, *J. Phys. Chem. A* **110**, 6173 (2006).

[319]H. Wang and M. Frenklach, *Combust. Flame* **110**, 173 (1997).

[320]C.-W. Zhou, V. V. Kislov, and A. M. Mebel, *J. Phys. Chem. A* **116**, 1571 (2012).

[321]D. R. Reed and S. R. Kass, *J. Mass. Spectrom.* **35**, 534 (2000).

[322]H. A. Lardin, R. R. Squires, and P. G. Wenthold, *J. Mass Spectrom.* **36**, 607 (2001).

[323]W. C. Lineberger, *Annu. Rev. Phys. Chem.* **64**, 21 (2013).

[324]Z. Marcinow, D. K. Clawson, and P. W. Rabideau, *Tetrahedron* **45**, 5441 (1989).

[325]L. M. Culberson, C. C. Blackstone, and A. Sanov, *J. Phys. Chem. A* **117**, 11760 (2013).

[326]C. Barckholtz, T. A. Barckholtz, and C. M. Hadad, *J. Am. Chem. Soc.* **121**, 491 (1999).

[327]H. F. Calcote, *Combust. Flame* **42**, 215 (1981).

[328]H. Richter, O. A. Mazyar, R. Sumathi, W. H. Green, and J. W. B. J. B. Howard, *J. Phys. Chem. A* **105**, 1561 (2001).

[329]R. G. Harvey and N. E. Geacintov, *Acc. Chem. Res.* **21**, 66 (1988).

[330]J. L. Durant, W. F. Busby, A. L. Lafleur, B. W. Penman, and C. L. Crespi, *Mutat. Res.* **371**, 123 (1996).

[331]J. Gao, G. Berden, and J. Oomens, *Astrophys. J.* **787**, 170 (2014).

[332]D. S. N. Parker, F. T. Zhang, Y. S. Kim, R. I. Kaiser, A. Landera, V. V. Kislov, A. M. Mebel, and A. G. G. M. Tielens, *Proc. Natl. Acad. Sci. USA* **109**, 53 (2012).

[333]R. I. Kaiser, D. S. N. Parker, and A. M. Mebel, *Annu. Rev. Phys. Chem.* **66**, 43 (2015).

[334]I. Cherchneff, *EAS Publications Series* **46**, 177 (2011).

[335]N. J. Demarais, Z. B. Yang, O. Martinez, N. Wehres, T. P. Snow, and V. M. Bierbaum, *Astrophys. J.* **746**, 32 (2012).

[336]M. H. Vuong and B. H. Foing, *Astron. Astrophys.* **363**, L5 (2000).

[337]V. L. Page, T. P. Snow, and V. M. Bierbaum, *Astrophys. J.* **584**, 316 (2003).

[338]V. Wakelam and E. Herbst, *Astrophys. J.* **680**, 371 (2008).

[339]J. Szczepanski, M. Vala, D. Talbi, O. Parisel, and Y. Ellinger, *J. Chem. Phys.* **98**, 4494 (1993).

[340]D. M. Hudgins and S. A. Sandford, *J. Phys. Chem. A* **102**, 329 (1998).

[341]A. J. Huneycutt, R. N. Casaes, B. J. McCall, C. Y. Chung, Y. P. Lee, and R. J. Saykally, *ChemPhysChem* **5**, 321 (2004).

[342]J. M. L. Martin, J. El-Yazal, and J.-P. François, *J. Phys. Chem.* **100**, 15358 (1996).

[343]A. Staicu, G. Rouillé, O. Sukhorukov, T. Henning, and F. Huisken, *Mol. Phys.* **102**, 1777 (2004).

[344]J. DeCoster, A. Ergut, Y. A. Levendis, H. Richter, J. B. Howard, and J. B. Carlson, *Prof. Combust. Inst.* **31**, 491 (2007).

[345]R. Ananthula, T. Yamada, and P. H. Taylor, *J. Phys. Chem. A* **110**, 3559 (2006).

[346]P. H. Kasai, P. A. Clark, and E. B. Whipple, *J. Am. Chem. Soc.* **92**, 2640 (1970).

[347]R. H. Chen, S. A. Kafafi, and S. E. Stein, *J. Am. Chem. Soc.* **111**, 1418 (1989).

[348]J. E. P. Syka, J. J. Coon, M. J. Schroeder, J Shabanowitz, and D. F. Hunt, *P. Natl. Acad. Sci. USA* **101**, 9528 (2004).

[349]J. Cioslowski, G. Liu, M. Martinov, P. Piskorz, and D. Moncrieff, *J. Am. Chem. Soc.* **118**, 5261 (1996).

[350]B. V. Unterreiner, M. Sierka, and R. Ahlrichs, *Phys. Chem. Chem. Phys.* **6**, 4377 (2004).

[351]M. J. Rossi, *Int. J. Chem. Kinet.* **40**, 395 (2008).

[352]J. B. Kim, M. L. Weichman, and D. M. Neumark, *J. Am. Chem. Soc.* **136**, 7159 (2014).

[353]M. L. Weichman, J. B. Kim, and D. M. Neumark, *J. Phys. Chem. A* **119**, 6140 (2015).

[354]L. M. Culberson, C. C. Blackstone, A. A. Wallace, and A. Sanov, *J. Phys. Chem. A* **119**, 9770 (2015).

[355]P. Li, D. E. Miser, S. Rabiei, R. T. Yadav, and M. R. Hajaligol, *Appl. Catal. B* **43**, 151 (2003).

[356]A. K. Kandalam, B. Chatterjee, S. N. Khanna, B. K. Rao, P. Jena, and B. V. Reddy, *Surf. Sci.* **601**, 4873 (2007).

[357]D. S. Newsome, *Cat. Rev. - Sci. Eng.* **21**, 275 (1980).

[358]C. Rhodes, G. J. Hutchings, and A. M. Ward, *Catal. Today* **23**, 43 (1995).

[359]L. G. Xu, S. Bao, R. J. O'Brien, D. J. Houpt, and B. H. Davis, *Fuel Sci. Technol. Int.* **12**, 1323 (1994).

[360]W. Weiss and W. Ranke, *Prog. Surf. Sci.* **70**, 1 (2002).

[361]V. Kesavan, D. Dhar, Y. Koltypin, N. Perkas, O. Palchik, A. Gedanken, and S. Chandrasekaran, *Pure Appl. Chem.* **73**, 85 (2001).

[362]M. M. Schubert, S. Hackenberg, A. C. van Veen, M. Muhler, V. Plzak, and R. J. Behm, *J. Catal.* **197**, 113 (2001).

[363]D. K. Böhme and H. Schwarz, *Angew. Chem. Int. Ed.* **44**, 2336 (2005).

[364]M. J. Cheng, K. Chenoweth, J. Oxgaard, A. van Duin, and W. A. Goddard, *J. Phys. Chem. C* **111**, 5115 (2007).

[365]Y. D. Kim, *Int. J. Mass Spectrom.* **238**, 17 (2004).

[366]G. E. Johnson, R. Mitrić, V. Bonačić-Koutecký, and A. W. Castleman, *Chem. Phys. Lett.* **475**, 1 (2009).

[367]K. R. Asmis, *Phys. Chem. Chem. Phys.* **14**, 9270 (2012).

[368]B. V. Reddy and S. N. Khanna, *Phys. Rev. Lett.* **93**, 068301 (2004).

[369]H. Schwarz, *Int. J. Mass Spectrom.* **237**, 75 (2004).

[370]S. J. Riley, E. K. Parks, G. C. Nieman, L. G. Pobo, and S. Wexler, *J. Chem. Phys.* **80**, 1360 (1984).

[371]Q. Sun, M. Sakurai, Q. Wang, J. Z. Yu, G. H. Wang, K. Sumiyama, and Y. Kawazoe, *Phys. Rev. B* **62**, 8500 (2000).

[372]D. N. Shin, Y. Matsuda, and E. R. Bernstein, *J. Chem. Phys.* **120**, 4150 (2004).

[373]S. Yin, W. Xue, X.-L. Ding, W.-G. Wang, S.-G. He, and M.-F. Ge, *Int. J. Mass Spectrom.* **281**, 72 (2009).

[374]K. S. Molek, C. Anfuso-Cleary, and M. A. Duncan, J. Phys. Chem. A **112**, 9238 (2008).

[375]M. Li, S.-R. Liu, and P. B. Armentrout, J. Chem. Phys. **131**, 144310 (2009).

[376]W. Xue, S. Yin, X.-L. Ding, S.-G. He, and M.-F. Ge, *J. Phys. Chem. A* **113**, 5302 (2009).

[377]M. C. Oliveira, J. Marçalo, M. C. Vieira, and M. A. A. Ferreira, *Int. J. Mass. Spectrom.* **185**, 825 (1999).

[378]Y. Xie, F. Dong, S. Heinbuch, J. J. Rocca, and E. R. Bernstein, *J. Chem. Phys.* **130**, 114306 (2009).

[379]N. M. Reilly, J. U. Reveles, G. E. Johnson, J. M. del Campo, S. N. Khanna, A. M. Koster, and A. W. Castleman, *J. Phys. Chem. C* **111**, 19086 (2007).

[380]N. M. Reilly, J. U. Reveles, G. E. Johnson, S. N. Khanna, and A. W. Castleman, *J. Phys. Chem. A* **111**, 4158 (2007).

[381]W. Xue, Z.-C. Wang, S.-G. He, Y. Xie, and E. R. Bernstein, *J. Am. Chem. Soc.* **130**, 15879 (2008).

[382]J. U. Reveles, G. E. Johnson, S. N. Khanna, and A. W. Castleman, J. Phys. Chem. C **114**, 5438 (2010).

[383]H. Wu, S. R. Desai, and L.-S. Wang, *J. Am. Chem. Soc.* **118**, 5296 (1996).

[384]G. V. Chertihin, W. Saffel, J. T. Yustein, L. Andrews, M. Neurock, A. Ricca, and C. W. Bauschlicher, *J. Phys. Chem.* **100**, 5261 (1996).

[385]N. O. Jones, B. V. Reddy, F. Rasouli, and S. N. Khanna, *Phys. Rev. B* **72**, 165411 (2005).

[386]S. L'opez, A. H. Romero, J. Mej'ia-L'opez, J. Mazo-Zuluaga, and J. Restrepo, *Phys. Rev. B* **80**, 085107 (2009).

[387]X.-L. Ding, W. Xue, Y.-P. Ma, Z.-C. Wang, and S.-G. He, *J. Chem. Phys.* **130**, 014303 (2009).

[388]B. F. Xu, C. L. Yang, M. S. Wang, and X. G. Ma, *Mol. Phys.* **109**, 1889 (2011).

[389]P. C. Engelking and W. C. Lineberger, *J. Chem. Phys.* **66**, 5054 (1977).

[390]A. S. C. Cheung, R. M. Gordon, and A. J. Merer, *J. Mol. Spectrosc.* **87**, 289 (1981).

[391]A. J. Merer, *Annu. Rev. Phys. Chem.* **40**, 407 (1989).

[392]Y. Gong, M. Zhou, and L. Andrews, *Chem. Rev.* **109**, 6765 (2009).

[393]L. S. Wang, J. W. Fan, and L. Lou, *Surf. Rev. Lett.* **3**, 695 (1996).

[394]G. L. Gutsev, C. W. Bauschlicher, H. J. Zhai, and L. S. Wang, *J. Chem. Phys.* **119**, 11135 (2003).

[395]D. M. Cox, D. J. Trevor, R. L. Whetten, E. A. Rohlfing, and A. Kaldor, *Phys. Rev. B* **32**, 7290 (1985).

[396]G. L. Gutsev and C. W. Bauschlicher, *J. Phys. Chem. A* **107**, 7013 (2003).

[397]H. Shiroishi, T. Oda, I. Hamada, and N. Fujima, *Eur. Phys. J. D* **24**, 85 (2003).

[398]H. Shiroishi, T. Oda, I. Hamada, and N. Fujima, *Polyhedron* **24**, 16 (2005).

[399]C. J. Cramer and D. G. Truhlar, Phys. Chem. Chem. Phys. **11**, 10757 (2009).

[400]A. J. Wachters, *J. Chem. Phys.* **52**, 1033 (1970).

[401]P. J. Hay, *J. Chem. Phys.* **66**, 4377 (1977).

[402]M. J. Frisch, G. W. Trucks, H. B. Schlegel, G. E. Scuseria, M. A. Robb, J. R. Cheeseman, G. Scalmani, V. Barone, B. Mennucci, G. A. Petersson, H. Nakatsuji, M. Caricato, X. Li, H. P. Hratchian, A. F. Izmaylov, J. Bloino, G. Zheng, J. L. Sonnenberg, M. Hada, M. Ehara, K. Toyota, R. Fukuda, J. Hasegawa, M. Ishida, T. Nakajima, Y. Honda, O. Kitao, H. Nakai, T. Vreven, J. A. Montgomery, J. E. Peralta, F. Ogliaro, M. Bearpark, J. J. Heyd, E. Brothers, K. N. Kudin, V. N. Staroverov, R. Kobayashi, J. Normand, K. Raghavachari, A. Rendell, J. C. Burant, S. S. Iyengar, J. Tomasi, M. Cossi, N. Rega, J. M. Millam, M. Klene, J. E. Knox, J. B. Cross, V. Bakken, C. Adamo, J. Jaramillo, R. Gomperts, R. E. Stratmann, O. Yazyev, A. J. Austin, R. Cammi, C. Pomelli, J. W. Ochterski, R. L. Martin, K. Morokuma, V. G. Zakrzewski, G. A. Voth, P. Salvador, J. J. Dannenberg, S. Dapprich, A. D. Daniels, Ö. Farkas, J. B. Foresman, J. V. Ortiz, J. Cioslowski, and D. J. Fox, *Gaussian 09, Revision C.01*, `http://www.gaussian.com`.

[403]K. M. Ervin, *PESCAL*, `http://wolfweb.unr.edu/~ervin/pes`.

[404]A. Fujishima and K. Honda, *Nature* **238**, 37 (1972).

[405]F. E. Osterloh, *Chem. Mater.* **20**, 35 (2008).

[406]Á. Valdés, Z.-W. Qu, G.-J. Kroes, J. Rossmeisl, and J. K. Nørskov, *J. Phys. Chem. C* **112**, 9872 (2008).

[407]M. Grätzel, *Nature* **414**, 338 (2001).

[408]A. J. Frank, N. Kopidakis, and J. van de Lagemaat, *Coordin. Chem. Rev.* **248**, 1165 (2004).

[409]M. R. Hoffmann, S. T. Martin, W. Choi, and D. W. Bahnemann, *Chem. Rev.* **95**, 69 (1995).

[410]D. Bahnemann, *Sol. Energy* **77**, 445 (2004).

[411]H. He, P. Zapol, and L. A. Curtiss, *J. Phys. Chem. C* **114**, 21474 (2010).

[412]S. N. Habisreutinger, L. Schmidt-Mende, and J. K. Stolarczyk, *Angew. Chem. Int. Ed.* **52**, 7372 (2013).

[413]H. Zhang and J. F. Banfield, *J. Mater. Chem.* **8**, 2073 (1998).

[414]A. Bendavid, P. J. Martin, Å. Jamting, and H. Takikawa, *Thin Solid Films* **355**, 6 (1999).

[415]T. Tachikawa, M. Fujitsuka, and T. Majima, *J. Phys. Chem. C* **111**, 5259 (2007).

[416]S. A. Shevlin and S. M. Woodley, *J. Phys. Chem. C* **114**, 17333 (2010).

[417]S. Li and D. A. Dixon, *J. Phys. Chem. A* **112**, 6646 (2008).

[418]Z. R. R. Tian, J. A. Voigt, J. Liu, B. McKenzie, and H. Xu, *J. Am. Chem. Soc.* **125**, 12384 (2003).

[419]C. Ducati, E. Barborini, G. Bongiorno, S. Vinati, P. Milani, and P. A. Midgley, *Appl. Phys. Lett.* **87**, 201906 (2005).

[420]M. G. Manera, P. D. Cozzoli, M. L. Curri, G. Leo, R. Rella, A. Agostiano, and L. Vasanelli, *Synthetic Met.* **148**, 25 (2005).

[421]G. K. Mor, K. Shankar, M. Paulose, O. K. Varghese, and C. A. Grimes, *Nano Lett.* **6**, 215 (2006).

[422]J. H. Park, S. Kim, and A. J. Bard, *Nano Lett.* **6**, 24 (2006).

[423]B. Liu and E. S. Aydil, *J. Am. Chem. Soc.* **131**, 3985 (2009).

[424]J. Sauer and H. J. Freund, *Catal. Lett.* **145**, 109 (2015).

[425]Y. Matsuda and E. R. Bernstein, *J. Phys. Chem. A* **109**, 314 (2005).

[426]K. Demyk, D. van Heijnsbergen, G. von Helden, and G. Meijer, *Astron. Astrophys.* **420**, 547 (2004).

[427]E. Janssens, G. Santambrogio, M. Brümmer, L. Wöste, P. Lievens, J. Sauer, G. Meijer, and K. R. Asmis, *Phys. Rev. Lett.* **96**, 233401 (2006).

[428]B. Helmich, M. Sierka, J. Dobler, and J. Sauer, *Phys. Chem. Chem. Phys.* **16**, 8441 (2014).

[429]H. Wu and L.-S. Wang, *J. Chem. Phys.* **107**, 8221 (1997).

[430]G. V. Chertihin and L. Andrews, *J. Am. Chem. Soc.* **117**, 1595 (1995).

[431]K. M. Perera and R. B. Metz, *J. Phys. Chem. A* **113**, 6253 (2009).

[432]E. C. Tyo, R. M. M. Nőßler, V. Bonačić-Koutecký, and A. W. Castleman, *Phys. Chem. Chem. Phys.* **13**, 4243 (2011).

[433]J. Zhuang, Z. H. Li, K. Fan, and M. Zhou, *J. Phys. Chem. A* **116**, 3388 (2012).

[434]S. Yin and E. R. Bernstein, *Phys. Chem. Chem. Phys.* **16**, 13900 (2014).

[435]G. V. Chertihin and L. Andrews, *J. Phys. Chem.* **99**, 6356 (1995).

[436]S. Brünken, H. S. P. Mller, K. M. Menten, M. C. McCarthy, and P. Thaddeus, *Astrophys. J.* **676**, 1367 (2008).

[437]X. J. Zhuang, A. Le, T. C. Steimle, R. Nagarajan, V. Gupta, and J. P. Maier, *Phys. Chem. Chem. Phys.* **12**, 15018 (2010).

[438]Y. Gong, Q. Zhang, and M. Zhou, *J. Phys. Chem. A* **111**, 3534 (2007).

[439]T. Albaret, F. Finocchi, and C. Noguera, *J. Chem. Phys.* **113**, 2238 (2000).

[440]S. Hamad, C. R. A. Catlow, S. M. Woodley, S. Lago, and J. A. Mejías, *J. Phys. Chem. B* **109**, 15741 (2005).

[441]Z. W. Qu and G. J. Kroes, *J. Phys. Chem. B* **110**, 8998 (2006).

[442]S. M. Woodley, S. Hamad, J. A. Mejías, and C. R. A. Catlow, *J. Mater. Chem.* **16**, 1927 (2006).

[443]M. Calatayud, L. Maldonado, and C. Minot, *J. Phys. Chem. C* **112**, 16087 (2008).

[444]M.-H. Weng, C. Chen, and S.-P. Ju, *Chinese J. Catal.* **30**, 384 (2009).

[445]I. Bandyopadhyay and C. M. Aikens, *J. Phys. Chem. A* **115**, 868 (2011).

[446]O. A. Syzgantseva, P. Gonzalez-Navarrete, M. Calatayud, S. Bromley, and C. Minot, *J. Phys. Chem. C* **115**, 15890 (2011).

[447]W. Zhang, Y. Han, S. Yao, and H. Sun, *Mater. Chem. Phys.* **130**, 196 (2011).

[448]L. L. Tang, L. W. Sai, J. J. Zhao, and R. F. Qiu, *J. Comput. Chem.* **33**, 163 (2012).

[449]N. Marom, M. Kim, and J. R. Chelikowsky, *Phys. Rev. Lett.* **108**, 106801 (2012).

[450]M. Y. Chen and D. A. Dixon, *J. Chem. Theory Comput.* **9**, 3189 (2013).

[451]S. G. Neogi and P. Chaudhury, *J. Comput. Chem.* **35**, 51 (2014).

[452]S. G. Li and D. A. Dixon, *J. Phys. Chem. A* **114**, 2665 (2010).

[453]K. R. Asmis, M. Brümmer, C. Kaposta, G. Santambrogio, G. von Helden, G. Meijer, K. Rademann, and L. Wöste, *Phys. Chem. Chem. Phys.* **4**, 1101 (2002).

[454]K. R. Asmis and J. Sauer, *Mass. Spectrom. Rev.* **26**, 542 (2007).

[455]S. G. Li and D. A. Dixon, *J. Phys. Chem. A* **111**, 11908 (2007).

[456]S. Grimme, *J. Comp. Chem.* **27**, 1787 (2006).

[457]E. P. Meagher and G. A. Lager, *Can. Mineral.* **17**, 77 (1979).

[458]M. Horn, C. F. Schwerdtfeger, and E. P. Meagher, *Kristallogr.* **136**, 273 (1972).

[459]T. L. Thompson and J. T. Yates, *Chem. Rev.* **106**, 4428 (2006).

[460]W. S. Epling, C. H. F. Peden, M. A. Henderson, and U. Diebold, *Surf. Sci.* **412**, 333 (1998).

[461]G. Lu, A. Linsebigler, and J. T. Yates, *J. Phys. Chem.* **98**, 11733 (1994).

[462]X. Chen and S. S. Mao, *Chem. Rev.* **107**, 2891 (2007).

[463]S. Sato and J. M. White, *J. Am. Chem. Soc.* **102**, 7206 (1980).

[464]M. A. Henderson, *Surf. Sci. Rep.* **66**, 185 (2011).

[465]B. O'Regan and M. Gratzel, *Nature* **353**, 737 (1991).

[466]K. Hashimoto, H. Irie, and A. Fujishima, *Jpn. J. Appl. Phys.* **44**, 8269 (2005).

[467]M. Anpo, S. Dohshi, M. Kitano, Y. Hu, M. Takeuchi, and M. Matsuoka, *Annu. Rev. Mater. Res.* **35**, 1 (2005).

[468]J. Schneider, M. Matsuoka, M. Takeuchi, J. Zhang, Y. Horiuchi, M. Anpo, and D. W. Bahnemann, *Chem. Rev.* **114**, 9919 (2014).

[469]M. Ni, M. K. H. Leung, D. Y. C. Leung, and K. Sumathy, *Renew. Sust. Energy Rev.* **11**, 401 (2007).

[470]M. L. Weichman, X. Song, M. R. Fagiani, S. Debnath, S. Gewinner, W. Schöllkopf, D. M. Neumark, and K. R. Asmis, *J. Chem. Phys.* **144**, 124308 (2016).

[471]C. H. Sun, L. M. Liu, A. Selloni, G. Q. Lu, and S. C. Smith, *J. Mater. Chem.* **20**, 10319 (2010).

[472]R. Mu, Z. j. Zhao, Z. Dohnálek, and J. Gong, *Chem. Soc. Rev.* **46**, 1785 (2017).

[473]V. E. Henrich, G. Dresselhaus, and H. J. Zeiger, *Solid State Commun.* **24**, 623 (1977).

[474]R. L. Kurtz, R. Stockbauer, T. E. Madey, E. Roman, and J. L. Desegovia, *Surf. Sci.* **218**, 178 (1989).

[475]M. B. Hugenschmidt, L. Gamble, and C. T. Campbell, *Surf. Sci.* **302**, 329 (1994).

[476]M. A. Henderson, *Surf. Sci.* **355**, 151 (1996).

[477]D. Brinkley, M. Dietrich, T. Engel, P. Farrall, G. Gantner, A. Schafer, and A. Szuchmacher, *Surf. Sci.* **395**, 292 (1998).

[478]L.-Q. Wang, K. F. Ferris, P. X. Skiba, A. N. Shultz, D. R. Baer, and M. H. Engelhard, *Surf. Sci.* **440**, 60 (1999).

[479]R. Schaub, P. Thostrup, N. Lopez, E. Lgsgaard, I. Stensgaard, J. K. Nrskov, and F. Besenbacher, *Phys. Rev. Lett.* **87**, 266104 (2001).

[480]G. S. Herman, Z. Dohnlek, N. Ruzycki, and U. Diebold, *J. Phys. Chem. B* **107**, 2788 (2003).

[481]S. Wendt, R. Schaub, J. Matthiesen, E. K. Vestergaard, E. Wahlstrm, M. D. Rasmussen, P. Thostrup, L. M. Molina, E. Lgsgaard, I. Stensgaard, B. Hammer, and F. Besenbacher, *Surf. Sci.* **598**, 226 (2005).

[482]M. Takeuchi, G. Martra, S. Coluccia, and M. Anpo, *J. Phys. Chem. B* **109**, 7387 (2005).

[483]O. Bikondoa, C. L. Pang, R. Ithnin, C. A. Muryn, H. Onishi, and G. Thornton, *Nat. Mater.* **5**, 189 (2006).

[484]Z. Zhang, O. Bondarchuk, B. D. Kay, J. M. White, and Z. Dohnálek, *J. Phys. Chem. B* **110**, 21840 (2006).

[485]L. E. Walle, A. Borg, E. M. J. Johansson, S. Plogmaker, H. Rensmo, P. Uvdal, and A. Sandell, *J. Phys. Chem. C* **115**, 9545 (2011).

[486]H. H. Kristoffersen, J. Ø. Hansen, U. Martinez, Y. Y. Wei, J. Matthiesen, R. Streber, R. Bechstein, E. Lægsgaard, F. Besenbacher, B. Hammer, and S. Wendt, *Phys. Rev. Lett.* **110**, 146101 (2013).

[487]Z. Geng, X. Chen, W. Yang, Q. Guo, C. Xu, D. Dai, and X. Yang, *J. Phys. Chem. C* **120**, 26807 (2016).

[488]S. Tan, H. Feng, Y. Ji, Y. Wang, J. Zhao, A. Zhao, B. Wang, Y. Luo, J. Yang, and J. G. Hou, *J. Am. Chem. Soc.* **134**, 9978 (2012).

[489]T. Zheng, C. Wu, M. Chen, Y. Zhang, and P. T. Cummings, *J. Chem. Phys.* **145**, 044702 (2016).

[490]M. Posternak, A. Baldereschi, and B. Delley, *J. Phys. Chem. C* **113**, 15862 (2009).

[491]H. Shi, Y.-C. Liu, Z.-J. Zhao, M. Miao, T. Wu, and Q. Wang, *J. Phys. Chem. C* **118**, 20257 (2014).

[492]A. W. Castleman, *Catal. Lett.* **141**, 1243 (2011).

[493]M. Schlangen and H. Schwarz, *Catal. Lett.* **142**, 1265 (2012).

[494]S. Yin and E. R. Bernstein, *Int. J. Mass Spectrom.* **321**, 49 (2012).

[495]H.-J. Zhai and L.-S. Wang, *Chem. Phys. Lett.* **500**, 185 (2010).

[496]H. Deng, K. P. Kerns, B. Guo, R. C. Bell, and A. W. Castleman, *Croat. Chem. Acta* **71**, 1105 (1998).

[497]H.-G. Xu, X.-N. Li, X.-Y. Kong, S.-G. He, and W.-J. Zheng, *Phys. Chem. Chem. Phys.* **15**, 17126 (2013).

[498]R.-Z. Li, H.-G. Xu, G.-J. Cao, X.-L. Xu, and W.-J. Zheng, *J. Chem. Phys.* **139**, 184303 (2013).

[499]P. C. Redfern, P. Zapol, L. A. Curtiss, T. Rajh, and M. C. Thurnauer, *J. Phys. Chem. B* **107**, 11419 (2003).

[500]T. Tsuchiya and J. L. Whitten, *J. Phys. Chem. C* **115**, 1635 (2011).

[501]L. B. Pandey and C. M. Aikens, *J. Phys. Chem. A* **116**, 526 (2012).

[502]D. Çakir and O. Gülseren, *J. Phys.: Condens. Matter* **24**, 305301 (2012).

[503]H. Du, A. D. Sarkar, H. Li, Q. Sun, Y. Jia, and R.-Q. Zhang, *J. Mol. Catal. A: Chem.* **366**, 163 (2013).

[504]E. Berardo, H.-S. Hu, S. A. Shevlin, S. M. Woodley, K. Kowalski, and M. A. Zwijnenburg, *J. Chem. Theory Comput.* **10**, 1189 (2014).

[505]F. Rodríguez-Hernández, D. C. Tranca, B. M. Szyja, R. A. van Santen, A. Martínez-Mesa, L. Uranga-Piña, and G. Seifert, *J. Phys. Chem. C* **120**, 437 (2016).

[506]M. Muuronen, S. M. Parker, E. Berardo, A. Le, M. A. Zwijnenburg, and F. Furche, *Chem. Sci.* **8**, 2179 (2017).

[507]A. Valdés and G.-J. Kroes, *J. Phys. Chem. C* **114**, 1701 (2010).

[508]Y.-F. Li and Z.-P. Liu, *J. Am. Chem. Soc.* **133**, 15743 (2011).

[509]Q. q. Meng, J. g. Wang, Q. Xie, H. q. Dong, and X. n. Li, *Catal. Today* **165**, 145 (2011).

[510]E. Berardo and M. A. Zwijnenburg, *J. Phys. Chem. C* **119**, 13384 (2015).

[511]T.-H. Wang, Z. Fang, N. W. Gist, S. Li, D. A. Dixon, and J. L. Gole, *J. Phys. Chem. C* **115**, 9344 (2011).

[512]Z. Fang and D. A. Dixon, *J. Phys. Chem. A* **117**, 3539 (2013).

[513]M. Chen, T. P. Straatsma, and D. A. Dixon, *J. Phys. Chem. A* **119**, 11406 (2015).

[514]J. D. Chai and M. Head-Gordon, *Phys. Chem. Chem. Phys.* **10**, 6615 (2008).

[515]Y. Minenkov, A. Singstad, G. Occhipinti, and V. R. Jensen, *Dalton Trans.* **41**, 5526 (2012).

[516]I. M. Alecu, J. Zheng, Y. Zhao, and D. G. Truhlar, *J. Chem. Theory Comput.* **6**, 2872 (2010).

[517]K. K. Irikura, *J. Phys. Chem. Ref. Data* **36**, 389 (2007).

[518]Y. Suda and T. Morimoto, *Langmuir* **3**, 786 (1987).

[519]S. H. Szczepankiewicz, A. J. Colussi, and M. R. Hoffmann, *J. Phys. Chem. B* **104**, 9842 (2000).

[520]K. S. Finnie, D. J. Cassidy, J. R. Bartlett, and J. L. Woolfrey, *Langmuir* **17**, 816 (2001).

[521]A. Yamakata, T. Ishibashi, and H. Onishi, *Bull. Chem. Soc. Jpn.* **75**, 1019 (2002).

[522]C. y. Wang, H. Groenzin, and M. J. Shultz, *Langmuir* **19**, 7330 (2003).

[523]R. Nakamura and Y. Nakato, *J. Am. Chem. Soc.* **126**, 1290 (2004).

[524]M. R. Fagiani, H. Knorke, T. K. Esser, N. Heine, C. T. Wolke, S. Gewinner, W. Schöllkopf, M.-P. Gaigeot, R. Spezia, M. A. Johnson, and K. R. Asmis, *Phys. Chem. Chem. Phys.* **18**, 26743 (2016).

[525]D. E. Manolopoulos, *J. Chem. Soc. Faraday Trans.* **93**, 673 (1997).

[526]G. C. Schatz, *Science* **288**, 1599 (2000).

[527]F. Fernández-Alonso and R. N. Zare, *Annu. Rev. Phys. Chem.* **53**, 67 (2002).

[528]D. H. Z. X. Yang, *Acc. Chem. Res.* **41**, 981 (2008).

[529]R. T. Skodje, *Adv. Quantum Chem.* **63**, 119 (2012).

[530]K. Liu, *Adv. Chem. Phys.* **149**, 1 (2012).

[531]R. T. Skodje, D. Skouteris, D. E. Manolopoulos, S. H. Lee, F. Dong, and K. Liu, *Phys. Rev. Lett.* **85**, 1206 (2000).

[532]W. Dong, C. Xiao, T. Wang, D. Dai, X. Yang, and D. H. Zhang, *Science* **327**, 1501 (2010).

[533]T. Wang, T. Yang, C. Xiao, Z. Sun, L. H. D. Dai, X. Yang, and D. H. Zhang, *J. Phys. Chem. Lett.* **5**, 3049 (2014).

[534]M. Qiu, Z. Ren, L. Che, D. Dai, S. A. Harich, X. Wan, X. Yang, C. Xu, D. Xie, M. Gustafsson, R. T. Skodje, Z. Sun, and D. H. Zhang, *Science* **311**, 1440 (2006).

[535]J. Z. H. Zhang and W. H. Miller, *J. Chem. Phys.* **92**, 1811 (1990).

[536]S. E. Bradforth, D. W. Arnold, D. M. Neumark, and D. E. Manolopoulos, *J. Chem. Phys.* **99**, 6345 (1993).

[537]S. L. Holmgren, M. Waldman, and W. Klemperer, *J. Chem. Phys.* **67**, 4414 (1977).

[538]M. H. Alexander, S. Gregurick, and P. J. Dagdigian, *J. Chem. Phys.* **101**, 2887 (1994).

[539]J. F. Castillo, D. E. Manolopoulos, K. Stark, and H.-J. Werner, *J. Chem. Phys* **104**, 6531 (1996).

[540]D. E. Manolopoulos, *Nature* **419**, 266 (2002).

[541]B. Fu, X. Xu, and D. H. Zhang, *J. Chem. Phys.* **129**, 011103 (2008).

[542]I. V. Koptyug, K. V. Kovtunov, S. R. Burt, M. S. Anwar, C. Hilty, S. I. Han, A. Pines, and R. Z. Sagdeev, *J. Am. Chem. Soc.* **129**, 5580 (2007).

[543]T. A. Grinev, A. A. Buchachenko, and R. V. Krems, *ChemPhysChem* **8**, 815 (2007).

[544]A. Weaver and D. M. Neumark, *Faraday Discuss.* **91**, 5 (1991).

[545]C. Bartels, C. Hock, J. Huwer, R. Kuhnen, J. Schwöbel, and B. von Issendorff, *Science* **323**, 1323 (2009).

[546]M. D. Feit and J. A. Fleck, *J. Chem. Phys.* **78**, 301 (1983).

[547]D. T. Colbert and W. H. Miller, *J. Chem. Phys.* **96**, 1982 (1992).

[548]D. E. Manolopoulos, *J. Chem. Phys.* **117**, 9552 (2002).

[549]J. A. Nichols, R. A. Kendall, S. J. Cole, and J. Simons, *J. Phys. Chem.* **95**, 1074 (1991).

[550]T. B. Adler, G. Knizia, and H.-J. Werner, *J. Chem. Phys.* **127**, 221106 (2007).

[551]G. Knizia, T. B. Adler, and H.-J. Werner, *J. Chem. Phys.* **130**, 054104 (2009).

[552]T. H. Dunning, *J. Chem. Phys.* **90**, 1007 (1989).

[553]F. Weigend, *Phys. Chem. Chem. Phys.* **4**, 4285 (2002).

[554]F. Weigend, A. Kohn, and C. Hattig, *J. Chem. Phys.* **116**, 3175 (2002).

[555]H.-J. Werner, P. J. Knowles, G. Knizia, F. R. Manby, M. Schütz, P. Celani, T. Korona, R. Lindh, A. Mitrushenkov, G. Rauhut, K. R. Shamasundar, T. B. Adler, R. D. Amos, A. Bernhardsson, A. Berning, D. L. Cooper, M. J. O. Deegan, A. J. Dobbyn, F. Eckert, E. Goll, C. Hampel, A. Hesselmann, G. Hetzer, T. Hrenar, G. Jansen, Y. L. C. Köppl, A. W. Lloyd, R. A. Mata, A. J. May, S. J. McNicholas, W. Meyer, M. E. Mura, A. Nicklass, D. P. ONeill, P. Palmieri, D. Peng, K. Pflüger, R. Pitzer, M. Reiher, T. Shiozaki, H. Stoll, A. J. Stone, R. Tarroni, T. Thorsteinsson, and M. Wang, *MOLPRO, version 2012.1, a package of ab initio programs*, `http://www.molpro.net`.

[556]K. Stark, "Dynamik einer chemischen elementarreaktion auf einer neuen ab initio potential-energie-oberfläche: das system $F + H_2 \longrightarrow HF + H$", PhD thesis (Universität Stuttgart, 1996).

[557]B. Hartke and H.-J. Werner, *Chem. Phys. Lett.* **280**, 430 (1997).

[558]C. X. Xu, D. Q. Xie, and D. H. Zhang, *Chinese J. Chem. Phys.* **19**, 96 (2006).

[559]G. L. Li, H.-J. Werner, F. Lique, and M. H. Alexander, *J. Chem. Phys.* **127**, 174302 (2007).

[560]J. Chen, Z. G. Sun, and D. H. Zhang, *J. Chem. Phys.* **142**, 024303 (2015).

[561]H.-J. Werner, M. Kallay, and J. Gauss, *J. Chem. Phys.* **128**, 034305 (2008).

[562]S. A. Nizkorodov, W. W. Harper, and D. J. Nesbitt, *Faraday Disc.* **113**, 107 (1999).

[563]M. H. Alexander, D. E. Manolopoulos, and H.-J. Werner, *J. Chem. Phys.* **113**, 11084 (2000).

[564]E. Garand, J. Zhou, D. E. Manolopoulos, M. H. Alexander, and D. M. Neumark, *Science* **319**, 72 (2008).

[565]Z. G. Sun and D. H. Zhang, *Int. J. Quantum Chem.* **115**, 689 (2015).

[566]D. R. Herschbach, *Discuss. Faraday Soc.* **33**, 149 (1962).

[567]Y. T. Lee, J. D. McDonald, P. R. LeBreton, and D. R. Herschbach, *Rev. Sci. Instrum.* **40**, 1402 (1969).

[568]H. Eyring, *J. Chem. Phys.* **3**, 107 (1935).

[569]D. G. Truhlar, B. C. Garrett, and S. J. Klippenstein, *J. Phys. Chem.* **100**, 12771 (1996).

[570]H. Guo and K. Liu, *Chem. Sci.* **7**, 3992 (2016).

[571]R. N. Zare, *Science* **279**, 1875 (1998).

[572]T. Yang, J. Chen, L. Huang, T. Wang, C. Xiao, Z. Sun, D. Dai, X. Yang, and D. H. Zhang, *Science* **347**, 60 (2015).

[573]K. Liu, *Annu. Rev. Phys. Chem.* **67**, 91 (2016).

[574]J. B. Kim, M. L. Weichman, T. F. Sjolander, D. M. Neumark, J. Kłos, M. H. Alexander, and D. E. Manolopoulos, *Science* **349**, 510 (2015).

[575]J. A. DeVine, M. L. Weichman, X. Zhou, J. Ma, B. Jiang, H. Guo, and D. M. Neumark, *J. Am. Chem. Soc.* **138**, 16417 (2016).

[576]S. E. Bradforth, D. W. Arnold, R. B. Metz, A. Weaver, and D. M. Neumark, *J. Phys. Chem.* **95**, 8066 (1991).

[577]A. W. Ray, J. Agarwal, B. B. Shen, H. F. Schaefer, and R. E. Continetti, *Phys. Chem. Chem. Phys.* **18**, 30612 (2016).

[578]G. C. Schatz, J. M. Bowman, and A. Kuppermann, *J. Chem. Phys.* **63**, 674 (1975).

[579]R. E. Wyatt and M. J. Redmon, *Chem. Phys. Lett.* **96**, 284 (1983).

[580]R. N. Zare, *Science* **311**, 1383 (2006).

[581]Z. Ren, Z. Sun, D. Zhang, and X. Yang, *Rep. Prog. Phys.* **80**, 026401 (2017).

[582]R. Otto, J. Ma, A. W. Ray, J. S. Daluz, J. Li, H. Guo, and R. E. Continetti, *Science* **343**, 396 (2014).

[583]T. Westermann, J. B. Kim, M. L. Weichman, C. Hock, T. I. Yacovitch, J. Palma, D. M. Neumark, and U. Manthe, *Angew. Chem. Int. Ed.* **53**, 1122 (2014).

[584]*Active Thermochemical Tables (ATcT) values based on ver. 1.118 of the Thermochemical Network, October 2015, Editor: B. Ruscic*, `http://ATcT.anl.gov`.

[585]H. Feng, K. R. Randall, and H. F. Schaefer, *J. Phys. Chem. A* **119**, 1636 (2015).

[586]W. A. Glauser and M. L. Koszykowski, *J. Phys. Chem.* **95**, 10705 (1991).

[587]J. T. Jodkowski, M.-T. Rayez, J.-C. Rayez, T. Bérces, and S. Dóbé, *J. Phys. Chem. A* **102**, 9219 (1998).

[588]U. Meier, H. H. Grotheer, and T. Just, *Chem. Phys. Lett.* **106**, 97 (1984).

[589]M. A. Wickramaaratchi, D. W. Setser, H. Hildebrandt, B. Körbitzer, and H. Heydtmann, *Chem. Phys.* **94**, 109 (1985).

[590]T. Khatoon and K. Hoyermann, *Ber. Bunsen-Ges. Phys. Chem.* **92**, 669 (1988).

[591]J. L. Durant, *J. Phys. Chem.* **95**, 10701 (1991).

[592]S. Dóbé, T. Bérces, F. Temps, H. G. Wagner, and H. Ziemer, *25th Symp. Int. Combust. Proc.* **25**, 775 (1994).

[593]B. D. Wladkowski, A. L. L. East, J. E. Mihalick, W. D. Allen, and J. I. Brauman, *J. Chem. Phys.* **100**, 2058 (1994).

[594]L. Sun, K. Song, W. L. Hase, M. Sena, and J. M. Riveros, *Int. J. Mass Spectrom.* **227**, 315 (2003).

[595]J. M. Gonzales, C. Pak, R. S. Cox, W. D. Allen, H. F. Schaefer, A. G. Császár, and G. Tarczay, *Chem. Eur. J.* **9**, 2173 (2003).

[596]J. Ma and H. Guo, *J. Phys. Chem. Lett.* **6**, 4822 (2015).

[597]H. Guo, *J. Chem. Phys.* **108**, 2466 (1998).

[598]B. Jiang, J. Li, and H. Guo, *Int. Rev. Phys. Chem.* **35**, 479 (2016).

[599]J. Li, Y. Li, and H. Guo, *J. Chem. Phys.* **138**, 141102 (2013).

[600]J. Manz, R. Meyer, E. Pollak, and J. Romelt, *Chem. Phys. Lett.* **93**, 184 (1982).

[601]J. Manz, R. Meyer, and H. H. R. Schor, *J. Chem. Phys.* **80**, 1562 (1984).

[602]D. G. Fleming, J. Manz, K. Sato, and T. Takayanagi, *Angew. Chem. Int. Ed.* **53**, 13706 (2014).

[603]R. D. Levine and S. F. Wu, *Chem. Phys. Lett.* **11**, 557 (1971).

[604]B. Jiang and H. Guo, *J. Chem. Phys.* **139**, 054112 (2013).

[605]J. Li, B. Jiang, and H. Guo, *J. Chem. Phys.* **139**, 204103 (2013).

[606]B. J. Braams and J. M. Bowman, *Int. Rev. Phys. Chem.* **28**, 577 (2009).

[607]L. M. Raff, R. Komanduri, M. Hagan, and S. T. S. Bukkapatnam, *Neural Networks in Chemical Reaction Dynamics* (Oxford University Press, Oxford, 2012).

[608]J. Li, R. Dawes, and H. Guo, *J. Chem. Phys.* **137**, 094304 (2012).

[609]J. Li, B. Jiang, and H. Guo, *J. Chem. Phys.* **138**, 074309 (2013).

[610]J. C. Light and T. Carrington, *Adv. Chem. Phys.* **114**, 263 (2000).

[611]R. Chen and H. Guo, *J. Chem. Phys.* **105**, 3569 (1996).

[612] *NIST Computational Chemistry Comparison and Benchmark Database, NIST Standard Reference Database Number 101, Release 18, October 2016, Editor: R. D. Johnson*, `http://cccbdb.nist.gov`.

Index of Abbreviations Used

ASE	Amplified spontaneous emission
BBO	Barium borate
COM	Center of mass
cw	continuous wave
DBS	Dipole-bound state
DC	Direct current
DFG	Difference frequency generation
DFT	Density functional theory
DIB	Diffuse interstellar band
EA	Electron affinity
eBE	Electron binding energy
eKE	Electron kinetic energy
EL	Even-Lavie
ESI	Electrospray ionization
FC	Franck-Condon
FEL	Free electron laser
fwhm	full-width at half maximum
HOMO	Highest-occupied molecular orbital
HT	Herzberg-Teller
IR	Infrared
ISM	Interstellar medium
IRMPD	Infrared multiple-photon photodissociation
IRPD	Infrared photodissociation
JT	Jahn-Teller
LUMO	Lowest-occupied molecular orbital
MCP	Microchannel plate
MEVELER	Maximum-entropy velocity Legendre reconstruction
MO	Molecular orbital
MOM	Maximum overlap method
MS	Mass spectrometer

PAD	Photoelectron angular distribution
PAH	Polycyclic aromatic hydrocarbon
PC	Product complex
PES	Photoelectron spectroscopy *or* Potential energy surface
PIP-NN	Permutation invariant polynomial-neural network
QMF	Quadrupole mass filter
RC	Reactant complex
RF	Radio frequency
RT	Renner-Teller
SEVI	Slow photoelectron velocity-map imaging
SO	Spin-orbit
TDDFT	Time-dependent density functional theory
TE	Term energy
TMS	Trimethylsilyl
TOFMS	Time-of-flight mass spectrometer
TS	Transition state
UV	Ultraviolet
VAP	Vibrational adiabatic potential
VMI	Velocity-map imaging
ZEKE	Zero electron kinetic energy
ZPE	Zero-point energy

Publications from Graduate Work

1. J. A. DeVine*, **Marissa L. Weichman***, B. Laws, M. C. Babin, G. Balerdi, S. T. Gibson, R. W. Field, J. Ma, H. Guo, and D. M. Neumark. Signatures of isomerization in the vinylidene photoelectron spectrum (in preparation, **equal authorship*)

2. **M. L. Weichman** and D. M. Neumark. Slow photoelectron velocity-map imaging of cryo-cooled anions: New developments and applications. *Annu. Rev. Phys. Chem.* (in preparation).

3. **M. L. Weichman**, S. Debnath, J. T. Kelly, S. Gewinner, W. Schöllkopf, D. M. Neumark, and K. R. Asmis. Vibrational action spectroscopy of dissociative water adsorption on gas-phase titanium dioxide cluster anions. *Top. Catal.* (in preparation).

4. **M. L. Weichman**, L. Cheng, J. B. Kim, J. F. Stanton, and D. M. Neumark. Low-lying vibronic level structure of the ground state of the methoxy radical: Slow-electron velocity map imaging (SEVI) spectra and Köppel-Domcke-Cederbaum (KDC) vibronic Hamiltonian calculations. *J. Chem. Phys.* (under review).

5. **M. L. Weichman**, J. A. DeVine, M. C. Babin, J. Li, J. Ma, H. Guo, and D. M. Neumark. Feshbach resonances in the exit channel of the $F + CH_3OH \rightarrow HF + CH_3O$ reaction via transition state spectroscopy. *Nat. Chem.* (under review).

6. J. A. DeVine, **M. L. Weichman**, M. C. Babin, and D. M. Neumark. Slow photoelectron velocity-map imaging of cold *tert*-butyl peroxide. *J. Chem. Phys.* **147**, 013915 (2017).

7. J. A. DeVine, **M. L. Weichman**, S. J. Lyle, and D. M. Neumark. High-Resolution photoelectron imaging of cryogenically cooled α-and β-furanyl anions. *J. Mol. Spectrosc.* **332**, 16 (2017).

8. J. A. DeVine, **M. L. Weichman**, J. Ma, B. Jiang, H. Guo, and D. M. Neumark. Non-adiabatic effects on excited singlet and triplet states of vinylidene observed with slow photoelectron velocity-map imaging. *J. Am. Chem. Soc.* **138**, 16417 (2016).

9. **M. L. Weichman**, J. A. DeVine, and D. M. Neumark. High-resolution photoelectron imaging of cryogenically cooled Fe_4O^- and Fe_5O^-. *J. Chem. Phys.* **145**, 054302 (2016).

10. **M. L. Weichman**, X. Song, M. R. Fagiani, S. Debnath, D. M. Neumark, and K. R. Asmis. Gas phase vibrational spectroscopy of cold $(TiO_2)_n^-$ (n=3-8) clusters. *J. Chem. Phys.* **144**, 124308 (2016).

11. **M. L. Weichman**, J. A. DeVine, D. S. Levine, J. B. Kim, and D. M. Neumark. Isomer-specific vibronic structure of the 9-, 1-, and 2-anthracenyl radicals via slow photoelectron velocity-map imaging. *Proc. Natl. Acad. Sci. USA* **113**, 1698 (2016).

12. J. B. Kim, **M. L. Weichman**, T. F. Sjolander, D. M. Neumark, J. Kłos, M. H. Alexander, and D. E. Manolopoulos. Spectroscopic observation of resonances in the $F + H_2$ reaction. *Science* **349**, 510 (2015).

13. **M. L. Weichman**, J. B. Kim, and D. M. Neumark. Slow photoelectron velocity-map imaging spectroscopy of the ortho-hydroxyphenoxide anion. *J. Phys. Chem. A* **119**, 6140 (2015).

14. J. B. Kim, **M. L. Weichman**, and D. M. Neumark. Low-lying states of FeO and FeO^- by slow photoelectron spectroscopy. *Mol. Phys.* **113**, 2105 (2015).

15. **M. L. Weichman**, J. B. Kim, J. A. DeVine, D. S. Levine, and D. M. Neumark. Vibrational and electronic structure of the α- and β-naphthyl radicals via slow photoelectron velocity-map imaging. *J. Am. Chem. Soc.* **137**, 1420 (2015).

16. J. B. Kim, **M. L. Weichman**, and D. M. Neumark. Assignment of electronic bands in the photoelectron spectrum of the VO_2^- anion. *J. Chem. Theory Comput.* **10**, 5235 (2014).

17. J. B. Kim, **M. L. Weichman**, and D. M. Neumark. Slow photoelectron velocity-map imaging spec- troscopy of the Fe_3O^- and Co_3O^- anions. *J. Chem. Phys.* **141**, 174307 (2014).

18. J. B. Kim, **M. L. Weichman**, and D. M. Neumark. Structural isomers of Ti_2O_4 and Zr_2O_4 anions identified by slow photoelectron velocity-map imaging spectroscopy. *J. Am. Chem. Soc.* **136**, 7159 (2014).

19. **M. L. Weichman**, J. B. Kim, and D. M. Neumark. Rovibronic structure in slow photoelectron velocity-map imaging spectroscopy of CH_2CN^- and CD_2CN^-. *J. Chem. Phys.* **140**, 104305 (2014).

20. J. B. Kim, **M. L. Weichman**, and D. M. Neumark. Vibronic structure of VO_2 probed by slow photoelectron velocity-map imaging spectroscopy. *J. Chem. Phys.* **140**, 034307 (2014).

21. T. Westermann, J. B. Kim, **M. L. Weichman**, C. Hock, T. I. Yacovitch, J. Palma, D. M. Neumark, and U. Manthe. Resonances in the entrance channel of the $F + CH_4 \longrightarrow HF + CH_3$ reaction. *Angew. Chem., Int. Ed.* **53**, 1122 (2014).

22. J. B. Kim, **M. L. Weichman**, and D. M. Neumark. High-resolution anion photoelectron spectra of TiO_2^-, ZrO_2^-, and HfO_2^- obtained by slow electron velocity-map imaging. *Phys. Chem. Chem. Phys.* **50**, 20973 (2013).

23. **M. L. Weichman**, J. B. Kim, and D. M. Neumark. Vibrational fine structure of C_5 via anion slow photoelectron velocity-map imaging. *J. Chem. Phys.* **139**, 144314 (2013).

24. J. B. Kim, **M. L. Weichman**, T. I. Yacovitch, C. Shih, and D. M. Neumark. Slow photoelectron velocity-map imaging spectroscopy of the C_9H_7 (indenyl) and $C_{13}H_9$ (fluorenyl) anions. *J. Chem. Phys.* **139**, 104301 (2013).

25. C. Hock, J. B. Kim, **M. L. Weichman**, T. I. Yacovitch, and D. M. Neumark. Slow photoelectron velocity-map imaging spectroscopy of cold negative ions. *J. Chem. Phys.* **137**, 244201 (2012).